Alcoholism link to faulty GABA clearance *pp. 1298 & 1321*

Overlap in neuropsychiatric genetics *p. 1313*

Testing General Relativity on galaxy scales *p. 1342*

Science

$15
22 JUNE 2018
sciencemag.org

AAAS

AZTEC HUMAN SACRIFICE

Skulls bear witness to large-scale ritual killing *p. 1288*

CONTENTS

1294
Monarchs in peril

22 JUNE 2018 • VOLUME 360 • ISSUE 6395

1288

NEWS

IN BRIEF

IN DEPTH

FEATURE

INSIGHTS

PERSPECTIVES

POLICY FORUM

BOOKS *ET AL.*

Published by AAAS

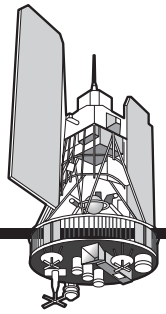

1303
Saving forests by satellites

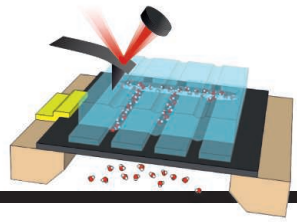

1302 & 1339
Water in a tight space

ON THE COVER

In the Aztec city of Tenochtitlan in the 16th century, the skulls of human sacrificial victims were slipped onto wooden posts and displayed on a monumental rack. Archaeologists at Mexico's National Institute of Anthropology and History discovered the remains of the rack and two accompanying skull towers during recent excavations in downtown Mexico City. See page 1288.
Photo: Henry Romero/REUTERS

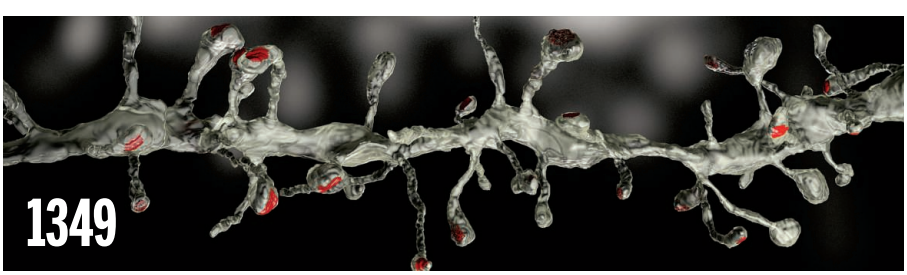

SCIENCE (ISSN 0036-8075) is published weekly on Friday, except last week in December, by the American Association for the Advancement of Science, 1200 New York Avenue, NW, Washington, DC 20005. Periodicals mail postage (publication No. 484460) paid at Washington, DC, and additional mailing offices. Domestic individual membership, including subscription (12 months): $165 ($74 allocated to subscription). Domestic institutional subscription (51 issues): $1808; Foreign postage extra: Mexico, Caribbean (surface mail) $55; other countries (air assist delivery): $89. First class, airmail, student, and emeritus rates on request. Canadian rates with GST available upon request, GST #125488122. Publications Mail Agreement Number 1069624. **Printed in the U.S.A.**
Change of address: Allow 4 weeks, giving old and new addresses and 8-digit account number. **Postmaster:** Send change of address to AAAS, P.O. Box 96178, Washington, DC 20090–6178. **Single-copy sales:** $15 each plus shipping and handling; bulk rate on request. **Authorization to reproduce** material for internal or personal use under circumstances not falling within the fair use provisions of the Copyright Act is granted by AAAS to libraries and others who use Copyright Clearance Center (CCC) Pay-Per-Use services provided that $35.00 per article is paid directly to CCC, 222 Rosewood Drive, Danvers, MA 01923. The identification code for *Science* is 0036-8075. *Science* is indexed in the *Reader's Guide to Periodical Literature* and in several specialized indexes.

CREDITS: (CLOCKWISE FROM TOP LEFT) GRAPHIC: ADAPTED BY KELLIE HOLOSKI/*SCIENCE*; KALININ *ET AL.*; S. EL-BOUSTANI *ET AL.*

Science
AAAS
1200 New York Avenue, NW, Washington, DC 20005
Clarendon House, Clarendon Road, Cambridge, UK CB2 8FH

EDITORIAL

Emerging stem cell ethics

It has been 20 years since the first derivation of human embryonic stem cells. That milestone marked the start of a scientific and public fascination with stem cells, not just for their biological properties but also for their potentially transformative medical uses. The next two decades of stem cell research animated an array of bioethical debates, from the destruction of embryos to derive stem cells to the creation of human-animal hybrids. Ethical tensions related to stem cell clinical translation and regulatory policy are now center stage and a topic of global discussion this week at the International Society for Stem Cell Research (ISSCR) annual meeting in Melbourne, Australia. Care must be taken to ensure that entry of stem cell–based products into the medical marketplace does not come at too high a human or monetary price.

Despite great strides in understanding stem cell biology, very few stem cell–based therapeutics are as yet used in standard clinical practice. Some countries have responded to patient demand and the imperatives of economic competition by promulgating policies to hasten market entry of stem cell–based treatments. Japan, for example, created a conditional approvals scheme for regenerative medicine products and has already put one stem cell treatment on the market based on preliminary evidence of efficacy. Italy provisionally approved a stem cell product under an existing European Union early access program. And last year, the United States introduced an expedited review program to smooth the path for investigational stem cell–based applications, at least 16 of which have been granted already. However, early and perhaps premature access to experimental interventions has uncertain consequences for patients and health systems.

A staggering amount of public money has been spent on stem cell research globally. Those seeking to develop stem cell products may now not only leverage that valuable body of resulting scientific knowledge but also find that their costs for clinical testing are markedly reduced by deregulation. How should this influence affordability and access? The state and the taxpaying public's interests should arguably be reflected in the pricing of stem cell products that were developed through publicly funded research and the regulatory subsidies. Detailed programs for recouping taxpayers' investments in stem cell research and development must be established.

Rushing new commercial stem cell products into the market also entails considerations inherent to the ethics of using pharmaceuticals and medical devices. For example, once a product is approved for a given indication, it becomes possible for physicians to prescribe it for "off-label use." We have already witnessed the untoward effects of the elevated expectations that stem cells can serve as a kind of cellular panacea, a misconception that underlies the direct-to-consumer marketing of unproven uses of stem cells. Once off-label use of approved products becomes an option, there may be a new flood of untested therapeutic claims with which to contend. The ISSCR and the United States Federation of State Medical Boards have both recently issued guidelines on clinical translation and use, but adoption and enforcement remain key issues.

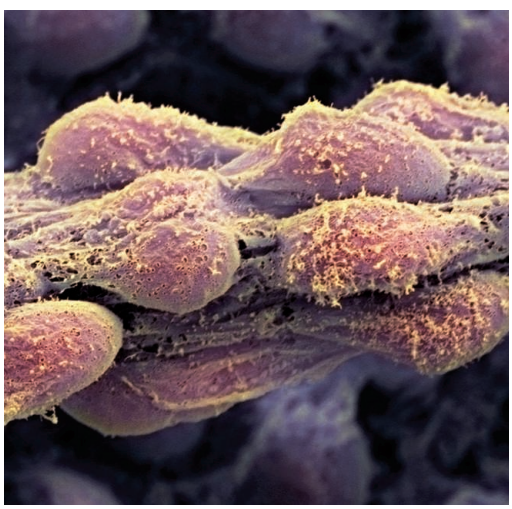

"...stem cell research animated an array of bioethical debates..."

The new frontiers of stem cell–based medicine also raise questions about the use of fast-tracked products. In countries where healthcare is not considered a public good, who should pay for post-market efficacy testing? Patients already bear a substantial burden of risk when they volunteer for experimental interventions. Frameworks that ask them to pay to participate in medical research warrant much closer scrutiny than has been seen thus far.

Striking the proper balance between streamlining review processes and ensuring that there is sufficient evidence before bringing products into clinical use is a perennial predicament for patients, payers, scientists, clinicians, and regulators. For stem cell treatments, attaining this balance will require frank and open discussion between all stakeholders, including the patients it seeks to benefit and the taxpayers who make it possible.

–Douglas Sipp, Megan Munsie, Jeremy Sugarman

Douglas Sipp
is a researcher at RIKEN and project professor at Keio University, Tokyo, Japan. sipp@cdb.riken.jp

Megan Munsie
is an associate professor in the School of Biomedical Sciences, University of Melbourne, Parkville, Australia. megan.munsie@unimelb.edu.au

Jeremy Sugarman
is a professor in the Berman Institute of Bioethics and the School of Medicine, Johns Hopkins University, Baltimore, MD, USA. jsugarman@jhu.edu

PHOTO: PROFESSOR MIODRAG STOJKOVIC/SCIENCE SOURCE

10.1126/science.aau4720

NEWS

> “There’s so much research on this that if people paid attention at all to the science, they would never do this.”
>
> **Charles Nelson**, a Harvard University pediatrics professor, in *The Washington Post*, on the “catastrophic” health effects of separating children from parents at the U.S. border.

IN BRIEF

Edited by **Jeffrey Brainard**

RESEARCH FUNDING

Europe plans big defense science boost

A Polish army PT-91 tank during North Atlantic Treaty Organization military drills in Latvia in 2017.

The European Commission in Brussels on 13 June proposed spending €13 billion on military R&D from 2021 to 2027, a move that would have been “unthinkable” in the recent past, Federica Mogherini, the commission’s foreign affairs and security chief, acknowledged. Almost all defense research in the European Union is now funded at the national level or through specific agreements between governments. The proposed European Defence Fund would include €4.1 billion for research—a 20-fold increase over an existing pilot fund—issued through competitively awarded grants for which companies, universities, and research institutes will be eligible to apply. To justify the new fund, commissioners cited terrorist attacks and Russia’s 2014 annexation of Crimea. “Both Europeans and our partners in the world expect the EU to be more and more a security provider, in our region and beyond,” Mogherini said. However, about 700 European researchers have signed a petition against any form of EU spending for military research.

New U.K. fund for innovation

ENTREPRENEURSHIP | The British Business Bank, a public company owned by the U.K. government, unveiled last week a £2.5 billion fund called British Patient Capital that will make long-term investments in technology companies and others with high potential for growth. In 2016, a government commission called for the fund, saying a lack of access to such financing was constraining development of these companies in the United Kingdom. The government will fund British Patient Capital over 10 years. An initial outlay of £400 million will significantly boost total equity investments in small- and medium-size businesses in the United Kingdom, which totaled about £3.6 billion in 2015. The new fund could offset moves by the European Union’s European Investment Fund (EIF), which cut its investments in the United Kingdom after the country triggered the Brexit process. Last year, EIF investments there fell by 91%, to £53 million.

Google starts AI center in Africa

RESEARCH FACILITIES | Google plans to open an artificial intelligence (AI) research center in Ghana’s capital, Accra, later this year, its first such laboratory in Africa. The tech giant’s AI division announced last week that it plans to collaborate with local researchers as well as policymakers on the potential uses of AI on the continent. Google did not provide numbers about the facility’s size. The company, which maintains AI research centers in Beijing, Paris, and other cities outside the United States, is raising its profile in Africa; earlier this year it launched a hub for startups in Lagos, Nigeria. In May, Facebook launched a similar hub in Lagos, its first in Africa.

Students report less sex, drugs

PUBLIC HEALTH | Fewer U.S. high school students report having sex and taking illicit drugs, but other risky activity remains alarmingly high, according to a biennial report released last week by the U.S. Centers for Disease Control and Prevention. Even as sexual activity declined, fewer

PHOTO: INTS KALNINS/REUTERS

Published by AAAS

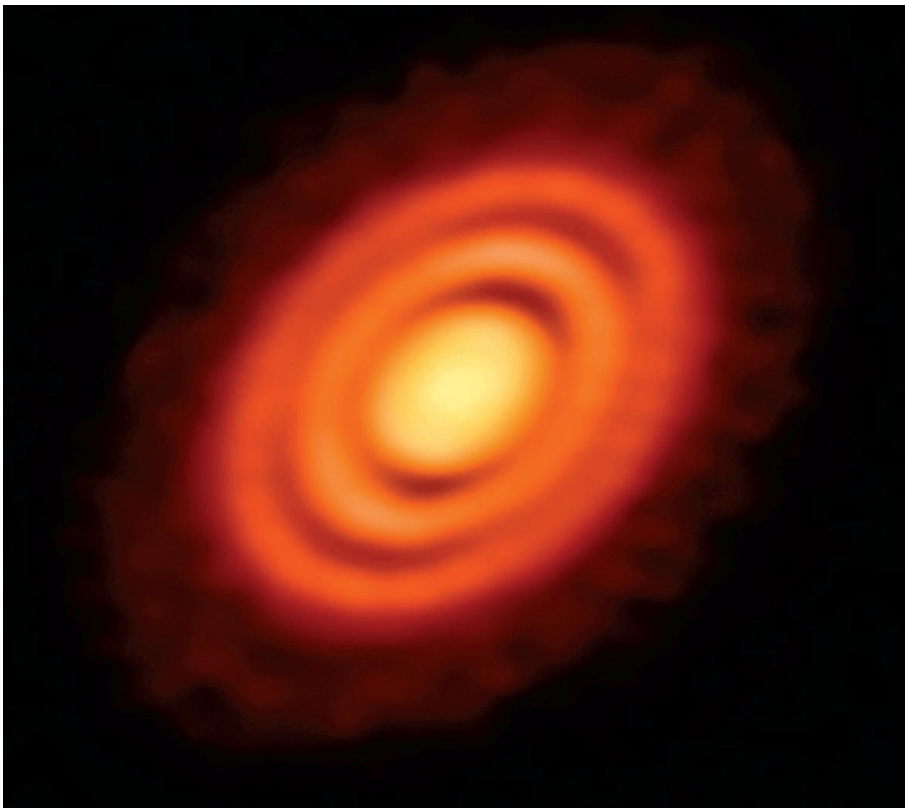

ASTRONOMY

New planets leave gas clues

Researchers using the Atacama Large Millimeter/submillimeter Array (ALMA) in Chile have detected three newborn planets by the way they disrupt gas swirling around a star just 4 million years old. They are the first exoplanets discovered by ALMA, an array of 66 radio dishes. ALMA has spotted concentric gaps in disks of dust and gas around young stars, but the array doesn't have the resolution to see the planets suspected to have swept the gaps clear. On 13 June in *The Astrophysical Journal Letters*, researchers report a new technique to show that newborn planets indeed orbit in the gaps. By looking for tiny Doppler shifts in the wavelengths of light emitted by carbon monoxide gas in the disk, the astronomers could detect the gravitational disturbance of the Jupiter-size planets as they swung past. The star, HD 163296, is 330 light-years from Earth.

reported using condoms during their most recent intercourse, increasing their risks of HIV and other sexually transmitted diseases. And nearly one in seven students reported misusing prescription opioids, for example by taking them without a prescription—a behavior that can lead to future injection drug use and risks of overdosing and contracting HIV. Gay, lesbian, and bisexual students reported experiencing significantly higher levels of violence in school, including bullying and sexual violence, and higher risks for suicide, depression, substance use, and poor academic performance than other students did. Nearly 15,000 students took the survey.

Health behaviors of U.S. high school students

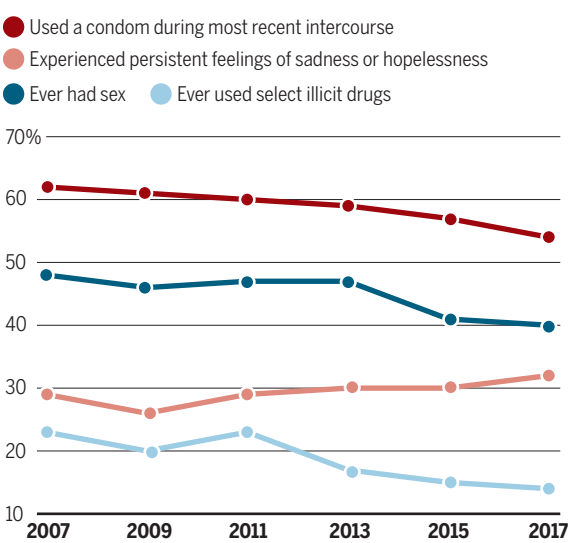

Co-authors group by gender

WORKPLACE | Researchers in the life sciences tend to prefer publishing with co-authors of the same gender, according to a preprint published on 14 June on bioRxiv. But, bucking the trend, papers in high-profile journals are more likely to be authored by members of both genders, supporting existing research showing that mixed-gender teams produce higher quality work. The new study also found that the tendency of authors to self-segregate by gender is stronger as the ratio of women to men among a journal's authors increases—a result that surprised the study's authors, who hypothesized that women might choose female co-authors most often when they are in the minority. The study's authors—Luke Holman of the University of Melbourne in Australia and Claire Morandin of the University of Helsinki—said they could not determine why authors tend to self-segregate by gender, but speculated that it might reflect men's bias against women or women's desire to avoid sexual harassment by men. However, female researchers, who are already behind men in average salaries and grants, may limit their networking opportunities if they co-publish mostly with women. The authors examined 36 million authors of 9 million papers published from 2002 to 2016 and indexed on PubMed.

Sea of Galilee to be refilled

CONSERVATION | Israel said on 10 June that it will begin pumping desalinated water into the Sea of Galilee starting next year to alleviate the effects of a 5-year drought. The shortage has brought the lake—and Israel's water table—to its lowest levels in a century. The 16,000-hectare lake, Israel's largest store of freshwater, is expected to develop high salinity and algal blooms if the water level falls much lower. In past decades, the country tapped the lake for drinking and agriculture, but it has reduced removals from about 400 million cubic meters a year to about 30 million to 40 million cubic meters. Israel already relies heavily on desalination to supply its cities and farms, and the government aims to double production to 1100 million cubic meters by 2030 with the help of two new desalination plants.

Researchers prepare for coastal surveys of seabird colonies in Cape Dorset in Canada.

Arctic research proves costly

RESEARCH FUNDING | The cost of studying seabirds in the Arctic is eight times greater than for similar studies at lower latitude sites, researchers reported in a 4 June article in *Arctic Science*. Funding is often insufficient to cover these costs, the authors note, limiting the ability of scientists to collect the data needed to understand how Arctic ecosystems are responding to climate change. Based on actual expeditions, the authors estimated the costs of typical Arctic field camps in Alaska, Canada, Greenland, and Norway. Travel accounted for nearly half the price tag. Other costs included conducting consultations in person with indigenous communities, which is sometimes required to receive a research permit.

Dark energy search delayed

ASTRONOMY | The launch of the European Space Agency's Euclid mission to study dark energy will be delayed by 2 years to 2022 because of problems with its infrared sensors, managers said last week. Euclid is likely to remain the first space telescope of its kind to launch, ahead of NASA's planned Wide Field Infrared Survey Telescope. By measuring the way gravity distorts the shapes of billions of galaxies, researchers hope to figure out how dark energy is accelerating the expansion of the universe. The infrared sensors, a NASA contribution to the mission, failed tests on arrival in Europe and must be remade. "Development of the new devices in NASA is proceeding very well," project manager Giuseppe Racca says.

THREE QS

A straight-talking U.S. science envoy

Epidemiologist Michael Osterholm of the University of Minnesota in Minneapolis speaks bluntly—which doesn't always sit well in government circles. Last week, he became one of five new U.S. Department of State science envoys. He'll address antibiotic resistance caused by overuse of the drugs in both animals and humans, and he'll focus on working with low- and middle-income countries, where resistance is growing fastest. This interview has been edited for clarity and length. (Read a longer version of this interview at https://scim.ag/QAOsterholm.)

Q: President Donald Trump's administration has been heavily criticized for not seeking the advice of the scientific community. Are you concerned?

A: I have not been a supporter of any administration for the last six administrations. What's important to me is the science. I'm just another tire on the vehicle trying to make things better for antibiotic resistance. It's a tough topic to get people to see as a priority.

Q: You're well known for always speaking your mind.

A: I will do that here. This is not a Democratic or Republican issue. Conservative or liberal, we're at risk, and it's growing dramatically with time. The only real enemies with regard to antibiotic resistance are the bugs themselves.

Q: Do you anticipate that you could be fired because of your views?

A: I don't. This is not a political position and doesn't require political sign off. I've been very impressed with the people I've worked with at [the Department of] State. When I went to work with the [George W.] Bush administration after 9/11 there were complicated issues, and I had an agreement with [Health and Human Services] Secretary Tommy Thompson that I'd say what was on my mind and if I couldn't, I'd leave. Let's hope I can accomplish things.

Budgets would boost NIH, NSF

RESEARCH FUNDING | Appropriations committees in the U.S. Congress last week approved healthy increases for several science agencies, providing much more than what President Donald Trump's administration requested for the 2019 fiscal year that starts in October. A House of Representatives subcommittee approved $38.3 billion for the National Institutes of Health, an increase of 3% over what Congress appropriated for this year. The Senate appropriations committee, meanwhile, allocated $6.4 billion for NASA's science division, a 3% rise. Like a bill approved earlier by the House appropriations committee, the Senate bill would restore the $10-million-a-year Carbon Monitoring System, a research program to study how sinks and sources of carbon can be remotely monitored from space, which the Trump administration quietly killed this year. The Senate spending bill would give the National Science Foundation $8.1 billion, a 4% increase. The two chambers ultimately must reconcile their spending bills.

#MeToo spurs firing, resignations

WORKPLACE | Thomas Brutnell, a leader in the field of photosynthesis and grass biology, was fired by the Donald Danforth Plant Science Center in St. Louis, Missouri, after a sexual misconduct investigation, President James Carrington announced on 14 June. Carrington said in a statement that the center had investigated a complaint of "inappropriate conduct and comments of a sexual nature." Brutnell declined comment through his lawyers in a statement citing "the privacy of all parties." In a separate development on 14 June, cognitive scientists Celeste Kidd and Steven Piantadosi resigned from the University of Rochester in New York, citing the institution's decision not to punish or fire T. Florian Jaeger, a linguist there who was accused of sexual harassment. The pair also said university administrators retaliated against them for joining others in making the allegations. The university in January accepted an external report concluding that Jaeger had not sexually harassed students or violated university policies (*Science*, 19 January, p. 262). He is set to return to the classroom this fall. Kidd and Piantadosi will take up tenure-track positions at the University of California, Berkeley.

SCIENCEMAG.ORG/NEWS
Read more news from *Science* online.

PHOTO: JENNIFER PROVENCHER

Published by AAAS

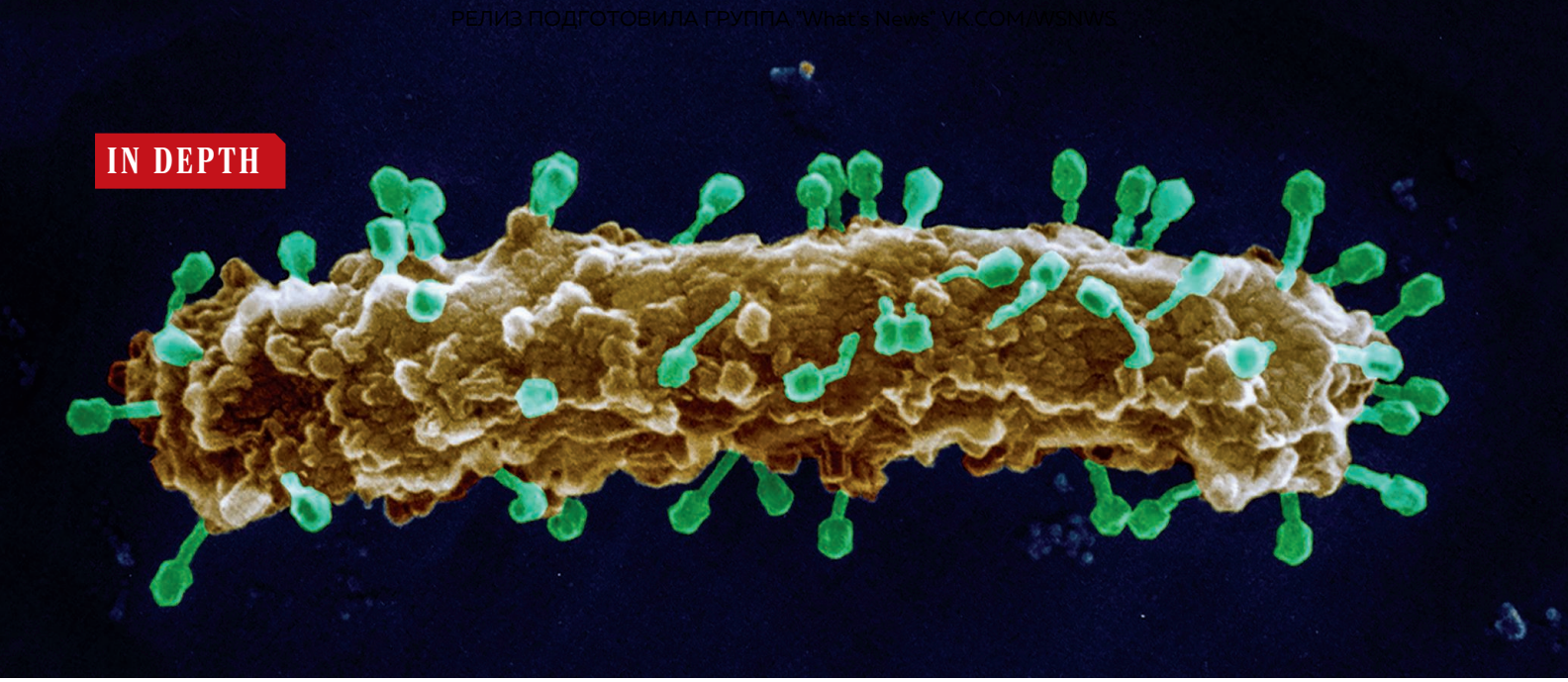

IN DEPTH

BIOMEDICINE

U.S. center will fight infections with viruses

Proving ground for phage therapy will organize full clinical trials of the approach

By **Kelly Servick**

One piece of good news can make all the difference. In the fight against antibiotic-resistant infections, a decades-old approach based on bacteria-slaying viruses called phages has been sidelined by technical hurdles, dogged by regulatory confusion, and largely ignored by drug developers in the West. But 2 years ago, researchers at the University of California, San Diego (UCSD), used phages to knock out an infection that nearly killed a colleague. Propelled by that success and a handful of others since, UCSD is now launching a clinical center to refine phage treatments and help companies bring them to market.

A first in North America, the center will initially consist of 16 UCSD researchers and physicians. It aims to be a proving ground for a treatment that has long been available in parts of Eastern Europe, but that still lacks the support of rigorous clinical trials. "There have been just a ton of failures and false starts," says Paul Bollyky, a microbiologist and physician at Stanford University Medical Center in Palo Alto, California, who studies phages. "The fact that a major American medical center is going to set up an ongoing enterprise around phage therapy … that's kind of a game changer for the field, at least in the United States."

Turning phages—found in soil, water, and sewage—into treatments isn't straightforward. Because each of the millions of phage strains in nature targets a specific bacterium, putting them to use means finding the specific phages that attack the menace at hand. Still, clinical centers overseas, in Georgia and Poland, have reported encouraging results with phages over the years. And the rise of antibiotic-resistant infections has prompted a handful of U.S. companies and research centers to reconsider the approach.

The case that mobilized the UCSD team hit close to home. In 2015, UCSD psychologist Tom Patterson was airlifted home after a vacation in Egypt when a drug-resistant strain of the bacterium *Acinetobacter baumannii* invaded his pancreas. As available antibiotics failed and Patterson fell into a coma, his wife, UCSD epidemiologist Steffanie Strathdee, launched an international effort to find strains of phage that might save him. After treatment with a variety of phages donated by San Diego–based biotech AmpliPhi Biosciences, Texas A&M University, and the U.S. Navy, Patterson made a dramatic recovery.

"Everybody's been talking about this case," Bollyky says. "Not only did he survive the treatment, which can't be taken for granted, but he also got better, and miraculously so." Patterson received some of the phages intravenously—an approach considered risky because toxins from bacteria used to grow the phages could linger in the mixture. His recovery helped allay safety fears, and it turned Strathdee into a self-described "phage wrangler," who helped match other patients with the right mixture of experimental phages. Since her husband's recovery, the UCSD team has successfully cleared infections in five more people with phage cocktails, under a U.S. Food and Drug Administration (FDA) process designed for emergencies where no approved treatments are available.

But a string of anecdotes does little to answer key scientific questions: What is the safest and most effective way to administer phages? How well do phages target the site of infection? How quickly are bacteria likely to develop resistance? "Those are the kinds of things you have to ask in structured clinical trials," says Robert Schooley, a UCSD physician and infectious disease researcher who treated Patterson and oversaw the other recent cases.

So he and Strathdee proposed the new clinical center, which will launch with a 3-year, $1.2 million grant from UCSD. The Center for Innovative Phage Applications and Therapeutics (IPATH) won't manufacture any phage treatments itself, but it will collaborate with companies and academic groups outside UCSD on multicenter clinical trials. IPATH will initially focus on treating patients with chronic, drug-resistant infections related to organ transplants, implanted devices such as pacemakers or joint replacements, and cystic fibrosis. Schooley is discussing possible trials with a team at the National Institute of Allergy and Infectious Diseases, and with two companies that have provided phages to patients

IMAGE: EYE OF SCIENCE/SCIENCE SOURCE

Phages like these studding an *Escherichia coli* bacterium target specific bacteria, complicating their use in medicine.

at UCSD: AmpliPhi and Adaptive Phage Therapeutics (APT), based in Gaithersburg, Maryland, which has licensed the Navy's phage collection.

Running phages through modern clinical testing has proved difficult in the past. A European Union–sponsored trial known as PhagoBurn was all but derailed by a series of setbacks (*Science*, 24 June 2016, p. 1506). "It was not an ideal trial, let me say it like that," says Jean-Paul Pirnay, a bioengineer at Queen Astrid Military Hospital in Brussels, one of the partners in PhagoBurn. A key obstacle was the fact that the trial targeted burn wounds, which often harbor multiple bacterial infections. That made it hard to test the effects of a phage therapy aimed at just one species. Designed to include 220 patients, the trial ultimately recruited only 27, and it has not yet published its results.

The anticipated trials at UCSD, on the other hand, will focus on patients with a single, known bacterial infection, Schooley says. But he admits it will still be tricky to design trials that isolate the effect of phages without withholding other potentially beneficial treatments, including antibiotics. (Ultimately, Schooley and many others expect phages to work in tandem with antibiotics—not to replace them.)

IPATH collaborators will also have to navigate a drug approval system suited to more conventional treatments. Because a phage cocktail will often have to be custom-designed for an individual, regulatory agencies may not have a single product to evaluate for safety and efficacy. But after initial talks with FDA, Greg Merril, APT's CEO, is confident the agency will be flexible. He plans to seek approval for an entire library of phages—about 100 for each bacterial species—from which doctors could create a cocktail of one to five phages for a patient.

In the meantime, Strathdee says the UCSD team plans to keep securing phages for individual cases under FDA's emergency pathway. She and Schooley already get several inquiries a week from patients and families fighting drug-resistant infections. "We hope to not send people with superbugs away, but to welcome them with open arms," she says. "Right now, they don't have anywhere to go."

Pirnay, whose team finds and formulates phages to treat infections related to battlefield injuries, has a piece of advice for the UCSD group: "Be careful not to create too high an expectancy with the public," he says. "Even when you do not say that you will be able to treat everything, you create a demand with desperate patients." ■

PHOTO: ALEXANDRE MENEGHINI/REUTERS/NEWSCOM

PUBLIC HEALTH

Reports of inner-ear damage deepen diplomat controversy

As mystery symptoms reported in Cuba spread to China, some blame an attack; others see "suggestion and paranoia"

By **Richard Stone**

The mystery began late in 2016. Personnel attached to the U.S. embassy in Havana developed symptoms such as headaches, dizziness, and insomnia after hearing strange loud sounds or feeling a sensation of pressure. Since then, dozens of diplomats have been withdrawn from Cuba, and international tensions have risen. This month, the mystery spread, with reports from the U.S. Department of State that "a number" of diplomats at its consulate in Guangzhou, China, had been flown home with symptoms similar to those reported in Cuba—where two more diplomats have reportedly fallen ill. Yet 18 months in, an explanation is nowhere in sight, although hypotheses have proliferated.

Former Secretary of State Rex Tillerson blamed a deliberate "health attack" for the Cuba ailments, whereas some neuroscientists and psychologists—and a panel of Cuban scientists—have written them off as the result of stress. Some unaffected diplomats from the Havana embassy agree. "There was a perfect storm of suggestion and paranoia," one told *Science,* speaking on condition of anonymity.

But a few researchers are finding hints of a physical cause. In February, a team at the University of Pennsylvania described neurological deficits in embassy personnel who had reported symptoms. And in unpublished results, Michael Hoffer, an otolaryngologist at the University of Miami in Florida, and his colleagues describe a unique vestibular and cognitive disorder in two dozen people evacuated from the Havana embassy. They believe some kind of directed energy device may have caused inner-ear damage.

Taking both teams' observations together, "It seems like something's going on," says Lee Goldstein of Boston University, who studies neurodegenerative diseases. But, he adds, "We're still very much in the early days of trying to figure this out."

The first to fall ill was a U.S. intelligence agent in Havana. The "index case," as Hoffer calls him, complained to the embassy doctor of ear pain, tinnitus, vertigo, and feeling "cognitively not perfect." The agent said he had heard "a really odd, loud noise that seemed to follow him in the room," says Hoffer, who examined him in February. "When he opened the front door, the sound went away." Other U.S. personnel reported similar symptoms.

At the end of March 2017, recalls the U.S. diplomat who spoke with *Science,* then-Ambassador Jeffrey DeLaurentis summoned personnel with security clearances—about 30 in all—for a classified briefing in a special installation in the embassy: a steel conex box suspended on pylons that's shielded from surveillance. The "working hypothesis," the diplomat says, was the victims were being targeted by a long-range acoustic device. Embassy security officers advised their colleagues to record harassing sounds and report any symptoms. In April 2017, the embassy clued in all members of its diplomatic corps and advised people to sleep in the middle of a room, away from windows.

Most personnel have been evacuated from the U.S. embassy in Havana, leaving only a skeleton crew.

"Everybody was in a frenzy about it," says a second U.S. diplomat who was stationed in Havana at the time with two young children. "We had a big window in the front of the house. It was a horrible feeling. We just thought, 'Oh my God, we're in harm's way,'" she says. "You start to feel paranoid."

Hoffer, a former military doctor who had treated concussion victims in Iraq, was enlisted to assess the ailing diplomats. His team had been working on better tests for concussion in athletes, together with University of Miami neurophysiologist Bonnie

Levin, otolaryngologist Carey Balaban of the University of Pittsburgh in Pennsylvania, and engineers at Neuro Kinetics, Inc., also in Pittsburgh. In one test, the patient wears goggles that project a moving field of light points while a camera observes eye movements. In healthy subjects, the eyes reflexively track the lights. People with a head injury are often unable to focus on them at all. The goggles can also perform other eye movement tests sensitive to concussions.

Hoffer and colleagues tested several dozen Havana embassy personnel who had been flown to Miami. About half flunked a critical eye movement test, and more than two dozen reported dizziness or vertigo. In those individuals, Balaban says, further tests implicated damage to the ear's otolith organs, the utricle and the saccule, key to sensing gravity. "That's prima facie evidence the diplomats are not making this up," Hoffer says.

"I agree with that," Goldstein says, but he is skeptical of speculation about what might be causing the injuries. Balaban and his colleagues venture that a directed energy source could have damaged the exquisitely sensitive utricle and saccule. Maintaining balance became so taxing, they say, that victims reported concussionlike symptoms, finding it hard to think and concentrate. Hoffer acknowledges, however, that some patients may have had preexisting injuries. One had been stationed in Afghanistan and may have been exposed to a blast there. (His team's findings are under review at a medical journal, he says.)

In January, after an investigation that included fieldwork in Havana, the Federal Bureau of Investigation found no evidence for an attack with powerful energy beams. But the Department of Defense is giving the possibility a closer look. U.S. Navy acoustic expert Kurt Yankaskas, who runs the noise-induced hearing loss program at the Office of Naval Research in Arlington, Virginia, thinks an energy weapon is a possibility, although "it would have to have been tight-beamed and high frequency." One candidate, he says, is so-called hypersonic sound, generated by the interference of ultrasonic waves, which the Navy has evaluated as a means of communicating on deafening aircraft carrier decks.

Whatever the symptoms' cause, only a minority of embassy staff were stricken. The Department of State dispatched Hoffer and University of Miami physical therapist James Buskirk to Havana in April 2017 to perform tests on several dozen of the remaining personnel. "A lot of people at the embassy wanted reassurance they weren't affected," Buskirk says. None had experienced symptoms, and they all scored normally on the tests.

Other researchers and physicians maintain that mass psychogenic illness could explain some, if not all, of the symptoms. A panel of Cuban scientists that evaluated U.S. evidence and gathered its own data concluded in December 2017 that U.S. recordings of a grating, supposedly unnatural sound match the chirping of the Jamaican field cricket, a notoriously noisy insect that's common in Cuba (*Science*, 8 December 2017, p. 1236). People's state of mind determined whether they developed symptoms, the first diplomat asserts. "I don't know anybody who at one point thought we were under no risk and then subsequently decided that they were a victim."

He himself heard a mysterious sound one night last June. "Standing in the atrium of my house, it was so loud and metallic, my brain literally hurt," he says. He called the embassy security officer, who came over and recorded the sound. But his housekeeper knew right away it was a Jamaican field cricket. "She grew up on a farm. She's like, 'Oh yeah, they drive people crazy.'"

The second diplomat echoes that experience. The sound, she says, "was eerie. A really nasty sound. Not like your head is going to explode, but it's very unpleasant." Then she and her family heard it on several more occasions outdoors, for example, while walking their dog. "That was reassuring. We realized it had to be the crickets."

She acknowledges that over time, a divide widened between "the true believers" and those like her who are skeptical that there was an attack. At the same time, she says, she's open-minded to plausible explanations for the mystery illness.

Both U.S. and Cuban authorities are struggling to provide them. On 5 June, Secretary of State Mike Pompeo announced the creation of a task force that will lead an interagency probe. And earlier this month, the president of the Cuban Academy of Sciences (ACC) in Havana, neurophysiologist Luis Velázquez Pérez, proposed that ACC and the U.S. National Academy of Sciences (NAS) in Washington, D.C., team up to try to solve the mystery. (A spokesperson for NAS could not comment on whether it will respond.) John Van Horn, a neuroscientist at the University of Southern California in Los Angeles, hopes the research will go forward. "Opened and reasoned scientific scrutiny of these cases" is needed, he says, "to reach a more precise conclusion than that some evil boogeyman has developed a supersecret sound gun and is using it specifically against foreign diplomats."

"I have every incentive to know the truth," the second diplomat says. "It's in our best interest to know if there's something that could damage us or our kids." ■

Richard Stone, formerly Science*'s international editor, is now senior science editor at Tangled Bank Studios in Chevy Chase, Maryland.*

Sounds and fury

A mystery illness among U.S. diplomats in Cuba and China has raised international tensions and sparked debate about possible causes.

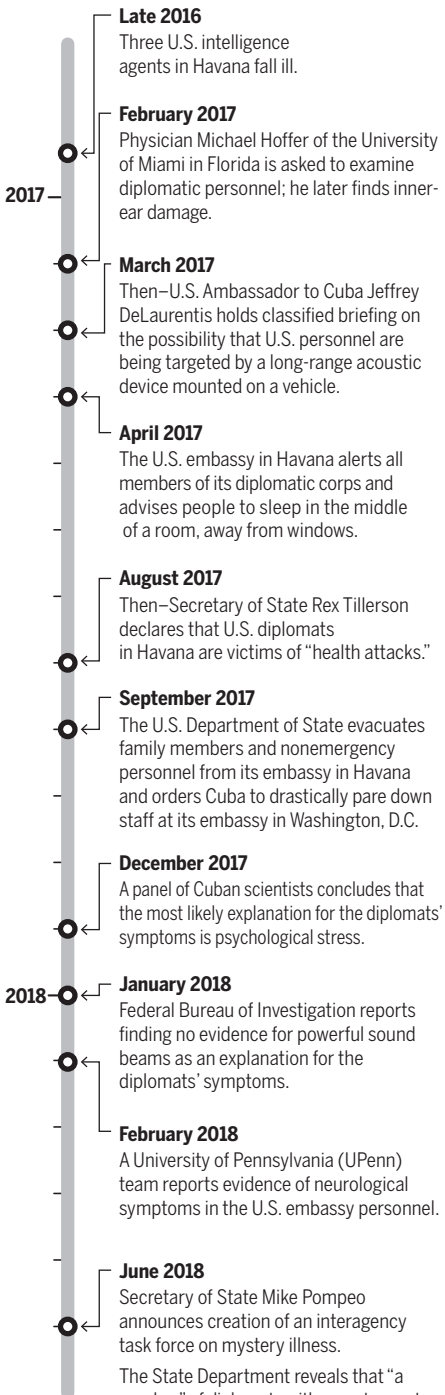

GRAPHIC: V. ALTOUNIAN/*SCIENCE*

GEOPHYSICS

Rising bedrock may delay ice sheet collapse

Its burden lightening, crust beneath West Antarctic glaciers is rebounding at a fast pace

By **Katie Langin**

The news last week out of Antarctica was sobering. According to a consensus estimate published in *Nature*, the continent has lost 3 trillion tons of ice in the past 25 years—most of it from the vulnerable West Antarctic Ice Sheet, where the loss rate tripled over the study period. Although West Antarctica contributed just 6 millimeters of sea level rise in that time, scientists say ice-sheet collapse there could raise global sea levels by 3 meters in the coming centuries. The accelerating loss could be a sign that the catastrophe has already been set in motion.

But a study on p. 1335 offers a glimmer of hope, documenting a process that could slow the collapse. As ice melts and the load on the crust lightens, the bedrock beneath West Antarctica is rising rapidly. In places it could rise 8 meters over the coming century—potentially protecting the ice from the warm seawater that is melting it from below. "It may just buy the world a few extra decades," says Rick Aster, a seismologist at Colorado State University in Fort Collins and an author of the new study.

The West Antarctic Ice Sheet is vulnerable because its bed lies far below sea level, forming a giant basin that slopes inland to a depth of more than a kilometer. Glaciers—"rivers" of ice—shed ice into the ocean. For the moment, some are snagged on ridges in the sea floor, slowing their flow. But as the warming ocean erodes them from below, they could retreat behind the ridges. Seawater would then pour into the basin, lifting ice off the bedrock and melting it in a runaway process. "It's a very unstable situation," says Natalya Gomez, a geophysicist at McGill University in Montreal, Canada.

The bowl under West Antarctica was created during the last ice age, when the weight of the ice, much thicker at the time, pressed down on the bedrock. But the rock was ready to spring back. "The earth acts like a memory foam mattress," says Valentina Barletta, a geophysicist at the Technical University of Denmark in Kongens Lyngby who led the new study. Some rebound occurs immediately, as soon as ice melts. But some takes place more slowly, as the gummy rock of the deeper mantle gradually readjusts to the lighter burden.

Gomez models this process and had found that rising bedrock might slow ice retreat, by raising the bowl and the ridges that stabilize the glaciers. But just how much help crustal rebound can offer depends on how fast it takes place, which reflects how hot and gooey the underlying mantle is.

To measure the rebound, Barletta and her colleagues tracked tiny changes in elevation using six GPS sensors that they fixed to ice-free bedrock in locations around the Amundsen Sea—the epicenter of West Antarctic ice loss that includes the rapidly receding Thwaites and Pine Island glaciers.

Pine Island Glacier, one of the most vulnerable in West Antarctica, is being melted from below by seawater.

PHOTO: MARTIN JAKOBSSON

Soon after the sensors were deployed, between 2010 and 2012, the team noticed they were rising fast, says Terry Wilson, a polar geologist at The Ohio State University in Columbus who led the deployment. But it took 2 or 3 years before the team realized, "Oh geez, this is real," she says.

They found that, in some places, the bedrock was rising more than 4 centimeters per year—one of the fastest rebound rates in the world. "That's huge," says Robin Bell, a geophysicist at Columbia University who wasn't involved in the study. "It shows that the earth is gooey there, a lot gooier than we thought." Bell says another finding, reported in *Nature* last week, shows that the process happened in the past. The study found that the West Antarctic Ice Sheet shrank at the end of the last ice age 12,000 years ago, but began growing again as the rebound effect took hold. "It shows you how dynamic the planet can be and how quickly it can respond to moving ice," Bell says.

The mantle is so gooey under West Antarctica that it is readjusting to ice lost decades or centuries ago, not the retreat of ice age glaciers thousands of years ago, the more standard time frame for mantle rebound, Barletta says. And the uplift will accelerate as the region sheds more ice weight. Barletta predicts that, in a century, it will be three times faster. By then, she says, the bedrock in some locations will have rebounded by about 8 meters, lifting the ice sheets along with it and lowering water levels where the vulnerable glaciers meet the ocean.

But some scientists say no amount of rebound will prevent ice sheet collapse in the long term, given the pace of carbon emissions and global warming. "It's not a get out of jail free card," says Ted Scambos, a glaciologist at the National Snow and Ice Data Center in Boulder, Colorado. "It's more of a refinement on the pace of [ice sheet] collapse," he says, especially if we continue "stomping on the climate gas pedal." Ingo Sasgen, a geophysicist at the Alfred Wegener Institute in Bremerhaven, Germany, agrees. "It's still a rather slow process compared to melting," he says. "If you have a very strong warming from the ocean, the ice sheet will disintegrate whatever the solid earth does." ■

EVOLUTION

Neanderthal brain organoids come to life

Human "minibrains" with gene from our extinct relative have intriguing differences

By **Jon Cohen**

Until now, researchers wanting to understand the Neanderthal brain and how it differed from our own had to study a void. The best insights into the neurology of our mysterious, extinct relatives came from analyzing the shape and volume of the spaces inside their fossilized skulls.

But a recent marriage of three hot fields—ancient DNA, the genome editor CRISPR, and "organoids" built from stem cells—offers a provocative, if very preliminary, new option. At least two research teams are engineering stem cells to include Neanderthal genes and growing them into "minibrains" that reflect the influence of that ancient DNA.

None of this work has been published, but Alysson Muotri, a geneticist at the University of California, San Diego (UCSD) School of Medicine, described his group's Neanderthal organoids for the first time this month at a UCSD conference called Imagination and Human Evolution. His team has coaxed stem cells endowed with Neanderthal DNA into pea-size masses that mimic the cortex, the outer layer of real brains. Compared with cortical minibrains made with typical human cells, the Neanderthal organoids have a different shape and differences in their neuronal networks, including some that may have influenced the species's ability to socialize. "We're trying to recreate Neanderthal minds," Muotri says.

"I'm a little envious," says Todd Preuss, a neuroanatomist at Emory University's Yerkes National Primate Research Center in Atlanta who is retiring just as this approach to studying brain evolution takes hold. "It's still a long haul to get from organoids to real brains, but if the technique can be developed enough to give us more information about normal tissue structure, then you've got something that's probably very useful."

Svante Pääbo, director of the Max Planck Institute for Evolutionary Anthropology in Leipzig, Germany, expects the work to draw skepticism because it's so difficult to figure out which genetic differences are "functionally relevant," and the organoids only represent the early stage of brain development. "Organoids are far from being able to tell us how adult brains function," says Pääbo, who led the team that deciphered the Neanderthal genome by rescuing DNA from their bones. His group has also started to make organoids with Neanderthal brain genes, but he stresses that the technique can introduce unintended mutations. "There are lots of control experiments to do, and then I'm quite hopeful we'll overcome those doubts," says Pääbo, who plans to compare Neanderthal brain organoids to those made from chimpanzee or modern human cells.

Muotri focused on one of approximately 200 protein-coding genes that differ between Neanderthals and modern humans. Known as *NOVA1*, it plays a role in early brain development in modern humans and also is linked to autism and schizophrenia. Because it controls splicing of RNA from other genes, it likely helped produce more than 100 novel brain proteins in Neanderthals. Conveniently, just one DNA base pair differs between the Neanderthal gene and the modern human one.

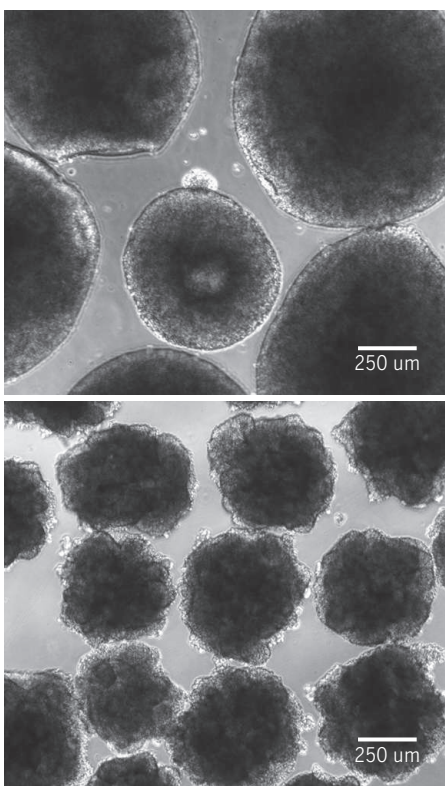

Compared with brain organoids grown from ordinary human cells (top), those with a Neanderthal gene variant (bottom) differ in appearance and behavior.

Muotri and his co-workers start with skin cells from a "neurotypical person"—someone without any known genetic defects linked to neurological disorders—and manipulate their genomes to turn them into pluripotent stem cells. Using CRISPR, the team then targets *NOVA1* and swaps in the Neanderthal base pair to replace the modern human one. To avoid being misled by the "off-target" DNA changes made by CRISPR as well as genetic errors that can occur from producing the stem cells, they sequence the resulting cells and discard any that have unintended mutations.

It takes several months to grow the Neanderthal DNA–containing stem cells into organoids—"We call them Neanderoids," Muotri says. Comparing them with modern human brain organoids made under identical conditions, his team found that the neuronal cells with the Neanderthalized *NOVA1* migrate more quickly within an organoid as they form structures. "We think it's related to the shape of the organoid, but we have no idea what it means," says Muotri, noting that the Neanderoids have a "popcorn" shape, whereas modern human cortical organoids are spherical. The Neanderoid neurons also make fewer synaptic connections, creating what resembles an abnormal neuronal network.

Several of these differences mirror what Muotri has found studying neuronal development in the brains of children with autism. "I don't want families to conclude that I'm comparing autistic kids to Neanderthals, but it's an important observation," says Muotri, who has a stepson with autism. "In modern humans, these types of changes are linked to defects in brain development that are needed for socialization. If we believe that's one of our advantages over Neanderthals, it's relevant."

Muotri has developed the modern human brain organoids to the stage where his team can detect oscillating electrical signals within the balls of tissue. They are now wiring the organoids to robots that resemble crabs, hoping the organoids will learn to control the robots' movements. Ultimately, Muotri wants to pit them against robots run by brain Neanderoids.

"It's kind of wild," says Simon Fisher, a geneticist who heads the Max Planck Institute for Psycholinguistics in Nijmegen, the Netherlands, who famously engineered mice to have a mutated human gene linked to speech disorders. "It's creative science." ■

IMAGES: ALYSSON MUOTRI

MeerKAT's 64 dishes can study the way hydrogen gas moves around galaxies.

PHOTO: SOUTH AFRICAN RADIO ASTRONOMY OBSERVATORY

ASTRONOMY

Radio arrays take shape in the global south

South Africa's MeerKAT will form part of the multicontinent Square Kilometre Array

By **Daniel Clery**

On the wide-open plains of the Karoo, a semiarid desert northeast of Cape Town, South Africa, the largest and most powerful radio telescope in the Southern Hemisphere is listening to the sky. The last of 64 13.5-meter dishes was installed in late 2017, and next month, South African President Cyril Ramaphosa will officially open the facility, known as MeerKAT. Spread across 8 kilometers, the dishes have a collecting area similar to that of the great workhorse of astrophysics, the Karl G. Jansky Very Large Array (VLA) near Socorro, New Mexico. But with new hardware designs and a powerful supercomputer to process data, the newcomer could have an edge on its 40-year-old northern cousin.

"For certain studies, it will be the best" in the world, says Fernando Camilo, chief scientist of the South African Radio Astronomy Observatory in Cape Town, which operates MeerKAT. Sensitive across a wide swath of the radio spectrum, MeerKAT can study how hydrogen gas moves into galaxies to fuel star formation. With little experience, South Africa has "a major fantastic achievement," says Heino Falcke of Radboud University in Nijmegen, the Netherlands. The new telescope also signals a wider shift to the global south for radio astronomers, as they gear up to build the ambitious Square Kilometre Array (SKA) in South Africa and Australia.

MeerKAT, which stands for Karoo Array Telescope along with the Afrikaans word for "more," is one of several precursor instruments for the SKA, which, if built, will be Earth's largest radio array by far. That effort got a boost this week as Spain agreed to join 10 countries backing the SKA, including project leaders Australia, South Africa, and the United Kingdom. The first phase of the SKA could begin in 2020 at a cost of €798 million. It would add another 133 dishes to MeerKAT, extending it across 150 kilometers, and place 130,000 smaller radio antennas across Australia—but only if member governments agree to fully fund the work. Months of delicate negotiations lie ahead. "In every country, people are having that discussion on what funding is available," Falcke says.

With MeerKAT's 64 dishes now in place, engineers are learning how to process the data they gather. In a technique called interferometry, computers correlate the signals from pairs of dishes to build a much sharper image than a single dish could produce. For early science campaigns last year, 16 dishes were correlated. In March, the new supercomputer came online, and the team hopes to be fully operational by early next year. "It's going to be a challenge," Camilo says.

MeerKAT's dishes are smaller than the VLA's, but having more of them puts it in "a sweet spot of sensitivity and resolution," Camilo says. Its dishes are split into a densely packed core, which boosts sensitivity, and widely dispersed arms, which increase resolution. The VLA can opt for sensitivity or resolution, but not both at once—and only after the slow process of moving its 27 dishes into a different configuration.

The combination makes MeerKAT ideal for mapping hydrogen, the fuel of star and galaxy formation. Because of a spontaneous transition in the atoms of neutral hydrogen, the gas constantly emits microwaves with a wavelength of 21 centimeters. Stretched to radio frequencies by the expansion of the universe, these photons land in the telescope's main frequency band. It should have the sensitivity to map the faint signal to greater distances than before, and the resolution to see the gas moving in and around galaxies.

MeerKAT will also watch for pulsars, dense and rapidly spinning stellar remnants. Their metronomic radio wave pulses serve as precise clocks that help astronomers study gravity in extreme conditions. "By finding new and exotic pulsars, MeerKAT can provide tests of physics," says Philip Best of the University of Edinburgh. Falcke wants to get a better look at a highly magnetized pulsar discovered in 2013. He hopes it will shed light on the gravitational effects of the leviathan it orbits: the supermassive black hole at the center of the Milky Way.

Other SKA precursors are taking shape. The Australian SKA Pathfinder (ASKAP) at the Murchison Radio-astronomy Observatory in Western Australia is testing a novel survey technology with its 36 12-meter dishes that could be used in a future phase of the SKA. Whereas a conventional radio dish has a single-element detector—the equivalent of a single pixel—the ASKAP's detectors have 188 elements, which should help it quickly map galaxies across large areas of the sky.

Nearby is the Murchison Widefield Array (MWA), a patchwork of 2048 antennas, each about a meter across, that look like metallic spiders. Sensitive to lower frequencies than MeerKAT, the MWA can pick up the neutral hydrogen signal from as far back as 500 million years after the big bang, when the first stars and galaxies were lighting up the universe. Astronomers have been chasing the faint signal for years, and earlier this year, one group reported a tentative detection (*Science*, 2 March, p. 969). "We're really curious to see if it can be replicated," says MWA Director Melanie Johnston-Hollitt of Curtin University in Perth, Australia.

If the MWA doesn't deliver a verdict, the SKA, with 130,000 similar antennas, almost certainly will. Although the MWA may detect the universe lighting up, the SKA intends to map out where it happened. ■

A canceled trial sought to determine whether a single drink a day could have heart benefits.

RESEARCH ETHICS

NIH kills alcohol trial, starts hunt for other suspect studies

Agency says research protocol was skewed to find benefits of moderate drinking

By **Meredith Wadman**

After an investigation found senior officials at the National Institutes of Health (NIH) in Bethesda, Maryland, secretly and improperly wooed the alcoholic beverage industry to fund a study of the potential heart benefits of moderate drinking, NIH Director Francis Collins last week shut down the $100 million clinical trial just 4 months into its expected 10-year span.

The conduct of officials at the National Institute on Alcohol Abuse and Alcoholism (NIAAA) in Bethesda was "way outside of the acceptable culture of our noble institution," Collins said at a 15 June meeting of his advisory council. He ordered a sweeping, 2-month review by each of NIH's 27 institutes and centers aimed at ferreting out any similarly compromised research elsewhere.

The announcement capped months of controversy surrounding the Moderate Alcohol and Cardiovascular Health (MACH) trial, which planned to enroll 7800 participants in a study of whether one drink a day protects against heart disease and diabetes. The study, meant to deliver a clear verdict on the possible heart benefits of low-dose alcohol, began recruiting participants in February. The next month, however, *The New York Times* revealed that NIAAA officials had solicited funding from the alcoholic beverage industry—in all, beverage companies would contribute $68 million—and had seen to it that a principal investigator (PI) whom the officials favored ran the trial. Three days later, Collins announced that a working group of external advisers would review the trial. In May, NIH suspended enrollment after 105 participants had signed up.

The advisers' 165-page report concludes NIAAA staffers broke NIH rules by directly soliciting companies for donations, and then withheld information about that effort from staff at NIH and the Foundation for the National Institutes of Health, a congressionally chartered nonprofit that is intended to allow private donors to support NIH studies while preventing them from influencing designs or outcomes. In one email cited by investigators, an NIAAA staffer counseled another not to respond to a colleague's question about the activities, while allowing, "We can't keep him totally in the dark." Another email, apparently intended for an industry source, was composed by an NIAAA staffer and run past the PI, who approved it. The message read, in part: "One of the important findings will be showing that moderate drinking is safe." Ultimately, five companies donated funds to the MACH trial: Anheuser-Busch InBev, based in Leuven, Belgium; Carlsberg Breweries of Copenhagen; Diageo, based in London; Heineken, in Amsterdam; and Pernod Ricard USA, based in New York City.

The report says NIAAA staffers also manipulated the grant application process to ensure that a favored scientist—Kenneth Mukamal of Beth Israel Deaconess Medical Center and Harvard Medical School in Boston—won awards to plan and then run the trial. Mukamal, who had given presentations to industry groups stressing the "unique opportunity" such a trial presented, was the only applicant for both grants.

"Many of the [NIH staff] who have seen the working group report were frankly shocked to see that so many lines were crossed," Collins said. It was clear, he said, that backers of the study had shaped the trial protocol to ensure an outcome favorable to the sponsors. NIH epidemiologists who reviewed the study said it did not enroll enough people or follow them for long enough to determine whether moderate alcohol consumption increases cancer risks, potentially offsetting any heart benefits. They also faulted the protocol for not including heart failure—which can be caused by alcohol—as a primary endpoint. The MACH trial, they concluded, "could show benefits while missing the harms."

Mukamal responded with a vigorous defense of the trial's integrity. In a statement "on behalf of the [MACH] investigators," he wrote: "We stand fully and forcefully behind the scientific integrity of the [MACH] trial protocol and team. … Every design consideration was carefully and deliberately vetted with no input or direction whatsoever from private sponsors." NIAAA has spent $4 million of the $20 million it had committed to the trial, and the foundation has disbursed $11.8 million in industry funds.

Researchers concerned about industry influence on research applauded NIH's decision to kill the trial. Collins did "the right thing," says Adriane Fugh-Berman, who studies pharmaceutical marketing practices at the Georgetown University Medical Center in Washington, D.C. "It was the only tenable decision that could be made—both the scientific and ethical aspects of the research have been fatally compromised," says Michael Siegel, an epidemiologist and former NIAAA grantee at Boston University who has studied the impact of alcohol advertising on adolescents.

Fugh-Berman would like NIH to go further and renounce all industry funding of research—even unrestricted donations. NIH's Office of Management Assessment is also investigating the MACH trial's genesis and fundraising, focusing on whether employees violated NIH policy or federal regulations. Its probe is not yet complete. ■

With reporting by Jocelyn Kaiser.

PHOTO: ISTOCK.COM/JAYSONPHOTOGRAPHY

CONSERVATION BIOLOGY

Chinese grave reveals vanished gibbon genus

Humans and climate change drove once-revered ape extinct in the past 2000 years

By **Gretchen Vogel**

Swinging from branch to branch with loud and often melodic calls, gibbons are a dramatic presence in forests they inhabit. Eighth century Chinese poet Li Bai described their haunting voices: "*While on the cliffs of the Yangtze Gorges, gibbons ceaselessly cry/Ten thousand folds of mountains, my skiff has slipped them by.*"

Today, no gibbons live anywhere near the Yangtze River gorges Li traversed, and the apes that remain elsewhere in China have fur patterns different from those often depicted in classical Chinese paintings. But given their prominence in art, researchers assumed the animals must once have swung through the treetops of central China. Now, physical evidence of a vanished gibbon has turned up in an unexpected place: a tomb that may have been built for the grandmother of China's first emperor, nearly 2300 years ago. The skull and jaw found in the tomb are so distinctive that scientists conclude they belonged to a member of a now-extinct gibbon genus.

The skull "is really a fantastic find," says Thomas Geissmann, a gibbon expert at the University of Zurich in Switzerland who was not involved in the research. "I don't doubt for a second that it's a new species, and probably a new genus. … We can assume that this vast area of central China [once] had many other species" of gibbon. With surviving gibbons also facing extinction, the new find could boost motivation to protect them by highlighting how much has already been lost, says Samuel Turvey, a conservation biologist at the Zoological Society of London who, with his colleagues, describes the ancient skull on p. 1346.

Turvey, who studies human-caused extinctions, combs historical records and museum collections for evidence about past biodiversity. In 2011, at the Shaanxi Provincial Institute of Archaeology in Xi'an, China, he came across artifacts from the tomb, which was discovered in 2004 on the outskirts of Xi'an, the capital of Shaanxi province and once a powerful imperial city. Based on the tomb's location and the artifacts it contained, archaeologists Ding Yan and Zhang Tianen of the Shaanxi institute, who helped lead the excavations, dated it to the Warring States period, about 2250 years ago. They concluded it may have been built for Lady Xia, the grandmother of China's first emperor, Qin Shi Huang. Qin ruled from 256 B.C.E. until 210 B.C.E., united much of China and was buried near Xi'an with his famous terra cotta army.

The collection's primate bones caught Turvey's attention. "Historically there are accounts of gibbons" in central China, he says, "but it is very, very far from any gibbon populations today." The tomb also contained skeletons of leopards, lynx, black bears, cranes, and a range of domestic animals. The wild animals were all from the region, so the gibbon probably also lived nearby, says archaeologist Hu Songmei of the Shaanxi institute. Gibbons were common high-status pets, and burial chambers were often arranged so that the deceased "could continue to enjoy the life they knew when still alive," Hu says. Because the emperor was presumably involved in his grandmother's funeral preparations, Turvey says, "It's not a total flight of fancy to think that he might have seen this specific gibbon."

Gibbons are a common motif in classical Chinese artworks such as this 15th century painting.

IMAGE: FREER GALLERY OF ART AND ARTHUR M. SACKLER GALLERY, SMITHSONIAN INSTITUTION, WASHINGTON, D.C.; GIFT OF CHARLES LANG FREER, F1911.272

Chinese authorities did not let the team sample the bone for DNA, which could have helped determine the animal's kinship with existing gibbons. Instead, Turvey worked with Helen Chatterjee, an expert on gibbons at University College London, and colleagues to measure key points on the skull and teeth and compare the dimensions with those of the four living genera of gibbons. Their statistical analysis found both the skull and molars were so distinct from all of today's gibbons that the fossil belonged to a separate genus.

That fits with what we know of gibbons, Chatterjee says. Gibbon populations can easily become isolated from each other because the apes spend their lives in the treetops and can't cross gaps in the canopy created by rivers or other barriers. That has spurred extreme genetic diversity—the four genera alive today have different numbers of chromosomes, she notes.

The team named the new species *Junzi imperialis*. "*Junzi*" is a Chinese word for scholar-officials, who were often associated with gibbons because the animals were considered wiser and nobler than mischievous monkeys. The animals' arms were thought to help them channel chi, "a bit like Jedi masters," Chatterjee says.

As for what *J. imperialis* looked like, classical paintings may hold some clues. They depict gibbons with a wide variety of colors and facial markings, frequently different from any of today's gibbon species. Turvey says *J. imperialis* "may be the tip of the iceberg," and a whole suite of gibbon species that were common across China in previous centuries have already gone extinct.

The Imperial Chinese reverence for gibbons apparently didn't extend to preserving their habitat. The razing of forests for agriculture in recent centuries, and perhaps the onset of a cooler, drier climate in central China, apparently spelled disaster for *J. imperialis*. The same dynamic is at play for today's gibbons, says David Chivers, a primatologist who retired from the University of Cambridge in the United Kingdom. One species, on China's Hainan island, has only two dozen individuals left. "Remove the forest and they're gone," he says of the apes. "We've got to stop the forest being cut down. That's the only way to save them." ■

With reporting by Bian Huihui in Shanghai, China.

FEATURES

FEEDING THE GODS

Hundreds of skulls testify to the monumental scale of human sacrifice in the Aztec capital

By **Lizzie Wade**, *in Mexico City*

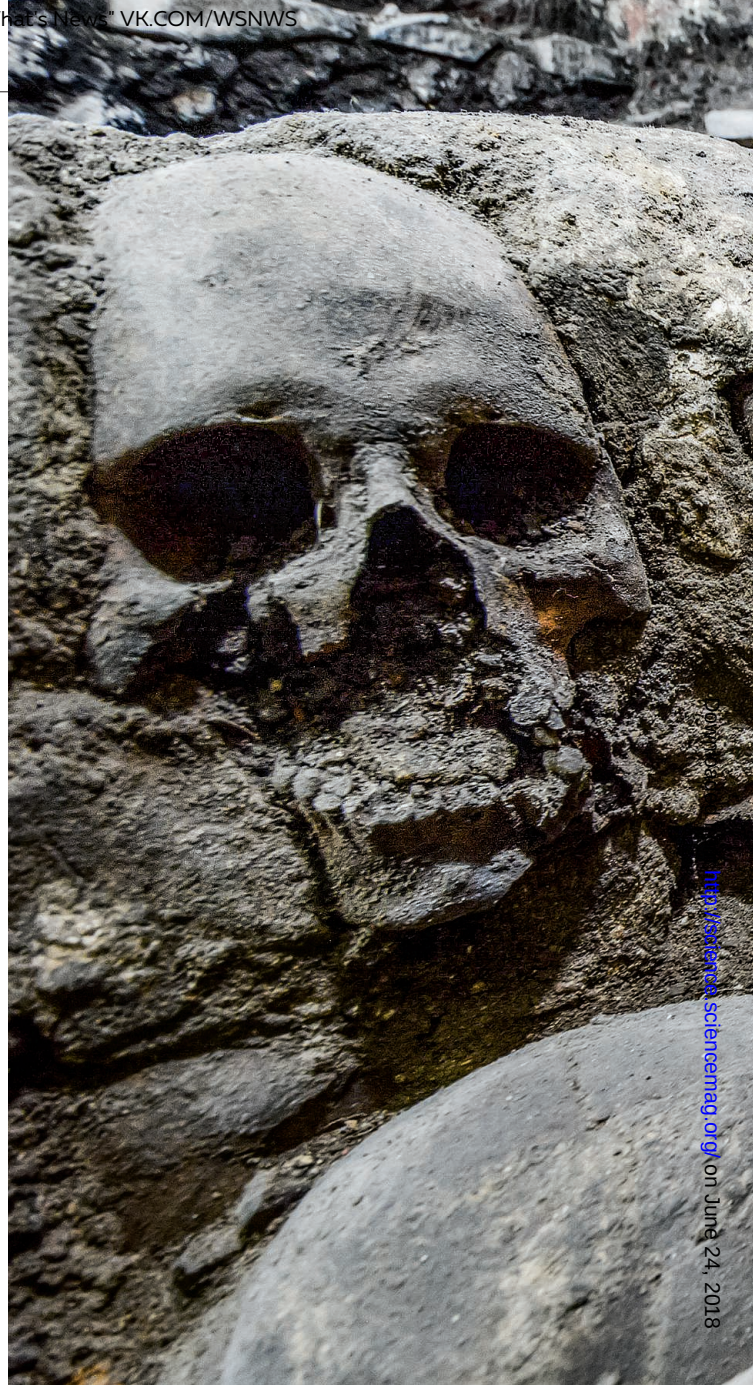

The priest quickly sliced into the captive's torso and removed his still-beating heart. That sacrifice, one among thousands performed in the sacred city of Tenochtitlan, would feed the gods and ensure the continued existence of the world.

Death, however, was just the start of the victim's role in the sacrificial ritual, key to the spiritual world of the Mexica people in the 14th to the 16th centuries.

Priests carried the body to another ritual space, where they laid it face-up. Armed with years of practice, detailed anatomical knowledge, and obsidian blades sharper than today's surgical steel, they made an incision in the thin space between two vertebrae in the neck, expertly decapitating the body. Using their sharp blades, the priests deftly cut away the skin and muscles of the face, reducing it to a skull. Then, they carved large holes in both sides of the skull and slipped it onto a thick wooden post that held other skulls prepared in precisely the same way. The skulls were bound for Tenochtitlan's *tzompantli*, an enormous rack of skulls built in front of the Templo Mayor—a pyramid with two temples on top. One was dedicated to the war god, Huitzilopochtli, and the other to the rain god, Tlaloc.

Eventually, after months or years in the sun and rain, a skull would begin to fall to pieces, losing teeth and perhaps even its jaw. The priests would remove it to be fashioned into a mask and placed in an offering, or use mortar to add it to two towers of skulls that flanked the *tzompantli*. For the Aztecs—the larger cultural group to which the Mexica belonged—those skulls were the seeds that would ensure the continued existence of humanity. They were a sign of life and regeneration, like the first flowers of spring.

But the Spanish conquistadors who marched into Tenochtitlan in 1519 saw them differently. For them, the skulls—and the entire practice of human sacrifice—evinced the Mexica's barbarism

IMAGES: (LEFT TO RIGHT) 1587 AZTEC MANUSCRIPT, THE CODEX TOVAR/WIKIMEDIA COMMONS; RAÚL BARRERA RODRÍGUEZ

and justified laying waste to the city in 1521. The Spanish tore down the Templo Mayor and the *tzompantli* in front of it, paved over the ruins, and built what would become Mexico City. And the great rack and towers of skulls passed into the realm of historical mystery.

Some conquistadors wrote about the *tzompantli* and its towers, estimating that the rack alone contained 130,000 skulls. But historians and archaeologists knew the conquistadors were prone to exaggerating the horrors of human sacrifice to demonize the Mexica culture. As the centuries passed, scholars began to wonder whether the *tzompantli* had ever existed.

Archaeologists at the National Institute of Anthropology and History (INAH) here can now say with certainty that it did. Beginning in 2015, they discovered and excavated the remains of the skull rack and one of the towers underneath a colonial period house on the street that runs behind Mexico City's cathedral. (The other tower, they suspect, lies under the cathedral's back courtyard.) The scale of the rack and tower suggests they held thousands of skulls, testimony to an industry of human sacrifice unlike any other in the world. Now, archaeologists are beginning to study the skulls in detail, hoping to learn more about Mexica rituals and the postmortem treatment of the bodies of the sacrificed. The researchers also wonder who the victims were, where they lived, and what their lives were like before they ended up marked for a brutal death at the Templo Mayor.

A codex written after the conquest by a Spanish priest (left) depicts Tenochtitlan's enormous skull rack, or *tzompantli*. Now, archaeologists have discovered and excavated the rack's remains (right).

"This is a world of information," says archaeologist Raúl Barrera Rodríguez, director of INAH's Urban Archaeology Program and leader of the team that found the *tzompantli*. "It's an amazing thing, and just the kind of discovery many of us had hoped

Sacrifice city

For the Mexica, human sacrifice was key to the health of the world. Recent finds show that a vast rack of skulls (reconstruction below) stood in a temple at the heart of their capital, Tenochtitlan.

The island capital of Tenochtitlan
The Mexica built their capital city on an island in the now-drained Lake Texcoco. At its apex, the city had a population of about 250,000 and was the seat of an empire that stretched to southern Mexico. The temple complex in the middle of the island was the political and religious heart of the city state.

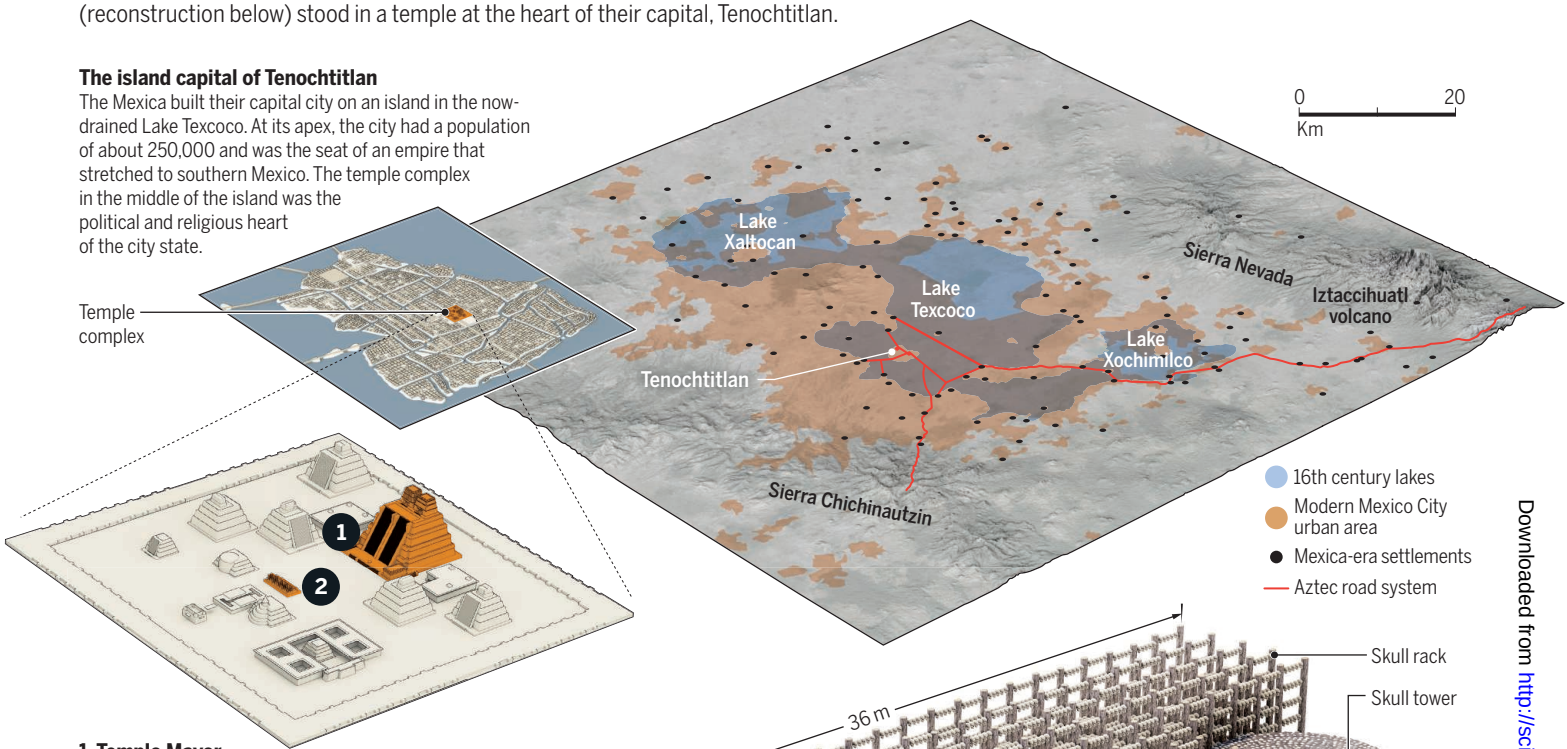

1 Templo Mayor
Most sacrifices in Tenochtitlan were performed in public at the top of the Templo Mayor. The sacrifices played a vital role in the Mexica's cosmology, and may have also helped the young empire control conquered populations.

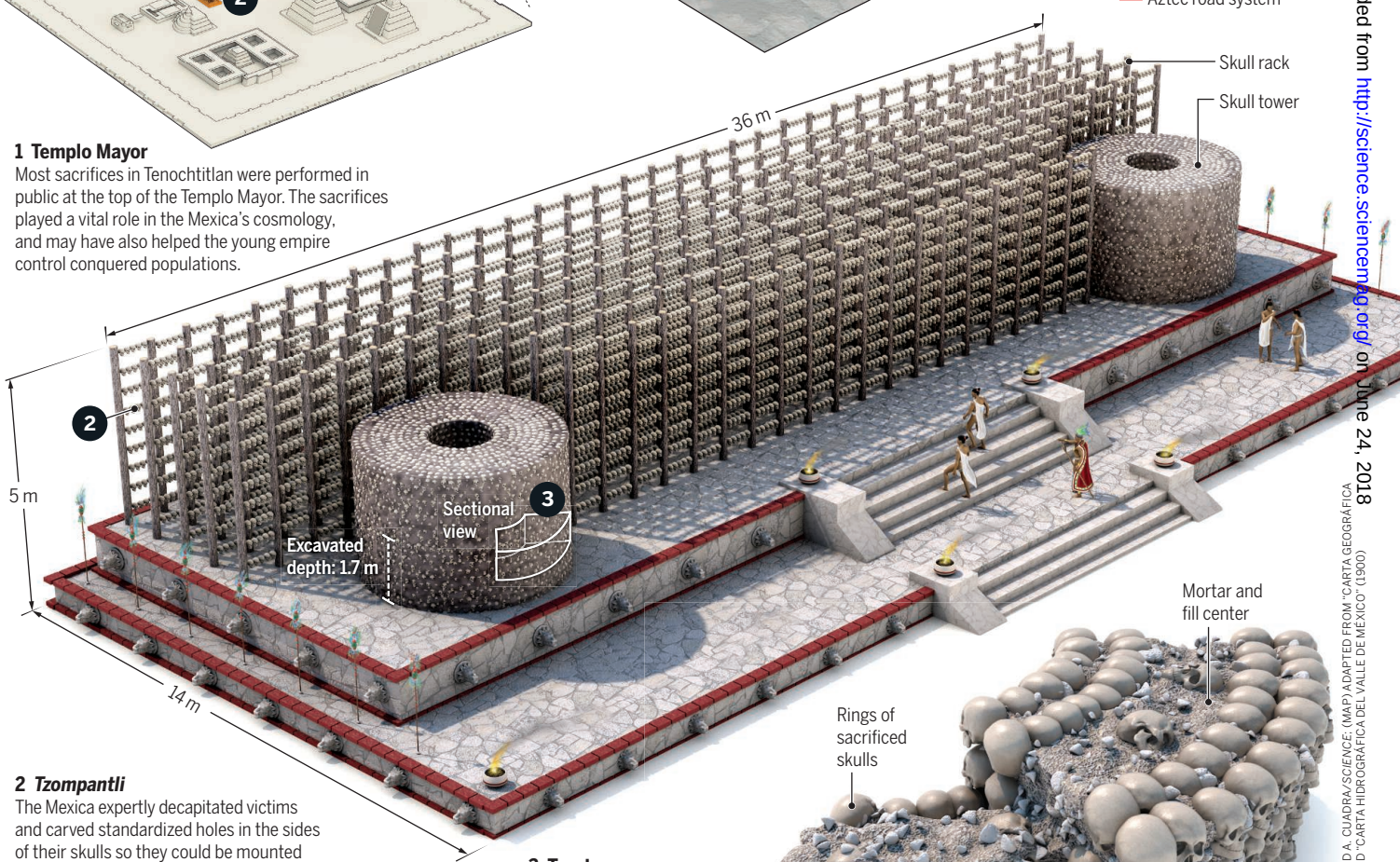

2 *Tzompantli*
The Mexica expertly decapitated victims and carved standardized holes in the sides of their skulls so they could be mounted onto the posts of a rack called the *tzompantli*, which held thousands of skulls.

3 Two towers
Built from skulls and mortar, towers at least 1.7 meters tall and likely taller flanked the *tzompantli*. These were built in phases, with skulls on the outer rings facing outward, and those on the inner rings facing inward.

CREDITS: (GRAPHIC) C. BICKEL AND A. CUADRA/*SCIENCE*; (MAP) ADAPTED FROM "CARTA GEOGRÁFICA DEL DISTRITO FEDERAL" (1899) AND "CARTA HIDROGRÁFICA DEL VALLE DE MÉXICO" (1900)

Published by AAAS

for," agrees John Verano, a bioarchaeologist at Tulane University in New Orleans, Louisiana, who studies human sacrifice. He and other researchers hope the skulls will clarify the role of large-scale human sacrifice in Mexica religion and culture—and whether, as scholars suspect, it played a key part in building their empire.

THE DISCOVERY of the *tzompantli* began the same way all the Urban Archaeology Program's digs do: with a planned construction project in the heart of downtown Mexico City. Whenever someone wants to build in a seven-block area around the Templo Mayor, Barrera Rodríguez's team must excavate first, salvaging whatever remains of the colonial and especially Mexica city beneath. The finds are often significant and surprisingly intact. The Templo Mayor itself came to light in the 1970s, when INAH archaeologists were called in after city electrical workers stumbled on an imposing circular statue of the goddess Coyolxauhqui, who was killed and dismembered by her brother Huitzilopochtli.

Much of the temple had survived to be discovered. The Mexica built it in seven phases between 1325 and 1521, each corresponding to the reign of a king. Each phase was built over and around the earlier ones, embedding the Templo Mayor's history within it like a set of Russian nesting dolls. Although the Spanish destroyed the temple's final phase, the smaller temples from earlier reigns were paved over but left relatively unscathed. Those ruins are now part of the Templo Mayor Museum. But many structures that surrounded the ruins remained hidden beneath the dense colonial city—and now, the modern megalopolis.

So when Barrera Rodríguez got the call to excavate a site just a few buildings down from where Guatemala Street dead-ends into the Templo Mayor complex, he knew the dig could lead to a major discovery. Starting in February 2015, his team dug about 20 test pits, unearthing modern debris, colonial porcelain, and, finally, the basalt slabs of a Mexica period floor. Then, he remembers, "Hundreds of skull fragments began to appear." In more than 2 decades of excavating in downtown Mexico City, he had never seen anything like it.

Barrera Rodríguez and INAH archaeologist and field supervisor Lorena Vázquez Vallín knew from colonial maps of Tenochtitlan that the *tzompantli*, if it existed, could be somewhere near their dig. But they weren't sure that's what they were seeing until they found the postholes for the skull rack. The wooden posts themselves had long since decayed, and the skulls once displayed on them had shattered—or been purposely crushed by the conquistadors. Still, the size and spacing of the holes allowed them to estimate the *tzompantli*'s size: an imposing rectangular structure, 35 meters long and 12 to 14 meters wide, slightly larger than a basketball court, and likely 4 to 5 meters high (see graphic, p. 1290). From their knowledge of the eras of the Templo Mayor, archaeologists estimate that the particular phases of the *tzompantli* they found were likely built between 1486 and 1502, although human sacrifice had been practiced in Tenochtitlan since its founding in 1325.

Nearby, the researchers also found skulls apparently stuck together with mortar—remnants of one of the towers flanking the *tzompantli*, where most skulls once exhibited on its posts ended their postmortem journey. The team spent a second season, from October 2016 to June 2017, excavating the *tzompantli* and the tower. At its largest, the tower was nearly 5 meters in diameter and at least 1.7 meters tall. Combining the two historically documented towers and the rack, INAH archaeologists now estimate that several thousand skulls must have been displayed at a time.

Other Mesoamerican cultures also engaged in human sacrifice and built *tzompantlis*. But, "The Mexica certainly brought this to an extreme," says Vera Tiesler, a bioarchaeologist at the Autonomous University

INAH archaeologists collected nearly 200 skulls from the tower flanking the *tzompantli*. Isotope and DNA studies, now underway, are expected to reveal that victims came from all over Mesoamerica.

PHOTOS: HÉCTOR MONTAÑO/INAH

of Yucatán in Mérida, Mexico. In her work at the Mayan city of Chichen Itza, founded some 700 years before Tenochtitlan and more than 1000 kilometers away, she found six skulls with holes in their sides that she suspects were once displayed on the posts of a *tzompantli*. However, the holes in each skull were less regular and uniform than those in the Tenochtitlan skulls. "That makes me think it was not a standardized practice yet," she says. "Tenochtitlan was the maximum expression [of the *tzompantli* tradition]."

Human sacrifice occupied a particularly important place in Mesoamerica. Many of the region's cultures, including the Maya and the Mexica, believed that human sacrifice nourished the gods. Without it, the sun would cease to rise and the world would end. And sacrificial victims earned a special, honored place in the afterlife.

Ritual killings in traditional cultures elsewhere in the world, including Asia and Europe, point to additional roles for the practice (*Science*, 18 May 2012, p. 834), and may help explain why the Mexica took it to such an extreme. "All premodern societies make some kind of offering," Verano says. "And in many societies, if not all, the most valuable sacrifice is human life." Social scientists who study religion have shown that costly offerings and painful rituals, such as the bloodletting ceremonies the Mexica also practiced, can help define and strengthen group identity—especially in societies that have grown too large for everyone to know everyone else (*Science*, 28 August 2015, p. 918).

Some researchers also argue that killing captives or subjects both establishes and reinforces hierarchy in large, complex societies. A 2016 *Nature* paper, for example, linked human sacrifice to the development of social stratification in dozens of traditional Austronesian cultures.

Many researchers say that, for the Mexica, political power as well as religious belief is likely key to understanding the scale of the practice. Theirs was a relatively young empire; during their 200-year reign, they conquered territory all over central and southern Mexico, sometimes facing tremendous resistance from local communities (some of which would later ally with the Spanish against the empire). Spanish chronicles describe Tenochtitlan's sacrificial victims as captives brought back from wars, such as those fought with their archenemy, the nearby republic of Tlaxcala (*Science*, 17 March 2017, p. 1114). Subject peoples in the Mexica Empire were also sometimes required to send individuals as tribute. "The killing of captives, even in a ritual context, is a strong political statement," Verano says. "It's a way to demonstrate power and political influence—and, some people have said, it's a way to control your own population."

"The more powerful a state was, the more victims it could dedicate," says Ximena Chávez Balderas, an INAH bioarchaeologist who spent years studying the remains of sacrificial victims in offerings in the Templo Mayor; she is now Verano's doctoral student at Tulane. The religious significance and political messaging of human sacrifice "go hand in hand," she says.

Some of the skulls displayed on the *tzompantli* were transformed into masks; this one's nose is an obsidian blade like those used in human sacrifice.

OVER TWO SEASONS of excavations, INAH archaeologists collected 180 mostly complete skulls from the tower as well as thousands of skull fragments. Now, those finds sit in a lab next to the Templo Mayor ruins, being painstakingly examined by a team led by INAH anthropologist Jorge Gómez Valdés. Cut marks on the skulls leave no doubt they were defleshed after death, and the decapitation technique appears clean and uniform. "[Mexica priests] had extremely impressive anatomical knowledge, which was passed down from generation to generation," Chávez Balderas says.

Goméz Valdés found that about 75% of the skulls examined so far belonged to men, most between the ages of 20 and 35—prime warrior age. But 20% were women, and 5% belonged to children. Most victims seemed to be in relatively good health before they were sacrificed. "If they are war captives, they aren't randomly grabbing the stragglers," Gómez Valdés says. The mix of ages and sexes also supports another Spanish claim, that many victims were slaves sold in the city's markets expressly to be sacrificed.

Chávez Balderas identified a similar distribution of sex and age in her studies of victims in smaller offerings within the Templo Mayor itself, which often contained skulls from the *tzompantli* that had been decorated and turned into eerie masks. Her colleagues also analyzed isotopes of strontium and oxygen that the teeth and bones had absorbed. The isotopes in teeth reflect the geology of a person's surroundings during childhood, whereas isotopes in bones show where a person lived before death. The results confirmed that the victims were born in various parts of Mesoamerica but had often spent significant time in Tenochtitlan before they were sacrificed. "They aren't foreigners who were brought into the city and directly to the ritual," Chávez Balderas says. "They were assimilated into the society of Tenochtitlan in some way." Barrera Rodríguez says some historical accounts record cases of captive warriors living with the families of their captors for months or years before being sacrificed.

Samples for isotopic analysis as well as ancient DNA studies have already been taken from many of the *tzompantli* skulls, Gómez Valdés says. He, too, expects to find a diversity of origins, especially because the *tzompantli* skulls display a variety of intentional dental and cranial modifications, which were practiced by different cultural groups at different times. If so, the skulls could yield information that extends far beyond how the victims died. "Hypothetically, in this *tzompantli*, you have a sample of the population from all over Mesoamerica," Vázquez Vallín says. "It's unparalleled."

Bioarchaeologist Tiffiny Tung of Vanderbilt University in Nashville, who studies human sacrifice in the Andes, says she is excited to see what the INAH team can learn from the skulls about sacrificial rituals and the genetic diversity of Mesoamerica just before the conquest. "We can go down literally to the individual person and tell that person's story. And then we can pull back and tell the story … about these big communities," she says. Once imbued with a sacred, but silent, role in the city where they died, those victims may finally speak again. ■

PHOTO: MOSTARDI PHOTOGRAPHY/ALAMY STOCK PHOTO

INSIGHTS

PERSPECTIVES

ECOLOGY

Mechanisms behind the monarch's decline

Migratory failure may contribute to the dwindling of this iconic butterfly's population

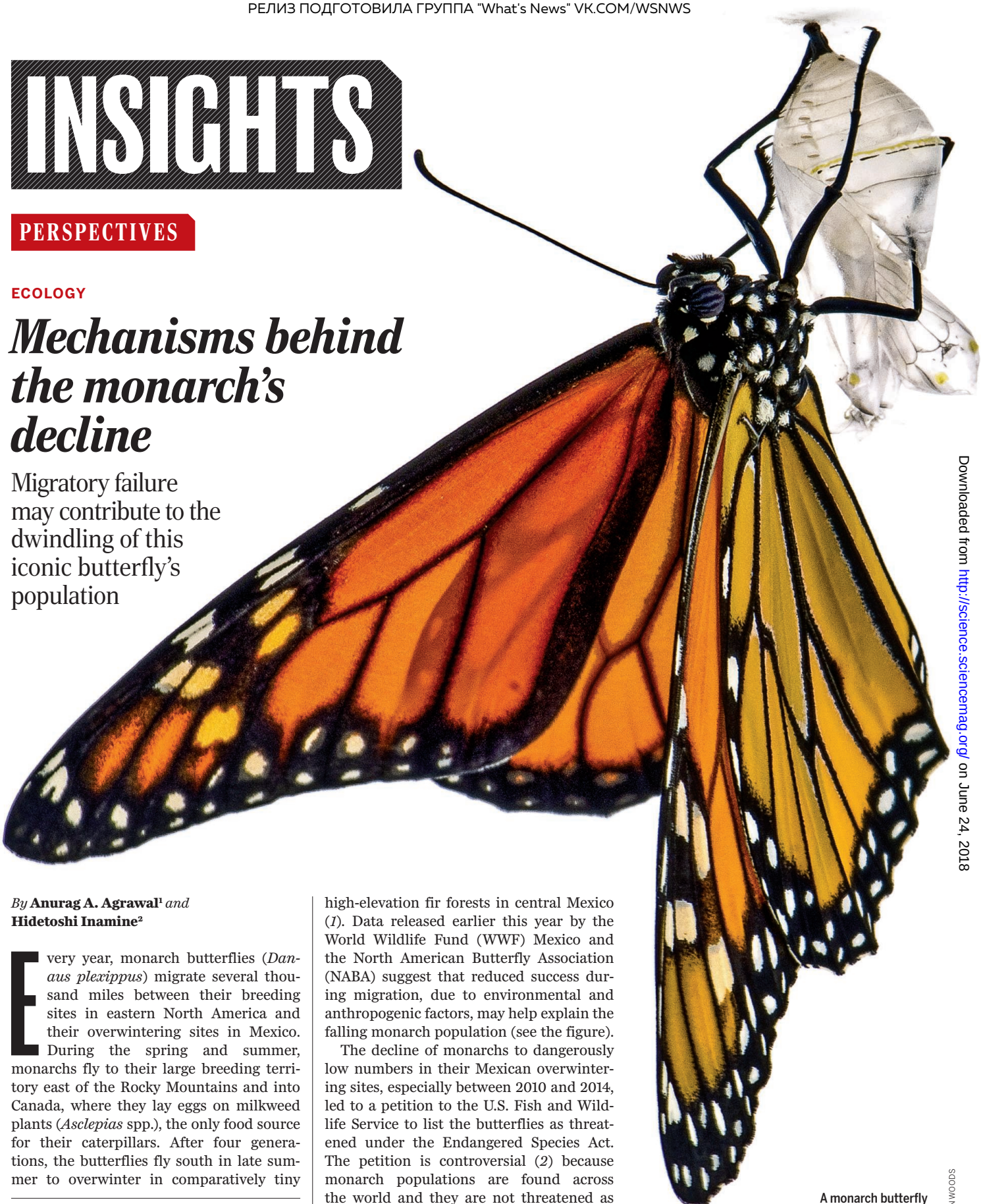

A monarch butterfly (*Danaus plexippus*), soon after emerging from its chrysalis

PHOTO: ELLEN WOODS

By **Anurag A. Agrawal**[1] *and* **Hidetoshi Inamine**[2]

Every year, monarch butterflies (*Danaus plexippus*) migrate several thousand miles between their breeding sites in eastern North America and their overwintering sites in Mexico. During the spring and summer, monarchs fly to their large breeding territory east of the Rocky Mountains and into Canada, where they lay eggs on milkweed plants (*Asclepias* spp.), the only food source for their caterpillars. After four generations, the butterflies fly south in late summer to overwinter in comparatively tiny high-elevation fir forests in central Mexico (*1*). Data released earlier this year by the World Wildlife Fund (WWF) Mexico and the North American Butterfly Association (NABA) suggest that reduced success during migration, due to environmental and anthropogenic factors, may help explain the falling monarch population (see the figure).

The decline of monarchs to dangerously low numbers in their Mexican overwintering sites, especially between 2010 and 2014, led to a petition to the U.S. Fish and Wildlife Service to list the butterflies as threatened under the Endangered Species Act. The petition is controversial (*2*) because monarch populations are found across the world and they are not threatened as a species. However, the sustainability of their long-distance migration in the Americas is in question, and understanding the

[1]*Department of Ecology and Evolutionary Biology, Cornell University, Ithaca, NY, USA.* [2]*Department of Biology, Pennsylvania State University, University Park, PA, USA. Email: agrawal@cornell.edu*

mechanisms driving their decline is crucial to reversing the trend. Monarchs have experienced a decline over decades and face diverse threats, including extreme weather, pesticides, habitat loss, and disease (table S1). The U.S. Fish and Wildlife Service is required by law to reach a decision about federal protection by June 2019.

Population dynamics of migratory animals must be understood in terms of ecological limits across the whole cycle of breeding, migration, and overwintering (*3*). For monarchs, this challenging task has been advanced not only by traditional academic work, but by 25 years of monitoring by nongovernmental organizations like the WWF and by large numbers of citizen scientists (table S2). This collaborative effort has provided clear evidence for a precipitous decline of monarchs during overwintering in Mexico and during their first generation in spring in the gulf states of the southern United States (*4*). However, evidence of this decline diminishes during the next three summer generations as monarchs migrate to the Midwest and Northeast of the United States and into Canada (see the figure).

Agricultural intensification, particularly the widespread adoption of herbicide-tolerant crops in the Midwest, has reduced the availability of milkweed as a food source for monarch caterpillars, and this has been championed as the cause of the monarch's decline (*5*). Although the number of eggs produced regionally has declined substantially in the Midwest (*6*), this trend is ambiguous in the Northeast and in broadscale counts of adult butterflies (*4*, *7*). Mortality during the annual autumnal migration to Mexico has received less attention, but its potential role in the decline was implicated by studies attempting to connect the abundance of migrating butterflies in late summer to the abundance of those that arrived in Mexico (*4*, *8*, *9*).

Mortality during migration threatens other migratory animals (*10*) and may have increased in recent years for monarchs, potentially contributing to the declines in the overwintering population. For example, the abundance of monarchs was one of the highest in decades in the Northeast during the 2017 breeding season, but in the subsequent winter, the population was well below historic levels in Mexico. The autumn of 2017 was the hottest in over 100 years, and the extended warmth induced an extra generation of butterflies late in summer. This delayed much of the monarch migration, potentially changing the rate of migratory success. Stress during the breeding season and migration may affect not only migratory success, but also the likelihood of overwinter survival and the subsequent northbound migration in spring. Continued degradation of the fir forests in the Monarch Butterfly Biosphere Reserve in Mexico could also explain declining numbers through reduced migratory success (*11*–*13*).

Butterfly migrants cease to rely on milkweed at the end of the summer. Instead, they depend on floral nectar from a range of plants, water to drink, and safe passage for their journey to Mexico. Thus, the connection between the summer and winter abundance, and factors that may disrupt migratory success, is critical for guiding monarch conservation (*4*, *8*, *9*).

Regardless of whether summer monarch abundance correlates with winter abundance on average, it is clear that migratory success is highly variable from one year to the next (see the figure). The latest data from 2017 are a case in point, showing no obvious correlation between summer and winter abundances. If nectar resources, landscape quality, and intact overwintering sites con-

Threats to migratory success

Monarch butterflies overwinter in Mexico and breed primarily in the Midwestern and Northeastern United States and Canada. Conservation efforts are focused on protecting overwintering forests in Mexico and restoring milkweed in breeding areas. Migratory mortality may also play a role in falling populations at overwintering sites (see graph to the right), but the connectivity between summer and winter populations is complex and little understood.

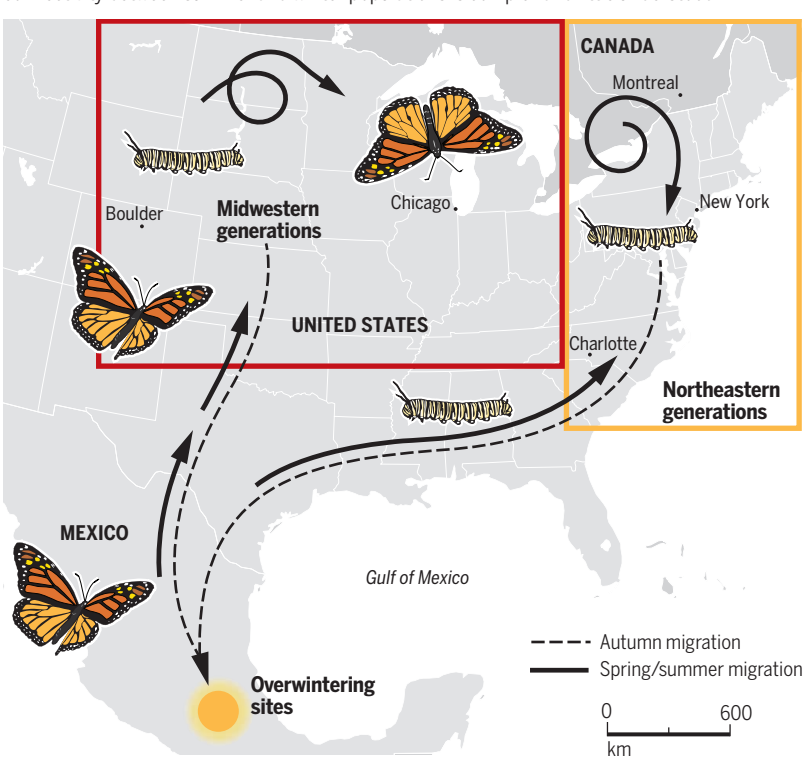

GRAPHIC: N. CARY/SCIENCE

Populations at overwintering sites. Over the past 25 years, monarch populations have fallen substantially at their overwintering sites in fir forests in Mexico. Data from WWF Mexico.

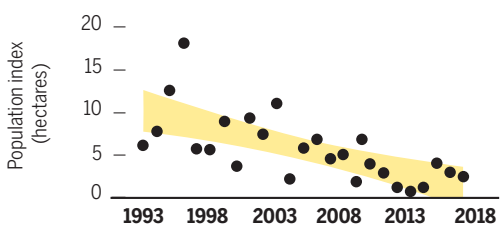

Populations in the Midwest and Northeast. Populations fluctuate widely from year to year, with no obvious trend or pattern. See supplementary materials for data sources and analysis.

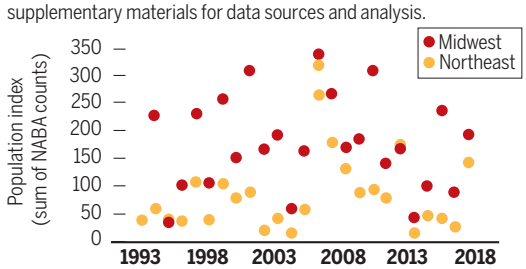

Relative population index for each region by year. Values are standardized by the 10-year average for that region (2008–2017). Population estimates in the breeding season are often not associated with those of the overwintering sites.

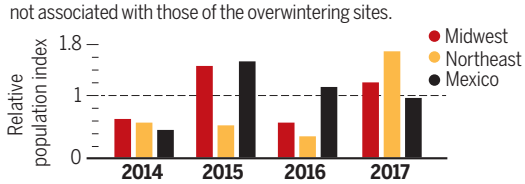

Published by AAAS

tinue to degrade, the discordance between summer and winter abundances may amplify. Contributing factors reducing the success of the monarch migration may also include sublethal effects of pesticides, road mortality, and increasing levels of disease (table S1). Planting regionally native milkweeds could buffer the monarch's population but will not alleviate migratory mortality.

Recent evidence points to a decline beginning >45 years ago in another U.S. population of monarchs, which migrates within California (*14*). Such long-term and broadscale negative population trends suggest continent-wide changes that transcend single explanations such as herbicide-tolerant crops.

Modeling efforts are helping to elucidate the causes of the shrinking monarch populations (*13*), but as is the case for most declining species, multiple stressors likely conspire. Long-term monitoring must continue but is especially important in the southern United States and northern Mexico to estimate population sizes midmigration to and from the overwintering sites. Statistical analysis of the >25 years of monarch tagging data will likely shed light on migratory mortality and would be a boon from the hard work of citizen scientists (*15*). Beyond migratory mortality, latent negative effects of environmental and anthropogenic factors experienced during migration may affect overwintering itself and are in need of attention. ■

REFERENCES AND NOTES

1. A. A. Agrawal, *Monarchs and Milkweed: A Migrating Butterfly, a Poisonous Plant, and Their Remarkable Story of Coevolution* (Princeton Univ. Press, Princeton, NJ, 2017).
2. D. Wagner, T. Gilligan, J. Shuey, *News Lepid. Soc.* **56**, 190 (2014).
3. P. P. Marra, E. B. Cohen, S. R. Loss, J. E. Rutter, C. M. Tonra, *Biol. Lett.* **11**, 20150552 (2015).
4. H. Inamine, S. P. Ellner, J. P. Springer, A. A. Agrawal, *Oikos* **125**, 1081 (2016).
5. J. M. Pleasants *et al.*, *PLOS ONE* **12**, e0181245 (2017).
6. J. M. Pleasants, K. S. Oberhauser, *Insect Conserv. Divers.* **6**, 135 (2013).
7. S. P. Saunders, L. Ries, K. S. Oberhauser, W. E. Thogmartin, E. F. Zipkin, *Ecography* **41**, 278 (2018).
8. L. Ries, D. J. Taron, E. Rendón-Salinas, *Ann. Entomol. Soc. Am.* **108**, 691 (2015).
9. G. Badgett, A. K. Davis, *Ann. Entomol. Soc. Am.* **108**, 700 (2015).
10. D. S. Wilcove, M. Wikelski, *PLOS Biol.* **6**, e188 (2008).
11. O. Vidal, J. López-García, E. Rendón-Salinas, *Conserv. Biol.* **28**, 177 (2014).
12. L. P. Brower *et al.*, *Am. Entomol.* **62**, 92 (2016).
13. W. E. Thogmartin *et al.*, *Open Science* **4**, 170760 (2017).
14. A. E. Espeset *et al.*, *Oecologia* **181**, 819 (2016).
15. A. K. Davis, *Insect Conserv. Divers.* **8**, 103 (2015).

SUPPLEMENTARY MATERIALS

www.sciencemag.org/content/360/6395/1294/suppl/DC1

ACKNOWLEDGMENTS

Cornell University's Atkinson Center for a Sustainable Future provided support, J. Springer (NABA) compiled the citizen science data, and J. Thaler and two anonymous reviewers provided comments.

10.1126/science.aat5066

ANTHROPOLOGY

How did Homo sapiens *evolve?*

Genetic and fossil evidence challenges current models of modern human evolution

By **Julia Galway-Witham** *and* **Chris Stringer**

Over the past 30 years, understanding of *Homo sapiens* evolution has advanced greatly. Most research has supported the theory that modern humans had originated in Africa by about 200,000 years ago, but the latest findings reveal more complexity than anticipated. They confirm interbreeding between *H. sapiens* and other hominin species, provide evidence for *H. sapiens* in Morocco as early as 300,000 years ago, and reveal a seemingly incremental evolution of *H. sapiens* cranial shape. Although the cumulative evidence still suggests that all modern humans are descended from African *H. sapiens* populations that replaced local populations of archaic humans, models of modern human origins must now include substantial interactions with those populations before they went extinct. These recent findings illustrate why researchers must remain open to challenging the prevailing theories of modern human origins.

> ***"...researchers must remain open to challenging the prevailing theories of modern human origins."***

Although living humans vary in traits such as body size, shape, and skin color, they clearly belong to a single species, *H. sapiens*, characterized by shared features such as a narrow pelvis, a large brain housed in a globular braincase, and reduced size of the teeth and surrounding skeletal architecture. These traits distinguish modern humans from other now-extinct humans (members of the genus *Homo*), such as the Neandertals in western Eurasia (often classified as *H. neanderthalensis*) and, by inference, from the Denisovans in eastern Eurasia (a genetic sister group of Neandertals). How did *H. sapiens* relate to these other humans in evolutionary and taxonomic terms, and how do those relationships affect evolving theories of modern human origins?

By the 1980s, the human fossil record had grown considerably, but it was still insufficient to demonstrate whether *H. sapiens* had evolved from local ancestors across much of the Old World (multiregional evolution) or had originated in a single region and then dispersed from there (single origin). In 1987, a study using mitochondrial DNA from living humans (*1*) indicated a recent and exclusively African origin for modern humans. In the following year, one of us coauthored a review of the fossil and genetic data, expanding on that discovery and supporting a recent African origin (RAO) for our species (*2*).

The RAO theory posits that by 60,000 years ago, the shared features of modern humans had evolved in Africa and, via population dispersals, began to spread from there across the world. Some paleoanthropologists have resisted this single-origin view and the narrow definition of *H. sapiens* to exclude fossil humans such as the Neandertals (*3*). In subsequent decades, genetic and fossil evidence supporting the RAO theory continued to accumulate, such as in studies of the genetic diversity of African and non-African modern humans (*4*) and the geographic distribution of early *H. sapiens* fossils (*5*), and this model has since become dominant within mainstream paleoanthropology. In recent years, however, new fossil discoveries, the growth of ancient DNA research, and improved dating techniques have raised questions about whether the RAO theory of *H. sapiens* evolution needs to be revised or even abandoned.

Different views on the amount of genetic and skeletal shape variation that is reasonably subsumed within a species definition directly affect developing models of human origins. For many researchers, the anatomical distinctiveness of modern humans and Neandertals has been sufficient to place them in separate species; for example, variation in traits such as cranial shape and the anatomy of the middle and inner ears are greater between Neandertals and *H. sapiens* than between well-recognized species of apes (*6*). Yet, Neandertal genome sequences and the discovery of past interbreeding between Neandertals and *H. sapiens* (*7*) provide support for their belonging to the same species

Centre for Human Evolution Research (CHER), Department of Earth Sciences, Natural History Museum, London SW7 5BD, UK. Email: j.galway-witham@nhm.ac.uk; c.stringer@nhm.ac.uk

under the biological species concept, and this finding has revived multiregionalism (*8*). The recent recognition of Neandertal art (*9*) further narrows—or for some researchers removes—the perceived behavioral gap between the two supposed species.

These challenges to the uniqueness of *H. sapiens* were a surprise to many and question assignments of hominin species in the fossil record. However, the limitations of the biological species concept have long been recognized (*10*). If it were to be implemented rigorously, many taxa within mammals—such as those in *Equus*, a genus that includes horses, donkeys, and zebras—would have to be merged into a single species. Nevertheless, in our view, species concepts need to have a basis in biology. Hence, the sophisticated abilities of Neandertals, however interesting, are not indicative of their belonging to *H. sapiens*. The recently recognized interbreeding between the late Pleistocene lineages of *H. sapiens*, Neandertals, and Denisovans is nonetheless important, and the discovery of even more compelling evidence to support Neandertals and modern humans belonging to the same species would have a profound effect on models of the evolution of *H. sapiens* (*8*).

Until recently, the oldest known fossils of *H. sapiens* came from east Africa, dated to 150,000 to 200,000 years ago (*5*); these specimens display most of the features that we associate with members of our lineage. Many researchers interpreted the emergence of this suite of traits in Africa, before *H. sapiens* dispersals into Eurasia, as important evidence in favor of RAO. However, recent research suggests that the derived traits of modern humans did not evolve together; rather, a modern-looking face appeared first, with a globular braincase evolving later (*11*). This pattern is exemplified by the cranial fossils from Jebel Irhoud, Morocco, which were recently redated to ~300,000 years old and which many researchers consider to be the oldest known examples of the *H. sapiens* lineage (*12*). The Jebel Irhoud specimens appear to represent an early iteration of the species in which some traits (such as a less-projecting face) were already present, but the typical braincase shape of modern humans had yet to evolve.

The apparently prolonged evolution of *H. sapiens* has raised questions about the extent of anatomical modernity that is necessary or sufficient for classifications of early *H. sapiens*. This has led to suggestions that ancient hominin populations in China (represented by the Dali fossil, which is roughly contemporaneous with those from Jebel Irhoud) could have been involved in modern human origins. If this is the case, it challenges the exclusivity of Africa in the evolution of the derived traits of *H. sapiens*, providing sup-

Recent African origin, with modifications

Recent discoveries provide insight into scenarios of how *H. sapiens* spread around the world.

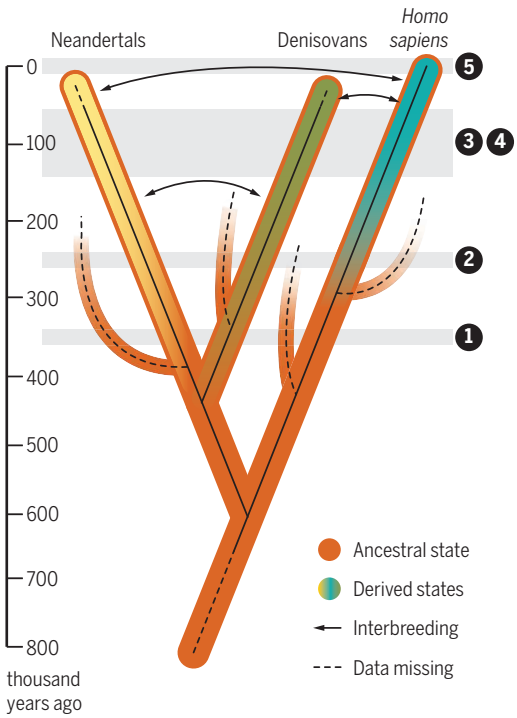

1 Neandertal and Denisovan traits are beginning to emerge in Eurasia.

2 Neandertal and Denisovan traits continue to develop and spread; traits associated with *H. sapiens* begin to emerge across Africa; Africa and Eurasia remain isolated.

3 Novel *H. sapiens* traits evolve in Africa; *H. sapiens* disperse into Eurasia, with areas of interbreeding at the overlapping ranges with Neandertals and Denisovans (RAOWH).

4 Alternatively, *H. sapiens* traits spread into Eurasia, with more extensive blending between *H. sapiens*, Neandertals, and Denisovans; novel *H. sapiens* traits evolve in Africa, but the interbreeding between the various species may catalyze the evolution of new traits (AM).

5 Portions of Neandertal and Denisovan genes are distributed across populations of *H. sapiens* today.

Maps showing schematic slices through phylogeny

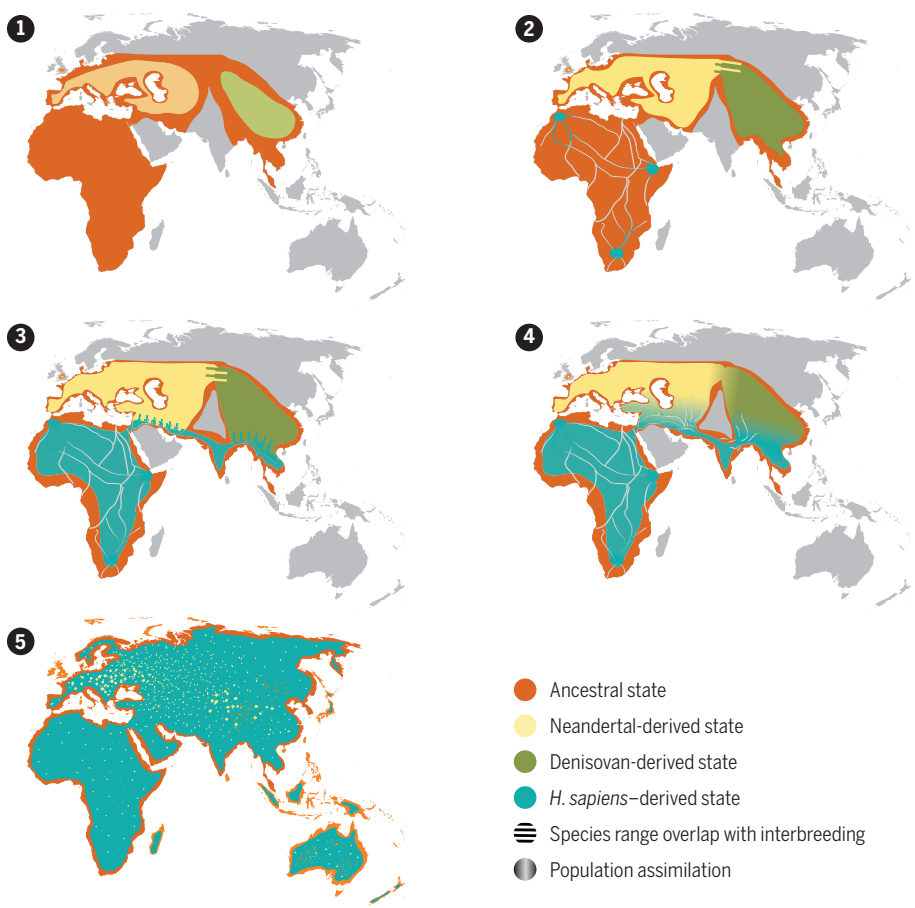

GRAPHIC: N. DESAI/*SCIENCE*

port for multiregionalism. However, resemblances between the Dali and Jebel Irhoud crania seem to be mainly based on primitive retentions rather than evolutionary novelties. The supposedly derived facial shape of early members of *H. sapiens,* such as those at Jebel Irhoud, may actually be more ancient, possibly tracing back to the common ancestor with Neandertals (*5*) (see the figure).

The apparently more deeply rooted origin of *H. sapiens* adds to the problem of how scientists can delineate *H. sapiens* from other species in an evolutionarily meaningful way and suggests that the species did not evolve as recently as previously envisaged. However, evidence of evolutionary novelty in the fossil record of putative *H. sapiens* still appears relatively recently in Africa, compared to a multiregional view of human evolution (in which *H. sapiens* began to evolve at least 1.8 million years ago). Within Africa, it is currently unclear whether the origin of *H. sapiens* was localized, as in some early RAO formulations, or involved a process similar to multiregional evolution, but operating purely within the continent (*5*, *13*).

With only a few dissenters, the strictest versions of both RAO (which denies interbreeding with other lineages or species) and multiregionalism (which argues for an interbreeding network of one species over the past ~1.8 million years) are now generally regarded as falsified. Instead, two intermediate theories best accommodate the complex interactions between hominin taxa ~40,000 to 100,000 years ago (*8*, *14*): RAO with hybridization (RAOWH) and the assimilation model (AM) (see the figure).

The two theories differ in their reconstructions of the processes by which the DNA of dispersing *H. sapiens* populations mixed with those of other populations outside of Africa. AM emphasizes demic diffusion, in which populations of African-derived *H. sapiens* and Eurasian Neandertals and Denisovans would have mixed over wide areas. Genes would have flowed gradually between these regional populations, catalyzing genetic and anatomical changes and leading to the spread of modern traits. In contrast, RAOWH envisages *H. sapiens* genes as largely entering and traversing Eurasia within the bodies of dispersing humans of African origin. Along the way there were successful hybridization events with indigenous populations, but these were effectively absorbing fragmented populations of indigenes in a relatively rapid replacement process, where they overlapped. Debate continues over what constitutes necessary or sufficient evidence for either theory.

The low percentage of surviving Neandertal DNA in the human genome seems to reflect a replacement process, but the much greater amount (~6%) of Neandertal plus Denisovan-like DNA persisting in some extant Oceanian populations (*7*) may indicate more extensive interactions. In addition, growing evidence for a longer-term coexistence of *H. sapiens* and other lineages outside of Africa extends the potential for interactions in both time and space, consistent with AM (*15*). It may be that at the scale of human generations, the processes resembled assimilation, whereas viewed through the lens of deeper time, they look more like the replacement envisaged in RAOWH.

RAO has required modifications in light of new data over the past 30 years, but the accumulation of evidence still points to the evolution of the shared anatomical features of *H. sapiens* as an African phenomenon. How the ancestral populations interacted within Africa now looks unclear (*5*, *13*). Genomes have not been successfully reconstructed from African fossils older than about 15,000 years, but if such data become available, they will hopefully clarify many of the remaining uncertainties. With the growing influx of new analytical techniques and discoveries within and outside Africa, it is imperative that researchers continue to rigorously challenge our theories and that they remain aware of their limitations. ■

"...evidence of evolutionary novelty in the fossil record of putative* H. sapiens *still appears relatively recently in Africa..."

REFERENCES AND NOTES

1. R. L. Cann, M. Stoneking, A. C. Wilson, *Nature* **325**, 31 (1987).
2. C. B. Stringer, P. Andrews, *Science* **239**, 1263 (1988).
3. M. Wolpoff, R. Caspari, *Race and Human Evolution* (Simon and Schuster, London, 1997).
4. N. Yu *et al.*, *Genetics* **161**, 269 (2002).
5. C. B. Stringer, *Philos. Trans. R. Soc. London Ser. B* **371**, 20150237 (2016).
6. A. Stoessel, P. Gunz, R. David, F. Spoor, *J. Hum. Evol.* **91**, 1 (2016).
7. R. Nielsen *et al.*, *Nature* **541**, 302 (2017).
8. C. B. Stringer, *Trends Ecol. Evol.* **29**, 248 (2014).
9. D. L. Hoffmann *et al.*, *Science* **359**, 912 (2018).
10. F. E. Zachos, *Species Concepts in Biology: Historical Development, Theoretical Foundations and Practical Relevance* (Springer, 2016).
11. S. Neubauer, J.-J. Hublin, P. Gunz, *Sci. Adv.* **4**, eaao5961 (2018).
12. J.-J. Hublin *et al.*, *Nature* **546**, 289 (2017).
13. E. Scerri, *New Sci.* **238**, 34 (2018).
14. F. H. Smith *et al.*, *Quat. Int.* **450**, 126 (2017).
15. C. J. Bae, K. Douka, M. D. Petraglia, *Science* **358**, eaai9067 (2017).

ACKNOWLEDGMENTS

The authors' work is supported by the Calleva Foundation and the Human Origins Research Fund.

10.1126/science.aat6659

NEUROSCIENCE

Aberrant choice behavior in alcoholism

Impaired neurotransmitter clearance in the amygdala is implicated in alcoholism

By **Rainer Spanagel**

More than 2 billion people worldwide regularly drink alcohol. Alcohol is a component cause of more than 200 diseases and causes ~3.3 million deaths per year globally (*1*). The major disease burden comes from harmful alcohol consumption and alcohol dependence. Not everyone who regularly consumes alcohol becomes dependent: ~15% become engaged in harmful and compulsive alcohol drinking (*2*). Patients suffering from alcohol dependence no longer have the freedom to choose between alternative rewards because alcohol drinking dictates what should be done next, namely, shaping activities for the next drink. On page 1321 of this issue, Augier *et al.* (*3*) demonstrate that aberrant choice behavior—that is, choosing alcohol over an alternative reward—is a key driver for the transition from controlled to compulsive alcohol use. They also provide a mechanistic understanding of this aberrant choice behavior that could lead to new treatment opportunities.

Why do only a subset of individuals exhibit this aberrant choice behavior and become dependent on alcohol? Alcoholism is the result of cumulative responses to alcohol exposure, the genetic makeup of an individual, and environmental perturbations over time. This complex gene-environment interaction leads to heterogeneity in disease course (*4*). There are several key processes that drive the progression to alcoholism: the formation of habits (*5*), the development of increased craving for alcohol in response to conditioned cues and stress (*6*), and increasingly impaired behavioral control (*7*). Augier *et al.* introduce aberrant choice behavior—

Institute of Psychopharmacology, Central Institute of Mental Health, University of Heidelberg, Mannheim, Germany. Email: rainer.spanagel@zi-mannheim.de

characterized by reduced sensitivity to alternative rewards—as another key driver for the transition to compulsive alcohol use.

We have little understanding of the neurobiological and molecular mechanisms underlying aberrant choice behavior. This is because an appropriate animal model has been lacking. Augier *et al.* provide an animal model in which they developed a choice-based method to identify rats that self-administer alcohol at the expense of a high-value alternative, a sweet saccharin solution, and assessed whether these animals show other characteristics of clinical alcoholism.

Of 620 rats, 95 (15%) preferred alcohol and developed signs of alcohol dependence, such as increased motivation to obtain alcohol and continued use despite adverse consequences. Specifically, rats continued to self-administer alcohol despite quinine taste or delivery of a shock punishment contingent on alcohol delivery, which are clear indications of compulsivity and no longer being under behavioral control. The proportion of rats exhibiting this aberrant choice behavior and characteristics of alcoholism is remarkable because it corresponds to the proportion of humans that develop alcohol dependence among those that regularly consume alcohol. The value of animal models for understanding human psychiatric disorders is increasingly criticized because preclinical studies often produce false-positive results that do not translate to the clinical situation. However, it should be noted that for other drugs of abuse, such as cocaine (*8*), the proportion of animals reaching addiction criteria also corresponds precisely to the prevalence rates of addicts within a user population.

Why does only a subset of laboratory rats show aberrant choice behavior? Augier *et al.* investigated the underlying molecular differences between rats that prefer the saccharin solution and the alcohol-preferring subgroup. Differential gene expression analyses in brain areas known to be involved in mediating the symptoms of clinical alcoholism (*9*) revealed pronounced differences in the amygdala between the two groups. Pathway analysis identified a cluster of differentially regulated genes implicated in γ-aminobutyric acid (GABA)–mediated neurotransmission. In particular, the gene encoding GABA transporter 3 (GAT-3) was decreased in the amygdala of alcohol-preferring rats. GABA is the most important inhibitory transmitter in the rodent and human brain, and GABA transporters regulate the amount of extracellular GABA. Reduced amounts of GAT-3 are indicative of increased extracellular GABA concentrations and thus enhanced constant (tonic) inhibition. In a series of electrophysiological and functional experiments, Augier *et al.* confirmed this assumption. In particular, they showed that decreased expression of GAT-3 in the amygdala of saccharin-preferring rats is sufficient to promote alcohol choice at the expense of a high-value alternative. Therefore, reduced GABA clearance within the central amygdala is a candidate mechanism for aberrant choice behavior and the subsequent development of alcohol dependence. Furthermore, reduced GAT-3 concentrations were found in the amygdala of deceased alcoholics, confirming this candidate mechanism in the human brain (see the figure). The central amygdala is known to be recruited during the transition to alcohol dependence and may serve as a potential integrative hub between anxiety disorders and alcohol dependence (*10*), which commonly co-occur in humans. Indeed, the alcohol-preferring rats show higher anxiety-like behavior (*3*).

The study of Augier *et al.* underlines the value of animal models for exploring addictive behavior (*11*). But are these findings of clinical relevance and do they provide insight for drug development? Small molecules targeting GABA clearance are a promising avenue. Such drugs could not only prevent an alcohol-preferring phenotype but might also be beneficial for the treatment of alcohol dependence, especially in those individuals with comorbid anxiety disorder. It is difficult to develop drugs that can enhance GAT-3 activity, but several small molecules that target increased extracellular GABA concentrations through their effects on other targets are under clinical development. One potent mechanism to lower extracellular GABA is the activation of presynaptically located metabotropic $GABA_B$ receptors ($GABA_B$-Rs) (*12*). Baclofen acts mainly as an agonist of $GABA_B$-Rs and is clinically used in France for treating alcohol dependence under a temporary recommendation by the French drug regulatory agency. However, several large clinical trials of baclofen show no or minimal efficacy for relapse prevention (*13, 14*), and the European Medicines Agency did not approve baclofen. Another drug, sodium oxybate, which acts as a $GABA_B$-R agonist and also binds to several other receptors (for example, extrasynaptic GABA receptors), is clinically used in Austria and Italy. It might be that sodium oxybate can normalize impaired GABA clearance in the amygdala. This assumption, however, needs experimental validation. Nevertheless, data from more than 260,000 alcohol-dependent patients treated with sodium oxybate show a good benefit-risk ratio, especially in drinkers with very high alcohol consumption (*15*). Given that life expectancy of alcohol-dependent patients with very high drinking levels is reduced by 22 years compared with the general population and ~90,000 of those drinkers die prematurely each year in the European Union (*15*), there is a pressing need for more effective treatments. ■

Regulating aberrant choice

Reduced GAT-3 levels augment extracellular GABA concentrations and thus enhance tonic inhibition within the amygdala. Medications such as sodium oxybate and baclofen may normalize enhanced tonic inhibition.

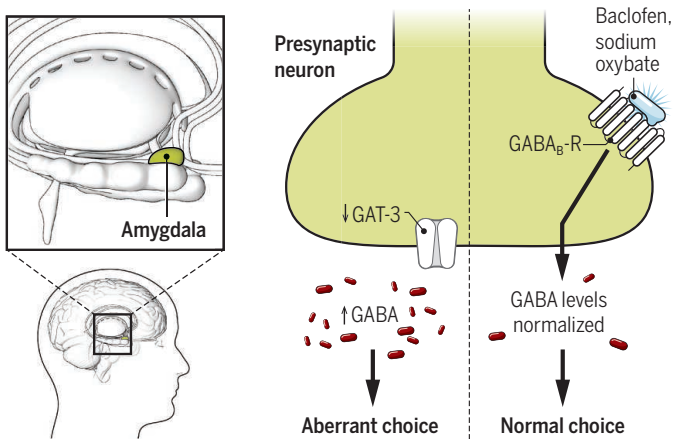

GRAPHIC: V. ALTOUNIAN/*SCIENCE*

REFERENCES AND NOTES

1. World Health Organization, Global status report on alcohol and health 2014 (WHO, Geneva, 2014).
2. J. C. Anthony *et al.*, *Exp. Clin. Psychopharmacol.* **2**, 244 (1994).
3. E. Augier *et al.*, *Science* **360**, 1321 (2018).
4. R. Spanagel, *Physiol. Rev.* **89**, 649 (2009).
5. B. J. Everitt, T. W. Robbins, *Annu. Rev. Psychol.* **67**, 23 (2016).
6. K. C. Berridge, T. E. Robinson, *Am. Psychol.* **71**, 670 (2016).
7. R. Z. Goldstein, N. D. Volkow, *Nat. Rev. Neurosci.* **12**, 652 (2011).
8. V. Deroche-Gamonet *et al.*, *Science* **305**, 1014 (2004).
9. H. R. Noori *et al.*, *Addict. Biol.* **17**, 827 (2012).
10. N. W. Gilpin *et al.*, *Biol. Psychiatry* **77**, 859 (2015).
11. R. Spanagel, *Dialogues Clin. Neurosci.* **19**, 247 (2017).
12. R. Agabio, G. Colombo, *Front. Neurosci.* **8**, 140 (2014).
13. E. M. Beraha *et al.*, *Eur. Neuropsychopharmacol.* **26**, 1950 (2016).
14. M. Reynaud *et al.*, *Alcohol Alcohol.* **52**, 439 (2017).
15. W. van den Brink *et al.*, *Addict. Biol.* **23**, 966 (2018).

ACKNOWLEDGMENTS

D&A Pharma, which produces sodium oxybate, supported an expert opinion dossier written by R.S. and others.

10.1126/science.aau0668

PLANT PATHOLOGY

Receptor networks underpin plant immunity

Plant-pathogen coevolution led to complex immune receptor networks

By **Chih-Hang Wu, Lida Derevnina, Sophien Kamoun**

Plants are attacked by a multitude of pathogens and pests, some of which cause epidemics that threaten food security. Yet a fundamental concept in plant pathology is that most plants are actively resistant to most pathogens and pests. Plants fend off their innumerable biotic foes primarily through innate immune receptors that detect the invading pathogens and trigger a robust immune response. The conceptual basis of such interactions was elegantly articulated by Harold H. Flor, who, in 1942, proposed the hypothesis that single genes in plants and pathogens define the outcome of their interactions; that is, a plant harboring a specific gene displays resistance against a pathogen that carries an interacting virulence gene (*1*). This gene-for-gene model was hugely insightful and influential—it has helped to guide applied and basic research on disease resistance. However, recent findings are taking the field beyond this simplified binary view of plant-pathogen interactions. Plants carry extremely diverse and dynamic repertoires of immune receptors that are interconnected in complex ways. Conversely, plant pathogens secrete a diversity of virulence proteins and metabolites called effectors, and pathogen genomics has revealed hundreds of effector genes in many species. These effectors have evidently evolved to favor pathogen infection and spread, but a subset of them inadvertently activate plant immune receptors. The emerging paradigm is that dynamic webs of genetic and biochemical networks underpin the early stages of plant-pathogen interactions.

Three layers of network complexity underpin plant response to pathogens (see the figure). First, sensor immune receptors can directly or indirectly detect molecules derived from pathogens. Second, many sensor receptors require coreceptors, helper receptors, or receptor-like regulatory scaffolds to translate pathogen recognition events into immune responses. Third, receptor complexes recruit distinct, but overlapping, downstream signaling components to generate a multifaceted innate immune response. Cross-talk at the receptor level is prevalent in plant immune networks and contributes to adjusting phenotypic outputs to biotic and abiotic environmental conditions, such as light and temperature (*2*, *3*).

Plant immune receptors are classed into cell surface receptors, including receptor-like kinases (RLKs) and receptor-like proteins (RLPs), or intracellular receptors of the nucleotide-binding domain and leucine-rich repeat–containing (NLR) family, both of which appear to form intricate receptor networks to mediate immune responses. The network feature of cell surface receptors is well established. RLKs and RLPs form various preformed and pathogen-activated complexes at the cell plasma membrane, which recruit receptor-like cytoplasmic kinases (RLCKs) to activate downstream immune signaling (*4*, *5*). RLKs in the somatic embryogenesis receptor kinase (SERK) family, such as SERK3 [also called BRASSINOSTEROID-ASSOCIATED KINASE 1 (BAK1)], participate in diverse cellular processes involved in development and immunity (*4*). Systemic analysis revealed that the extracellular leucine-rich repeat (LRR) domains of RLKs govern interactions between different receptors, forming an intricate network with multiple operational modules. Several RLKs, such as SERK3/BAK1 and ARTICULATION POINT EXECUTIVE (APEX), serve as interconnected cross-talk nodes or articulation points that help maintain network integrity. This reflects their essential roles in integrating multiple environmental stimuli and ensuring appropriate response modulation (*3*). Another RLK, SUPPRESSOR OF BIR1-1 (SOBIR1), is genetically and biochemically linked to RLPs in a network that also includes SERK3/BAK1 (*5*). An increased understanding of cell surface receptor networks and their connections to downstream components would enable manipulation of network nodes and fine-tuning of signaling outputs.

NLR proteins also engage in genetic and biochemical interactions that are more complex than anticipated (*6*, *7*). Many NLRs, which sense host-translocated pathogen effectors, require other NLR proteins to function, forming connections that vary from NLR pairs to networks. NLR pairs often operate through negative regulation, with the sensor NLR releasing its inhibition of helper NLR autoactivity upon pathogen perception. The concept of NLR networks is more recent, culminated through observations that some helper NLRs are functionally redundant and are required for the activities of multiple sensor NLRs. In asterid

Plant receptor networks

There are three mechanistic layers that contribute to immune complexity; each layer is represented by network nodes that may display functional redundancy, differential dependency (represented by arrow intensity), and specificity. These layers may also be targeted by pathogen effectors. This contrasts with the simplified binary view of the gene-for-gene hypothesis.

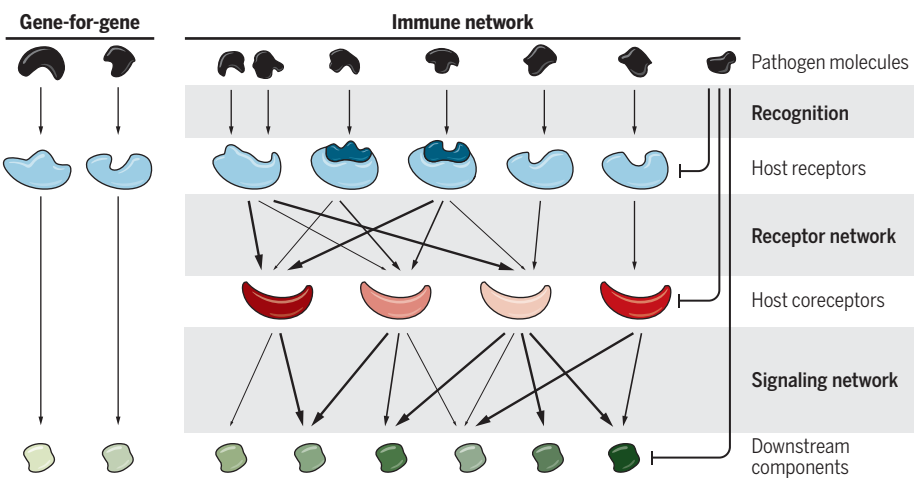

GRAPHIC: ADAPTED BY A. KITTERMAN/*SCIENCE*

The Sainsbury Laboratory, Norwich Research Park, Norwich NR4 7UH, UK. Email: sophien.kamoun@tsl.ac.uk

plants, such as tomato and tobacco, NRCs (NLR-required for cell death proteins) and NRC-dependent NLRs form a complex genetic network that operates against various pathogens and pests (*7*). The NRC network has evolved from an ancestral NLR pair that expanded to half of all NLRs in some asterid species. Similarly, paralogs of the plant *Arabidopsis thaliana* ACTIVATED DISEASE RESISTANCE PROTEIN 1 (ADR1) helper NLR family are required for the function of several *A. thaliana* NLRs, although their evolutionary relationships are currently unknown (*8*). Whether additional phylogenetic clades of NLRs and cell surface receptors form evolutionarily defined networks remains to be determined. It will be interesting to further explore the network architecture of these highly diversified receptors in an evolutionary context, as this may unravel genetic and biochemical relationships among plant immune receptors.

Networks require finely-tuned regulation for optimal function. Receptor network homeostasis is achieved through different regulatory processes, including gene expression, receptor complex formation, and activation of signal transduction. Genes encoding paired NLRs overwhelmingly occur in a head-to-head genomic configuration, possibly because they share the same promoter elements for coregulation (*9*). Presumably, tight coexpression is important for optimal function and to avoid autoimmunity and fitness costs. How plants regulate genetically unlinked receptors that engage in complex networks remains poorly understood. Transcription factors, chromatin regulation, alternative splicing, and small RNAs are among the mechanisms that modulate NLR transcript dosage and maintain network homeostasis (*10*, *11*). Plants have also evolved regulatory mechanisms to control receptor complex formation. Cell surface receptors form ligand-dependent complexes with other receptor proteins, which may function as bona fide coreceptors or as regulatory scaffolds that establish signaling complexes (*3*). Homeostasis by negative biochemical regulation is also a common process. Cell surface receptor complexes are negatively regulated by RLCKs, pseudokinases, phosphatases, and E3 ubiquitin ligases, resulting in multiple paths of network feedback mechanisms (*5*).

Why have immune receptor systems evolved into complex network architectures? Networks enhance evolvability and maintain robustness, prominent features of immunity in many biological systems (*12*). A key feature of plant immune receptor networks is the uncoupling of plant pathogen perception from initiation of downstream signaling and immune response. Thus, receptors devoted to sensing pathogen molecules are free to expand and evolve rapidly with reduced constraints. In addition, functionally redundant core elements bypass the need for specific signaling mechanisms against each pathogen and increase resilience to environmental or internal disturbances. The SERK family of RLKs and the NRC family of NLRs are examples of core elements that display some degree of redundancy (*4*, *7*). Such elements ensure that the immune system remains operational whenever a receptor becomes nonfunctional owing to mutation, deletion, or immunosuppression by pathogens.

Plant pathogens counteract host immunity by deploying effectors that target the multiple layers of immune networks. Pathogen effectors are highly redundant and repeatedly suppress key host pathways, but their activities can also activate NLR immunity (*13*). Thus, effector redundancy can be viewed as a form of evolutionary bet hedging (whereby an organism suffers a fitness disadvantage in normal conditions for increased fitness under stress) that enables pathogen populations to keep up with plant immunity. Conversely, redundant nodes in immune receptor networks may help the plant evade suppression by pathogen effectors, further contributing to the robustness of the immune system. That pathogen effectors can act as both triggers and suppressors of receptor-mediated immunity further highlights the complex coevolutionary dynamics that drive these interactions.

"...understanding of receptor network topology directly affects strategies for retooling the immune system of crop plants..."

How does the network view of plant immune systems affect breeding for disease resistance? The effectiveness of the plant immune system rests on its capacity to detect invading pathogens. To date, most approaches to improve plant immune receptors have focused on expanding their pathogen detection spectrum (*14*). A detailed understanding of receptor network topology directly affects strategies for retooling the immune system of crop plants for enhanced disease resistance. These include boosting the expression of coreceptors to intensify the immune response mediated by multiple receptors. Network architecture can be manipulated for broader receptor-coreceptor connections to extend the capacity of the immune network. Transfer of individual receptor genes across distantly related crops often fails. Delivery of receptor-coreceptors as paired or subnetwork units may increase the success of broadening disease resistance in crops. Finally, given that pathogens have evolved effectors to target immune receptors, it should be possible to generate receptor variants that evade pathogen suppression. This could prove particularly useful when the pathogen-targeted receptor is a critical node in the immune network.

A new field, studying plant immune receptor networks, is emerging. We postulate that Flor's intuitive gene-for-gene model is superseded by the systems view that plant immune receptors form networks with complex topology (*3*, *4*, *7*). Although some plant immune receptors may function as singletons, possibly combining both recognition and signaling activities into a single molecule, most cell surface and intracellular immune receptors appear to engage other receptors to function. In the network context, node connectivity between pathogen effectors and sensor receptors, sensors, and helper or coreceptors, as well as helpers and signaling elements, is dynamic and obeys rules of specificity and signal strength. Receptor networks also govern immunity in animals, with Toll-like cell surface receptors forming homo- or heterocomplexes, and NLRs such as neuronal apoptosis inhibitory protein (NAIP) immune receptors forming inflammasome megacomplexes with their NLRC4 (NLR family CARD domain–containing protein 4) helper (*6*, *15*). Some plant receptors are known to form complexes, but the degree to which they form megacomplexes similar to inflammasomes is unclear. Decrypting the biochemical codes that rule receptor-network wiring will help define the molecular basis of host immunity. Ultimately, an improved knowledge of immune systems could enable optimal use and deployment of immune receptors in agriculture. ■

REFERENCES

1. H. H. Flor, *Phytopathology* **32**, 653 (1942).
2. Y. Belkhadir, Y. Jaillais, *New Phytol.* **206**, 522 (2015).
3. E. Smakowska-Luzan *et al.*, *Nature* **553**, 342 (2018).
4. X. Ma *et al.*, *Trends Plant Sci.* **21**, 1017 (2016).
5. D. Couto, C. Zipfel, *Nat. Rev. Immunol.* **16**, 537 (2016).
6. J. D. G. Jones *et al.*, *Science* **354**, 1174 (2016).
7. C.-H. Wu *et al.*, *Proc. Natl. Acad. Sci. U.S.A.* **114**, 8113 (2017).
8. V. Bonardi *et al.*, *Proc. Natl. Acad. Sci. U.S.A.* **108**, 16463 (2011).
9. J. C. Stein *et al.*, *Nat. Genet.* **50**, 285 (2018).
10. Y. Lai, T. Eulgem, *Mol. Plant. Pathol.* **19**, 1267 (2017).
11. Y. Zhang *et al.*, *Mol. Biol. Evol.* **33**, 2692 (2016).
12. H. Kitano, K. Oda, *Mol. Syst. Biol.* **2**, 2006.0022 (2006).
13. J. Win *et al.*, *Cold Spring Harb. Symp. Quant. Biol.* **77**, 235 (2012).
14. S. Cesari, *New Phytol.* **219**, 17 (2018).
15. N. Gay *et al.*, *Nat. Rev. Immunol.* **14**, 546 (2014).

10.1126/science.aat2623

CHEMISTRY

Feel the dielectric force

The dielectric constant of water confined in nanoscale channels is far below that of bulk water

By **Sergei V. Kalinin**

Water is the foundational element of life. Its high melting and boiling temperatures relative to analogs such as hydrogen sulfide are a precondition to life. The density maximum at 4°C makes ice float, ensuring that lakes and oceans do not freeze on the bottom. The high surface tension of water enables insects to walk on its surface. Its high dielectric constant makes it an excellent solvent, a key property for many geochemical, biological, and technological processes. These properties can be traced to the strong hydrogen bonding in liquid water (*1*–*3*). On page 1339 of this issue, Fumagalli *et al.* (*4*) report on another property of liquid water that relates to its hydrogen bonding: the dielectric constant in thin water layers.

The behavior of water near interfaces and in confined systems is even more complex than the properties of bulk water. Both biological and energy applications are affected by the structure and energetics of electrochemical double layers formed by adsorbed and solvated ions. But although the importance of dielectric phenomena in water on these length scales is well recognized, experimental data have remained elusive. Macroscopic electrochemical data provide only the gross characteristics of interface capacitance that cannot be partitioned into components. Measurements in nanoscale devices that allow fundamental studies of ferroelectric materials cannot be extended to liquid layers.

Fumagalli *et al.* now report an elegant study of the dielectric properties of water under spatial confinement. They unambiguously demonstrate the presence of an anomalous or dead layer with a dielectric constant of only ~2—well below ~81 for liquid water—and a thickness of two to three molecules. These advances are made possible by the combination of two key technologies of modern nanoscience: scanning probe microscopy (SPM) and the fabrication of nanopatterned two-dimensional (2D) materials. SPM enables measurement of minute atomic-level forces (*5*, *6*) and, from these forces, magnetic, electrical, electromechanical, and elastic phenomena (*7*). In particular, Fumagalli *et al.* exploit the exquisite sensitivity of SPM to capacitive forces, which in turn are directly related to the dielectric properties of the material below the tip and can—with careful analysis of system geometry—be used for quantitative dielectric measurements (*8*).

However, SPM measurements yield information only on a product of the dielectric constant and the characteristic object size (in the current system, this is the depth of the channel). The second key element of this work is the use of 2D materials made from boron nitride (BN), a good dielectric that provides flat, clean surfaces. Traditionally, these materials are explored for their distinct electronic, optical, and transport properties (*9*–*11*), but for Fumagalli *et al.*, they serve as a structural material. The authors used a combination of patterning and deposition to create nanopatterned channels of varying depths, from subnanometer to hundreds of nanometers. They used surface deformation of the material, measured with SPM, to determine the degree of filling of the channel.

The authors took systematic measurements of dielectric forces as a function of channel depths, providing information of the average dielectric constant of water in the channels. They found this dependence to be well approximated by the two-capacitor model, in which one capacitor represents the water layer with bulk properties and the other represents the interfacial water, which is somewhat similar to the approach used for the analysis of ferroelectric dead layers (*12*, *13*). From this, they determined the characteristic thickness and dielectric constant of the dead layer (see the figure).

The spatial confinement of the water layer with subnanometer precision, together with force-based electrostatic measurements, allowed quantitative dielectric measurements in volumes that are a million times smaller than those studied with macroscopic techniques. The authors thereby definitively answer a question that has long vexed the scientific community.

The study is likely to both advance understanding of the properties of water and enable technological advances. Understanding electrostatic interactions in confined water volumes is key to understanding the biological functionalities of membranes, protein assembly, and myriad behaviors that underpin living systems. Knowledge of the dielectric behavior of water on small length scales is equally important to understanding energy and electrochemical systems. These data also provide a reference point with which to calibrate the performance of molecular dynamics and density functional calculations. Furthermore, the author's approach can be used to probe dielectric and ionic properties of self-assembled monolayers and to explore dynamic electric and dielectric responses in actively driven electrochemical systems. Their methodology thus opens a window to dielectric behaviors on nanometer scales, all through feeling the dielectric force. ■

Zooming in on the dead layer

By measuring electrostatic forces above a water-filled channel as a function of channel depth, Fumagalli *et al.* show that ultrathin water has a dielectric constant of ~2, below that of BN.

Deep channel

The electrostatic force above the channel is mostly determined by the conventional layer.

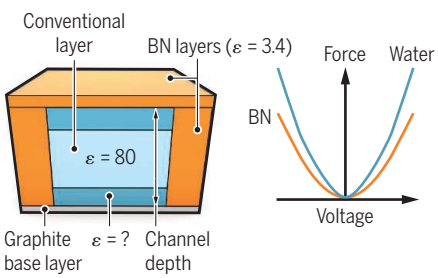

Shallow channel

The electrostatic force above the channel is mostly determined by the dead layer.

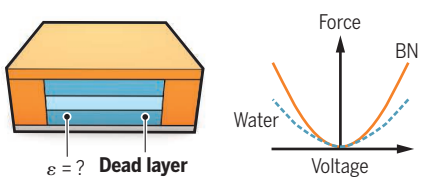

GRAPHIC: C. BICKEL/*SCIENCE*

The Institute for Functional Imaging of Materials and the Center for Nanophase Materials Sciences, Oak Ridge National Laboratory, Oak Ridge, TN 37831, USA. Email: sergei2@ornl.gov

REFERENCES

1. M. W. Mahoney, W. L. Jorgensen, *J. Chem. Phys.* **112**, 8910 (2000).
2. F. H. Stillinger, A. Rahman, *J. Chem. Phys.* **60**, 1545 (1974).
3. J. R. Errington, P. G. Debenedetti, *Nature* **409**, 318 (2001).
4. L. Fumagalli *et al.*, *Science* **360**, 1339 (2018).
5. C. Gerber, H. P. Lang, *Nat. Nanotechnol.* **1**, 3 (2006).
6. G. Binnig *et al.*, *Phys. Rev. Lett.* **56**, 930 (1986).
7. S. V. Kalinin, A. Gruverman, Eds., *Scanning Probe Microscopy: Electrical and Electromechanical Phenomena at the Nanoscale* (Springer, 2007), vols. 1 and 2.
8. G. Gramse *et al.*, *Nanotechnology* **20**, 395702 (2009).
9. A. K. Geim, K. S. Novoselov, *Nat. Mater.* **6**, 183 (2007).
10. A. K. Geim, I. V. Grigorieva, *Nature* **499**, 419 (2013).
11. K. S. Novoselov *et al.*, *Proc. Natl. Acad. Sci. U.S.A.* **102**, 10451 (2005).
12. C. Zhou, D. M. Newns, *J. Appl. Phys.* **82**, 3081 (1997).
13. A. A. Sirenko *et al.*, *Nature* **404**, 373 (2000).

10.1126/science.aat9875

POLICY FORUM

FOREST LOSS

Combating deforestation: From satellite to intervention

Near–real-time monitoring and response are possible

By **Matt Finer[1], Sidney Novoa[2], Mikaela J. Weisse[3], Rachael Petersen[3], Joseph Mascaro[4], Tamia Souto[1], Forest Stearns[4], Raúl García Martinez[2]**

Tropical forests are critically important for human livelihoods, climate stability, and biodiversity conservation but remain threatened (*1*). Recent years have seen major strides in documenting historical and annual tropical forest loss with satellites (*2*). Now, a convergence of satellite technologies and analytical capabilities makes it increasingly possible to monitor deforestation in near real time, on the scale of days, weeks, or months, rather than years (*3*, *4*). This advance creates greater potential for near–real-time action as well and could play a key role in achieving local, national, and international forest, biodiversity, and climate policy goals, as there is a global imperative to address deforestation. Challenges remain, however, to attaining effective policy action based on the new technology. On the basis of lessons learned from pioneering work in Brazil and Peru, we suggest at least two key factors for successfully linking the technical and policy realms. On the technical side, it is critical to capitalize on continually improving satellite technology to better detect, understand, and prioritize deforestation events. On the policy side, institution building, along with related civil-society engagement, is needed to facilitate effective action within complex government frameworks. We outline a five-step protocol for near–real-time tropical deforestation monitoring, with the goal of bridging the gap between technology and policy.

MORE AND BETTER EYES IN THE SKY

The number of Earth observation satellites, and the quality and accessibility of the imagery they provide, has greatly improved in recent years (see the first figure) (*5*), making satellite imagery the most consistent and effective tool for large-scale forest monitoring. Satellite-based monitoring has four key considerations: spatial resolution, temporal resolution, sensor type, and data access. Spatial resolution (that is, pixel size) has been steadily increasing since the 1970s (see the first figure), trending from coarse (>250 m) to medium (10 to 30 m) to high (<5 m). Temporal resolution (frequency of imagery for any given location) has also improved. Until recently, there had been a trade-off between spatial and temporal resolution, with higher-resolution sensors covering less area per day. For example, NASA's coarse-resolution MODIS (Moderate Resolution Imaging Spectroradiometer) sensor collects optical imagery of every point daily, whereas medium-resolution Landsat has a revisit time of 16 days. However, constellations of miniature satellites (such as the 175 satellites of the company Planet) address the trade-off, by providing high-resolution (3 m) optical imagery with near-daily frequency (*6*).

Though cloud cover often limits the availability of usable optical satellite imagery, radar sensors can penetrate clouds. The European Space Agency's new Sentinel-1 satellites offer medium-resolution radar data on a regular basis for every point on Earth (for example, every 12 days in the Amazon), regardless of the weather conditions.

Cost can limit access to some imagery. Although coarse- and medium-resolution imagery from U.S. and European governments is freely available (MODIS, Landsat, and Sentinel), high-resolution imagery from companies such as Planet (including RapidEye), DigitalGlobe, and Airbus is available commercially and tends to be costly. However, the public- versus commercial-access gap is closing. For example, Europe's new Sentinel-2 satellite freely offers 10-m-resolution optical imagery every 4 days (*7*), and Sentinel-1 is the first radar satellite that provides freely available data. Planet now displays monthly 5-m-resolution cloud-free mosaics online.

Along with improvements in resolution and access, increased computing power, such as by Google Earth Engine, has enabled effective processing of the massive amounts of satellite data.

POWER IN THE PROTOCOL

The challenge remains to harness improving satellite technology and unprecedented data streams into a strategic and effective monitoring system that can ultimately be used by decision-makers to reduce defor-

[1]Amazon Conservation Association, Washington, DC 20005, USA. [2]Asociación para la Conservación de la Cuenca Amazónica (ACCA), Lima, Peru. [3]World Resources Institute, Washington, DC 20002, USA. [4]Planet, San Francisco, CA 94103, USA. Email: mfiner@amazonconservation.org

Trends in earth observation satellites

Data reflect 488 earth observation satellites launched since 1972 by commercial and government providers (excluding military). We followed methods established in (*5*) and added satellites from the Union of Concerned Scientists database and public launch information from SpaceFlightNow and Planet. See the supplementary materials for details.

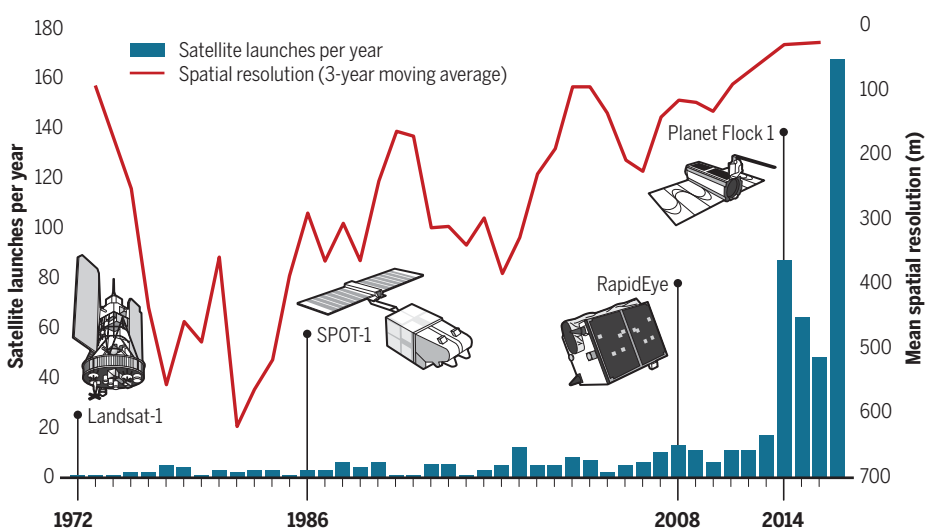

GRAPHIC: ADAPTED BY KELLIE HOLOSKI/*SCIENCE*

estation. We propose a five-step near–real-time deforestation-monitoring protocol designed primarily for government and civil society. This comprehensive protocol, based on recent monitoring initiatives in the Amazon (*8*, *9*) and insights from the international Global Forest Watch partnership, is particularly aimed at tropical countries that are designing strategies to confront deforestation. One of our main motivations is to help convert cutting-edge technological data into actionable information, a transformation that has thus far been lacking on a global scale.

Forest loss detection

The first step is to detect forest loss as precisely and quickly as possible. Advances in automated forest-loss detection have followed those of satellites. The original near–real-time detection systems, starting in the early 2000s, utilized coarse-resolution MODIS imagery, including well-known systems in Brazil [DETER (Real-Time System for Detection of Deforestation; government) and SAD (Deforestation Alert System; civil society)] and Terra-i and FORMA (Forest Monitoring for Action) from international organizations.

More recently, detection systems have incorporated medium-resolution Landsat imagery. In 2009, researchers at the Carnegie Institution for Science developed CLASlite (Carnegie Landsat Analysis System–Lite), pioneering Landsat-based forest-loss detection software. In 2016, researchers at the University of Maryland developed GLAD (Global Land Analysis and Discovery), the first fully automated, Landsat-based alert system (*10*). In 2017, the Peruvian government, which previously used GLAD, developed its own Landsat-based alert system.

Most recently, the Brazilian SAD alerts were further innovated by incorporating Sentinel imagery, both optical and radar. Thus, sensing capability for automated forest-loss alerts has improved resolution by two orders of magnitude (from 1000 to 10 m) in less than a decade and can see through clouds. Future alerts may improve to 3 m, with Planet imagery.

Given the widespread nature of small-scale deforestation events (*11*), medium-resolution (Landsat and Sentinel)–based alerts have replaced coarse-resolution (MODIS)–based alerts as the standard. As a practical option, GLAD alerts now cover more than 20 tropical countries, essentially providing pantropical coverage. These alerts are free datasets, updated weekly, that indicate 30 m–by–30 m pixels of likely forest loss. For Brazil and Peru, there are also more specialized alerts.

Prioritization of data

Alerts may yield thousands, even millions, of raw data points (pixels) on a regular basis and can quickly become overwhelming, especially at larger scales. Thus, prioritizing alert data is often necessary, for example, by incorporating important spatial data such as protected areas, indigenous territories, or any specific area of interest. Kernel density analysis identifies deforestation hot spots, allowing users to focus on geographic areas with the highest concentrations of recent forest loss (*12*). Other prioritization techniques include visually scanning for large clusters or linear features that indicate anthropogenic clearing and adding river and terrain information to screen for forest loss that is likely due to natural causes. In the future, machine learning may aid prioritization by highlighting the most important alerts on the basis of pattern (size and density), shape (linear), and location (overlap with areas of interest).

"...effective government institution building is the key element to ensuring that near–real-time forest monitoring information is utilized."

Identification of drivers

To convert priority alerts to actionable information, they need to be validated, to verify that the highlighted pixels are indeed deforestation, and investigated, to determine the driver (cause).

Alerts can typically be validated by visually checking the underlying medium-resolution imagery (Landsat or Sentinel). Also, new mobile apps, such as Forest Watcher, facilitate field verification. Drones, which can fly targeted missions under cloud cover, will likely play increasing roles in providing local information.

After validation, visual analysis of high-resolution imagery is an effective and efficient technique to determine the driver. Our protocol focuses on identification of the direct driver, the immediate action at the local level that is causing the forest loss. For example, important direct drivers in the Amazon include agriculture (both large and small scale), logging roads, and gold mining (see second figure). In turn, identification of the direct driver aids identification of the indirect driver, such as a market force, that often determines the appropriate policy action. For example, the response to a new mining operation will be different, and involve different government agencies, than the response to a new oil palm plantation.

In cases where high-resolution imagery is cost-prohibitive, there are improving free alternatives. At 10-m resolution, Sentinel-2 is sufficient to distinguish most drivers. Further, Planet now offers 5-m-resolution visual maps online, updated monthly.

In the future, machine learning could greatly enhance identification of major deforestation drivers (such as mining and agriculture) and even identify specific crop types (oil palm, cacao, coffee, soy, and so on) from satellite imagery.

Timely communication of results

The next challenge is to communicate important results when traditional methods, such as published reports or peer-reviewed articles, are not time-effective options. Although the operative audience is government officials, as described in the next step below, there is scientific, educational, and governance (transparency) value in reaching a wider public audience that includes civil society, journalists, researchers, and the private sector. It is often difficult to predict the exact group of actors that will seize on any given set of new findings, so it is strategic to cast a wide net, as this step is important in bridging the gap between the technical and policy components.

Civil society has developed approaches that may serve as a model. Launched in 2015, Monitoring of the Andean Amazon Project (MAAP) specializes in publishing concise, timely, web-based reports about ongoing near–real-time monitoring efforts in the Andean Amazon. Reports often feature high-resolution imagery both before and after recent deforestation events. All reports are reviewed by preselected expert committees before publication. Particularly sensitive findings, such as illegal activity that may be subject to an intervention, are passed directly to relevant government entities before being made public.

Global Forest Watch has recently built off this approach, expanding to a global scale with the "Places to Watch" initiative (*13*). Brief, web-based reports highlight the most consequential cases of recent deforestation identified by GLAD alerts around the tropics.

Impact to reduce deforestation

The ultimate goal is that the steps above lead to actual policy or conservation action. On the basis of recent experience in the Amazon, first in Brazil and now also in Peru, effective government-institution building is the key element to ensuring that near–real-time forest monitoring information is utilized.

Detecting deforestation and identifying drivers in the Peruvian Amazon

Detecting forest loss with Landsat-based GLAD alerts (top) and identifying deforestation drivers with high spatial and temporal resolution Planet imagery (bottom).

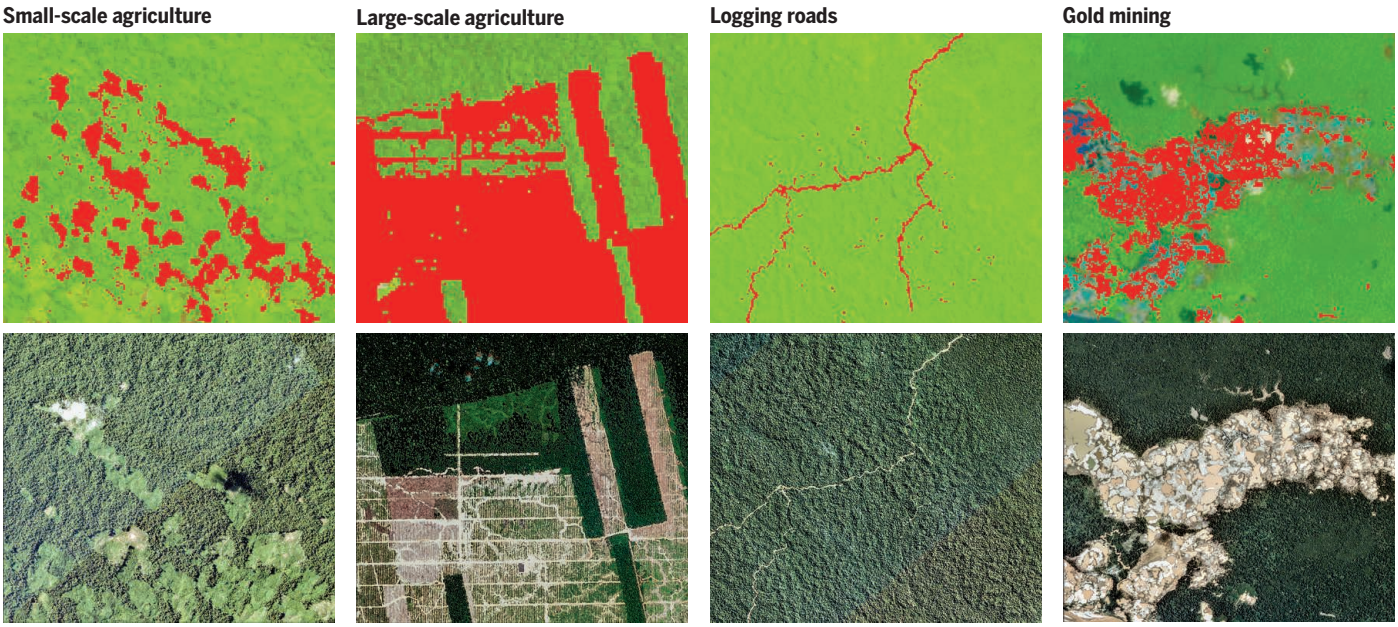

IMAGES: (TOP ROW) GLOBAL FOREST WATCH; (BOTTOM ROW) PLANET

Streamlined coordination between the array of government ministries and agencies to process and respond to the technical information is critical. In a pioneering effort, the effective use of MODIS-based deforestation alerts (DETER) was widely credited with helping to curb surging deforestation in the Brazilian Amazon in the early 2000s. Notably, the Brazilian government increased its capacity to physically and legally respond to the alerts by improving coordination across 15 ministries (including the federal police, army, and public prosecutor) (*14*, *15*).

Similar institution building is now taking place in Peru, which is constructing a National System of Monitoring and Control, led by the National Forest Service and Wildlife Authority (SERFOR), to coordinate actions related to the generation, analysis, and response to deforestation information among government entities. This system is specifically designed to build the government infrastructure for efficient, data-driven policy action, including laying out responsibilities and pathways for the complex array of actors. Notably, in addition to generating and receiving forest-loss information (that is, detection), SERFOR conducts both a technical and legal analysis of the data before sending the information to decision-makers. This technical and legal analysis also provides detailed guidance to authorities on how to prioritize deforestation events, on the basis of factors such as driver, area, and land designation, to facilitate prompt decision-making.

Although Brazil and Peru are the most advanced examples, other countries are making progress as well. Colombia is now producing quarterly early-warning reports to identify the most-active deforestation fronts across the country. These reports are an input for the strengthening of coordinated actions between the environment ministry, regional authorities, and the military. The Indonesian government is also using near–real-time monitoring data as an additional source of information to improve law enforcement in the forestry sector.

Civil society has also emerged as a key actor related to institution building. Brazil, again, led the way with the development of an independent alert system (SAD) in addition to the government-generated alerts. This independent data generation and analysis by civil society set an important precedent, with implications for improving transparency, spurring innovation, and creating public pressure.

In Peru, the civil society–designed protocol presented in this paper served as an initial model for the emerging National System of Monitoring and Control. The protocol was modified and expanded on to fit Peru's complex government structure but serves as a good example of how civil society, and the protocol itself, may assist institution building. In Uganda, civil society (led by the Jane Goodall Institute) is training government rangers to use GLAD alerts to identify and respond to new deforestation fronts.

Advancing satellite technology has made near–real-time deforestation monitoring increasingly feasible for a growing number of countries and actors. Our protocol may serve as a foundation for efforts to effectively link the technological advances with the ultimate goal of policy action to reduce deforestation. ■

REFERENCES AND NOTES

1. J. Barlow *et al.*, *Nature* **535**, 144 (2016).
2. M. Hansen *et al.*, *Science* **342**, 850 (2013).
3. J. Lynch, M. Maslin, H. Balzter, M. Sweeting, *Nature* **496**, 293 (2013).
4. A. K. Pratihast *et al.*, *PLOS ONE* **11**, e0150935 (2016).
5. A. S. Belward, J. O. Skøien, *ISPRS J. Photogramm. Remote Sens.* **103**, 115 (2015).
6. D. Butler, *Nature* **505**, 143 (2014).
7. J. Li, D. P. Roy, *Remote Sens.* **9**, 902 (2017).
8. M. Finer, S. Novoa, "Patterns and Drivers of Deforestation in the Peruvian Amazon. MAAP: Synthesis #2" (Monitoring of the Andean Amazon Project, 2017).
9. E. Worsham, C. Clark, R. Fehrman, "Scaling pathways: Case study. Imazon: Using data and partnerships to save the Amazon" (Innovation Investment Alliance and CASE at Duke, 2017).
10. M. C. Hansen *et al.*, *Environ. Res. Lett.* **11**, 034008 (2016).
11. M. Kalamandeen *et al.*, *Sci. Rep.* **8**, 1600 (2018).
12. N. L. Harris *et al.*, *Environ. Res. Lett.* **12**, 024012 (2017).
13. M. J. Weisse, R. Petersen, S. Sargent, S. Gibbes, "Places to watch: Identifying high-priority forest disturbance from near-real time satellite data" (World Resources Institute, Washington, DC, 2017).
14. D. Nepstad *et al.*, *Science* **344**, 1118 (2014).
15. J. Assunção, C. Gandour, R. Rocha, *Environ. Dev. Econ.* **20**, 697 (2015).

ACKNOWLEDGMENTS

This work was partially funded by the International Conservation Fund of Canada and the Norwegian Agency for Development Cooperation. We thank C. Garcia, J. Swenson, and M. Silman for reviewing the manuscript.

SUPPLEMENTARY MATERIALS

www.sciencemag.org/content/360/6395/1303/suppl/DC1

10.1126/science.aat1203

BOOKS *et al.*

Many of the building blocks of emotion are present in animals, but they may manifest in unique ways.

NEUROSCIENCE

Hard feelings

A pair of neuroscientists finds that investigating emotions is easier done than said

By **Elizabeth Bauer**

Ask a roomful of neuroscientists to define the term "emotion" and you will trigger a lively discussion. Some will argue that emotions involve conscious experiences that can be studied only in humans. Others might counter that insects and other invertebrates exhibit some of the emotion building blocks seen in mammals. Some will contend that different emotions correspond to anatomically distinct areas of the brain, whereas others argue that emotions are produced in a highly distributed manner. Still others will bring up the 19th-century psychologist William James's argument that emotions are a consequence, not a cause, of behavior.

In *The Neuroscience of Emotion*, Ralph Adolphs and David J. Anderson argue that before we can study it, we must first define what we mean by "emotion." Only then, they maintain, can we form appropriate and testable hypotheses.

Colleagues at Caltech, the authors bring different experimental backgrounds to the topic of emotion. Adolphs studies the neural basis of human social behavior. Anderson uses rodents and fruitflies as model organisms to investigate how internal states elicit emotional behaviors. Their book is less a catalog of recent neuroscientific discoveries and more a conceptual framework for investigating emotional behaviors both in humans and in other animals.

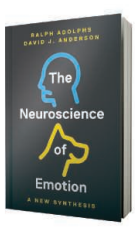

The Neuroscience of Emotion
A New Synthesis
Ralph Adolphs and David J. Anderson
Princeton University Press, 2018. 372 pp.

Adolphs and Anderson begin by contending that emotions are biological phenomena that cause behavioral and physiological changes in the brain and body and—in some species—subjective feelings. If emotions are a class of internal brain states expressed in measurable ways, they argue, we can study the neurobiological implementation of these states separately from subjective conscious feelings, meaning both humans and other animals are potential subjects. They go on to define, in detail, the basic properties of an emotion, including valence, scalability, persistence, automaticity, and generalization.

There is a tight logic running throughout *The Neuroscience of Emotion* that integrates theories of emotions, recent studies, and commonsense analogies. The authors confront, for example, the popular but erroneous view that fear is in the amygdala. This belief arose because activity in the amygdala can be correlated with feelings of fear in humans. But just as monitoring the speedometer of a car enables us to predict how fast it is moving without telling us anything about how the car works, increased activity in a particular brain region does not necessarily tell us anything about the causal mechanism of emotion.

Cutting-edge methods (such as optogenetics and pharmacogenetics) allow for the functional dissection of the neural circuits that cause emotional behavior in animals. Using these techniques, we have learned, for example, that the central nucleus of the amygdala contains as many as seven different neuronal subtypes that participate in phenomena including fear, learning, and appetitive behaviors. Conventional drugs and electrical stimulation tend to act indiscriminately on all cells, meaning it's possible that such interventions might cancel out any potential effects a treatment might have had by stimulating or inhibiting conflicting cell types simultaneously.

Chapters on emotions in rodents highlight aspects of the emotional experience that we currently do not understand and provide specific suggestions for future research. How are some of the basic properties of emotions, such as persistence and generalizability, encoded, for example? And how do cortical projections from subcortical areas allow for interactions between emotions and cognitive processes?

Verbal reports by human subjects can conflate actual emotional states and the conscious experience of emotions. To combat this, the authors suggest designing experiments to emphasize one component or the other. Subjects could be presented with a spider, for example, to incite fear, or—if the subjects' perceptions of the experience are desired—they could be asked to recollect emotional experiences from their lives.

The book finishes with a critique of current theories of emotion and suggestions for future research. The authors ask, for example, if there might be emotions that are unique to a certain species—and even if there might be emotions unique to individuals within a species. And will we one day understand emotions well enough to be able to build robots that have an internal emotional life?

Adolphs and Anderson openly acknowledge that they do not provide a comprehensive theory of emotion. Indeed, despite the existence of substantial research on the subject, we are left with the impression that we actually know remarkably little about emotions at present. But their enthusiasm for the topic is genuine and makes *The Neuroscience of Emotion* compelling and engaging. ■

The reviewer is at the Department of Biology, Barnard College, New York, NY 10027, USA. Email: ebauer@barnard.edu

10.1126/science.aat9119

SCIENCE LIVES

The Victorian dynamo

A long-awaited biography does justice to John Tyndall, a pioneering climate researcher and science advocate

The Ascent of John Tyndall
Victorian Scientist, Mountaineer, and Public Intellectual
Roland Jackson
Oxford University Press, 2018. 592 pp.

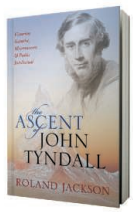

By **Sarah Dry**

In his day, the Victorian physicist and science popularizer John Tyndall was as famous and controversial a figure as Charles Darwin. Unlike Darwin, Tyndall slipped into obscurity following his death in 1893. This is a shame. He has much to teach us about the prominent role of science in Victorian culture.

A lively, charismatic figure, Tyndall left behind a copious correspondence and an engagingly written journal, all of which has been exploited by Roland Jackson in a long-awaited biography. Jackson's book arrives just in time to help situate Tyndall's work on heat in the atmosphere—which has recently seen him dubbed an anachronistic "father" of global warming—within the context of a life bursting with science and much else besides.

Born to an Anglo-Irish family in County Carlow, Ireland, Tyndall came to England as a jobbing surveyor but, thanks to his charismatic lecturing style, quickly ascended to the heights of scientific society. In 1853, he became professor of natural philosophy at the Royal Institution, following in the footsteps of Humphry Davy and Michael Faraday.

Using his prominent position and powerful alliances with like-minded scientists (among them Thomas Huxley, Darwin's "bulldog"), Tyndall became an outspoken advocate for a newly emboldened form of science. "We claim, and we shall wrest, from theology the entire domain of cosmological theory" was his most notorious rallying cry, designed to rattle the cages of the Anglican establishment.

Science, for Tyndall, had the power to illuminate every aspect of a world that never stopped eliciting his sense of wonder. He loved to tinker, building devices with which to test the connections between natural phenomena; the unity of nature was a key conceptual touchstone for him.

He put his considerable experimental skills to work doing research on fundamental physical phenomena such as light, heat, sound, and magnetism. This included work on the absorption of heat by different gases (including carbon dioxide and water vapor), as well as studies of the motion of glaciers, the color of the sky, and the vibrations of so-called "sensitive flames" caused by sound waves. He also put the same basic insights to work in intensely practical matters, often of public safety, consulting for the government on the best technology for lighthouses and foghorns and how to filter the air in firemen's respirators.

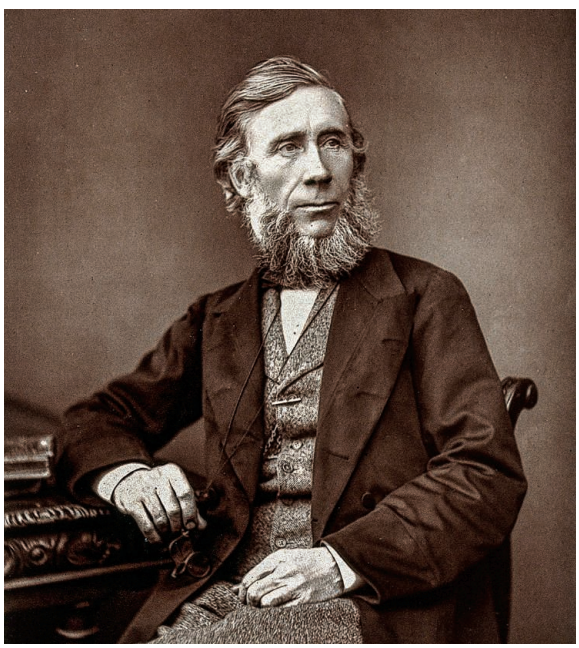

Wiry and vigorous, John Tyndall found spiritual sustenance outside of church walls and thought nothing of walking 15 miles on a Sunday.

Tyndall's social life was, if anything, even busier and more varied than his research life. Both the poet Alfred Lord Tennyson and the philosopher and historian Thomas Carlyle were boyhood heroes who became close friends.

Tyndall was also notable for his European connections. Unusually for the time, he studied for his Ph.D. in Marburg, Germany, under Robert Bunsen and later translated works by German chemists and physicists into English.

As important as Tyndall's social contacts were, in Jackson's telling, the sheer quantity of details becomes overwhelming—as indeed it was for Tyndall. Nature provided not only a key site of scientific inquiry but also an increasingly necessary respite from the stress of his busy urban life. In the Alps, he sought escape from the city but found relief not in rest but in a different kind of activity—vigorous exercise, often accompanied by risky ascents, and similarly intense field measurements of glacier flow, meteorological phenomena, and floating matter in the air.

Jackson recounts Tyndall's fascinating life with impressive clarity. By keeping his focus so tightly on Tyndall the man, however, he loses the opportunity to draw key conclusions about Victorian science more generally. Tyndall mixed scientific celebrity with risk-taking and experimental finesse. His movements between the lecture theater, the laboratory, and the mountains, to say nothing of his social climbing, tell us what it took to make authoritative statements about nature at a time when the cultural value of science was vehemently debated.

Tyndall's fame owed much to his writing, especially his thrilling accounts of his mountaineering exploits (which included an early ascent of the Weisshorn and a shoulder of the Matterhorn) and his engaging books on heat, sound, and water. These remained in print after his death and were read by many who later cited them as having inspired them to become scientists.

Tyndall's death, in 1893 at the age of 73, was accidental. His wife, Louisa, some 25 years younger than him, accidentally administered an extra dose of his sleeping medication. "My darling," said Tyndall when he realized what had happened, "you have killed your John."

Grief and guilt inspired Louisa to write a biography that would do justice to her husband, but she was unable to complete the task. When she died, some 47 years after Tyndall, his entire generation had also gone. And so it is that Roland Jackson's admirably complete biography is the first serious biography to appear since a patchy production appeared in 1945, soon after Louisa's death. It's about time. ■

10.1126/science.aat6293

The reviewer is the author of The Newton Papers: The Strange and True Odyssey of Isaac Newton's Manuscripts *(Oxford University Press, Oxford, 2014). Email: sarahdry@gmail.com*

LETTERS

Edited by **Jennifer Sills**

Evaluating human trials: FDA's role

In their Policy Forum "Bystander risk, social value, and ethics of human research" (13 April, p. 158), S. K. Shah *et al.* discuss the difficulty of determining the risk to bystanders and the benefit to society inherent in human challenge trials (HCTs) in which healthy people are infected with a virus such as Zika. They recommend forming ad hoc Comprehensive Ethics Review Committees, which they assert could address potential risks better than a standard institutional review board. We agree that third-party risks and social value are important considerations in clinical trial evaluation but point out that the U.S. Food and Drug Administration (FDA) is already authorized and well equipped to address these issues. Objective expert reviewers routinely formally evaluate the scientific, clinical, and ethical aspects of all clinical studies performed under the FDA's Investigational New Drug (IND) process (*1*).

An IND application is required for challenge studies in which live organisms are administered to subjects to assess vaccine effectiveness or to study disease pathogenesis or the host response to the organism. The FDA has considerable experience in addressing risk to human subjects enrolled into clinical trials as well as evaluating risks to bystanders and in assessing the social value of HCTs. The FDA's review process combines the necessary scientific and regulatory expertise to appropriately evaluate risks and apply rational risk minimization strategies.

The FDA is authorized to require studies with potential third-party risks, such as those potentially associated with live-attenuated vaccines and with human challenge trials, to be performed under appropriate containment with explicit consideration for these risks (including potential sexual and environmental transmission). The FDA also evaluates manufacturing and safety testing of challenge strains. If risks are deemed unreasonable or are inadequately described in the Investigator Brochure, the FDA can place a study on "clinical hold." The FDA can also convene its Vaccines and Related Biological Products Advisory Committee (*2*) to provide public expert discussion and recommendations regarding relevant scientific and human subject protection issues, as occurred in the evaluation of the benefit and risks of HCTs to assess the effectiveness of cholera vaccines.

Philip R. Krause* and Marion F. Gruber
Office of Vaccines Research and Review, Center for Biologics Evaluation and Research, FDA, Silver Spring, MD 20993, USA.
*Corresponding author. Email: philip.krause@fda.hhs.gov

REFERENCES

1. U.S. FDA, Investigational New Drug (IND) application (2017); www.fda.gov/drugs/developmentapprovalprocess/howdrugsaredevelopedandapproved/approvalapplications/investigationalnewdrugindapplication/default.htm.
2. U.S. FDA, Vaccines and Related Biological Products Advisory Committee (2018); www.fda.gov/AdvisoryCommittees/CommitteesMeetingMaterials/BloodVaccinesandOtherBiologics/VaccinesandRelatedBiologicalProductsAdvisoryCommittee/.

10.1126/science.aau0591

Response

Krause and Gruber offer the U.S. Food and Drug Administration (FDA) as part of the solution to the problems we have identified. We agree that the FDA could helpfully assist with the review of specific protocols for Zika human challenge trials (HCTs), especially given the need to update our panel's conclusions based on current knowledge about Zika virus. However, comprehensive ethical review of different programs of research beyond Zika human challenge trials is also necessary moving forward; here, the FDA may have a more limited role to play.

The Zika HCT ethics panel we served on did not review a specific protocol; rather, it addressed the general ethical considerations related to a potential program of Zika HCT research. We determined that Zika HCTs could be ethically justifiable but were premature to conduct in February 2017. These conclusions were based on a snapshot of what was known at the time and should be updated based on new information: The current epidemiology of Zika virus makes it more difficult to conduct vaccine trials, and better data are now available on potential risks through sexual transmission to bystanders not enrolled in the study (*1*). A multidisciplinary expert committee should revisit how to minimize risks to participants and bystanders, whether the social value of Zika HCTs justifies any remaining risks, and other related ethical issues (*2*). Krause and Gruber offer a useful path forward by proposing FDA review mechanisms that could convene such a committee.

The broader issues for which we suggested the solution of Comprehensive Ethics Review Committees (CERCs) could also benefit from FDA involvement. We proposed that CERCs could essentially replicate what our panel accomplished by assessing proposed programs of research with a focus on bystander risk and highly contingent social value. Krause and Gruber correctly note that the FDA has the expertise to help assess and minimize bystander risk, and with appropriate ethical expertise, the FDA could also address whether any residual risk to bystanders can be justified. With regard to assessing the value of a trial that is contingent on other factors, an opinion from the FDA on the acceptability of a particular

PHOTO: LILLIAN SUWANRUMPHA/AFP/GETTY IMAGES

A Bangkok city worker fumigates to kill Zika-carrying mosquitoes. The search for a Zika vaccine continues.

type of trial (such as a Zika HCT) within a clinical development strategy (*3*) would be incredibly useful.

However, expecting the FDA to review every protocol raising controversial ethical issues like bystander risk and highly contingent social value (including, but not limited to, Zika human challenge trials) may tax its capacity. In addition, the FDA only has jurisdiction over sponsor submissions, which limits its ability to address these issues unless they are tied to specific protocols subject to FDA authority. Finally, the FDA is charged with ensuring scientific quality and the safety of subjects, not bystanders (*4*), and it expressly defers to institutional review boards when reviewing the social value of research (*5*). Nevertheless, we welcome the willingness of the FDA to help advance our proposal for a more comprehensive approach to research ethics review.

S. K. Shah,[1]* J. Kimmelman,[2] A. D. Lyerly,[3] H. F. Lynch,[4] F. G. Miller,[5] R. Palacios,[6] C. A. Pardo,[7] C. Zorrilla[8]
[1]Treuman Katz Center for Pediatric Bioethics, University of Washington and Seattle Children's Research Institute, Seattle, WA 98101, USA. [2]Biomedical Ethics Unit, McGill University, Montreal, QC H3A 1X1, Canada. [3]Center for Bioethics and Department of Social Medicine, University of North Carolina at Chapel Hill, Chapel Hill, NC 27599, USA. [4]Department of Medical Ethics and Health Policy, Perelman School of Medicine, University of Pennsylvania, Philadelphia, PA 19104, USA. [5]Weil Cornell Medical College, New York, NY 10065, USA. [6]Instituto Butantan, São Paulo, Brazil. [7]Department of Neurology, Neurovirus Emerging in the Americas Study (NEAS), Johns Hopkins University, Baltimore, MD 21205, USA. [8]University of Puerto Rico School of Medicine, San Juan, PR 00921, USA.
*Corresponding author. Email: shahsk@uw.edu

REFERENCES

1. P. S. Mead *et al.*, *N. Engl. J. Med.* **378**, 1377 (2018).
2. S. K. Shah *et al.*, "Ethical considerations for Zika virus human challenge trials" (2017); www.niaid.nih.gov/sites/default/files/EthicsZikaHumanChallengeStudiesReport2017.pdf.
3. H. D. Marston, N. Lurie, L. L. Borio, A. S. Fauci, *N. Engl. J. Med.* **375**, 1209 (2016).
4. Code of Federal Regulations, Title 21, Section 312.42 (2017).
5. Code of Federal Regulations, Title 21, Section 56.111(a)(2) (2017).

10.1126/science.aau0865

Casualties of human-wildlife conflict

In their Letter "Pesticides thwart condor conservation" (11 May, p. 612), P. A. E. Alarcón and S. A. Lambertucci advocate a ban on carbofuran use in developing countries to prevent wildlife poisoning [e.g., (*1*)]. We agree that pesticides should be restricted. However, pesticide bans are insufficient. After many countries banned strychnine, people continued to set poisoned baits for predators with other toxins, such as aldicarb, carbofuran, and endosulfan (*2*, *3*). Commercialization of aldicarb has been forbidden in the European Union since 2003 (*4*) and carbofuran and endosulfan since 2007 (*5*, *6*). Yet, more than 10 years later, they are still heavily used to illegally kill predators across Europe (*3*, *6*). People willing to poison the animals they perceive as vermin can always find a way to access toxins. To effectively address the problem, we must consider its root: human-wildlife conflict.

Human-wildlife conflict occurs when the behavior of a wild animal species—mostly high-profile animals such as top predators and mega-herbivores—poses a direct and recurring threat to people's livelihoods and, in response, humans persecute the species (*7*). When humans attempt to kill the targeted species with a nonselective control method such as poison, other species are killed unintentionally. This is usually the case when condors and other nontargeted predators and scavengers feed on poisoned baits set for conflictive predators (*1*, *8*). Human-wildlife conflict is also behind the intentional killing of Andean condors (*Vultur gryphus*) in areas where these birds have been accused of killing livestock (*9*).

Given that human thoughts and actions ultimately determine the course and resolution of human-wildlife conflicts (*10*), the success of efforts to conserve condors and other scavengers and predators will rely on interdisciplinary research and management approaches that integrate natural and social sciences. For example, social scientists can provide insight into decision-making about wildlife and highlight connections between social and ecological systems (*11*). Meanwhile, marketing techniques honed by social scientists can influence attitudes, perceptions, and behaviors of individuals, and ultimately societies, with the objective of advancing conservation goals (*12*). Together with widespread stakeholder participation, including scientists, politicians, farmers, and hunters, these approaches offer a more cost-effective way to mitigate conflicts and increase tolerance of wildlife.

Juan M. Grande,[1,2]* Santiago Zuluaga,[1,2] Silvio Marchini[3]
[1]Instituto de Ciencias de la Tierra y Ambientales de La Pampa–Consejo Nacional de Investigaciones Científicas y Técnicas (INCITAP-CONICET), Santa Rosa 6300, La Pampa, Argentina. [2]Centro para el Estudio y Conservación de las Aves Rapaces en Argentina, Facultad de Ciencias Exactas y Naturales, Universidad Nacional de La Pampa (CECARA-FCEyN-UNLPam), Santa Rosa 6300, La Pampa, Argentina. [3]Department of Forest Science, Luiz de Queiroz College of Agriculture, University of São Paulo, Piracicaba, SP 13418-900, Brazil.
*Corresponding author. Email: manuhola@yahoo.es

REFERENCES

1. BirdLife International, "34 Andean Condors found dead in Argentina—the poisoning needs to stop" (2018); www.birdlife.org/worldwide/news/34-andean-condors-found-dead-argentina-poisoning-needs-stop.
2. M. Hernández, A. Margalida, *Ecotoxicology* **17**, 264 (2008).
3. N. Ruiz-Suárez *et al.*, *Sci. Total Environ.* **505**, 1093 (2015).
4. 2003/199/EC: Council Decision of 18 March 2003 concerning the non-inclusion of aldicarb in Annex I to Council Directive 91/414/EEC and the withdrawal of authorisations for plant protection products containing this active substance (2003); https://eur-lex.europa.eu/eli/dec/2003/199/oj.
5. 2007/416/EC: Commission Decision of 13 June 2007 concerning the non-inclusion of carbofuran in Annex I to Council Directive 91/414/EEC and the withdrawal of authorisations for plant protection products containing that substance (2007); http://data.europa.eu/eli/dec/2007/416/oj.
6. A. De Roma *et al.*, *J. Vet. Diagn. Invest.* **29**, 122 (2017).
7. C. Inskip, A. Zimmermann, *Oryx* **43**, 18 (2009).
8. D. Ogada, *Ann. N.Y. Acad. Sci.* **1322**, 1 (2016).
9. V. B. Cailly Arnulphi, S. A. Lambertucci, C. E. Borghi, *PLOS ONE* **12**, 1 (2017).
10. M. J. Manfredo, A. A. Dayer, *Hum. Dimens. Wildl.* **9**, 1 (2004).
11. D. J. Decker, S. J. Riley, W. F. Siemer, *Human Dimensions of Wildlife Management* (Johns Hopkins University Press, Baltimore, ed. 2, 2012).
12. A. J. Wright *et al.*, *Ocean Coast. Manag.* **115**, 41 (2015).

10.1126/science.aau2465

TECHNICAL COMMENT ABSTRACTS

Comment on "Sterilizing immunity in the lung relies on targeting fungal apoptosis-like programmed cell death"

Abdel Aouacheria, Kyle W. Cunningham, J. Marie Hardwick, Zdena Palková, Ted Powers, Fedor F. Severin, Libuše Váchová

Shlezinger *et al.* (Reports, 8 September 2017, p. 1037) report that the common fungus *Aspergillus fumigatus*, a cause of aspergillosis, undergoes caspase-dependent apoptosis-like cell death triggered by lung neutrophils. However, the technologies they used do not provide reliable evidence that fungal cells die via a protease signaling cascade thwarted by a fungal caspase inhibitor homologous to human survivin.
Full text: dx.doi.org/10.1126/science.aar6910

Response to Comment on "Sterilizing immunity in the lung relies on targeting fungal apoptosis-like programmed cell death"

Neta Shlezinger, Henriette Irmer, Sourabh Dhingra, Sarah R. Beattie, Robert A. Cramer, Gerhard H. Braus, Amir Sharon, Tobias M. Hohl

Aouacheria *et al.* question the interpretation of contemporary assays to monitor programmed cell death with apoptosis-like features (A-PCD) in *Aspergillus fumigatus*. Although our study focuses on fungal A-PCD for host immune surveillance and infectious outcomes, the experimental approach incorporates multiple independent A-PCD markers and genetic manipulations based on fungal rather than mammalian orthologs to circumvent the limitations associated with any single approach.
Full text: dx.doi.org/10.1126/science.aas9457

TECHNICAL COMMENT

FUNGAL PATHOGENS

Comment on "Sterilizing immunity in the lung relies on targeting fungal apoptosis-like programmed cell death"

Abdel Aouacheria[1], Kyle W. Cunningham[2], J. Marie Hardwick[3]*, Zdena Palková[4], Ted Powers[5], Fedor F. Severin[6], Libuše Váchová[7]

Shlezinger *et al*. (Reports, 8 September 2017, p. 1037) report that the common fungus *Aspergillus fumigatus*, a cause of aspergillosis, undergoes caspase-dependent apoptosis-like cell death triggered by lung neutrophils. However, the technologies they used do not provide reliable evidence that fungal cells die via a protease signaling cascade thwarted by a fungal caspase inhibitor homologous to human survivin.

Shlezinger *et al*. (*1*) reported the existence of an "apoptosis-like" programmed death pathway in the opportunistic pathogen *Aspergillus fumigatus*, a multicellular fungus responsible for life-threatening infections. However, this conclusion is compromised by several technical problems with their methods. These arise from the use of mammalian apoptosis assays designed to detect biochemical events that are not present or molecularly defined in fungi. A related problem stems from the assumption that fungal proteins with limited sequence homology to mammalian apoptosis regulators will function analogously in fungal cells. In this study, a chemical sensor and a small-molecule inhibitor of mammalian apoptosis regulators [caspases and the IAP (inhibitor of apoptosis) family of proteins, respectively] were applied to fungal cells with the expectation of binding to distant fungal homologs but without direct evidence for such. Furthermore, the proposed fungal target proteins (metacaspases and BIR1) appear to lack the corresponding binding sites for these chemical reagents. Thus, the evolutionary divide between fungi and mammals appears to be too great for what might seem like a safe extrapolation regarding apoptosis—generally defined in mammals as the classic biochemical and morphological consequence of caspase-3 or -7 activation.

Using a transgenic strain of *A. fumigatus* with a dual fluorescent probe to distinguish dying cells from dead cells, Shlezinger *et al*. report that mold conidia exposed to oxidative stress in vitro, or engulfed by neutrophils in vivo, exhibit features of apoptotic mammalian cells prior to loss of viability. The authors measured fungal caspase activity by flow cytometry or fluorescence microscopy using fluorescein isothiocyanate (FITC)–conjugated tripeptide Val-Ala-Asp (VAD) fused to fluoromethylketone (FMK). FITC-VAD-FMK is a mammalian caspase reporter that mimics the required Asp cleavage site found in natural substrates of mammalian caspases. The FMK moiety results in tight binding to the caspase active-site cysteine, potently inhibiting caspase activity. By binding to active caspases, the fluorescent FITC moiety is retained in animal cells for easy detection.

However, despite careful scrutiny, sequence-based bioinformatics approaches have failed to detect caspase homologs in fungal genomes, or more generally in nonmetazoan organisms (*2*). *A. fumigatus* encodes two metacaspases (CasA and CasB) (*3*), which are also cysteine proteases related to animal caspases. However, metacaspases cleave their substrates after Arg and Lys, rather than Asp (*4*), the key residue in FITC-VAD-FMK. This raises a critical question: What enzymatic activities are responsible for the FITC-VAD-FMK caspase reporter activity in dying fungi? One possibility is that peptide-FMK reporters are promiscuous. They have been reported to bind or inhibit other classes of cysteine proteases in mammalian cells including cathepsins (*5*), and for these reasons have fallen from favor for use in mammalian models (*6*). Similarly, FITC-VAD-FMK could potentially monitor vacuolar cathepsins in fungi, but it can also nonspecifically label living nonpermeabilized yeast cells (*7*). Given its promiscuity, FITC-VAD-FMK could theoretically bind fungal metacaspases. However, although a double knockout of both *A. fumigatus* metacaspases CasA and CasB exhibited cell growth abnormalities, it was not resistant to cell death induced by oxidative stress or other stimuli tested (*3*).

Shlezinger *et al*. took a different approach to address a causal role for fungal caspase-like activities, leading to the identification of a virulence mechanism. They found that fungal strains overexpressing *A. fumigatus* BIR1 (AfBIR1) are resistant to oxidative stress (H_2O_2) in vitro and are more virulent in mice. AfBIR1 shares amino acid sequence similarity to a family of mammalian IAP proteins that, like AfBIR1, contain baculovirus IAP repeat (BIR) domains. The authors' proposed model suggests that AfBIR1 behaves similarly to the human IAP protein survivin, based on the assumption that survivin inhibits apoptotic caspases. However, survivin is not a caspase inhibitor and it lacks the sequences found in the BIR region of mammalian XIAP and *Drosophila* IAP1 that directly inhibit caspases (*8*, *9*). To provide evidence that endogenous AfBIR1 regulates caspase-like activity while overcoming the lethality caused by *AfBIR1* deletion, Shlezinger *et al*. sought to inhibit AfBIR1 by treating fungal conidia and mice with S12, a small molecule reported to inhibit survivin (*10*). S12 was originally identified through chemical and computational screens for compounds that target a cavity located near the survivin dimerization interface.

[1]ISEM, Institut des Sciences de l'Evolution de Montpellier, Université de Montpellier, CNRS, EPHE, IRD, Montpellier, France. [2]Department of Biology, Johns Hopkins University, Baltimore, MD 21218, USA. [3]Department of Molecular Microbiology and Immunology, Johns Hopkins University School of Public Health, Baltimore, MD 21205, USA. [4]Faculty of Science, Charles University, BIOCEV, Vestec, Czech Republic. [5]Department of Molecular and Cellular Biology, University of California, Davis, CA 95616, USA. [6]Belozersky Institute of Physico-Chemical Biology, Moscow State University, Moscow 119991, Russia. [7]Institute of Microbiology of the Czech Academy of Sciences, BIOCEV, Vestec, Czech Republic.
***Corresponding author. Email: hardwick@jhu.edu**

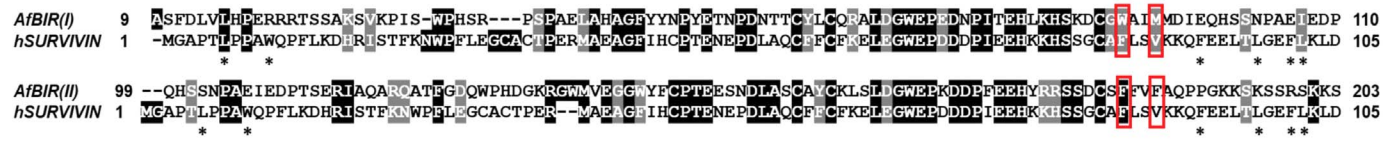

Fig. 1. Amino acid residues in the single BIR domain of human survivin (BIRC5) required for binding S12 are not well conserved in either of the BIR domains of AfBIR1. Human survivin (NP_001159) is aligned using ClustalW to both BIR domains of *A. fumigatus* BIR1 (XP_752777). Disruption of either Phe^{86} or Val^{89} (red frames) in survivin inhibits S12 binding; asterisks mark residues forming the interface between survivin dimers (*10*). Amino acid abbreviations: A, Ala; C, Cys; D, Asp; E, Glu; F, Phe; G, Gly; H, His; I, Ile; K, Lys; L, Leu; M, Met; N, Asn; P, Pro; Q, Gln; R, Arg; S, Ser; T, Thr; V, Val; W, Trp; Y, Tyr.

However, residues critical for S12 binding to survivin are not well conserved in AfBIR1 (Fig. 1). Thus, studies to verify direct binding of S12 to AfBIR1 are needed, as their interaction cannot be inferred solely on the basis of multiple sequence alignments.

The other hallmark of mammalian apoptosis used throughout the Shlezinger *et al.* study is nuclear DNA fragmentation, which is quantified using TUNEL (terminal deoxynucleotidyl transferase–mediated deoxyuridine triphosphate nick end labeling) assays. The TUNEL assay is useful for labeling the new ends of nuclear DNA after caspase-dependent activation of the mammalian DNase CAD (caspase-activated deoxyribonuclease) (*11*). However, the TUNEL assay is not specific to apoptosis and detects DNA breaks resulting from nonapoptotic cell death (*12*). DNA fragmentation and many other features of dying mammalian cells have been observed in a diverse range of nonmetazoan taxa, including protists, microalgae, yeast, bacteria, and plants. However, the genes directly responsible are largely unknown. Thus, the central unanswered question is whether the fungal factors responsible for TUNEL reactivity, caspase-like activity, or other mammalian readouts play an active and causal role in fungal cell death, or whether they only serve to mark dead and dying cells with degrading DNA, vacuolar permeability, and depletion of ATP.

Shlezinger *et al.* provide convincing genetic arguments that host phagocyte NOX [reduced nicotinamide adenine dinucleotide phosphate (NADPH) oxidase] mediates the demise of ingested fungal conidia. The possibility that a NOX-derived reactive oxygen species induces a FITC-VAD-FMK–traceable signal modulated by AfBIR is also intriguing, but more evidence will be required to distinguish this model from other possibilities, including direct killing of the engulfed pathogens by neutrophils without pro-death contributions from fungal "caspase-like activities." Some fungal species have orthologs of the mammalian necroptosis mediator MLKL or the mammalian pyroptosis mediator DNFA5/gasdermin (*13*, *14*). Even if these pro-necrotic death factors also do not promote regulated death pathways in fungi, this does not deny the existence of genetically controlled fungal cell death, especially in fungi with elaborate morphological forms (*15*).

REFERENCES AND NOTES

1. N. Shlezinger *et al.*, *Science* **357**, 1037–1041 (2017).
2. R. A. V. Bell, L. A. Megeney, *Cell Death Differ.* **24**, 1359–1368 (2017).
3. D. L. Richie *et al.*, *Mol. Microbiol.* **63**, 591–604 (2007).
4. L. A. Bouvier, G. T. Niemirowicz, E. Salas-Sarduy, J. J. Cazzulo, V. E. Alvarez, *FEBS J.* **285**, 1097–1110 (2018).
5. J. Rozman-Pungerčar *et al.*, *Cell Death Differ.* **10**, 881–888 (2003).
6. M. Poreba, A. Strózyk, G. S. Salvesen, M. Drag, *Cold Spring Harb. Perspect. Biol.* **5**, a008680 (2013).
7. L. Váchová, Z. Palková, *FEMS Yeast Res.* **7**, 12–21 (2007).
8. J. Chai *et al.*, *Cell* **104**, 769–780 (2001).
9. S. J. Riedl *et al.*, *Cell* **104**, 791–800 (2001).
10. A. Berezov *et al.*, *Oncogene* **31**, 1938–1948 (2012).
11. M. Enari *et al.*, *Nature* **391**, 43–50 (1998).
12. B. Grasl-Kraupp *et al.*, *Hepatology* **21**, 1465–1468 (1995).
13. A. Daskalov *et al.*, *Proc. Natl. Acad. Sci. U.S.A.* **113**, 2720–2725 (2016).
14. J. Gregan, L. Van Laer, L. D. Lieto, G. Van Camp, S. E. Kearsey, *Biochim. Biophys. Acta* **1638**, 179–186 (2003).
15. A. P. Gonçalves, J. Heller, A. Daskalov, A. Videira, N. L. Glass, *Front. Microbiol.* **8**, 1837 (2017).

ACKNOWLEDGMENTS

Funding: Supported by the Fondation ARC and the Ligue Contre le Cancer Comité du Gard (A.A.); NIH grants RO1 NS083373, R21 NS096677, and RO1 GM077875 (J.M.H.); NIH grant R21 AI115016 (K.W.C.); and the CZ.1.05/1.1.00/02.0109 BIOCEV by ERDF and MEYS (Z.P. and L.V.). **Author contributions:** All authors contributed to and approved the manuscript. Authors are listed alphabetically. **Competing interests:** We declare no competing interests.

7 December 2017; accepted 10 May 2018
10.1126/science.aar6910

TECHNICAL RESPONSE

FUNGAL PATHOGENS

Response to Comment on "Sterilizing immunity in the lung relies on targeting fungal apoptosis-like programmed cell death"

Neta Shlezinger[1], Henriette Irmer[2], Sourabh Dhingra[3], Sarah R. Beattie[3], Robert A. Cramer[3], Gerhard H. Braus[2], Amir Sharon[4]*, Tobias M. Hohl[1,5]*

Aouacheria *et al*. question the interpretation of contemporary assays to monitor programmed cell death with apoptosis-like features (A-PCD) in *Aspergillus fumigatus*. Although our study focuses on fungal A-PCD for host immune surveillance and infectious outcomes, the experimental approach incorporates multiple independent A-PCD markers and genetic manipulations based on fungal rather than mammalian orthologs to circumvent the limitations associated with any single approach.

Our manuscript reports that human and mouse leukocytes trigger A-PCD in inhaled mold conidia as a mechanism of mucosal barrier immune surveillance (*1*). We distinguish fungal A-PCD from metazoan apoptosis and from accidental cell death; the latter process is defined as "virtually immediate and ... insensitive to pharmacologic or genetic interventions of any kind" (*2*). According to a recently published 2018 guideline (*3*), the A-PCD process observed in conidia during cellular interactions with innate immune cells is best understood as a regulated cell death subroutine with apoptosis-like features. Our study relied on a combination of assays to monitor markers of conidial A-PCD (i.e., nuclear condensation and histone degradation, fungal caspase-like activities, DNA double-strand breaks, and viability by clonogenic assay), in accordance with accepted practice (*4*–*7*).

The Comment by Aouacheria *et al*. (*8*) highlights differences between animal apoptosis and fungal A-PCD, and points to longstanding knowledge gaps in the study of regulated cell death in fungi. In particular, the fungal factors responsible for TUNEL reactivity or caspase-like activity, or those that trigger fungal cell death in mammalian cell death assays, remain undefined (*9*). Notably, the authors' assertion regarding the low specificity of individual assays holds true for mammalian cells as well. Thus, although we fully agree with the authors that improvements in methodologies will advance the study of fungal cell death, our study did not aim to answer this general question. In addition, Aouacheria *et al*. raise several issues that require clarification.

First, at the outset, the authors state that "Shlezinger *et al*. reported the existence of an 'apoptosis-like' programmed death pathway in the opportunistic pathogen *Aspergillus fumigatus*, a multicellular fungus responsible for life-threatening infections." A-PCD in fungi, and specifically in *A. fumigatus*, is well known and broadly supported by numerous studies conducted over the past 20 years [reviewed in (*7*)]. Among filamentous molds, the best-understood examples of regulated cell death processes include heterokaryon incompatibility (*10*, *11*), appressorium morphogenesis (*12*), senescence (*13*, *14*), and the development of reproductive structures and infectious propagules (*15*). We make no such claim of discovery; in fact, the existence of A-PCD in fungi was the basis for our research hypothesis.

Second, Aouacheria *et al*. criticize the use of the fluorescein isothiocyanate (FITC)–conjugated tripeptide Val-Ala-Asp fused to fluoromethylketone (FITC-VAD-FMK) as a marker of fungal A-PCD. Fungal genomes encode metacaspases, cysteine-dependent proteases that share structural properties with metazoan caspases and hydrolyze proteins after Arg or Lys rather than Asp residues (*16*). Deletion of the two *A. fumigatus* metacaspases, CasA and CasB, does not render cells sensitive to oxidative stress and does not attenuate a FITC-VAD-FMK signal under these conditions (*17*); the dependency of *Aspergillus* cell death routines on metacaspase activity varies according to the specific stimulus (*18*, *19*). Nonetheless, a substantial body of work demonstrates that the pan-caspase inhibitor Z-VAD-FMK effectively inhibits the activation of apoptosis-like cell death in fungal cells (*4*, *20*–*22*) and in particular in *A. fumigatus* (*18*). On the basis of these studies, FITC-VAD-FMK has been used extensively for detection of caspase-like activity in yeast and filamentous fungi (*23*–*26*). In addition, numerous studies reported that activation of fungal apoptotic cell death correlated with the appearance of caspase-like activities with a substrate specificity similar to that of initiator caspases [with Val-Glu-Ile-Asp (VEID)– and Ile-Glu-Thr-Asp (IETD)–hydrolyzing activities] that could be abolished by Z-VAD-FMK (*15*, *24*, *27*, *28*). Together with our findings, the above studies support a model in which unidentified caspase-like protease(s) act in fungal A-PCD downstream of BIR1-dependent regulation. Thus, the identification and functional characterization of putative *A. fumigatus* cysteine proteases in A-PCD represents an important direction of future research.

Our results do not support the notion that FITC-VAD-FMK "can also nonspecifically label living nonpermeabilized yeast cells." We detected a fluorescent signal in live *A. fumigatus* conidia that were engulfed by innate immune cells in vivo. If the probe were incorporated nonspecifically by live conidia in the murine lung, we would predict detection of the same signal in free conidia found in infected airways of the same animal. This was not the case.

Third, the authors state that "Shlezinger *et al*. took a different approach to address a causal role for fungal caspase-like activities, leading to the identification of a virulence mechanism" and that the manuscript assumes "that AfBIR1 behaves similarly to the human inhibitor of apoptosis (IAP) protein survivin, based on the assumption that survivin inhibits apoptotic caspases." It is critical to note that AfBIR1 belongs to a conserved family of proteins in fungi (and animals) that encode a BIR domain (*4*, *16*), the hallmark of IAP proteins. Because all other characterized fungal proteins that contain a BIR domain exert anti-PCD activity (*17*–*21*), we functionally analyzed AfBIR1 to establish a direct relationship among AfBIR1-dependent regulation of conidial A-PCD, fungal virulence, innate immune surveillance in the lung, and infectious outcomes. Although we monitored fungal caspase-like activity during A-PCD and its dependency on AfBIR1 expression levels, the precise mechanism by which this regulation occurs represents a focus for follow-up studies. Thus, the premise for our experiments and conclusions rests on a body of work conducted in fungal rather than mammalian systems that collectively strongly supports a role for fungal BIR1 orthologs in regulated cell death processes.

Fourth, the authors criticize the use of S12 as an AfBIR1 inhibitor. Because a genetic loss-of-function approach was not possible, we used a complementary pharmacologic approach to target the fungal BIR domain. The impact of S12 on oxidative stress–induced A-PCD correlated with

[1]Infectious Disease Service, Department of Medicine, Memorial Sloan Kettering Cancer Center, New York, NY 10075, USA. [2]Department of Molecular Microbiology and Genetics, Institute for Microbiology and Genetics, and Göttingen Center for Molecular Biosciences, University of Göttingen, D-37077 Göttingen, Germany. [3]Department of Microbiology and Immunology, Geisel School of Medicine, Dartmouth College, Hanover, NH 03755, USA. [4]Department of Molecular Biology and Ecology of Plants, Tel Aviv University, Tel Aviv 69978, Israel. [5]Immunology Program, Sloan Kettering Institute, Memorial Sloan Kettering Cancer Center, New York, NY 10075, USA.
***Corresponding author. Email: hohlt@mskcc.org (T.M.H.); amirsh@tauex.tau.ac.il (A.S.)**

AfBIR1 expression levels in different strains. In vivo, administration of S12 accelerated fungal clearance, in contrast to the delayed clearance and invasive disease caused by an increase in AfBIR1 expression. Thus, the results of the S12 experiments are in line with and extend complementary genetic gain-of-function experiments. However, further work is necessary to demonstrate direct binding of S12 with AfBIR1.

Our results support a model in which the respiratory innate immune system triggers NADPH oxidase–dependent A-PCD in inhaled mold conidia and advance the concept that a higher eukaryote can exploit a regulated cell death process in a lower eukaryote to maintain barrier immunity. Although the Comment by Aouacheria *et al.* does not detract from these conclusions, it enlightens longstanding conceptual and technical questions related to fungal A-PCD, highlights important knowledge gaps for future research and advancement of the field as a whole, and engenders a lively conversation about these fascinating topics.

REFERENCES

1. N. Shlezinger *et al.*, *Science* **357**, 1037–1041 (2017).
2. L. Galluzzi *et al.*, *Cell Death Differ.* **22**, 58–73 (2015).
3. D. Carmona-Gutierrez *et al.*, *Microb. Cell* **5**, 4–31 (2018).
4. A. Sharon, A. Finkelstein, N. Shlezinger, I. Hatam, *FEMS Microbiol. Rev.* **33**, 833–854 (2009).
5. C. P. Semighini, S. D. Harris, *Methods Mol. Biol.* **638**, 269–279 (2010).
6. D. Carmona-Gutierrez *et al.*, *Cell Death Differ.* **17**, 763–773 (2010).
7. A. P. Gonçalves, J. Heller, A. Daskalov, A. Videira, N. L. Glass, *Front. Microbiol.* **8**, 1837 (2017).
8. A. Aouacheria *et al.*, *Science* **360**, eaar6910 (2018).
9. J. M. Hardwick, W. C. Cheng, *Dev. Cell* **7**, 630–632 (2004).
10. A. Daskalov *et al.*, *PLOS Biol.* **13**, e1002059 (2015).
11. A. Daskalov *et al.*, *Proc. Natl. Acad. Sci. U.S.A.* **113**, 2720–2725 (2016).
12. C. Veneault-Fourrey, M. Barooah, M. Egan, G. Wakley, N. J. Talbot, *Science* **312**, 580–583 (2006).
13. A. Hamann, D. Brust, H. D. Osiewacz, *Mol. Microbiol.* **65**, 948–958 (2007).
14. L. Knuppertz, V. Warnsmann, A. Hamann, C. Grimm, H. D. Osiewacz, *Autophagy* **13**, 1037–1052 (2017).
15. C. Thrane, U. Kaufmann, B. M. Stummann, S. Olsson, *Fungal Genet. Biol.* **41**, 361–368 (2004).
16. L. Tsiatsiani *et al.*, *Cell Death Differ.* **18**, 1279–1288 (2011).
17. D. L. Richie *et al.*, *Mol. Microbiol.* **63**, 591–604 (2007).
18. S. A. Mousavi, G. D. Robson, *Fungal Genet. Biol.* **39**, 221–229 (2003).
19. S. A. Mousavi, G. D. Robson, *Microbiology* **150**, 1937–1945 (2004).
20. R. S. Al-Dhaheri, L. J. Douglas, *J. Med. Microbiol.* **59**, 149–157 (2010).
21. X. Wang, Y. Wang, Y. Zhou, X. Wei, *Mycologia* **106**, 881–888 (2014).
22. F. Shirazi *et al.*, *Antimicrob. Agents Chemother.* **57**, 4360–4368 (2013).
23. E. Herker *et al.*, *J. Cell Biol.* **164**, 501–507 (2004).
24. P. Hauptmann *et al.*, *Mol. Microbiol.* **59**, 765–778 (2006).
25. F. Shirazi, R. E. Lewis, D. P. Kontoyiannis, *Microb. Cell* **2**, 445–450 (2015).
26. M. Johansson, X. Chen, S. Milanova, C. Santos, D. Petranovic, *FEMS Yeast Res.* **16**, fow007 (2016).
27. F. Madeo *et al.*, *Curr. Genet.* **41**, 208–216 (2002).
28. N. Guaragnella, A. Bobba, S. Passarella, E. Marra, S. Giannattasio, *FEBS Lett.* **584**, 224–228 (2010).

5 February 2018; accepted 10 May 2018
10.1126/science.aas9457

RESEARCH

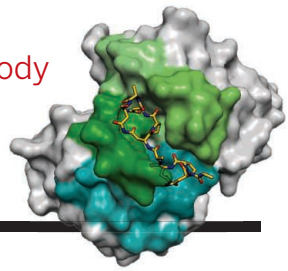

Malaria antigen-antibody interaction

Imkeller et al., *p. 1358*

IN *SCIENCE* JOURNALS

Edited by **Caroline Ash**

EVOLUTIONARY BIOLOGY

Hybrid camouflage variation

Snowshoe hares molt from a brown coat to a white coat in winter. In some populations, however, where winter snow is less extensive, hares molt from a brown coat to a brown coat. Jones *et al*. show that regulation of the pigmentation gene *Agouti* is responsible for the winter coat color change. Hybridization with jackrabbits has led to introgression around this gene that facilitates the brown winter morph. Hybridization appears to have provided important adaptive variation to the snowshoe hare. —SNV

Science, this issue p. 1355

Hybrid snowshoe hares can stay brown in snowless winters.

ENVIRONMENTAL STUDIES

China's plastic waste import ban

China, the world's top plastic waste importer, implemented a permanent ban on importing nonindustrial plastic waste beginning on 31 December 2017. Brooks *et al.* examined how this ban may affect countries that had previously exported difficult-to-manage plastic waste to China. Through analyzing 28 years of data on imports and exports from the United Nations Comtrade Database, they found that China has imported 45% of the world's plastic waste since 1992. This means that an estimated 111 million metric tons of plastic waste will have to be redirected by 2030 because of this ban. The analysis further highlights how, for decades, higher-income countries have been exporting plastic waste to lower-income countries that do not have robust waste management infrastructures. —PJB

Sci. Adv. 10.1126/sciadv.aat0131 (2018).

ANTHROPOLOGY

The noblewoman's ape

Human activities are causing extinctions across a wide array of taxa. Yet there has been no evidence of humans directly causing extinction among our relatives, the apes. Turvey *et al*. describe a species of gibbon found in a 2200- to 2300-year-old tomb ascribed to a Chinese noblewoman. This previously unknown species was likely widespread, may have persisted until the 18th century, and may be the first ape species to have perished as a direct result of human activities. This discovery may also indicate the existence of unrecognized primate diversity across Asia. —SNV

Science, this issue p. 1346

PAIN

Dialing down the opioids

The pain relief afforded by morphine and other opioids comes with the cost of behavioral side effects and high addiction potential. He *et al*. found that the analgesic response to morphine could be enhanced by compounds that activate the peripheral sensory neuron–localized receptor MrgC11 in mice and MrgX1 in humans. Activation of MrgC11 promoted its interaction with the μ-opioid receptor. This interaction enabled the use of lower morphine doses to achieve pain relief in mice, without the tolerance and locomotor side effects typically associated with the drug. —LKF

Sci. Signal. **11**, eaao3134 (2018).

IMMUNODEFICIENCIES

Fingers on the trigger

Hyper–immunoglobulin E syndromes (HIESs) are rare genetic immunodeficiency diseases characterized by bacterial infections, chronic mucocutaneous candidiasis, allergies, and skeletal abnormalities associated with impaired T helper 17 (T_H17) cell immunity. Béziat *et*

CREDITS: (FROM TOP) K. IMKELLER *ET AL.*; MAURITIUS IMAGES GMBH/ALAMY STOCK PHOTO

Published by AAAS

al. and Frey-Jakobs *et al.* have studied patients with an autosomal recessive form of HIES and identified mutations in the zinc finger transcription factor ZNF341 as the culprit. Loss-of-function mutations encoding truncated forms of ZNF341 interfered with its ability to recognize a bipartite binding site located in the promoter of STAT3, the transcription factor mutated in most cases of autosomal dominant HIES. ZNF341-supported transcription of STAT3 is a key upstream regulatory step needed to trigger the T_H17 differentiation pathway. These findings reveal a previously unappreciated layer of transcriptional regulation controlling JAK-STAT signaling. —IW

Sci. Immunol. **3**, eaat4956, eaat4941 (2018).

QUANTUM CRITICALITY

A nanostructure quantum simulator

Phase transitions occurring at absolute zero temperature, or quantum phase transitions (QPTs), can be grouped into broad categories called universality classes. The classification is based on the properties of the transition rather than the microscopic details of the underlying system. Iftikhar *et al.* exploited this fact to study QPTs in clean, tunable nanostructures, rather than in complex materials, where they most often occur. Within a single nanostructure, two different classes of QPTs with profoundly different characters were studied and comprehensively characterized. —JS

Science, this issue p. 1315

GEOPHYSICS

A quick rebound for Antarctic crust

Earth's crust deforms under the load of glaciers and ice sheets. When these masses are removed, the crust rebounds at a time scale determined by the viscosity of the upper mantle. Using GPS, Barletta *et al.* found that the viscosity of the mantle under the West Antarctic Ice Sheet is much lower than expected. This means that as ice is lost, the crust rebounds much faster than previously expected. Although estimates of total ice loss have to be revised upward, the surprising finding indicates that the ice sheet may stabilize against catastrophic collapse. —BG

Science, this issue p. 1335

GRAVITATION

Testing General Relativity on galaxy scales

Einstein's theory of gravity, General Relativity (GR), has been tested precisely within the Solar System. However, it has been difficult to test GR on the scale of an individual galaxy. Collett *et al.* exploited a nearby gravitational lens system, in which light from a distant galaxy (the source) is bent by a foreground galaxy (the lens). Mass distribution in the lens was compared with the curvature of space-time around the lens, independently determined from the distorted image of the source. The result supports GR and eliminates some alternative theories of gravity. —KTS

Science, this issue p. 1342

NEUROSCIENCE

Rebalancing strength between synapses

Activation of a neuronal pathway is often associated with inhibition of surrounding pathways. How locally coordinated synaptic plasticity occurs in vivo is not known, nor is its role in shaping neuronal responses. El-Boustani *et al.* paired optogenetic stimulation of single neurons with a visual input and were able to shift the neuron's receptive field toward the target location. Spines that expressed structural long-term potentiation had receptive fields overlapping the target stimulus but were surrounded by spines that expressed receptive fields away from the target. —PRS

Science, this issue p. 1349

IN OTHER JOURNALS

Edited by **Sacha Vignieri** *and* **Jesse Smith**

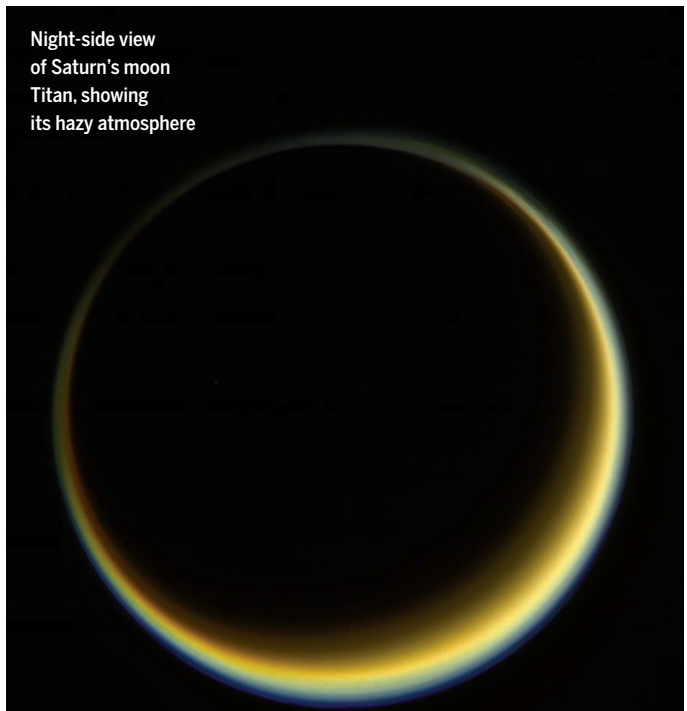

Night-side view of Saturn's moon Titan, showing its hazy atmosphere

PLANETARY SCIENCE

Benzene ice clouds in Titan's atmosphere

Titan, the largest moon of Saturn, has a thick atmosphere composed mostly of nitrogen, with smaller amounts of organic molecules such as methane and benzene. Vinatier *et al.* have analyzed infrared spectra of Titan obtained by the Cassini spacecraft during flybys of the moon. In addition to the expected gas-phase species, colder regions show a spectral signature consistent with solid benzene. After eliminating alternative explanations, the authors conclude that stratospheric clouds of benzene ice are present, particularly over Titan's south pole. The clouds are analogous to high-altitude cirrus clouds on Earth, which are composed of solid water-ice crystals. —KTS

Icarus **310**, 89 (2018).

ORGANIC CHEMISTRY

Making a triple negative

The trifluoromethanesulfonyl (Tf) group is remarkably adept at stabilizing negative charge: It boasts highly withdrawing fluorines and sulfur-oxygen bonds that can delocalize electrons through resonance. Höfler *et al.* took full advantage of these properties in generating a molecule with three independent anionic carbon centers. The synthetic reaction coupled triformylmethane with three equivalents of Tf_2CH_2, after which a base deprotonated all three Tf-substituted carbon centers. The compound was characterized by crystallography and showed trigonal-planar geometries at each charged carbon. —JSY

Angew. Chem. Int. Ed. 10.1002/anie.201803647 (2018).

PHOTO: NASA/JPL-CALTECH/SPACE SCIENCE INSTITUTE

Two different photoreceptors allow an annelid to choose its depth.

PLANKTONIC NEUROSCIENCE

Paired photoreceptors function as an oceanic depth gauge

Ciliary photoreceptors, which are typical of vertebrates, differ in morphology and in type of opsins from the rhabdomeric photoreceptors characteristic of annelids. Larvae of the marine annelid *Platynereis dumerilii* have both kinds of photoreceptors. Verasztó *et al*. worked out the circuits and responses driven by this pairing. The ciliary photoreceptors respond to ultraviolet (UV) light, causing the larvae to swim away from it. The rhabdomeric photoreceptors respond to blue light and drive a phototactic response. At the ocean surface, the UV-avoidance response dominates, driving larvae downward, whereas at greater depths, the phototactic response dominates, driving larvae toward the surface. When the swim-upward signal balances out the swim-downward signal, the larvae have found their favorite depth. —PJH

eLife 10.7554/eLife.36440 (2018).

ONCOLOGY

A ray of hope for advanced breast cancer

Immunotherapies are revolutionizing cancer treatment. Yet certain common cancer types, such as breast cancer, are often missing from the immunotherapy conversation. One reason is that breast cancers express relatively few neoantigens, or mutant tumor-associated proteins that are targeted by the immune system. A case study now shows that in the setting of adoptive T cell therapy, this problem can be circumvented, resulting in a dramatic clinical response. Zacharakis *et al*. report that a patient with metastatic breast cancer showed complete durable remission of her disease after being treated with autologous tumor-infiltrating lymphocytes that had been enriched ex vivo for reactivity to just four neoantigens. This study lays the groundwork for studies of other cancers assumed to be refractory to immunotherapy. — PAK

Nat. Med. 10.1038/s41591-018-0040-8 (2018).

SLEEP

A good excuse to sleep in

Most of us don't get as much sleep as we should, which is often due to hectic weekday schedules. Akerstedt *et al.* reveal that all is not lost—sleeping in on the weekends may have beneficial effects on our health. In a 13-year study of more than 43,000 subjects, the researchers compared the duration of sleep on weekdays versus weekends with overall mortality. Individuals (<65 years old) who caught less than 5 hours of sleep a night had a higher death rate than those that regularly had 7 hours of sleep. But when the weekday short sleepers compensated with long sleep on weekends, no difference in mortality was observed. —PNK

J. Sleep Res. 10.1111/jsr.12712 (2018).

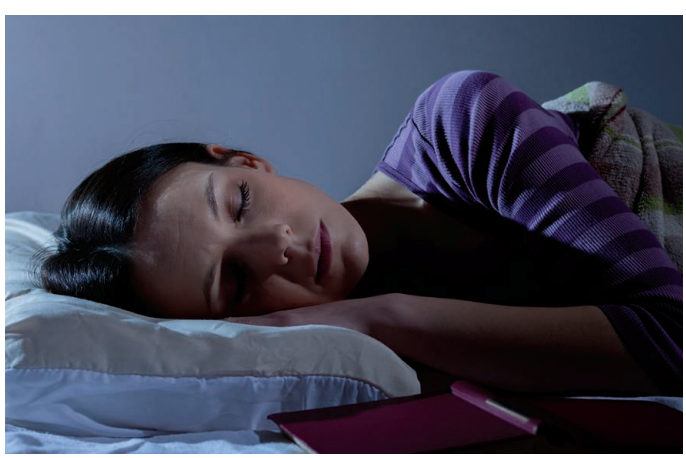

Sleeping in on the weekend may make up for less sleep during the week.

CLIMATE CHANGE

Warming in Greenland's past

To project how much sea level will rise in response to ongoing climate warming, one of the things we need to know is how sensitive the rate of Greenland Ice Sheet melting is to rising temperatures. McFarlin *et al.* present results from a set of sediment cores from a small nonglacial lake in the highlands of northwest Greenland, which contain deposits from the Holocene and the Last Interglacial (LIG). They found midge assemblages indicating peak July temperatures that were 4.0° to 7.0°C warmer than modern temperatures during the early Holocene and at least 5.5° to 8.5°C warmer during the LIG. This perspective of extreme warming suggests that even larger changes than predicted for this region over the coming century may be in store. —HJS

Proc. Natl. Acad. Sci. U.S.A. 10.1073/pnas.1720420115 (2018).

NEUROSCIENCE

The human prefrontal cortex is special

The size and surface area of the cerebral cortex varies dramatically across mammals. It is well known that the human cortex is by far the largest among primates. However, there is no agreement about whether the human prefrontal cortex is larger, in relative terms, than those of other primates. Donahue *et al*. compared structural brain scan datasets from humans, chimpanzees, and macaques. They found a greater proportion of prefrontal cortex gray matter volume in humans than in the two nonhuman primate species, and they observed an even greater difference between species for white matter volume in the prefrontal cortex. This part of the association cortex, which is implicated in higher cognition and affect, is thus disproportionately large in humans relative to other primates. —PRS

Proc. Natl. Acad. Sci. U.S.A. **115**, E5183 (2018).

PHOTOS: (FROM TOP) MARTIN GÜHMANN (CC BY-SA 4.0); MLADEN MITRINOVIC/SHUTTERSTOCK

ALSO IN *SCIENCE* JOURNALS

Edited by **Caroline Ash**

ECOLOGY

Where have all the monarchs gone?

North American monarch butterfly populations have declined at their Mexican overwintering sites in recent years. The picture is less clear for monarch summer breeding sites in the United States and Canada. In a Perspective, Agrawal and Inamine report on recent survey results and conclude that several stressors affect monarch populations, including reduced availability of milkweed plants for caterpillars, stress during migration, and degradation of fir forest at the overwintering sites in Mexico. Migratory success is highly variable from one year to the next, complicating efforts to conserve monarch populations. —JFU

Science, this issue p. 1294

ANTHROPOLOGY

Out of Africa, with a difference

According to the recent African origin model, modern humans emerged in Africa by about 200,000 years ago. They spread across the rest of the world, successively replacing archaic populations along the way. In a Perspective, Galway-Witham and Stringer show that recent evidence calls for modification of this influential model. Fossil evidence indicates that modern humans may have evolved for longer than previously thought. Genetic evidence for mixing between modern humans and archaic populations, such as Neandertals and Denisovans, makes it difficult to clearly delineate species boundaries between them. Genomic data for African fossils older than 15,000 years will help to resolve these questions. —JFU

Science, this issue p. 1296

PLANT PATHOLOGY

Networks in plant immunity

Plant defenses against pathogens have traditionally been viewed as pairwise matching of a resistance gene in a host plant to a virulence gene in a pathogen (Flor's gene-for-gene hypothesis). In a Perspective, Wu *et al.* discuss emerging data that show that plant immune responses function as a network in which key nodes coordinate the host response to multiple pathogen factors. —GKA

Science, this issue p. 1300

PSYCHIATRIC GENOMICS

Brainstorming diseases

Consistent classification of neuropsychiatric diseases is problematic because it can lead to misunderstanding of etiology. The Brainstorm Consortium examined multiple genome-wide association studies drawn from more than 200,000 patients for 25 brain-associated disorders and 17 phenotypes. Broadly, it appears that psychiatric and neurologic disorders share relatively little common genetic risk. However, different and independent pathways can result in similar clinical manifestations (e.g., psychosis, which occurs in both schizophrenia and Alzheimer's disease). Schizophrenia correlated with many psychiatric disorders, whereas the immunopathological affliction Crohn's disease did not, and posttraumatic stress syndrome was also largely independent of underlying traits. Essentially, the earlier the onset of a disorder, the more inheritable it appeared to be. —LMZ

Science, this issue p. 1313

SIGNAL TRANSDUCTION

Mechanisms of drug action

Advanced mass spectrometry methods enable monitoring of tens of thousands of phosphorylation sites in proteins. This technology can potentially distinguish cellular signaling pathways that produce beneficial effects from those that produce unwanted side effects. Liu *et al*. treated mice with various agonists of the kappa opioid receptor (a G protein–coupled receptor) and monitored changes in phosphorylation over time in different brain regions. The phosphorylation patterns revealed distinct patterns of signaling in various brain tissues, some of which were associated with unwanted side effects. —LBR

Science, this issue p. 1314

ALCOHOL DEPENDENCY

Finding the vulnerable minority

"Only" about 10 to 15% of people exposed to alcohol develop alcohol-related problems. The behavioral repertoire of people confronted with opportunities to consume alcohol involves numerous choices between this drug reward and healthy alternatives. Augier *et al*. established a choice procedure that begins to address alcohol addiction in rats (see the Perspective by Spanagel). They found that a minority of outbred rats continued to self-administer alcohol even when a high-value alternative (such as sugar) was available. That minority displayed a remarkable constellation of behavioral traits resembling the human clinical condition, including a high motivation to obtain alcohol and continued use despite adverse consequences. The cause was impaired GABA (γ-aminobutyric acid) clearance in the central amygdala. Postmortem tissue analysis supported the possibility of a similar pathology in human alcoholism. —SMH

Science, this issue p. 1298; see also p. 1321

ATTOSECOND DYNAMICS

Time and place of electron exit

Until about a decade ago, laser-induced ionization was considered instantaneous. Since then, applications of attosecond laser pulses have shown multiple subtle and complex factors that influence the precise timing of electron ejection from atoms and surfaces. Vos *et al*. measured the corresponding attosecond dynamics of dissociative photoionization in a diatomic molecule, carbon monoxide. By imaging the charged fragments, the timing could be correlated with the specific spatial portion of the molecule from which the electron wave packet emerged. —JSY

Science, this issue p. 1326

CHIRAL RESOLUTION

Taking enantiomers for a spin

There are two common ways to distinguish mirror-image molecules, or enantiomers. The first relies on their distinct interactions with circularly polarized light, the second on their interactions with a pure enantiomer of some other molecule. Now Banerjee-Ghosh *et al*. report a conceptually different approach to chiral resolution. Experiments showed that, depending on the direction of magnetization, chiral oligopeptides, oligonucleotides, and amino acids have enantiospecific differences in initial adsorption rates on ferromagnetic surfaces. This effect is attributed to enantiospecific induced spin polarization. —JSY

Science, this issue p. 1331

WATER PROPERTIES

Water's surface dielectric

Theoretical studies predict that the inhibition of rotational motion of water near a solid surface will decrease its local dielectric constant. Fumagalli *et al*. fabricated thin channels in insulating hexagonal boron nitride on top of conducting graphene layers (see the Perspective by Kalinin). The channels, which varied in height from 1 to 300 nanometers, were filled with water and capped with a boron nitride layer. Modeling of the capacitance measurements made with an atomic force microscope tip revealed a surface-layer dielectric constant of 2, compared with the bulk value of 80 for water. —PDS

Science, this issue p. 1339; see also p. 1302

TISSUE ENGINEERING

Disjointed no more

Temporomandibular joint (TMJ) dysfunction causes pain and limits movement of the jaw joint. Thinning of the TMJ disc, a fibrocartilage structure that allows for smooth joint movement, is an early sign of TMJ dysfunction. To help prevent joint degeneration, Vapniarsky *et al.* implanted engineered discs derived from rib cartilage cells into a minipig model of TMJ disc thinning. The implants exhibited biomechanical and biochemical properties similar to those of native discs, improved closure of disc defects, reduced osteoarthritis scores, and relieved degenerative changes in the jaw joint. —CC

Sci. Transl. Med. **10**, eaaq1802 (2018).

IMMUNOLOGY

Surface antibody maturation

Affinity maturation in B cells generates antibodies with increasingly enhanced antigen-binding properties. Imkeller *et al*. investigated the maturation of human B cells that express protective antibodies against the circumsporozoite protein of the malaria-causing parasite *Plasmodium falciparum* (PfCSP). The repetitive structure of PfCSP induces mutations in B cells, facilitating direct interactions between two repeat-bound antibodies against PfCSP, which enhance antigen affinity and B cell activation. Such interactions may optimize binding and promote clustering of surface antibodies in general. —STS

Science, this issue p. 1358

RESEARCH ARTICLE SUMMARY

PSYCHIATRIC GENOMICS

Analysis of shared heritability in common disorders of the brain

The Brainstorm Consortium†

INTRODUCTION: Brain disorders may exhibit shared symptoms and substantial epidemiological comorbidity, inciting debate about their etiologic overlap. However, detailed study of phenotypes with different ages of onset, severity, and presentation poses a considerable challenge. Recently developed heritability methods allow us to accurately measure correlation of genome-wide common variant risk between two phenotypes from pools of different individuals and assess how connected they, or at least their genetic risks, are on the genomic level. We used genome-wide association data for 265,218 patients and 784,643 control participants, as well as 17 phenotypes from a total of 1,191,588 individuals, to quantify the degree of overlap for genetic risk factors of 25 common brain disorders.

RATIONALE: Over the past century, the classification of brain disorders has evolved to reflect the medical and scientific communities' assessments of the presumed root causes of clinical phenomena such as behavioral change, loss of motor function, or alterations of consciousness. Directly observable phenomena (such as the presence of emboli, protein tangles, or unusual electrical activity patterns) generally define and separate neurological disorders from psychiatric disorders. Understanding the genetic underpinnings and categorical distinctions for brain disorders and related phenotypes may inform the search for their biological mechanisms.

RESULTS: Common variant risk for psychiatric disorders was shown to correlate significantly, especially among attention deficit hyperactivity disorder (ADHD), bipolar disorder, major depressive disorder (MDD), and schizophrenia. By contrast, neurological disorders appear more distinct from one another and from the psychiatric disorders, except for migraine, which was significantly correlated to ADHD, MDD, and Tourette syndrome. We demonstrate that, in the general population, the personality trait neuroticism is significantly correlated with almost every psychiatric disorder and migraine. We also identify significant genetic sharing between disorders and early life cognitive measures (e.g., years of education and college attainment) in the general population, demonstrating positive correlation with several psychiatric disorders (e.g., anorexia nervosa and bipolar disorder) and negative correlation with several neurological phenotypes (e.g., Alzheimer's disease and ischemic stroke), even though the latter are considered to result from specific processes that occur later in life. Extensive simulations were also performed to inform how statistical power, diagnostic misclassification, and phenotypic heterogeneity influence genetic correlations.

CONCLUSION: The high degree of genetic correlation among many of the psychiatric disorders adds further evidence that their current clinical boundaries do not reflect distinct underlying pathogenic processes, at least on the genetic level. This suggests a deeply interconnected nature for psychiatric disorders, in contrast to neurological disorders, and underscores the need to refine psychiatric diagnostics. Genetically informed analyses may provide important "scaffolding" to support such restructuring of psychiatric nosology, which likely requires incorporating many levels of information. By contrast, we find limited evidence for widespread common genetic risk sharing among neurological disorders or across neurological and psychiatric disorders. We show that both psychiatric and neurological disorders have robust correlations with cognitive and personality measures. Further study is needed to evaluate whether overlapping genetic contributions to psychiatric pathology may influence treatment choices. Ultimately, such developments may pave the way toward reduced heterogeneity and improved diagnosis and treatment of psychiatric disorders. ■

ON OUR WEBSITE

Read the full article at http://dx.doi.org/10.1126/science.aap8757

The list of author affiliations is available in the full article online.
†Corresponding authors: Verneri Anttila (verneri.anttila@gmail.com); Aiden Corvin (acorvin@tcd.ie); Benjamin M. Neale (bneale@broadinstitute.org)
Cite this article as The Brainstorm Consortium, *Science* **360**, eaap8757 (2018). DOI: 10.1126/science.aap8757

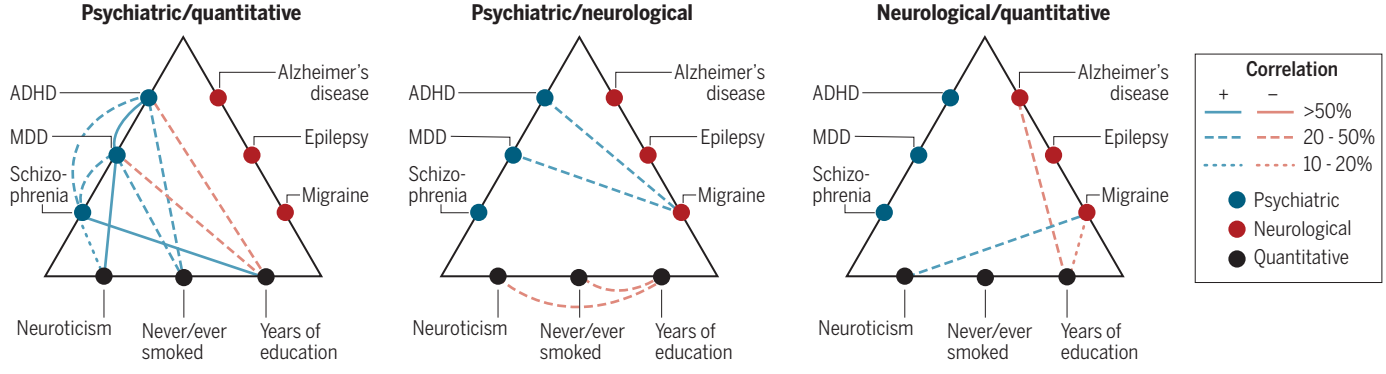

Subsection of genetic risk correlations among brain disorders and quantitative phenotypes. Heritability analysis of brain disorders points to pervasive sharing of genetic risk among psychiatric disorders. These correlations are largely absent among neurological disorders but are present for both groups in relation to neurocognitive quantitative phenotypes. Only significant correlations shown. Line color and solidity indicate direction and magnitude of correlation, respectively.

RESEARCH ARTICLE

PSYCHIATRIC GENOMICS

Analysis of shared heritability in common disorders of the brain

The Brainstorm Consortium*†

Disorders of the brain can exhibit considerable epidemiological comorbidity and often share symptoms, provoking debate about their etiologic overlap. We quantified the genetic sharing of 25 brain disorders from genome-wide association studies of 265,218 patients and 784,643 control participants and assessed their relationship to 17 phenotypes from 1,191,588 individuals. Psychiatric disorders share common variant risk, whereas neurological disorders appear more distinct from one another and from the psychiatric disorders. We also identified significant sharing between disorders and a number of brain phenotypes, including cognitive measures. Further, we conducted simulations to explore how statistical power, diagnostic misclassification, and phenotypic heterogeneity affect genetic correlations. These results highlight the importance of common genetic variation as a risk factor for brain disorders and the value of heritability-based methods in understanding their etiology.

The classification of brain disorders has evolved over the past century, reflecting the medical and scientific communities' assessments of the presumed root causes of clinical phenomena such as behavioral change, loss of motor function, spontaneous movements, or alterations of consciousness. Directly observable phenomena (such as the presence of emboli, protein tangles, or unusual electrical activity patterns) generally define and separate neurological disorders from psychiatric disorders (*1*). Understanding the genetic underpinnings and categorical distinctions between brain disorders may be helpful in informing the search for the biological pathways underlying their pathophysiology (*2*, *3*).

Studies of twins and families have indicated that, in general, brain disorders (excepting those caused by trauma, infection, or cancer) show substantial heritability (*4*). Epidemiological and twin studies have explored patterns of phenotypic overlaps (*5*–*7*), and comorbidity has been reported for many pairs of disorders, including bipolar disorder and migraine (*8*), stroke and major depressive disorder (MDD) (*9*), epilepsy and autism spectrum disorder (ASD), and epilepsy and attention deficit hyperactivity disorder (ADHD) (*10*, *11*). Furthermore, direct etiological links may also exist—e.g., mutations in the same ion channel genes confer pleiotropic risk for multiple distinct brain phenotypes (*12*–*14*). Genome-wide association studies (GWASs) have demonstrated that individual common risk variants can overlap across traditional diagnostic boundaries (*15*, *16*) and that disorders such as schizophrenia, MDD, and bipolar disorder can have genetic correlations (*17*).

*All authors with their affiliations are listed at the end of this paper.
†Collaborators and affiliations are listed in the supplementary materials.

GWASs have also demonstrated that common genetic variation contributes to the heritability of brain disorders. Generally, this occurs via the combination of many common variants—examples include Alzheimer's disease (*18*), bipolar disorder (*19*), migraine (*20*), Parkinson's disease (*21*), and schizophrenia (*22*)—each with a small individual effect. In addition to locus discovery, the degree of distinctiveness (*23*) across neurological and psychiatric phenotypes can be evaluated with the introduction of novel heritability-based methods (*24*) and sufficiently large sample sizes for robust heritability analysis. These analyses can shed light on the nature of these diagnostic boundaries and explore the extent of shared common variant genetic influences.

Study design

The Brainstorm Consortium, a collaboration among GWAS meta-analysis consortia for 25 disorders (Table 1), was assembled to perform a comprehensive heritability and correlation analysis of brain disorders. We included meta-analyses of any common brain disorders for which we could identify a GWAS meta-analysis consortium of sufficient size for heritability analysis. The total study sample consists of 265,218 cases of different brain disorders and 784,643 controls (Table 1) and includes at least one representative of most ICD-10 (10th revision of the International Statistical Classification of Diseases and Related Health Problems) blocks covering mental and behavioral disorders and diseases of the central nervous system (CNS). Also included are 1,191,588 samples for 13 behavioral-cognitive phenotypes (n = 744,486 individuals) traditionally viewed as brain-related, as well as 4 additional phenotypes (n = 447,102 individuals) selected to represent known, well-delineated etiological processes {immune disorders (Crohn's disease), vascular disease (coronary artery disease), and anthropomorphic measures [height and body mass index (BMI)]} (Table 2).

GWAS summary statistics for the 42 disorders and phenotypes were centralized and underwent uniform quality control and processing (*25*). To avoid potential bias arising from ancestry differences, we used European-only meta-analyses for each disorder and generated new meta-analyses for those datasets where the original sample sets had diverse ancestries. Clinically relevant subtypes from three disorders (epilepsy, migraine, and ischemic stroke) were also included; in these cases, the subtype datasets are parts of the top-level dataset (Table 1).

We have developed a heritability estimation method, linkage disequilibrium score (LDSC) regression (*24*), which was used to calculate heritability estimates and correlations, as well as to estimate their statistical significance from block jackknife–based standard errors. More formally, we estimate the common variant heritability (h^2g) of each disorder, defined as the proportion of phenotypic variance in the population that could theoretically be explained by an optimal linear predictor formed using the additive effects of all common (minor allele frequency >5%) autosomal single-nucleotide polymorphisms (SNPs). The genetic correlation for a pair of phenotypes is then defined as the correlation between their optimal genetic predictors. Heritability for binary disorders and phenotypes was transformed to the liability scale. We further performed a weighted least-squares regression analysis to evaluate whether differences relating to study makeup (such as sample size) were correlated with the magnitude of the correlation estimates. Finally, we performed a heritability partitioning analysis (*25*) by means of stratified LD score regression to examine whether the observed heritability for the disorders or phenotypes was enriched into any of the tissue-specific regulatory regions or functional category partitions of the genome, using 10 top-level tissue-type and 53 functional partitions from Finucane *et al.* (*26*). Simulated phenotype data was then generated under different scenarios by permuting 120,267 genotyped individuals from the UK Biobank (*25*) to evaluate statistical power and aid in interpreting the results (*25*).

Heritability estimates and their error sources

We observed a similar range of heritability estimates among the disorders and the behavioral-cognitive phenotypes (fig. S1, A and B, and table S1 and S2), roughly in line with previously reported estimates from smaller datasets (table S3). Three ischemic stroke subtypes (cardioembolic, large-vessel disease, and small-vessel disease) as well as the "agreeableness" personality measure from the NEO Five-Factor Inventory (*27*) had insufficient evidence of additive heritability for robust analysis and thus were excluded from further examination (*25*). The only observed correlation between heritability estimates and factors relating to study makeup (table S4 and fig. S1,

Table 1. Brain disorder phenotypes used in the Brainstorm project. Indented phenotypes are part of a larger whole (e.g., the epilepsy study contains the samples from both focal epilepsy and generalized epilepsy). "Anxiety disorders" refers to a meta-analysis of five subtypes (generalized anxiety disorder, panic disorder, social phobia, agoraphobia, and specific phobias). References are listed in table S1 and data availability in table S13. PGC-ADD2, Psychiatric Genomics Consortium (PGC) Attention Deficit Disorder Working Group; PGC-ED, PGC Eating Disorder Working Group; ANGST, Anxiety Neuro Genetics STudy; PGC-AUT, PGC Autism Spectrum Disorder Working Group; PGC-BIP2, PGC Bipolar Disorder Working Group; PGC-MDD2, PGC Major Depressive Disorder Working Group; PGC-OCDTS, PGC Obsessive Compulsive Disorder and Tourette Syndrome Working Group; PGC-PTSD, PGC Posttraumatic Stress Disorder Working Group; PGC-SCZ2, PGC Schizophrenia Working Group; IGAP, International Genomics of Alzheimer's Project; ILAE, International League Against Epilepsy Consortium on Complex Epilepsies; ISGC, International Stroke Genetics Consortium; METASTROKE, a consortium of the ISGC; IHGC, International; Headache Genetics Consortium; IMSGC, International Multiple Sclerosis Genetics Consortium; IPDGC, International Parkinson's Disease Genomics Consortium. " indicates same as above.

Psychiatric disorders				Neurological disorders			
Disorder	**Source**	**Cases**	**Controls**	**Disorder**	**Source**	**Cases**	**Controls**
Attention deficit hyperactivity disorder	PGC-ADD2	12,645	84,435	Alzheimer's disease	IGAP	17,008	37,154
Anorexia nervosa	PGC-ED	3495	10,982	Epilepsy	ILAE	7779	20,439
Anxiety disorders	ANGST	5761	11,765	Focal epilepsy	"	4601*	17,985*
Autism spectrum disorder	PGC-AUT	6197	7377	Generalized epilepsy	"	2525*	16,244*
Bipolar disorder	PGC-BIP2	20,352	31,358	Intracerebral hemorrhage	ISGC	1545	1481
Major depressive disorder	PGC-MDD2	66,358	153,234	Ischemic stroke	METASTROKE	10,307	19,326
Obsessive-compulsive disorder	PGC-OCDTS	2936	7279	Cardioembolic stroke	"	1859*	17,708*
Posttraumatic stress disorder	PGC-PTSD	2424	7113	Early onset stroke	"	3274*	11,012*
Schizophrenia	PGC-SCZ2	33,640	43,456	Large-vessel disease	"	1817*	17,708*
Tourette syndrome	PGC-OCDTS	4220	8994	Small-vessel disease	"	1349*	17,708*
				Migraine	IHGC	59,673	316,078
				Migraine with aura	"	6332*	142,817*
				Migraine without aura	"	8348*	136,758*
				Multiple sclerosis	IMSGC	5545	12,153
				Parkinson's disease	IPDGC	5333	12,019
Total psychiatric		158,028	365,993	Total neurologic		107,190	418,650

*Sample count for a phenotype that is part of a larger group.

C to F) was a modest correlation between age of disorder onset and heritability, suggesting that early onset brain disorders tend to be more heritable. Because some of our interpretation of the results depends on lack of observed correlation, we explored the behavior of observed correlation versus power (fig. S2A), standard errors (fig. S2B), and the individual results (fig. S2, C and D) to identify where we can be reasonably robust in claiming lack of correlation.

The common variant heritability estimates for the psychiatric and neurological disorders were generally somewhat lower than previously reported estimates from common variants (table S5). When comparing estimates reported here with those previously reported in studies with smaller sample sizes (*28*), a similar pattern was observed for the behavioral-cognitive traits, with the exception of "openness," "neuroticism," and "never/ever smoked" (defined as those who have never smoked versus those who have smoked at some point) suggesting that some attenuation in heritability is observed when moving to larger sample sizes. Measures related to cognitive ability, such as childhood cognitive performance [heritability estimate of 0.19 (SE: 0.03)] and years of education [heritability estimate of 0.30 (SE: 0.01)], yielded estimates that were more consistent with previous estimates of the heritability of intelligence (*29*, *30*), suggesting that the cognitive measures may be less prone to phenotypic measurement error and/or have a higher heritability overall than the personality measures.

These heritability estimates should be interpreted somewhat cautiously, as they reflect the phenotype ascertained in each study and will be deflated in the presence of diagnostic heterogeneity, ascertainment errors, or unusual contributions of high-impact rare variants. To evaluate potential sources of these differences, we explored three approaches (*25*): evaluating the differences in real data, simulation work (table S5), and quantifying the magnitude of effect for potentially implied misclassification (table S6).

In comparison with heritability estimates obtained using twin and family data, the more diverse selection and survival biases in the underlying data may attenuate the heritability estimates and correlations, as may increased within-disorder heterogeneity introduced by the larger meta-analyses. A related explanation for the lower estimates of heritability may be that increasing sample sizes have led to expanded inclusion criteria, meaning that less severely affected cases with a lower overall burden of risk factors (both genetic and environmental) might be included, which in turn would attenuate estimates of heritability. However, the successful identification of genome-wide significant loci suggests that these larger samples are nevertheless very useful for genetic studies, and the simulation results suggest that this has, at most, a limited effect on estimated genetic correlations (fig. S9). Even so, some of the pairs of phenotypes included here lack sufficient power for robust estimation of genetic correlations. Moreover, our analyses examine only the properties of common variant contributions; extending these analyses to include the effects of rare variants may further inform the extent of genetic overlap. For example, epilepsy and ASD show substantial overlap in genetic risk from de novo loss-of-function mutations (*31*), in contrast to the limited common variant sharing observed in this study. This may suggest that the rare and common variant contributions to genetic overlap may behave differently and that incorporating the two variant classes into a single analysis may provide further insight into brain disorder pathogenesis.

To address the possibility of methodological differences contributing to the differences in the estimates, and although LDSC and GREML have previously been shown to yield similar estimates from the same data (*24*), we performed our own comparison in Alzheimer's disease data (*32*) (selected on the basis of data availability). In Alzheimer's disease, the previously published heritability estimate [0.24 (SE: 0.03)] is significantly different

Table 2. Behavioral-cognitive and additional phenotypes used in the study. Indented phenotypes are part of a larger whole (e.g., samples in the college attainment analysis are a subset of those in the analysis for years of education). (d), dichotomous phenotype; (q), quantitative phenotype. References and phenotype definitions are listed in table S2, and data availability in table S13. SSGAC, Social Science Genetic Association Consortium; CTG, Complex Trait Genetics Lab; GPC, Genetics of Personality Consortium; TAG, Tobacco and Genetics Consortium; GIANT, Genetic Investigation of ANthropometric Traits consortium; Cardiogram, CARDIoGRAMplusC4D Consortium; IIBDGC, International Inflammatory Bowel Disease Genetics Consortium.

Phenotype	Source	Samples
Behavioral-cognitive phenotypes		
Cognitive		
Years of education (q)	SSGAC	293,723
College attainment (d)	"	120,917*
Cognitive performance (q)	"	17,989*
Intelligence (d)	CTG	78,308
Personality measures		
Subjective well-being	SSGAC	298,420
Depressive symptoms	"	161,460*
Neuroticism (q)	"	170,911*
Extraversion (q)	GPC	63,030*
Agreeableness (q)	"	17,375*
Conscientiousness (q)	"	17,375*
Openness (q)	"	17,375*
Smoking-related		
Never/ever smoked (d)	TAG	74,035
Cigarettes per day (q)	TAG	38,617*
Additional phenotypes		
BMI (q)	GIANT	339,224
Height (q)	"	253,288*
Coronary artery disease (d)	Cardiogram	86,995
Crohn's disease	IIBDGC	20,883
Total		1,124,048

*Sample counts represent overlap with preceding dataset.

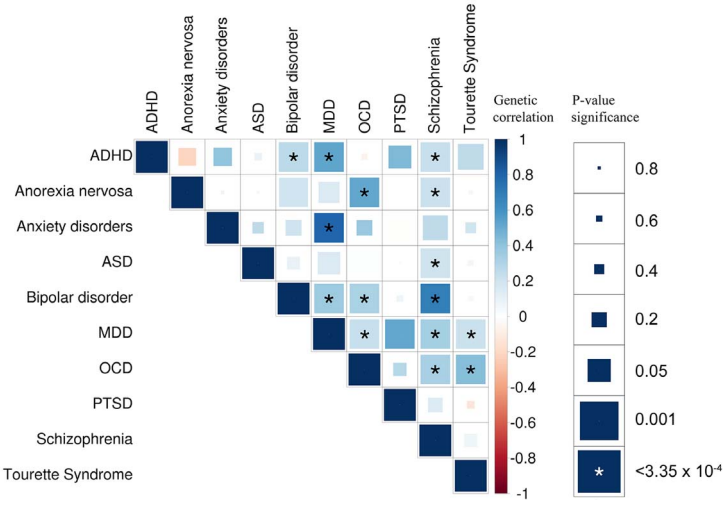

Fig. 1. Genetic correlations across psychiatric phenotypes. The color of each box indicates the magnitude of the correlation, and the size of the box indicates its significance (LDSC), with significant correlations filling each square completely. Asterisks indicate genetic correlations that are significantly different from zero after Bonferroni correction.

from the estimate in the current study [0.13 (SE: 0.02)]. These differences may reflect implicit heterogeneity in a much larger case collection used in the current study (effective sample size 10,494 versus 46,669) and the potential reasons listed above, but they could also be due to methodological variability (most of the previous approximations listed in table S3 are estimated with a different methodology). To evaluate this, we applied the same analytical process used in this paper to the summary statistics of the GERAD (Genetic and Environmental Risk in Alzheimer's Disease) cohort (3941 cases and 7848 controls) from the Alzheimer's disease meta-analysis, where the previous heritability estimate was calculated. There, we obtained a heritability estimate of 0.25 (SE: 0.04), which agrees closely with the published estimate of 0.24 (SE: 0.03), suggesting that the different approximations may reflect differences between datasets rather than methodological variability.

Correlations among brain disorders

We observed widespread sharing across psychiatric disorders (Fig. 1 and fig. S3) by expanding the number of brain disorder pairs studied beyond those previously reported (*17*), but similar sharing was not observed among neurological disorders. Among the psychiatric disorders, schizophrenia showed significant genetic correlation with most of the psychiatric disorders, whereas MDD was positively (though not necessarily significantly) correlated with every other disorder tested. Further, schizophrenia, bipolar disorder, anxiety disorders, MDD, and ADHD each showed a high degree of correlation to the four others [average genetic correlation (r_g) = 0.40] (table S7A). Anorexia nervosa, obsessive-compulsive disorder (OCD), and schizophrenia also demonstrated significant sharing among themselves (Fig. 1), as did Tourette syndrome (TS), OCD, and MDD, as well as ASD and schizophrenia. Posttraumatic stress disorder (PTSD) showed no significant correlation with any of the other psychiatric phenotypes (though some correlation to ADHD and MDD was observed), and both ASD and TS appear to potentially be more distinct from the other psychiatric disorders. The modest power of the ASD, PTSD, and TS meta-analyses, however, limits the strength of this conclusion (fig. S2C).

Neurological disorders showed a more limited extent of genetic correlation than that of the psychiatric disorders (Fig. 2, fig. S4, and table S7A), suggesting greater diagnostic specificity and/or more distinct etiologies. Parkinson's disease, Alzheimer's disease, generalized epilepsy, and multiple sclerosis (MS) showed little to no correlation with other brain disorders. The highest degree of genetic correlation among the neurological disorders was observed for focal epilepsy (average r_g = 0.46, excluding the other epilepsy datasets), though none of the correlations were significant, reflecting the relatively modest power of the current focal epilepsy meta-analysis (fig. S2C). However, the modest heritability and the broad pattern of sharing observed for focal epilepsy may be consistent with heterogeneity and

potentially even diagnostic misclassification across a range of neurological conditions.

In the cross-category correlation analysis, the observed pattern is consistent with limited sharing across the included neurological and psychiatric disorders (Fig. 3; average r_g = 0.03). The only significant cross-category correlations were with migraine, suggesting that this disorder may share some of its genetic architecture with psychiatric disorders: migraine and ADHD (r_g = 0.26, P = 8.81 × 10^{-8}), migraine and TS (r_g = 0.19, P = 1.80 × 10^{-5}), and migraine and MDD (r_g = 0.32, P = 1.42 × 10^{-22} for all migraine; r_g = 0.23, P = 5.23 × 10^{-5} for migraine without aura; r_g = 0.28, P = 1.00 × 10^{-4} for migraine with aura).

We observed several significant genetic correlations between the behavioral-cognitive or additional phenotypes and brain disorders (Fig. 4 and table S7B). Results for cognitive traits were dichotomous among psychiatric phenotypes (fig. S5A), with ADHD, anxiety disorders, MDD, and TS showing negative correlations to the cognitive measures and anorexia nervosa, ASD, bipolar disorder, and OCD showing positive correlations. Schizophrenia showed more mixed results, with a significantly negative correlation to intelligence but a positive correlation to years of education. Among neurological phenotypes (fig. S5B), the correlations were either negative or null, with Alzheimer's disease, epilepsy, intracerebral hemorrhage (ICH), ischemic stroke, early onset stroke, and migraine showing significantly negative correlations. Correlations between college attainment and years of education with bipolar disorder (*24*), Alzheimer's disease, and schizophrenia have been previously reported (*33*).

Among the personality and symptom measures, significant positive correlations were observed between neuroticism and anorexia nervosa, anxiety disorders, migraine, migraine without aura, MDD, OCD, schizophrenia, and TS [fig. S6, A and B; replicating previously reported correlations with MDD and schizophrenia (*34*)]; between depressive symptoms and ADHD, anxiety disorder, bipolar disorder, MDD, and schizophrenia; and between subjective well-being and anxiety disorder, bipolar disorder, and MDD. For smoking-related measures, the only significant genetic correlations were between never/ever smoked and MDD (r_g = 0.33, P = 3.10 × 10^{-11}) as well as ADHD (r_g = 0.37, P = 3.15 × 10^{-6}).

Among the additional phenotypes, the two examples of disorders with well-defined etiologies had different results. Crohn's disease, representing immunological pathophysiology, showed no correlation with any of the study phenotypes, whereas the phenotype representing vascular pathophysiology (coronary artery disease) showed significant correlation to MDD (r_g = 0.19, P = 8.71 × 10^{-5}) as well as the two stroke-related phenotypes (r_g = 0.69, P = 2.47 × 10^{-6} to ischemic stroke and r_g = 0.86, P = 2.26 × 10^{-5} to early onset stroke), suggesting shared genetic effects across these phenotypes. Significant correlations were also observed for BMI, which was positively correlated with ADHD and MDD, and negatively correlated with anorexia nervosa [as previously reported with a different dataset (*24*)] and schizophrenia.

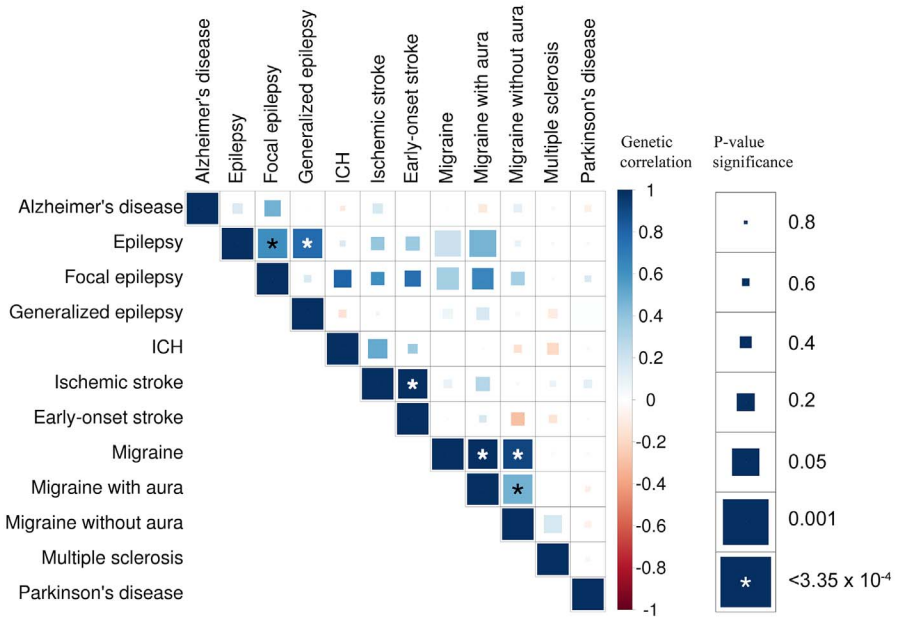

Fig. 2. Genetic correlations across neurological phenotypes. The color of each box indicates the magnitude of the correlation, and the size of the box indicates its significance (LDSC), with significant correlations filling each square completely. Asterisks indicate genetic correlations that are significantly different from zero after Bonferroni correction. Some phenotypes have substantial overlaps (Table 1)—for instance, all cases of generalized epilepsy are also cases of epilepsy. Asterisks indicate significant genetic correlation after multiple testing correction.

Our enrichment analysis (fig. S7 and tables S8 to S12) demonstrated significant heritability enrichments between the CNS and generalized epilepsy, MDD, TS, college attainment, intelligence, neuroticism, and the never/ever smoked trait; between depressive symptoms and adrenal/pancreatic cells and tissues; as well as between hematopoietic cells (including immune system cells) and MS (fig. S7, A and B, and tables S8 and S9). We replicated the reported (CNS) enrichment for schizophrenia, bipolar disorder, and years of education (tables S8 and S9) and observed the reported enrichments for BMI (CNS), years of education (CNS), height (connective tissues and bone, cardiovascular system, and other), and Crohn's disease (hematopoietic cells) from the same datasets (fig. S7, C and D) (*26*). The psychiatric disorders with large numbers of identified GWAS loci (bipolar disorder, MDD, and schizophrenia) and migraine, which was the only cross-correlated neurological disorder, show enrichment to conserved regions (tables S10 and S12), whereas the other neurological disorders with similar numbers of loci (MS, Alzheimer's disease, and Parkinson's disease) do not (fig. S7, A and B). Enrichment to conserved regions was also observed for neuroticism, intelligence, and college attainment and to H3K9ac peaks for BMI (tables S11 and S12).

Discussion

By integrating and analyzing the genome-wide association summary statistic data from consortia of 25 brain disorders, we find that psychiatric disorders broadly share a considerable portion of their common variant genetic risk, especially across schizophrenia, MDD, bipolar disorder, anxiety disorder, and ADHD, whereas neurological disorders are more genetically distinct. Across categories, psychiatric and neurologic disorders share relatively little common genetic risk, suggesting that multiple different and largely independently regulated etiological pathways may give rise to similar clinical manifestations [e.g., psychosis, which manifests in both schizophrenia (*35*) and Alzheimer's disease (*36*)]. Except for migraine, which appears to share some genetic architecture with psychiatric disorders, the existing clinical delineation between neurology and psychiatry is corroborated at the level of common variant risk for the studied disorders.

On the basis of the observed results, we performed some exploratory analyses to address concerns about diagnostic overlap and misclassification, which are particularly relevant to psychiatric disorders, owing to their spectral nature. Given that the broad and continuous nature of psychiatric disorder spectra has long been clinically recognized (*37*–*39*) and that patients can, in small numbers, progress from one diagnosis to another (*40*), we evaluated to what extent this kind of diagnostic overlap could explain the observed correlations. Genetic correlation could arise if, for example, patients progress through multiple diagnoses over their lifetime or if some specific diagnostic boundaries between phenotype pairs are particularly porous to misclassification (table S5). Although, for instance, migraine and

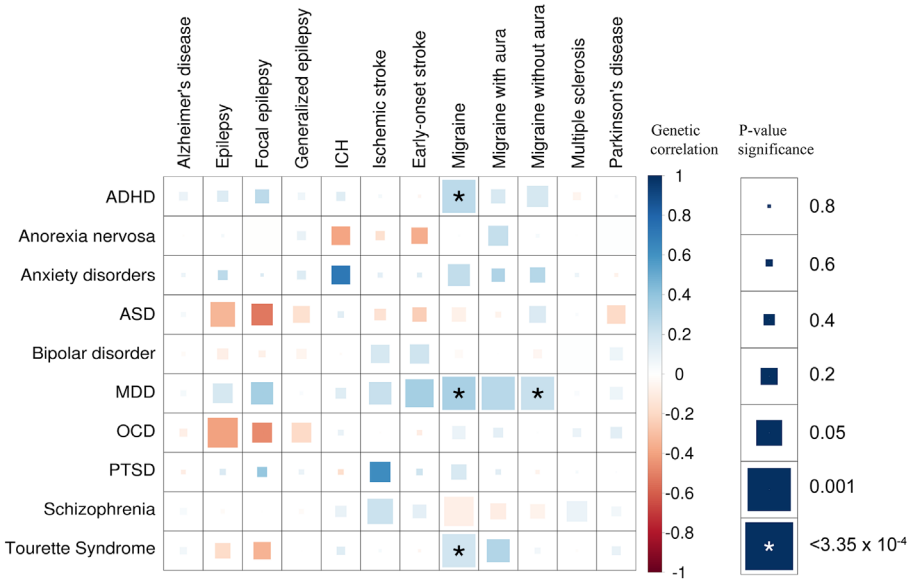

Fig. 3. Genetic correlations across neurological and psychiatric phenotypes. The color of each box indicates the magnitude of the correlation, and the size of the box indicates its significance (LDSC), with significant correlations filling each square completely. Asterisks indicate genetic correlations that are significantly different from zero after Bonferroni correction.

schizophrenia are unlikely to be mistaken for one another, there may be more substantial misclassification between particular psychiatric disorders, consistent with the clinical controversies in classification. Previous work (*41*) suggests that substantial misclassification (on the order of 15 to 30%, depending on whether it is uni- or bidirectional) is required to introduce false levels of genetic correlation. We found that the observed levels of correlation are unlikely to appear in the absence of underlying genetic correlation (table S6), as it is apparent that a very high degree of misclassification (up to 79%) would be required to produce the observed correlations in the absence of any true genetic correlation and that reasonably expected misclassification would have limited impact on the observed r_g (fig. S8). Therefore, these results suggest true sharing of a substantial fraction of the common variant genetic architecture among psychiatric disorders as well as between behavioral-cognitive measures and brain disorders. We also performed large-scale simulations to explore the effect of sample size, polygenicity, and degree of correlation on power to detect significant correlations. First, we established that the observed heritability of the simulated misclassified traits in the UK Biobank data behaves as would be theoretically expected (fig. S9A) and that the effects on observed correlation (fig. S9, B and C) are in line with the estimates from family data (*41*). Reasonably low levels of misclassification or changes to the exact level of heritability appear unlikely to induce significant correlations, as observed in the power analysis (fig. S10), though a lower observed heritability caused by substantial misclassification (fig. S9A) will decrease the power to estimate true genetic overlap.

The high degree of genetic correlation among the psychiatric disorders adds further evidence that current clinical diagnostics do not reflect specific genetic etiology for these disorders and that genetic risk factors for psychiatric disorders do not respect clinical diagnostic boundaries. Rather, this finding suggests a more interconnected genetic etiology, in contrast to that of neurological disorders, and underscores the need to refine psychiatric diagnostics. This study may provide important "scaffolding" to support a framework for investigating mental disorders, incorporating many levels of information to understand basic dimensions of brain function.

The observed positive genetic correlations are consistent with a few hypothetical scenarios. For example, this observation may reflect the existence of some portion of common genetic risk factors conferring risks for multiple psychiatric disorders and where other distinct additional factors, both genetic and nongenetic, contribute to the eventual clinical presentation. The presence of significant genetic correlation may also reflect the phenotypic overlap between any two disorders; for example, the sharing between schizophrenia and ADHD might reflect underlying difficulties in executive functioning, which are well-established in both disorders (*42*), and that the shared risk arises from a partial capture of its shared genetic component. Similarly, we might speculate that a shared mechanism underlying cognitive biases may extend from overvalued ideas to delusions (ranging from anorexia nervosa and OCD to schizophrenia), and that this heritable intermediate trait confers pleiotropic risk to multiple outcomes. This kind of latent variable could give rise to the observed genetic correlation between disorders, owing to the shared portion of variation affecting that variable. Though a combination of these is likely, more genome-wide significant loci are needed to evaluate these overlaps at the locus level.

Conversely, the low correlations observed across neurological disorders suggest that the current classification reflects relatively specific genetic etiologies, although the limited sample size for some of these disorders and the lack of inclusion of disorders conceived as "circuit-based" (e.g., restless legs syndrome, sleep disorders, and possibly essential tremor) constrain the full generalizability of this conclusion. On the basis of our observations, degenerative disorders (such as Alzheimer's and Parkinson's diseases) would therefore not be expected to share their polygenic risk profiles with a neuroimmunological disorder (such as MS) or neurovascular disorder (such as ischemic stroke). Similarly, we see limited evidence for the reported comorbidity between migraine with aura and ischemic stroke (*43*) (r_g = 0.29, P = 0.099); however, the standard errors of this comparison are too high to draw strong conclusions. At the disorder subtype level, migraine with and without aura (r_g = 0.48, P = 1.79 × 10^{-5}) show substantial genetic correlation, whereas focal and generalized epilepsy (r_g = 0.16, P = 0.388) show much less.

The few significant correlations across neurology and psychiatry—namely, between migraine and ADHD, MDD, and TS—suggest modest shared etiological overlap across the neurology-psychiatry distinction. The comorbidity of migraine with MDD, TS, and ADHD has been previously reported in epidemiological studies (*44*–*47*), whereas the previously reported comorbidity between migraine and bipolar disorder seen in epidemiological studies (*48*) was not reflected in our estimate of genetic correlation (r_g = −0.03, P = 0.406).

Several phenotypes show only very low-level correlations with any of the other disorders and phenotypes that we studied, despite large sample size and robust evidence for heritability, which suggests that their common variant genetic risk may largely be unique. Alzheimer's disease, Parkinson's disease, and MS show extremely limited sharing with the other phenotypes and with each other. Neuroinflammation has been implicated in the pathophysiology of each of these conditions (*49*–*51*), as it has for migraine (*52*) and many psychiatric conditions, including schizophrenia (*53*), but no considerable shared heritability was observed with either of those conditions nor with Crohn's disease, nor did we observe enrichment for immune-related tissues in the functional partitioning (fig. S7) as observed for Crohn's disease. Although this does not preclude the sharing of individual neuroinflammatory mechanisms in these disorders, the large-scale lack of shared common variant genetic influences supports the distinctiveness of disorder etiology. Further, we observed significant enrichment of heritability for immunological cells and tissues in MS only, showing that inflammation-specific regulatory marks in the genome do not show overall enrichment for common variant risk for either Alzheimer's or Parkinson's diseases [though this does not preclude

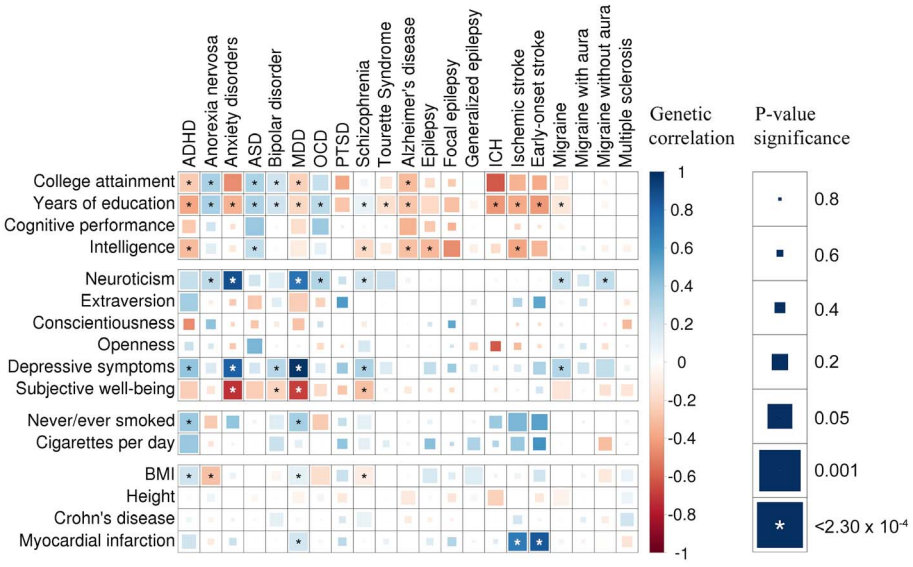

Fig. 4. Genetic correlations across brain disorders and behavioral-cognitive phenotypes. The color of each box indicates the magnitude of the correlation, and the size of the box indicates its significance (LDSC), with significant correlations filling each square completely. Asterisks indicate genetic correlations that are significantly different from zero after Bonferroni correction.

the effects of specific, not particularly polygenic neuroinflammatory mechanisms (*54*)]. Among psychiatric disorders, ASD and TS showed a similar absence of correlation with other disorders, although this may reflect small sample sizes.

Analysis of the Big Five personality measures suggest that the current sample sizes may be large enough for correlation testing. Neuroticism, which has by far the largest sample size, shows several significant correlations. Most significant of these was to MDD (r_g = 0.737, $P = 5.04 \times 10^{-96}$), providing evidence for the link between these phenotypes, as reported for polygenic risk scores (*55*) and twin studies (*56*, *57*); as well as other psychiatric disorders (Fig. 4 and table S7B). The correlation between MDD and anxiety disorders, with a similar pattern of correlation and the dimensional measures of depressive symptoms, subjective well-being, and neuroticism suggests that they all tag a similar underlying etiology. The significant correlation between coronary artery disease and MDD supports the link between MDD and CAD (*58*), and the observed correlation between ADHD and smoking initiation (r_g = 0.374, $P = 3.15 \times 10^{-6}$) is consistent with the epidemiological evidence of overlap (*59*) and findings from twin studies (*60*).

For the neurological disorders, five (Alzheimer's disease, intracerebral hemorrhage, ischemic and early onset stroke, and migraine) showed significant negative genetic correlation to the cognitive measures, whereas two (epilepsy and focal epilepsy) showed moderate negative genetic correlation (fig. S5). For Alzheimer's disease, poor cognitive performance in early life has been linked to increased risk for developing the disorder (*61*), but to our knowledge no such connection has been reported for other phenotypes. Among the psychiatric disorders, ADHD, anxiety disorders, and MDD show a significant negative correlation to cognitive and education attainment measures, whereas the remaining five of the eight psychiatric disorders (anorexia nervosa, ASD, bipolar disorder, OCD, and schizophrenia) showed significant positive genetic correlation with one or more cognitive measures. These results suggest the existence of a link between cognitive performance in early life and the genetic risk for both psychiatric and neurological brain disorders. The basis of the genetic correlations between education, cognition, and brain disorders may have a variety of root causes, including indexing performance differences on the basis of behavioral dysregulation (e.g., ADHD relating to attentional problems during cognitive tests), or may reflect ascertainment biases in certain disorders conditional on impaired cognition (e.g., individuals with lower cognitive reserve being more rapidly identified for Alzheimer's disease), but the results could also suggest a direct link between the underlying etiologies.

BMI shows significant positive genetic correlation to ADHD, consistent with a meta-analysis linking ADHD to obesity (*62*), and negative genetic correlation with anorexia nervosa, OCD, and schizophrenia. This is consistent with evidence for enrichment of BMI heritability in CNS tissues (*26*) that suggest neuronal involvement (*63*); this may also provide a partial genetic explanation for lower BMI in anorexia nervosa patients even after recovery (*64*). Given that no strong correlations were observed between BMI and any of the neurological phenotypes, BMI's brain-specific genetic architecture may be more closely related to behavioral phenotypes. Ischemic stroke and BMI show surprisingly little genetic correlation in this analysis (r_g = 0.07, P = 0.26), suggesting that although BMI is a risk factor for stroke (*65*), there is little evidence for shared common genetic effects. These analyses also suggest that the reported reduced rates of cardiovascular disease in individuals with histories of anorexia nervosa (*66*, *67*) are more likely due to BMI-related secondary effects. The limited evidence of genetic correlation of anorexia nervosa with intracerebral hemorrhage, ischemic stroke, early onset stroke, and coronary artery disease suggests that any lower cardiovascular mortality is more likely due to direct BMI-related effects rather than to genetic risk variants.

The genetic correlation results presented here indicate that the clinical boundaries for the studied psychiatric phenotypes do not reflect distinct underlying pathogenic processes. This suggests that genetically informed analyses may provide a basis for restructuring of psychiatric nosology, consistent with twin- and family-based results. In contrast, neurological disorders show greater genetic specificity, and although it is important to emphasize that while some brain disorders are underrepresented here, our results demonstrate the limited evidence for widespread common genetic risk sharing between psychiatric and neurological disorders. However, we provide strong evidence that both psychiatric and neurological disorders show robust correlations with cognitive and personality measures, indicating avenues for follow-up studies. Further analysis is needed to evaluate whether overlapping genetic contributions to psychiatric pathology may influence treatment choices. Ultimately, such developments are promising steps toward reducing diagnostic heterogeneity and eventually improving the diagnostics and treatment of psychiatric disorders.

Materials and methods summary

We collected GWAS meta-analysis summary statistics for 25 brain disorders and 17 other phenotypes from various consortia and, where necessary, generated new, non–sex-stratified European cohort–only versions of the meta-analyses (*25*). All datasets underwent uniform quality control (*25*). For each trait, by using the LDSC framework (*24*), the total additive common SNP heritability present in the summary statistics (h^2g) was estimated by regressing the association χ^2 statistic of a SNP against the total amount of common genetic variation tagged by that SNP, for all SNPs. Genetic correlations (r_g; i.e., the genome-wide average shared genetic risk) for pairs of phenotypes were estimated by regressing the product of z-scores, rather than the χ^2 statistic, for each phenotype and for each SNP. Significance was assessed by Bonferroni multiple testing correction via estimating the number of independent brain disorder phenotypes via matrix decomposition (*25*). Functional and partitioning analyses for the GWAS datasets were also performed using LDSC regression. Power analyses and simulation work to aid in interpretation of the results were conducted using genotype data from the UK Biobank resource (*25*).

REFERENCES AND NOTES

1. J. B. Martin, The integration of neurology, psychiatry, and neuroscience in the 21st century. *Am. J. Psychiatry* **159**, 695–704 (2002). doi: 10.1176/appi.ajp.159.5.695; pmid: 11986119
2. J. W. Smoller, Disorders and borders: Psychiatric genetics and nosology. *Am. J. Med. Genet. B. Neuropsychiatr. Genet.* **162**, 559–578 (2013). doi: 10.1002/ajmg.b.32174; pmid: 24132891
3. T. R. Insel, P. S. Wang, Rethinking mental illness. *JAMA* **303**, 1970–1971 (2010). doi: 10.1001/jama.2010.555; pmid: 20483974
4. T. J. Polderman *et al*., Meta-analysis of the heritability of human traits based on fifty years of twin studies. *Nat. Genet.* **47**, 702–709 (2015). doi: 10.1038/ng.3285; pmid: 25985137
5. K. S. Kendler, C. A. Prescott, J. Myers, M. C. Neale, The structure of genetic and environmental risk factors for common psychiatric and substance use disorders in men and women. *Arch. Gen. Psychiatry* **60**, 929–937 (2003). doi: 10.1001/archpsyc.60.9.929; pmid: 12963675
6. R. Jensen, L. J. Stovner, Epidemiology and comorbidity of headache. *Lancet Neurol.* **7**, 354–361 (2008). doi: 10.1016/S1474-4422(08)70062-0; pmid: 18339350
7. J. Nuyen *et al*., Comorbidity was associated with neurologic and psychiatric diseases: A general practice-based controlled study. *J. Clin. Epidemiol.* **59**, 1274–1284 (2006). doi: 10.1016/j.jclinepi.2006.01.005; pmid: 17098570
8. R. M. Hirschfeld *et al*., Screening for bipolar disorder in the community. *J. Clin. Psychiatry* **64**, 53–59 (2003). doi: 10.4088/JCP.v64n0111; pmid: 12590624
9. A. Pan, Q. Sun, O. I. Okereke, K. M. Rexrode, F. B. Hu, Depression and risk of stroke morbidity and mortality: A meta-analysis and systematic review. *JAMA* **306**, 1241–1249 (2011). doi: 10.1001/jama.2011.1282; pmid: 21934057
10. A. Lo-Castro, P. Curatolo, Epilepsy associated with autism and attention deficit hyperactivity disorder: Is there a genetic link? *Brain Dev.* **36**, 185–193 (2014). doi: 10.1016/j.braindev.2013.04.013; pmid: 23726375
11. E. N. Bertelsen, J. T. Larsen, L. Petersen, J. Christensen, S. Dalsgaard, Childhood Epilepsy, Febrile Seizures, and Subsequent Risk of ADHD. *Pediatrics* **138**, e20154654 (2016). doi: 10.1542/peds.2015-4654; pmid: 27412639
12. C. G. de Kovel *et al*., Recurrent microdeletions at 15q11.2 and 16p13.11 predispose to idiopathic generalized epilepsies. *Brain* **133**, 23–32 (2010). doi: 10.1093/brain/awp262; pmid: 19843651
13. T. D. Graves, M. G. Hanna, Neurological channelopathies. *Postgrad. Med. J.* **81**, 20–32 (2005). doi: 10.1136/pgmj.2004.022012; pmid: 15640425
14. J. Haan, G. M. Terwindt, A. M. van den Maagdenberg, A. H. Stam, M. D. Ferrari, A review of the genetic relation between migraine and epilepsy. *Cephalalgia* **28**, 105–113 (2008). pmid: 18197881
15. S. Debette *et al*., Common variation in PHACTR1 is associated with susceptibility to cervical artery dissection. *Nat. Genet.* **47**, 78–83 (2015). doi: 10.1038/ng.3154; pmid: 25420145
16. S. M. Purcell *et al*., Common polygenic variation contributes to risk of schizophrenia and bipolar disorder. *Nature* **460**, 748–752 (2009). pmid: 19571811
17. Cross-Disorder Group of the Psychiatric Genomics Consortium, Genetic relationship between five psychiatric disorders estimated from genome-wide SNPs. *Nat. Genet.* **45**, 984–994 (2013). doi: 10.1038/ng.2711; pmid: 23933821
18. J. C. Lambert *et al*., Meta-analysis of 74,046 individuals identifies 11 new susceptibility loci for Alzheimer's disease. *Nat. Genet.* **45**, 1452–1458 (2013). doi: 10.1038/ng.2802; pmid: 24162737
19. T. W. Mühleisen *et al*., Genome-wide association study reveals two new risk loci for bipolar disorder. *Nat. Commun.* **5**, 3339 (2014). doi: 10.1038/ncomms4339; pmid: 24618891
20. V. Anttila *et al*., Genome-wide meta-analysis identifies new susceptibility loci for migraine. *Nat. Genet.* **45**, 912–917 (2013). doi: 10.1038/ng.2676; pmid: 23793025
21. M. A. Nalls *et al*., Large-scale meta-analysis of genome-wide association data identifies six new risk loci for Parkinson's disease. *Nat. Genet.* **46**, 989–993 (2014). doi: 10.1038/ng.3043; pmid: 25064009
22. Schizophrenia Working Group of the Psychiatric Genomics Consortium, Biological insights from 108 schizophrenia-associated genetic loci. *Nature* **511**, 421–427 (2014). doi: 10.1038/nature13595; pmid: 25056061
23. N. Solovieff, C. Cotsapas, P. H. Lee, S. M. Purcell, J. W. Smoller, Pleiotropy in complex traits: Challenges and strategies. *Nat. Rev. Genet.* **14**, 483–495 (2013). doi: 10.1038/nrg3461; pmid: 23752797
24. B. Bulik-Sullivan *et al*., An atlas of genetic correlations across human diseases and traits. *Nat. Genet.* **47**, 1236–1241 (2015). doi: 10.1038/ng.3406; pmid: 26414676
25. See materials and methods and other supplementary materials.
26. H. K. Finucane *et al*., Partitioning heritability by functional annotation using genome-wide association summary statistics. *Nat. Genet.* **47**, 1228–1235 (2015). doi: 10.1038/ng.3404; pmid: 26414678
27. M. H. de Moor *et al*., Meta-analysis of genome-wide association studies for personality. *Mol. Psychiatry* **17**, 337–349 (2012). doi: 10.1038/mp.2010.128; pmid: 21173776
28. R. A. Power, M. Pluess, Heritability estimates of the Big Five personality traits based on common genetic variants. *Transl. Psychiatry* **5**, e604 (2015). doi: 10.1038/tp.2015.96; pmid: 26171985
29. C. M. Haworth *et al*., The heritability of general cognitive ability increases linearly from childhood to young adulthood. *Mol. Psychiatry* **15**, 1112–1120 (2010). doi: 10.1038/mp.2009.55; pmid: 19488046
30. I. J. Deary *et al*., Genetic contributions to stability and change in intelligence from childhood to old age. *Nature* **482**, 212–215 (2012). doi: 10.1038/nature10781; pmid: 22258510
31. S. De Rubeis *et al*., Synaptic, transcriptional and chromatin genes disrupted in autism. *Nature* **515**, 209–215 (2014). doi: 10.1038/nature13772; pmid: 25363760
32. S. H. Lee *et al*., Estimation and partitioning of polygenic variation captured by common SNPs for Alzheimer's disease, multiple sclerosis and endometriosis. *Hum. Mol. Genet.* **22**, 832–841 (2013). doi: 10.1093/hmg/dds491; pmid: 23193196
33. A. Okbay *et al*., Genome-wide association study identifies 74 loci associated with educational attainment. *Nature* **533**, 539–542 (2016). doi: 10.1038/nature17671; pmid: 27225129
34. D. J. Smith *et al*., Genome-wide analysis of over 106 000 individuals identifies 9 neuroticism-associated loci. *Mol. Psychiatry* **21**, 749–757 (2016). doi: 10.1038/mp.2016.49; pmid: 27067015
35. P. F. Buckley, B. J. Miller, D. S. Lehrer, D. J. Castle, Psychiatric comorbidities and schizophrenia. *Schizophr. Bull.* **35**, 383–402 (2009). doi: 10.1093/schbul/sbn135; pmid: 19011234
36. C. G. Lyketsos *et al*., Mental and behavioral disturbances in dementia: Findings from the Cache County Study on Memory in Aging. *Am. J. Psychiatry* **157**, 708–714 (2000). doi: 10.1176/appi.ajp.157.5.708; pmid: 10784462
37. R. Kendell, A. Jablensky, Distinguishing between the validity and utility of psychiatric diagnoses. *Am. J. Psychiatry* **160**, 4–12 (2003). doi: 10.1176/appi.ajp.160.1.4; pmid: 12505793
38. A. S. Cristino *et al*., Neurodevelopmental and neuropsychiatric disorders represent an interconnected molecular system. *Mol. Psychiatry* **19**, 294–301 (2014). doi: 10.1038/mp.2013.16; pmid: 23439483
39. D. A. Regier *et al*., Limitations of diagnostic criteria and assessment instruments for mental disorders. Implications for research and policy. *Arch. Gen. Psychiatry* **55**, 109–115 (1998). doi: 10.1001/archpsyc.55.2.109; pmid: 9477922
40. T. M. Laursen, E. Agerbo, C. B. Pedersen, Bipolar disorder, schizoaffective disorder, and schizophrenia overlap: A new comorbidity index. *J. Clin. Psychiatry* **70**, 1432–1438 (2009). doi: 10.4088/JCP.08m04807; pmid: 19538905
41. N. R. Wray, S. H. Lee, K. S. Kendler, Impact of diagnostic misclassification on estimation of genetic correlations using genome-wide genotypes. *Eur. J. Hum. Genet.* **20**, 668–674 (2012). doi: 10.1038/ejhg.2011.257; pmid: 22258521
42. E. G. Willcutt, A. E. Doyle, J. T. Nigg, S. V. Faraone, B. F. Pennington, Validity of the executive function theory of attention-deficit/hyperactivity disorder: A meta-analytic review. *Biol. Psychiatry* **57**, 1336–1346 (2005). doi: 10.1016/j.biopsych.2005.02.006; pmid: 15950006
43. J. T. Spector *et al*., Migraine headache and ischemic stroke risk: An updated meta-analysis. *Am. J. Med.* **123**, 612–624 (2010). doi: 10.1016/j.amjmed.2009.12.021; pmid: 20493462
44. O. B. Fasmer, A. Halmøy, K. J. Oedegaard, J. Haavik, Adult attention deficit hyperactivity disorder is associated with migraine headaches. *Eur. Arch. Psychiatry Clin. Neurosci.* **261**, 595–602 (2011). doi: 10.1007/s00406-011-0203-9; pmid: 21394551
45. N. Breslau, R. B. Lipton, W. F. Stewart, L. R. Schultz, K. M. Welch, Comorbidity of migraine and depression: Investigating potential etiology and prognosis. *Neurology* **60**, 1308–1312 (2003). doi: 10.1212/01.WNL.0000058907.41080.54; pmid: 12707434
46. K. R. Merikangas, J. Angst, H. Isler, Migraine and psychopathology. Results of the Zurich cohort study of young adults. *Arch. Gen. Psychiatry* **47**, 849–853 (1990). doi: 10.1001/archpsyc.1990.01810210057008; pmid: 2393343
47. G. Barabas, W. S. Matthews, M. Ferrari, Tourette's syndrome and migraine. *Arch. Neurol.* **41**, 871–872 (1984). doi: 10.1001/archneur.1984.04050190077018; pmid: 6589980
48. R. S. McIntyre *et al*., The prevalence and impact of migraine headache in bipolar disorder: Results from the Canadian Community Health Survey. *Headache* **46**, 973–982 (2006). doi: 10.1111/j.1526-4610.2006.00469.x; pmid: 16732843
49. M. T. Heneka *et al*., Neuroinflammation in Alzheimer's disease. *Lancet Neurol.* **14**, 388–405 (2015). doi: 10.1016/S1474-4422(15)70016-5; pmid: 25792098
50. E. C. Hirsch, S. Hunot, Neuroinflammation in Parkinson's disease: A target for neuroprotection? *Lancet Neurol.* **8**, 382–397 (2009). doi: 10.1016/S1474-4422(09)70062-6; pmid: 19296921
51. E. M. Frohman, M. K. Racke, C. S. Raine, Multiple sclerosis—the plaque and its pathogenesis. *N. Engl. J. Med.* **354**, 942–955 (2006). doi: 10.1056/NEJMra052130; pmid: 16510748
52. C. Waeber, M. A. Moskowitz, Migraine as an inflammatory disorder. *Neurology* **64** (Suppl 2), S9–S15 (2005). doi: 10.1212/WNL.64.10_suppl_2.S9; pmid: 15911785
53. J. Steiner *et al*., Increased prevalence of diverse N-methyl-D-aspartate glutamate receptor antibodies in patients with an initial diagnosis of schizophrenia: Specific relevance of IgG NR1a antibodies for distinction from N-methyl-D-aspartate glutamate receptor encephalitis. *JAMA Psychiatry* **70**, 271–278 (2013). doi: 10.1001/2013.jamapsychiatry.86; pmid: 23344076
54. L. Jones *et al*., Convergent genetic and expression data implicate immunity in Alzheimer's disease. *Alzheimers Dement.* **11**, 658–671 (2015). doi: 10.1016/j.jalz.2014.05.1757; pmid: 25533204
55. M. H. M. de Moor *et al*., Meta-analysis of Genome-wide Association Studies for Neuroticism, and the Polygenic Association With Major Depressive Disorder. *JAMA Psychiatry* **72**, 642–650 (2015). doi: 10.1001/jamapsychiatry.2015.0554; pmid: 25993607
56. K. S. Kendler, M. Gatz, C. O. Gardner, N. L. Pedersen, Personality and major depression: A Swedish longitudinal, population-based twin study. *Arch. Gen. Psychiatry* **63**, 1113–1120 (2006). doi: 10.1001/archpsyc.63.10.1113; pmid: 17015813
57. R. E. Ørstavik, K. S. Kendler, N. Czajkowski, K. Tambs, T. Reichborn-Kjennerud, The relationship between depressive personality disorder and major depressive disorder: A population-based twin study. *Am. J. Psychiatry* **164**, 1866–1872 (2007). doi: 10.1176/appi.ajp.2007.07010045; pmid: 18056242
58. H. Hemingway, M. Marmot, Evidence based cardiology: Psychosocial factors in the aetiology and prognosis of coronary heart disease. Systematic review of prospective cohort studies. *BMJ* **318**, 1460–1467 (1999). doi: 10.1136/bmj.318.7196.1460; pmid: 10346775
59. F. J. McClernon, S. H. Kollins, ADHD and smoking: From genes to brain to behavior. *Ann. N. Y. Acad. Sci.* **1141**, 131–147 (2008). doi: 10.1196/annals.1441.016; pmid: 18991955
60. T. Korhonen *et al*., Externalizing behaviors and cigarette smoking as predictors for use of illicit drugs: A longitudinal study among Finnish adolescent twins. *Twin Res. Hum. Genet.* **13**, 550–558 (2010). doi: 10.1375/twin.13.6.550; pmid: 21142931
61. D. A. Snowdon *et al*., Linguistic ability in early life and cognitive function and Alzheimer's disease in late life. Findings from the Nun Study. *JAMA* **275**, 528–532 (1996). doi: 10.1001/jama.1996.03530310034029; pmid: 8606473
62. S. Cortese *et al*., Association Between ADHD and Obesity: A Systematic Review and Meta-Analysis. *Am. J. Psychiatry* **173**, 34–43 (2016). doi: 10.1176/appi.ajp.2015.15020266; pmid: 26315982
63. A. E. Locke *et al*., Genetic studies of body mass index yield new insights for obesity biology. *Nature* **518**, 197–206 (2015). doi: 10.1038/nature14177; pmid: 25673413
64. L. Mustelin *et al*., Long-term outcome in anorexia nervosa in the community. *Int. J. Eat. Disord.* **48**, 851–859 (2015). doi: 10.1002/eat.22415; pmid: 26059099
65. T. Kurth *et al*., Prospective study of body mass index and risk of stroke in apparently healthy women. *Circulation* **111**, 1992–1998 (2005). doi: 10.1161/01.CIR.0000161822.83163.B6; pmid: 15837954
66. S. R. Korndörfer *et al*., Long-term survival of patients with anorexia nervosa: A population-based study in Rochester, Minn. *Mayo Clin. Proc.* **78**, 278–284 (2003). doi: 10.4065/78.3.278; pmid: 12630579

67. P. F. Sullivan, Discrepant results regarding long-term survival of patients with anorexia nervosa? *Mayo Clin. Proc.* **78**, 273–274 (2003). doi: 10.4065/78.3.273; pmid: 12630577

ACKNOWLEDGMENTS

We thank the members of the Neale and Daly laboratories for helpful discussions; R. Hoskins, J. Wessman, and J. Martin for comments on the manuscript; M. Whittall for inspiration; S. Knemeyer for help with the summary figure; C. Hammond for organizational assistance; and the patients and participants of the respective consortia for their participation. Data on coronary artery disease have been contributed by CARDIoGRAMplusC4D investigators and have been downloaded from www.cardiogramplusc4d.org. matSpD (Matrix Spectral Decomposition method) is available at neurogenetics.qimrberghofer.edu.au/matSpD/. This research was conducted using the UK Biobank resource (application 18597). **Funding:** This work was supported by grants 1R01MH10764901 and 5U01MH09443203 from the National Institute of Mental Health, as well as the Orion Farmos Research Foundation (V.A.) and the Fannie and John Hertz Foundation (H.K.F.). Consortium specific funding is detailed in the supplementary materials ("Study-specific acknowledgments"). **Author contributions:** V.A., A.C., and B.M.N. conceived of and coordinated the study; V.A., B.B.S., H.K.F., R.W., and P.T. contributed methodology; B.B.S. and H.K.F. contributed software; V.A. and B.M.N. conducted the statistical analysis; B.M.N. obtained funding and provided resources; R.W., J.B., L.D., V.E.-P., G.F., P.G., R.M., N.P., S.R., Z.W., and D.Y. were responsible for curation of disorder-specific data; P.H.L. and C.C. helped with data interpretation; V.A. and B.M.N. wrote the original draft, and all authors contributed to review and editing; V.A. provided the visualization; G.B., C.B., M.Daly, M.Dichgans, S.V.F., R.G., P.H., K.K., B.K., C.A.M., A.P., J.S., P.S., J.W., N.W., C.C., A.P., J.S., P.S., J.R., A.C., and B.M.N. provided supervision and project administration; and the remaining authors contributed disorder-specific sample collection and/or analysis. Consortium-specific personnel lists can be found in the supplementary materials. **Competing interests:** The authors declare no competing interests. **Data and materials availability:** Data sources for the GWAS summary statistics used in the study and their availability, as well as the study-specific acknowledgments, are provided in the supplementary materials (table S13 and supplementary text, respectively).

The Brainstorm Consortium

Verneri Anttila[1,2,3]*, Brendan Bulik-Sullivan[1,3], Hilary K. Finucane[2,3,4,5], Raymond K. Walters[1,2,3], Jose Bras[6,7], Laramie Duncan[1,2,3,8], Valentina Escott-Price[9,10], Guido J. Falcone[11,12,13], Padhraig Gormley[1,2,3,11], Rainer Malik[14], Nikolaos A. Patsopoulos[3,15], Stephan Ripke[1,2,3,16], Zhi Wei[17], Dongmei Yu[2,11], Phil H. Lee[2,11], Patrick Turley[1,3], Benjamin Grenier-Boley[18,19,20], Vincent Chouraki[18,19,20,21], Yoichiro Kamatani[22,23], Claudine Berr[24,25,26], Luc Letenneur[27,28], Didier Hannequin[29,30], Philippe Amouyel[18,19,20,21], Anne Boland[31], Jean-François Deleuze[31], Emmanuelle Duron[32,33], Badri N. Vardarajan[34], Christiane Reitz[35], Alison M. Goate[36], Matthew J. Huentelman[37], M. Ilyas Kamboh[38], Eric B. Larson[39,40], Ekaterina Rogaeva[41], Peter St George-Hyslop[41,42], Hakon Hakonarson[43,44,45], Walter A. Kukull[46], Lindsay A. Farrer[47], Lisa L. Barnes[48,49,50], Thomas G. Beach[51], F. Yesim Demirci[38], Elizabeth Head[52], Christine M. Hulette[53], Gregory A. Jicha[54], John S.K. Kauwe[55], Jeffrey A. Kaye[56], James B. Leverenz[57], Allan I. Levey[58], Andrew P. Lieberman[59], Vernon S. Pankratz[60], Wayne W. Poon[61], Joseph F. Quinn[62,63], Andrew J. Saykin[64], Lon S. Schneider[65], Amanda G. Smith[66], Joshua A. Sonnen[67,68], Robert A. Stern[69], Vivianna M. Van Deerlin[70], Linda J. Van Eldik[52], Denise Harold[71], Giancarlo Russo[72], David C. Rubinsztein[73,74], Anthony Bayer[75], Magda Tsolaki[76,77], Petra Proitsi[78], Nick C. Fox[79,6], Harald Hampel[80,81,82,83], Michael J. Owen[84,85], Simon Mead[86], Peter Passmore[87], Kevin Morgan[88], Markus M. Nöthen[89,90], Martin Rossor[91], Michelle K. Lupton[92,93], Per Hoffmann[89,90,94,95], Johannes Kornhuber[96], Brian Lawlor[97], Andrew McQuillin[98], Ammar Al-Chalabi[99,100], Joshua C. Bis[101], Agustin Ruiz[102,103], Mercè Boada[102], Sudha Seshadri[104,105,106], Alexa Beiser[107,108,106], Kenneth Rice[109], Sven J. van der Lee[110], Philip L. De Jager[111], Daniel H. Geschwind[112,113,114], Matthias Riemenschneider[115], Steffi Riedel-Heller[116], Jerome I. Rotter[117], Gerhard Ransmayr[118], Bradley T. Hyman[12,13], Carlos Cruchaga[120], Montserrat Alegret[102], Bendik Winsvold[121,122], Priit Palta[123,124], Kai-How Farh[125,3], Ester Cuenca-Leon[11,3,2], Nicholas Furlotte[126], Tobias Kurth[127], Lannie Ligthart[128], Gisela M.Terwindt[129], Tobias Freilinger[130,131], Caroline Ran[132], Scott D.Gordon[92], Guntram Borck[133], Hieab H.H. Adams[110,134], Terho Lehtimäki[135], Juho Wedenoja[136,137], Julie E. Buring[138], Markus Schürks[139], Maria Hrafnsdottir[140], Jouke-Jan Hottenga[128,141], Brenda Penninx[142], Ville Artto[143], Mari Kaunisto[123], Salli Vepsäläinen[143], Nicholas G. Martin[92], Grant W. Montgomery[92,144], Mitja I. Kurki[1,3,11,123], Eija Hämäläinen[123], Hailiang Huang[1,2,145], Jie Huang[146,147], Cynthia Sandor[148], Caleb Webber[148,10], Bertram Muller-Myhsok[149,150,151], Stefan Schreiber[152,153], Veikko Salomaa[154], Elizabeth Loehrer[155], Hartmut Göbel[156], Alfons Macaya[157], Patricia Pozo-Rosich[158,159], Thomas Hansen[160,161], Thomas Werge[161,162,163], Jaakko Kaprio[123,137], Andres Metspalu[124], Christian Kubisch[164], Michel D. Ferrari[129], Andrea C. Belin[132], Arn M. J. M. van den Maagdenberg[166,129], John-Anker Zwart[167], Dorret Boomsma[168,128], Nicholas Eriksson[126], Jes Olesen[160], Daniel I. Chasman[169,13], Dale R. Nyholt[170], Andreja Avbersek[171], Larry Baum[172], Samuel Berkovic[173], Jonathan Bradfield[174], Russell Buono[175,176,177], Claudia B. Catarino[171,178], Patrick Cossette[179], Peter De Jonghe[180,181,182], Chantal Depondt[183], Dennis Dlugos[184,185], Thomas N. Ferraro[186,187], Jacqueline French[188], Helle Hjalgrim[189], Jennifer Jamnadas-Khoda[171,190], Reetta Kälviäinen[192,193], Wolfram S. Kunz[194,195], Holger Lerche[131], Costin Leu[196], Dick Lindhout[197,198], Warren Lo[199,200], Daniel Lowenstein[201], Mark McCormack[202,203], Rikke S. Møller[204,205], Anne Molloy[206], Ping-Wing Ng[207,208], Karen Oliver[209], Michael Privitera[210,211], Rodney Radtke[212], Ann-Kathrin Ruppert[213], Thomas Sander[213], Steven Schachter[214,12,13], Christoph Schankin[215,216], Ingrid Scheffer[217,218,219], Susanne Schoch[220], Sanjay M. Sisodiya[221,222], Philip Smith[223], Michael Sperling[224], Pasquale Striano[225], Rainer Surges[226,227], G. Neil Thomas[228], Frank Visscher[229], Christopher D. Whelan[202], Federico Zara[230], Erin L. Heinzen[231], Anthony Marson[232,233], Felicitas Becker[234,235], Hans Stroink[236], Fritz Zimprich[237], Thomas Gasser[238,239], Raphael Gibbs[240], Peter Heutink[239,238], Maria Martinez[241,242], Huw R. Morris[221], Manu Sharma[243], Mina Ryten[221], Kin Y. Mok[7,245], Sara Pulit[246,247,3], Steve Bevan[248], Elizabeth Holliday[249], John Attia[250,251], Thomas Battey[11,253], Giorgio Boncoraglio[254,255], Vincent Thijs[219,256], Wei-Min Chen[257], Braxton Mitchell[258,259], Peter Rothwell[260], Pankaj Sharma[261,262], Cathie Sudlow[263], Astrid Vicente[264,265], Hugh Markus[266], Christina Kourkoulis[3,119,11], Joana Pera[267], Miriam Raffeld[3,11,119,268], Scott Silliman[269], Vesna Boraska Perica[270], Laura M. Thornton[271], Laura M. Huckins[272], N. William Rayner[273,274,275], Cathryn M. Lewis[276], Monica Gratacos[277], Filip Rybakowski[278], Anna Keski-Rahkonen[279], Anu Raevuori[280,279], James I. Hudson[281], Ted Reichborn-Kjennerud[282,283], Palmiero Monteleone[284], Andreas Karwautz[285], Katrin Mannik[124,286], Jessica H. Baker[271], Julie K. O'Toole[287], Sara E. Trace[288], Oliver S. P. Davis[289], Sietske G. Helder[290,276], Stefan Ehrlich[291], Beate Herpertz-Dahlmann[292], Unna N. Danner[293,294], Annemarie A. van Elburg[293,294], Maurizio Clementi[295], Monica Forzan[296], Elisa Docampo[297,298], Jolanta Lissowska[299], Joanna Hauser[300], Alfonso Tortorella[301], Mario Maj[302], Fragiskos Gonidakis[303], Konstantinos Tziouvas[304], Hana Papezova[305,306], Zeynep Yilmaz[271], Gudrun Wagner[307], Sarah Cohen-Woods[308], Stefan Herms[89,90,94,95], Antonio Julià[311], Raquel Rabionet[312,313,314,315], Danielle M. Dick[316], Samuli Ripatti[123,137,317], Ole A. Andreassen[318,319], Thomas Espeseth[318,320,321], Astri J. Lundervold[322,321], Vidar M. Steen[323,324], Dalila Pinto[325,326,327,328], Stephen W. Scherer[330,331], Harald Aschauer[332], Alexandra Schosser[333,334], Lars Alfredsson[335], Leonid Padyukov[336], Katherine A. Halmi[337], James Mitchell[338,339], Michael Strober[340], Andrew W. Bergen[341,342], Walter Kaye[343], Jin Peng Szatkiewicz[271], Bru Cormand[312,313,314,344], Josep Antoni Ramos-Quiroga[345,346,348,347], Cristina Sánchez-Mora[346,345,348], Marta Ribasés[346,345,348], Miguel Casas[349,350,345,351], Amaia Hervas[352], Maria Jesús Arranz[353], Jan Haavik[354,355], Tetyana Zayats[354,1], Stefan Johansson[356,324], Nigel Williams[9], Astrid Dempfle[357], Aribert Rothenberger[358], Jonna Kuntsi[359], Robert D. Oades[360], Tobias Banaschewski[361], Barbara Franke[362,363,364], Jan K. Buitelaar[365,366], Alejandro Arias Vasquez[367], Alysa E. Doyle[119,13], Andreas Reif[368], Klaus-Peter Lesch[369,370,371], Christine Freitag[372], Olga Rivero[371], Haukur Palmason[140], Marcel Romanos[373], Kate Langley[374,84], Marcella Rietschel[375], Stephanie H. Witt[375], Soeren Dalsgaard[376,163,377], Anders D. Børglum[378,163,379,380], Irwin Waldman[381], Beth Wilmot[382], Nikolas Molly[383], Claiton H.D. Bau[384,385], Jennifer Crosbie[386,387], Russell Schachar[388,387], Sandra K. Loo[389], James J. McGough[390], Eugenio H. Grevet[385,392], Sarah E. Medland[92], Elise Robinson[1,2,5], Lauren A. Weiss[393,394,395], Elena Bacchelli[396], Anthony Bailey[397,398], Vanessa Bal[393,394,395], Agatino Battaglia[399], Catalina Betancur[400], Patrick Bolton[359,401], Rita Cantor[402], Patrícia Celestino-Soper[403], Geraldine Dawson[404], Silvia De Rubeis[325,326,407], Frederico Duque[406,405], Andrew Green[408,409], Sabine M. Klauck[410], Marion Leboyer[411,412,413], Pat Levitt[414,65], Elena Maestrini[396], Shrikant Mane[415,416], Daniel Moreno-De-Luca[417], Jeremy Parr[418,419,420], Regina Regan[409,421], Abraham Reichenberg[272], Sven Sandin[325,326,422], Jacob Vorstman[423,424], Thomas Wassink[425], Ellen Wijsman[426,109], Edwin Cook[427], Susan Santangelo[429,430], Richard Delorme[431,432], Bernadette Rogé[433,434,435], Tiago Magalhaes[421,436], Dan Arking[437], Thomas G. Schulze[438,439,375,440,441], Robert C. Thompson[442,443], Jana Strohmaier[375,444], Keith Matthews[445,446], Ingrid Melle[447,448], Derek Morris[449], Douglas Blackwood[450], Andrew McIntosh[450], Sarah E. Bergen[422], Martin Schalling[451,452], Stéphane Jamain[411,412,413], Anna Maaser[90,89], Sascha B. Fischer[94,458], Céline S. Reinbold[94,458], Janice M. Fullerton[454,455], José Guzman-Parra[456,457], Fermin Mayoral[456,457], Peter R. Schofield[454,455], Sven Cichon[94,458,460], Thomas W. Mühleisen[460,458], Franziska Degenhardt[461], Johannes Schumacher[461], Michael Bauer[462], Philip B. Mitchell[463,464], Elliot S. Gershon[465], John Rice[466], James B. Potash[440], Peter P. Zandi[467], Nick Craddock[84], I. Nicol Ferrier[418], Martin Alda[468,469], Guy A. Rouleau[470,471], Gustavo Turecki[472], Roel Ophoff[474,475], Carlos Pato[476], Adebayo Anjorin[473], Eli Stahl[272,317], Markus Leber[477], Piotr M. Czerski[478], Cristiana Cruceanu[479,480], Ian R. Jones[481], Danielle Posthuma[482,483], Till F.M. Andlauer[149,484], Andreas J. Forstner[90,89,95,94,486], Fabian Streit[375], Bernhard T. Baune[487], Tracy Air[487], Grant Sinnamon[489,490], Naomi R. Wray[144,488], Donald J. MacIntyre[491], David Porteous[492], Georg Homuth[493], Margarita Rivera[494,276], Jakob Grove[163,379,378,495], Christel M. Middeldorp[496,497,128], Ian Hickie[498], Michele Pergadia[120], Divya Mehta[499,500], Johannes H. Smit[142,502,503], Rick Jansen[142], Eco de Geus[128,502], Erin Dunn[11,501], Qingqin S. Li[504], Matthias Nauck[505,506], Robert A. Schoevers[507], Aartjan TF Beekman[142,508], James A. Knowles[509], Alexander Viktorin[422], Paul Arnold[510,511,424], Cathy L. Barr[512,388,387], Gabriel Bedoya-Berrio[513], O. Joseph Bienvenu[514], Helena Brentani[515], Christie Burton[388], Beatriz Camarena[516], Carolina Cappi[515], Danielle Cath[518,519], Maria Cavallini[520], Daniele Cusi[521], Sabrina Darrow[522], Damiaan Denys[524,525], Eske M. Derks[92], Andrea Dietrich[517,526], Thomas Fernandez[523], Martijn Figee[524,325], Nelson Freimer[474], Gloria Gerber[11], Marco Grados[440], Erica Greenberg[119], Gregory L. Hanna[443], Andreas Hartmann[527,528,529], Matthew E. Hirschtritt[393,395], Pieter J. Hoekstra[526], Alden Huang[530,390], Chaim Huyser[531,532], Cornelia Illmann[119], Michael Jenike[13], Samuel Kuperman[533], Bennett Leventhal[522], Christine Lochner[534], Gholson J. Lyon[535], Fabio Macciardi[536], Marcos Madruga-Garrido[538], Irene A. Malaty[537], Athanasios Maras[539], Lauren McGrath[540], Eurípedes C. Miguel[541], Pablo Mir[542,543], Gerald Nestadt[440], Humberto Nicolini[544,545], Michael S. Okun[546,547,548], Andrew Pakstis[416], Peristera Paschou[550], John Piacentini[390], Christopher Pittenger[549], Kerstin Plessen[551,552], Vasily Ramensky[553], Eliana M. Ramos[554], Victor Reus[393,395], Margaret A. Richter[555,556], Mark A. Riddle[514], Mary M. Robertson[557], Veit Roessner[558], Maria Rosário[559,560], Jack F. Samuels[440], Paul Sandor[556,561,562], Dan J. Stein[563,534], Fotis Tsetsos[564], Filip Van Nieuwerburgh[565], Sarah Weatherall[11], Jens R. Wendland[566], Tomasz Wolanczyk[567], Yulia Worbe[568,569,570], Gwyneth Zai[556], Fernando S. Goes[440], Nicole McLaughlin[571,572], Paul S. Nestadt[440], Hans-Jorgen Grabe[573], Christel Depienne[574,575,576], Anuar Konkashbaev[577], Nuria Lanzagorta[545], Ana Valencia-Duarte[578,579], Elvira Bramon[98], Nancy Buccola[580], Wiepke Cahn[581], Murray Cairns[582,583,584], Siow A. Chong[585], David Cohen[586,587], Benedicto Crespo-Facorro[588,348], James Crowley[288], Michael Davidson[589,590], Lynn DeLisi[591,13], Timothy Dinan[592,593], Gary Donohoe[594], Elodie Drapeau[272,325,326], Jubao Duan[595,596], Lieuwe Haan[524,597], David Hougaard[598], Sena Karachanak-Yankova[599], Andrey Khrunin[600], Janis Klovins[601], Vaidutis Kučinskas[602], Jimmy Lee Chee Keong[603], Svetlana Limborska[604], Carmel Loughland[605,250], Jouko Lönnqvist[154,606], Brion Maher[467], Manuel Mattheisen[607,608,609], Colm McDonald[610,611], Kieran C. Murphy[612], Igor Nenadic[613,614], Jim van Os[581,615,616], Christos Pantelis[617,618,219], Michele Pato[476], Tracey Petryshen[2,11], Digby Quested[619,620], Panos Roussos[272], Alan R. Sanders[621,596], Ulrich Schall[250], Sibylle G. Schwab[622], Kang Sim[623,624,585], Hon-Cheong So[625,626,627], Elisabeth Stögmann[237], Mythily Subramaniam[585,624], Draga Toncheva[599], John Waddington[202], James Walters[84,85], Mark Weiser[590,628], Wei Cheng[271], Robert Cloninger[629], David Curtis[630,631], Pablo V. Gejman[596,621], Frans Henskens[632,633,251], Morten Mattingsdal[447,634], Sang-Yun Oh[635,636], Rodney Scott[250,251,637], Bradley Webb[638], Gerome Breen[639,640], Claire Churchhouse[1,2,3], Cynthia M. Bulik[641,422], Mark Daly[1,2,3], Martin Dichgans[14,150], Stephen V. Faraone[642], Rita Guerreiro[6,7], Peter Holmans[9], Kenneth S. Kendler[643], Bobby Koeleman[644], Carol A. Mathews[645,548], Alkes Price[3,5], Jeremiah Scharf[2,3,11,646,12,13], Pamela Sklar[272], Julie Williams[9,10], Nicholas W. Wood[7,630], Chris Cotsapas[3,647], Aarno Palotie[1,2,3,11,12,13,123], Jordan W. Smoller[2,11], Patrick Sullivan[641,648], Jonathan Rosand[3,11,12,13], Aiden Corvin[2,649]*†, Benjamin M. Neale[1,2,3]*†

[1]Analytic Translational Genetics Unit, Massachusetts General Hospital and Harvard Medical School, Boston, Massachusetts, USA. [2]Stanley Center for Psychiatric Research, Broad Institute of MIT and

Harvard, Cambridge, Massachusetts, USA. [3]Program in Medical and Population Genetics, Broad Institute of MIT and Harvard, Cambridge, Massachusetts, USA. [4]Department of Mathematics, Massachusetts Institute of Technology, Cambridge, Massachusetts, USA. [5]Department of Epidemiology, Harvard T.H. Chan School of Public Health, Boston, Massachusetts, USA. [6]UK Dementia Research Institute, University College London, London, UK. [7]Department of Molecular Neuroscience, Institute of Neurology, University College London, London, UK. [8]Department of Psychiatry and Behavioral Science, Stanford University, Stanford, California, USA. [9]Cardiff University, Medical Research Council Center for Neuropsychiatric Genetics & Genomics, Institute of Psychology, Medicine & Clinical Neuroscience, Cardiff, UK. [10]Dementia Research Institute, Cardiff University, Cardiff, UK. [11]Center for Genomic Medicine, Massachusetts General Hospital, Boston, MA, USA. [12]Department of Neurology, Massachusetts General Hospital, Boston, MA, USA. [13]Harvard Medical School, Boston, MA, USA. [14]Institute for Stroke and Dementia Research (ISD), University Hospital, LMU Munich, Munich, Germany. [15]Department of Neurology, Brigham & Women's Hospital, Harvard Medical School, Boston, MA, USA. [16]Charite Universitatsmedizin Berlin, Berlin, Germany. [17]Department of Computer Science, New Jersey Institute of Technology, New Jersey, USA. [18]INSERM U1167 LabEx DISTALZ, Lille, France. [19]Institut Pasteur de Lille, U1167, Lille, France. [20]Université de Lille, U1167, RID-AGE, Risk Factors and Molecular Determinants of Aging-Related Diseases, Lille, France. [21]Centre Hosp. Univ Lille, Lille, France. [22]Laboratory for Statistical Analysis, RIKEN Center for Integrative Medical Sciences, Yokohama, Japan. [23]Center for Genomic Medicine, Kyoto University Graduate School of Medicine, Kyoto, Japan. [24]INSERM U1061 - Neuropsychiatry: Epidemiological and Clinical Research, Montpellier, France. [25]University of Montpellier, Montpellier, France. [26]Memory Research and Resources Center, Department of Neurology, Montpellier University Hospital Gui de Chauliac, Montpellier, France. [27]INSERM, UMR 1219, Bordeaux, France. [28]University of Bordeaux, Bordeaux, France. [29]Rouen University Hospital, Rouen, France. [30]Inserm U1245, Rouen, France. [31]Centre National de Recherche en Génomique Humaine (CNRGH), Institut de biologie François Jacob, CEA, Evry, France. [32]Department of Gerontology, Hôpital Broca, AH-HP, Paris, France. [33]Hôpital Paul Brousse Université Paris Sud XI, Le Kremlin-Bicêtre, Paris, France. [34]Gertrude H. Sergievsky Center and Dept of Neurology, Columbia University, New York, NY, USA. [35]Columbia University, New York, NY, USA. [36]Department of Neuroscience, Icahn School of Medicine at Mount Sinai, New York, NY, USA. [37]Translational Genomics Research Institute, Neurogenomics Division, Phoenix, AZ, USA. [38]University of Pittsburgh, Pittsburgh, PA, USA. [39]Kaiser Permanente Washington Health Research Institute, Seattle, WA, USA. [40]Department of Medicine, University of Washington, WA, USA. [41]Tanz Centre for Research in Neurodegenerative Diseases, University of Toronto, Toronto, Canada. [42]Cambridge Institute for Medical Research, University of Cambridge, Cambridge, UK. [43]Center for Applied Genomics of The Children's Hospital of Philadelphia, Philadelphia, PA, USA. [44]Division of Human Genetics, Children's Hospital of Philadelphia, Philadelphia, PA, USA. [45]Department of Pediatrics, The Perelman School of Medicine, University of Pennsylvania, Philadelphia, PA, USA. [46]National Alzheimer Coordinating Center (NACC), Department of Epidemiology, University of Washington, Seattle, WA, USA. [47]Department of Medicine, Boston University School of Medicine, Boston, MA, USA. [48]Rush Alzheimers Disease Center, Chicago, IL, USA. [49]Department of Neurological Sciences, Rush Medical College, Chicago, IL, USA. [50]Department of Behavioral Sciences, Rush Medical College, Chicago, IL, USA. [51]Banner Sun Health Research Institute, Sun City, AZ, USA. [52]Sanders-Brown Center on Aging, University of Kentucky, Lexington, KY, USA. [53]Department of Pathology, Duke University School of Medicine, Durham, NC, USA. [54]College of Medicine, University of Kentucky, Lexington, KY, USA. [55]Department of Biology, Brigham Young University, Provo, UT, USA. [56]Layton Aging & Alzheimer's Disease Center, Oregon Health & Science University, Portland, OR, USA. [57]Lou Ruvo Center for Brain Health, Neurological Institute, Cleveland Clinic, Cleveland, OH, USA. [58]Department of Neurology, School of Medicine, Emory University, Atlanta, GA, USA. [59]Department of Pathology, University of Michigan Medical School, Ann Arbor, MI, USA. [60]University of New Mexico Health Sciences Center, Albuquerque, NM, USA. [61]Institute for Memory Impairments and Neurological Disorders, University of California, Irvine, CA, USA. [62]Department of Neurology, Oregon Health and Science University, Portland, OR, USA. [63]Department of Neurology and Parkinson's Disease Research Education and Clinical Care Center (PADRECC), Portland Veterans Affairs Medical Center, Portland, OR, USA. [64]Indiana Alzheimer Disease Center, Indiana University School of Medicine, Indianapolis, IN, USA. [65]Keck School of Medicine of the University of Southern California, Los Angeles, CA, USA. [66]Byrd Alzheimer's Institute, University of South Florida, Tampa, FL, USA. [67]Department of Pathology, University of Utah, Salt Lake City, UT, USA. [68]Department of Pathology, University of Washington, Seattle, WA, USA. [69]Boston University School of Medicine, Boston, MA, USA. [70]Department of Pathology and Laboratory Medicine, Perelman School of Medicine, University of Pennsylvania, Philadelphia, PA, USA. [71]School of Biotechnology, Dublin City University, Glasnevin, Dublin, Ireland. [72]Functional Genomics Center Zurich, ETH/UZH-Zurich, Zurich, Switzerland. [73]Department of Medical Genetics, Cambridge Institute for Medical Research, Cambridge, UK. [74]UK Dementia Research Institute, Cambridge, UK. [75]School of Medicine, Cardiff University, Cardiff, UK. [76]1st and 3rd Departments of Neurology, Aristotle University of Thessaloniki, Thessaloniki, Greece. [77]Greek Association of Alzheimer's Disease and Related Disorders, Thessaloniki, Greece. [78]Maurice Wohl Clinical Neuroscience Institute, Institute of Psychiatry, Psychology and Neuroscience, King's College London, London, UK. [79]Dementia Research Centre, UCL Institute of Neurology, London, UK. [80]Sorbonne University, GRC n° 21, Alzheimer Precision Medicine (APM), AP-HP, Pitié-Salpêtrière Hospital, Paris, France. [81]Institute of Memory and Alzheimer's Disease (IM2A), Department of Neurology, Pitié-Salpêtrière Hospital, AP-HP, Paris, France. [82]Brain & Spine Institute (ICM), INSERM U 1127, CNRS UMR 7225, Paris, France. [83]AXA Research Fund & Sorbonne University Chair, Paris, France. [84]MRC Centre for Neuropsychiatric Genetics and Genomics, Cardiff University, Cardiff, UK. [85]Institute of Psychological Medicine and Clinical Neurosciences, School of Medicine, Cardiff University, Cardiff, UK. [86]Institute of Prion Diseases and MRC Prion Unit, University College London, London, UK. [87]Centre for Public Health, Queens University Belfast, Belfast, UK. [88]Human Genetics, School of Life Sciences, University of Nottingham, Nottingham UK. [89]Department of Genomics, Life & Brain Center, University of Bonn, Bonn, Germany. [90]Institute of Human Genetics, School of Medicine, University of Bonn & University Hospital Bonn, Bonn, Germany. [91]Department of Neurodegeneration, UCL Institute of Neurology, London, UK. [92]QIMR Berghofer Medical Research Institute, Brisbane, Australia. [93]Institute of Psychiatry Psychology and Neuroscience, Kings College London, UK. [94]Institute of Medical Genetics and Pathology, University Hospital Basel, Basel, Switzerland. [95]Human Genomics Research Group, Department of Biomedicine, University of Basel, Basel, Switzerland. [96]Department of Psychiatry and Psychotherapy, Friedrich-Alexander-Universität Erlangen-Nürnberg University Hospital, Erlangen, Germany. [97]Department of Psychiatry and Global Brain Health Institute, Trinity College, Dublin, Ireland. [98]Division of Psychiatry, Molecular Psychiatry Laboratory, University College London, London, UK. [99]Maurice Wohl Clinical Neuroscience Institute, Department of Basic and Clinical Neuroscience, King's College London, London, UK. [100]King's College Hospital, London, UK. [101]Cardiovascular Health Research Unit, Department of Medicine, University of Washington, Seattle, WA, USA. [102]Fundació ACE, Institut Català de Neurociències Aplicades, Barcelona, Spain and Universitat Internacional de Catalunya, Barcelona, Spain. [103]Facultat de Medicina i Ciències de la Salut, Universitat Internacional de Catalunya (UIC), Barcelona, Spain. [104]Glenn Biggs Institute for Alzheimer's and Neurodegenerative Diseases, University of Texas Health Sciences Center, San Antonio, Texas, USA. [105]Neurology and Neurogenetics Core, Framingham Heart Study, Framingham, MA, USA. [106]School of Medicine, Boston University, Boston, MA, USA. [107]School of Public Health, Boston University, Boston, MA, USA. [108]Framingham Heart Study, Framingham, MA, USA. [109]Department of Biostatistics, University of Washington, Seattle, WA, USA. [110]Department of Epidemiology, Erasmus Medical Centre, Rotterdam, the Netherlands. [111]Center for Translational & Computational Neuroimmunology, Columbia University Medical Center, New York, NY, USA. [112]Neurogenetics Program, Departments of Neurology and Human Genetics, David Geffen School of Medicine, University of California, Los Angeles, Los Angeles, CA, USA. [113]Center For Autism Research and Treatment, Semel Institute, David Geffen School of Medicine, University of California, Los Angeles, Los Angeles, CA, USA. [114]Institute for Precision Health, University of California, Los Angeles, Los Angeles, CA, USA. [115]Department of Psychiatry, Saarland University Hospital, Homburg, Germany. [116]Institute of Social Medicine, Occupational Health and Public Health (ISAP), University of Leipzig, Leipzig, Germany. [117]Institute for Translational Genomics and Population Sciences, Departments of Pediatrics and Medicine, LABioMed at Harbor-UCLA Medical Center, Torrance, CA, USA. [118]Department of Neurology II, Kepler University Clinic, Johannes Kepler University, Linz, Austria. [119]Massachusetts General Hospital, Boston, MA, USA. [120]Washington University School of Medicine, St. Louis, MO, USA. [121]Communication and Research Unit for Musculoskeletal Disorders (FORMI), Oslo University Hospital, Oslo, Norway. [122]Department of Neurology, Oslo University Hospital, Oslo, Norway. [123]Institute for Molecular Medicine Finland (FIMM), HiLIFE, University of Helsinki, Helsinki, Finland. [124]Estonian Genome Center, Institute of Genomics, University of Tartu, Tartu, Estonia. [125]Illumina Inc., San Diego, CA, USA. [126]23andMe Inc., Mountain View, CA, USA. [127]Institute of Public Health, Charité – Universitätsmedizin Berlin, Berlin, Germany. [128]Department of Biological Psychology, Vrije Universiteit Amsterdam, Amsterdam, The Netherlands. [129]Department of Neurology, Leiden University Medical Center, Leiden, The Netherlands. [130]Institute for Stroke and Dementia Research, Klinikum der Universitaet Muenchen, Munich, Germany. [131]Department of Neurology and Epileptology, Hertie Institute for Clinical Brain Research, University of Tuebingen, Tuebingen, Germany. [132]Department of Neuroscience, Karolinska Institutet, Stockholm, Sweden. [133]Institute of Human Genetics, University of Ulm, Ulm, Germany. [134]Department of Radiology and Nuclear Medicine, Erasmus Medical Centre, Rotterdam, the Netherlands. [135]Department of Clinical Chemistry, Fimlab Laboratories and Finnish Cardiovascular Research Center-Tampere, Faculty of Medicine and Life Sciences, University of Tampere, Tampere, Finland. [136]Department of Ophthalmology, University of Helsinki and Helsinki University Hospital, Helsinki, Finland. [137]Department of Public Health, University of Helsinki, Helsinki, Finland. [138]Brigham and Women's Hospital, Boston, MA. [139]Department of Neurology, University Hospital Essen, Germany. [140]Landspitali National University Hospital, Reykjavik, Iceland. [141]Avera Institute for Human Genetics, Sioux Falls, SD, USA. [142]Department of Psychiatry, VU University Medical Center, Amsterdam, The Netherlands. [143]Department of Neurology, Helsinki University Central Hospital, Helsinki, Finland. [144]Institute for Molecular Bioscience, University of Queensland, Brisbane, Australia. [145]Department of Medicine, Harvard Medical School, Boston, MA, USA. [146]Boston VA Research Institute, Boston, MA, USA. [147]Brigham Women's Hospital Division of Aging, Harvard Medical School, Boston, MA, USA. [148]Department of Physiology, Anatomy and Genetics, University of Oxford, Oxford, UK. [149]Max Planck Institute of Psychiatry, Munich, Germany. [150]Munich Cluster for Systems Neurology (SyNergy), Munich, Germany. [151]Institute of Translational Medicine, University of Liverpool, Liverpool, UK. [152]Institute of Clinical Molecular Biology, Kiel University and University Hospital Schleswig-Holstein, Kiel, Germany. [153]Clinic of Internal Medicine I, University Hospital Schleswig-Holstein, Kiel, Germany. [154]National Institute for Health and Welfare, Helsinki, Finland. [155]Department of Environmental Health, Harvard T.H. Chan School of Public Health, Boston, MA, USA. [156]Kiel Pain and Headache Center, Kiel, Germany. [157]Pediatric Neurology Research Group, Vall d'Hebron Research Institute, Autonomous University of Barcelona, Barcelona, Spain. [158]Headache Unit, Neurology Department, Hospital Vall d'Hebron, Barcelona, Spain. [159]Headache Research Group, VHIR, Autonomous University of Barcelona, Barcelona, Spain. [160]Danish Headache Center, Rigshospitalet Glostrup and University of Copenhagen, Copenhagen, Denmark. [161]Institute of Biological Psychiatry, Roskilde, Denmark. [162]Department of Clinical Sciences, University of Copenhagen, Copenhagen, Denmark. [163]Lundbeck Foundation Initiative for Integrative Psychiatric Research, iPSYCH, Aarhus, Denmark. [164]Institute of Human Genetics, University Medical Center Hamburg-Eppendorf, Hamburg, Germany. [165]Karolinska Institutet, Stockholm, Sweden. [166]Department of Human Genetics, Leiden University Medical Center, Leiden, The Netherlands. [167]Division of Clinical Neuroscience, Oslo University Hospital and University of Oslo, Oslo, Norway. [168]Netherlands Twin Register, Vrije Universiteit, Amsterdam, the Netherlands. [169]Division of Preventive Medicine, Brigham and Women's Hospital, Boston, MA, USA. [170]Statistical and Genomic Epidemiology Laboratory, Institute of Health and Biomedical Innovation, Queensland University of Technology, Brisbane, Queensland, Australia. [171]Department of Clinical and Experimental Epilepsy, UCL Institute of Neurology, London, UK. [172]Centre for Genomic Sciences, University of Hong Kong, Hong Kong. [173]Epilepsy Research Centre, University of Melbourne, Heidelberg, Australia. [174]Quantinuum Research LLC, San Diego, CA, USA. [175]Cooper Medical School of Rowan University, Camden, NJ, USA. [176]Thomas Jefferson University Hospital, Philadelphia, PA, USA. [177]Children's Hospital of Philadelphia, Philadelphia, PA, USA. [178]Epilepsy Society, Chalfont-St-Peter, Bucks, UK. [179]Centre de Recherche du Centre Hospitalier de l'Universite de Montreal and Department of Neurosciences, Université de Montréal, Montréal, Canada. [180]Neurogenetics Group, VIB-CMN, Antwerp, Belgium. [181]University of Antwerp, Antwerp, Belgium. [182]Department of Neurology, Antwerp University Hospital, Antwerp, Belgium. [183]Department of Neurology, Hôpital Erasme, Université Libre de Bruxelles, Brussels, Belgium. [184]Division of Neurology, Children's Hospital of Philadelphia, Philadelphia, PA, USA. [185]Perelman School of Medicine at the University of Pennsylvania, Philadelphia, PA, USA. [186]Department of Biomedical Sciences, Cooper Medical School of Rowan University, Camden, NJ, USA. [187]Department of Psychiatry, Center for Neurobiology and Behavior, Perelman School of Medicine at the University of Pennsylvania, Philadelphia, PA, USA. [188]NYU School of Medicine, New York, NY, USA. [189]Amplexa Genetics A/S, Odense, Denmark. [190]Institute of Mental Health, University of Nottingham, Nottingham, UK. [191]Human Genetics, School of Life Sciences,

University of Nottingham, Nottingham UK. [192]Epilepsy Center/ Neurocenter, Kuopio University Hospital, Kuopio, Finland. [193]Institute of Clinical Medicine, School of Medicine, Faculty of Health Sciences, University of Eastern Finland, Kuopio, Finland. [194]Department of Epileptology, University Bonn Medical Center, Bonn, Germany. [195]Institute of Experimental Epileptology and Cognition Research, University Bonn Medical Center, Bonn, Germany. [196]Department of Clinical and Experimental Epilepsy, NIHR University College London Hospitals Biomedical Research Centre, UCL Institute of Neurology, London. [197]Department of Genetics, University Medical Center Utrecht, the Netherlands. [198]Epilepsy Foundation in the Netherlands (SEIN), Heemstede, the Netherlands. [199]Departments of Pediatrics and Neurology, Ohio State University, Columbus, OH, USA. [200]Nationwide Children's Hospital, Columbus, OH, USA. [201]Department of Neurology, University of California, San Francisco, CA, USA. [202]Department of Molecular and Cellular Therapeutics, Royal College of Surgeons in Ireland, Dublin, Ireland. [203]Center for Molecular Medicine, University Medical Center Utrecht, Utrecht, the Netherlands. [204]Danish Epilepsy Centre, Filadelfia, Dianalund, Denmark. [205]Institute for Regional Health Services, University of Southern Denmark, Odense, Denmark. [206]Trinity College Dublin, Dublin, Ireland. [207]United Christian Hospital, Hong Kong. [208]Hong Kong Sanatorium and Hospital, Hong Kong. [209]Epilepsy Research Centre, University of Melbourne, Austin Health, Heidelberg, Australia. [210]Department of Neurology, University of Cincinnati, Cincinnati, OH, USA. [211]UC Gardner Neuroscience Institute, Cincinnati, OH, USA. [212]Department of Neurology, Duke University School of Medicine, Durham, NC, USA. [213]Cologne Center for Genomics (CCG), University of Cologne, Cologne, Germany. [214]Department of Neurology, Beth Israel Deaconess Medical Center, Boston, MA, USA. [215]Department of Neurology, Inselspital, Bern University Hospital, University of Bern, Switzerland. [216]Department of Neurology, University of Munich Hospital, Grosshadern, University of Munich, Germany. [217]Department of Medicine, The University of Melbourne, Austin Health, Melbourne, Victoria, Australia. [218]Department of Paediatrics, Royal Children's Hospital, The University of Melbourne, Melbourne, Victoria, Australia. [219]Florey Institute of Neuroscience and Mental Health, Melbourne, Victoria, Australia. [220]Institute of Neuropathology, Bonn University Medical School, Bonn, Germany. [221]UCL Institute of Neurology, London, UK. [222]Chalfont Centre for Epilepsy, Bucks, UK. [223]University Hospital of Wales, Cardiff, UK. [224]Department of Neurology, Thomas Jefferson University, Philadelphia, PA, USA. [225]Pediatric Neurology and Muscular Diseases Unit-Department of Neurosciences, Rehabilitation, Ophthalmology, Genetics, Maternal and Child Health University of Genoa, "G. Gaslini" Institute, Genova, Italy. [226]Department of Epileptology, University Hospital Bonn, Bonn, Germany. [227]Section of Epileptology, Department of Neurology, University Hospital RWTH Aachen, Aachen, Germany. [228]Institute of Applied Health Research, University of Birmingham, UK. [229]Department of Neurology, Admiraal De Ruyter Hospital, Goes, The Netherlands. [230]Laboratory of Neurogenetics, G. Gaslini Institute, Genova, Italy. [231]Institute for Genomic Medicine, Columbia University Medical Center, New York, NY, USA. [232]University of Liverpool, Liverpool, UK. [233]Walton Centre NHS Foundation Trust, Liverpool, UK. [234]Department of Neurology and Epileptology, University Hospital Tuebingen, Tuebingen, Germany. [235]Department of Neurology, University of Ulm, Ulm, Germany. [236]CWZ Hospital, Nijmegen, Netherlands. [237]Department of Neurology, Medical University of Vienna, Austria. [238]Hertie-Institute for Clinical Brain Research, University of Tübingen, Tübingen, Germany. [239]German Center for Neurodegenerative Diseases (DZNE), Tübingen, Germany. [240]Laboratory of Neurogenetics, National Institute on Aging, National Institutes of Health, Bethesda, MD, USA. [241]INSERM U1220, IRSD, Toulouse, France. [242]Université Paul Sabatier, Toulouse, France. [243]Centre for Genetic Epidemiology, Institute for Clinical Epidemiology and Applied Biometery, University of Tubingen, Germany. [244]Department of Molecular Neuroscience, Institute of Neurology, University College London, London, UK. [245]Division of Life Science, Hong Kong University of Science and Technology, Hong Kong Special Administrative Region, China. [246]Department of Genetics, Center for Molecular Medicine, University Medical Center Utrecht, Utrecht, The Netherlands. [247]Big Data Institute, Li Ka Shing Centre for Health Information and Discovery, University of Oxford, Oxford, UK. [248]University of Lincoln, Lincoln, UK. [249]Faculty of Health and Medicine, University of Newcastle, Callaghan, Australia. [250]University of Newcastle, Callaghan, Australia. [251]Hunter Medical Research Institute, Newcastle, Australia. [252]Center for Genomic Medicine, Massachusetts General Hospital, Boston, MA, USA. [253]Division of Neurocritical Care and Emergency Neurology, Massachusetts General Hospital, Boston, MA, USA. [254]Department of Cerebrovascular Diseases, Fondazione IRCCS Istituto Neurologico Carlo Besta, Milano, Italy. [255]PhD Program in Neuroscience, University Milano-Bicocca, Monza, Italy. [256]Austin Health, Heidelberg, Australia. [257]University of Virginia Center for Public Health Genomics, University of Virginia, Charlottesville, VA, USA. [258]Dept of Medicine, University of Maryland School of Medicine, Baltimore, MD, USA. [259]Geriatrics Research and Education Clinical Center, Baltimore Veterans Administration Medical Center, Baltimore, MD, USA. [260]Centre for Prevention of Stroke and Dementia, Nuffield Department of Clinical Neurosciences, University of Oxford, Oxford, UK. [261]Institute of Cardiovascular Research, Royal Holloway University of London, London, UK. [262]Ashford & St Peters NHS Foundation Trust, Surrey, UK. [263]University of Edinburgh, Edinburgh, UK. [264]Instituto Nacional de Saúde Doutor Ricardo Jorge, Lisboa, Portugal. [265]Biosystems and Integrative Sciences Institute - BioISI, University of Lisboa, Lisboa, Portugal. [266]Department of Clinical Neurosciences, University of Cambridge, Cambridge, UK. [267]Department of Neurology, Jagiellonian University Medical College, Kraków, Poland. [268]The Warren Alpert Medical School of Brown University, Providence, RI, USA. [269]Department of Neurology, College of Medicine-Jacksonville, University of Florida, Jacksonville, FL, USA. [270]University of Split School of Medicine, Split, Croatia. [271]University of North Carolina at Chapel Hill, Chapel Hill, NC, USA. [272]Icahn School of Medicine at Mount Sinai, New York, NY, USA. [273]Wellcome Centre for Human Genetics, Nuffield Department of Medicine, University of Oxford, Oxford, UK. [274]Oxford Centre for Diabetes, Endocrinology and Metabolism, Nuffield Department of Medicine, University of Oxford, Oxford, UK. [275]Department of Human Genetics, Wellcome Sanger Institute, Hinxton, Cambridgeshire, UK. [276]MRC Social, Genetic and Developmental Psychiatry Centre, King's College London, London, UK. [277]Genes and Disease Programme, Centre for Genomic Regulation (CRG), Barcelona, Spain. [278]Department of Adult Psychiatry, Poznan University of Medical Sciences, Poland. [279]Clinicum, Department of Public Health, University of Helsinki, Finland. [280]Department of Adolescent Psychiatry, Helsinki University Central Hospital, Helsinki, Finland. [281]Harvard Medical School/McLean Hospital, Belmont, MA, USA. [282]Norwegian Institute of Public Health, Oslo, Norway. [283]University of Oslo, Oslo, Norway. [284]Department of Medicine, Surgery and Dentistry "Scuola Medica Salernitana", University of Salerno,Italy. [285]Eating Disorders Unit, Department of Child and Adolescent Psychiatry, Medical University of Vienna, Vienna, Austria. [286]Center for Integrative Genomics, University of Lausanne, Lausanne, Switzerland. [287]Kartini Clinic, Portland, OR, USA. [288]Department of Psychiatry, University of North Carolina at Chapel Hill, Chapel Hill, NC, USA. [289]MRC Integrative Epidemiology Unit and Bristol Medical School, University of Bristol, Bristol, UK. [290]Zorg op Orde BV, Leidschendam, The Netherlands. [291]Division of Psychological & Social Medicine and Developmental Neurosciences, Faculty of Medicine, Technischen Universität Dresden, Dresden, Germany. [292]Department of Child & Adolescent Psychiatry & Psychosomatic Medicine of University Clinics, RWTH Aachen, Aachen, Germany. [293]Altrecht Eating Disorders Rintveld, Altrecht Mental Health Institute, Zeist, The Netherlands. [294]Faculty of Social Sciences, University of Utrecht, Utrecht, the Netherlands. [295]Medical Genetics Unit, Department SDB, University of Padova, Padova, Italy. [296]UOC Genetica ed Epidemiologica Clinica Az. Ospedaliera, Padova, Italy. [297]Department of Human Genetics, CHU Sart-Tilman, University of Liège, Liège, Belgium. [298]Department of Rheumatology, CHU Sart-Tilman, University of Liège, Liège, Belgium. [299]Department of Cancer Epidemiology and Prevention, Cancer Center and M. Sklodowska-Curie Institute of Oncology, Warsaw, Poland. [300]Department of Psychiatry, University of Medical Sciences, Poznan, Poland. [301]Department of Psychiatry, University of Perugia, Perugia, Italy. [302]Department of Mental and Physical Health and Preventive Medicine, University of Campania "luigi Vanvitelli", Naples, Italy. [303]Eating Disorders Unit, 1st Psychiatric Department, National and Kapodistrian University of Athens, Athens, Greece. [304]Aglaia Kyriakou Childrens Hospital, Athens, Greece. [305]Eating Disorders Unit, Department of Psychiatry, First Faculty of Medicine, Charles University, Prague, Czech Republic. [306]General University Hospital, Prague, Czech Republic. [307]Medical University of Vienna, Austria. [308]School of Psychology, Flinders University, Adelaide, Australia. [309]Division of Medical Genetics, University Hospital Basel, Basel, Switzerland. [310]Genomics Research Group, Department of Biomedicine, University of Basel, Basel, Switzerland. [311]Vall d'Hebron Research Institute, Barcelona, Spain. [312]Institut de Recerca Sant Joan de Déu, Barcelona, Spain. [313]Institut de Biomedicina de la Universitat de Barcelona (IBUB), Barcelona, Spain. [314]Department of Genetics, Microbiology & Statistics, Faculty of Biology, University of Barcelona, Barcelona, Spain. [315]Centre for Genomic Regulation (CRG), Barcelona, Spain. [316]Departments of Psychology and Human & Molecular Genetics, College Behavioral and Emotional Health Institute, Virginia Commonwealth University, Richmond, Virginia. [317]Broad Institute of MIT and Harvard, Cambridge, USA. [318]NORMENT, Div. of Mental Health and Addiction, University of Oslo, Oslo, Norway. [319]Oslo University Hospital, Oslo, Norway. [320]Department of Psychology, University of Oslo, Norway. [321]K. G. Jebsen Centre for Research on Neuropsychiatric Disorders, University of Bergen, Bergen, Norway. [322]Department of Biological and Medical Psychology, University of Bergen, Bergen, Norway. [323]NORMENT, K.G. Jebsen Center for Psychosis Research, Department of Clinical Science, University of Bergen, Norway. [324]Department of Medical Genetics, Haukeland University Hospital, Bergen, Norway. [325]Department of Psychiatry, Icahn School of Medicine at Mount Sinai, New York, NY, USA. [326]Seaver Autism Center for Research and Treatment, Icahn School of Medicine at Mount Sinai, New York, NY, USA. [327]Department of Genetics and Genomic Sciences, and Institute for Genomics and Multiscale Biology, Icahn School of Medicine at Mount Sinai, New York, NY, USA. [328]The Mindich Child Health & Development Institute, Icahn School of Medicine at Mount Sinai, New York, NY, USA. [329]Friedman Brain Institute, Icahn School of Medicine at Mount Sinai, New York, NY, USA. [330]McLaughlin Centre and Department of Molecular Genetics, University of Toronto, Toronto, Canada. [331]The Centre for Applied Genomics, Hospital for Sick Children, Toronto, Canada. [332]Biopsychosocial Corporation, Vienna, Austria. [333]Department of Psychiatry and Psychotherapy, Medical University of Vienna, Vienna, Austria. [334]Zentren für Seelische Gesundheit, BBRZ-Med, Vienna, Austria. [335]Institute of Environmental Medicine, Karolinska Institutet, Stockholm, Sweden. [336]Rheumatology Unit, Department of Medicine, Karolinska Institutet and Karolinska University Hospital, Solna, Sweden. [337]Weill Cornell Medical College, New York, New York, USA. [338]School of Medicine, University of North Dakota, Grand Forks, ND, USA. [339]Neuropsychiatric Research Institute, Fargo, ND, USA. [340]Department of Psychiatry & Biobehavioral Sciences, Semel Institute for Neuroscience & Human Behavior, David Geffen School of Medicine, University of California at Los Angeles, Los Angeles, CA, USA. [341]BioRealm, Walnut, California, USA. [342]Oregon Research Institute, Eugene, OR, USA. [343]Department of Psychiatry, University of California San Diego, La Jolla, CA, USA. [344]Centro de Investigación Biomédica en Red de Enfermedades Raras (CIBERER), Instituto de Salud Carlos III, Madrid, Spain. [345]Department of Psychiatry, Hospital Universitari Vall d'Hebron, Barcelona, Spain. [346]Psychiatric Genetics Unit, Group of Psychiatry, Mental Health and Addiction, Vall d'Hebron Research Institute (VHIR), Universitat Autònoma de Barcelona, Barcelona, Spain. [347]Department of Psychiatry and Legal Medicine, Universitat Autònoma de Barcelona, Barcelona, Spain. [348]Biomedical Network Research Centre on Mental Health (CIBERSAM), Instituto de Salud Carlos III, Madrid, Spain. [349]Universitat Autònoma de Barcelona, Barcelona, Spain. [350]Programa Corporatiu "Neurodevelopment Disorders along Life Span", Institut Català de la Salut, Barcelona, Spain. [351]Clinica Galatea y PAIMM, Mental Health Program for Impaired Physicians, Barcelona, Spain. [352]Child and Adolescent Mental Health Unit, Hospital Universitario Mútua de Terrassa, Barcelona, Spain. [353]Fundació Docència i Recerca Mútua Terrassa. [354]K.G. Jebsen Centre for Neuropsychiatric Disorders, Department of Biomedicine, University of Bergen, Norway. [355]Division of Psychiatry, Haukeland University Hospital, Bergen, Norway. [356]K.G. Jebsen Centre for Neuropsychiatric Disorders, Department of Clinical Science, University of Bergen, Norway. [357]Institute of Medical Informatics and Statistics, Kiel University, Kiel, Germany. [358]Child and Adolescent Psychiatry/Psychotherapy, University Medical Center, Goettingen, Germany. [359]Institute of Psychiatry, Psychology and Neuroscience, King's College London, London, UK. [360]Clinic for Child and Adolescent Psychiatry and Psychotherapy, University of Duisburg-Essen, Essen, Germany. [361]Child and Adolescent Psychiatry and Psychotherapy, Central Institute of Mental Health, Medical Faculty Mannheim, University of Heidelberg, Mannheim, Germany. [362]Department of Human Genetics, Radboud University Medical Center, Nijmegen, The Netherlands. [363]Department of Psychiatry, Radboud University Medical Center, Nijmegen, The Netherlands. [364]Donders Institute for Brain, Cognition and Behaviour, Radboud University, Nijmegen, The Netherlands. [365]Department of Cognitive Neuroscience, Donders Institute for Brain, Cognition and Behavior, Radboud University Medical Centre, Nijmegen, The Netherlands. [366]Karakter Child and Adolescent Psychiatry University Center, Nijmegen, The Netherlands. [367]Department of Psychiatry & Human Genetics, Donders Institute for Brain, Cognition and Behaviour, Radboud University Medical Center, Nijmegen, The Netherlands. [368]Department of Psychiatry, Psychosomatic Medicine and Psychotherapy, University Hospital Frankfurt, Frankfurt am Main, Germany. [369]Laboratory of Psychiatric Neurobiology, Institute of Molecular Medicine, I.M. Sechenov First Moscow State Medical University, Moscow, Russia. [370]Department of Translational Psychiatry, School for Mental Health and Neuroscience (MHeNS), Maastricht University, Maastricht, The Netherlands. [371]Division of Molecular Psychiatry, Center of Mental Health, University of Wuerzburg, Wuerzburg, Germany. [372]Department of Child and Adolescent Psychiatry, Psychosomatics and Psychotherapy, University Hospital Frankfurt, Goethe University, Frankfurt am Main, Germany. [373]Center of Mental Health, Department of Child and Adolescent

Psychiatry, Psychosomatics and Psychotherapy, University Hospital of Wuerzburg, Wuerzburg, Germany. [374]School of Psychology, Cardiff University, UK. [375]Central Institute of Mental Health, Department of Genetic Epidemiology in Psychiatry, Medical Faculty Mannheim, University of Heidelberg, Mannheim, Germany. [376]National Centre for Register-based Research, Aarhus University, Aarhus, Denmark. [377]Hospital of Telemark, Kragerø, Norway. [378]Department of Biomedicine and Human Genetics, Aarhus University, Aarhus, Denmark. [379]Center for Integrative Sequencing (iSEQ), Aarhus University, Aarhus, Denmark. [380]Aarhus Genome Center, Aarhus, Denmark. [381]Department of Psychology, Emory University, Atlanta, GA, USA. [382]Department of Medical Informatics and Clinical Epidemiology, Oregon Health & Science University, Portland, OR, USA. [383]Department of Psychological and Brain Sciences, University of Iowa, Iowa City, IA, USA. [384]Departamento de Genética, Universidade Federal do Rio Grande do Sul, Porto Alegre, Brazil. [385]ADHD Outpatient Clinic, Hospital de Clínicas de Porto Alegre, Porto Alegre, Brazil. [386]Neurosciences and Mental Health Program, Research Institute, Hospital for Sick Children, Toronto, Canada. [387]University of Toronto, Toronto, Canada. [388]Hospital for Sick Children, Toronto, Canada. [389]Department of Psychiatry, University of California, Los Angeles, Los Angeles, CA, USA. [390]Semel Institute for Neuroscience & Human Behavior, David Geffen School of Medicine, University of California at Los Angeles, Los Angeles, CA, USA. [391]ADHD Outpatient Clinic, Hospital de Clínicas de Porto Alegre, Porto Alegre, Brazil. [392]Department of Psychiatry, Faculdade de Medicina, Universidade Federal do Rio Grande do Sul, Porto Alegre, Brazil. [393]Department of Psychiatry, University of California, San Francisco, San Francisco, CA, USA. [394]Institute for Human Genetics, University of California, San Francisco, San Francisco, CA, USA. [395]Weill Institute for Neurosciences, University of California, San Francisco, San Francisco, CA, USA. [396]Department of Pharmacy and Biotechnology, University of Bologna, Bologna, Italy. [397]Department of Psychiatry, University of British Columbia, Vancouver, Canada. [398]Institute of Mental Health, University of British Columbia, Vancouver, Canada. [399]Stella Maris Clinical Research Institute for Child and Adolescent Neuropsychiatry, Pisa, Italy. [400]Sorbonne Université, INSERM, CNRS, Neuroscience Paris Seine, Institut de Biologie Paris Seine, Paris, France. [401]NIHR Biomedical Research Centre in Mental Health Maudsley Hospital, London, UK. [402]Department of Human Genetics, David Geffen School of Medicine, University of California at Los Angeles, Los Angeles, CA, USA. [403]LifeOmic, Indianapolis, IN, USA. [404]Department of Psychiatry and Behavioral Sciences, Duke University, Durham, NC, USA. [405]University Clinic of Pediatrics, Faculty of Medicine, University of Coimbra, Coimbra, Portugal. [406]Child Developmental Center, Hospital Pediátrico, Centro Hospitalar e Universitário de Coimbra, Coimbra, Portugal. [407]Mindich Child Health and Development Institute, Icahn School of Medicine at Mount Sinai, New York, NY, USA. [408]Dept of Clinical Genetics, Our Lady's Children's Hospital, Crumlin, Dublin, Ireland. [409]School of Medicine and Medical Science, University College Dublin, Dublin, Ireland. [410]Division of Molecular Genome Analysis and Division of Cancer Genome Research, German Cancer Research Center (DKFZ), Heidelberg, Germany. [411]Inserm U955, Psychiatrie Translationnelle, Créteil, France. [412]Faculté de Médecine, Université Paris Est, Créteil, France. [413]Fondation FondaMental, Créteil, France. [414]Children's Hospital Los Angeles, Los Angeles, CA, USA. [415]Yale Center for Genome Analysis, Yale University, New Haven, CT, USA. [416]Department of Genetics, Yale University School of Medicine, New Haven, CT, USA. [417]Division of Child and Adolescent Psychiatry, Department of Psychiatry and Human Behavior, Brown University, Providence, RI, USA. [418]Institute of Neuroscience, Newcastle University, Newcastle, UK. [419]Newcastle Upon Tyne Hospitals NHS Foundation Trust, Newcastle, UK. [420]Northumberland, Tyne & Wear NHS Foundation Trust, Northumberland, UK. [421]Genomics Medicine Ireland, Dublin, Ireland. [422]Department of Medical Epidemiology and Biostatistics, Karolinska Institutet, Stockholm, Sweden. [423]Department of Psychiatry, Hospital for Sick Children and University of Toronto, Toronto, Canada. [424]Program in Genetics and Genome Biology, Hospital for Sick Children, Toronto, Canada. [425]Department of Psychiatry, Carver College of Medicine, University of Iowa, Iowa City, IA, USA. [426]Division of Medical Genetics, Department of Medicine, University of Washington, Seattle, WA, USA. [427]Department of Psychiatry, University of Illinois at Chicago, Chicago, IL, USA. [428]Tufts University School of Medicine, Portland, ME, USA. [429]Center for Psychiatric Research, Maine Medical Center Research Institute, Portland, ME, USA. [430]Department of Psychiatry, Tufts University School of Medicine, Boston, MA, USA. [431]Child and Adolescent Psychiatry Department, Robert Debre Hospital, APHP, Paris, France. [432]Human Genetics and Cognitive Functions, Institut Pasteur, Paris, France. [433]Centre d'Etudes et de Recherches en Psychopathologie et Psychologie de la Santé (CERPPS), Université Toulouse Jean Jaurès, Toulouse, France. [434]CERESA, Toulouse, France. [435]Institut Universitaire de France, Paris, France. [436]Academic Centre on Rare Diseases University College Dublin (ACoRD/UCD), Dublin, Ireland. [437]McKusick-Nathans Institute of Genetic Medicine, Johns Hopkins University School of Medicine, Baltimore, MD, USA. [438]Institute of Psychiatric Phenomics and Genomics (IPPG), University Hospital, LMU Munich, Munich, Germany. [439]Department of Psychiatry and Psychotherapy, University Medical Center Göttingen, Göttingen, Germany. [440]Department of Psychiatry and Behavioral Sciences, Johns Hopkins University, Baltimore, MD, USA. [441]Human Genetics Branch, National Institute of Mental Health, National Institutes of Health, US Department of Health and Human Services, Bethesda, MD, USA. [442]Molecular and Behavioral Neuroscience Institute, University of Michigan, Ann Arbor, MI, USA. [443]Department of Psychiatry, University of Michigan, Ann Arbor, MI, USA. [444]SRH University Heidelberg, Academy for Psychotherapy, Heidelberg, Germany. [445]Division of Neuroscience, School of Medicine, University of Dundee, Dundee, UK. [446]Advanced Interventions Service, NHS Tayside, Dundee, UK. [447]NORMENT, K.G. Jebsen Centre for Psychosis Research, Institute of Clinical Medicine, University of Oslo, Oslo, Norway. [448]Division of Mental Health and Addiction, Oslo University Hospital, Oslo, Norway. [449]Cognitive Genetics and Cognitive Therapy Group, Neuroimaging, Cognition and Genomics (NICOG) Centre, School of Psychology and Discipline of Biochemistry, National University of Ireland Galway, Galway, Ireland. [450]Division of Psychiatry, University of Edinburgh, Edinburgh, UK. [451]Department of Molecular Medicine and Surgery, Karolinska Institutet, Stockholm, Sweden. [452]Center for Molecular Medicine, Karolinska University Hospital, Stockholm, Sweden. [453]Université Paris Est, Faculté de Médecine, Créteil, France. [454]Neuroscience Research Australia, Sydney, Australia. [455]School of Medical Sciences, University of New South Wales, Sydney, Australia. [456]Unidad de Salud Mental, Hospital Regional Universitario de Malaga, Malaga, Spain. [457]Instituto de Investigación Biomédica de Málaga (IBIMA), Malaga, Spain. [458]Department of Biomedicine, University of Basel, Basel, Switzerland. [459]Institute of Medical Genetics and Pathology, University Hospital Basel, Basel, Switzerland. [460]Institute of Neuroscience and Medicine (INM-1), Research Centre Jülich, Jülich, Germany. [461]Institute of Human Genetics, University of Bonn, Bonn, Germany. [462]Department of Psychiatry and Psychotherapy, University Hospital Carl Gustav Carus, Technische Universität Dresden, Dresden, Germany. [463]School of Psychiatry, University of New South Wales, Sydney, Australia. [464]Black Dog Institute, Sydney, Australia. [465]University of Chicago, Chicago, IL, USA. [466]Washington University, St. Louis, MO, USA. [467]Department of Mental Health, Johns Hopkins Bloomberg School of Public Health, Baltimore, MD, USA. [468]Department of Psychiatry, Dalhousie University, Halifax, Canada. [469]National Institute of Mental Health, Klecany, Czech Republic. [470]Montreal Neurological Institute, McGill University, Montréal, Canada. [471]Department of Neurology and Neurosurgery, McGill University, Montréal, Canada. [472]Department of Psychiatry, McGill University, Montréal, Canada. [473]University College London, London, UK. [474]Center for Neurobehavioral Genetics, Semel Institute for Neuroscience & Human Behavior, University of California at Los Angeles, Los Angeles, CA, USA. [475]UMC Utrecht, Utrecht, The Netherlands. [476]SUNY Downstate Medical Center, Brooklyn, NY, USA. [477]Hospital for Psychiatry and Psychotherapy, Cologne, Germany. [478]Laboratory of Psychiatric Genetics, Department of Psychiatry, Poznan University of Medical Sciences, Poznan, Poland. [479]Douglas Mental Health University Institute, McGill University, Montreal, Canada. [480]Department of Translational Research in Psychiatry, Max-Planck Institute of Psychiatry, Munich, Germany. [481]National Centre for Mental Health, MRC Centre for Neuropsychiatric Genetics and Genomics, Cardiff University, Cardiff, UK. [482]Department Complex Trait Genetics, Center for Neurogenomics and Cognitive Research, VU University, Amsterdam, The Netherlands. [483]Department Clinical Genetics, VU University Medical Center, Amsterdam Neuroscience, Amsterdam, The Netherlands. [484]Department of Neurology, Klinikum rechts der Isar, Technical University of Munich, Munich, Germany. [485]Institute of Human Genetics, University of Bonn, Bonn, Germany. [486]Department of Psychiatry (UPK), University of Basel, Basel, Switzerland. [487]Discipline of Psychiatry, University of Adelaide, Adelaide, Australia. [488]Queensland Brain Institute, University of Queensland, Brisbane, Australia. [489]Bela Menso Brain and Behaviour Centre, James Cook University, Varsity Lakes, Australia. [490]Bond University, Faculty of Society and Design, Robina, Australia. [491]Division of Psychiatry, Centre for Clinical Brain Sciences, University of Edinburgh, Edinburgh, UK. [492]Centre for Genomic and Experimental Medicine, University of Edinburgh, Edinburgh, UK. [493]Interfaculty Institute for Genetics and Functional Genomics, University Medicine Greifswald, Greifswald, Germany. [494]Department of Biochemistry and Molecular Biology II, Institute of Neurosciences, Center for Biomedical Research, University of Granada, Granada, Spain. [495]Bioinformatics Research Centre, Aarhus University, Aarhus, Denmark. [496]Child Health Research Centre, University of Queensland, Brisbane, Australia. [497]Child and Youth Mental Health Service, Children's Health Queensland Health and Hospital Service, Brisbane, Australia. [498]Brain and Mind Centre, University of Sydney, Sydney, Australia. [499]School of Psychology and Counselling, Faculty of Health, Institute of Health and Biomedical Innovation, Queensland University of Technology, Queensland, Australia. [500]University of Queensland, Brisbane, Australia. [501]Department of Psychiatry, Harvard Medical School, Boston, MA, USA. [502]Amsterdam Public Health Research Institute, VU Medical Center, Amsterdam, the Netherlands. [503]Department of Research and Innovation, GGZ Ingeest, Specialized Mental Health Care, Amsterdam, the Netherlands. [504]Janssen Research & Development LLC, Titusville, NJ, USA. [505]Institute of Clinical Chemistry and Laboratory Medicine, University Medicine Greifswald, Greifswald, Germany. [506]German Centre for Cardiovascular Research (DZHK e.V.), Partner Site Greifswald, Greifswald, Germany. [507]Research School of Behavioural and Cognitive Neurosciences, Department of Psychiatry, University Medical Center Groningen, University of Groningen, Groningen, the Netherlands. [508]Department of Psychiatry GGZ INGEEST, Amsterdam, the Netherlands. [509]Department of Cell Biology, SUNY Downstate Medical Center, Brooklyn, NY, USA. [510]Mathison Centre for Mental Health Research & Education, Hotchkiss Brain Institute, Cumming School of Medicine, University of Calgary, Calgary, Canada. [511]Departments of Psychiatry and Medical Genetics, Cumming School of Medicine, University of Calgary, Calgary, Canada. [512]Krembil Research Institute, University Health Network, Toronto, Canada. [513]Grupo de Genética Molecular, Instituto de Biología, Facultad de Ciencias Exactas y Naturales, Universidad de Antioquia, Medellín, Colombia. [514]Johns Hopkins University School of Medicine, Baltimore, MD, USA. [515]Department of Psychiatry, Sao Paulo Medical School, University of Sao Paulo, Sao Paulo, Brazil. [516]Depto. Farmacogenética, Instituto Nacional de Psiquiatria Ramon de la Fuente Muñiz, Mexico City, Mexico. [517]University of Groningen, Groningen, the Netherlands. [518]Department of Psychiatry, University of Groningen and University Medical Center, Groningen, the Netherlands. [519]Department of Specialized Trainings, GGZ Drenthe Mental Health Care Services, Assen, the Netherlands. [520]Ospedale San Raffaele, Milano, Italy. [521]Bio4Dreams Srl, Milan, Italy. [522]University of California, San Francisco, CA, USA. [523]Yale University School of Medicine, New Haven, CT, USA. [524]Department of Psychiatry, Academic Medical Center, University of Amsterdam, Amsterdam, the Netherlands. [525]Netherlands Institute for Neuroscience, Royal Netherlands Academy of Arts and Sciences, Amsterdam, the Netherlands. [526]Department of Child and Adolescent Psychiatry, University Medical Center Groningen, University of Groningen, Groningen, The Netherlands. [527]Centre National Maladie 'Syndrome Rare Gilles de la Tourette', Groupe Hospitalier Pitié-Salpêtrière, Paris, France. [528]Assistance Publique-Hôpitaux de Paris, Département de Neurologie, Groupe Hospitalier Pitié-Salpêtrière, Paris, France. [529]Sorbonne Universités, UPMC Université Paris 06, UMR S 1127, CNRS UMR 7225, ICM, Paris, France. [530]Bioinformatics Interdepartmental Program, University of California, Los Angeles, Los Angeles, CA, USA. [531]De Bascule, Amsterdam, The Netherlands. [532]Department of Child and Adolescent Psychiatry, Academic Medical Center, University of Amsterdam, Amsterdam, the Netherlands. [533]Carver College of Medicine, University of Iowa, Iowa City, IA, USA. [534]MRC Unit on Risk & Resilience in Mental Disorders, Department of Psychiatry, University of Cape Town, Cape Town, South Africa. [535]Cold Spring Harbor Laboratory, Cold Spring Harbor, NY, USA. [536]Department of Psychiatry and Human Behavior, University of California, Irvine, Irvine, CA, USA. [537]Department of Neurology, University of Florida, Gainesville, FL, USA. [538]Sección de Neuropediatría, Instituto de Biomedicina de Sevilla, Hospital Universitario Virgen del Rocío/CSIC/Universidad de Sevilla, Seville, Spain. [539]Yulius Academy, Yulius Mental Health Organization, Barendrecht, The Netherlands. [540]Department of Psychology, University of Denver, Denver, CO, USA. [541]Faculdade de Medicina FMUSP, Universidade de São Paulo, São Paulo, Brazil. [542]Unidad de Trastornos del Movimiento, Servicio de Neurología y Neurofisiología Clínica, Instituto de Biomedicina de Sevilla, Hospital Universitario Virgen del Rocío/CSIC/Universidad de Sevilla, Seville, Spain. [543]Centro de Investigación Biomédica en Red sobre Enfermedades Neurodegenerativas (CIBERNED), Madrid, Spain. [544]National Institute of Genomic Medicine (INMEGEN), Ciudad de México, Mexico. [545]Clinical Research, Grupo Médico Carracci, Mexico City, Mexico. [546]Departments of Neurology and Neurosurgery, University of Florida, Gainesville, FL, USA. [547]Fixel Center for Neurological Diseases, University of Florida, Gainesville, FL, USA. [548]McKnight Brain Institute, University of Florida, Gainesville, FL, USA. [549]Department of Psychiatry, Yale School of Medicine, New Haven, CT, USA. [550]Department of Biological Sciences, Purdue University, West Lafayette, Indiana, USA. [551]Division of Adolescent and Child Psychiatry, Department of Psychiatry, Lausanne University Hospital, Lausanne, Switzerland. [552]Child and Adolescent Mental Health Centre, Mental Health Services Capital Region Copenhagen, University of

Copenhagen, Copenhagen, Denmark. [553]Moscow Institute of Physics and Technology, Dolgoprudny, Institusky 9, Moscow, Russia. [554]Department of Psychiatry, David Geffen School of Medicine, University of California at Los Angeles, Los Angeles, CA, USA. [555]Frederick W. Thompson Anxiety Disorders Centre, Sunnybrook Health Sciences Centre, Toronto, Canada. [556]Department of Psychiatry, University of Toronto, Toronto, Canada. [557]Division of Neuropsychiatry, University College London, London, UK. [558]Department of Child and Adolescent Psychiatry, Faculty of Medicine, Technischen Universität Dresden, Dresden, Germany. [559]Child and Adolescent Psychiatry Unit (UPIA), Department of Psychiatry, Federal University of São Paulo, Brazil. [560]Yale Child Study Center, Yale University School of Medicine, New Haven, CT, USA. [561]University Health Network, University of Toronto, Toronto, Canada. [562]Youthdale Treatment Centers, Toronto, Canada. [563]Groote Schuur Hospital, Cape Town, South Africa. [564]Department of Molecular Biology and Genetics, Democritus University of Thrace, Alexandroupolis, Greece. [565]Laboratory of Pharmaceutical Biotechnology, Ghent University, Ghent, Belgium. [566]Pfizer, Inc., New York, NY, USA. [567]Department of Child Psychiatry, Medical University of Warsaw, Warsaw, Poland. [568]Sorbonne Université, Faculty of Médecine, Paris, France. [569]Reference center for Gilles de la Tourette syndrome, Pitie-Salpetriere Hospital, Paris, France. [570]Department of Physiology, Saint Antoine Hospital, Paris, France. [571]Butler Hospital, Providence, RI, USA. [572]Alpert Medical School of Brown University, Providence, RI, USA. [573]Department of Psychiatry and Psychotherapy, University Medicine Greifswald, Greifswald, Germany. [574]Institute of Human Genetics, University Hospital Essen, University Duisburg-Essen, Essen, Germany. [575]INSERM, U 1127, CNRS UMR 7225, Sorbonne Universités, UPMC Univ Paris 06 UMR S 1127, Paris, France. [576]IGBMC, CNRS UMR 7104/INSERM U964/Université de Strasbourg, Illkirch, France. [577]Vanderbilt University Medical Center, Nashville, TN, USA. [578]Escuela de Ciencias de la Salud, Universidad Pontificia Bolivariana, Medellín, Colombia. [579]Laboratorio de Genética Molecular, SIU, Universidad de Antioquia, Medellín, Colombia. [580]School of Nursing, Louisiana State University Health Sciences Center, New Orleans, LA, USA. [581]Brain Center Rudolf Magnus, University Medical Center Utrecht, Utrecht, The Netherlands. [582]School of Biomedical Sciences and Pharmacy, The University of Newcastle, Callaghan, Australia. [583]Priority Research Centre for Brain and Mental Health Research, Hunter Medical Research Institute, Newcastle, Australia. [584]Schizophrenia Research Institute, Sydney, Australia. [585]Institute of Mental Health, Singapore, Singapore. [586]Assistance Publique - Hopitaux de Paris, GH Pitié-Salpêtrière, Paris, France. [587]Sorbonne Université, CNRS UMR 7222 Institut des Systèmes Intelligents et Robotiques, Paris, France. [588]Departments of Medicine and Psychiatry, School of Medicine University of Cantabria-IDIVAL, University Hospital Marqués de Valdecilla, Santander, Spain. [589]Minerva Neurosciences Inc., Waltham, MA, USA. [590]Sackler School of Medicine, Tel Aviv University, Tel Aviv, Israel. [591]VA Boston Healthcare System, Boston, MA, USA. [592]APC Microbiome Ireland, University College Cork, Cork, Ireland. [593]Department of Psychiatry, University College Cork, Cork, Ireland. [594]Neuroimaging, Cognition and Genomics (NICOG) Centre, School of Psychology, National University of Ireland Galway, Galway, Ireland. [595]Center for Psychiatric Genetics, NorthShore University HealthSystem Research Institute, Evanston, IL, USA. [596]Department of Psychiatry and Behavioral Neuroscience, University of Chicago, Chicago, IL, USA. [597]Arkin, Amsterdam, the Netherlands. [598]Department for Congenital Disorders, Statens Serum Institut, Copenhagen, Denmark. [599]Department of Medical Genetics, Medical University, Sofia, Bulgaria. [600]Department of Molecular Bases of Human Genetics, Institute of Molecular Genetics, Russian Academy of Sciences, Moscow, Russia. [601]Latvian Biomedical Research and Study Centre, Riga, Latvia. [602]Vilnius University, Vilnius, Lithuania. [603]Institute of Mental Health, Lee Kong Chian School of Medicine, Nanyang Technological University, Singapore, Singapore. [604]Department of Human Genetics, Institute of Molecular Genetics, Russian Academy of Sciences, Moscow, Russia. [605]Hunter New England Local Health District, Newcastle, Australia. [606]Department of Psychiatry, University of Helsinki, Helsinki, Finland. [607]Department of Psychiatry, Psychosomatics and Psychotherapy, Center of Mental Health, University Hospital Wuerzburg, Wuerzburg, Germany. [608]Department of Biomedicine, Aarhus University, Aarhus, Denmark. [609]Department of Clinical Neuroscience, Centre for Psychiatry Research, Karolinska Institutet, Stockholm, Sweden. [610]Centre for Neuroimaging and Cognitive Genomics (NICOG), National University of Ireland, Galway, Galway, Ireland. [611]NCBES Galway Neuroscience Centre, National University of Ireland, Galway, Galway, Ireland. [612]Department of Psychiatry, Royal College of Surgeons in Ireland, Dublin, Ireland. [613]Philipps-Universität Marburg and Marburg University Hospital UKGM, Marburg, Germany. [614]Department of Psychiatry and Psychotherapy, Jena University Hospital, Jena, Germany. [615]Maastricht University Medical Centre, Maastricht, the Netherlands. [616]Department of Psychosis Studies, Institute of Psychiatry, King's College London, London, UK. [617]Melbourne Neuropsychiatry Centre, Department of Psychiatry, University of Melbourne & Melbourne Health, Victoria, Australia. [618]Centre for Neural Engineering, Department of Electrical and Electronic Engineering, University of Melbourne, Victoria, Australia. [619]Oxford Health NHS Foundation Trust, Oxford, UK. [620]Department of Psychiatry, University of Oxford, Oxford, UK. [621]Department of Psychiatry and Behavioral Sciences, NorthShore University HealthSystem Research Institute, Evanston, IL, USA. [622]Faculty of Science, Medicine and Health, University of Wollongong, Wollongong, Australia. [623]Yong Loo Lin School of Medicine, National University of Singapore, Singapore. [624]Lee Kong Chian School of Medicine, Nanyang Technological University, Singapore, Singapore. [625]School of Biomedical Sciences, Chinese University of Hong Kong, Shatin, Hong Kong. [626]KIZ-CUHK Joint Laboratory of Bioresources and Molecular Research of Common Diseases, Kunming Institute of Zoology, Chinese Academy of Sciences, Kunming, China. [627]Chinese University of Hong Kong, Hong Kong. [628]Sheba Medical Center, Ramat Gan, Israel. [629]Departments of Psychiatry and Genetics, Washington University School of Medicine, St. Louis, MO, USA. [630]UCL Genetics Institute, University College London, London, UK. [631]Centre for Psychiatry, Barts and the London School of Medicine and Dentistry, London, UK. [632]School of Medicine & Public Health, University of Newcastle, Callaghan, Australia. [633]Priority Research Centre for Health Behaviour, University of Newcastle, Callaghan, Australia. [634]Research Unit, Sørlandet Hospital, Kristiansand, Norway. [635]Department of Statistics and Applied Probability, University of California, Santa Barbara, CA, USA. [636]Computational Research Division, Lawrence Berkeley National Laboratory, University of California at Berkeley, Berkeley, CA, USA. [637]NSW Health Pathology, Newcastle, Australia. [638]Virginia Institute for Psychiatric and Behavioral Genetics, Department of Psychiatry, Virginia Commonwealth University, Richmond, VA, USA. [639]Institute of Psychiatry, Psychology & Neuroscience, Social Genetics & Developmental Psychiatry Center, MRC, Kings College London, London, UK. [640]NIHR Maudsley Biomedical Research Centre, South London & Maudsley NHS Trust & King's College London, London, UK. [641]Departments of Psychiatry and Nutrition, University of North Carolina at Chapel Hill, Chapel Hill, NC, USA. [642]Departments of Psychiatry and of Neuroscience and Physiology, SUNY Upstate Medical University, Syracuse, NY, USA. [643]Department of Psychiatry, Virginia Commonwealth University, Richmond, VA, USA. [644]Division Biomedical Genetics, University Medical Center Utrecht, Utrecht, the Netherlands. [645]Department of Psychiatry and UF Genetics Institute, University of Florida, Gainesville, FL, USA. [646]Division of Cognitive and Behavioral Neurology, Brigham and Women's Hospital, Boston, MA, USA. [647]Department of Neurology, Yale School of Medicine, New Haven, CT, USA. [648]Department of Genetics and Psychiatry, University of North Carolina School of Medicine, Chapel Hill, North Carolina, USA. [649]Neuropsychiatric Genetics Research Group, Department of Psychiatry, Trinity College Dublin, Dublin, Ireland.
***Corresponding author. Email: verneri.anttila@gmail.com (V.A.); acorvin@tcd.ie (A.C.); bneale@broadinstitute.org (B.M.N.)**
†These authors contributed equally to this work.

SUPPLEMENTARY MATERIALS

www.sciencemag.org/content/360/6395/eaap8757/suppl/DC1
Materials and Methods
Supplementary Text
Consortium Memberships
Figs. S1 to S10
Tables S1 to 13
References (*68*–*108*)

15 April 2016; resubmitted 7 February 2017
Accepted 24 April 2018
10.1126/science.aap8757

RESEARCH ARTICLE SUMMARY

SIGNAL TRANSDUCTION

In vivo brain GPCR signaling elucidated by phosphoproteomics

Jeffrey J. Liu, Kirti Sharma, Luca Zangrandi, Chongguang Chen, Sean J. Humphrey, Yi-Ting Chiu, Mariana Spetea, Lee-Yuan Liu-Chen, Christoph Schwarzer*, Matthias Mann*

INTRODUCTION: The G protein–coupled receptor (GPCR) superfamily is a major drug target for neurological diseases. Functionally selective agonists activate GPCRs, such as the kappa opioid receptor (KOR), in a pathway-specific manner that may lead to drugs with fewer side effects. For example, KOR agonists that trigger beneficial antinociceptive, antipruritic, and anticonvulsant effects while causing minimal or no undesirable dysphoric, aversive, or psychotomimetic effects would be invaluable in light of the current opioid epidemic. However, functional selectivity observed in vitro frequently has little predictive value for behavioral outcomes.

RATIONALE: Obtaining a systems view of GPCR signaling in the brain may overcome the gap between in vitro pharmacology and in vivo testing. Recent breakthroughs in mass spectrometry–based proteomics have enabled us to quantify tens of thousands of phosphorylation events simultaneously in a high-throughput fashion. Using the KOR as a GPCR model, we applied this technology to achieve a global overview of the architecture of brain phosphoproteome in five mouse brain regions, in which we examined signaling induced by structurally and behaviorally diverse agonists.

RESULTS: Through the quantification of 50,000 different phosphosites, this approach yielded a brain region–specific systems view of the phosphoproteome, providing a context to understand KOR signaling in vivo. We observed strong regional specificity of KOR signaling attributable to differences in protein-protein interaction networks, neuronal contacts, and the different tissues in neuronal circuitries. Agonists with distinct signaling profiles elicited differential dynamic phosphorylation of synaptic proteins, thereby linking GPCR signaling to the modulation of brain functions. The most prominent changes occurred on synaptic proteins associated with dopaminergic, glutamatergic, and γ-aminobutyric acid–mediated (GABAergic) signaling and synaptic vesicle release. The large-scale dephosphorylation of synaptic proteins in the striatum after 5 min of agonist stimulation was partially blocked by protein phosphatase 2A (PP2A) inhibitors, underscoring the involvement of PP2A in KOR-mediated synaptic functions. Pathway analysis revealed enrichment of mTOR (mechanistic target of rapamycin) signaling by agonists associated with aversion. Strikingly, mTOR inhibition during KOR activation abolished aversion while preserving therapeutic antinociceptive and anticonvulsant effects. Parallel characterization of phosphoproteomic changes related to KOR-mediated mTOR activation in a cell line model provided additional mechanistic insights at the level of the signaling cascade.

ON OUR WEBSITE

Read the full article at http://dx.doi.org/10.1126/science.aao4927

CONCLUSION: We dissected the signaling pathways associated with desired and undesired outcomes of KOR activation in vivo and applied this knowledge to suppress the latter. Our work demonstrates the utility of combining phosphoproteomics with pharmacological tools and behavioral assessments as a general approach for studying GPCR signaling in vivo. Together with appropriate in vitro cellular systems, individual pathways can be characterized in depth, providing a rational basis for GPCR drug discovery. ■

The list of author affiliations is available in the full article online.
*Corresponding author. Email: mmann@biochem.mpg.de (M.M.); schwarzer.christoph@i-med.ac.at (C.S.)
Cite this article as J. J. Liu *et al.*, *Science* **360**, eaao4927 (2018). DOI: 10.1126/science.aao4927

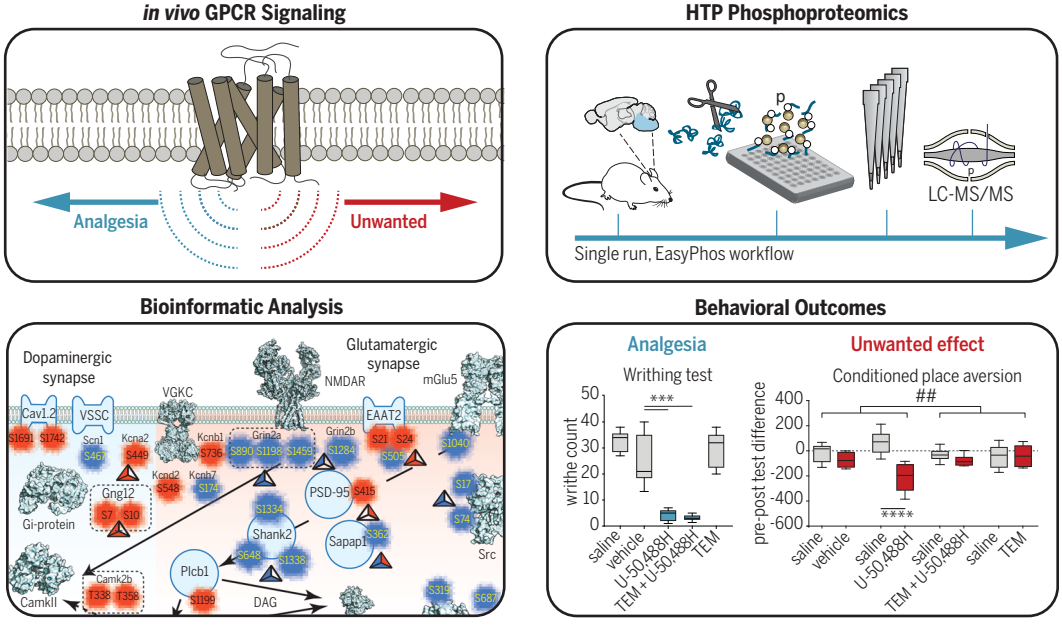

High-throughput phosphoproteomics to characterize in vivo brain GPCR signaling. Subsequent bioinformatic analysis enables prediction and modulation of downstream signaling pathways, which are correlated with unwanted effects but not the therapeutic outcome.

RESEARCH ARTICLE

SIGNAL TRANSDUCTION

In vivo brain GPCR signaling elucidated by phosphoproteomics

Jeffrey J. Liu[1], Kirti Sharma[1], Luca Zangrandi[2], Chongguang Chen[3], Sean J. Humphrey[1], Yi-Ting Chiu[3], Mariana Spetea[4], Lee-Yuan Liu-Chen[3], Christoph Schwarzer[2]*, Matthias Mann[1,5]*

A systems view of G protein–coupled receptor (GPCR) signaling in its native environment is central to the development of GPCR therapeutics with fewer side effects. Using the kappa opioid receptor (KOR) as a model, we employed high-throughput phosphoproteomics to investigate signaling induced by structurally diverse agonists in five mouse brain regions. Quantification of 50,000 different phosphosites provided a systems view of KOR in vivo signaling, revealing novel mechanisms of drug action. Thus, we discovered enrichment of the mechanistic target of rapamycin (mTOR) pathway by U-50,488H, an agonist causing aversion, which is a typical KOR-mediated side effect. Consequently, mTOR inhibition during KOR activation abolished aversion while preserving beneficial antinociceptive and anticonvulsant effects. Our results establish high-throughput phosphoproteomics as a general strategy to investigate GPCR in vivo signaling, enabling prediction and modulation of behavioral outcomes.

The G protein–coupled receptor (GPCR) superfamily encompasses drug targets in numerous therapeutic areas, including cancer (*1*) and cardiac (*2*) and neurological (*3*) diseases. Stimulation of a single GPCR, such as the kappa opioid receptor (KOR), often activates parallel pathways, each leading to distinctive pharmacological outcomes. For example, KOR activation triggers beneficial analgesic (*4*), antipruritic (*5*, *6*), and anticonvulsant/antiepileptic (*7*) signaling (*8*) as well as undesirable dysphoria or aversion and psychotomimetic effects (*8*, *9*) (Fig. 1A). Recently, some KOR agonists were described that do not induce conditioned place aversion (CPA) in mice (*10*, *11*), in contrast to endogenous and classical agonists. Functional selectivity, a GPCR signaling paradigm derived from in vitro (*12*, *13*) and structural (*14*, *15*) experiments, was used to explain this phenomenon (*16*, *17*). However, functional selectivity in cells transfected with KOR is not directly translatable to cells naturally expressing KOR (*18*) or to behavioral effects in vivo (*19*). The complexity of brain circuitry hinders the in vitro–in vivo correlation through heterogeneity at protein, cellular, and neural pathway levels (*20*). Thus, it is imperative to develop an unbiased approach that directly investigates GPCR (and specifically KOR) signaling in vivo, thereby elucidating the largely elusive downstream signaling consequences of GPCR activation in the brain.

Developments in mass spectrometry (MS)–based proteomics in general, and phosphoproteomics in particular, now enable the near-comprehensive characterization of proteomes and tens of thousands of phosphorylation events (*21*–*24*). Application of MS to study GPCR signaling has been limited to assaying the phosphorylation state of a single receptor (*25*) or small-scale phosphoproteomics on in vitro cell lines (*26*–*28*) or ex vivo cells (*29*). We recently described the EasyPhos technology, which streamlines phosphoproteomics to such an extent that hundreds of phosphoproteomes can be measured in a short time and at uncompromised depth of coverage, enabling time-course studies of dynamic and signaling events in vivo (*30*, *31*). Here, we applied this technology along with behavioral and pharmacological investigations to attain a systems view of KOR signaling induced by diverse agonists in temporally and spatially resolved areas of the mouse brain.

Brain phosphoproteomic architecture

We administered five KOR agonists intracisternally (i.c.) in dosages established to be effective in pharmacological and behavioral experiments (Fig. 1B and Table 1). After short (5 min) and long (30 min) intervals after injection, we dissected four brain regions that express KOR at different levels (striatum, hippocampus, cortex, and medulla oblongata) and one without detectable KOR expression (cerebellum) (Fig. 1C). In total, including biological replicates (three per experimental condition) and follow-up experiments, we measured more than 300 single-shot label-free phosphoproteomic samples using the high-throughput EasyPhos platform (*30*) (Fig. 1D). Together, this yielded more than 60,000 different identified phosphosites mapping to ~6700 brain proteins. This is the most comprehensive coverage of any organ phosphoproteome reported to date, underscoring the diversity and importance of phosphorylation-based regulation in the brain (Fig. 1E).

To obtain a general overview of the architecture of the brain phosphoproteome, we performed principal components analysis (PCA), which revealed that the phosphoproteomes of each brain region cluster tightly and are distinct from other regions. This indicates that each region possesses a unique phosphoproteome signature. Furthermore, brain regions that share a similar developmental origin exhibit similarities in their phosphoproteome (Fig. 2A, component 2). The region-specific nature of the phosphoproteome is partly driven by the underlying differences in the proteomes, because proteins highly expressed in one brain region (e.g., striatum) often also yield prominent phosphopeptides in the same region (Fig. 2, B and C). In particular, expression levels of kinases (*32*) (the "kinome") correlated significantly with the abundance of phosphopeptides containing the corresponding linear motifs (Fig. 2D). Thus, proteome and kinase expression in different regions partially shapes the brain phosphoproteome. The complexity within the brain phosphoproteome is in contrast to the homogeneity of in vitro cell lines. We observed that 85% of synaptic proteins were phosphorylated, which is of particular interest given previous reports of the importance of phosphorylation in the regulation of synaptic plasticity (*33*).

Approximately 50,000 of the identified phosphorylation sites were quantifiable (Fig. 1F). As established in our recent studies using EasyPhos technology, reproducibility between biological replicates was robust, with an average Pearson correlation of ~0.85 (fig. S1). Injection of the reference KOR agonist U-50,488H significantly perturbed ~5% of these sites, with different ligand perturbation patterns in distinct brain regions (Fig. 1G). After 5 min of U-50,488H stimulation, we observed maximum perturbation in the striatum (1000 sites), and progressively less in the order of hippocampus > cortex > medulla oblongata, in line with the expression level of KOR in the respective brain regions (*34*). In the cerebellum, where KOR is not detectable, there were hardly any regulated sites, providing a strong validation of our technology (Fig. 1G). Furthermore, we found that in the four KOR-expressing brain regions (striatum, hippocampus, cortex, and medulla oblongata), the regulated sites were not detected in the brains of KOR knockout mice (KOR-KO), which demonstrates the specificity of ligand effects in the brain (fig. S2). Overall, these results show that phosphoproteomics

[1]Department of Proteomics and Signal Transduction, Max Planck Institute of Biochemistry, 82152 Martinsried, Germany. [2]Department of Pharmacology, Medical University of Innsbruck, 6020 Innsbruck, Austria. [3]Center for Substance Abuse Research and Department of Pharmacology, Temple University Lewis Katz School of Medicine, Philadelphia, PA 19140, USA. [4]Department of Pharmaceutical Chemistry, Institute of Pharmacy and Center for Molecular Biosciences Innsbruck (CMBI), University of Innsbruck, 6020 Innsbruck, Austria. [5]Novo Nordisk Foundation Center for Protein Research, Faculty of Health Sciences, University of Copenhagen, 2200 Copenhagen, Denmark.
***Corresponding author. Email: mmann@biochem.mpg.de (M.M.); schwarzer.christoph@i-med.ac.at (C.S.)**

enables observation of KOR-modulated signaling in a brain region–specific fashion.

KOR signaling is brain region–specific

Next, we spatially and temporally analyzed U-50,488H–regulated sites determined to be significant by analysis of variance (ANOVA). U-50,488H activates inhibitory G proteins ($G_{i/o}$) and induces internalization of KOR through β-arrestin2 recruitment (*35*). Inhibition of Ca^{2+} channels modulates release of neurotransmitters such as γ-aminobutyric acid (GABA), dopamine, and glutamate, and negatively regulates signaling mediated by all three neurotransmitters. Accordingly, our bioinformatics analysis of regulated phosphosites (*36*) revealed significant enrichment of Gene Ontology (GO) terms such as "inhibition of adenylate cyclase activity by G protein signaling pathway," "positive regulation of receptor internalization," and "regulation of neurotransmitter secretion." This unbiased approach also highlighted mechanisms not yet linked to KOR activation, such as "RNA splicing" (fig. S3A). In line with this, the phosphorylation states of numerous membrane proteins, such as voltage-gated sodium channels and neurotransmitter transporters, are altered by KOR activation (fig. S3B).

Like the basal brain phosphoproteome, phosphosites clustered tightly by replicates. Interestingly, the PCA map was dynamic in time, with the relative positions of the cortex, medulla, hippocampus, and striatum changing drastically between the time points (Fig. 3, A and B). In the first component, the striatum deviated most from the other regions at the 5-min interval, whereas the cortex diverged mostly at 30 min, which suggests that U-50,488H perturbation is most profound in the striatum at early time points and in the cortex at later time points. The striatum is part of the mesolimbic pathway and the cortex is part of the mesocortical pathway; these are the two most prominent pathways in KOR signaling (also reflected in the relatively high KOR expression in both regions). Unlike in vitro cell model systems, each brain region comprises elaborated connections of heterogeneous neurons. In this complex background, we also discovered U-50,488H–mediated KOR signaling to be highly region-specific. For example, we found that U-50,488H–regulated sites in the striatum were specific to this region—a result that also held for the other brain regions (Fig. 3C and fig. S4).

At the level of known functional sites, we observed dephosphorylation of the dopamine- and cyclic adenosine monophosphate (cAMP)–regulated neuronal phosphoprotein (DARPP-32) on phosphorylated Ser^{97} (pS97) and of the tyrosine kinase Src on pS17 exclusively in the striatum. The *raf* proto-oncogene serine/threonine protein kinase Raf1 was dephosphorylated at pS259 only in the cortex, and the extracellular signal–regulated kinase ERK1 was phosphorylated at Thr^{203} and Tyr^{205} (pT203/pY205) only in the hippocampus (Fig. 3D). We further investigated the regional specificity of ERK1 phosphorylation using immunohistochemistry. This latter observation validates the phosphoproteomics findings and reveals that elevated ERK1 phosphorylation is specifically located on hippocampal mossy fibers (Fig. 3E).

In contrast to the basal phosphoproteome, which was partly shaped by the proteome and particularly by the kinome (Fig. 2), no correlation between U-50,488H–regulated phosphorylation events and the region-specific proteome or basal phosphoproteome was observed (fig. S5). This implies that region-specific regulation is not just a function of expression levels of kinases and substrates, but results from more complex factors such as different protein-protein interaction networks, neuronal contacts, or the position of the tissue in neuronal circuitries. Indeed, mapping the U-50,488H–regulated phosphorylation events onto known interaction networks (*37*) highlighted the signaling pathways relevant to the specific physiological functions of each brain region, including the GO terms "neurotransmitter secretion" and "dopaminergic synapses" (enriched in striatum) and "axon guidance," "long-term potentiation," and "calcium signaling" (enriched in hippocampus), which was not the case for the basal phosphoproteome (fig. S6).

Next, we contrasted signaling of the initially investigated agonist U-50,488H with that of 6′GNTI (*38*), which possesses a different signaling profile (Table 1). Depending on the brain region and time point, U-50,488H and 6′GNTI shared 30 to 50% of regulated sites. Substantial differences were apparent in the first component of a PCA between U-50,488H and 6′GNTI after 5 min of stimulation in the striatum and hippocampus, but not in the medulla oblongata and cortex. After 30 min of stimulation, the ligand differences were greatly reduced in the striatum but were more pronounced in other regions, especially the cortex (fig. S7). Because the i.c. injected doses of each ligand were similar across brain regions and time points, these region- and time-dependent changes between ligands may reflect the position of the regions in distinct brain circuitry, but also may reflect differences in pharmacokinetic effects and biodistribution of these two agonists.

KOR signaling in the striatal synaptic phosphoproteome

Some KOR agonists induce aversive states, primarily through activation of medium spiny neurons in the nucleus accumbens (NAc) of the

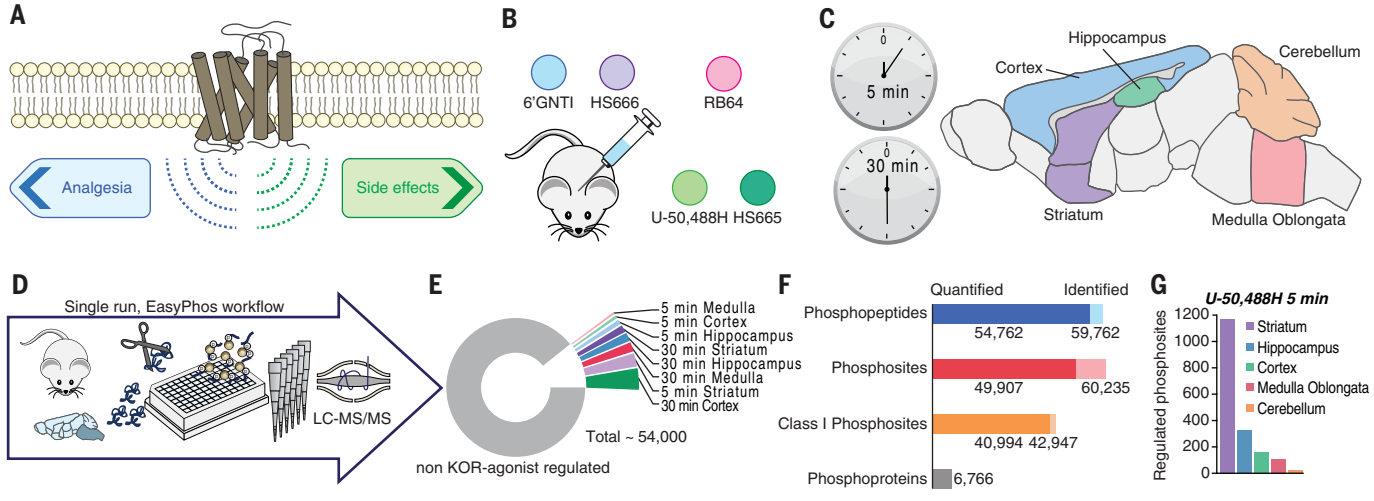

Fig. 1. High-throughput phosphoproteomics of in vivo KOR-mediated GPCR signaling. (**A**) KOR signaling activates antinociception while inducing unwanted side effects. (**B**) Five KOR agonists were administrated i.c. to mice with U-50,488H as the reference KOR agonist. (**C**) Drug-treated groups of mice were killed 5 or 30 min after injection in each experimental group (n = 3 per group). Five brain regions were dissected and processed for phosphoproteomic studies. (**D**) The single-run EasyPhos workflow. (**E**) Of ~50,000 quantifiable phosphosites, fewer than 5% were perturbed by the U-50,488H treatment. (**F**) Overall statistics of the brain phosphoproteome. (**G**) The magnitude of U-50,488H–induced perturbation differs among brain regions. The striatum has the most detectable perturbation with more than 1000 sites, whereas the cerebellum has fewer observable U-50,488H–induced perturbation.

Table 1. KOR ligands: In vitro pharmacological profiles and behavioral responses. Conditioned place aversion is designated "yes" or "no" depending on whether it was observed at the dosage applied in the present phosphoproteomic experiments. The applied dose is that used in the present study. EC_{50}, concentration of the ligand at half of the maximal response; E_{max}, maximal response elicited from a given ligand; n.a., not available.

Ligands	Binding affinity, human KOR	G protein activation, human KOR		β-arrestin2 recruitment, human KOR		Conditioned place aversion	Anticonvulsant effect (range)	Antinociceptive effect (range)	Applied dose (nmol)
	K_i (nM)	EC_{50} (nM)	E_{max} (%)	EC_{50} (nM)	E_{max} (%)				
U-50,488H	0.68 (*71*)	43 (*38*)	100 (*38*)	2 (*38*)	100 (*38*)	Yes (100 nmol) (*11*) Yes (2.5 mg/kg) (*7*)	6 to 20 mg/kg (*7*)	3 to 10 nmol (*11*) 1 to 5 mg/kg (*44*)	20
6′GNTI	1.15 (*72*)	1.6 (*38*)	64 (*38*)	n.a. (*38*)*	n.a. (*38*)*	No (1 to 30 nmol) (*7*)	3 to 30 nmol (*7*)	10 nmol (*73*)	30
RB64	0.59 (*74*)	5.29 (*60*)	101 (*60*)	391 (*60*)	104 (*60*)	Yes (3 mg/kg) (*9*)	n.a.	3 mg/kg (*9*)	3†
HS665	0.49 (*55*)	3.62 (*55*)	90.0 (*55*)	463 (*11*)	55 (*11*)	Yes (30 nmol) (*11*)	n.a.	3 to 10 nmol (*11*) 1.25 to 5 mg/kg (*44*)	10
HS666	5.90 (*55*)	35.0 (*55*)	53.4 (*55*)	449 (*11*)	24 (*11*)	No (150 nmol) (*11*)	n.a.	3 to 30 nmol (*11*) 2 to 10 mg/kg (*75*)	30

*EC_{50} and E_{max} for β-arrestin2 recruitment of 6′GNTI are controversial and reported with different values in the literature. EC_{50} = 5.9 nM and E_{max} = 12% (*18*), and EC_{50} = 7.38 nM and E_{max} = 34.7% (*63*). †Highest solubility.

ventral striatum (*17*, *39*). To gain deeper insight, we used five structurally distinct KOR agonists, each with distinct signaling profiles and in vivo behavioral responses (Table 1). The unbiased PCA analysis of the phosphoproteomic experimental results revealed clustering of samples treated with U-50,488H (20 nmol) and HS665 (10 nmol) on one side and treated with 6′GNTI (30 nmol) and HS666 (30 nmol) on the other in the first component. Samples treated with RB64 (3 nmol) were clustered between these but were more similar to those treated with U-50,488H and HS665 (fig. S8). Further bioinformatic analysis showed significant enrichment for the GO annotations "potassium channel complex," "cell junction," and "excitatory synapse" (fig. S9A) (*40*) based on the sites regulated by U-50,488H, HS665, and RB64 but not by 6′GNTI and HS666. This prompted us to focus on differential phosphorylation of synaptic proteins, particularly because dynamic phosphorylation of synaptic proteins in the striatum affects synaptic plasticity (*33*) and membrane trafficking (*41*).

Overall, large-scale dynamic phosphorylation changes on synaptic proteins were present at the 5-min interval and ebbed away at the 30-min interval (fig. S9B). The most prominent dynamic phosphorylation changes mediated by U-50,488H, HS665, and RB64, but not by 6′GNTI and HS666, involved synaptic proteins associated with dopaminergic, glutamatergic, and GABAergic signaling and synaptic vesicle release. This included a down-regulation of the phosphorylation state of the *N*-methyl-D-aspartate (NMDA) receptor and many of its scaffolding proteins, dynamins (Ser^{851} on Dnm1), members of the SNARE complex, and a multitude of ion channels (Fig. 4A).

We were especially intrigued by DARPP-32, a downstream effector of dopaminergic signaling that is also regulated by glutamatergic signaling. DARPP-32 is a potent inhibitor of protein phosphatase 1 (PP1) and plays an important role in synaptic plasticity (*42*). Dynamic phosphorylation of DARPP-32 in general, and Ser^{97} specifically, is regulated by various drugs of abuse (*43*, *44*) and is correlated with nuclear accumulation of DARPP-32 and the control of gene expression related to long-term synaptic plasticity (*43*). From the MS measurements, we found Ser^{97} to be specifically dephosphorylated at 5 min after application of U-50,488H in the striatum by a factor of 2. Immunohistochemistry clearly showed this dephosphorylation in both the caudate putamen (CPu) and NAc, the two main loci of the striatum. This effect was specific to Ser^{97}, whereas Ser^{192} was not regulated (Fig. 4C).

Other interesting ligand-directed dynamic phosphorylation events include the cannabinoid receptor 1 (CB1). The phosphorylation level of CB1 at Ser^{317} was shown to correlate with CB1 activity; mounting evidence links CB1 activation with KOR activation (*45*–*47*). Our current data suggest that cross-talk between CB1 and KOR may at least be partially regulated through dynamic phosphorylation of CB1 at Ser^{317} (Fig. 4, A and C).

Among the kinases, down-regulation of Src kinase at Ser^{74} is noteworthy because of the known role of Src in phosphorylating many of the above-mentioned substrates and regulating synaptic plasticity (*48*). Other sites of interest include Ser^{7} of G protein gamma subunit 12, which is an immediate downstream effector of KOR, and Ser^{1459} of the NMDA receptor 2a subunit.

When comparing the effects of the five agonists, we observed that 6′GNTI and HS666 did not significantly regulate the abovementioned phosphosites, whereas HS665 and RB64 affected some but not all of the sites regulated by U-50,488H (Fig. 3C). This may reflect differential activation of pathways through KOR, but may also be influenced by differences in biodistribution, the applied dosage, efficacy, or pharmacokinetic or off-target effects that are undetected using our method. However, viewing the phosphoproteomic changes of synaptic proteins as a whole, U-50,488H, HS665, and RB64 exhibited greater similarity to each other than to 6′GNTI and HS666, even though each ligand induced a somewhat unique perturbation to the phosphoproteome (Fig. 3A and fig. S10). This illustrates the importance of investigating the molecular basis of in vivo GPCR signaling at the systems level instead of at the individual phosphorylation level.

These examples illustrate the complexity and subtlety of the differential regulation of various signaling pathways in the nervous systems by these two ligand classes in the important context of the synapse.

Phosphatases participate in KOR striatal U-50,488H–mediated signaling

The large-scale dephosphorylation of synaptic proteins in the striatum after 5 min of stimulation by U-50,488H but not 6′GNTI raised the question of whether they specifically activate Ser/Thr phosphatases. To test this hypothesis, we injected mice i.c. with three functionally distinct phosphatase inhibitors: fostriecin, a protein phosphatase 2A (PP2A) and protein phosphatase 4 (PP4) inhibitor; calyculin A, a PP1 and PP2A inhibitor; and tautomycetin, a selective PP1 inhibitor (Fig. 5). One hour after treatment, mice received U-50,488H; brains were dissected 5 min later, and their striatum was processed for phosphoproteomic measurements as previously described.

Consistent with our hypothesis, we found 300 phosphorylation sites in the striatum for which dephosphorylation was abolished in the presence of one or more phosphatase inhibitors. This establishes that phosphatases play an important role in U-50,488H–mediated signaling. About half of these phosphatase-sensitive sites belong to synaptic proteins, in agreement with the importance of phosphatases in synaptic functions (*49*). In addition, GO enrichment analysis of the proteins regulated by phosphatase revealed enrichment of "clathrin-dependent endocytosis,"

"synaptic vesicle priming," and "small GTPase regulator activity," which suggests that U-50,488H–mediated but not 6′GNTI-mediated pathway(s) may be involved in neurotransmitter release and membrane receptor trafficking (fig. S11).

Among the 300 phosphatase-sensitive sites, a minor cluster was insensitive to tautomycetin pretreatment (Fig. 5A). Unlike the other two inhibitors, tautomycetin selectively inhibits PP1 but not PP2A; therefore, these sites are most likely mediated by PP2A. In this group of sites, we were especially intrigued by the aforementioned phosphorylation of Ser^{317} of the CB1 receptor and Ser^{762} of the $GABA_B$ receptor (Fig. 5B), both well-known GPCRs. Thus, phosphoproteomics can reveal additional mechanistic details in the complexity of in vivo GPCR signaling through the phosphorylation of coexpressed GPCRs. Together, these results highlight the importance of phosphatases in GPCR signaling at synapses.

Conditioned place aversion, but not antinociceptive or anticonvulsant effects, is ablated by mTOR pathway blockade

The bioinformatic analysis of the sites differentially regulated by U-50,488H, HS665, and RB64 but not by 6′GNTI and HS666 also revealed that the mechanistic target of rapamycin (mTOR) signaling pathway was enriched in the striatum at the 5-min interval and in the cortex at 30 min (Fig. 6, A and B). In the striatum, mTOR was the most significantly regulated pathway, whereas in the cortex it was among the top five. This interesting finding from our unbiased phosphoproteomics approach links to previous reports of mTOR involvement in ketamine-induced and fluoxetine (Prozac)–induced antidepressant effects in a region-dependent manner (*50*, *51*) as well as dysfunction of the mTOR pathway in the prefrontal cortex of patients with major depressive disorders (*52*).

U-50,488H is well established to produce CPA in rodents (*53*, *54*). A recent report indicated that through central injection in mice, 6′GNTI did not cause CPA, although it showed robust antiseizure activity similar to U-50,488H (*7*). RB64 was also reported to produce a unique spectrum of behavioral activities, including CPA in mice (*9*). HS665 and HS666 are recently synthesized KOR-specific agonists (*55*). HS665, but not HS666, was reported to produce profound CPA (*11*) (Table 1). Combined with our present observation that only U-50,488H, HS665, and RB64, but not 6′GNTI and HS666, induce mTOR signaling, this led us to hypothesize that pretreating mice with an mTOR inhibitor could abolish the aversive behavior induced by U-50,488H.

We investigated the effects of pretreatment with temsirolimus, an mTOR inhibitor, at a dose of 8 mg/kg. Mice were pretreated for 1 hour with temsirolimus, saline, or vehicle controls before receiving U-50,488H or saline injection for each conditioning session (Fig. 6C). As expected, treatment with U-50,488H induced a highly significant response in the CPA assay, consistent with previous findings that this KOR agonist induced aversive effects in mice. Pretreatment with the mTOR inhibitor abolished the CPA induced by U-50,488H alone (Fig. 6C). This shows that mTOR blockade indeed suppressed the aversive effects linked to KOR activation, which is in agreement with our hypothesis. The anticonvulsive effect of U-50,488H as assessed in the pentylenetetrazole (PTZ) (tail vein infusion)–induced seizure model (Fig. 6D) and the antinociceptive effect assessed in the acetic acid–induced writhing test (Fig. 6E) were unaffected by mTOR inhibition.

Probing the downstream molecular mechanism of mTOR activation, we found that U-50,488H, HS665, and RB64 on one hand and 6′GNTI and HS666 on the other differentially regulated phosphorylation sites of proteins involved in translation, including Eif4b (Ser^{504}) and Rps6 (Ser^{240}, Ser^{244}) (fig. S12). Both proteins are part of the mTOR signaling pathway, and their phosphorylation sites are regulated by the kinases involved in the same pathway. A body of evidence already links mTOR-mediated alteration of protein synthesis with synaptic plasticity, learning, and memory, specifically through long-term potentiation and depression (*56*). Our present data specifically connect KOR activation to depressive/aversive behavior involving the activation of mTOR, possibly through its effect on protein translation; hence, this connection can be pharmacologically separated.

To investigate the upstream mechanism that activates mTOR, we used the neuroblastoma cell line (Neuro 2A) with stable expression of mouse KOR. Cells were pretreated with vehicle or pertussis toxin (PTX) (200 ng/ml), a specific inhibitor of the $G_{i/o}$ signaling pathway, for 2 hours, followed by vehicle or U-50,488H (10 μM) for 30 min. Phosphoproteomic analysis of these cells revealed that mTOR signaling was the most enriched pathway in cells treated with U-50,488H or with U-50,488H + PTX ($P < 10^{-8}$) but not in cells treated with PTX alone, indicating that mTOR signaling is activated in a G protein–independent manner (fig. S13). Specifically, we discovered that Ser^{939} of Tsc2 was phosphorylated by U-50,488H treatment in a PTX-insensitive manner (fig. S14). Phosphorylation of Tsc2 by Akt modulates mTOR signaling (*57*), and we found an additional group

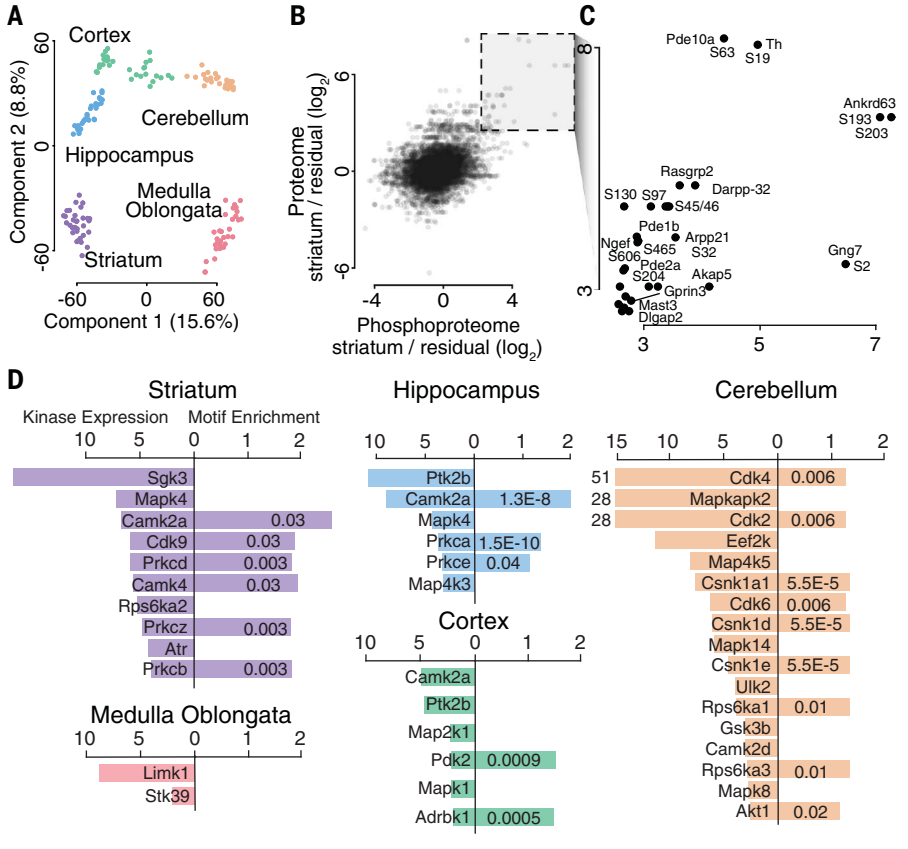

Fig. 2. Unstimulated brain phosphoproteomic architecture. (**A**) Principal components analysis (PCA) of all brain samples. The first and second components are shown. (**B**) Welch *t* test difference between striatum and rest of brain (residual) at the phosphoproteomic level (*x* axis) and the proteomic level (*y* axis); Pearson correlation = 0.53. (**C**) Zoom-in of plot in (B) for proteins that are highly expressed in the striatum. (**D**) Differential kinase expression in each region in comparison to residual (left) and motif enrichment (right) of the same kinase, when the motif is available. The motif enrichment is the result of the Fisher exact test on phosphosites that exhibit high intensity in each region relative to the residual. The number on each bar indicates the *P* value of the enrichment.

of Akt substrates to be influenced by U-50,488H that were also PTX-insensitive (fig. S15) among molecules that likely mediate G protein–independent signaling. Akt was previously discovered to be downstream of KOR activation in the cultured primary striatal neurons (*18*), indicating that Akt activation might be an interesting line of research to pursue.

Along with the mTOR pathway, we also found the mitogen-activated protein kinase (MAPK) pathway to be enriched in U-50,488H and U-50,488H + PTX stimulated Neuro 2A cells. Early activators such as Sos1 and Raf1 were dephosphorylated in a PTX-insensitive manner (fig. S14). Activation of the MAPK pathway has already been linked to KOR G protein–independent signaling pathways and KOR-mediated aversion (*16*, *17*). Thus, our current data establish that both mTOR and the MAPK pathways are activated in a G protein–independent manner. This leads us to speculate that these two G protein–independent signaling pathways are activated in a similar fashion to activation downstream of the insulin receptor: MAPK through the Grb2-Sos1-Raf branch, and mTOR activation through the Akt-Tsc2 branch (fig. S14).

Discussion

This study offers a systems view of in vivo brain GPCR signaling. Even though specifically KOR-mediated signals derive from interaction of ligands with the same GPCR, signaling pathways are channeled toward distinct physiological effectors in each brain region and at each time point. We found that the basal phosphoproteome in different regions correlates with the abundance of the proteome and the kinome. This was not the case for the regulated phosphoproteome, reflecting the importance of additional factors such as protein interaction networks, neuron-neuron contacts, and brain circuitry in the makeup of the regulated phosphoproteome. This was apparent from signaling propagation to brain areas with minimal KOR expression at later time points. Such results emphasize that a more complex concept of GPCR signaling, which accounts for diversity of cell types and cell-cell communication in addition to in vitro concepts such as functional selectivity, is necessary for a better understanding of the subtleties of in vivo GPCR signaling.

Our study has also established that the phosphoproteomic approach could disentangle beneficial antinociceptive and anticonvulsant effects from unwanted KOR-mediated side effects such as aversion at the pathway level, and possibly could use this knowledge to separate one from the other. This in vivo approach bypasses the need of in vitro characterization of ligands and minimizes the risk associated with in vitro–in vivo translation. Although temsirolimus, the mTOR inhibitor used here, is an FDA-approved chemotherapy agent, clinical application of these results would likely require a specific modulation of the mTOR network that results in the desired behavioral outcomes.

We propose phosphoproteomics combined with pharmacological tools and behavioral assessments as a general approach for studying GPCR signaling in vivo. Together with appropriate in vitro cellular systems, detailed molecular mechanisms of individual pathways can be characterized, leading to a more rational approach for GPCR drug discovery. Our approach bridges in vitro–based and purely behavioral studies, offering the opportunity to discover, without a priori assumptions, signaling pathways that can be pharmacologically manipulated to achieve specific therapeutic benefits.

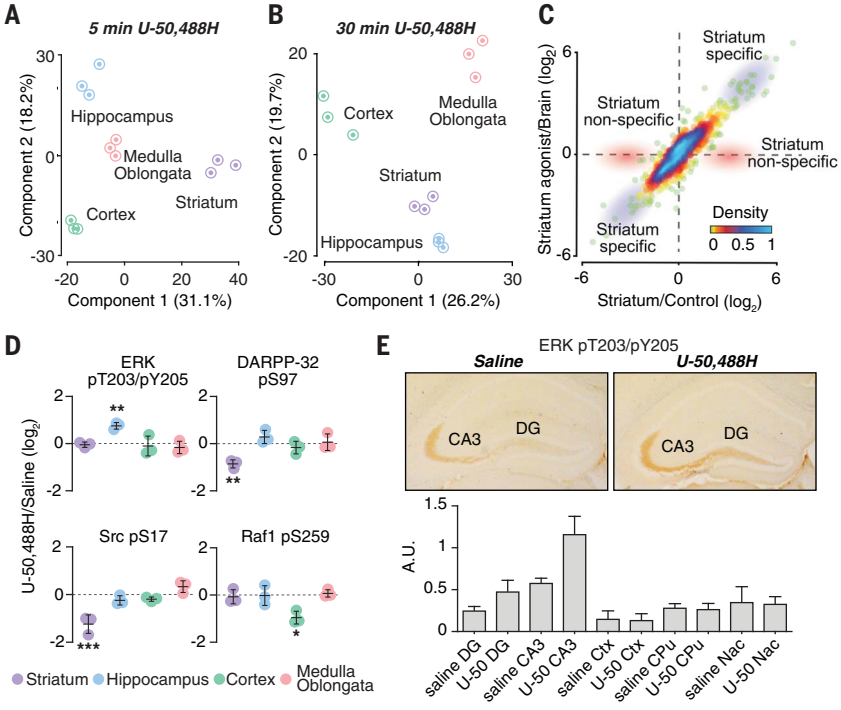

Fig. 3. Region-specific outcomes of U-50,488H–induced activation of KOR. (**A**) PCA of normalized spatial and temporal U-50,488H–regulated sites (significant by ANOVA) versus their respective saline controls at the 5-min time point. (**B**) Same as (A) at the 30-min time point. (**C**) Scatterplot showing striatum-specific U-50,488H signaling. The *x* axis denotes the $\log_2$ intensity difference of striatum samples between U-50,488H and saline control; the *y* axis denotes the $\log_2$ intensity difference between all the striatum samples and those from the other brain regions. U-50,488H–regulated sites that are striatum-specific fall on the diagonal, as indicated by the area shaded in blue; U-50,488H–regulated sites that are in common among all brain regions fall on the *x* axis, as indicated by the area shaded in red. (**D**) Quantification of selected sites in four brain regions. The *y* axis denotes the $\log_2$ intensity difference between U-50,488H and saline samples in the respective regions. Error bars represent mean ± SD. (**E**) Immunohistochemistry of ERK pT203/pY205. Top: Representative images of stained hippocampus with saline or U-50,488H treatment; specific regions in hippocampus are indicated within the images (n = 4 per group). Bottom: Histogram showing quantification of ERK pT203/pY205 immunoreactivity in various regions including the hippocampus. CA3, cornu ammonis field 3; Ctx, cortex; CPu, caudate putamen (a subregion of striatum); DG, dentate gyrus; NAc, nucleus accumbens (a subregion of striatum). Error bars represent mean ± SD (n = 4). Data in (C) to (E) were collected 5 min after injection. A.U., arbitrary units.

Materials and methods

Animals

All animal care and experimental procedures were approved by the Austrian Animal Experimentation Ethics Board in compliance with the European Convention for the Protection of Vertebrate Animals Used for Experimental and Other Scientific Purposes ETS no. 123.

We investigated prodynorphin knockout (pDyn-KO) and KOR knockout (KOR-KO) mice (male, adult) in the phosphoproteomic and most behavioral studies. CD1 mice (male, adult) were used in the writhing test. pDyn-KO mice (*58*) and KOR-KO mice (*59*) were backcrossed onto the C57BL/6N background over 10 generations. For breeding and maintenance, mice were group housed (maximum of five animals per cage) with free access to food and water. Temperature was fixed at 23°C and 60% humidity with a 12-hour light-dark cycle (lights on 7 a.m. to 7 p.m.). Mice of the same strain and age were arbitrarily sorted into groups, splitting litters into different groups. For the animal experiments, the experimenter was blinded to the treatments of the animals.

Phosphoproteomic experiments were carried out in pDyn-KO mice to minimize the influence of endogenous dynorphins. Endogenous dynorphins are released under stressful situations such as handling. They are considered unbiased full agonists and their release during the treatment

is likely to influence the phosphorylation profile especially of biased, partial agonists. Indeed, comparing the profiles of 6′GNTI on wild-type and pDyn-KO mice resulted in comparable, yet less reproducible, phosphorylation patterns.

KOR agonists

We investigated five KOR ligands: U-50,488H, HS665, RB64, 6′GNTI, and HS666. An overview of their in vitro pharmacological profiles and behavioral effects is presented in Table 1. 6′GNTI, generated in the laboratory of P. Portoghese, is used as tool ligand to study KOR pharmacology in vitro and in vivo. It was demonstrated to produce antinociception in mice after central intrathecal administration (*46*) and anticonvulsant effects without inducing conditioned place aversion after central i.c. administration in mice (*7*). HS665 and HS666 are structurally distinct KOR ligands from the class of diphenethylamines from the laboratory of H. Schmidhammer, displaying interesting pharmacological profiles (*11*, *40*, *60*). HS665 is a potent, selective, and full agonist for KOR G protein activation. It produces antinociception and CPA in mice (*61*, *62*). HS666 is a selective KOR partial agonist (*11*). RB64 was generated in the laboratory of B. Roth as an analog of salvinorin A. As a KOR full agonist, RB64 was established to have a unique spectrum of activities in vivo by producing analgesia (without causing sedation) and CPA in mice (*9*). All compounds were applied dissolved in saline at the relevant concentration except of RB64, which was only soluble in saline containing 10% dimethyl sulfoxide (DMSO).

In phosphoproteomic experiments, KOR ligands (U-50,488H, 20 nmol; 6′GNTI, 30 nmol; HS665, 10 nmol; HS666, 30 nmol; RB64, 3 nmol) were injected i.c. into pDyn-KO mice under mild (2%) sevofluorane anesthesia in a fixed volume of 3 µl. Each experimental group included three mice. After 5 or 30 min, animals were killed by cervical displacement; the brain was removed from the skull and microdissected immediately. The hippocampus, striatum, cortex, cerebellum, medulla oblongata, and olfactory bulbs were flash-frozen in liquid nitrogen at 2:15, 3:05, 3:30, 3:50, 4:10, and 5:00 min after decapitation. Central application of drugs avoids several pharmacokinetic effects and therefore is considered to yield better comparability. Moreover, 6′GNTI does not permeate the blood brain barrier in sufficient amounts. U-50,488H was purchased from Tocris; 6′GNTI was a gift from the NIDA Drug Supply Program; HS665 and HS666 were synthesized according to the published procedure (*61*); and RB64 was a generous gift from B. Roth laboratory.

Phosphatase inhibitors

The phosphatase inhibitors tautomycetin (0.05 mg/kg), fostriecin (0.05 mg/kg), and calyculin (0.01 mg/kg) (all from Tocris) were applied intraperitoneally (i.p.) 1 hour before KOR agonists. All of these phosphatase inhibitors are soluble in saline at the dosage applied.

Pertussis toxin and Neuro 2A cells

FmK6H-N2A cells were subcultured in a 100-mm plate in complete medium [GIBCO 41500-034, minimum essential medium supplemented with 10% fetal bovine serum and blasticidin (1 µg/ml)] and allowed to grow to 80% confluency (~8×10^6 cells) in a CO_2 incubator. The cells were washed and incubated with serum-free medium for 1 hour. The pertussis toxin (PTX, List Biological Laboratories Inc., Campbell, CA) was added to the cell medium at 0.2 µg/ml and allowed reaction for 1 hour in the incubator. The cells were then

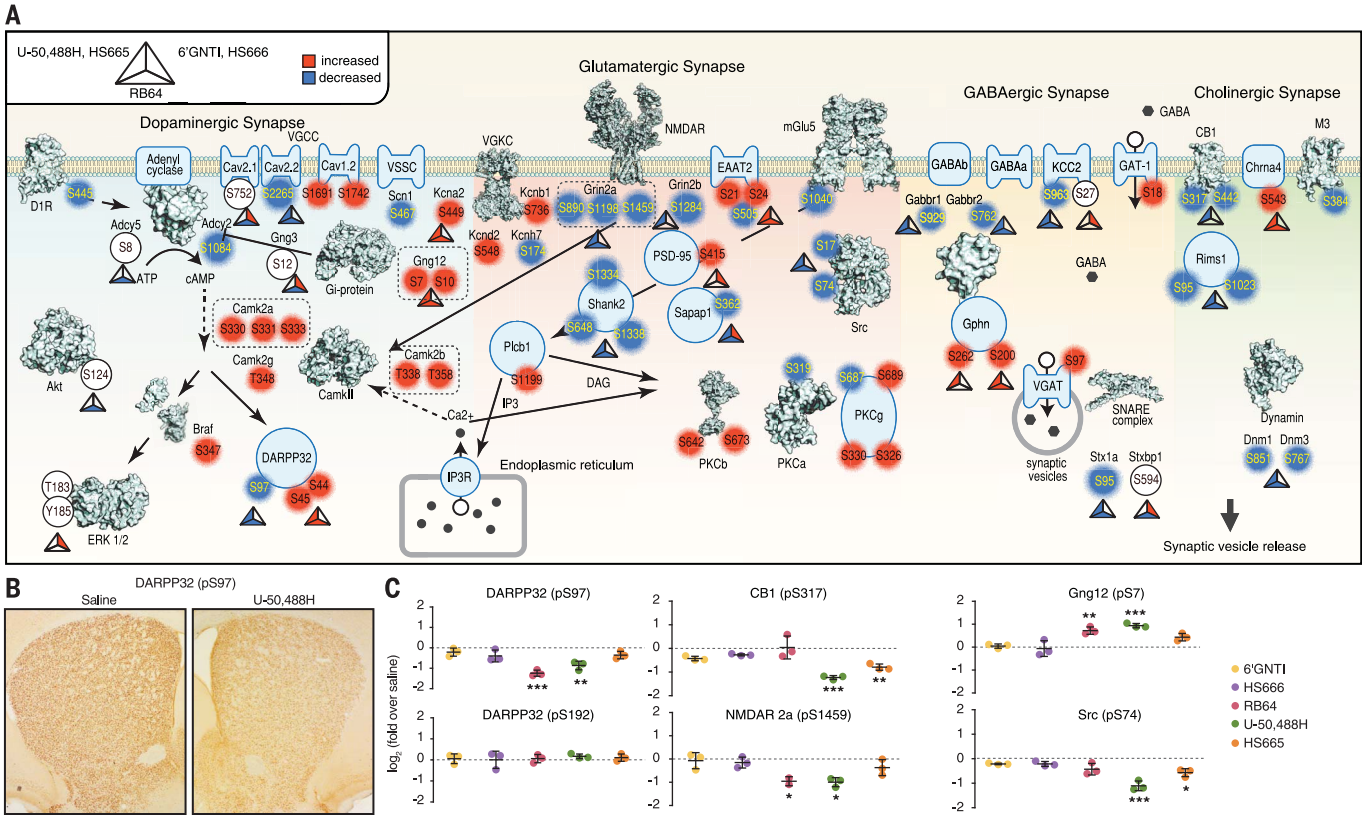

Fig. 4. KOR-mediated signaling at synapses after 5 min. (**A**) Proteins assigned to different KEGG pathways, with particular phosphosites of each protein indicated by the position of the site in a circle. Empty, red, and blue circles indicate no change, increase, and decrease of phosphorylation by U-50,488H stimulation, respectively. Significant U-50,488H–altered sites are chosen from the pairwise Welch *t* test between U-50,488H and saline samples, with cutoff of $P < 0.05$ and difference of >70% in each direction. Triangles next to the circles indicate changes of phosphorylation mediated by three different groups of KOR agonists according to their bioinformatics clustering (fig. S8). The coloring is the same as above. (**B**) Immunohistochemistry in a coronal section of striatum using an antibody to DARPP-32 p97, showing decreased immunoreactivity by U-50,488H treatment ($n = 4$ per group). (**C**) Quantification of selected phosphosites from (A). Samples were analyzed by ANOVA post hoc Dunnett test. *$P < 0.05$, **$P < 0.01$, ***$P < 0.001$ versus saline (control) group. Error bars represent mean ± SD ($n = 3$).

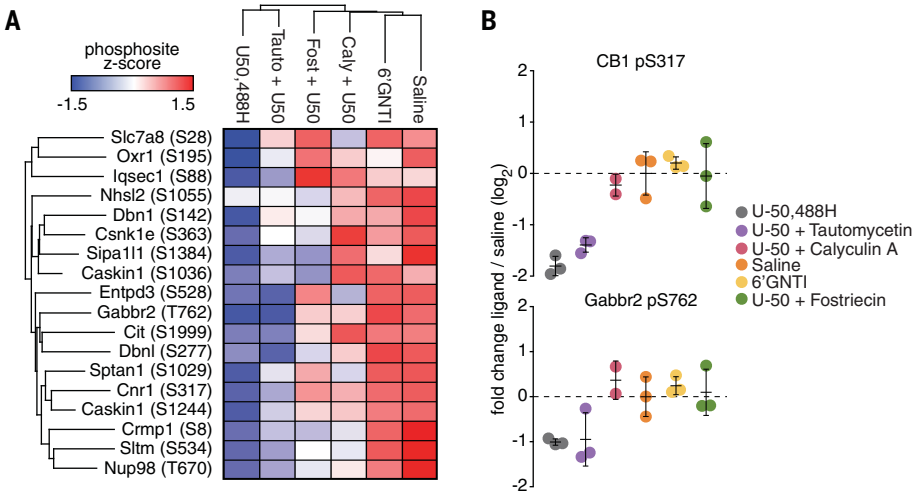

Fig. 5. PP2A mediates U-50,488H actions. (**A**) Heat map of the hierarchical clustering results of U-50,488H–induced changes in PP2A substrates. These sites are dephosphorylated after U-50,488H application with or without tautomycetin (Tauto) pretreatment (PP1-specific inhibitor). But they are not affected by 6′GNTI or by pretreatment with the PP2A inhibitors fostriecin (Fost) or calyculin (Caly) combined with U-50,488H stimulation. The median intensity of three biological replicates in each condition was *z*-scored and colored as shown in the scale bar. (**B**) Selected sites from (A). The *y* axis is the $\log_2$ difference between each condition and saline control. Error bars represent mean ± SD (n = 3).

further treated for 30 min with 10 μM U-50,488H or vehicle. The cells were quickly washed with PBS buffer, collected in PBS containing 1 mM EDTA, and centrifuged. The cell pellets were immediately dissolved in sample buffer (4% SDS, 50 mM Tris, pH 7.4) with the aid of three short bursts of sonication. Samples were then stored at −80°C for subsequent phosphoproteomic analysis.

Phosphoproteomic sample preparation

Frozen brain tissues were transferred into "lysing matrix D" tubes, which contained 1.4-mm ceramic beads (MP Biomedicals) with 400 μl of lysis buffer (100 mM Tris pH 8.5, 4% SDS). Samples were then lysed using Fastprep 24 (MP Biomedicals) at 4 m/s. Samples were then spun down at the maximum speed for 90 min. Frozen cell samples were processed in the same lysis buffer.

After heating for 10 min at 95°C, cold acetone was added to each tube to induce protein precipitation to reach 4:1 (acetone: sample v/v). Protein precipitates were redissolved into 500 μl of the resuspension buffer [100 mM ammonium bicarbonate (ABC), 100 mM Tris pH 8.5, 10% 2,2,2-trifluoroethanol (TFE), 10 mM tris (2-carboxyehtyl)phosphine (TCEP), 40 mM 2-choloroacetamide (CAA)]. After incubation at 50°C for 10 min, samples were transferred into a 96–deep well plate (DWP), from which the protein concentration was determined using the BCA assay. From then on, all the following steps were performed in parallel. The EasyPhos protocol was applied to the samples as described (*30*). Briefly, samples were treated with trypsin and LysC at 100:1 (protein:enzyme w/w) with agitation (2000 rpm) at 37°C; 150 μl of 3.2 M KCl, 55 μl of 150 mM KH_2PO_4, 800 μl of acetonitrile (ACN), and 95 μl of trifluoroacetic acid (TFA) were added to each sample. Digested peptides were enriched with TiO_2 beads (10:1 beads:protein w/w) at 40°C for 5 min at 2000 rpm. Afterward, the phosphopeptide-containing TiO_2 beads were further washed with 4 ml of wash buffer (60% ACN, 1% TFA) and treated with elution buffer (40% ACN, 15% NH_4OH). Eluted phosphopeptides were concentrated in a SpeedVac for 15 min at 45°C; during this process, volatile chemicals such as NH_4OH and ABC were removed. Samples were then desalted using StageTips packed with SDB-RPS membranes and then concentrated in a SpeedVac until dry. A 6-μl volume of MS loading buffer (2% ACN, 0.3% TFA) was added to the samples, which were then sonicated for 5 min in a water bath sonicator.

High-performance liquid chromatography and MS measurements

Samples were loaded onto 50-cm columns packed in-house with C18 1.9 μM ReproSil particles (Dr. Maisch GmbH), with an EASY-nLC 1000 system (Thermo Fisher Scientific) coupled to the MS (Q Exactive HF, Thermo Fisher Scientific). A homemade column oven maintained column temperature at 50°C. Peptides were introduced onto the column with buffer A (0.1% formic acid) and eluted with a 140-min gradient of 5 to 25% of buffer B (60% ACN, 0.1% formic acid), both at a flow rate of 300 nl/min.

A data-dependent acquisition (TopN) MS method was used, in which one full scan (300 to 1600 m/z, R = 60,000 at 200 m/z) at a target of 3×10^6 ions was first performed, followed by 10 data-dependent MS/MS scans with higher-energy collisional dissociation [target 10^5 ions, max ion fill time 120 ms, isolation window 1.6 m/z, normalized collision energy 27%, underfill ratio 40%, R = 15,000 at 200 m/z]. Dynamic exclusion of 60 s and apex trigger (4 to 7 s) were enabled.

Bioinformatic workflow and data analysis

The raw MS spectra were processed using MaxQuant version 1.5.5.2 (*61*). We applied a false discovery rate (FDR) < 0.01 at the level of peptide-spectrum matching, protein assembly, and modifications identification. We estimated protein, peptide, and site FDR using a target-decoy approach with the reverse sequence database. This step was performed in the Andromeda search engine (*62*) integrated in the MaxQuant environment. Searches were performed using the Mouse UniProt FASTA database (September 2014). In addition to the default settings, phospho (STY) was selected as a "variable modification" to enable the identification of peptides containing phosphorylated Ser, Thr, or Tyr residues. The "match between runs" (MBR) feature was enabled, with a matching time window of 1 min.

Further bioinformatics analysis was conducted in Perseus (version 1.5.2.17) (*63*), Microsoft Excel, and R statistical computing software. Annotations were extracted from Gene Ontology (GO) (*64*) and the Kyoto Encyclopedia of Genes and Genomes (KEGG). The synaptic proteins were annotated according to the synaptome database (http://metamoodics.org/SynaptomeDB/) (*65*). Kinase-substrate relationships were based on the phosphositeplus database (phosphosite.org) (*66*). Interaction network analysis was performed with the web-based string database (string-db.org), using the active data source of "Experiments" and "Database" and the biogrid interaction data depository (https://thebiogrid.org/). Cytoscape (version 3.3.0) and its plugin jActiveModules were used to analyze the architecture of subnetworks and to visualize the interaction data (*67*); t tests were conducted using the Welch t-test formula implemented into the Perseus environment unless stated otherwise. Multiple sample comparison was performed using ANOVA with post hoc Dunnett test and the "multicomp" package in R.

For convenience of data handling, all samples were first transformed into a $\log_2$ scale and data normalization was performed. Briefly, after valid value filtering, a median subtract was performed. This is based on the assumption that the majority of the phosphoproteome is unperturbed by the ligand stimulation. In cases where a batch effect was observed (e.g., when experiments were measured in separate MS sessions), normalization by PCA component subtraction was performed. The component in PCA that was correlated with the batch effect was removed by multiplying each sample by its own normalization factor.

To alleviate the "missing value" problem, we performed stringent valid value filtering requiring at least 30% of valid values in all groups, at least 70% of valid values in at least one group, and 50% valid values across all samples. In addition, we removed any columns where quantified values were fewer than 10% of the mean

valid values within the group. In each brain region, we usually encountered 11,000+ sites after this stringent filtering. When comparing the phosphoproteome across regions, we quantified 6000 to 7000 sites after filtering. For most of the analysis, whenever possible we did not perform imputation. If necessary, we imputed the missing values from a random Gaussian-shaped distribution applying a downshift of 1.5 times the standard deviation of the global dataset, and a width of 0.5 times the standard deviation. This effectively simulated values toward the lower end of the intensity distribution, as expected.

PCA, a hybrid hierarchical *k*-means clustering algorithm, and categorical enrichment tests (Fisher exact test) were performed in the Perseus environment. The detailed description can be found in (*63*). The PCA analysis was performed on the basis of singular value decomposition. The categorical enrichment tests were performed in the following steps: We first performed ANOVA on samples from one region and time point (background) using a post hoc Dunnett test. To ensure the simplicity of the test, we pooled U-50,488H, HS665, and RB64 into one group and 6′GNTI and HS666 into another. We then selected groups of phosphosites that passed a threshold of $P < 0.05$ for the former but $P > 0.05$ for the latter. A Fisher exact test was used to test categorical enrichment of the above-mentioned phosphosites using the "background" mentioned above. The ANOVA post hoc Dunnett test was performed for phosphoproteomic analysis using R.

Interaction network analysis

Interaction network analysis was performed using pairwise Welch *t* tests (for example, between U-50,488H and saline samples) to determine U-50,488H–regulated sites in each brain region after 5 min of stimulation. Proteins carrying significantly regulated phosphorylation sites were subsequently used as input for interaction analysis using the String database and Cytoscape plugin "jActiveModule" (*67*). In the jActiveModule analysis, the Biogrid mouse interaction network was also used as an input. The jActiveModule analysis was originally designed to find the highly connected modules or subnetworks, which exhibit similar responses to an experimental condition. We further designated the response as changes in the phosphorylation level in our experiments. The consensus networks between these two approaches in each brain region were selected and displayed.

Categorical enrichment analysis

A Fisher exact test was performed to reveal annotations and pathways that are significantly enriched in the regulated group for each brain region. The output of this test is a *P* value (indicating a degree of significance) and an enrichment factor (indicating the level of enrichment with respect to the background).

The "annotation matrix" algorithm described previously (*36*) was also used to identify cellular mechanisms and processes proteins harboring large-scale dynamic phosphorylation alterations. We reasoned that multiple dynamic phosphorylation perturbation on proteins that belong to the same cellular mechanism are likely to occur if the pathway is recruited. Therefore, we performed nonparametric Mann-Whitney *U* tests between phosphosites carrying the same annotation against the background.

Immunohistochemistry

Immunohistochemistry was performed as described (*68*). Briefly, mice were anesthetized with thiopental (150 mg/kg i.p.). As soon as they fell asleep (~1 min after injection), drugs were injected intracisternally and mice were perfused 5 min after drug treatment with 4% paraformaldehyde in PBS (50 mM phosphate-buffered saline, pH 7.2). Immunohistochemistry was performed on coronal 40-μm vibratome sections incubated free-floating in blocking solution (10% normal goat serum and 0.3% Triton X-100 in TBS) for 90 min. Primary antibodies against pDARPP-32 (1:400; Cell Signaling Technology,

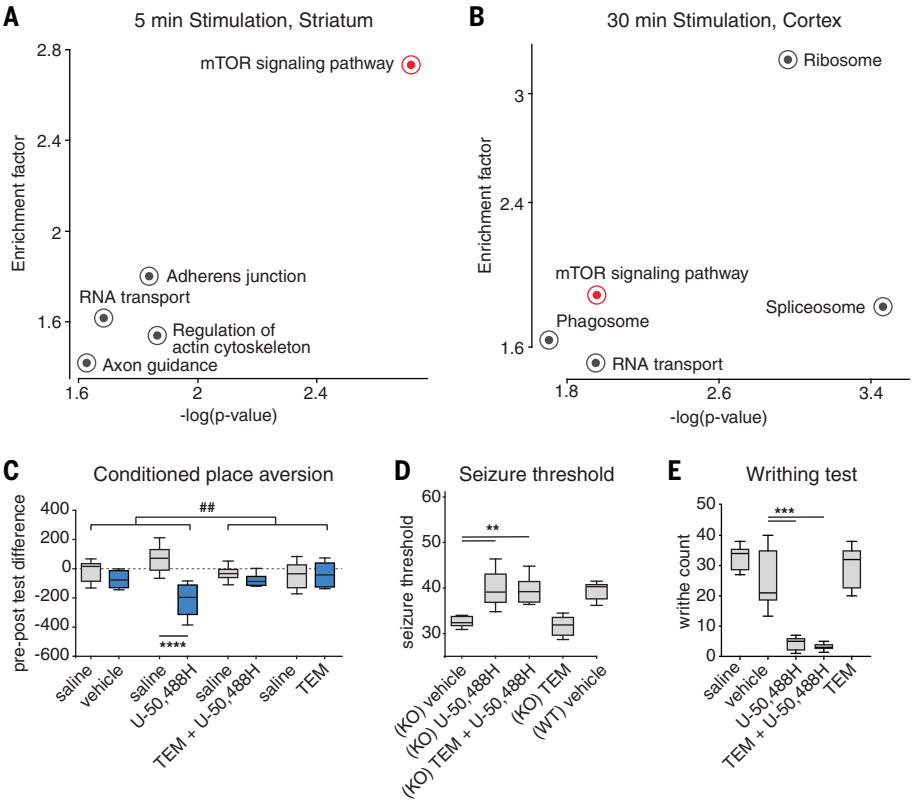

Fig. 6. Blockade of mTOR signaling inhibits conditioned place aversion but does not influence anticonvulsant or antinociceptive effects. (**A**) Fisher exact test on the group of sites that are significantly regulated only by U-50,488H and HS665 in the striatum after 5 min of KOR activation. (**B**) Same as (A) but in cortex after 30 min of stimulation. The *x* axis is the negative log of the *P* value obtained from the Fisher exact test; the *y* axis is the relative difference between the percentages of significantly differentially regulated sites that carried the depicted annotations over the percentage of all sites that carried the same annotation. (**C**) Conditioned place aversion in pDyn-KO mice (U-50,488H, 2.5 mg/kg; $n = 6$ to 8 per group). Three-way ANOVA with post hoc Šidák correction for multiple comparison was performed with time spent in each chamber as the first factor, treatment of U-50,488H as the second factor, and treatment of temsirolimus (TEM) as the third factor. The interaction term between the first factor and TEM yields $P = 0.0074$, whereas TEM alone does not induce significant changes, demonstrating that TEM treatment has a highly significant effect on U-50,488H–mediated aversion. The results of post hoc comparison between time spent in each chamber is indicated. $^{****}P < 0.0001$, $^{\#\#}P < 0.01$. (**D**) PTZ-induced seizure threshold in pDyn-KO mice (U-50,488H, 20 mg/kg; $n = 5$ per group). KO, pDyn-KO; WT, wild type. Two-way ANOVA with post hoc Dunnett multiple-comparisons test and vehicle as control was performed with treatment of U-50,488H as the first factor and treatment of TEM as the second factor. U-50,488H treatment was significant ($P < 0.0001$), but treatment of TEM was not significant ($P = 0.5809$). Post hoc Dunnett multiple-comparisons tests are shown. $^{**}P < 0.01$. (**E**) Writhing test in CD1 mice (U-50,488H, 2 mg/kg; $n = 6$ per group). A two-tailed *t* test showed no significant difference between saline and vehicle. Two-way ANOVA with post hoc Dunnett multiple-comparisons test and vehicle as control was performed with the same factors as in (D). U-50,488H treatment was significant ($P < 0.0001$); treatment of TEM was not ($P = 0.7627$). Post hoc Dunnett multiple-comparisons tests are shown. $^{***}P < 0.001$. Bars represent mean ± SEM.

#D11A5) or pERK, (1:400; Cell Signaling Technology, #9101) were applied overnight at room temperature followed by horseradish peroxidase–conjugated secondary antibodies (1:500, Dako) and 3,3′-diaminobenzidine for detection.

Animal behavioral experiments

Drug preparation

U-50,488H was dissolved in sterile physiological saline (0.9%). Temsirolismus (Tocris) was prepared in 10% DMSO and 3% Tween 20 in sterile physiological saline (0.9%). Vehicle (10% DMSO and 3% Tween 20 in physiological saline) or test compounds were administered in a volume of 10 μl per 1 g body weight.

Conditioned place avoidance

The conditioned place avoidance (CPA) tests were conducted in pDyn-KO mice using a custom-made, three-chamber apparatus (*69*). The conditioning procedure comprised a pretest session, four consecutive training days [two training sessions per day, one each for drug (afternoon) or saline (morning) with a minimum interval of 4 hours], and a CPA test on day 6. Pretest and CPA test session lengths were 15 min, and the conditioning sessions lasted 30 min (*7*). Drugs were assigned to the chambers in an unbiased design. For conditioning, all mice received vehicle 60 min before saline in the morning. In the afternoon, two groups of mice received temsirolimus (8 mg/kg in vehicle) 60 min before injection of either U-50,488H (2.5 mg/kg) or saline. Two other groups received vehicle 60 min before injection of either U-50,488H (2.5 mg/kg) or saline. The difference in time spent in the drug-paired versus the saline-paired box before and after conditioning was evaluated. Each experimental group included six to eight animals.

Pentylenetetrazole-induced seizures

A threshold for pentylenetetrazole (PTZ)–induced seizures was measured through infusion of PTZ (10 mg/ml in saline) through the tail vein in freely moving pDyn-KO mice as described (*7*). Animals were pretreated with either vehicle or temsirolimus (8 mg/kg i.p.) 60 min before PTZ infusion and with saline or U-50,488H (20 mg/kg i.p.) 30 min before PTZ infusion. Infusion was stopped at the first appearance of tonic-clonic seizures. Threshold was calculated from volume injected and body weight (*7*). Each experimental group included five animals.

Writhing test

Writhing was induced in CD1 mice by i.p. injection of a 0.6% acetic acid aqueous solution according to the described procedure (*40*). Groups of mice received saline, vehicle (10% DMSO and 3% Tween 20 in physiological saline), temsirolismus (8 mg/kg), or U-50,488H (2 mg/kg) alone or together with temsirolismus (8 mg/kg). Drugs or controls were administered s.c. to mice; 5 min before testing (25 min after drug or controls), each animal received i.p. acetic acid solution. Temsirolismus was administered 1 hour before U-50,488H. Each mouse was placed in individual transparent Plexiglas chambers, and the number of writhes was counted during a 10-min observation period. Each experimental group included six animals.

Statistical analysis

Behavioral data were analyzed with either two-tailed *t* test or two-way ANOVA using a Dunnett test for multiple comparisons as a post hoc test (except CPA, where a three-way ANOVA with post hoc Šidák correction for multiple comparison was performed) and graphically processed with GraphPad Prism 5.0 Software (GraphPad Prism Software Inc., San Diego, CA). Data are presented as mean ± SEM, with significance set at $P < 0.05$.

REFERENCES AND NOTES

1. R. T. Dorsam, J. S. Gutkind, G-protein-coupled receptors and cancer. *Nat. Rev. Cancer* **7**, 79–94 (2007). doi: 10.1038/nrc2069; pmid: 17251915
2. L. A. Capote, R. Mendez Perez, A. Lymperopoulos, GPCR signaling and cardiac function. *Eur. J. Pharmacol.* **763** (Pt B), 143–148 (2015). doi: 10.1016/j.ejphar.2015.05.019; pmid: 25981298
3. K. Szafran *et al*., Potential role of G protein-coupled receptor (GPCR) heterodimerization in neuropsychiatric disorders: A focus on depression. *Pharmacol. Rep.* **65**, 1498–1505 (2013). doi: 10.1016/S1734-1140(13)71510-X; pmid: 24552997
4. P. F. Vonvoigtlander, R. A. Lahti, J. H. Ludens, U-50,488: A selective and structurally novel non-Mu (kappa) opioid agonist. *J. Pharmacol. Exp. Ther.* **224**, 7–12 (1983). pmid: 6129321
5. J. Morgenweck, K. J. Frankowski, T. E. Prisinzano, J. Aubé, L. M. Bohn, Investigation of the role of βarrestin2 in kappa opioid receptor modulation in a mouse model of pruritus. *Neuropharmacology* **99**, 600–609 (2015). doi: 10.1016/j.neuropharm.2015.08.027; pmid: 26318102
6. Y. Togashi *et al*., Antipruritic activity of the kappa-opioid receptor agonist, TRK-820. *Eur. J. Pharmacol.* **435**, 259–264 (2002). doi: 10.1016/S0014-2999(01)01588-6; pmid: 11821035
7. L. Zangrandi, J. Burtscher, J. P. MacKay, W. F. Colmers, C. Schwarzer, The G-protein biased partial κ opioid receptor agonist 6′-GNTI blocks hippocampal paroxysmal discharges without inducing aversion. *Br. J. Pharmacol.* **173**, 1756–1767 (2016). doi: 10.1111/bph.13474; pmid: 26928671
8. K. M. Raehal, L. M. Bohn, β-arrestins: Regulatory role and therapeutic potential in opioid and cannabinoid receptor-mediated analgesia. *Handb. Exp. Pharmacol.* **219**, 427–443 (2014). doi: 10.1007/978-3-642-41199-1_22; pmid: 24292843
9. K. L. White *et al*., The G protein-biased κ-opioid receptor agonist RB-64 is analgesic with a unique spectrum of activities in vivo. *J. Pharmacol. Exp. Ther.* **352**, 98–109 (2015). doi: 10.1124/jpet.114.216820; pmid: 25320048
10. T. F. Brust *et al*., Biased agonists of the kappa opioid receptor suppress pain and itch without causing sedation or dysphoria. *Sci. Signal.* **9**, ra117 (2016). doi: 10.1126/scisignal.aai8441; pmid: 27899527
11. M. Spetea *et al*., Selective κ receptor partial agonist HS666 produces potent antinociception without inducing aversion after i.c.v. administration in mice. *Br. J. Pharmacol.* **174**, 2444–2456 (2017). doi: 10.1111/bph.13854; pmid: 28494108
12. S. A. Martins *et al*., Towards the miniaturization of GPCR-based live-cell screening assays. *Trends Biotechnol.* **30**, 566–574 (2012). doi: 10.1016/j.tibtech.2012.07.004; pmid: 22921755
13. R. Schröder *et al*., Deconvolution of complex G protein-coupled receptor signaling in live cells using dynamic mass redistribution measurements. *Nat. Biotechnol.* **28**, 943–949 (2010). doi: 10.1038/nbt.1671; pmid: 20711173
14. J. J. Liu, R. Horst, V. Katritch, R. C. Stevens, K. Wüthrich, Biased signaling pathways in β2-adrenergic receptor characterized by 19F-NMR. *Science* **335**, 1106–1110 (2012). doi: 10.1126/science.1215802; pmid: 22267580
15. A. Manglik *et al*., Structure-based discovery of opioid analgesics with reduced side effects. *Nature* **537**, 185–190 (2016). doi: 10.1038/nature19112; pmid: 27533032
16. M. R. Bruchas *et al*., Stress-induced p38 mitogen-activated protein kinase activation mediates kappa-opioid-dependent dysphoria. *J. Neurosci.* **27**, 11614–11623 (2007). doi: 10.1523/JNEUROSCI.3769-07.2007; pmid: 17959804
17. J. M. Ehrich *et al*., Kappa Opioid Receptor-Induced Aversion Requires p38 MAPK Activation in VTA Dopamine Neurons. *J. Neurosci.* **35**, 12917–12931 (2015). doi: 10.1523/JNEUROSCI.2444-15.2015; pmid: 26377476
18. C. L. Schmid *et al*., Functional selectivity of 6′-guanidinonaltrindole (6′-GNTI) at κ-opioid receptors in striatal neurons. *J. Biol. Chem.* **288**, 22387–22398 (2013). doi: 10.1074/jbc.M113.476234; pmid: 23775075
19. L. M. Bohn, M. J. Lohse, M. N. Nitabach, P. H. Taghert, M. J. Smit, Exploring the Biology of G Protein-Coupled Receptors from In Vitro to In Vivo. *Mol. Pharmacol.* **88**, 534–535 (2015). doi: 10.1124/mol.115.100750; pmid: 26162863
20. S. M. Spangler, M. R. Bruchas, Optogenetic approaches for dissecting neuromodulation and GPCR signaling in neural circuits. *Curr. Opin. Pharmacol.* **32**, 56–70 (2017). doi: 10.1016/j.coph.2016.11.001; pmid: 27875804
21. R. Aebersold, M. Mann, Mass-spectrometric exploration of proteome structure and function. *Nature* **537**, 347–355 (2016). doi: 10.1038/nature19949; pmid: 27629641
22. N. M. Riley, J. J. Coon, Phosphoproteomics in the Age of Rapid and Deep Proteome Profiling. *Anal. Chem.* **88**, 74–94 (2016). doi: 10.1021/acs.analchem.5b04123; pmid: 26539879
23. K. Sharma *et al*., Ultradeep human phosphoproteome reveals a distinct regulatory nature of Tyr and Ser/Thr-based signaling. *Cell Rep.* **8**, 1583–1594 (2014). doi: 10.1016/j.celrep.2014.07.036; pmid: 25159151
24. A. F. Altelaar, J. Munoz, A. J. Heck, Next-generation proteomics: Towards an integrative view of proteome dynamics. *Nat. Rev. Genet.* **14**, 35–48 (2013). doi: 10.1038/nrg3356; pmid: 23207911
25. K. N. Nobles *et al*., Distinct phosphorylation sites on the β2-adrenergic receptor establish a barcode that encodes differential functions of β-arrestin. *Sci. Signal.* **4**, ra51 (2011). doi: 10.1126/scisignal.2001707; pmid: 21868357
26. G. L. Christensen *et al*., Quantitative phosphoproteomics dissection of seven-transmembrane receptor signaling using full and biased agonists. *Mol. Cell. Proteomics* **9**, 1540–1553 (2010). doi: 10.1074/mcp.M900550-MCP200; pmid: 20363803
27. K. Xiao *et al*., Global phosphorylation analysis of beta-arrestin-mediated signaling downstream of a seven transmembrane receptor (7TMR). *Proc. Natl. Acad. Sci. U.S.A.* **107**, 15299–15304 (2010). doi: 10.1073/pnas.1008461107; pmid: 20686112
28. R. T. Kendall *et al*., The beta-arrestin pathway-selective type 1A angiotensin receptor (AT1A) agonist [Sar1,Ile4,Ile8]angiotensin II regulates a robust G protein-independent signaling network. *J. Biol. Chem.* **286**, 19880–19891 (2011). doi: 10.1074/jbc.M111.233080; pmid: 21502318
29. J. D. Hoffert *et al*., Dynamics of the G protein-coupled vasopressin V2 receptor signaling network revealed by quantitative phosphoproteomics. *Mol. Cell. Proteomics* **11**, M111 014613 (2012).
30. S. J. Humphrey, S. B. Azimifar, M. Mann, High-throughput phosphoproteomics reveals in vivo insulin signaling dynamics. *Nat. Biotechnol.* **33**, 990–995 (2015). doi: 10.1038/nbt.3327; pmid: 26280412
31. M. S. Robles, S. J. Humphrey, M. Mann, Phosphorylation Is a Central Mechanism for Circadian Control of Metabolism and Physiology. *Cell Metab.* **25**, 118–127 (2017). pmid: 27818261
32. K. Sharma *et al*., Cell type- and brain region-resolved mouse brain proteome. *Nat. Neurosci.* **18**, 1819–1831 (2015). doi: 10.1038/nn.4160; pmid: 26523646
33. H. K. Lee, Synaptic plasticity and phosphorylation. *Pharmacol. Ther.* **112**, 810–832 (2006). doi: 10.1016/j.pharmthera.2006.06.003; pmid: 16904750
34. C. Schwarzer, 30 years of dynorphins—new insights on their functions in neuropsychiatric diseases. *Pharmacol. Ther.* **123**, 353–370 (2009). doi: 10.1016/j.pharmthera.2009.05.006; pmid: 19481570
35. S. Dogra, P. N. Yadav, Biased agonism at kappa opioid receptors: Implication in pain and mood disorders. *Eur. J. Pharmacol.* **763** (Pt B), 184–190 (2015). doi: 10.1016/j.ejphar.2015.07.018; pmid: 26164787
36. S. Tyanova *et al*., Proteomic maps of breast cancer subtypes. *Nat. Commun.* **7**, 10259 (2016). doi: 10.1038/ncomms10259; pmid: 26725330
37. See "Interaction network analysis" above. String database and "jActiveModule" were used.
38. M. L. Rives, M. Rossillo, L. Y. Liu-Chen, J. A. Javitch, 6′-Guanidinonaltrindole (6′-GNTI) is a G protein-biased κ-opioid receptor agonist that inhibits arrestin recruitment.

J. Biol. Chem. **287**, 27050–27054 (2012). doi: 10.1074/jbc.C112.387332; pmid: 22736766
39. A. T. Knoll, W. A. Carlezon Jr., Dynorphin, stress, and depression. *Brain Res.* **1314**, 56–73 (2010). doi: 10.1016/j.brainres.2009.09.074; pmid: 19782055
40. See "Categorical enrichment analysis" above.
41. K. M. Turner, R. D. Burgoyne, A. Morgan, Protein phosphorylation and the regulation of synaptic membrane traffic. *Trends Neurosci.* **22**, 459–464 (1999). doi: 10.1016/S0166-2236(99)01436-8; pmid: 10481193
42. P. Calabresi *et al*., Dopamine and cAMP-regulated phosphoprotein 32 kDa controls both striatal long-term depression and long-term potentiation, opposing forms of synaptic plasticity. *J. Neurosci.* **20**, 8443–8451 (2000). doi: 10.1523/JNEUROSCI.20-22-08443.2000; pmid: 11069952
43. A. Stipanovich *et al*., A phosphatase cascade by which rewarding stimuli control nucleosomal response. *Nature* **453**, 879–884 (2008). doi: 10.1038/nature06994; pmid: 18496528
44. M. Hamada *et al*., Nicotine regulates DARPP-32 (dopamine- and cAMP-regulated phosphoprotein of 32 kDa) phosphorylation at multiple sites in neostriatal neurons. *J. Pharmacol. Exp. Ther.* **315**, 872–878 (2005). doi: 10.1124/jpet.105.090852; pmid: 16040813
45. X. Wang *et al*., CB1 receptor antagonism prevents long-term hyperexcitability after head injury by regulation of dynorphin-KOR system and mGluR5 in rat hippocampus. *Brain Res.* **1646**, 174–181 (2016). doi: 10.1016/j.brainres.2016.05.055; pmid: 27262683
46. S. P. Welch, M. Eads, Synergistic interactions of endogenous opioids and cannabinoid systems. *Brain Res.* **848**, 183–190 (1999). doi: 10.1016/S0006-8993(99)01908-3; pmid: 10612710
47. R. E. Hampson, J. Mu, S. A. Deadwyler, Cannabinoid and kappa opioid receptors reduce potassium K current via activation of Gs proteins in cultured hippocampal neurons. *J. Neurophysiol.* **84**, 2356–2364 (2000). doi: 10.1152/jn.2000.84.5.2356; pmid: 11067978
48. M. W. Salter, L. V. Kalia, Src kinases: A hub for NMDA receptor regulation. *Nat. Rev. Neurosci.* **5**, 317–328 (2004). doi: 10.1038/nrn1368; pmid: 15034556
49. D. G. Winder, J. D. Sweatt, Roles of serine/threonine phosphatases in hippocampal synaptic plasticity. *Nat. Rev. Neurosci.* **2**, 461–474 (2001). doi: 10.1038/35081514; pmid: 11433371
50. M. M. Harraz, R. Tyagi, P. Cortés, S. H. Snyder, Antidepressant action of ketamine via mTOR is mediated by inhibition of nitrergic Rheb degradation. *Mol. Psychiatry* **21**, 313–319 (2016). doi: 10.1038/mp.2015.211; pmid: 26782056
51. S. K. Hwang *et al*., Everolimus improves neuropsychiatric symptoms in a patient with tuberous sclerosis carrying a novel TSC2 mutation. *Mol. Brain* **9**, 56 (2016). doi: 10.1186/s13041-016-0222-6; pmid: 27216612
52. C. S. Jernigan *et al*., The mTOR signaling pathway in the prefrontal cortex is compromised in major depressive disorder. *Prog. Neuropsychopharmacol. Biol. Psychiatry* **35**, 1774–1779 (2011). doi: 10.1016/j.pnpbp.2011.05.010; pmid: 21635931
53. R. F. Mucha, A. Herz, Motivational properties of kappa and mu opioid receptor agonists studied with place and taste preference conditioning. *Psychopharmacology* **86**, 274–280 (1985). doi: 10.1007/BF00432213; pmid: 2994144
54. R. Bals-Kubik, A. Herz, T. S. Shippenberg, Evidence that the aversive effects of opioid antagonists and kappa-agonists are centrally mediated. *Psychopharmacology* **98**, 203–206 (1989). doi: 10.1007/BF00444692; pmid: 2569217
55. M. Spetea, I. P. Berzetei-Gurske, E. Guerrieri, H. Schmidhammer, Discovery and pharmacological evaluation of a diphenethylamine derivative (HS665), a highly potent and selective κ opioid receptor agonist. *J. Med. Chem.* **55**, 10302–10306 (2012). doi: 10.1021/jm301258w; pmid: 23134120
56. J. O. Lipton, M. Sahin, The neurology of mTOR. *Neuron* **84**, 275–291 (2014). doi: 10.1016/j.neuron.2014.09.034; pmid: 25374355
57. K. Inoki, Y. Li, T. Zhu, J. Wu, K. L. Guan, TSC2 is phosphorylated and inhibited by Akt and suppresses mTOR signalling. *Nat. Cell Biol.* **4**, 648–657 (2002). doi: 10.1038/ncb839; pmid: 12172553
58. S. Loacker, M. Sayyah, W. Wittmann, H. Herzog, C. Schwarzer, Endogenous dynorphin in epileptogenesis and epilepsy: Anticonvulsant net effect via kappa opioid receptors. *Brain* **130**, 1017–1028 (2007). doi: 10.1093/brain/awl384; pmid: 17347252
59. F. Simonin *et al*., Disruption of the kappa-opioid receptor gene in mice enhances sensitivity to chemical visceral pain, impairs pharmacological actions of the selective kappa-agonist U-50,488H and attenuates morphine withdrawal. *EMBO J.* **17**, 886–897 (1998). doi: 10.1093/emboj/17.4.886; pmid: 9463367
60. K. L. White *et al*., Identification of novel functionally selective κ-opioid receptor scaffolds. *Mol. Pharmacol.* **85**, 83–90 (2014). doi: 10.1124/mol.113.089649; pmid: 24113749
61. S. Tyanova, T. Temu, J. Cox, The MaxQuant computational platform for mass spectrometry-based shotgun proteomics. *Nat. Protoc.* **11**, 2301–2319 (2016). doi: 10.1038/nprot.2016.136; pmid: 27809316
62. J. Cox *et al*., Accurate proteome-wide label-free quantification by delayed normalization and maximal peptide ratio extraction, termed MaxLFQ. *Mol. Cell. Proteomics* **13**, 2513–2526 (2014). doi: 10.1074/mcp.M113.031591; pmid: 24942700
63. S. Tyanova *et al*., The Perseus computational platform for comprehensive analysis of (prote)omics data. *Nat. Methods* **13**, 731–740 (2016). doi: 10.1038/nmeth.3901; pmid: 27348712
64. M. Ashburner *et al*., Gene ontology: Tool for the unification of biology. *Nat. Genet.* **25**, 25–29 (2000). doi: 10.1038/75556; pmid: 10802651
65. M. Pirooznia *et al*., SynaptomeDB: An ontology-based knowledgebase for synaptic genes. *Bioinformatics* **28**, 897–899 (2012). doi: 10.1093/bioinformatics/bts040; pmid: 22285564
66. P. V. Hornbeck *et al*., PhosphoSitePlus: A comprehensive resource for investigating the structure and function of experimentally determined post-translational modifications in man and mouse. *Nucleic Acids Res.* **40**, D261–D270 (2012). doi: 10.1093/nar/gkr1122; pmid: 22135298
67. M. S. Cline *et al*., Integration of biological networks and gene expression data using Cytoscape. *Nat. Protoc.* **2**, 2366–2382 (2007). doi: 10.1038/nprot.2007.324; pmid: 17947979
68. C. Schwarzer, G. Sperk, C. Rauca, W. Pohle, Neuropeptide Y and somatostatin immunoreactivity in the rat hippocampus after moderate hypoxia. *Naunyn Schmiedebergs Arch. Pharmacol.* **354**, 67–71 (1996). doi: 10.1007/BF00168708; pmid: 8832590
69. K. Kummer *et al*., Conditioned place preference for social interaction in rats: Contribution of sensory components. *Front. Behav. Neurosci.* **5**, 80 (2011). pmid: 22232578
70. J. A. Vizcaíno *et al*., 2016 update of the PRIDE database and its related tools. *Nucleic Acids Res.* **44**, D447–D456 (2016). doi: 10.1093/nar/gkv1145; pmid: 26527722
71. J. Zhu *et al*., Cloning of a human kappa opioid receptor from the brain. *Life Sci.* **56**, PL201–PL207 (1995). doi: 10.1016/0024-3205(94)00507-0; pmid: 7869844
72. S. K. Sharma, R. M. Jones, T. G. Metzger, D. M. Ferguson, P. S. Portoghese, Transformation of a kappa-opioid receptor antagonist to a kappa-agonist by transfer of a guanidinium group from the 5′- to 6′-position of naltrindole. *J. Med. Chem.* **44**, 2073–2079 (2001). doi: 10.1021/jm010095v; pmid: 11405645
73. M. Waldhoer *et al*., A heterodimer-selective agonist shows in vivo relevance of G protein-coupled receptor dimers. *Proc. Natl. Acad. Sci. U.S.A.* **102**, 9050–9055 (2005). doi: 10.1073/pnas.0501112102; pmid: 15932946
74. F. Yan *et al*., Structure-based design, synthesis, and biochemical and pharmacological characterization of novel salvinorin A analogues as active state probes of the kappa-opioid receptor. *Biochemistry* **48**, 6898–6908 (2009). doi: 10.1021/bi900605n; pmid: 19555087
75. F. Erli *et al*., Highly Potent and Selective New Diphenethylamines Interacting with the κ-Opioid Receptor: Synthesis, Pharmacology, and Structure-Activity Relationships. *J. Med. Chem.* **60**, 7579–7590 (2017). doi: 10.1021/acs.jmedchem.7b00981; pmid: 28825813

ACKNOWLEDGMENTS

We thank B. Roth and D. Itzhak for their critical and helpful comments; G. Sowa, I. Paron, and K. Mayr for expert assistance with the MS measurement; and J. Rudolph, S. Tyanova, and G. Borner for valuable advice on bioinformatics analysis. 6′-GNTI was provided by the NIDA drug supply program to C.S. RB-64 was a generous gift from B. Roth. **Funding:** Supported by the Max Planck Society for the Advancement of Science; an EMBO long-term fellowship and the Max Planck Institute stipend program (J.J.L.); Austrian Research Fund (FWF) grants I-977-B24, P-30430-BBL, and W-1206-B05 (C.S.); and NIH grants DA013429, DA041359, and AT006899 (L.-Y.L.-C.). **Author contributions:** J.J.L., C.S., L.-Y.L.-C., and M.M. initiated the project; J.J.L., C.S., and M.S. designed experiments; L.Z. and C.S. performed mice ligand injection and dissections, supervised by C.S.; J.J.L. performed sample preparation and mass spectrometry experiments with help from S.J.H.; J.J.L. performed bioinformatic analysis with help from K.S.; C.C. and Y.C. performed the PTX experiments supervised by L.-Y.L.-C.; C.S. supervised and performed phosphatase inhibitor experiments, immunohistochemistry, conditioned place aversion, and PTZ-induced seizure experiments; M.S. provided HS665 and HS666 and performed the writhing test; M.M. supervised the mass spectrometry experiments and data analysis; J.J.L., C.S., M.S., and M.M. wrote the manuscript with editing and input from K.S., S.H., M.S., and L.-Y.L.-C.; and the project was conceived by J.J.L., C.S., and L.-Y.L.-C. The mTOR behavioral response was first discovered by L.-Y.L.-C. and reproduced by C.S. **Data and materials availability:** Mass spectrometry–based proteomics data have been deposited to the ProteomeXchange Consortium via the PRIDE (*70*) partner repository with the dataset identifier PXD006637. N2A-FmK6H cells are available from L.-Y.L.-C. under a material transfer agreement.

SUPPLEMENTARY MATERIALS

www.sciencemag.org/content/360/6395/eaao4927/suppl/DC1
Figs. S1 to S15
Table S1

27 July 2017; accepted 27 April 2018
10.1126/science.aao4927

RESEARCH ARTICLE

QUANTUM CRITICALITY

Tunable quantum criticality and super-ballistic transport in a "charge" Kondo circuit

Z. Iftikhar[1], A. Anthore[1,2], A. K. Mitchell[3], F. D. Parmentier[1]*, U. Gennser[1], A. Ouerghi[1], A. Cavanna[1], C. Mora[4], P. Simon[5], F. Pierre[1]†

Quantum phase transitions (QPTs) are ubiquitous in strongly correlated materials. However, the microscopic complexity of these systems impedes the quantitative understanding of QPTs. We observed and thoroughly analyzed the rich strongly correlated physics in two profoundly dissimilar regimes of quantum criticality. With a circuit implementing a quantum simulator for the three-channel Kondo model, we reveal the universal scalings toward different low-temperature fixed points and along the multiple crossovers from quantum criticality. An unanticipated violation of the maximum conductance for ballistic free electrons is uncovered. The present charge pseudospin implementation of a Kondo impurity opens access to a broad variety of strongly correlated phenomena.

Continuous second-order quantum phase transitions (QPTs)—which take place at absolute zero temperature as a control parameter such as the magnetic field is tuned—are accompanied by the development of a highly correlated quantum critical state. With increasing temperature, this state extends over a broadening range of parameters further away from the critical point. In this regime of quantum criticality, the properties of the system obey scaling laws determined by the QPT universality class and do not depend on microscopic details. Although QPTs are ubiquitous in contemporary theoretical physics and have been observed in a multitude of highly correlated materials (*1*), it remains challenging to realize them in simple, well-controlled experimental systems.

Tunable nanostructures provide a path to a microscopic understanding of QPTs that circumvents the complexity of real-world highly correlated materials. So far, however, the rare examples that exhibit a second-order QPT (*2*–*6*) demonstrate only a single quantum critical point (associated with the two-channel Kondo effect, described below); although it is a non-Fermi liquid, this critical point can be treated with a perturbative approach in the low-temperature limit (*7*, *8*). By contrast, we realized and characterized completely a circuit that embodies the three-channel Kondo model, with three fully tunable channels connected to a magnetic impurity emulated by the charge states of a metallic island. Within the same nanostructure, this gives us access to two universality classes of quantum criticality (associated with the two-channel and three-channel Kondo effects) that manifest profoundly dissimilar physics. For instance, the quantum critical point for two symmetric Kondo channels can be understood in terms of free electrons and Majorana fermions (*7*, *8*), whereas for three symmetric channels, it involves ($\mathbb{Z}_3$) parafermions with irreducibly strong interactions (*9*). The demonstrated high-precision implementation qualifies our device as an analog quantum simulator, providing quantitative experimental solutions for the three-channel Kondo model.

The multichannel Kondo model

The multichannel Kondo model, which is a generalization of the original (one channel) Kondo model, gives rise to archetypal QPTs and collective, non-Fermi liquid behaviors from a minimal Hamiltonian. Although introduced to account for the different atomic orbitals in metals (*10*–*12*), it has developed over the years into a central testing ground for strongly correlated and quantum critical physics and is a benchmark for many-body theoretical methods (*7*, *11*–*19*). The model describes a local Kondo spin S (of 1/2 here) coupled antiferromagnetically to N independent free-electron continua (Fig. 1A, $N = 3$)

$$H_{\mathrm{NCK}} = \sum_{i=1}^{N} J_i \mathbf{s_i} \cdot \mathbf{S} + H_{\mathrm{continua}} \qquad (1)$$

where H_{NCK} is the N-channel Kondo Hamiltonian, $\mathbf{s_i}$ is the local spin density of electron continuum (channel) i at the Kondo spin $\mathbf{S}$ location, $J_i > 0$ is the coupling strengths (here assumed isotropic), and H_{continua} is the free-electron continua Hamiltonian. The conventional single-channel model ($N = 1$) exhibits universal scaling but no second-order QPT or non-Fermi liquid physics. As the temperature T is reduced, the electrons progressively screen the Kondo spin, resulting for $T \to 0$ in an idle spin-singlet (*11*). By contrast, for $N \geq 2$, there is a competition between channels to screen the $S = 1/2$ Kondo impurity, which develops into second-order QPTs. Each number of identical channels corresponds to a different class of quantum criticality (*16*), with specific non-Fermi liquid physics (*12*) and collective excitations revealed by, for example, a divergent specific heat coefficient c/T as $T \to 0$. The marginal two-channel case corresponds to a logarithmic c/T divergence (*12*), whereas power law c/T divergences are predicted for $N \geq 3$ (*12*).

Kondo "charge" pseudospin implementation

Experimentally, Kondo nanostructures are usually small quantum dots (*20*–*23*), in which coherent electron cotunneling merges the distinct electrical contacts into one Kondo channel (*24*, *25*) [except in the two-channel devices in (*2*, *5*, *26*, *27*)]. By contrast, in the recently demonstrated (*6*) "charge" Kondo approach (*14*, *28*, *29*), the charge Kondo impurity **S** is not a magnetic spin but a pseudospin-1/2 (Fig. 1B, red arrow) built from the macroscopic quantum states describing the overall charge Q of a small metallic island (Fig. 1B, red disk). We extended this concept to three independent Kondo channels. In the most straightforward case of a weakly connected island whose charge is well quantized (*30*), the Kondo spin $S = \{\downarrow, \uparrow\}$ directly maps on the island's two charge states of lowest energy $\{Q, Q + e\}$. All the other charge configurations are indeed frozen out and can be ignored at low temperatures $T \ll E_{\mathrm{C}}/k_{\mathrm{B}}$ ($E_{\mathrm{C}} = e^2/2C$ is the charging energy, e is the electron charge, C is the island geometric capacitance, and k_{B} is the Boltzmann constant). The charge pseudospin energy degeneracy is obtained by tuning (with a gate voltage V_{g}) the device at the degeneracy point between the charge states Q and $Q + e$. Detuning V_{g} away from charge degeneracy is completely analogous to applying a magnetic field on usual magnetic Kondo impurities (*28*). The island charge Kondo pseudospin S is, however, not coupled to the real spin of electrons. Instead, it is flipped by transferring electrons in and out of the island, through the connected electrical channels (Fig. 1B, red dashed lines). This mechanism takes the form of a Kondo (pseudo-) spin-exchange coupling: Introducing an electron pseudospin s (Fig. 1B, blue arrow), which corresponds to the electron localization inside ($s = \downarrow$) or outside ($s = \uparrow$) of the island, the tunneling of an electron flips both its localization pseudospin s as well as the island overall charge pseudospin S. A well-developed Kondo effect requires a continuum of electronic states

[1]Centre de Nanosciences et de Nanotechnologies (C2N), CNRS, Univ. Paris-Sud, Université Paris-Saclay, 91120 Palaiseau, France. [2]Univ. Paris Diderot, Sorbonne Paris Cité, 75013 Paris, France. [3]School of Physics, University College Dublin, Dublin 4, Ireland. [4]Laboratoire Pierre Aigrain, Ecole Normale Supérieure–PSL Research University, CNRS, UPMC Univ. Paris 06–Sorbonne Universités, Univ. Paris Diderot-Sorbonne Paris Cité, 75005 Paris, France. [5]Laboratoire de Physique des Solides, CNRS, Univ. Paris-Sud, Université Paris-Saclay, 91405 Orsay, France.
*Present address: Service de Physique de l'État Condensé, CEA, CNRS, Université Paris Saclay, CEA-Saclay 91191 Gif-sur-Yvette, France.
†Corresponding author. Email: frederic.pierre@u-psud.fr

for both localization pseudospins. This implies a continuous density of states in the metallic island (in contrast with small quantum dots). The different conduction channels constitute here separate Kondo channels. Also, the same physics is predicted at $T \ll E_C/k_B$ for arbitrary connection strengths (*14*, *31*, *32*), except perfectly ballistic contacts, despite the coexistence of many charge states in a quantum superposition near the ballistic limit (*30*). In practice, we found from numerical renormalization group (NRG) calculations performed over a broad range of coupling strengths that $T \lesssim E_C/20k_B$ ensures negligible deviations from universal Kondo physics (*32*).

Each of the Kondo/conduction channels passes through a different quantum point contact (QPC) individually formed and tuned by means of field effect in a high-mobility Ga(Al)As two-dimensional electron gas (*32*). Single channels, polarized in real electron spin, are obtained by immersing the device into a large magnetic field ($B \simeq 2.7$ T, corresponding to the regime of the integer quantum Hall effect at filling factor $\nu = 3$). The Kondo channel couplings J_i ($i \in \{1, 2, 3\}$) are individually characterized by the "intrinsic" (unrenormalized by Kondo or Coulomb effects) transmission probability τ_i across the single open transport channel of QPC$_i$. The micrometer-scale separation between QPCs enables independent fine tuning (~0.1%) and high-precision characterization [$\lesssim 2\%$, with a large dc bias voltage suppressing Kondo/Coulomb renormalization (*32*)] of the Kondo channels, over the full range $\tau_i \in [0, 1]$. Such fine tuning of the connected channels to identical couplings is crucial for approaching the frustrated, symmetric Kondo critical points. The two-channel Kondo (2CK) configurations are implemented by setting $\tau_1 \simeq \tau_3 \equiv \tau$ and $\tau_2 = 0$, whereas for the three-channel Kondo (3CK) configurations $\tau_1 \simeq \tau_2 \simeq \tau_3 \equiv \tau$. With the charging energy $E_C \simeq k_B \times 0.3$ K (separately obtained from Coulomb diamond measurements) and high-precision shot-noise thermometry (*33*), the device is completely characterized. The knowledge of these parameters allows for a full quantitative microscopic understanding (*19*, *28*, *29*). In practice, Kondo physics is observed through the renormalized QPC conductances G_i measured in situ. Because the symmetry between channels is found preserved by renormalization (at an experimental accuracy of ~$0.003e^2/h$), we generally display the averages $G_{1,3} \equiv (G_1 + G_3)/2$ and $G_{1,2,3} \equiv (G_1 + G_2 + G_3)/3$ when investigating the symmetric 2CK and 3CK configurations, respectively.

The high-precision implementation/quantum simulation of the charge Kondo model is validated in Fig. 1, C and D, and the different two-channel and three-channel Kondo behaviors are qualitatively illustrated. The renormalized conductance across channels tuned to "intrinsic" $\tau \simeq 0.90$ (Fig. 1, C and D, squares) or 0.68 (Fig. 1, C and D, triangles) is displayed for $T \simeq 7.9$ and 29 mK while sweeping the gate voltage V_g. The charge degeneracy point is identified as the conductance peak ($\delta V_g = 0$). The good match, without any fit parameters, between the conductance data and the quantitative predictions of the charge Kondo model derived analytically for two near ballistic channels at low temperature (Fig. 1C, continuous line) (*29*, *32*) attests to the accurate device characterization and to its precise implementation of the model for arbitrary Kondo pseudospin energy splitting (*19*, *32*). At large δV_g, the conductance is systematically reduced upon lowering T as usually expected from plain charge quantization. At $\delta V_g = 0$ and for two or three symmetric channels set to $\tau \simeq 0.68$, we observed instead a conductance increase with T owing to the Kondo renormalization of weakly connected channels. At the larger $\tau \simeq 0.90$, 2CK and 3CK exhibit qualitatively different conductance renormalizations at $\delta V_g = 0$, with opposite signs.

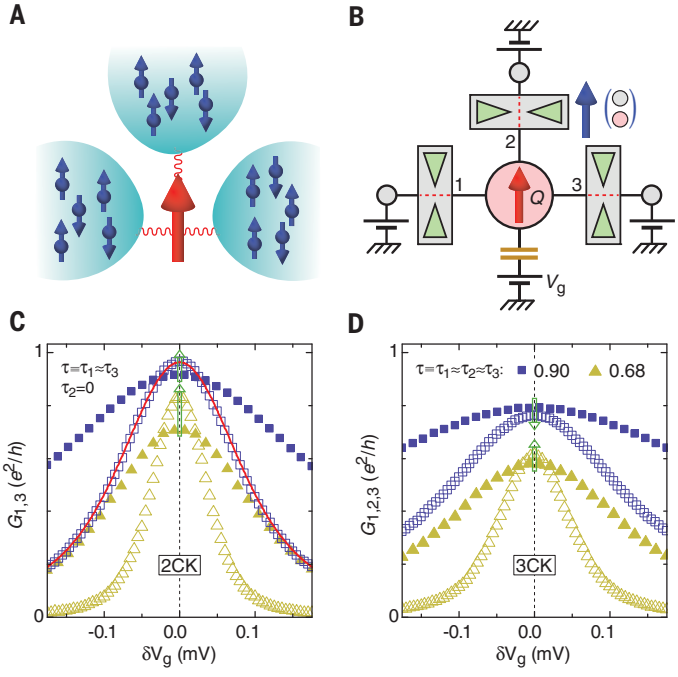

Fig. 1. Multichannel Kondo model and charge implementation. (**A**) In the Kondo model, a local spin (red arrow) is antiferromagnetically coupled to the spin of electrons (blue arrows). Each Kondo channel corresponds to one distinct electron continuum (three continua are shown here). (**B**) Sample schematic realizing the charge pseudospin implementation of the three-channel Kondo model. A micrometer-scale metallic island (red disk) is connected to large electrodes (small gray disks) through three QPCs (green split gates), each set to a single (spin-polarized) conduction channel (red dashed lines) indexed by $i \in \{1, 2, 3\}$. (**C** and **D**) Quantum channels conductance measured versus gate voltage V_g is displayed over half a Coulomb oscillation period $\Delta \simeq 0.7$ mV (several sweeps including different consecutive peaks are averaged). Measurements at $T \simeq 7.9$ and 29 mK are shown, respectively, as open and full symbols for two (C) or three (D) symmetric channels. The squares correspond to an "intrinsic," unrenormalized transmission probability across the connected QPCs of $\tau \simeq 0.90$, and triangles to that of $\tau \simeq 0.68$. The red continuous line (C) displays the $T = 7.9$ mK prediction for two channels both set to $\tau = 0.90$ (*32*). Green arrows indicate the direction of conductance change at $\delta V_g = 0$ as temperature is reduced.

Observation of an intermediate nontrivial fixed point

The above findings corroborate the theoretical expectations for the different 2CK and 3CK low-temperature conductance fixed points (*29*, *34*). Both 2CK and 3CK quantum critical fixed points are associated with an intermediate value of the renormalized Kondo coupling $0 < |J| < \infty$ (*10*, *12*). In previous experiments on small quantum dots (*2*, *5*), the 2CK intermediate coupling could not be established. Indeed, T was not low enough with respect to the scaling Kondo temperature T_K to show a saturation; furthermore, asymmetries between electrical channels (*15*) can lead to a trivial intermediate asymptotic value of the measured conductance, which therefore does not necessarily imply an intermediate coupling in these spin Kondo devices. Moreover, the intermediate coupling character of the 2CK fixed point is not entirely invariable but depends on the choice of representation (*7*, *8*, *14*, *29*). In particular, the 2CK fixed point can be described as a noninteracting system involving two Majorana modes [one free, one in the strong coupling limit (*7*)]. This dual strong-coupling character of the 2CK fixed point also materializes in the present charge Kondo implementation: Here, $G_{1,3}$ constitutes an alternative probe of the coupling between electrons and charge Kondo impurity, which flows not toward an intermediate value per electrical channel but toward the maximum free-electron quantum limit $G_{2CK} = e^2/h$ (*29*). By contrast, the genuinely intermediate character of the interacting 3CK fixed point is predicted to show up directly in charge Kondo circuits, as a flow of the conductance per channel $G_{1,2,3}$ toward the nontrivial intermediate universal conductance $G_{3CK} = 2\sin^2(\pi/5)e^2/h \simeq 0.691e^2/h$ (*34*).

The precise 2CK and 3CK low-temperature universal conductance fixed points are experimentally established by measuring the temperature evolution of $G_{1,3}$ and $G_{1,2,3}$, respectively, for a broad range of symmetric channel settings [$\tau \in (0.56, 0.985)$]. For this purpose, and until explicitly specified otherwise, the device is tuned

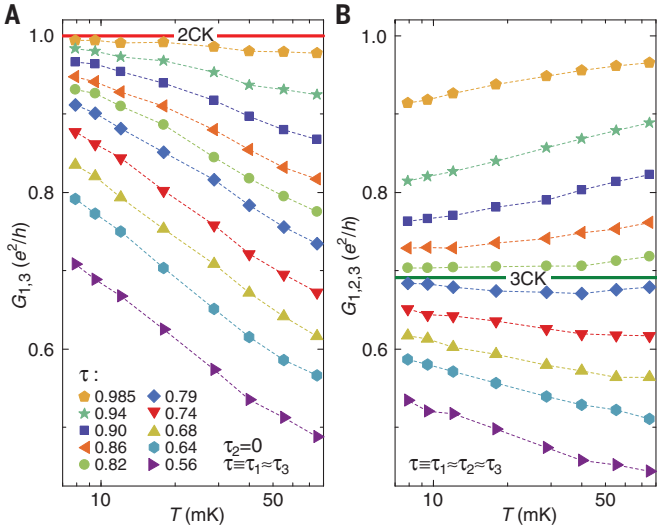

Fig. 2. Quantum critical fixed points. (**A** and **B**) The conductance of (A) two or (B) three symmetric channels measured at the charge degeneracy point ($\delta V_g = 0$) is plotted as symbols versus temperature on a logarithmic scale. Each set of identical symbols connected by dashed lines corresponds to the same device setting (τ). The predicted (A) 2CK and (B) 3CK low-temperature fixed points for the conductance per channel in the present charge Kondo implementation are shown as horizontal continuous lines [$G_{2CK} = e^2/h$, $G_{3CK} = 2\sin^2(\pi/5)e^2/h$].

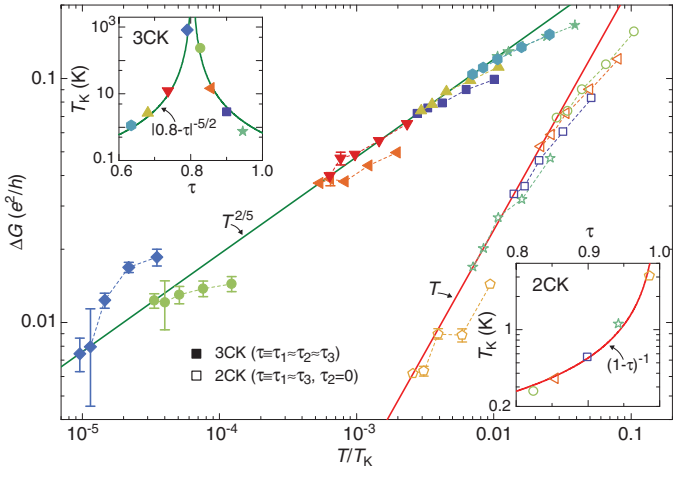

Fig. 3. Non-Fermi liquid scaling exponents. The absolute difference between symmetric channels conductance at charge degeneracy and predicted Kondo fixed point ($\Delta G \equiv |G_{1,3} - G_{2CK}|$ and $\Delta G \equiv |G_{1,2,3} - G_{3CK}|$) is plotted as symbols (open and solid for 2CK and 3CK, respectively) versus T/T_K in a log-log scale for $T \in \{7.9, 9.5, 12, 18, 29\}$ mK. Statistical error bars are shown when larger than symbols. The red and green continuous straight lines display the predicted power-law scaling at $T/T_K \ll 1$ for the conductance per channel in the present charge 2CK and 3CK implementations, respectively. The scaling Kondo temperature T_K is adjusted separately for each tuning τ of the symmetric channels (insets, corresponding symbols). This is done by matching the lowest-temperature data point $\Delta G(T \simeq 7.9$ mk) with the corresponding displayed power law. Continuous lines in insets show the predicted power-law divergences of T_K versus τ for 2CK (bottom right inset) and 3CK (top left inset).

at charge degeneracy ($\delta V_g = 0$), where Kondo effect is expected. Measurements of $G_{1,3}$ and $G_{1,2,3}$ versus T in logarithmic scale are shown as symbols in Fig. 2. In the 2CK configuration (Fig. 2A), whatever the setting τ, we found that $G_{1,3}$ always grows as T is reduced. This observation validates the predicted e^2/h Kondo fixed point (Fig. 2A, horizontal red line), at an experimental accuracy of $0.006e^2/h$ (*6*). Upon lowering T in the 3CK configuration (Fig. 2B), $G_{1,2,3}$ systematically grows when below $0.68e^2/h$ (and for $T \leq 40$ mK) and decreases when above $0.70e^2/h$. This validates the predicted 3CK universal conductance fixed point $G_{3CK} \simeq 0.69e^2/h$ (horizontal green line) at an experimental accuracy of $\pm 0.01e^2/h$. This constitutes direct experimental evidence of an intermediate non-Fermi liquid fixed point.

Universal scalings toward quantum criticality

First, we characterized the power-law exponents when approaching the 2CK and 3CK low-temperature fixed points and found them to be different from the characteristic T^2 for Fermi liquids. For this purpose, the distances ΔG between measured $G_{1,3}$ and $G_{1,2,3}$ and, respectively, the theoretically predicted fixed points G_{2CK} and G_{3CK} are plotted in Fig. 3 versus T/T_K. The continuous straight lines show the universal power-law scalings asymptotically predicted at low T/T_K for the conductance in the present charge Kondo implementation: $\Delta G \propto T$ for 2CK (*19*, *29*, *35*) and $\Delta G \propto T^{2/5}$ for 3CK (*12*, *13*, *32*) [further discussion is provided in (*32*)]. Comparing with the data requires us to, for each τ, fix the corresponding scaling Kondo temperature $T_K(\tau)$. Symbols in the Fig. 3 insets represent the experimentally extracted values of T_K versus τ, which were obtained for each tuning τ by matching the lowest-temperature data point with the displayed theoretical power law. The data-theory comparison in the main Fig. 3 panel is therefore in the conductance evolution as temperature is increased. We found that sufficiently close to the fixed points ($\Delta G \lesssim 0.1e^2/h$), the experiment is consistent with predictions. The precision is here limited by the increasing relative experimental uncertainty as ΔG is reduced. A direct extraction of the temperature exponents from the $\Delta G < 0.1e^2/h$ data at $T \in \{7.9, 12\}$ mK (satisfying the NRG universality criteria $T \lesssim E_C/20k_B \simeq 15$ mK) gives $\alpha_{2CK} = 0.83 \pm 0.08$ for 2CK and $\alpha_{3CK} = 0.42 \pm 0.17$ for 3CK.

We then investigated the full 2CK and 3CK universal renormalization flows. Measurements (symbols) are now compared in Fig. 4, A to C, with NRG calculations spanning the whole range of T/T_K (Fig. 4, continuous black lines) (*32*). In Fig. 4, A and B, respectively, $G_{1,3}$ and $G_{1,2,3}$ are plotted versus $\log(T/T_K)$. Following standard procedures, the theoretical scaling Kondo temperature T_K was normalized so that the NRG universal conductance takes a value equal to half that of the Kondo fixed point at $T = T_K$. As in Fig. 3, the experimental $T_K(\tau)$ (symbols in Fig. 4 insets) are adjusted by matching data with theory at $T \simeq 7.9$ mK. These $T_K(\tau)$ remain therefore identical to those in the insets of Fig. 3 as long as NRG calculations and asymptotic power laws are indistinguishable (for $T_K \gg 7.9$ mK). We observed a quantitative agreement between the data and the universal NRG prediction over six (2CK) or eight (3CK) orders of magnitude in T/T_K. A direct comparison of the same measurements and predictions is shown in Fig. 4C in a scale-invariant representation that does not involve rescaling the temperature in units of T_K, by displaying $\partial G_{1,3}/\partial\log(T)$ versus $G_{1,3}$ and $\partial G_{1,2,3}/\partial\log(T)$ versus $G_{1,2,3}$. In this representation, data points correspond to experimental measurements of the so-called β-function that determines the corresponding 2CK or 3CK renormalization group equation for the conductance. In Fig. 4C, the straight dashed lines near 2CK and 3CK fixed points (Fig. 4C, arrows) represent the predicted non-Fermi liquid power-law behaviors discussed in the previous paragraph. Comparing with the experimental slope therefore complements the approach in Fig. 3. Also shown is the experimental "analog quantum simulation" of the universal 3CK β-function at $G_{1,2,3} > G_{3CK}$, out of reach of NRG calculations.

Last, we explored the quantitative relationship between scaling Kondo temperature T_K and microscopic model parameter τ (Figs. 3 and 4, insets). At small $\tau \lesssim 0.5$, the same expected exponential behavior $T_K \simeq (E_C/10k_B)\exp(-\pi^2/\sqrt{4\tau})$ is observed for 2CK and 3CK (*29*). At larger τ, T_K appears to diverge at a specific setting τ_c, with extracted T_K values orders of magnitude above

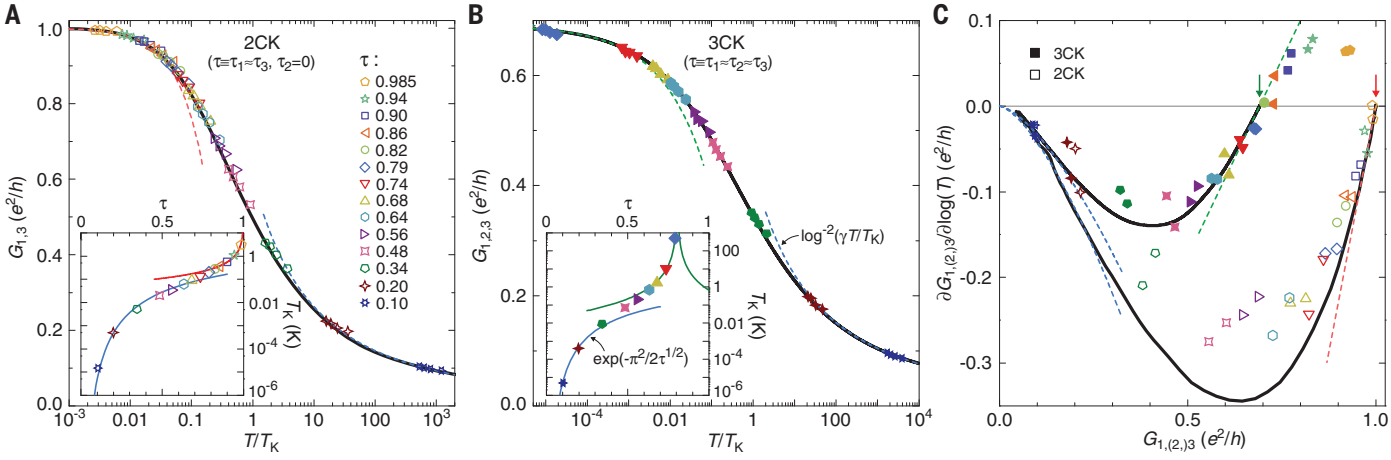

Fig. 4. Universal renormalization flow to quantum criticality. The measured conductance of the two or three connected, symmetric channels is shown as symbols (open and solid for 2CK and 3CK, respectively) for a broad range of settings τ. (**A** and **B**) Data ($T \in \{7.9, 9.5, 12, 18\}$ mK) and predictions are plotted versus T/T_K in log scale. The corresponding experimental T_K are shown in insets as symbols versus τ, together with theoretical predictions for tunnel contacts $\tau \ll 1$ (light-blue continuous lines) and for very large T_K at $|\tau - \tau_c| \ll 1$ [respectively, red and green continuous lines for 2CK and 3CK in insets of (A) and (B)]. (**C**) Direct data-theory comparison (no T/T_K rescaling) with $\partial G_{1,3}/\partial \log(T)$ plotted versus $G_{1,3}$ and $\partial G_{1,2,3}/\partial \log(T)$ plotted versus $G_{1,2,3}$. The discrete experimental differentiation is performed with measurements at $T \in \{7.9, 12, 18\}$ mK. Kondo fixed points are indicated by arrows. Black continuous lines are NRG calculations of the universal renormalization flows [2CK in (A) and (C) and 3CK in (B) and (C)]. Colorized dashed lines shown at low T/T_K [(A) and (B)], and close to the Kondo fixed points (C), display the predicted low-temperature power laws for 2CK [red in (A) and (C)] and 3CK [green in (B) and (C)]. Light blue dashed lines shown at large T/T_K [(A) and (B)], and for small channels conductance (C), represent the predicted high-temperature logarithmic scaling proportional to $\log^{-2}(\gamma T/T_K \gg 1)$, with the slightly different 2CK and 3CK prefactors and γ here used as fit parameters.

the high-energy cutoff $E_C/k_B \simeq 300$ mK (in which case, universal Kondo physics can only be probed at $T/T_K \ll 1$). For 2CK, theory predicts a divergence at $\tau_c = 1$ as $T_K(1-\tau \ll 1) \propto 1/(1-\tau)$, which is displayed by the identical continuous red lines in the insets of Figs. 3 and 4A (*29*) [(*31*, *36*), the prediction of a peaked $T_K(J)$]. For 3CK, the observed value $\tau_c \simeq 0.8$ is higher than $G_{3CK}h/e^2 \simeq 0.69$. This is caused by the conductance suppression by Coulomb interaction at temperatures $T \gtrsim E_C/k_B$, before the development of universal Kondo physics at low temperatures. Assuming theoretically that T_K diverges at τ_c, we generally find (*32*) that a low-temperature conductance power law $\Delta G \propto T^\alpha$ corresponds to a power-law divergence as $T_K \propto |\tau - \tau_c|^{-1/\alpha}$. The observed close agreement between experimental $T_K(|\tau - \tau_c| \ll 1)$ in 2CK and 3CK configurations with, respectively, $T_K \propto |\tau - 1|^{-1}$ (Figs. 3 and 4A, insets, red lines) and $T_K \propto |\tau - 0.8|^{-5/2}$ (Figs. 3 and 4B, insets, green lines) therefore further establishes the predicted non-Fermi liquid Kondo exponents for two ($\alpha_{2CK} = 1$) and three ($\alpha_{3CK} = 2/5$) symmetric channels.

Crossover from quantum criticality

As the temperature is increased [up to some limit; here, $T \lesssim \min(T_K, E_C/k_B)$], the quantum critical regime is generally expected to span over a larger range of system parameters, away from the $T = 0$ quantum critical point (Fig. 5A). The so-called crossover temperature T_{co} delimits quantum criticality from below, with the critical point itself corresponding to $T_{co} = 0$. Generically, the crossover from quantum criticality as temperature is lowered should follow universal curves versus the reduced parameter T/T_{co}. Indeed, T_{co} is the only relevant temperature scale, encapsulating all microscopic details, provided that the high-energy cutoff for quantum criticality is much higher. In tunable circuits, the crossover from 2CK quantum criticality was explored versus Kondo channels asymmetry (*5*, *6*) and, in the different implementation of a spin-polarized quantum dot embedded into a dissipative circuit, versus the difference between resonant dot level and Fermi energy (*4*). These experiments corroborate the existence of a universal T/T_{co} scaling, as well as the predicted quadratic increase of T_{co} for small deviations from the 2CK critical point (*12*, *15*, *18*). We explored the disparate universal and exotic behaviors along the different crossovers induced by breaking the Kondo (pseudo)spin degeneracy or the channel symmetry, observed the development of the quantum phase transition across the symmetric 3CK quantum critical point, and demonstrated "super-ballistic" conductances.

In a first step, we investigated the so-far-unexplored crossover from 2CK and 3CK quantum criticality induced by breaking the energy degeneracy of the Kondo impurity, with the connected channels remaining symmetric. We established (i) the different 2CK and 3CK power-law dependence $T_{co} \propto |\Delta E|^\gamma$ for small energy splitting of the charge pseudospin $\Delta E = 2E_C \delta V_g/\Delta \ll E_C$, with $\Delta \simeq 0.7$ mV being the gate voltage period; (ii) a generalized expression of T_{co} for arbitrary ΔE; and (iii) the theoretical universal crossover curves $\tilde{G}_{2CK}(T/T_{co})$ and $\tilde{G}_{3CK}(T/T_{co})$, obtained analytically in (*19*, *29*) for 2CK and by NRG here for 3CK.

The crossover temperature T_{co} is defined so that the conductance is halfway between the quantum critical regime ($\approx G_{2CK}$ or $\approx G_{3CK}$, at $T_{co} \ll T \ll T_K$) and the Fermi liquid regime (≈ 0, at $T_{co} \gg T$)—that is, $G_{1,3}(\Delta E, T = T_{co}) \equiv G_{2CK}/2$ or $G_{1,2,3}(\Delta E, T = T_{co}) \equiv G_{3CK}/2$. In practice, we fixed the electronic temperature T and adjusted the energy splitting $\Delta E \propto \delta V_g$ in order to obtain this midway conductance value, if possible. In Fig. 5, B and C, this corresponds to the crossings between continuous and horizontal dashed lines, where the experimentally extracted crossover temperature directly reads $T_{co}^{expt}(\Delta E) = T$. Symbols in Fig. 5, D and E, display T_{co}^{expt} versus ΔE for the settings τ where $T_{co} \propto \Delta E^\gamma$ is expected (*32*). The predicted corresponding power laws are shown as continuous lines ($T_{co} \propto \Delta E^2$ for 2CK, $T_{co} \propto \Delta E^{5/3}$ for 3CK) (*12*). Fitting separately, for each τ, the $T_{co}^{expt}(\Delta E) \leq 12$ mK data (fulfilling the universality NRG criteria) yield the values of γ displayed as symbols in the insets of Fig. 5, D and E. A statistical analysis of these values gives $\gamma_{2CK} = 2.01 \pm 0.04$ and $\gamma_{3CK} = 1.69 \pm 0.02$ for the crossovers from 2CK and 3CK, respectively, which is in close agreement with theory.

The theoretically predicted universal crossover curves $\tilde{G}_{2CK}(T_{co}/T)$ and $\tilde{G}_{3CK}(T_{co}/T)$, shown as thick dashed lines in Fig. 5, B and C, right hand sides, are compared with conductance data. Continuous lines in Fig. 5, B and C, left hand sides represent the conductance measured at different temperatures versus gate voltage for $\tau_{1,3} \simeq 0.94$ (Fig. 5B) and $\tau_{1,2,3} \simeq 0.82$ (Fig. 5C). These settings correspond to well-developed quantum critical regimes $T \ll T_K$ (small ΔG), a necessary condition to investigate $\tilde{G}_{2CK}$ and $\tilde{G}_{3CK}$ down to small T_{co}/T. In Fig. 5, B and C, right hand sides, the gate voltage sweeps at different temperatures

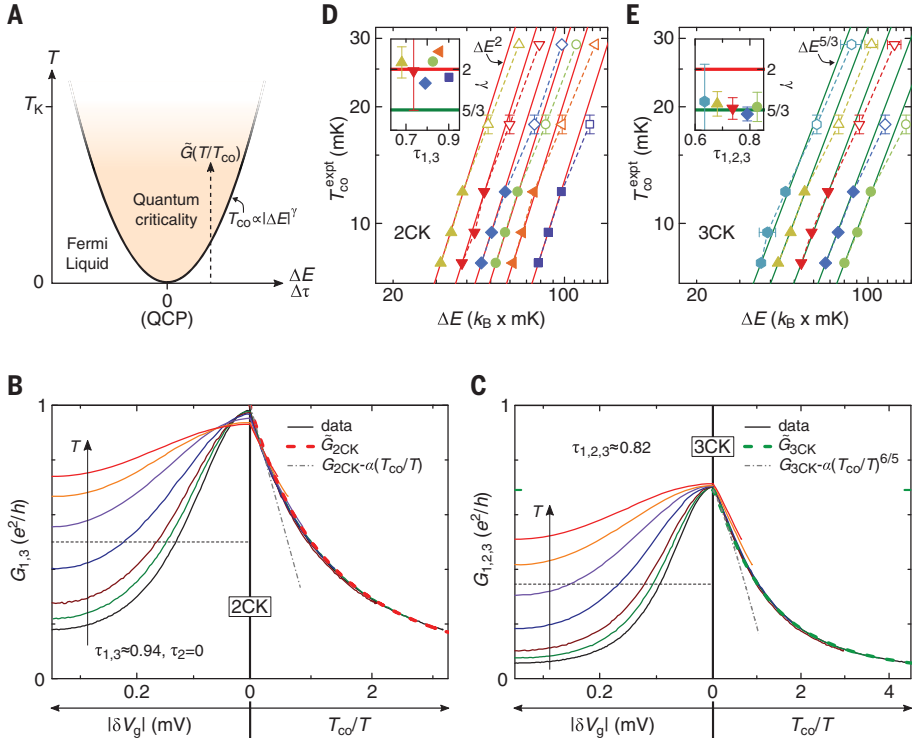

Fig. 5. Crossover from quantum criticality by pseudospin degeneracy breaking. (**A**) Quantum criticality extends as T rises. It is delimited from below by the crossover temperature T_{co}, which increases as a power law for small parameter-space distances from the critical point (for example, charge pseudospin energy splitting $\Delta E \propto \delta V_g$, channels asymmetry $\Delta\tau$). Along the crossover, theory predicts universal T/T_{co} scalings [for example, $G_i(T, \Delta E) = \tilde{G}(T/T_{co})$]. (**B** and **C**) The conductance of (B) two and (C) three symmetric channels set, respectively, to $\tau_{1,3} \simeq 0.94$ and $\tau_{1,2,3} \simeq 0.82$, are plotted as continuous lines versus $|\delta V_g|$ (left side) and T_{co}/T (right side) for $T \in \{7.9, 9.5, 12, 18, 29, 40, 55\}$ mK. Colored thick dashed lines (gray dash-dotted lines) shown in right sides display the theoretical universal crossover curves $\tilde{G}_{2CK}$ and $\tilde{G}_{3CK}$ (the predicted $T_{co}/T \ll 1$ power laws). The only fit parameter is an unknown fixed prefactor for the 3CK crossover scale T_{co} [no fit parameters in (B)]. (**D** and **E**) Experimental crossover temperatures T_{co}^{expt} are plotted as symbols in a log-log scale versus ΔE, for (D) two and (E) three symmetric channels. Each set of symbols connected by dashed lines represents one device setting $\tau_{1,3}$ or $\tau_{1,2,3}$ (insets). Full symbols correspond to $T_{co}^{expt} \leq 12$ mK. Straight continuous lines display the predicted power laws $T_{co} \propto \Delta E^{\gamma}$, with $\gamma = 2$ for 2CK and $\gamma = 5/3$ for 3CK. Fitting $T_{co}^{expt}(\Delta E) \leq 12$ mK separately for each τ yields the values of γ shown as symbols in the insets with the fit standard error.

(continuous lines) fall on top of one another when plotted versus calculated T_{co}/T, demonstrating the predicted universal character of the crossover from quantum criticality. Moreover, we found a precise match between experimental universal curves and theoretical predictions $\tilde{G}_{2CK}$ and $\tilde{G}_{3CK}$. T_{co} is obtained from experimental parameters by using generalized expressions that remain valid for arbitrary gate voltage beyond the power law at small detuning. For the charge 2CK device with near ballistic channels, the full quantitative expression derived in (*29*) was used in Fig. 5B: $T_{co} \simeq 1.444 E_C(1-\tau_{1,3})\sin^2(\pi\delta V_g/\Delta)$. The data-$\tilde{G}_{2CK}$ comparison in Fig. 5B is therefore without any fit parameter. For 3CK, we expect from NRG calculations the similar generalization $T_{co} = \lambda_{3CK}\sin^{5/3}(\pi\delta V_g/\Delta)$ (*32*), which was used in Fig. 5C. Because the prefactor $\lambda_{3CK}(\tau, E_C)$ is not known, the value $\lambda_{3CK} = 36$ mK was freely adjusted in the data-$\tilde{G}_{3CK}$ comparison shown in Fig. 5C.

In a second step, the development of the 3CK QPT driven by the channels' competition to screen the Kondo spin is plainly observed through the conductance renormalization flow of asymmetric channels upon lowering temperature (Fig. 6). The Kondo charge pseudospin is energy degenerate ($\delta V_g = 0$), $QPC_{1,3}$ are tuned symmetric ($\tau_1 \simeq \tau_3$), and τ_2 is adjusted separately. Displayed in Fig. 6 as colored lines with arrowheads is the temperature evolution of the measured conductances G_2 (vertical axis) and $G_{1,3}$ (horizontal axis) from 55 to 7.9 mK (arrowhead at lowest T); each line corresponds to a different device setting. In total, 15 × 14 settings of $\{\tau_2, \tau_1 \simeq \tau_3\}$ were measured, with $\tau_{1,2,3}$ picked among 14 fixed values ranging from 0.1 to 0.985 (*32*) and including also $\tau_2 = 0$. The data closest to the Fig. 6 diagonal gray line correspond to three channels tuned symmetric ($\tau_1 \simeq \tau_2 \simeq \tau_3$). Below the diagonal, where $\tau_2 < \tau_1 \simeq \tau_3$, the data flow toward the predicted 2CK fixed point (Fig. 6, red disk, at $G_{1,3} = e^2/h$ and $G_2 = 0$). Above the diagonal, where $\tau_2 < \tau_1 \simeq \tau_3$ so that a flow toward the 1CK fixed point involving QPC_2 is expected (blue disk, at $G_{1,2,3} = 0$), we observed a monotonous decrease of the conductance $G_{1,3}$ across the less strongly coupled QPCs. By contrast, G_2 first rises, markedly oversteps the free-electron quantum limit e^2/h (up to +25%), and then decreases toward the zero conductance 1CK fixed point as T is further reduced.

The nonmonotonous behavior of G_2 when higher than $G_{1,3}$ might appear counterintuitive. A flow toward the low-temperature 1CK "strong coupling" fixed point is expected, which corresponds to a renormalized Kondo coupling growing monotonously ($J_2 \to \infty$). However, J_2 connects with the tunnel coupling/hopping integral of electrons across QPC_2 in the charge Kondo mapping, and free-electron theory predicts a nonmonotonous dependence of the conductance with the hopping integral [with a maximum for the value that best preserves translational invariance, and $G_2(J_2 \to \infty) = 0$]. By contrast, the present measurement of a conductance that exceeds the maximum possible value for noninteracting electrons in the ballistic limit is highly nontrivial and was not anticipated (although reproduced by our NRG calculations). Such a super-ballistic conductance, also in an intermediate temperature range and of similar amplitude, was coincidently observed in clean graphene constrictions (*37*) and explained as a collective viscous flow of the electronic fluid induced by electron-electron collisions (*38*). We speculate that the electron-electron interactions mediated by the Kondo impurity within the electronic channel across QPC_2, expected to be particularly strong near the turning point where G_2 is maximum, might also result in such a viscous electronic fluid behavior. One specificity of our system is that the super-ballistic magnitude and the temperature range in which it takes place can be controlled in situ, by separately adjusting the channels.

The experimental findings are compared with NRG calculations of the universal crossover flow from 3CK quantum criticality, induced by an initially minute asymmetry between G_2 and $G_{1,3}$ (*32*). These are displayed in Fig. 6 as two thick gray lines originating from the 3CK fixed point, with arrows pointing toward lower temperatures. For $G_{1,3} > G_2$, NRG predicts a monotonous crossover flow from 3CK to 2CK conductance fixed points that closely matches the nearby data. For $G_2 > G_{1,3}$, the universal NRG crossover flow from 3CK to 1CK reproduces the observed nonmonotonous behavior, confirms the naively expected vanishing of G_2 at the 1CK fixed point, and establishes that a super-ballistic conductance exceeding by ~20% the free-electron maximum limit follows from the 3CK model, which is in quantitative agreement with the experiment.

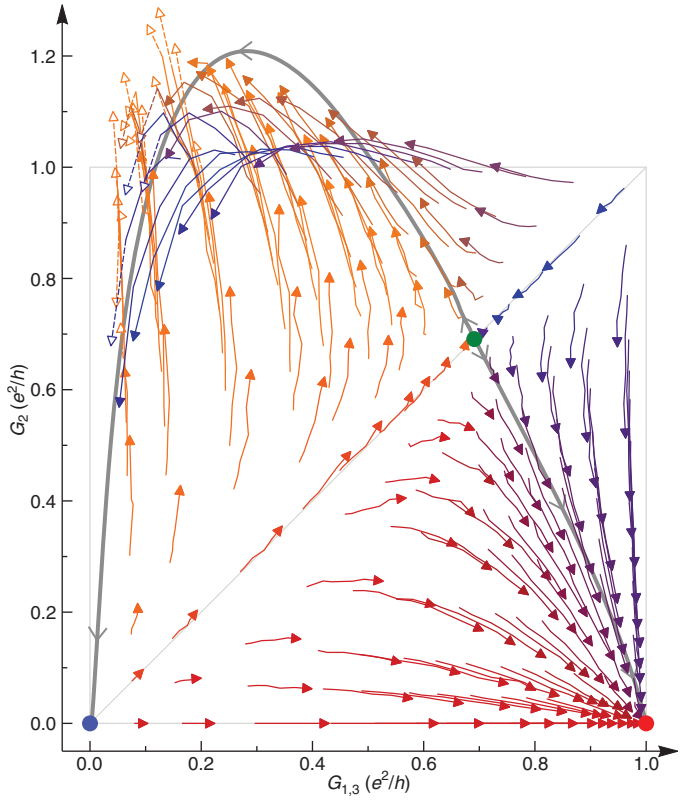

Fig. 6. Three-channel Kondo renormalization flow with super-ballistic conductances. Each colored line with an arrowhead displays the measured channels' conductance at T = 55, 40, 29, 18, 12, and 7.9 mK (arrowhead is shown at lowest T) for a fixed device tuning ($\tau_1 \approx \tau_3$, τ_2) at charge degeneracy ($\delta V_g = 0$). The lines' colors reflect the direction (the angle) of the vector connecting lowest- and highest-temperature data points, to improve readability. Because QPC_1 and QPC_3 are set symmetric [$\tau_1 \approx \tau_3$ tuned among 14 values from 0.1 to 0.985 (*32*)], only the renormalized average $G_{1,3}$ is shown on the horizontal axis. QPC_2 is separately adjusted to a coupling τ_2 selected among the same 14 values and also $\tau_2 = 0$. For the solid lines and solid arrows, the experimental standard error of G_2h/e^2 and $G_{1,3}h/e^2$ is below 0.05 (usually well below). For the dashed lines and open arrows, the standard error of G_2h/e^2 is between 0.05 and 0.1. The green, red, and blue disks correspond, respectively, to the predicted 3CK, 2CK, and 1CK low-temperature fixed points. The thick gray lines represent NRG calculations of the universal crossover flows from 3CK (*32*), with arrows pointing to lower temperatures. The conductance G_2 can markedly exceed the maximum free electron limit e^2/h.

Although experimental and NRG flows point to the same direction near 3CK and 1CK fixed points, clear crossings are also visible in intermediate regimes above the diagonal, including between different experimental device settings. These mostly take place between flows involving opposite renormalization directions of G_2, as expected from the nonmonotonous relationship between G_2 and Kondo coupling J_2 that specifically shows up above the diagonal.

Outlook

The observation of super-ballistic conductance opens a research path for low-power electronics. Although the present implementation has no clear application potential, it forms a powerful platform from which to understand the underlying mechanisms of behaviors that arise in diverse clean systems with strong electron-electron interactions. We anticipate that similar metal-semiconductor hybrids will form building blocks for a wide range of investigations of the strongly correlated electron physics, and in particular the emergence of exotic parafermion quasiparticles (*7*, *9*, *35*). Measurements of complementary observables—such as charge susceptibility, fluctuations, and heat current—as well as investigations of the dynamical and out-of-equilibrium responses could unveil yet hidden facets of the exotic underlying physics. Furthermore, direct generalizations of the present charge Kondo implementation should grant access to quantitative investigations of many thus-far-inaccessible strongly correlated phenomena (*16*, *39*), including the nanoengineered competition between Kondo channels, dissipation [specific proposal in (*40*)], fractional quantum Hall effect, and multiple impurities.

REFERENCES AND NOTES

1. S. Sachdev, *Quantum Phase Transitions* (Cambridge Univ. Press, 2011).
2. R. M. Potok, I. G. Rau, H. Shtrikman, Y. Oreg, D. Goldhaber-Gordon, *Nature* **446**, 167–171 (2007).
3. H. T. Mebrahtu *et al*., *Nature* **488**, 61–64 (2012).
4. H. Mebrahtu *et al*., *Nat. Phys.* **9**, 732–737 (2013).
5. A. J. Keller *et al*., *Nature* **526**, 237–240 (2015).
6. Z. Iftikhar *et al*., *Nature* **526**, 233–236 (2015).
7. V. J. Emery, S. Kivelson, *Phys. Rev. B Condens. Matter* **46**, 10812–10817 (1992).
8. P. Coleman, L. B. Ioffe, A. M. Tsvelik, *Phys. Rev. B Condens. Matter* **52**, 6611–6627 (1995).
9. I. Affleck, M. Oshikawa, H. Saleur, *Nucl. Phys. B* **594**, 535–606 (2001).
10. P. Nozières, A. Blandin, *J. Phys.* **41**, 193–211 (1980).
11. A. C. Hewson, *The Kondo Problem to Heavy Fermions* (Cambridge Univ. Press, 1997).
12. D. L. Cox, A. Zawadowski, *Adv. Phys.* **47**, 599–942 (1998).
13. I. Affleck, A. W. W. Ludwig, *Phys. Rev. B Condens. Matter* **48**, 7297–7321 (1993).
14. K. A. Matveev, *Phys. Rev. B Condens. Matter* **51**, 1743–1751 (1995).
15. M. Pustilnik, L. Borda, L. I. Glazman, J. von Delft, *Phys. Rev. B* **69**, 115316 (2004).
16. M. Vojta, *Philos. Mag.* **86**, 1807–1846 (2006).
17. R. Bulla, T. A. Costi, T. Pruschke, *Rev. Mod. Phys.* **80**, 395–450 (2008).
18. E. Sela, A. K. Mitchell, L. Fritz, *Phys. Rev. Lett.* **106**, 147202 (2011).
19. A. K. Mitchell, L. A. Landau, L. Fritz, E. Sela, *Phys. Rev. Lett.* **116**, 157202 (2016).
20. D. Goldhaber-Gordon *et al*., *Nature* **391**, 156–159 (1998).
21. S. M. Cronenwett, T. H. Oosterkamp, L. P. Kouwenhoven, *Science* **281**, 540–544 (1998).
22. J. Nygård, D. H. Cobden, P. E. Lindelof, *Nature* **408**, 342–346 (2000).
23. M. R. Buitelaar, A. Bachtold, T. Nussbaumer, M. Iqbal, C. Schönenberger, *Phys. Rev. Lett.* **88**, 156801 (2002).
24. L. I. Glazman, M. E. Raikh, *JETP Lett.* **47**, 452 (1988).
25. T. K. Ng, P. A. Lee, *Phys. Rev. Lett.* **61**, 1768–1771 (1988).
26. Y. Oreg, D. Goldhaber-Gordon, *Phys. Rev. Lett.* **90**, 136602 (2003).
27. S. Florens, P. Simon, S. Andergassen, D. Feinberg, *Phys. Rev. B* **75**, 155321 (2007).
28. K. A. Matveev, *Sov. Phys. JETP* **72**, 892 (1991).
29. A. Furusaki, K. A. Matveev, *Phys. Rev. B Condens. Matter* **52**, 16676–16695 (1995).
30. S. Jezouin *et al*., *Nature* **536**, 58–62 (2016).
31. E. Lebanon, A. Schiller, F. B. Anders, *Phys. Rev. B* **68**, 041311 (2003).
32. Materials and methods are available as supplementary materials.
33. Z. Iftikhar *et al*., *Nat. Commun.* **7**, 12908 (2016).
34. H. Yi, C. L. Kane, *Phys. Rev. B* **57**, R5579–R5582 (1998).
35. L. Landau, E. Cornfeld, E. Sela, Charge fractionalization in a Kondo device. *Phys. Rev. Lett.* **120**, 186801 (2018).
36. C. Kolf, J. Kroha, *Phys. Rev. B* **75**, 045129 (2007).
37. R. Krishna Kumar *et al*., *Nat. Phys.* **13**, 1182–1185 (2017).
38. H. Guo, E. Ilseven, G. Falkovich, L. S. Levitov, *Proc. Natl. Acad. Sci. U.S.A.* **114**, 3068–3073 (2017).
39. G. Kotliar, D. Vollhardt, *Phys. Today* **57**, 53–59 (2004).
40. K. Le Hur, *Phys. Rev. Lett.* **92**, 196804 (2004).

ACKNOWLEDGMENTS

We thank I. Affleck, S. Florens, L. Fritz, L. Glazman, C. Kane, K. Matveev, Y. Nazarov, E. Sela, G. Zarand, and F. Zhang for discussions. **Funding:** This work was supported by the French RENATECH network and the national French program "Investissements d'Avenir" (Labex NanoSaclay, ANR-10-LABX-0035). **Author contributions:** Z.I. and F.P. performed the experiment; Z.I., A.A., and F.P. analyzed the data; A.K.M. performed the NRG developments; C.M. and P.S. extended the analytical predictions; F.D.P. fabricated the sample with inputs from A.A.; U.G., A.C., and A.O. grew the 2DEG; and F.P. led the project and wrote the manuscript, with inputs from Z.I., A.A., A.K.M., U.G, C.M., and P.S. **Competing interests:** The authors declare no competing financial interests. **Data and materials availability:** The displayed experimental data are provided in a separate supplementary file (Data file S1). Correspondence and requests for materials should be addressed to F.P. (frederic.pierre@u-psud.fr).

SUPPLEMENTARY MATERIALS

www.sciencemag.org/content/360/6395/1315/suppl/DC1
Materials and Methods
Supplementary Text
Figs. S1 to S5
References (*41*–*52*)
Data File S1

1 May 2017; accepted 19 April 2018
Published online 3 May 2018
10.1126/science.aan5592

ALCOHOL DEPENDENCY

A molecular mechanism for choosing alcohol over an alternative reward

Eric Augier[1]*, Estelle Barbier[1], Russell S. Dulman[2], Valentina Licheri[3], Gaëlle Augier[1], Esi Domi[1], Riccardo Barchiesi[1], Sean Farris[4], Daniel Nätt[1], R. Dayne Mayfield[4], Louise Adermark[3], Markus Heilig[1]

Alcohol addiction leads to increased choice of alcohol over healthy rewards. We established an exclusive choice procedure in which ~15% of outbred rats chose alcohol over a high-value reward. These animals displayed addiction-like traits, including high motivation to obtain alcohol and pursuit of this drug despite adverse consequences. Expression of the γ-aminobutyric acid (GABA) transporter GAT-3 was selectively decreased within the amygdala of alcohol-choosing rats, whereas a knockdown of this transcript reversed choice preference of rats that originally chose a sweet solution over alcohol. GAT-3 expression was selectively decreased in the central amygdala of alcohol-dependent people compared to those who died of unrelated causes. Impaired GABA clearance within the amygdala contributes to alcohol addiction, appears to translate between species, and may offer targets for new pharmacotherapies for treating this disorder.

Alcohol use accounts for almost 5% of global disease burden (*1*), and the harm from alcohol use has been estimated to exceed that due to heroin or cocaine (*2*). Basic neuroscience has identified brain circuits and molecular mechanisms that contribute to drug and alcohol reward, craving, and relapse (*3*, *4*). These advances have, however, had limited impact on the treatment of addictive disorders, suggesting that research in model organisms needs to incorporate additional processes (*3*, *5*).

Once established, alcohol addiction—hereafter equated with alcoholism—is a chronic relapsing disorder in which alcohol use becomes compulsive, i.e., continues despite negative consequences (*6*). Understanding the transition from controlled to compulsive alcohol use is a critical challenge for addiction research. In humans, only a subset of users transition to compulsive drug use (*7*, *8*). In contrast, in commonly used animal models, nearly all rats learn to self-administer addictive drugs, including alcohol (*9*). This points to the possibility that focusing on self-administration may be insufficient to identify key mechanisms of addiction (*5*, *10*).

This realization has prompted important conceptual advances. When rats are allowed to self-administer cocaine over a prolonged period of time, only a minority of them develop compulsive drug taking (*11*, *12*). Furthermore, most rats will cease to self-administer cocaine when a high-value alternative becomes available, but a subset of animals continue self-administration despite the presence of an alternative (*13*, *14*). Indeed, in epidemiological studies, only a minority of exposed people develop addiction (*5*, *10*).

Here, we set out to identify molecular mechanisms underlying the choice of alcohol over a natural reward. We first established an exclusive choice-based method to identify rats that continue to self-administer alcohol at the expense of a high-value alternative, a sweet solution, and assessed whether these animals show other characteristics of clinical alcoholism (*15*). We then used gene expression profiling to identify a molecular mechanism that mediates compulsive alcohol drinking at the expense of other high-value options.

Intense sweetness outcompetes alcohol reward in most but not all rats

Sweetness is a fundamental reward that is highly conserved between humans and other animals (*16*). To tap into its value without the confound of caloric content, we used as alternative reward a solution of the noncaloric sweetener saccharin. In a first experiment (see fig. S1 for experimental timelines), rats (n = 32) were trained to self-administer 20% alcohol for about 10 weeks until reaching stable response rates on a fixed-ratio 3 (FR-3) reinforcement schedule (fig. S2, A and B). They were then offered daily sessions of mutually exclusive choice between alcohol and 0.04% saccharin (Fig. 1A). Overall, despite not having previously been trained to respond to saccharin, rats quickly started to choose more saccharin than alcohol (Fig. 1B). The percentage of choice for saccharin over alcohol became even higher when a more rewarding concentration of saccharin, 0.2%, was introduced (Fig. 1C, significant effect of the saccharin concentration: $F_{1,31}$ = 21.56, p < 0.0001, η^2 = 0.41).

Once operant responding had stabilized, the rats only chose alcohol over the alternative reward 26.2% of the time (Fig. 1C). However, although the vast majority of rats strongly preferred saccharin, a minority, 4 rats out of 32 in the first experiment (12.5% of the population, Fig. 1D, left) continued to choose alcohol despite having access to a high-value alternative (alcohol-preferring, AP). Although this was a small number, it aligns well with human addiction rates (*7*, *8*) and prompted us to expand the study of individual differences in choice behavior. Ultimately, this percentage was stable across a large number of rats from successive batches (see below; Fig. 1D, right). Alcohol preference was not influenced by holding prior history of alcohol and saccharin self-administration identical (fig. S3).

Extensive pre-exposure to saccharin does not affect subsequent alcohol choice

People who go on to develop addictive disorders have typically had extensive exposure to sweet reward prior to initiating alcohol use. We therefore tested whether this kind of preexposure would affect subsequent alcohol choice. A separate group of rats was offered the opportunity to drink a 0.2% saccharin solution or water (experiment 2, n = 32 per group) in their home cage for 4 weeks, before operant training was initiated. Rats that had access to the sweet solution consumed extensive amounts of saccharin during the first week of exposure (101.6 ± 6.8 ml/day) and maintained this consumption throughout their 4 weeks of exposure (week 4: 89.8 ± 5.4 ml/day; fig. S4A). There was no significant difference in acquisition of alcohol self-administration between saccharin- and water-preexposed animals (fig. S4B, no main effect of group: saccharin versus water, $F_{1,61}$ = 0.13, p = 0.72; main effect of sessions, $F_{29,1769}$ = 5.28, p < 0.001; η^2 = 0.08 but no interaction between group and sessions: $F_{29,1769}$ = 0.98, p = 0.48). Extensive preexposure to saccharin also left acquisition of the choice procedure unaffected (fig. S4C, no main effect of group: saccharin versus water, $F_{1,57}$ = 0.40, p = 0.53; main effect of sessions, $F_{18,1026}$ = 7.82, p <0.001; η^2 = 0.12 but no interaction between group and sessions: $F_{18,1026}$ = 1.00, p = 0.45).

Once responding had stabilized, both groups strongly favored the sweet solution (22.3 ± 3.8% alcohol choice for the saccharin-exposed group versus 20.6 ± 4.0% for the water-exposed group; fig. S4D, no main effect of group: saccharin versus water, $F_{1,61}$ = 0.32, p = 0.57). Again, a subpopulation of animals chose alcohol over saccharin (fig. S4E, n = 3 in each group). Extensive preexposure to the sweet solution did not affect sampling (fig. S4F) or completed trials ($F_{1,61}$ = 0.56, p = 0.46). Thus, the alcohol choice observed in experiment 1 was not sensitive to the individual's prior history of sweet-reward exposure.

Finally, we investigated whether AP rats would persist in working for alcohol if the alternative reward was readily available. We used a modified choice paradigm in which rats had continuous access to both sources of reinforcement and found that AP rats maintained a strong preference for alcohol despite the concurrent availability of saccharin throughout five consecutive sessions (fig. S5).

[1]Center for Social and Affective Neuroscience, IKE, Linköping University, Linköping, 581 83, Sweden. [2]Center for Alcohol Research in Epigenetics, Department of Psychiatry, University of Illinois, Chicago, IL 60612, USA. [3]Department of Psychiatry and Neurochemistry, Sahlgrenska Academy, University of Göteborg, 413 90 Göteborg, Sweden. [4]The Waggoner Center for Alcohol and Addiction Research, University of Texas, Austin, TX 78712, USA.
*Corresponding author. Email: eric.augier@liu.se

Alcohol-choosing rats show addiction-like behaviors

Owing the low frequency of the AP phenotype, we repeated the first experiment on several batches of rats and screened them for preference during the choice procedure before carrying out further behavioral testing (Fig. 1D, right). We then characterized the subpopulation of animals that chose alcohol over saccharin with regard to addiction-like behaviors (experiments 3 and 4) and compared them to the much larger subpopulation of rats that stopped working for alcohol when an alternative high-value option was available (saccharin-preferring, SP). Only 95 rats out of 620 tested on the choice procedure continued to choose alcohol despite having access to a high-value alternative (15.3% of the population).

We first assessed the motivation of AP and SP rats to obtain and consume alcohol or saccharin using a progressive ratio reinforcement schedule (*17*). AP rats showed a higher motivation to obtain alcohol than SP rats (Fig. 1E, left bars), whereas the motivation to obtain saccharin did not statistically differ between the two groups (Fig. 1E, right bars; interaction between group (AP versus SP) × reinforcer (alcohol versus saccharin; $F_{1,90} = 31.13$, $p < 0.0001$; $\eta^2 = 0.26$; post hoc comparison AP versus SP rats for alcohol $p < 0.0001$, AP versus SP rats for saccharin $p = 0.33$).

We then investigated whether AP rats would maintain their alcohol drinking despite negative consequences: quinine adulteration or footshock punishment. AP rats showed a robust resistance to quinine adulteration (Fig. 1F, main effect of group, $F_{1,40} = 4.48$, $p < 0.05$; $\eta^2 = 0.10$). Their choice behavior remained unaffected even when alcohol was adulterated with a highly aversive concentration of quinine, 200 mg/liter. There was no statistical difference in the preference score for quinine alone when separately tested against water ($F_{1,40} = 0.09$, $p = 0.77$; fig. S6A), indicating that the resistance to quinine adulteration in AP rats was not due to an altered sensitivity to the quinine taste. Additionally, there was no statistical difference in preference score for a 0.2% solution of saccharin ($F_{1,40} = 0.51$, $p = 0.48$) or 20% ethanol ($F_{1,24} = 0.48$, $p = 0.49$),

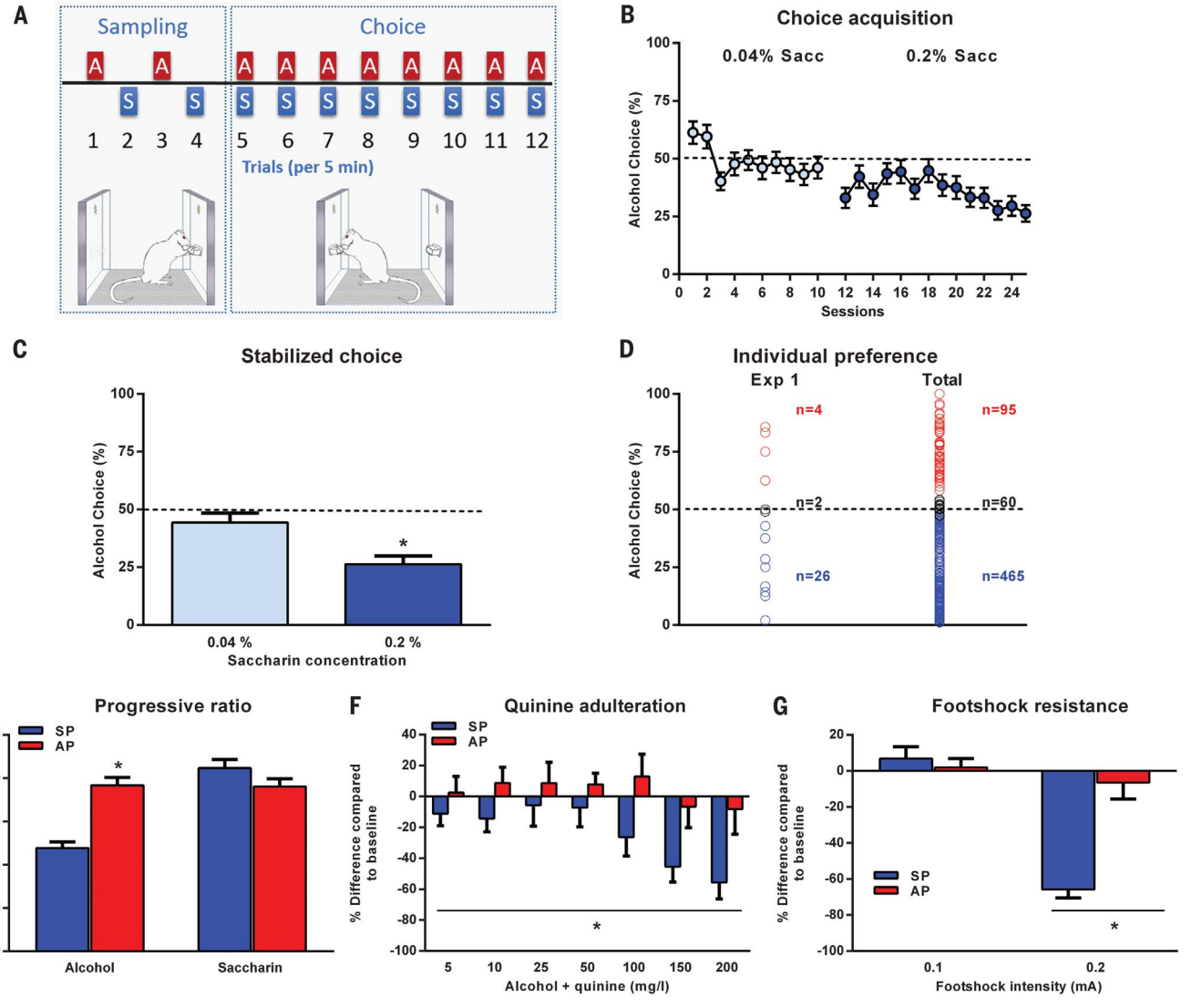

Fig. 1. Addiction-like behaviors in rats that choose alcohol over a high-value alternative reward. (**A**) Schematic representation of the discrete choice procedure. (**B**) Percentage alcohol choice (±SEM) during acquisition ($n = 32$). (**C**) Stabilized percentage alcohol choice (±SEM; $n = 32$) (**D**) Individual distribution. (**E**) Selectively elevated motivation to obtain alcohol but not saccharin in alcohol-choosing rats [mean breakpoint ± SEM during separate sessions of progressive ratio responding for 20% EtOH (left bars) or 0.2% saccharin (right bars; $n = 53$ for SP rats, 39 for AP rats)]. (**F**) Compulsive alcohol drinking in alcohol-choosing rats, shown by resistance to quinine adulteration of the alcohol solution (percentage change ± SEM in quinine-adulterated alcohol drinking; $n = 28$ for SP rats, 14 for AP rats). (**G**) Compulsive alcohol drinking, shown by resistance to footshock (percentage change ± SEM in footshock-punished alcohol self-administration; $n = 66$ for SP rats, 41 for AP rats).

indicating that alcohol preference during choice could not be explained by preexisting individual differences in preference for the taste of saccharin or alcohol.

Consistent with the quinine adulteration experiment, AP, but not SP, rats also maintained their responding for alcohol when drug delivery was paired with a contingent footshock punishment, (*18*) {Fig. 1G; Kruskal-Wallis nonparametric analysis of variance, significant group effect: [$H(3,218) = 73.7$, $p < 0.001$]; significant difference between AP and SP rats at 0.2 mA ($p < 0.001$), but not at 0.1 mA ($p = 1$)}. This was not caused by any difference in pain sensitivity between AP and SP rats (fig. S6B). Shock-resistant alcohol consumption in this procedure per se could potentially be explained by complex processes such as counterconditioning or latent inhibition (*19*). However, because of the strong correlation of shock resistance with alcohol choice and also with resistance to quinine adulteration, we believe that such a mechanism is less likely. Instead, the most parsimonious explanation appears to be that increased appetitive motivation of AP rats for alcohol allows them to overcome the aversion to footshock punishment.

Together, these results show that AP rats display a constellation of behavioral traits that resemble those considered diagnostic for addiction (*15*): (i) The user gives up valuable social and recreational activities because of substance use, here modeled by an increase in choice of alcohol over the high-value alternative reward, saccharin; (ii) the user shows an increased motivation to obtain and take the drug, spending excessive time and effort on its procurement and consumption, here modeled using an elevated breakpoint on a progressive-ratio schedule (*11*, *17*); and (iii) the user continues drug use despite its harmful and negative consequences, here modeled using continued alcohol self-administration despite quinine adulteration or delivery of a shock punishment contingent with drug delivery (*11*, *12*). Notably, the difference in total alcohol exposure during self-administration training and choice was minimal (fig. S7), making it unlikely that addiction-like behavior in AP rats resulted from alcohol exposure per se.

Locomotor reactivity to novelty does not predict alcohol choice

Because locomotor reactivity to a novel environment predicts aspects of cocaine seeking and taking (*20*, *21*), we investigated whether this behavioral marker would also be associated with alcohol choice and other alcohol-related behaviors (experiment 5). We found that neither alcohol self-administration nor alcohol choice was associated with reactivity to novelty (figs. S8 and S9); nor was reactivity to novelty associated with anxiety-like behaviors (fig. S10).

The GABA transporter GAT-3 is down-regulated in the amygdala of AP rats

To identify molecular substrates of alcohol choice, we carried out a gene expression screen in several brain regions thought to be involved in alcohol-taking behaviors in rodent models (*22*) (experiment 6). We used a custom Nanostring nCounter array that contains probes targeting 310 transcripts previously hypothesized to be involved in drug addiction (*23*, *24*). Using this highly sensitive and quantitative tool, we compared gene expression of AP and SP rats ($n = 7$ to 8 per group) in tissue punches from the nucleus accumbens (NAcc), caudate-putamen (CPU), prelimbic prefrontal cortex (PRL), infralimbic prefrontal cortex (IL), hippocampus (HIPP), and amygdala (AMG). This analysis found the highest number of significant changes in gene expression within the amygdala (Fig. 2A), with relatively few genes differentially expressed in the other five regions studied.

Pathway analysis showed that several genes implicated in γ-aminobutyric acid (GABA)–mediated transmission were expressed at significantly lower levels in the amygdala of AP rats (Fig. 2B and table S1). In particular, the expression of the GABA transporter GAT-3 (*Slc6a11*) was decreased. The mammalian genome contains four genes that encode high-affinity GABA transporters (GAT-1, *Slc6a1*; GAT-2, *Slc6a13*; GAT-3, *Slc6a11*; and BGT-1, *Slc6a12*) (*25*, *26*). GABA transporters are sodium- and chloride-dependent members of the solute carrier family 6 (Slc6) and mediate rapid clearance of GABA to maintain low extracellular GABA concentrations (*27*). These transporters are therefore likely to play an important role in controlling the actions of GABA, the principal inhibitory neurotransmitter of the brain (*28*).

Using quantitative polymerase chain reaction (qPCR), we confirmed the differential expression of GAT-3 detected by the Nanostring analysis. Because the three other genes of the GABA transporter family were not represented on our Nanostring panel, we assessed their expression using qPCR and found that GAT-1 and BGT-1 were also significantly down-regulated in the amygdala of AP rats; there was also a trend for lower GAT-2 expression (Fig. 2C). We used qPCR to

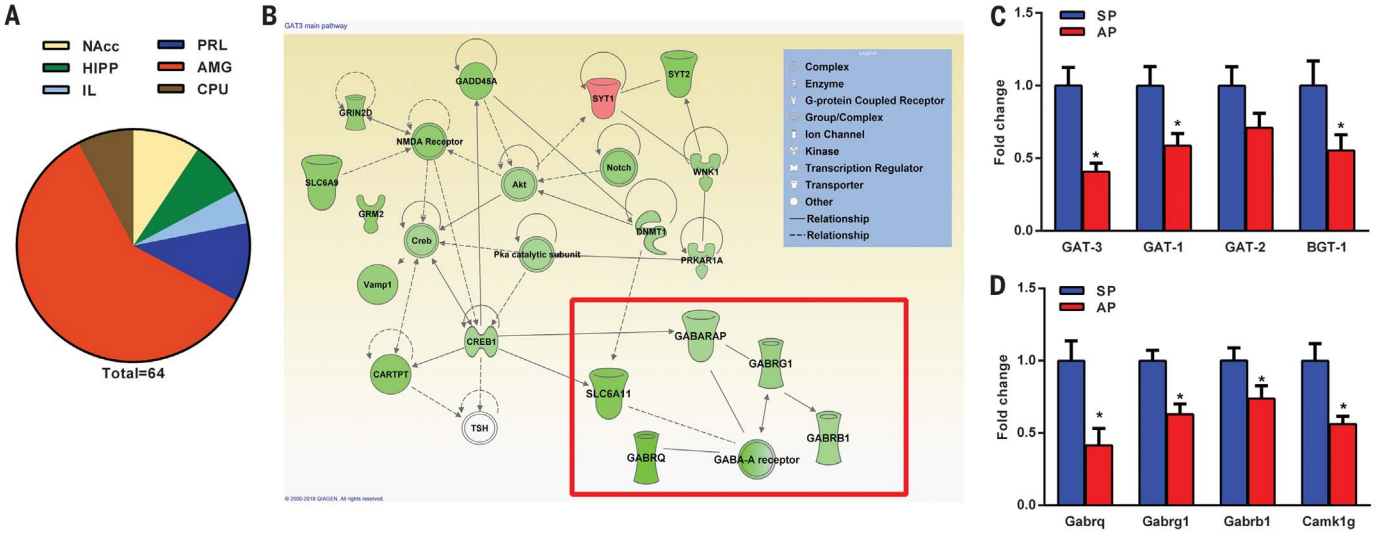

Fig. 2. The GABA transporter GAT-3 is down-regulated in the amygdala of AP rats. (**A**) A gene expression screen points to the amygdala (AMG) as a region of most prominent differential gene expression between AP and SP rats [other regions analyzed: nucleus accumbens (NAcc), caudate putamen (CPU), prelimbic prefrontal cortex (PRL), infralimbic prefrontal cortex (IL), and hippocampus (HIPP)]. (**B**) Pathway analysis shows that a gene network comprising several genes involved in GABAergic transmission is down-regulated in the amygdala of AP rats (green color indicates down-regulation in AP rats, whereas red color indicates up-regulation). (**C**) mRNA expression of GAT-3 and other GABA transporters is decreased in the amygdala of AP rats ($n = 7$ to 8 per group). (**D**) mRNA expression of several other genes involved in GABAergic transmission is decreased in the amygdala of AP rats ($n = 7$ to 8 per group).

confirm the down-regulation of additional genes involved in GABA-mediated transmission identified by the Nanostring screen. The expression of genes encoding several $GABA_A$ receptors subunits, *Gabrq*, *Gabrg1*, *Gabrb1*, was also lower in AP rats, presumably reflecting adaptations to an increased GABA tone due to down-regulated expression of transporters that clear extracellular GABA (Fig. 2D; for detailed statistics, see table S2). Results of the Nanostring and qPCR analyses were highly correlated (fig. S11). Thus, up-regulated GABA-mediated transmission in the amygdala represents a candidate mechanism for mediating alcohol choice, which is in agreement with and expands on prior work (*29*, *30*).

In further support of a role for GAT-3 in preclinical models of dependence, this transcript was also selectively down-regulated in the amygdala of the Indiana alcohol preferring rats P-rats (compared to their nonpreferring counterpart; $p < 0.01$, fig. S12). This strain has been selectively bred from Wistar rats for high alcohol drinking and has been proposed to model aspects of human alcoholism (*31*, *32*).

AP rats show increased tonic inhibition in central amygdala (CeA)

To establish whether decreased expression of GAT-3 results in an increased GABA tone in the amygdala of AP rats, we performed slice electrophysiology experiments (experiment 7). Field potential recordings revealed a significantly greater synaptic output from the CeA in AP rats compared to brain slices from SP rats (main effect of group: AP versus SP: $F_{1,34} = 17$, $p < 0.01$) (Fig. 3A). There was no group effect on neurotransmitter release probability, as assessed by paired pulse stimulation (Fig. 3B; SP versus AP: $t_{29} = 0.83$, $p > 0.05$). Disinhibition induced by the $GABA_A$ receptor antagonist bicuculline (20 μM) was significantly greater in slices from AP rats, indicating an enhanced GABA tone (AP versus SP: $F_{(1,23)} = 6.03$, $p < 0.05$) (Fig. 3C). These data provide consistent support for an increased tonic inhibition caused by elevated levels of extracellular GABA in AP rats, similar to that seen after induction of alcohol dependence (*30*). Because GABA-mediated transmission in the amygdala is believed to play an important role in the modulation of anxiety responses (*33*–*35*), we also assessed anxiety-like behaviors of AP and SP rats using the elevated plus-maze (*36*, *37*). In agreement with our electrophysiology findings, we observed higher anxiety-like behavior in AP rats (fig. S13).

GAT-3 knockdown in the CeA mimics the increased tonic inhibition of AP rats

We next examined whether the functional consequences of GAT-3 down-regulation in AP rats at a synaptic level could be mimicked using a viral knock-down (KD) approach. We injected rats with a short hairpin–mediated RNA (shRNA) adeno-associated virus (AAV) vector targeting *Slc6a11* in the amygdala (see fig. S14 for in vitro validation of the construct), and performed ex vivo electrophysiology in amygdala slices to assess the resulting changes in GABA-mediated neurotransmission. In agreement with our findings in AP rats, we observed a significantly greater synaptic output from the CeA in GAT-3 KD rats compared to brain slices from rats injected with the scrambled control vector (Fig. 3D; GAT-3 KD versus Scrambled: $F_{(1,40)} = 19$, $p < 0.001$). Again, there was no group effect on neurotransmitter release probability, as assessed by paired pulse stimulation (Fig. 3E; GAT-3 KD versus Scrambled: $t_{57} = 0.44$, $p > 0.05$); whereas disinhibition induced by the $GABA_A$ receptor antagonist bicuculline (20 μM) was significantly greater in slices from GAT-3 KD rats, indicative of an enhanced GABA tone (Fig. 3F; GAT-3 KD versus scrambled versus: $F_{(1,26)} = 7.70$, $p < 0.05$). Whole-cell recordings revealed no effect of GAT-3 KD on recorded spontaneous (sIPSCs) or miniature (mIPSCs) inhibitory postsynaptic currents, indicating that baseline activity of GABA-releasing neurons is unaltered (fig. S15, A to D). In contrast, there was no significant effect of bicuculline administration in the basolateral amygdala (main effect of group: $F_{1,19} = 1.43$, $p = 0.25$; main effect of time: $F_{15,285} = 4.82$, $p < 0.0001$; group × time interaction: $F_{15,285} = 0.35$, $p = 0.99$; fig. S15I). These results show that a KD of GAT-3 mimics the increased GABA tone in the CeA of AP rats.

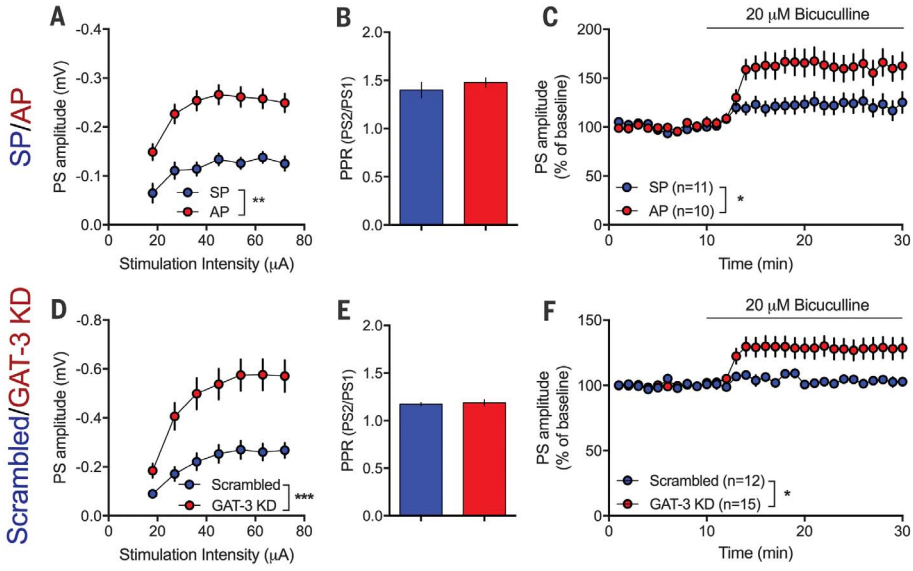

Fig. 3. Enhanced inhibitory tone in the CeA of AP rats, replicated by an shRNA knockdown of the GAT-3 transporter in SP rats. (**A** and **B**) Electrophysiological field potential recordings revealed an altered input/output function in AP rats as compared to SP rats, with no corresponding change in paired pulse ratio (PPR), indicative of postsynaptic alterations. (**C**) In addition, disinhibition resulting from administration of the $GABA_A$ receptor antagonist bicuculline was significantly enhanced in brain slices from AP rats. (**D** to **F**) The electrophysiological phenotype of AP rats was replicated by down-regulation of the GAT-3 transporter. Data are mean ± SEM. *n* = number of recordings, taken from at least five rats per treatment group.

A causal role of GAT-3 in amygdala for alcohol choice behavior

To establish a causal role of GAT-3 for alcohol choice, we injected a separate group of SP animals (experiment 8, $n = 31$) with the shRNA AAV vector targeting *Slc6a11* in the amygdala (fig. S16) and examined the consequences of down-regulated GAT-3 expression on choice between alcohol and the alternative high-value saccharin reward. Fluorescent in situ hybridization using RNAscope confirmed that *Slc6a11* was down-regulated in the CeA of GAT-3 KD animals compared to scrambled controls (Fig. 4, A and B; Mann-Whitney U = 1, two-sided exact $p = 0.009$). Using mass spectrometry (fig. S17), we also found that the knockdown of the *Slc6a11* transcript resulted in a significant decrease of the transporter protein (Fig. 4C; *t* test followed by a Benjamini-Hochberg multiple testing correction, $p < 0.001$).

We tested the effects of GAT-3 KD in the amygdala of rats preselected for high (~75% of baseline) levels of saccharin choice. In the first postsurgical week, we observed an initial increase of alcohol choice that was nonspecific, but behavior of control vector-injected animals returned to baseline within a week and remained at this level throughout the experiment. In contrast, beginning during week 2, we observed a shift of choice behavior toward alcohol in GAT-3 KD animals. This shift increased during week 3, coinciding with full expression of the shRNA vector, and was maintained for the remainder of the sessions (Fig. 4D, main effect of group, $F_{1,27} = 11.02$, $p < 0.01$; $\eta^2 = 0.29$; interaction between group and sessions, $F_{14,378} = 2.01$, $p < 0.05$; $\eta^2 = 0.07$). Once behavior was stable, the preference of GAT-3 KD animals was reversed, and they chose significantly more alcohol compared to control vector-treated animals (Fig. 4E, 47.1% alcohol choice versus 18.9%, $F_{1,27} = 18.71$,

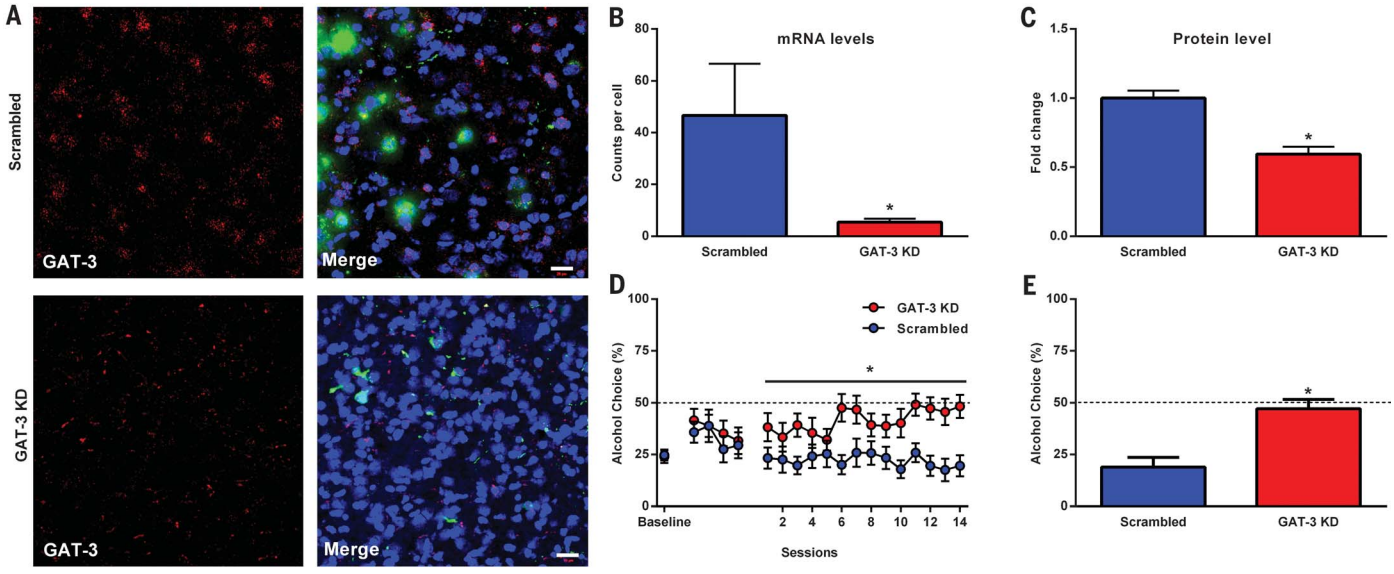

Fig. 4. shRNA knockdown of GAT-3 replicates alcohol-choice behavior. (**A**) Expression of *Slc6a11* (GAT-3) in the rat central amygdala measured by RNAscope. Red dots show the expression of *Slc6a11* (GAT-3). Blue labeling represents DAPI (4′,6-diamidino-2-phenylindole) staining, and green labeling confirms virus injection. (**B**) *Slc6a11* (GAT-3) mRNA levels after a viral-mediated knockdown (n = 5 to 6 per group). (**C**) Fold change in GAT-3 protein levels measured by mass spectrometry (n = 7 to 8 per group). (**D**) Percentage alcohol choice during acquisition. (**E**) Stabilized percentage alcohol choice (mean ± SEM) (n = 14 to 15 per group).

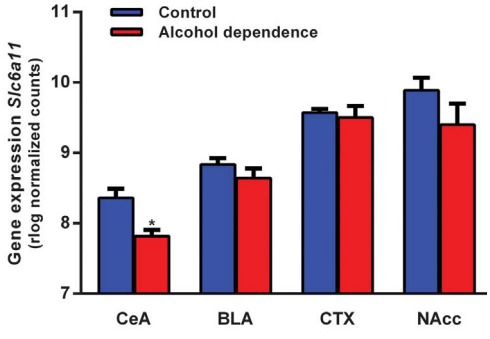

Fig. 5. GAT-3 is selectively down-regulated in the CeA of postmortem brains from individuals with confirmed alcohol dependence. Normalized read counts were extracted from an RNA-sequencing experiment of postmortem human brain samples. P values indicate a generalized linear model, with alcohol dependence as main factor, while simultaneously controlling for sex, ethnicity, smoking, and age. CeA, central nucleus of amygdala; BLA, basolateral amygdala; CTX, cortex; NAcc, nucleus accumbens. n = 29 for controls, 9 for alcohol-dependent individuals.

$p < 0.001$; $\eta^2 = 0.41$). GAT-3 down-regulation did not affect control behaviors (fig. S18). Thus, decreased expression of GAT-3 in the amygdala is sufficient to promote choice of alcohol at the expense of a high-value alternative. This effect of GAT-3 KD was specific for choice behavior and was achieved in the absence of effects on alcohol- or saccharin self-administration (experiment 9, fig. S20).

GAT-3 is specifically down-regulated in the CeA of alcohol-dependent people

Finally, we examined the potential translational validity of our findings. To do so, we carried out RNA sequencing of postmortem tissue samples from deceased human subjects with and without alcohol dependence (*38*). After correcting for common confounders such as age and smoking (table S3), patients with confirmed alcohol dependence showed down-regulation of GAT-3 in the CeA compared to controls (generalized linear model, p <0.01), but not in other brain regions (Fig. 5).

Concluding remarks

We developed a procedure in which rats are allowed a mutually exclusive choice between alcohol and a high-value alternative, a highly rewarding concentration of the noncaloric sweetener saccharin. Using this procedure, we found that the vast majority of outbred rats stopped responding to alcohol when offered the opportunity to access the high-value alternative reward. However, a subpopulation continued to choose alcohol despite the presence of the alternative. The frequency of this population was stable in multiple batches of animals, as confirmed by screening a total of 620 rats on the choice procedure.

Rats that chose alcohol over the high-value alternative displayed addiction-like behaviors, increased motivation to obtain alcohol, and continued use despite adverse consequences. These traits mimic key clinical diagnostic criteria for alcoholism. Furthermore, the percentage of AP rats (15.3%) is similar to human alcoholism rates (*7*, *8*).

The addiction-like phenotype in rats was associated with decreased expression of the GABA transporter GAT-3 in the amygdala, accompanied by down-regulation of several $GABA_A$ receptor subunit transcripts. The latter observation presumably reflects increased GABA tone due to lower clearance of extracellular GABA. Accordingly, AP rats showed increased GABA-mediated inhibition in the CeA in slice electrophysiology experiments. A viral-vector–mediated knockdown of *Slc6a11* mimicked this effect at the synaptic level and converted SP rats into AP rats in vivo. The latter finding demonstrates a causal role of *Slc6a11* for alcohol choice. Thus, increased GABAergic tone in the CeA due to reduced GABA uptake by GAT-3 transporters contributes to behaviors that are key for alcohol addiction.

Our findings are convergent with prior reports of increased GABA tone in CeA as a result of alcohol dependence and with results in which $GABA_A$ receptor agonists administered into CeA promote, whereas antagonists inhibit, alcohol self-administration (*29*, *30*). Our data provide strong support for a causal contribution of neuroadaptations affecting GABA signaling within the amygdala to the development of alcohol addiction. Furthermore, our findings suggest that preexisting differences in GABAergic gene expression in the CeA may also influence susceptibility to developing alcohol addiction. Collectively, these experiments identify impaired GABA clearance within CeA as a molecular mechanism that contributes to behavioral traits central to alcohol addiction.

REFERENCES AND NOTES

1. H. A. Whiteford *et al*., *Lancet* **382**, 1575–1586 (2013).
2. D. J. Nutt, L. A. King, L. D. Phillips; Independent Scientific Committee on Drugs, *Lancet* **376**, 1558–1565 (2010).
3. M. Heilig, D. H. Epstein, M. A. Nader, Y. Shaham, *Nat. Rev. Neurosci.* **17**, 592–599 (2016).
4. M. Heilig, W. H. Sommer, R. Spanagel, *Curr. Top. Behav. Neurosci.* **28**, 151–171 (2016).
5. S. H. Ahmed, *Neurosci. Biobehav. Rev.* **35**, 172–184 (2010).
6. F. A. Wagner, J. C. Anthony, *Neuropsychopharmacology* **26**, 479–488 (2002).
7. J. C. Anthony, in *Neuropsychopharmacology: The Fifth Generation of Progress*, K. L. Davis, D. Charney, J. T. Coyle, C. Nemeroff, Eds. (Lippincott Williams and Wilkins, Philadelphia, PA, 2002), chap. 109, pp. 1557–1573.
8. B. F. Grant *et al*., *JAMA Psychiatry* **72**, 757–766 (2015).
9. J. R. Weeks, *Science* **138**, 143–144 (1962).
10. T. E. Robinson, *Science* **305**, 951–953 (2004).
11. V. Deroche-Gamonet, D. Belin, P. V. Piazza, *Science* **305**, 1014–1017 (2004).
12. L. J. Vanderschuren, B. J. Everitt, *Science* **305**, 1017–1019 (2004).
13. M. Lenoir, F. Serre, L. Cantin, S. H. Ahmed, *PLOS ONE* **2**, e698 (2007).
14. L. Cantin *et al*., *PLOS ONE* **5**, e11592 (2010).
15. *Diagnostic and Statistical Manual of Mental Disorders* (American Psychiatric Association, Washington, DC, ed. 5, 2013).
16. K. C. Berridge, M. L. Kringelbach, *Psychopharmacology (Berl.)* **199**, 457–480 (2008).
17. W. Hodos, *Science* **134**, 943–944 (1961).
18. T. Seif *et al*., *Nat. Neurosci.* **16**, 1094–1100 (2013).
19. A. Dickinson, J. M. Pearce, *Psychol. Bull.* **84**, 690–711 (1977).
20. P. V. Piazza, J. M. Deminière, M. Le Moal, H. Simon, *Science* **245**, 1511–1513 (1989).
21. D. Belin, A. C. Mar, J. W. Dalley, T. W. Robbins, B. J. Everitt, *Science* **320**, 1352–1355 (2008).
22. R. Spanagel, *Physiol. Rev.* **89**, 649–705 (2009).
23. E. Barbier *et al*., *Mol. Psychiatry* **22**, 1746–1758 (2017).
24. G. K. Geiss *et al*., *Nat. Biotechnol.* **26**, 317–325 (2008).
25. J. Guastella *et al*., *Science* **249**, 1303–1306 (1990).
26. Q. R. Liu, B. López-Corcuera, S. Mandiyan, H. Nelson, N. Nelson, *J. Biol. Chem.* **268**, 2106–2112 (1993) [corrected].
27. F. Conti, A. Minelli, M. Melone, *Brain Res. Brain Res. Rev.* **45**, 196–212 (2004).
28. J. Bormann, *Trends Pharmacol. Sci.* **21**, 16–19 (2000).
29. N. W. Gilpin, M. A. Herman, M. Roberto, *Biol. Psychiatry* **77**, 859–869 (2015).
30. M. Roberto, S. G. Madamba, D. G. Stouffer, L. H. Parsons, G. R. Siggins, *J. Neurosci.* **24**, 10159–10166 (2004).
31. T. K. Li, L. Lumeng, W. J. McBride, M. B. Waller, J. M. Murphy, *NIDA Res. Monogr.* **66**, 41–49 (1986).
32. W. J. McBride, T. K. Li, *Crit. Rev. Neurobiol.* **12**, 339–369 (1998).
33. P. Botta *et al*., *Nat. Neurosci.* **18**, 1493–1500 (2015).
34. K. M. Tye *et al*., *Nature* **471**, 358–362 (2011).
35. P. Nuss, *Neuropsychiatr. Dis. Treat.* **11**, 165–175 (2015).
36. S. Pellow, P. Chopin, S. E. File, M. Briley, *J. Neurosci. Methods* **14**, 149–167 (1985).
37. S. L. Handley, S. Mithani, *Naunyn Schmiedebergs Arch. Pharmacol.* **327**, 1–5 (1984).
38. A. S. Warden, R. D. Mayfield, *Neuropharmacology* **122**, 161–174 (2017).

ACKNOWLEDGMENTS

We thank Y. Shaham, G. McNally, P.-V. Piazza, and M. Roberto for valuable comments. **Funding:** This work was supported by the Swedish Research Council (grant 2013-7434 to M.H.). L.A. was supported by the Stiftelsen Psykiatriska Forskningsfonden. **Author contributions:** E.A. and M.H. jointly conceptualized and designed the studies. E.A. designed and supervised experiments and analyzed and interpreted results. E.A., R.S.D., and G.A. performed the behavioral experiments. E.A., E.B., R.S.D., G.A., E.D., and R.B. performed the molecular analyses. E.B., G.A., and E.D. performed surgeries. L.A. and V.L. performed electrophysiological recordings. L.A. supervised electrophysiological experiments and assisted in manuscript preparation. S.F. and R.D.M. provided Illumina Sequencing data for the human postmortem analysis. D.N. performed bioinformatics analysis. E.A. and M.H. drafted the manuscript. All authors have read and approved the manuscript. **Competing interests:** The authors report no biomedical financial interests or potential conflicts of interest. **Data and materials availability:** All data are available in the main text or the supplementary materials.

SUPPLEMENTARY MATERIALS

www.sciencemag.org/content/360/6395/1321/suppl/DC1
Materials and Methods
Figs. S1 to S20
Tables S1 to S3
References (*39*–*54*)

20 June 2017; resubmitted 28 February 2018
Accepted 1 May 2018
10.1126/science.aao1157

ATTOSECOND DYNAMICS

Orientation-dependent stereo Wigner time delay and electron localization in a small molecule

J. Vos[1]*, L. Cattaneo[1], S. Patchkovskii[2], T. Zimmermann[3,4], C. Cirelli[1,5], M. Lucchini[1]†, A. Kheifets[6], A. S. Landsman[3,4], U. Keller[1]

Attosecond metrology of atoms has accessed the time scale of the most fundamental processes in quantum mechanics. Transferring the time-resolved photoelectric effect from atoms to molecules considerably increases experimental and theoretical challenges. Here we show that orientation- and energy-resolved measurements characterize the molecular stereo Wigner time delay. This observable provides direct information on the localization of the excited electron wave packet within the molecular potential. Furthermore, we demonstrate that photoelectrons resulting from the dissociative ionization process of the CO molecule are preferentially emitted from the carbon end for dissociative $^2\Sigma$ states and from the center and oxygen end for the $^2\Pi$ states of the molecular ion. Supported by comprehensive theoretical calculations, this work constitutes a complete spatially and temporally resolved reconstruction of the molecular photoelectric effect.

Attosecond metrology has characterized the dynamics of fundamental processes in quantum mechanics, such as the photoelectric effect in atoms. Streaking experiments and RABBITT (reconstruction of attosecond beating by interference of two-photon transitions) (*1*–*4*) have provided information on the timing of the photoionization process, known as Wigner time (τ_W) (*5*), defined as the energy derivative of the scattering phase ϕ_W of the electron wave packet (EWP) receding in the field of the ion: $\tau_W = \hbar \frac{\partial \phi_W}{\partial E}$, where $\hbar$ is Planck's constant h divided by 2π and E is energy. As the Wigner time delay, by its nature, is referenced to a freely propagating electron, it retrieves a photoionization time delay determined by the target-specific parameters of the scattering center (*5*).

At present, most photoionization time delay experiments have been performed on atomic targets [see (*6*) for a detailed review]. The experimental (*7*–*10*) and theoretical (*11*–*14*) study of molecular photoionization time delays, on the other hand, remains challenging because of the complexity of these targets. The congestion of electronic states accessible in the ionization process leads to many contributing channels of the same final energy, resulting in a multiplexed photoelectron (PE) spectrum. Additionally, molecules present a bond length–dependent spatial distribution of electron density in combination with a highly anisotropic potential landscape. This raises new questions about the angular dependence of the photoionization time delays in molecules (*11*, *15*) and the localization of the ionizing electron within the molecule (*16*, *17*). Recently, it has been shown that atomic photoionization time delays present a substantial angular dependence (*18*, *19*), and a more complex angular dependence is expected for molecules because of the lower degree of symmetry. Up to now, such questions associated with molecular targets remained unanswered because of the relative paucity of molecular photoionization time delay measurements.

Extending attosecond metrology measurements to the molecular domain involves considerable experimental and theoretical challenges. Here we show that molecular attosecond measurements provide access not only to the orientation- and energy-dependent photoionization time delays but also to the mean position of the ionization within the molecular potential of the diatomic carbon monoxide (CO) molecule. We thereby give a complete description of the molecular photoionization dynamics.

A quantity specific to molecular ionization processes, the stereo Wigner time delay (SWTD) τ_{SW} (*20*), presents a photoionization time delay that varies depending on the location within the molecular frame from which the EWP escapes.

$$\tau_{SW} = \tau_W(\text{carbon side}) - \tau_W(\text{oxygen side}) \quad (1)$$

Photoionization of the inner valence states of the CO molecule has been extensively studied in the past (*21*–*23*). In contrast to the isoelectronic, homonuclear N_2 molecule, the CO molecule is expected to show an SWTD caused by the asymmetry of the molecule's nuclear constituents. This symmetry breaking provides access to a complementary observable in addition to the traditional Wigner time delay, commonly extracted from attosecond pump-probe experiments. Although the Wigner time delay is specific to the molecular potential landscape, the self-referenced SWTD can be used to follow intramolecular photoionization dynamics on the attosecond time scale.

Identification of photoionization and dissociation channels

We ionized a supersonically expanded cold jet of CO molecules and detected the angle-resolved momenta of the (fragment) ions and electrons by using the cold target recoil ion momentum spectroscopy (COLTRIMS) (*24*, *25*) apparatus [see supplementary materials (SM) for details]. Photoionization dynamics were resolved by the interferometric pump-probe RABBITT technique (*26*, *27*), with attosecond extreme ultraviolet (XUV) pump pulses produced by high harmonic (HH) generation and a probe beam split off from the generating infrared (IR) field.

In contrast to an atomic ionization scenario, excitation energy stored in the CO^+ ion that is not released through PE emission can lead to dissociation (*22*). Three important ionization channels are thus accessible: the direct photoionization channel ($CO + h\nu \rightarrow CO^+ + e^-$, where

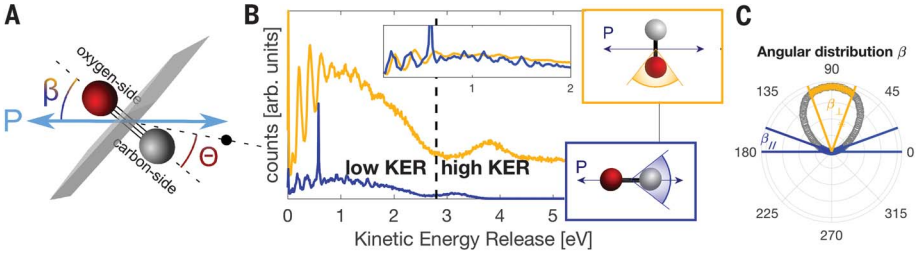

Fig. 1. KER as a function of molecular orientation. (**A**) Schematic representation of the selection based on the recoil angle with respect to the laser polarization axis P, indicated by β. The escaping side of the EWP (black) is indicated by the surface bisecting the molecular axis. (**B**) KER spectra separated in $\beta_\perp$ (orange) and $\beta_\parallel$ (blue), averaged over an angular range corresponding to an opening angle of ±20° (shaded area in blue- and orange-boxed illustrations). The inset highlights the vibrational structure observed in the low-KER (<2 eV) region. (**C**) Angular distribution of the recoil angle with respect to the field polarization axis β. The radius refers to the normalized yield. The selections of $\beta_\perp$ and $\beta_\parallel$ are highlighted in orange and blue, respectively.

[1]Department of Physics, ETH Zurich, 8093 Zurich, Switzerland. [2]Max Born Institute, 12489 Berlin, Germany. [3]Max Planck Institute for the Physics of Complex Systems, D-01187 Dresden, Germany. [4]Max Planck Korea, Department of Physics, Postech, Pohang, Gyeongbuk 37673, Republic of Korea. [5]Empa–Swiss Federal Laboratories for Materials Science & Technology, 8600 Dübendorf, Switzerland. [6]Research School of Physics and Engineering, The Australian National University, Canberra ACT 0200, Australia.
*Corresponding author. Email: jvos@phys.ethz.ch †Present address: Department of Physics, Politecnico di Milano, 20133 Milano, Italy.

ν is the photon frequency and e^- represents an electron) and two dissociative photoionization (DPI) channels ($CO + h\nu \rightarrow C^+ + O + e^-$ and $CO + h\nu \rightarrow O^+ + C + e^-$). Here, we focus on the DPI channel producing C^+ fragment ions.

Ideally, the photoionization dynamics would be studied in a state-resolved manner. However, the assignment of each PE-coincident (fragment) ion to an individual electronic state is generally not possible, as many states yield electrons with overlapping energy distributions due to ionization by different HHs present in the XUV spectrum. We enhanced the relative contribution of the electronic states by using angular resolution.

DPI events grant access to the recoil direction of the detected particles. This recoil frame coincides with the molecular frame when dissociation is fast compared with molecular rotation—that is, when the axial recoil approximation is valid (*28*). We verified that the axial recoil approximation is a valid assumption in our data treatment, with the partial exception of the $D^2\Pi$ state, which does not significantly influence the results (see SM section 3.10 for details). We thus ensured that the molecular orientation at the moment of ionization could be retrieved through the vector correlation of the detected particles (V_{C^+}, V_e, P) with respect to the laser polarization axis P without orienting the molecules (*29*, *30*). We separated DPI events according to the recoil angle with respect to the laser polarization axis, indicated by β (Fig. 1A) and henceforth referred to as the molecular orientation. We distinguished the distribution of the kinetic energy released upon dissociation (KER) for the cases where the recoil axis is oriented perpendicular ($\beta_\perp$) or parallel ($\beta_\parallel$) to the laser polarization (orange and blue curves in Fig. 1B). The energy of the neutral O fragment is reconstructed by conservation of the total momentum sum, so that the KER is given for both nuclei involved in the fragmentation channel. We identified two regions in the KER spectrum for perpendicular orientation, characterized by low KER (<2.8 eV) and high KER (>2.8 eV) values, and designated these regions $\beta_{\perp,\text{low KER}}$ and $\beta_{\perp,\text{high KER}}$, respectively. The vibrational structure in the low KER region can be attributed mostly to the $D^2\Pi$ state, with some contributions from the $3^2\Sigma^+$ state. However, because the $D^2\Pi$ state has an SWTD of almost zero, the partial breakdown of the axial recoil approximation has a negligible effect on the measured SWTDs (for full details see section 3.10 in the SM).

The DPI evolves along various potential energy surfaces (PESs), each converging to a specific dissociation limit and fragment ion (Fig. 2A). We simulated the nuclear dissociation dynamics of individual states by using the one-dimensional quantum nonadiabatic dynamics based on the multireference configuration interaction (MRCI)/def2-TZVPP PESs and nonadiabatic couplings (see SM). The main features observed in the simulations agree with the current and previous (*22*, *31*) experimental observations. The ratios of dissociation into the $C^+ + O$ channel for individual electronic states obtained from dissociation simulations were then combined with the photoionization cross sections to determine realistic contributions of states to RABBITT sidebands and thereby calculate SWTDs directly comparable to those in the experiment. The contributions of states to the three PE populations corresponding to $\beta_\parallel$, $\beta_{\perp,\text{low KER}}$, and $\beta_{\perp,\text{high KER}}$ determined from these simulations are summarized as follows: The PE spectrum in coincidence with recoil fragments emitted in the parallel orientation $\beta_\parallel$ is dominated by $^2\Sigma$ states, the $3^2\Sigma^+$ state at high energy and $4^2\Sigma^+$ at low energy. The PE spectrum corresponding to $\beta_{\perp,\text{low KER}}$ contains contributions from $D^2\Pi$ and $3^2\Sigma^+$ states, whereas the spectrum for $\beta_{\perp,\text{high KER}}$ is dominated by $3^2\Pi$. An energy correlation diagram showing the correlation between the KER and electron kinetic energy, and thus identifying reaction pathways (fig. S24), confirms these modeling results.

SWTD analysis

The dynamics of the photoionization are encoded in the phase of the escaping EWP, which can be retrieved by the interferometric XUV pump–IR probe technique called RABBITT (see SM) (*26*). In this technique, the outgoing PE, created after ionization with an XUV photon, undergoes an additional transition induced by the IR photon at the spatial and temporal overlap. Quantum path interference results in an oscillatory signal as a function of pump-probe delay τ, called a sideband (SB), which manifests between the single XUV photon absorption signals called HHs (Fig. 2B). The oscillatory signal is described by

$$\text{SB} \cong \cos(2\omega_{\text{IR}}\tau - \Delta\phi_{\text{tot}}) \cong \cos(2\omega_{\text{IR}}\tau - \Delta\phi_{\text{XUV}} - \Delta\phi_{\text{mol}}) \quad (2)$$

where ω_{IR} is the IR probe frequency. The total phase, $\Delta\phi_{\text{tot}}$, reflects the dynamic information for the escaping PE, including the attochirp of the ionizing XUV pulse ($\Delta\phi_{\text{XUV}}$) and a molecule-specific phase term, $\Delta\phi_{\text{mol}}$. The term $\Delta\phi_{\text{XUV}}$ results from the intrinsic emission delays in the HH generation process. The term $\Delta\phi_{\text{mol}}$ is characteristic of

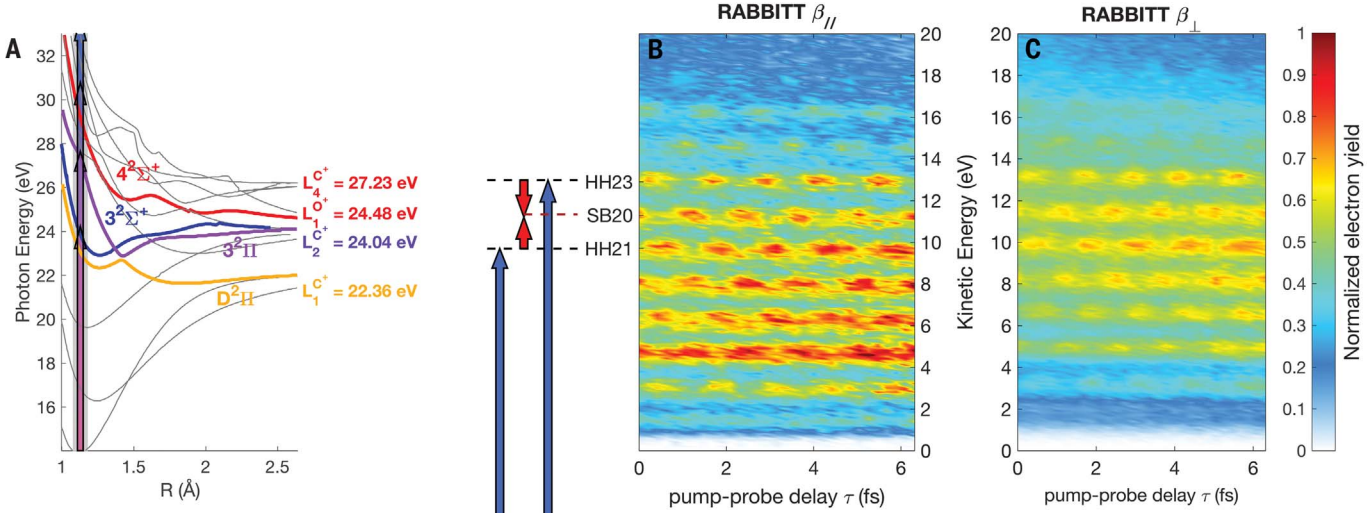

Fig. 2. Electronic states of the CO^+ molecular ion. (**A**) PESs of the most relevant electronic states (highlighted in orange, blue and purple, and red). The CO^+ ion dissociates after photoionization by the combined XUV and IR pulses, indicated by the arrows in the gray-shaded Franck-Condon region. The most relevant dissociation limits $L_1^{C^+}$, $L_2^{C^+}$, $L_4^{C^+}$, and $L_1^{O^+}$, adapted from (*22*), are indicated. R, internuclear distance. (**B**) The RABBITT trace showing the PE spectrum for molecules oriented along laser polarization, $\beta_\parallel$, recorded as a function of the pump-probe delay τ. The black and red dashed lines indicate high-order harmonics (induced by the XUV photons represented by the blue arrows) and sidebands (induced by a two-photon transition of an XUV photon and an IR photon, represented by the red arrows), respectively. (**C**) RABBITT trace for molecules with perpendicular orientation, $\beta_\perp$. Each RABBITT trace is normalized separately and does not reflect total electron counts.

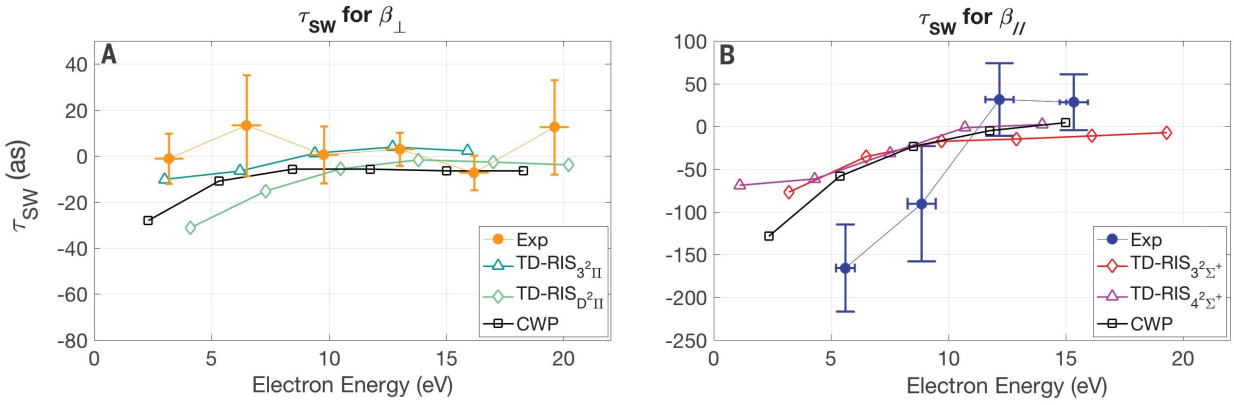

Fig. 3. Orientation- and energy-resolved SWTDs τ_{SW}. (**A**) SWTD for molecules oriented perpendicularly with respect to the laser field, integrated over the entire KER region. In this orientation the SWTDs are essentially zero within the span of the experimental error bar, which represents a combination of the 95% confidence interval for each measurement and the statistical error across all measurements weighted according to the uncertainty of the sideband fit. For a detailed analysis of the SWTDs in the low- and high-KER regions in perpendicular orientation, see fig. S24. Exp, experimental results. (**B**) For parallel orientation, $\beta_{\parallel}$, a highly negative SWTD is measured at low electron energies. In this configuration, the $3^2\Sigma^+$ state is the biggest contributor at high energies; at low energies, the $4^2\Sigma^+$ state contributes substantially. The experimental results are shown in comparison with the delays obtained by theory. A direct comparison between experiment and theory based on the CWP method is possible, as the SWTDs are shown integrated over all contributing states. In contrast, state-resolved SWTDs computed by TD-RIS are shown for dominant isolated states.

the individual system and can in turn be described by the sum of two terms: $\Delta\phi_{mol} = \Delta\phi_W + \Delta\phi_{CC}$, where $\Delta\phi_{CC}$ is the measurement-induced phase term that stems from the continuum-continuum transition in the IR field (*32*).

The phase term of interest is the target-specific Wigner phase, $\Delta\phi_W$, described as the phase shift referenced to a free propagating EWP. The phase shift is a relative measurement; thus, the subsequent Wigner time delay, given by $\tau_W = \Delta\phi_W/2\omega_{IR}$, necessarily requires a reference. In this stereospecific measurement we probe the photoionization dynamics associated with an intrinsic time delay in the molecule: specifically the photoionization time delay difference between PEs escaping from the carbon side versus the oxygen side. In this context an external reference is not required. Furthermore, the stereospecific measurement is insensitive to contributions from measurement-induced time delays. In particular, the attochirp contribution, $\Delta\phi_{XUV}$, cancels out in a comparison of the phase terms of sideband signals originating from the same neighboring harmonics. Additionally, assuming that the ionization probability is slowly varying with energy, $\Delta\phi_{CC}$ is removed because of the symmetric contribution of the long-range Coulomb potential (*32*). The stereo Wigner time is subsequently given by

$$\tau_{SW} = \frac{\Delta\phi_W(\text{carbon side}) - \Delta\phi_W(\text{oxygen side})}{2\omega_{IR}} \quad (3)$$

thereby yielding the absolute difference in Wigner time delay within the molecular potential.

The orientation-resolved RABBITT traces are separated according to the angle of the PE in the recoil frame (with an acceptance angle of 90°), indicated by Θ in Fig. 1A. Each RABBITT trace is subsequently analyzed by following the procedure described in a prior work (*3*). Briefly, the oscillating sideband signals are integrated over an energy range of roughly 1 eV (the precise energy range is indicated by the horizontal axis in Fig. 3) and fitted to Eq. 2 after being frequency-filtered by a fast Fourier transform (see SM).

The retrieved orientation-resolved SWTDs τ_{SW} are shown in Fig. 3. For perpendicular orientation, these SWTDs are shown to be within a range of ±35 as (attoseconds) (Fig. 3A). The two KER regions are not resolved for this orientation because the KER-resolved results $\beta_{\perp,low\ KER}$ and $\beta_{\perp,high\ KER}$ yield nearly identical results (see SM). Both the experimental and theoretical curves display virtually zero or slightly positive SWTDs across all electron energies. The experimental and theoretical results are in good agreement with each other.

On the contrary, we see a clearly different behavior in the energy-dependent SWTD for the parallel orientation (Fig. 3B). The blue experimental data points show that the SWTD evolves from a negative delay difference of −165 as at ~5.0 eV to a positive value of +30 as at 14.4 eV; that is, the SWTD changes from τ_W (carbon side) < τ_W (oxygen side) to its inverse with increasing electron kinetic energy.

Interpretation of the SWTDs

To understand the highly varying SWTD for parallel orientation, we used two complementary, independent theoretical models. The first model, the time-dependent resolution in ionic states (TD-RIS) method (*33*, *34*), describes the ionization dynamics initiated by the XUV pulse in a fully quantum mechanical manner, including the dynamics of electrons in the ion core. TD-RIS simulations do not account for the dynamics in the IR probe field and nuclear motion. The second model, the classical Wigner propagation (CWP) method, is based on the approximate, classical propagation of the Wigner function of the PE, including the IR field. Combining the CWP method with the quantum nonadiabatic dissociation dynamics, we compute the contributions of specific states to each RABBITT sideband and thereby the photoionization time delays, which are directly comparable to the experimental results.

In the perpendicular orientation, both TD-RIS and CWP methods predict small SWTDs, as is expected for symmetry reasons. Values from both theories compare well to the experimental values, which are close to zero within the error margin.

The most notable experimental trend for $\beta_{\parallel}$, the increasing negative SWTD toward lower PE energy, is qualitatively reproduced by both theoretical models. The difference between theoretical and experimental values at lower energies may be due in part to computational constraints that prevent either theory from accounting for higher-lying states. Given the spectrum of the XUV pump pulse, the states lying above $6^2\Sigma^+$ and $9^2\Pi$, which were not considered in the theoretical treatment, may contribute only to the lowest two sidebands.

On the basis of the experimental results, we may readily conclude that the molecular photoionization delays are very sensitive to the PE emission angle Θ and the molecular orientation β. Consequently, the stereoresolved measurements of dissociative states provide a way to determine the details of the ionization process that are inaccessible to angle-integrated measurements averaged over all molecular orientations.

To obtain further insight into the highly negative SWTDs measured in parallel orientation (Fig. 3B), we calculated the Wigner functions of

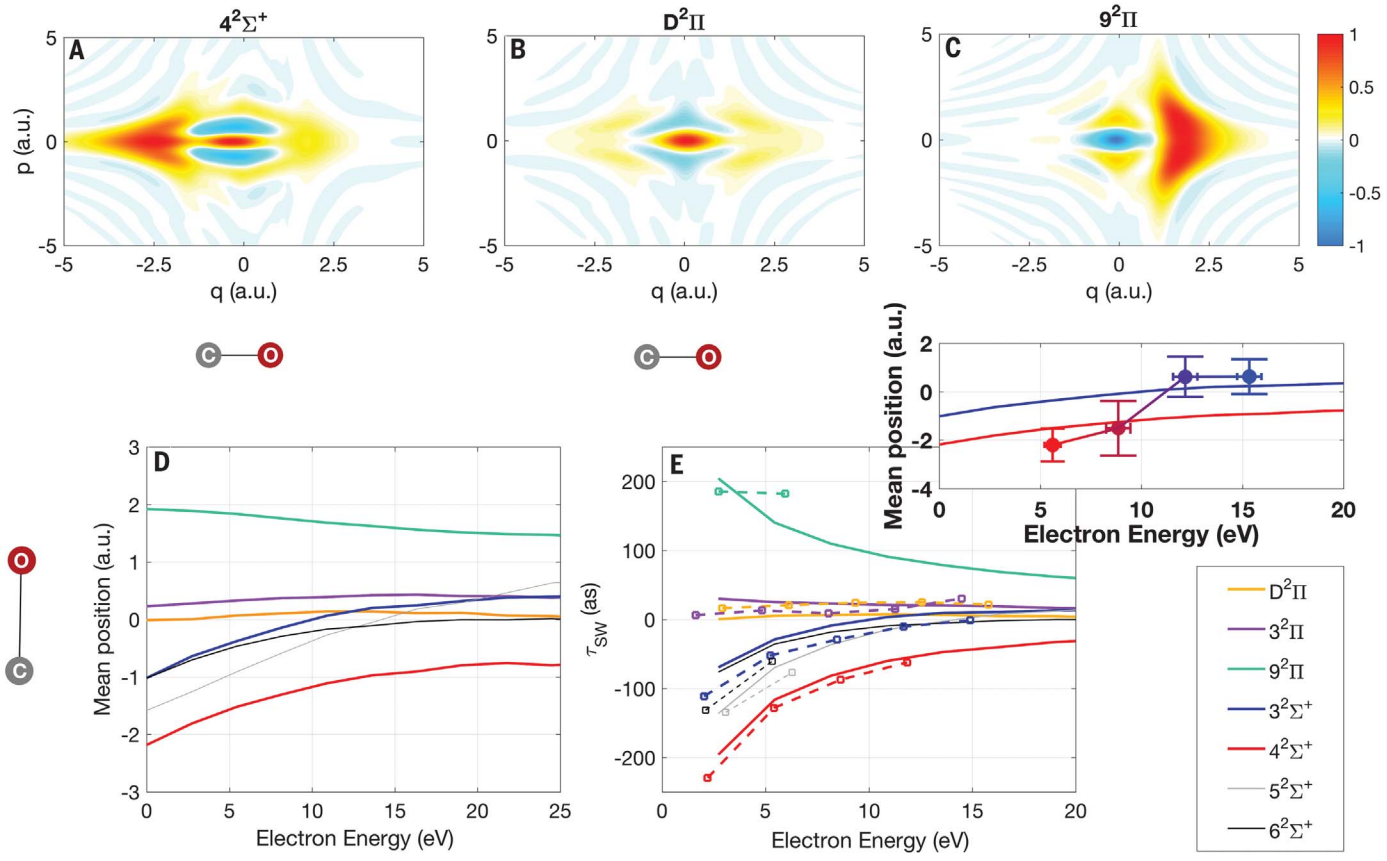

Fig. 4. SWTD and electron localization. Coordinate and momentum representations of the escaping electron at the instance of birth (provided by the source function) are shown for three representative electronic states: (**A**) $4^2\Sigma^+$, (**B**) $D^2\Pi$, and (**C**) $9^2\Pi$. The molecule is oriented parallel to the field and centered at q = 0, with the C side of the molecule placed on the left [C(q) = 1.07 a.u.] and the O side on the right [O(q) = 1.07 a.u.]. The $4^2\Sigma^+$ state shows a clear asymmetry along the molecular bond with a bias toward the carbon side. The $D^2\Pi$ state shows only a slight asymmetry toward the oxygen side, whereas the $9^2\Pi$ state is very strongly biased toward the oxygen side of the molecule. p, momentum. (**D**) The average electron position at the time of ionization, $q_I(E)$, as a function of electron energy for seven different states calculated by using the source functions, such as plotted in (A) to (C). (**E**) The SWTDs defined in Eq. 3 and computed for seven different states by using the CWP method (dashed lines) and $\tau_{\langle SW\rangle}$ defined in Eq. 4 and computed by using the mean position shown in (D) (solid lines). The inset shows $q_I(E)$ for the $3^2\Sigma^+$ (blue line) and $4^2\Sigma^+$(red line) states and the experimentally extracted mean position $q_{I,exp}(E)$ (solid circles on red-blue line) for parallel-oriented molecules. The error bars represent a combination of the weighted 95% confidence interval for each measurement and the statistical error across all measurements weighted according to the uncertainty of the sideband fit.

the dipole matrix element of the Dyson orbitals for each ionization channel (Fig. 4, A to C), which we refer to as the source function (see SM). This source function provides a coordinate and momentum representation of the EWP at the instance of birth. From Fig. 4 it is clear that a large (small) asymmetry of the source function translates into a large (small) SWTD. Because the source function is symmetric with respect to the sign of the initial PE momentum, the time difference can originate from either an asymmetry in the initial localization or an asymmetry in the molecular potential experienced by the departing electron. The comparison between the SWTDs and the dipole moments of the corresponding ionic states (see SM) suggests that the asymmetry of the molecular potential is not a decisive contributor.

The asymmetry of the source function with respect to position, on the other hand, correlates very well with the computed delays and seems to be the main factor determining the SWTD τ_{SW}. The source functions corresponding to large negative, zero, and large positive SWTDs are shown in Fig. 4, corresponding to the $4^2\Sigma^+$, $D^2\Pi$, and $9^2\Pi$ states, respectively. The $9^2\Pi$ state does not substantially contribute to the experimental RABBITT signal, and it is used only to illustrate the oxygen-leaning asymmetry that would result in large positive delays.

To show the correlation between the mean position of ionization, as computed with the CWP, and the τ_{SW} conclusively, we introduce a position interpretation of the mean SWTD

$$\tau_{\langle SW\rangle} = \frac{2q_I(E)}{\sqrt{2E}} \quad (4)$$

where E is the final kinetic energy of the ionized PE and $q_I(E)$ is the mean position of the electron at the moment of birth with respect to the geometric center of the molecule. In other words, q = 0 identifies the midway point along the CO bond. The simple $\tau_{\langle SW\rangle}$ is independent of the details of the molecular potential experienced by the ionized PE, meaning that it depends only on the mean electron position along the molecular axis and the final electron energy (Fig. 4D). Nevertheless, $\tau_{\langle SW\rangle}$ (Fig. 4E, solid lines) shows good agreement with the SWTDs for parallel orientation calculated by the full CWP method (Fig. 4E, dashed lines).

We can conclude that at low energies, τ_{SW} shows a clear bias toward the carbon side of the molecule for all $^2\Sigma$ states considered, resulting in negative delays (Fig. 4E, inset). In particular, the $4^2\Sigma^+$ state, which shows the highest asymmetry toward the carbon side in the source function, has the most negative delays. For example, the average position of ionization $q_I(E)$ = −1.55 atomic units (a.u., where 1 a.u. is ~0.529 angstrom)

at 5 eV of electron energy suggests that the SWTD is around −120 as, which is in agreement, within the error margin, with the experimental −165 as (Fig. 4, D and E). At higher electron energies, the average electron position at birth moves toward oxygen, resulting in positive displacements, in agreement with the experimental results. On the other hand, the $^2\Pi$ states, which become relatively more important in the perpendicular orientation, show rather positive ($D^2\Pi$ and $3^2\Pi$) or highly positive ($9^2\Pi$) SWTDs. The corresponding Wigner functions show no or very small bias toward oxygen for the $D^2\Pi$ and $3^2\Pi$ states, whereas a strong bias toward oxygen is observed for the $9^2\Pi$ state.

The excellent agreement between the SWTD τ_{SW} and the delay $\tau_{\langle SW \rangle}$ (Fig. 4E) suggests that Eq. 4 can be used to infer the mean position of the ionized PE from experimental measurements alone. This quantity, $q_{I,exp}$, shown in the inset of Fig. 4, is completely independent of any fitting parameters or simulations. We show that the experimentally extracted mean position of the excited EWP, $q_{I,exp}(E)$, starts to the left of the carbon atom and quickly moves right toward the oxygen atom with increasing energy of the absorbed photon. The SWTD thereby serves as an additional source of information for molecular photoionization dynamics next to the commonly extracted Wigner time delay. In particular, in CO, the SWTD measurements allow for a straightforward extraction of the relative mean position of the ionizing electron at the moment of ionization as a function of electron energy. Therefore, measurements of the SWTD could complete the description of Einstein's photoelectric effect in molecules by adding subangstrom spatial resolution to the existing attosecond temporal resolution.

The general applicability of this method is supported by auxiliary calculations (see SM), and it is plausible that this pattern holds for larger molecules as well, particularly if final state resolution can be obtained (*7*, *35*). Our work can serve as a benchmark not only for further experiments but also for the development of theoretical models, emphasizing the key role of the twofold dependence of the measured photoionization time delays on the molecular orientation and the intrinsic details of the molecular potential to understand more complex molecular dynamics.

REFERENCES AND NOTES

1. K. Klünder *et al.*, *Phys. Rev. Lett.* **106**, 143002 (2011).
2. M. Schultze *et al.*, *Science* **328**, 1658–1662 (2010).
3. L. Cattaneo *et al.*, *Opt. Express* **24**, 29060–29076 (2016).
4. M. Sabbar *et al.*, *Phys. Rev. Lett.* **115**, 133001 (2015).
5. E. P. Wigner, *Phys. Rev.* **98**, 145–147 (1955).
6. R. Pazourek, S. Nagele, J. Burgdörfer, *Rev. Mod. Phys.* **87**, 765–802 (2015).
7. M. Huppert, I. Jordan, D. Baykusheva, A. von Conta, H. J. Wörner, *Phys. Rev. Lett.* **117**, 093001 (2016).
8. S. Haessler *et al.*, *Phys. Rev. A* **80**, 011404 (2009).
9. L. Cattaneo *et al.*, *Nat. Phys.* 10.1038/s41567-018-0103-2 (2018).
10. C. Marceau *et al.*, *Phys. Rev. Lett.* **119**, 083401 (2017).
11. P. Hockett, E. Frumker, D. M. Villeneuve, P. B. Corkum, *J. Phys. B At. Mol. Opt. Phys.* **49**, 095602 (2016).
12. I. A. Ivanov, A. S. Kheifets, V. V. Serov, *Phys. Rev. A* **86**, 063422 (2012).
13. V. V. Serov, V. L. Derbov, T. Sergeeva, *Phys. Rev. A* **87**, 063414 (2013).
14. V. V. Serov, A. S. Kheifets, *J. Chem. Phys.* **147**, 204303 (2017).
15. P. Hockett, *J. Phys. B At. Mol. Opt. Phys.* **50**, 154002 (2017).
16. G. Sansone *et al.*, *Nature* **465**, 763–766 (2010).
17. Ch. Neidel *et al.*, *Phys. Rev. Lett.* **111**, 033001 (2013).
18. C. Cirelli *et al.*, *Nat. Commun.* **9**, 955 (2018).
19. S. Heuser *et al.*, *Phys. Rev. A* **94**, 063409 (2016).
20. A. Chacon, M. Lein, C. Ruiz, *Phys. Rev. A* **89**, 053427 (2014).
21. J. H. D. Eland, E. J. Duerr, *Chem. Phys.* **229**, 13–19 (1998).
22. M. Lebech, J. C. Houver, D. Dowek, *J. Chem. Phys.* **130**, 194307 (2009).
23. M. Lebech *et al.*, *J. Chem. Phys.* **136**, 094303 (2012).
24. R. Dörner *et al.*, *Phys. Rep.* **330**, 95–192 (2000).
25. J. Ullrich *et al.*, *Rep. Prog. Phys.* **66**, 1463–1545 (2003).
26. P. M. Paul *et al.*, *Science* **292**, 1689–1692 (2001).
27. H. G. Muller, *Appl. Phys. B* **74**, s17–s21 (2014).
28. R. N. Zare, *Mol. Photochem.* **4**, 1–37 (1972).
29. M. Lebech *et al.*, *J. Chem. Phys.* **118**, 9653–9663 (2003).
30. A. Lafosse *et al.*, *Phys. Rev. Lett.* **84**, 5987–5990 (2000).
31. P. Baltzer *et al.*, *J. Phys. B At. Mol. Opt. Phys.* **27**, 4915–4932 (1994).
32. J. M. Dahlström, A. L'Huillier, A. Maquet, *J. Phys. B At. Mol. Opt. Phys.* **45**, 183001 (2012).
33. M. Spanner, S. Patchkovskii, *Phys. Rev. A* **80**, 063411 (2009).
34. M. Spanner, S. Patchkovskii, *Chem. Phys.* **414**, 10–19 (2013).
35. A. E. Boguslavskiy *et al.*, *Science* **335**, 1336–1340 (2012).
36. J. Vos, Orientation-dependent stereo Wigner time delay and electron localization in a small molecule, Research Collection ETH Zurich (2018); doi:10.3929/ethz-b-000259345.

ACKNOWLEDGMENTS

Funding: J.V., L.C., C.C., and U.K. acknowledge support by the ERC advanced grant AttoClock-320401 within the Seventh Framework Program of the European Union and by the NCCR MUST, funded by the Swiss National Science Foundation. A.S.L. acknowledges the Max Planck Center for Attosecond Science (MPC-AS), MPK, and the National Research Foundation of Korea (grant 2016K1A4A4A01922028). **Author contributions:** J.V. and L.C. performed the measurements and analyzed the results. J.V., L.C., C.C., M.L., and U.K. evaluated and discussed the results. S.P., A.K., T.Z., and A.S.L. developed the theoretical models and performed the calculations. All authors discussed the results and contributed to the final manuscript. **Competing interests:** The authors declare no competing interests. **Data and materials availability:** Data presented in this study are available at Research Collection ETH Zurich (*36*).

SUPPLEMENTARY MATERIALS

www.sciencemag.org/content/360/6395/1326/suppl/DC1
Materials and Methods
Figs. S1 to S24
Tables S1 to S9
References (*37*–*52*)

25 July 2017; resubmitted 21 February 2018
Accepted 26 April 2018
10.1126/science.aao4731

REPORT

CHIRAL RESOLUTION

Separation of enantiomers by their enantiospecific interaction with achiral magnetic substrates

Koyel Banerjee-Ghosh[1]*, Oren Ben Dor[2]*, Francesco Tassinari[1]*, Eyal Capua[1], Shira Yochelis[2], Amir Capua[2], See-Hun Yang[3], Stuart S. P. Parkin[3,4], Soumyajit Sarkar[5], Leeor Kronik[5], Lech Tomasz Baczewski[6], Ron Naaman[1]†, Yossi Paltiel[2]†

It is commonly assumed that recognition and discrimination of chirality, both in nature and in artificial systems, depend solely on spatial effects. However, recent studies have suggested that charge redistribution in chiral molecules manifests an enantiospecific preference in electron spin orientation. We therefore reasoned that the induced spin polarization may affect enantiorecognition through exchange interactions. Here we show experimentally that the interaction of chiral molecules with a perpendicularly magnetized substrate is enantiospecific. Thus, one enantiomer adsorbs preferentially when the magnetic dipole is pointing up, whereas the other adsorbs faster for the opposite alignment of the magnetization. The interaction is not controlled by the magnetic field per se, but rather by the electron spin orientations, and opens prospects for a distinct approach to enantiomeric separations.

The relation between magnetism and chirality was the basis for an argument between two giants of science, Pasteur and Kelvin (*1*, *2*), over a century ago. Pasteur, after discovering that the chemistry of life showed a preference for molecules with a particular handedness (*3*, *4*), tried to carry out experiments aimed at finding asymmetric physical forces that could explain the biological homochirality (*5*). He attempted to induce handedness by stirring the reactants in a centrifuge and applying a magnetic field, but both attempts failed. In 2001, Ribo and co-workers reported that stirring solutions of achiral porphyrins could induce chiral-symmetry breaking in the resulting mesophases (*6*). Chiral supramolecular organization was also induced by vortex flow (*7*). However, further attempts to induce chirality by magnetic field failed (*8*). This lack of success is consistent with Kelvin's conclusion that "the magnetic rotation alone has neither left-handed nor right-handed quality" (*9*). Moreover, de Gennes has demonstrated that even the superposition of a magnetic field and an electric field, originally suggested by Curie (*10*), does not induce asymmetry in reactions (*11*). He claimed, however, that if the final state is out of equilibrium, asymmetry remains possible. Here we present another twist in this long-standing debate by demonstrating an enantioselective interaction of chiral molecules with a substrate magnetized perpendicular to its surface. The discrimination is mediated by a spin-specific interaction but not by the magnetic field per se.

Recent studies have shown that, when electrons move through chiral molecules, their transport is spin dependent, with the preferred spin orientation determined by the handedness of the molecule and the direction of motion (*12*, *13*). The effect, which by now is well established (*14*–*18*), is known as chirality-induced spin selectivity (CISS). As a corollary, charge redistribution in chiral molecules is also accompanied by enantiospecific spin polarization (*19*). These results led us to consider the possible interaction between chiral molecules with perpendicularly magnetized surfaces. This interaction should be spin sensitive by virtue of short-range magnetic-exchange interactions. Therefore, it could result in enantiospecificity through the above-mentioned relation between spin and chirality via the CISS phenomenon. If this were the case, it would facilitate the separation of a racemic mixture into its two enantiomeric components simply by allowing the mixture to interact with the magnetic substrate.

As a first examination, an L– or D–polyalanine (PAL)–based oligomer, a thiolated α-helix oligopeptide, SH-CAAAAKAAAAKAAAAKAAAAKAAAAKA-AAAKAAAAK (C, A, and K represent cysteine, alanine, and lysine, respectively), was exposed to a ferromagnetic (FM) cobalt film covered with 5 nm of gold for 2 s (see supplementary materials). This oligomer was chosen because of its stable helical structure and the existence of vast information on its adsorption on gold (*12*). The substrate configuration was chosen on the basis of prior studies, which have established that a thin layer of a noble metal like gold or platinum (up to about 10 nm), deposited on a ferromagnet, does not diminish magnetic or spin transport properties but protects the ferromagnet from oxidation (*20*–*22*). SiO_2 nanoparticles (NPs) were attached to the adsorbed PAL to act as a marker in the scanning electron microscope (SEM) images for the monolayer adsorption density. Figure 1A, (i) and (ii), shows SEM images of the L-enantiomer adsorbed on the FM substrate, with the latter magnetized up or down, respectively. The concentration of adsorbed particles in Fig. 1A, (i), is $4 \pm 0.4 \times 10^{10}$ NPs/cm^2, whereas in Fig. 1A, (ii), it is $6 \pm 1 \times 10^9$ NPs/cm^2. Results of the complementary experiment with D-PAL are shown in Fig. 1A, (iii) and (iv), with concentrations of $1 \pm 0.2 \times 10^{10}$ and $4 \pm 0.5 \times 10^{10}$ NPs/cm^2 found for the up- and down-magnetized substrate. As a control experiment, L- and D-enantiomers were also adsorbed on a nonmagnetic, pure gold substrate, with an external magnetic field applied either normally or antinormally to the substrate. In this case, no enantioselectivity was observed [see a full comparison in Fig. 1A, (v)]. In addition, the adsorption efficiency in this case was found to be between that of the FM substrate with the favored and unfavored spin alignment. Moreover, when the substrate was magnetized in-plane, no selective adsorption was observed. The experiments described here were conducted on 10 separate sets of samples, and the error analysis presented in the figures is based on particle-number counting at different parts of each sample. A complete discussion of the reproducibility of this experiment, as well as of the additional ones reported below, is provided in the supplementary materials.

The above results clearly demonstrate enantioselectivity in the adsorption process. We note that, in one magnetization direction, the L-PAL adsorption rate is 8 ± 2 times faster than that of D-PAL, whereas in the other magnetization direction, the D-PAL adsorption rate is 4 ± 1 times faster than that of L-PAL. However, the D-PAL purification level is lower than that of L-PAL, likely explaining the asymmetry in adsorption rate ratios (see supplementary materials). Furthermore, repetition of this experiment with a longer adsorption time (2 min) resulted in a reduction in the enantioselectivity of adsorption (see figs. S1 and S2), that is, the process exhibits substantial kinetic differences.

The kinetic effects in the selective adsorption are related to the adsorption-desorption kinetics typical to the formation of self-assembled monolayers of thiolated molecules (*23*). Specifically, it is well known that, when self-assembled monolayers are formed, the process is initially controlled by the rate of adsorption, the kinetics. At long time scales, the thermodynamics defines the adsorption, and, for two species that have the same energy for binding to a surface, the quantity of adsorbed molecules will be defined by their concentration. In the specific case described

[1]Department of Chemical and Biological Physics, Weizmann Institute of Science, Rehovot 76100, Israel. [2]Department of Applied Physics, Hebrew University, Jerusalem 91904, Israel. [3]IBM Research Division, Almaden Research Center, 650 Harry Road, San Jose, CA 95120, USA. [4]Max Planck Institute for Microstructure Physics, Halle (Saale) D-06120, Germany. [5]Department of Materials and Interfaces, Weizmann Institute of Science, Rehovot 76100, Israel. [6]Institute of Physics Polish Academy of Sciences, Al. Lotnikow 32/46, 02-668 Warszawa, Poland.
*These authors contributed equally to this work.
†Corresponding author. Email: ron.naaman@weizmann.ac.il (R.N.); paltiel@mail.huji.ac.il (Y.P.)

here, at short adsorption time, selectivity is observed because of the different rates of adsorption for the two enantiomers; however, at longer times, because the binding energies are identical, the two enantiomers will be equally adsorbed, and hence the enantioselectivity is reduced. See more on this subject below.

We next explored the separation of a racemic PAL mixture into its two enantiomeric components upon exposure to a magnetic substrate. The original mixture exhibited no circular dichroism (CD). As shown in Fig. 1B, (i), upon sequential exposure to 100 1 cm–by–1 cm substrates with up- or down-pointing magnetization, a clear CD signature corresponding to D- or L-PAL, respectively, was obtained from the residual solution. Furthermore, this signature is similar to that obtained for the pure enantiomers, as shown in Fig. 1B, (ii).

To implement a larger-scale enantioseparation apparatus, we coated a flow column on one side with a thin film consisting of 50 Al/5 Ti/0.3 Co/(0.7 Ni/0.3 Co)$_6$/5 Au (all numbers are in nm), magnetized externally either normally or antinormally to the surface. This particular film was chosen because it is a relatively soft magnet and could easily be magnetized with the external magnetic field (see supplementary materials). Figure 2 shows the CD spectra of a racemic [Cya-(Ala-Aib)$_5$-CO$_2$H] solution at the inlet and outlet of the apparatus for the two magnetization directions, where Cya is cystamine, Ala is alanine, and Aib is aminoisobutyric acid. Clearly, for a given magnetic direction, one enantiomer is adsorbed on the Au. The opposite enantiomer therefore accumulates in excess at the outlet and dominates the CD spectrum. The results here indicate once again that the L-enantiomer favors a surface that is magnetized up (that is, H^+), whereas the D-enantiomer favors the down magnetization (that is, H^-). Quantitative details are provided in the supplementary materials.

To monitor the kinetics of enantioselective adsorption directly, we monitored the fluorescence of double-stranded DNA (dsDNA) oligonucleotides (20 base pairs in length), to which a fluorescent dye was attached. The Cy-3 (cyanine) dye was tagged at the 3′ position (cytosine) of the dsDNA (see supplementary materials). In this case, the molecules were adsorbed on a Ni/Au surface, and the fluorescence was measured for different adsorption times and for different Ni magnetization directions (Fig. 3A). We verified that the same results were obtained with the Ni/Au as with the Co/Au substrates. Figure 3B shows the adsorption as a function of time and demonstrates that the adsorption rate is considerably different for up and down magnetization of the substrate.

To establish that the effect extended beyond oligopeptides and dsDNA, we probed the adsorption kinetics for a single amino acid, cysteine. Briefly, solutions of L- or D-cysteine were exposed to the same magnetic substrates used in prior experiments, with the magnetization pointing up or down. The change in concentration was measured by applying high-performance liquid chromatography (HPLC). We define the adsorption specificity as $\frac{A_D - A_U}{A_D + A_U}$, where A_D and A_U denote the quantity of adsorbed molecules measured for the two magnetization directions, namely, down or up, respectively. The results, presented in Fig. 3C, represent data averaged over four sets of experiments (see supplementary materials). They indicate that, for short adsorption times, the adsorption is enantioselective exactly as before. For long adsorption times, the selectivity is lost, a result which is, again, consistent with that obtained for PAL and which indicates different adsorption rates on the magnetized substrate. Clearly the kinetics vary for different molecules and

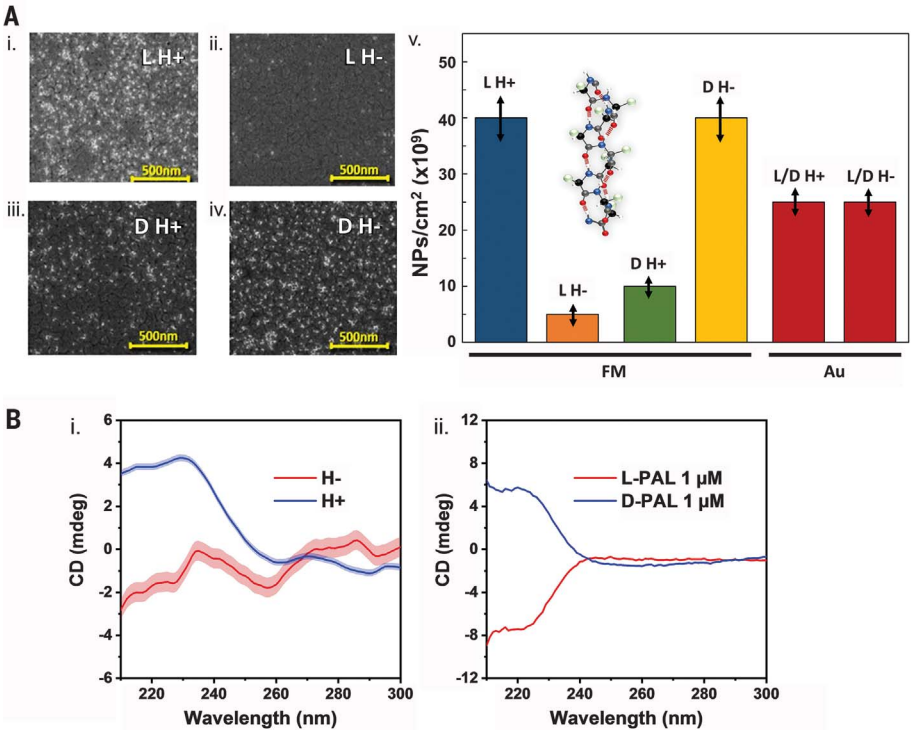

Fig. 1. Enantiospecific adsorption of a peptide. (**A**) Adsorption of the PAL oligopeptide [shown in inset of (v)] on FM samples (silicon with a 1.8-nm Co film and a 5-nm Au film), magnetized with the magnetic dipole pointing up (H^+) or down (H^-) relative to the substrate surface. SiO_2 nanoparticles were attached to the adsorbed oligopeptides. Panels (i) and (ii) L-PAL and (iii) and (iv) D-PAL were adsorbed for 2 s on a substrate magnetized up or down. Panel (v) summarizes the nanoparticle adsorption densities shown in (i) to (iv), compared with the adsorption density on Au with an applied external magnetic field (red bars). Double-headed arrows represent error bars. The errors are the standard deviation among 10 measurements conducted on each of the 10 samples, hence a total of 100 measurements. (**B**) Panel (i) shows the enantiospecific CD spectra of PAL, obtained from exposure of a racemic PAL mixture exhibiting no CD to a substrate with magnetization pointing down (red) or up (blue). CD spectra were obtained postadsorption. After the specific adsorption of one enantiomer, the resulting CD spectra clearly indicate the presence of the opposite enantiomer. The linewidth reflects the uncertainty of the results. Panel (ii) shows the CD spectra of the pure enantiomers, provided for comparison. mdeg, millidegrees.

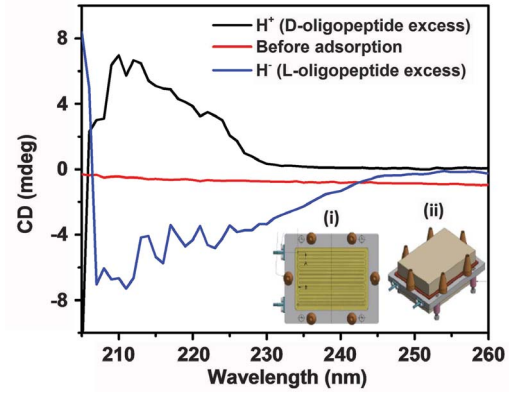

Fig. 2. Flow-based separation of enantiomers. CD spectra of a racemic D- and L-[Cya-(Ala-Aib)$_5$-CO$_2$H] oligopeptide mixture at the inlet (red) and outlet of a magnetic column (i), with an external (ii) magnetic field pointing up (black) or down (blue). Enantioseparation is clearly obtained.

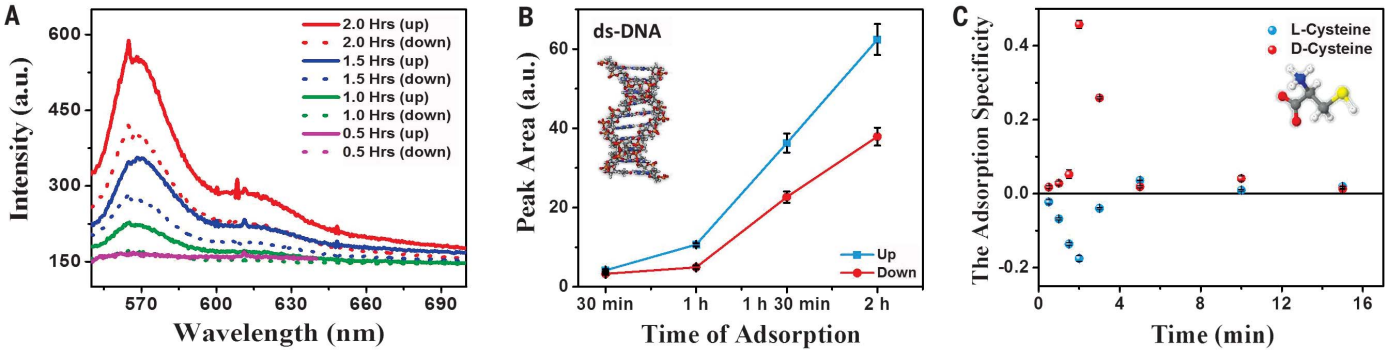

Fig. 3. Selective adsorption of dsDNA and cysteine. (**A**) Fluorescence spectrum measured from adsorbed dsDNA on a Si wafer coated with 8 Ti/100 Ni/8 Au (all numbers are in nm), with the magnet pointing up or down. a.u., arbitrary units. (**B**) Time dependence of the adsorption process, obtained when the magnetic dipole of the substrate is pointing up (blue) or down (red). (**C**) Adsorption specificity, defined as $\frac{A_D - A_U}{A_D + A_U}$, where A_D and A_U are HPLC-measured quantities of adsorbed cysteine on the magnetic substrate with magnetic moment pointing down or up, respectively, as a function of time. The size of the points on the graph represents the error in the adsorption specificity.

different concentrations, as indicated by the relatively slow process observed in dsDNA (Fig. 3B).

The above results demonstrate the generic nature of the effect. Unambiguous enantioselectivity, based on different adsorption rates, on a perpendicularly magnetized FM substrate is obtained throughout for a variety of chiral molecules and magnetic substrates. We now explain in more detail how this can be rationalized in terms of CISS-induced spin polarization in the chiral molecule, facilitating a selective magnetic-exchange interaction with the FM substrate. Under electric dipole polarization, induced by the substrate, an excess of electrons and holes on the negative and positive poles of the molecule, respectively, is obtained. This charge polarization is accompanied by spin polarization, as previously shown both experimentally and theoretically (*19*, *24*). The specific spin orientation at each pole depends on the chirality of the molecule (see Fig. 4A). The spin polarization results from the dynamic process of the electron redistribution in the chiral potential presented by the molecule.

If there is an exchange interaction between the molecular spin and the spin of the FM substrate, then the substrate-molecule interaction should be stabilized if the two spins are antiparallel (low-spin configuration) and destabilized if they are parallel (high-spin configuration), as shown in Fig. 4B. Indeed, a prior study found that adsorption of chiral molecules on a nonmagnetized FM substrate tends to magnetize it in opposite directions for opposite enantiomers (*25*).

The remaining question, then, is whether this spin interaction is large enough to promote enantioselectivity. To explore this, we assume that spin polarization has already been obtained through the dynamic CISS effect and study spin interaction with the FM substrate. The simplest model possible for net spin polarization is given by a H atom with a spin-polarized electron. We then represent the FM layer by a cube of Ni atoms with two atoms in each dimension, whose H-facing surface is oriented along the (111) direction of bulk Ni, with spins aligned parallel to each other owing to the FM interaction. The model we present is not a model of chirality; rather, it is a model for spin polarization. In fact, theory for the CISS effect is an ongoing topic of investigation [see, for example, reference (*24*)]. However, the model we present does show that the spin energetics can indeed drive the effect.

We performed density functional theory (DFT) calculations exploring the interaction energies as a function of distance, using the Perdew-Burke-Ernzerhof functional (*26*) (computational details are given in the supplementary materials). In one case, the H-atom spin was considered to be along the same direction of all the Ni atoms (high-spin, FM configuration) and in the other in the opposite direction (low-spin, anti-FM configuration). Clearly, this is but a crude model for the real system, whose accuracy is further limited by known limitations on charge (*27*) and spin (*28*) dissociation with conventional DFT. Nevertheless, the results, given in Fig. 4C, show that for all the distances up to about 0.35 nm, the total energy of the system for the high-spin configuration is higher than that of the low-spin configuration. The energy difference at the minimum of the potential is about 0.6 eV, which is well above thermal energy at room temperature. The H atom represents an extreme case of charge polarization (a full electron). Previous studies indicated that the polarization involves a spin of about a full electron (*19*, *29*). However, even if only $^1/_{10}$ of an electron charge is polarized, the difference between the two spin states would still easily allow for an observable effect.

To show that a similar effect is obtained with a more realistic molecular model, we considered a small chiral molecule, $CH_3C(OH)H(NH)$, whose radical character results in a net spin polarization in the gas phase. Interaction energy curves, similar to those shown in Fig. 4C, are given in fig. S3. Here, too, the energy difference is sizeable (~0.4 eV at the minimum of the potential) and decaying with increasing molecule-substrate separation, even though the spin on the atoms close to the surface is less than that of a full electron.

The curves of Fig. 4C show two binding-potential landscapes. If the molecule-surface interaction time is long enough, compared to the time it takes to cross from the upper potential to the lower one by spin orbit coupling or by hyperfine interaction, then the molecular spin orientation may flip, and the molecule will interact with the surface on the lower potential energy surface [see also (*30*) for a discussion in terms of "true" and "false" chirality]. However, at shorter times, each spin polarization will experience a different interaction potential and, therefore, different adsorption kinetics, consistent with the experimental results of Figs. 1 and 3B. It should be realized that, although the spin polarization controls the kinetics of the process, because of the spin flipping, on a long time scale, thermodynamics will prevail, namely, all the molecules will be adsorbed on the low–potential energy surface independent of the chirality. This process is related to the kinetics of monolayer formation in which molecules adsorb and desorb. After a long enough time, the transient spin effect diminishes, and the formation is controlled by concentration. It is important to appreciate that the "crossing time" between the potentials depends on molecular properties (spin orbit and hyperfine couplings) as well as on the number of collisions with the surface per second and, hence, will vary with concentration. Upon reaching thermodynamic equilibrium, molecules adsorb and desorb. Hence, molecules of the "wrong chirality" replace adsorbed molecules, and the selectivity diminishes. As can be realized from the data presented, the time scale to reach thermodynamics depends on the molecules and the experimental conditions, such as surface area versus concentration in the solution This is why the kinetics can actually be obtained only experimentally. We emphasize once again that the effect reported here is not associated with the direct interaction of chiral molecules with magnetic fields (*31*–*34*) but rather with the magnetic-exchange interaction of the spin-polarized molecules with the spin-polarized substrate [see Figs. 1A, (v), and 4B]. The direct interaction energy of an electron spin with a magnetic field is typically of the order of micro–electron volts, whereas the interaction energies

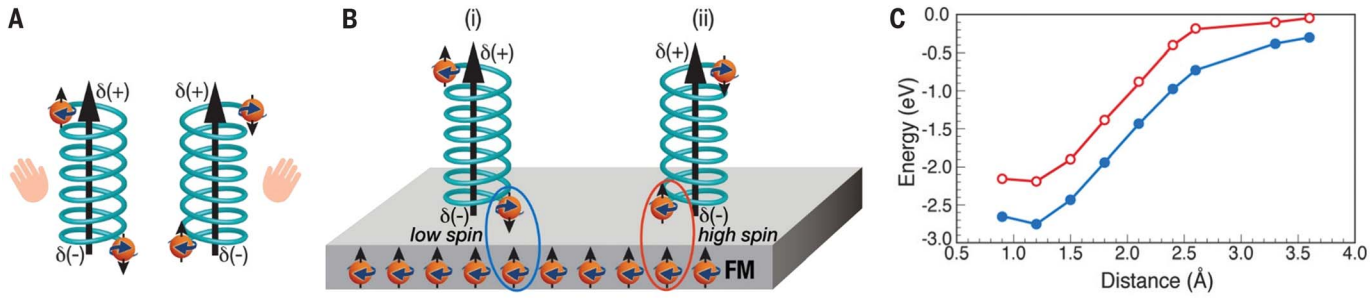

Fig. 4. Theoretical underpinnings. (**A**) A schematic cartoon of the polarization. The electrical polarization of the molecule is accompanied by spin polarization. The spin alignment at each electric pole depends on the specific enantiomer. The horizontal arrows indicate the rotation, and the vertical arrows indicate the spin direction. (**B**) Therefore, for a specific enantiomer, the interaction between the magnetized surface and the molecule (circled in blue and red) follows either a low-spin (i) or a high-spin (ii) potential, depending on the direction of magnetization of the substrate. (**C**) Calculated interaction energies as a function of distance between a hydrogen atom and a surface represented by a 2 atom–by–2 atom–by–2 atom cube of Ni atoms. All spins of the Ni atoms are aligned parallel to each other, and the H atom spin is aligned either parallel (red curve) or antiparallel (blue curve) to the spin of the Ni atoms. At longer distances, the two different configurations merge in terms of total energy, and that energy is considered as the zero of the energy axis.

obtained in Fig. 4C are at least five orders of magnitude greater.

Enantioselectivity is ubiquitous in nature, and many of the molecules in plants and living organisms have specific enantiomeric properties (*35*). Chiral recognition and enantiomeric selectivity are commonly assumed, both in nature and in artificial systems, to be related to a spatial effect, with the recognition process typically described by a "lock-and-key"–type model (*36*). Accordingly, chromatography-based enantioseparation requires the chiral substrate to be adjusted so that it interacts optimally with a specific enantiomer (*37*). Indeed, enantioseparation is an extremely important process in the pharmaceutical and chemical industries. Chromatography and electromigration techniques have long been the methods of choice in this field (*37*–*46*). However, despite intensive efforts, obtaining enantiomerically pure synthetic materials remains a challenge, as the cost of separation is relatively high and an extensive effort is required.

The enantioselective interaction of chiral molecules with a magnetic substrate, presented in this article, provides a potentially generic chromatographic method for enantioseparation, which does not require a specific separating column. Because the observed effect depends on the electrical polarizability of the system (that is accompanied by spin polarization) and because this polarization depends on the global structure of the chiral molecule, the method described here may also allow the separation of chiral molecules from a mixture of molecules, either chiral or achiral. In addition, this technique could potentially be applied for separating chiral molecules on the basis of their secondary structure and/or for separating two secondary structures of the same chiral molecule. Clearly, the efficiency of the method depends on the electric and spin polarization properties of the molecules and may vary considerably for different systems. We hope that this work will motivate further exploration of the detailed mechanisms and ultimate efficiency of this approach.

REFERENCES AND NOTES

1. L. D. Barron, *Chem. Soc. Rev.* **15**, 189–223 (1986).
2. T. Ruchon, M. Vallet, J.-Y. Thépot, A. Le Floch, R. W. Boyd, *C. R. Phys.* **5**, 273–277 (2004).
3. L. Pasteur, *Rev. Scient.* 3, vii: 2–6, in *Oeuvres de Louis Pasteur I* (1884), p. 369.
4. S. F. Mason, *Nature* **311**, 19–23 (1984).
5. P. Frank, W. A. Bonner, R. N. Zare, in *Chemistry for the 21st Century*, E. Keinan, I. Schechter, Eds. (Wiley, 2001), pp. 175–208.
6. K. Okano, O. Arteaga, J. M. Ribo, T. Yamashita, *Chemistry* **17**, 9288–9292 (2011).
7. K. Okano, T. Yamashita, *ChemPhysChem* **13**, 2263–2271 (2012).
8. B. L. Feringa, R. A. van Delden, *Angew. Chem. Int. Ed.* **38**, 3418–3438 (1999).
9. Lord Kelvin, *Baltimore Lectures on Molecular Dynamics and the Wave Theory of Light* (C. J. Clay and Sons, London, 1904).
10. P. Curie, *J. Phys.* **3**, 393–415 (1894).
11. P.-G. De Gennes, *C. R. Hebd. Seances Acad. Sci. B* **270**, 891 (1970).
12. R. Naaman, D. H. Waldeck, *Annu. Rev. Phys. Chem.* **66**, 263–281 (2015).
13. K. Michaeli, N. Kantor-Uriel, R. Naaman, D. H. Waldeck, *Chem. Soc. Rev.* **45**, 6478–6487 (2016).
14. T. J. Zwang, S. Hürlimann, M. G. Hill, J. K. Barton, *J. Am. Chem. Soc.* **138**, 15551–15554 (2016).
15. R. A. Rosenberg, D. Mishra, R. Naaman, *Angew. Chem.* **54**, 7295–7298 (2015).
16. A. C. Aragonès *et al.*, *Small* **13**, 1602519 (2017).
17. M. Kettner, D. K. Bhowmick, M. Bartsch, B. Göhler, H. Zacharias, *Adv. Mater. Interfaces* **3**, 1600595 (2016).
18. J. M. Abendroth *et al.*, *ACS Nano* **11**, 7516–7526 (2017).
19. A. Kumar *et al.*, *Proc. Natl. Acad. Sci. U.S.A.* **114**, 2474–2478 (2017).
20. M. Johnson, *J. Appl. Phys.* **75**, 6714–6719 (1994).
21. E. Y. Tsymbal, I. Zutic, Eds., *Handbook of Spin Transport and Magnetism* (CRC Press, 2012).
22. M. Johnson, *Science* **260**, 320–323 (1993).
23. D. K. Schwartz, *Annu. Rev. Phys. Chem.* **52**, 107–137 (2001).
24. K. Michaeli, V. Varade, R. Naaman, D. H. Waldeck, *J. Phys. Condens. Matter* **29**, 103002 (2017).
25. O. Ben Dor *et al.*, *Nat. Commun.* **8**, 14567 (2017).
26. J. P. Perdew, K. Burke, M. Ernzerhof, *Phys. Rev. Lett.* **77**, 3865–3868 (1996).
27. J. P. Perdew, R. G. Parr, M. Levy, J. L. Balduz, *Phys. Rev. Lett.* **49**, 1691–1694 (1982).
28. J. P. Perdew, A. Savin, K. Burke, *Phys. Rev. A* **51**, 4531–4541 (1995).
29. A. Kumar, E. Capua, C. Fontanesi, R. Carmieli, R. Naaman, *ACS Nano* **12**, 3892–3897 (2018).
30. L. D. Barron, *Chirality* **24**, 957–958 (2012).
31. H. J. Choi, M. H. Hyun, *Chem. Commun. (Camb.)* **42**, 6454–6456 (2009).
32. S. G. Kozlova, M. R. Ryzhikov, N. B. Kompankov, M. S. Zavakhina, *J. Phys. Chem. B* **120**, 7517–7521 (2016).
33. N. Micali *et al.*, *Nat. Chem.* **4**, 201–207 (2012).
34. L. D. Barron, *Science* **266**, 1491–1492 (1994).
35. L. D. Barron, *Nature* **405**, 895–896 (2000).
36. D. E. Koshland, *Angew. Chem. Int. Ed. Engl.* **33**, 2375–2378 (1994).
37. Y. Zhang, D.-R. Wu, D. B. Wang-Iverson, A. A. Tymiak, *Drug Discov. Today* **10**, 571–577 (2005).
38. J. Itoh, K. Fuchibe, T. Akiyama, *Angew. Chem. Int. Ed.* **45**, 4796–4798 (2006).
39. K. Gedrich *et al.*, *Inorg. Chem.* **49**, 4440–4446 (2010).
40. R. Vaidhyanathan *et al.*, *Angew. Chem. Int. Ed.* **45**, 6495–6499 (2006).
41. A. V. Davis, D. Fiedler, M. Ziegler, A. Terpin, K. N. Raymond, *J. Am. Chem. Soc.* **129**, 15354–15363 (2007).
42. T. Liu, Y. Liu, W. Xuan, Y. Cui, *Angew. Chem. Int. Ed.* **49**, 4121–4124 (2010).
43. S. Inagaki, J. Z. Min, T. Toyo'oka, *Anal. Chem.* **80**, 1824–1828 (2008).
44. B. S. Sekhon, *Int. J. Chemtech Res.* **2**, 1584–1594 (2010).
45. S.-C. Ng, T. Sun, H. S. O. Chan, *Tetrahedron Lett.* **43**, 2863–2866 (2002).
46. G. Gübitz, M. G. Schmid, *Electrophoresis* **25**, 3981–3996 (2004).

ACKNOWLEDGMENTS

We thank A. Brandis for performing the HPLC measurements. **Funding:** Y.P. and R.N. acknowledge the support of the John Templeton Foundation. R.N. acknowledges the support of the Israel Science Foundation and the European Research Council under the European Union's Seventh Framework Program (FP7/2007–2013)–ERC grant agreement n° 338720 CISS. Y.P. acknowledges the support of the Israel Science Foundation and the Ministry of Science Israel. O.B.D. acknowledges support from the Israeli Ministry of Science, Technology, and Space, grant number 0399174. L.T.B. acknowledges institutional support from the Institute of Physics Polish Academy of Sciences. **Author contributions:** K.B.-G. performed the experiments on the DNA and with the HPLC; O.B.D. performed the adsorption experiments on the oligopeptides; F.T. performed the experiments applying the CD; E.C. prepared the setup for the adsorption experiments; S.Y. prepared and characterized the oligopeptides; A.C., S.-H.Y., and S.S.P.P. designed, prepared, and characterized the Ni substrates; S.S. performed and analyzed the calculations; L.K. participated in planning and analyzing the calculations; L.T.B. designed, prepared, and characterized the Co surfaces; R.N. and Y.P. conceived the experiments; and L.K., Y.P., and R.N. wrote the manuscript. **Competing interests:** E.C., S.Y., R.N., and Y.P. filed a patent on magnetic separation of chiral compounds, U.S. application no. 62/636,903. **Data and materials availability:** All the data are presented in the manuscript and supplementary materials.

SUPPLEMENTARY MATERIALS

www.sciencemag.org/content/360/6395/1331/suppl/DC1
Materials and Methods
Figs. S1 to S5
References (*47*–*51*)

7 November 2017; resubmitted 4 February 2018
Accepted 25 April 2018
Published online 10 May 2018
10.1126/science.aar4265

GEOPHYSICS

Observed rapid bedrock uplift in Amundsen Sea Embayment promotes ice-sheet stability

Valentina R. Barletta[1,2]*, Michael Bevis[2], Benjamin E. Smith[3], Terry Wilson[2], Abel Brown[2], Andrea Bordoni[4], Michael Willis[5], Shfaqat Abbas Khan[1], Marc Rovira-Navarro[1,6], Ian Dalziel[7], Robert Smalley Jr.[8], Eric Kendrick[2], Stephanie Konfal[2], Dana J. Caccamise II[2], Richard C. Aster[9], Andy Nyblade[10], Douglas A. Wiens[11]

The marine portion of the West Antarctic Ice Sheet (WAIS) in the Amundsen Sea Embayment (ASE) accounts for one-fourth of the cryospheric contribution to global sea-level rise and is vulnerable to catastrophic collapse. The bedrock response to ice mass loss, glacial isostatic adjustment (GIA), was thought to occur on a time scale of 10,000 years. We used new GPS measurements, which show a rapid (41 millimeters per year) uplift of the ASE, to estimate the viscosity of the mantle underneath. We found a much lower viscosity (4×10^{18} pascal-second) than global average, and this shortens the GIA response time scale from tens to hundreds of years. Our finding requires an upward revision of ice mass loss from gravity data of 10% and increases the potential stability of the WAIS against catastrophic collapse.

The viscosity of Earth's upper mantle has a key role in Earth's response to surface mass variations, especially visible in glaciated areas, at both local and global spatial scales. Those glaciated areas, including Greenland and Antarctica, contributed over the period 2002 to 2010 to global mean sea-level rise at an estimated rate of +1.22 ± 0.17 mm/year (*1*). Over the same time interval, the ASE, with an area of less than 4% of the Antarctic Ice Sheet (AIS), contributed to global mean sea-level rise at a rate of +0.3 ± 0.02 mm/year (*1*, *2*), a fourth of the entire cryosphere contribution. Ice flow rates in the ASE region are increasing (*3*, *4*), and the grounding line, controlled by the marine ice-sheet instability (*5*, *6*) and subglacial geology (*7*), is retreating rapidly (*8*). Bedrock deforms due to a combination of Earth's instantaneous elastic response to contemporary ice changes and the delayed viscoelastic response to past deglaciation (fig. S1). Regions underlain by high-viscosity mantle are mostly sensitive to the ancient ice history, whereas in the presence of low viscosity, only the recent ice history is relevant. The response time of ice-related Earth deformations is determined by the mantle viscosity: Viscosities ~10^{18} to 10^{19} Pa s correspond to decadal to centennial time scales (*9*–*12*), and viscosities ~10^{20} to 10^{21} Pa s to millennial time scales (*13*, *14*). GIA models for the whole of Antarctica adopt upper mantle (UM) (down to 670 km) viscosities larger than 10^{20} Pa s and up to 10^{21} Pa s driven by deglaciation starting 21,000 years ago at the Last Glacial Maximum. One of the most used models, ICE6G (*13*), is characterized by a UM viscosity with a value of 5×10^{20} Pa s, an intermediate value among the range used by most GIA models, and it predicts the largest present-day uplift rate in ASE among the models.

In glaciated regions undergoing large ice mass losses, such as the ASE, the GIA contribution has a considerable impact on gravity-derived ice mass variation estimates, because the Earth response, driven by the upper mantle viscosity, provides a contribution to the gravity field that, if not corrected for, translates into an apparent mass increase (fig. S2). The upper mantle viscosity has also been found to be crucial in predictions of ice-sheet stability, where bedrock uplift and consequent sea-level fall near the grounding line (fig. S3) have been shown to be an important stabilizing factor in ice-sheet behavior (*15*), with lower viscosity and consequent more rapid uplift resulting in greater negative feedback (*16*, *17*). The impact of mantle viscosity on ice-sheet stability has been investigated (*16*, *17*) for a wide range of viscosities (10^{19} to 10^{21} Pa s) that could not be narrowed further due to of lack of direct constraints on absolute mantle viscosity under the AIS. This issue is especially pronounced in ASE where ongoing ice mass loss is the largest. In fact, relative mantle viscosity variations under the AIS have been inferred based on seismic tomography (*18*–*20*) but with poor constraints on absolute viscosity. Absolute viscosity can instead be constrained when it is dynamically derived from bedrock uplift rate or relative sea-level history. Finding low viscosity under sensitive areas of the marine ice sheet, such as ASE, would therefore have very important consequences on studies for estimating future ice-sheet stability and substantially reduce uncertainties regarding future ice mass loss projections. The possibility that the mantle viscosity in the ASE deviates significantly from the global average is supported by indications of geologically recent volcanism (*21*) and Cenozoic rifting in much of West Antarctica and limited evidence pointing to rift-related displacements of Oligocene age between the Thurston Island–Eights Coast and Marie Byrd Land crustal blocks flanking the Amundsen sector (*22*, *23*). In other glaciated regions (Patagonia, Alaska, Iceland, and North Antarctic Peninsula), large uplift rates measured by dense local GPS networks have been used to constrain low viscosity (*9*–*12*). For this reason, we installed GPS on bedrock around the ASE to better constrain the viscosity of the shallow mantle.

We analyzed the deformation rates (Fig. 1) using six GPS stations as part of a global geodetic analysis following a recently developed processing strategy (*24*, *25*). We found that the data indicate that ASE is undergoing one of the fastest GIA-related uplift rates ever recorded (up to 41 mm/year). In this work, we made use of solid Earth viscoelastic modeling to invert these data for the first estimate of absolute viscosity under ASE, using the new GPS solutions as constraints. To model uplift, we used a high-resolution approach (*12*, *26*) with a spatial resolution of 1 km, which is much higher than previous studies (*9*–*11*). Our compressible viscoelastic Earth model has a viscosity structure more complex than the single-layer mantle assumed in previous studies (*9*–*11*) and provides insight into the rheology of the whole upper mantle down to 670 km. The paucity of GPS constraints and the scarcity of glaciological information about local ice history forced us to thoroughly explore the impact of those uncertainties on the viscosity model. To accomplish this, we designed a new strategy for incorporating ice history that allows us to combine several independent components (denoted as Hx, with x being an index) with different weights. The most important ice history components are the well-observed, high-resolution, regional, yearly surface distribution of present-day ice changes (*27*), which have the spatial trend shown in Fig. 1A, and a total mass trend of −130 Gt/year, for the period 2002 to 2014 (denoted as H0), and the component representing ice history for the period 1900 to 2002, constructed by rescaling the spatial pattern in Fig. 1A (denoted as H1) based on increased ice flux since 1970 (*4*). We performed a grid search over physical parameters by comparing the modeled predictions with the observations (*27*). The inversion parameters for the Earth model are the thickness of the elastic lithosphere (LT) (ranging from 20 to 90 km) and the viscosities of three layers: shallow upper mantle (SUM) (from the base of the lithosphere to 200 km depth), the deeper upper mantle (DUM) (from 200 to 400 km depth), and the transition zone (TZ) (from

[1]DTU Space, National Space Institute, Geodynamics Department, Technical University of Denmark, Kgs. Lyngby, Denmark. [2]School of Earth Science, Ohio State University, Columbus, OH, USA. [3]University of Washington, Seattle, WA, USA. [4]DTU Compute, Technical University of Denmark, Kgs. Lyngby, Denmark. [5]University of Colorado Boulder, Boulder, CO, USA. [6]TU Delft, Delft, Netherlands. [7]Institute for Geophysics, University of Texas, Austin, TX, USA. [8]Center for Earthquake Research and Information, The University of Memphis, Memphis, TN, USA. [9]Colorado State University, Fort Collins, CO, USA. [10]Penn State University, State College, PA, USA. [11]Washington University in St. Louis, St. Louis, MO, USA.
*Corresponding author. Email: vr.barletta@gmail.com

400 to 670 km). We computed 807 different Earth models with about 10,000 variations of those models by linearly combining our results for different scenarios of ice history (*27*) (Fig. 1B).

We first verified that the instantaneous elastic contribution to the uplift rate caused by the present-day ice mass changes in the ASE region are only ~20% of the recorded signal at best (Fig. 1, C and D), in marked contrast to the generally elastically driven high-uplift rates observed in Greenland (*24*). The spatial pattern of the high uplift rates at the ASE excludes the possibility of an alternative geological origin, such as volcanic activity (*27*), and is also incompatible with Earth deformation models driven by deglaciation starting at the Last Glacial Maximum 21,000 years ago. Fig. 1C shows the predictions from model ICE6G (*13*), which are the largest among recent GIA models, in which a stiff mantle viscosity (>10^{20} Pa s) produces a smooth, uniform deformational response at the spatial scale of the ASE. This is in sharp contrast to the more spatially variable uplift that we measured with GPS (Fig. 1C), and it is evident in the residual signal (simply residual, in the following) obtained subtracting the modeled elastic uplift rates from those measured by the GPS. Horizontal GPS displacements, which are heterogeneous in both magnitude and direction (Fig. 1D), show similar spatial behavior. The horizontal motions depend strongly on the location of ice mass changes, and the residual motion vectors have directions that are close to those of the elastic response to modern-day ice changes (Fig. 1D). This indicates that these large GPS rates (Fig. 1) are a response to ice mass loss with a pattern that is consistent with present-day ice changes (*27*).

By comparing the residual with predictions from our viscoelastic modeling, we found that a viscosity range for the SUM between 10^{18} and 6.3 × 10^{18} Pa s ($\log_{10}$18.0 to $\log_{10}$18.8) is suitable to explain the deformation rates observed in ASE (*27*). Unexpectedly, we also find a better-fit viscosity model by decreasing the viscosity of deeper mantle layers (note the range of low viscosity in the axis of Fig. 2). The viscosities of SUM and DUM are not independent (blue line in Fig. 2A): that is, if we chose to fix DUM viscosity at excessively high values, a good fit is obtained for excessively low values for SUM, but still worse than our best fit to observations. Thus, the observations collected by our GPS network configuration are indeed sensitive to both shallow and the deeper mantle structure (*27*). Even more surprisingly, we found that the resolving power of the GPS network extends to the TZ (Fig. 2B). The relationship we found between DUM and TZ (blue line in Fig. 2B) shows that the TZ layer has a minor but detectable influence on observed bedrock motion (*27*).

We strongly constrained the upper mantle to a narrow range of low viscosity with our grid search (table S4 and Fig. 2); even considering uncertainties due to ice history reconstruction (*27*), fitting the observed signal with models results in R^2 = 0.96 (Fig. 3A). Our preferred model [lowest root mean square deviation (RMSD)], using the initial estimate for ice history (H0 + H1 in Fig. 1B, using a mass loss rate of 130 Gt/year for the period 2002 to 2014 and of 32.5 Gt/year for the period 1900 to 2002), has a 60-km-thick lithosphere, a shallow upper mantle of ~4 × 10^{18} ($\log_{10}$18.6) Pa s; a deeper upper mantle that is about four times stiffer, ~1.6 × 10^{19} ($\log_{10}$19.2) Pa s; and a transition zone value of 2.5 × 10^{19} ($\log_{10}$19.4) Pa s (Fig. 3A, Best 2). These values provide a good fit to the vertical and horizontal nonelastic signal (Fig. 3A) that is within the confidence intervals for the sites with the highest signal-to-noise ratio. In all cases, we found a model preference for an elastic lithosphere that is thicker than 50 km, with a clear, rapid deterioration of the fit for a thinner lithosphere (Fig. 2A). The best fits for elastic lithosphere thicknesses are between 50 and 60 km, which are consistent with seismological studies of the region (*18*).

We found that ASE has a rheological structure very different from those commonly used in global and regional dynamic Earth models (*13*, *14*), with the upper mantle viscosity being about two orders of magnitude lower. Low viscosity provides independent support for a hot mantle, as suggested by seismological results (*19*) and an elevated geothermal heat flux (*28*) in the region. Low viscosity is also supported by the characteristics of the subglacial geology that provide important boundary conditions for the evolution of the ice sheet (*7*, *29*). The low viscosity we found in deeper layers

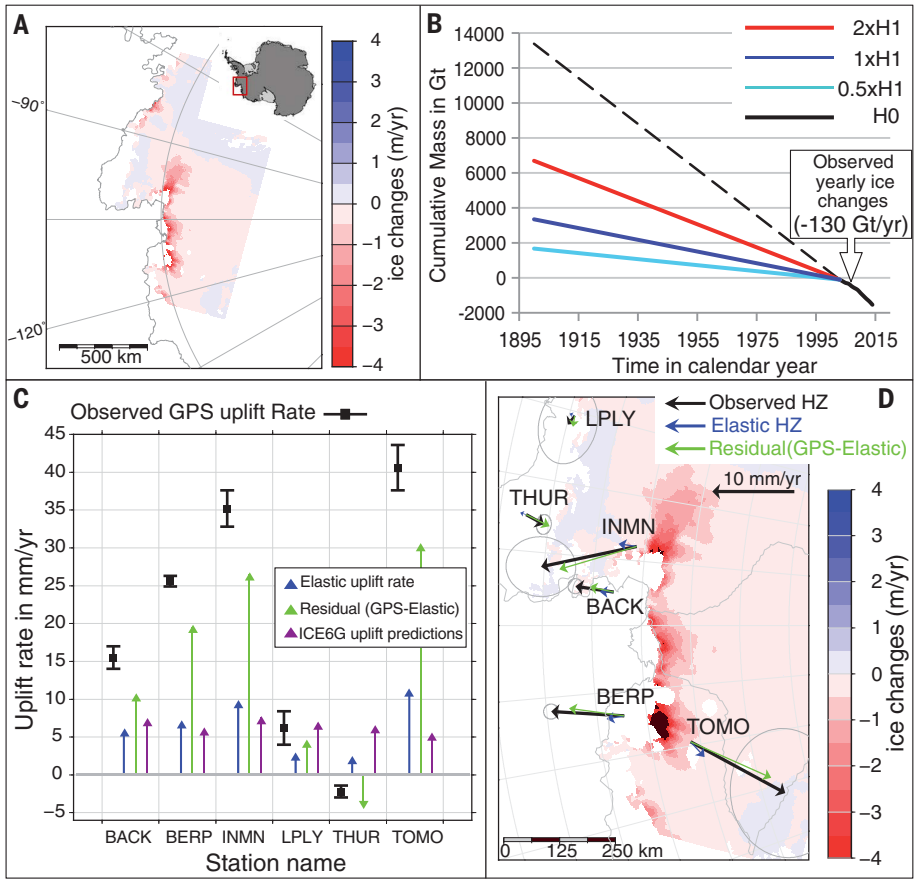

Fig. 1. Observations of bedrock motions and ice changes. (**A**) The average trend of ice mass changes in m/year of water equivalent for the 13 years 2002 to 2014 derived from satellite altimetry. (**B**) The cumulative total mass in Gt for the extrapolation of the ice history of the last century derived by rescaling of the pattern in (A). The black line represents the cumulative mass loss estimated from the yearly grids observed for the period 2002 to 2014, that is, the H0 ice history contribution. The blue solid line represents the cumulative mass loss for ice history contribution H1 for the period 1900 to 2002. We used the sum of the contribution for H0 and H1 as our initial estimate of mass change history. The black dashed line represents the ice history contribution obtained by extending the present-day rate to the past. The light blue and the red lines represent half and twice the rate of the H1 ice history contribution respectively. (**C** and **D**) show vertical (squares with error bars) and horizontal (arrows) observed GPS bedrock motion (black), respectively (reported in table S2). Horizontal motions are expressed in a frame that fixes, or nearly fixes, East Antarctica (*27*). Blue arrows show predicted elastic velocities (as in column 5 of table S2) using the observed ice mass changes shown in (A). Green arrows show the residual motions (observed uplift minus elastic predictions). Purple arrows—only for the vertical (C)—show the uplift prediction of the ICE6G (*13*) model. The ellipses in (D) represent uncertainties (±1 SD) for the associated observed horizontal velocity vectors. The background of (D) is the ice mass change in m/year of (A).

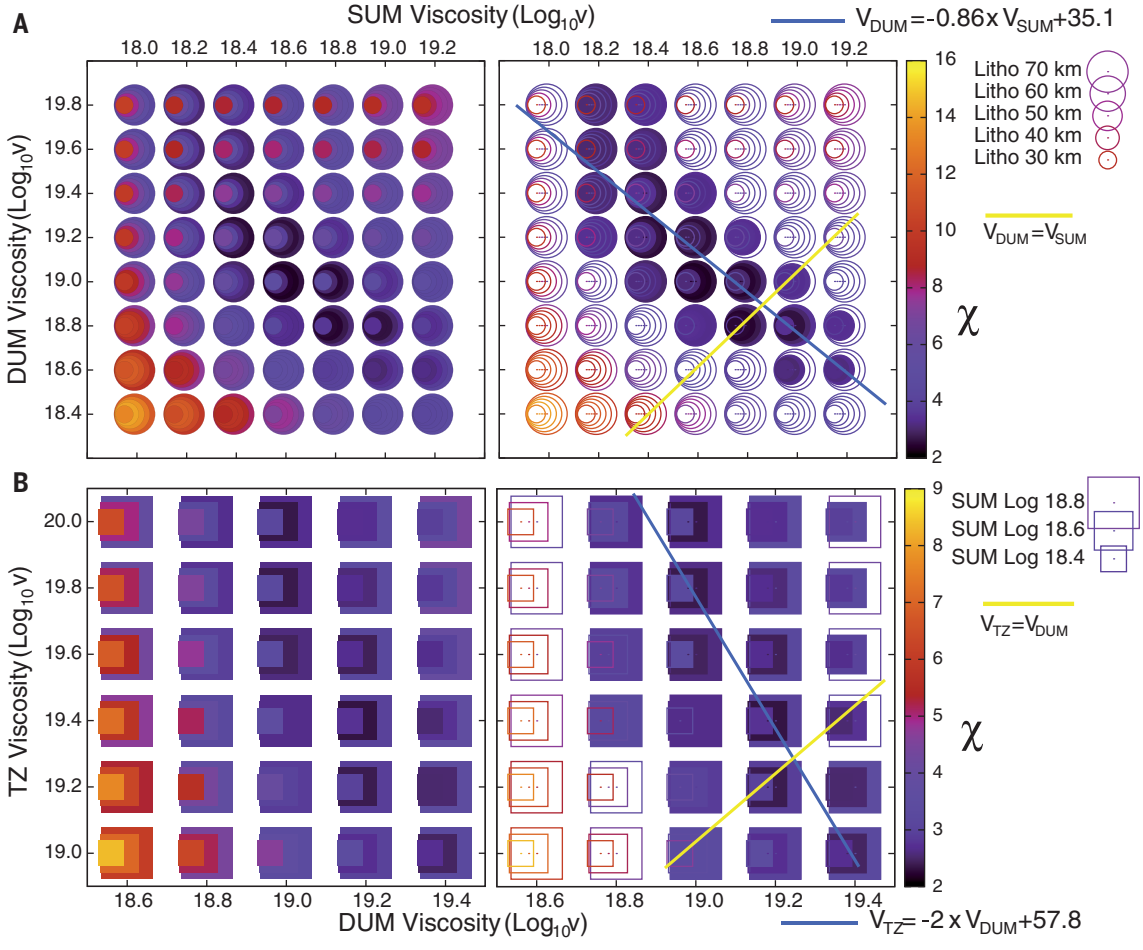

Fig. 2. Viscosity of the mantle to 670 km. (**A**) (Left) The misfit χ (color scale from 2 to 16) as a function of the shallow upper mantle (SUM) viscosity (*x* axis) and the deep upper mantle (DUM) viscosity (*y* axis) for transition zone (TZ) viscosity fixed at 7×10^{19} Pa s, for experiment E2 (*27*). Estimates of lithospheric thickness, ranging from 30 to 70 km, are shown by circle size (right), with solid circles showing the acceptable estimates within the 95% confidence interval. The blue line represents the best-fitting relation between the DUM and SUM viscosities. The yellow line divides the region where the SUM has a higher viscosity than the DUM, a configuration considered less likely. The best fit for this experiment is for LT 60 km, SUM $\log_{10}$ 18.6 Pa s, DUM $\log_{10}$ 19.0 Pa s (TZ $\log_{10}$ 19.84 Pa s) with a χ = 2.36. (**B**) (Left) The misfit χ (color scale from 2 to 9) as a function of the DUM viscosity (*x* axis) and the TZ viscosity (*y* axis) for three values of SUM viscosity (squares) and for fixed lithospheric thickness of 60 km for experiment E3 (*27*). (Right) Confidence interval, similar to the right plot in (A), applied to experiment E3 (*27*). The best fit for this experiment is for LT 60 km, SUM $\log_{10}$ 18.6 Pa s, DUM $\log_{10}$ 19.2 Pa s, and TZ $\log_{10}$ 19.4 Pa s with a χ = 2.32.

could be an indication of a plume-like thermal structure such as the one hypothesized in nearby Marie Byrd Land (*19*, *30*). Yet it can more confidently be attributed to a mantle chemically altered by hydrous fluids and volatile silicate melts generated by protracted Paleozoic-Cretaceous subduction (*31*). Low viscosity could characterize other areas of West Antarctica where geological and seismic evidence similarly suggests that the presence of a hot mantle (*19*, *28*, *30*) is more widespread under areas where surface bedrock exposure is rare or absent. The viscosity we estimated under ASE is dynamically constrained without any a priori geological assumptions and can be used to set a reference value for a regional Earth model based on seismic tomography, which has large absolute uncertainties when interpreted for viscosity.

Observed ASE bedrock uplift rates, due to the low-viscosity mantle and short time scale Earth response to ice changes (Fig. 3A), are higher than expected (*13*, *14*). The uplift rate is also predicted to accelerate with time (Fig. 3, B and C), producing an increasing impact on the gravity field. Both ice mass loss and the flow of mantle material perturb the time-variable gravity field observed by the Gravity Recovery and Climate Experiment (GRACE) satellite pair (fig. S2). The solid Earth effect results in an apparent mass increase that must be removed to estimate ice mass changes from observations of gravity changes. GRACE studies employ a constant rate of apparent mass change due to GIA of between +3.5 and +5.5 Gt/year water equivalent for the combined Pine Island and Thwaites glacier basins (*2*). Using our best local model, we calculated a much larger present-day apparent mass change of +16.7 Gt/year (*27*) for GRACE-derived mass trends over 2002 to 2014. This effect is, furthermore, not constant with time, as considered in previous studies (*1*, *2*), because it depends on recent ice mass changes. We estimate that apparent mass change will increase by >2% per year in coming decades even if the ice mass loss rate does not increase. We thus contend that published GRACE-derived ice mass loss estimates for ASE, for example, ~108 Gt/year (*1*) (drainage basins of Pine Island and Thwaites and Smith glaciers), are systematically underestimated by between 10.0 and 13.9 Gt/year, which is more than 10% of the total ice mass loss estimate for the ASE.

The extremely low upper mantle viscosity that we constrain supports the possibility of increased stability of the WAIS with respect to previous studies (*16*, *17*). Lower mantle viscosity leads to faster bedrock uplift in response to ice mass loss. Rapidly rising bedrock shallows the ocean at the grounding line and reduces the buoyancy forces experienced by the edge of the ice sheet while reducing the slope of the bed beneath the ice sheet (fig. S3). A laterally homogeneous viscosity of 10^{19} Pa s for the upper mantle has been used in the Earth modeling (*16*, *17*) and found to be sufficient to prevent collapse of WAIS under moderate climate warming scenarios and to delay it for the more extreme scenarios. The timing of the Earth response is completely determined by the viscosity structure, and we numerically estimated (*27*) the response-speed increase when using our preferred model. Even under the assumption that the current rate of ice thinning will be constant in the ASE over the next century, we found that the uplift rate will increase

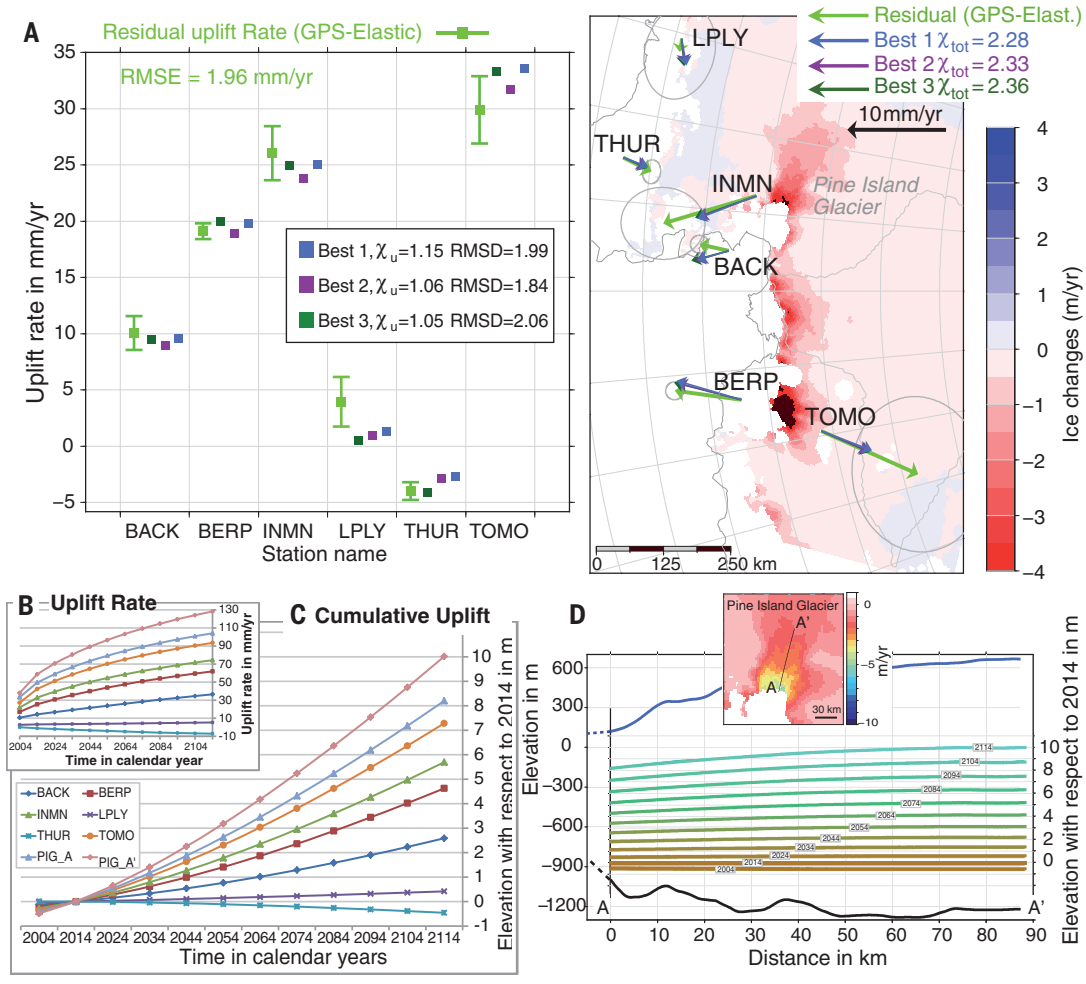

Fig. 3. Vertical and horizontal bedrock motion predictions. (**A**) The vertical (left) and horizontal (right) observed GPS minus elastic modeled residual velocities (green dot in left plot, green arrows in right plot) as in column 5 of table S2. Vertical and horizontal velocity predictions from three viscosity models providing good fit (R^2 = 0.96) are shown by the blue (Best 1), purple (Best 2), and dark green (Best 3) symbols. These models are our three best-fitting models (the total χ is reported in the legend of the right plot). In the text ,we indicate Best 2 as our preferred model because it has the lowest RMSD for the uplift rates. The error bars (left) are the weighted errors (error bar = SD/weight). The ellipses in (A) (right) represent uncertainties (±1 SD) for the associated residual horizontal velocity vectors. The weights are 1 except for LPLY and the horizontal for TOMO. Assuming that the current rate of ice thinning will be constant in the ASE throughout the next century, the evolution of uplift rates (**B**) and uplift (**C**) at the six GPS sites and points A and A′ of the profile along Pine Island Glacier are shown in (**D**). Ice mass loss in Pine Island Glacier (D, inset), and the elevation of the profile A-A′ for bedrock and ice [black and blue line from BEDMAP2 (*32*), respectively]. Bedrock variations along the profile AA′ from 2004 to 2114 with respect to 2014 are labeled.

(Fig. 3, B and C). In 100 years, uplift rates at the GPS sites will be between 2.5 and 3.5 times larger than currently observed (Fig. 3B), and the bedrock at the Pine Island Glacier grounding line will have risen by about 8 m compared to the present (Fig. 3, C and D). This is about three times higher than values shown to reduce runaway ice surface velocities within 100 years (*15*). The time required to build sufficient deformation to trigger the stabilization effect is much shorter (*27*) than in (*16*). Under low and medium climate forcing, with the onset of the stabilization feedback about two times faster (*27*), the condition for ice-sheet stability and its possible readvance can reasonably be expected to occur much earlier than predicted in previous studies (*16*, *17*). Based on our estimates, it might produce a deformation large enough and early enough in the deglaciation phase to prevent the complete collapse of the WAIS even under strong climate forcing. To investigate this last point, a full ice-Earth coupled simulation as in (*16*, *17*) that incorporates revised Earth properties is necessary. Earth structure can be expected to become increasingly relevant to the next generation of ice-Earth coupled models, where lateral variations under WAIS will be incorporated.

The weak Earth structure that we found under ASE and the related rapid stability feedback have a strong direct impact on WAIS evolution at the centennial time scale. The presence of such a low viscosity under ASE has effects on the millennial time scale also, with important implications on understanding of the potential WAIS collapse scenarios, as well as on the development of paleo ice-sheet history reconstructions and the associated long-term Earth deformation models (*13*, *14*), hopefully helping to improve the accuracy of future climate change prediction and sea-level projection.

REFERENCES AND NOTES

1. M. A. King *et al.*, *Nature* **491**, 586–589 (2012).
2. V. R. Barletta, L. S. Sørensen, R. Forsberg, *Cryosphere* **7**, 1411–1432 (2013).
3. E. Rignot *et al.*, *Nat. Geosci.* **1**, 106–110 (2008).
4. J. Mouginot, E. Rignot, B. Scheuchl, *Geophys. Res. Lett.* **41**, 1576–1584 (2014).
5. L. Favier *et al.*, *Nat. Clim. Chang.* **4**, 117–121 (2014).
6. IPCC, *Clim. Change* **2013**, 1535 (2013).
7. R. G. Bingham *et al.*, *Nature* **487**, 468–471 (2012).
8. E. Rignot, J. Mouginot, M. Morlighem, H. Seroussi, B. Scheuchl, *Geophys. Res. Lett.* **41**, 3502–3509 (2014).
9. A. Auriac *et al.*, *J. Geophys. Res. Solid Earth* **118**, 1331–1344 (2013).
10. A. Richter *et al.*, *Earth Planet. Sci. Lett.* **452**, 206–215 (2016).
11. C. F. Larsen, R. J. Motyka, J. T. Freymueller, K. A. Echelmeyer, E. R. Ivins, *Earth Planet. Sci. Lett.* **237**, 548–560 (2005).
12. G. A. Nield *et al.*, *Earth Planet. Sci. Lett.* **397**, 32–41 (2014).
13. W. R. Peltier, D. F. Argus, R. Drummond, *J. Geophys. Res. B Solid Earth* **120**, 450–487 (2015).
14. P. L. Whitehouse, M. J. Bentley, G. A. Milne, M. A. King, I. D. Thomas, *Geophys. J. Int.* **190**, 1464–1482 (2012).
15. S. Adhikari *et al.*, *Solid Earth* **5**, 569–584 (2014).
16. N. Gomez, D. Pollard, D. Holland, *Nat. Commun.* **6**, 8798 (2015).
17. H. Konrad, I. Sasgen, D. Pollard, V. Klemann, *Earth Planet. Sci. Lett.* **432**, 254–264 (2015).
18. D. S. Heeszel *et al.*, *J. Geophys. Res. B Solid Earth* **121**, 2015JB012616 (2016).
19. A. J. Lloyd *et al.*, *J. Geophys. Res. B Solid Earth* **120**, 8439–8460 (2015).
20. J. P. O'Donnell *et al.*, *Earth Planet. Sci. Lett.* **472**, 38–49 (2017).
21. H. F. J. Corr, D. G. Vaughan, *Nat. Geosci.* **1**, 122–125 (2008).
22. T. Kalberg, K. Gohl, G. Eagles, C. Spiegel, *Mar. Geophys. Res.* **36**, 263–279 (2015).
23. C. Spiegel *et al.*, *Global Planet. Change* **145**, 98–115 (2016).
24. M. Bevis *et al.*, *Proc. Natl. Acad. Sci. U.S.A.* **109**, 11944–11948 (2012).

25. M. Bevis, A. Brown, E. Kendrick, *J. Geod.* **87**, 311–321 (2013).
26. V. R. Barletta *et al.*, *Geophys. Res. Lett.* **33**, L14307 (2006).
27. Materials and methods are available as supplementary materials.
28. D. M. Schroeder, D. D. Blankenship, D. A. Young, E. Quartini, *Proc. Natl. Acad. Sci. U.S.A.* **111**, 9070–9072 (2014).
29. M. L. Pittard, B. K. Galton-Fenzi, J. L. Roberts, C. S. Watson, *Geophys. Res. Lett.* **43**, 3342–3350 (2016).
30. E. L. Emry *et al.*, *Geochem. Geophys. Geosyst.* **16**, 40–58 (2015).
31. C. A. Finn, R. D. Müller, K. S. Panter, *Geochem. Geophys. Geosyst.* **6**, (2005).
32. P. Fretwell *et al.*, *Cryosphere* **7**, 375–393 (2013).

ACKNOWLEDGMENTS

V.R.B. is indebted to C. Madison for important support in writing the manuscript. The authors thank DTU Computing Center (DCC), where the modeling simulations were performed, for the precious support provided. This research is a contribution to the SCAR SERCE program. **Funding:** This research was supported by the European Space Agency (ESA) in the framework of the project GOCE+ Antarctica - Dynamic Antarctic Lithosphere, the U.S. National Science Foundation Office of Polar Programs, and the U.S. Antarctic Program. VE-CLOV3RS was developed by V.R.B and A. Bordoni in a self-funded project. **Author contributions:** V.R.B. and M.B. planned the modeling strategy. V.R.B. computed the solid Earth predictions, performed the comparative analysis with the data, interpreted the results, prepared the figures, and wrote the original manuscript. M.B. provided GPS analysis, reference frame realization, trajectory analysis, interpretation, and writing. B.E.S. processed the altimetry data. T.W. supervised the work and provided input on the analysis, interpretation, and writing. A. Bordoni computed the Earth model Green's functions and advised on analysis, interpretation, and writing. S.A.K. computed elastic deformation for a double-blind test and contributed to writing. M.R.-N. provided ice history uncertainty assessment. M.W. advised on altimetry data and contributed to writing. A. Brown and E.K. performed GPS data analysis. D.J.C., I.D., E.K., S.K., R.S., M.W., and T.W. performed GPS fieldwork. D.J.C. provided GPS instrumental support. S.K. advised on the comparative analysis. D.A.W., R.C.A., and A.N. provided seismological Earth parameters and contributed to interpretation. T.W. and I.D. worked on tectonic framework issues. **Competing interests:** None declared. **Data and materials availability:** The POLENET GPS data are open and immediately available from the Data Archive Interface (DAI, www.unavco.org/data/gps-gnss/data-access-methods/dai2/app/dai2.html) of UNAVCO. The grids of ice mass changes derived with satellite altimetry are available at ftp://ftp.space.dtu.dk/pub/barletta/dZ_and_mass_estimates_Dec_10_2014.mat. Other relevant data are available at ftp://ftp.space.dtu.dk/pub/barletta. Code availability: The code VE-HResV2 computes the vertical and horizontal deformation given an input grid load and given the elastic or the viscoelastic Green's functions for an Earth model. It is available as Fortran code upon request to the author. The code VE-CLOV3RS v.3.5.6 computes the elastic and the viscoelastic Green's functions given an Earth model. The part of the code for the elastic Green's function (or elastic Love numbers) is available as executable upon request to the authors. The part of the code for the viscoelastic Green's function has been ported to high-performance clusters. It is still under development, and it is not user friendly at this stage. It is recommended that you ask the author to have it configured and run for you with your preferred Earth model. Both codes already have been used in other studies (*12*).

SUPPLEMENTARY MATERIALS

www.sciencemag.org/content/360/6395/1335/suppl/DC1
Supplementary Text
Figs. S1 to S13
Tables S1 to S4
References (*33*–*85*)

20 June 2017; accepted 25 April 2018
10.1126/science.aao1447

WATER PROPERTIES

Anomalously low dielectric constant of confined water

L. Fumagalli[1,2]*, A. Esfandiar[3], R. Fabregas[4,5], S. Hu[1,2], P. Ares[1,2], A. Janardanan[1,2], Q. Yang[1,2], B. Radha[1,2], T. Taniguchi[6], K. Watanabe[6], G. Gomila[4,5], K. S. Novoselov[1,2], A. K. Geim[1,2]*

The dielectric constant ε of interfacial water has been predicted to be smaller than that of bulk water (ε ≈ 80) because the rotational freedom of water dipoles is expected to decrease near surfaces, yet experimental evidence is lacking. We report local capacitance measurements for water confined between two atomically flat walls separated by various distances down to 1 nanometer. Our experiments reveal the presence of an interfacial layer with vanishingly small polarization such that its out-of-plane ε is only ~2. The electrically dead layer is found to be two to three molecules thick. These results provide much-needed feedback for theories describing water-mediated surface interactions and the behavior of interfacial water, and show a way to investigate the dielectric properties of other fluids and solids under extreme confinement.

Electric polarizability of interfacial water determines the strength of water-mediated intermolecular forces, which in turn affects phenomena such as surface hydration, ion solvation, molecular transport through nanopores, chemical reactions, and macromolecular assembly (*1*–*3*). The dielectric properties of interfacial water have attracted intense interest for many decades (*4*–*7*), yet no clear understanding has been reached (*8*–*11*). Theoretical (*12*–*14*) and experimental studies (*15*–*17*) have shown that water exhibits layered structuring near surfaces, which suggests that it may form ordered (ice-like) phases under ambient conditions. Such ordered water is generally expected to exhibit small polarizability because of surface-induced alignment of water molecular dipoles, which are then difficult to reorient by applying an electric field (*7*–*10*). Despite these extensive studies, the dielectric constant ε of interfacial water and its depth remain essentially unknown because measurements are challenging.

Previous experiments to assess ε of interfacial water mostly relied on broadband dielectric spectroscopy applied to large-scale naturally occurring systems such as nanoporous crystals, zeolite powders, and dispersions (*4*, *5*, *10*, *18*, *19*). These systems allow sufficient amounts of interfacial water for carrying out capacitance measurements, but the complex geometries require adjustable parameters and extensive modeling, which results in large and poorly controlled experimental uncertainties. For example, the extracted values of ε depended strongly on assumptions about the interfacial layer thickness. Given the lack of direct probes for measuring the polarizability of interfacial water, most evidence has come from molecular dynamics (MD) simulations, which also involve certain assumptions. These studies generally predict that the polarizability should be reduced by approximately an order of magnitude (*7*–*9*), but the quantitative accuracy of these predictions is unclear because the same simulation approach struggles to reproduce the known ε for bulk water phases (*20*).

Here, we used slit-like channels of various heights h that could be filled controllably with water. The channels were incorporated into a capacitance circuit with exceptionally high sensitivity to local changes in dielectric properties, which allowed us to determine the out-of-plane dielectric constant $\varepsilon_\perp$ of the water confined inside. We fabricated our devices by van der Waals assembly (*21*) of three atomically flat crystals of graphite and hexagonal boron nitride (hBN) following a method reported previously (*22*–*24*) (fig. S1). Graphite was used as a bottom layer for the assembly as well as the ground electrode in capacitance measurements (Fig. 1A). Next, a spacer layer was placed on top of graphite, an hBN crystal patterned into parallel stripes. The assembly was completed by placing another hBN crystal on top (Fig. 1, B and C). The spacer determined the channels' height h, and the other two crystals served as top and bottom walls. The reported channels were usually ~200 nm wide and several micrometers long. Each of our devices for a given h contained several channels in parallel (Fig. 1), which ensured high reproducibility of our measurements and reduced statistical errors. When required, the channels could be filled with water through a micrometer-size inlet etched in graphite from the back (*22*, *23*) (Fig. 1A).

To probe ε of water inside the channels, we used scanning dielectric microscopy based on electrostatic force detection with an atomic force microscope (AFM), adapting the approach described in (*25*). Briefly, by applying a low-frequency ac voltage between the AFM tip and the bottom electrode, we could detect the tip-substrate electrostatic force, which translated into the first derivative of the local capacitance dC/dz in the out-of-plane direction z. By raster-scanning the tip, a dC/dz (or "dielectric") image was acquired, from which local dielectric properties could be reconstructed (*24*). The device design allowed the AFM tip to be fully isolated from water inside the channels and to operate in a dry atmosphere. Note that the use of hBN is essential for these experiments. First, hBN is highly insulating, which allows the electric field generated by the AFM tip to reach the subsurface water without being screened. It is also highly beneficial to have hBN as the side walls (spacers) because this material provides a straightforward reference for comparison between the dielectric properties of hBN ($\varepsilon_\perp \approx 3.5$) (*26*) and the nearby water of the same thickness (Fig. 1C). As shown below, the latter arrangement yielded an unambiguous dielectric contrast, revealing that ε of confined water strongly changes with decreasing h independently of the modeling.

Unlike the previous reports (*22*, *23*), we chose to use relatively thin (30 to 80 nm) top crystals, which allowed us not only to reach closer to the subsurface water but also to ensure that the channels were fully filled during the capacitance measurements (see below) (fig. S2) (*24*). When there was no water inside, the top hBN exhibited notable sagging (*22*) (Fig. 1B). In Fig. 1, E to G, we show AFM topographic images for representative devices with $h \approx 10$ nm, 3.8 nm, and 1.4 nm, respectively, under dry conditions. All devices exhibited some sagging, the extent of which depended on the thickness of the top hBN (*22*) (black curves in Fig. 1, H to J). We used the areas that were not covered by the top hBN layer (cyan curves) to determine the channel heights h from the same images. Such initial imaging, as well as dielectric imaging after filling the channels, was carried out at low relative humidity (below 3%) and at room temperature.

Figure 2, A to C, shows AFM topographic images for the same three devices and the same scan areas as in Fig. 1, E to G, but after filling the channels with water, which was done by exposing the backside of our devices to deionized water (*22*) (Fig. 1A). After the channels were filled, the adhesion between the side and top walls decreased and the sagging diminished (Fig. 1C). The top hBN layer covering water-filled channels became straight with little topographic contrast remaining, independently of h (red curves in Fig. 1, H to J). The corresponding dielectric images for the discussed devices after their filling are shown in Fig. 2, D to F. They show very strong contrast that reverses with decreasing h. For the 10-nm channels, the red regions containing subsurface water indicate $\varepsilon_\perp$ greater than that of hBN, as expected (Fig. 2, D and G, red). For the 3.8-nm-thick water, the dielectric contrast disappeared (Fig. 2, E and G, cyan), whereas the

[1]School of Physics and Astronomy, University of Manchester, Manchester M13 9PL, UK. [2]National Graphene Institute, University of Manchester, Manchester M13 9PL, UK. [3]Department of Physics, Sharif University of Technology, P.O. Box 11155-9161, Tehran, Iran. [4]Departament d'Electrònica, Universitat de Barcelona, C/ Martí i Franquès 1, 08028 Barcelona, Spain. [5]Institut de Bioenginyeria de Catalunya, Barcelona Institute of Science and Technology, C/ Baldiri i Reixac 15-21, 08028 Barcelona, Spain. [6]National Institute for Materials Science, 1-1 Namiki, Tsukuba 305-0044, Japan.
*Corresponding author. Email: laura.fumagalli@manchester.ac.uk (L.F.); geim@manchester.ac.uk (A.K.G.)

1.4-nm-thick water exhibited the opposite, negative contrast (Fig. 2, F and G, blue). The images show that the polarizability of confined water strongly depends on its thickness h and reaches values less than that of hBN with its already modest $\varepsilon_\perp \approx 3.5$. As mentioned above, a reduction in $\varepsilon_\perp$ for strongly confined water is generally expected from atomistic simulations (*7*–*9*), but the observed decrease is much stronger than predicted ($\varepsilon_\perp \approx 10$) or commonly assumed (*24*).

To quantify the measured local capacitance and find $\varepsilon_\perp$ for different water thicknesses, we used a three-dimensional electrostatic model that takes into account the specific geometry of the measured devices and the AFM tips chosen (*24*)

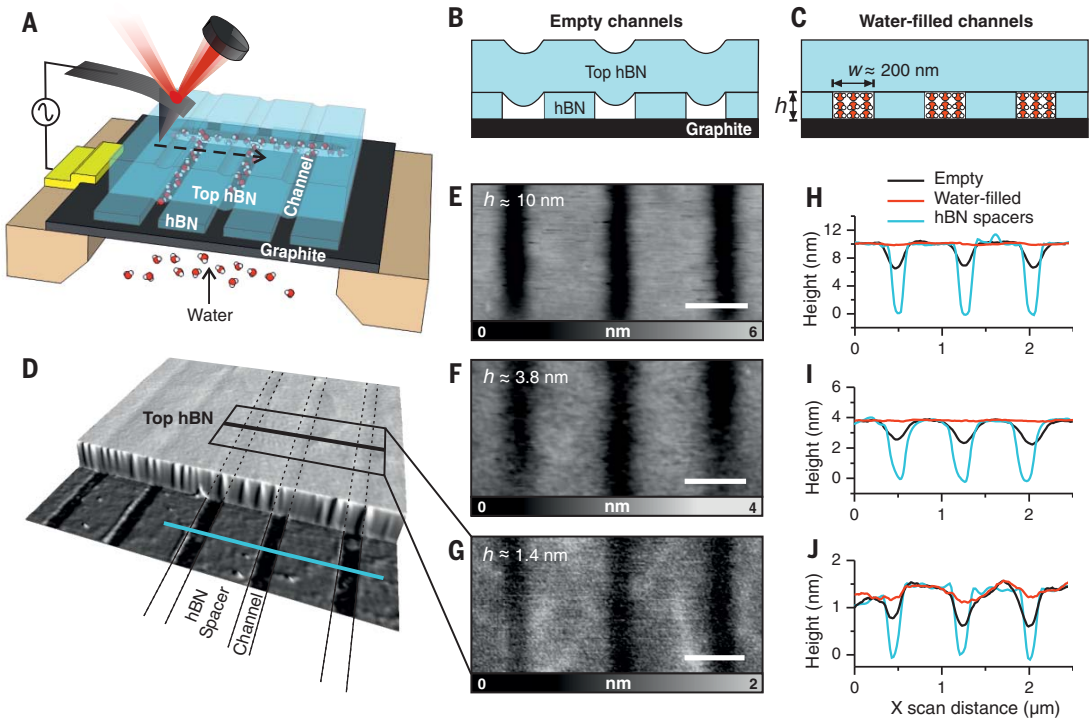

Fig. 1. Experimental setup for dielectric imaging. (**A**) Schematic illustration. The top layer and side walls made of hBN are shown in light blue; graphite serving as the ground electrode is in black. The three-layer assembly covers an opening in a silicon nitride membrane (light brown). The channels are filled with water from the back. The AFM tip served as the top electrode and was kept in a dry nitrogen atmosphere. (**B** and **C**) Cross-sectional schematics before (B) and after (C) filling the channels with water (not to scale). (**D**) Three-dimensional topography image of one of our devices. (**E** to **G**) AFM topography of the sagged top hBN for devices with different values of h before filling them with water. Scale bars, 500 nm. (**H** to **J**) Corresponding topography profiles for the top layer (black) and the part not covered by hBN (cyan) as indicated by color-coded lines in (D). Red curves: Same after filling with water.

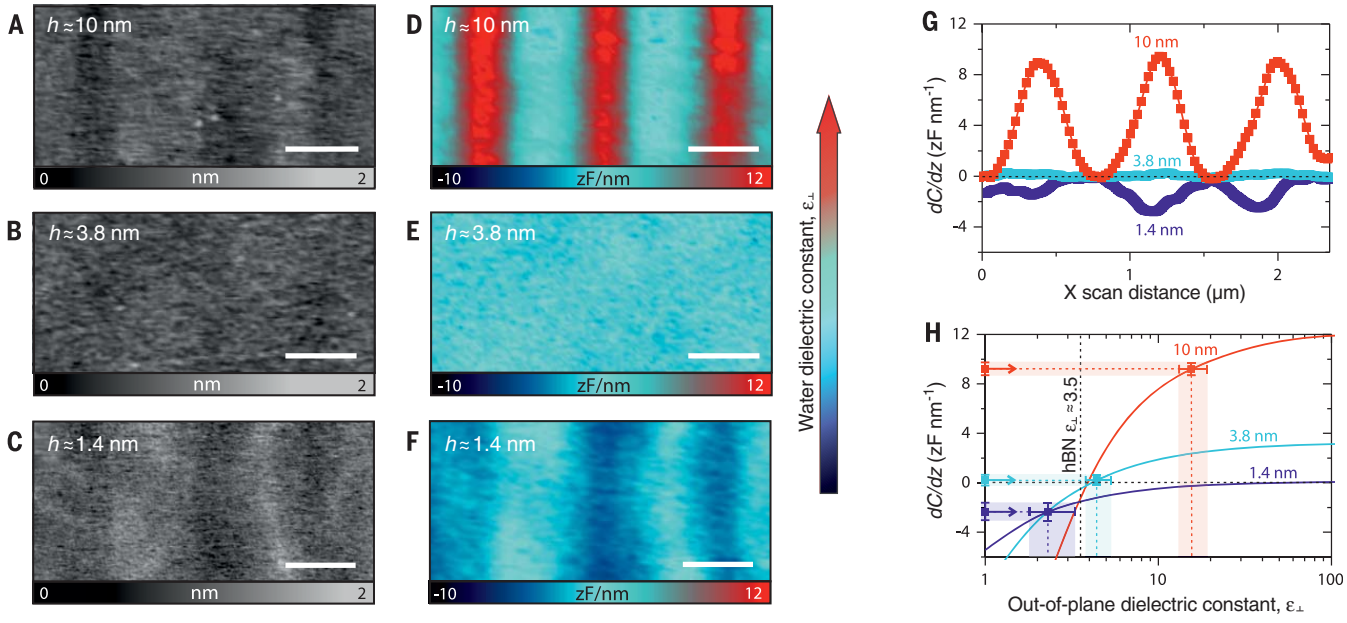

Fig. 2. Dielectric imaging of confined water. (**A** to **C**) Topographic images of the three devices in Fig. 1 after filling them with water. Scale bars, 500 nm. (**D** to **F**) Corresponding *dC/dz* images obtained by applying a tip voltage of 4 V at 1 kHz (other voltages and frequencies down to 300 Hz yielded similar images). Commercial cantilevers with tip radii of 100 to 200 nm were used to maximize the imaging sensitivity (*24*). (**G**) Averaged dielectric profiles across the channels in (D) to (F). (**H**) Simulated *dC/dz* curves as a function of $\varepsilon_\perp$ for the known geometries of the three studied devices (shown are the peak values in the middle of the channels). Symbols are the measured values of *dC/dz* from (G). Their positions along the x axis are adjusted to match the calculated curves. Bars and light-shaded regions denote standard errors as defined in (*24*).

(figs. S3 and S4). The model allows numerical calculation of dC/dz as a function of $\varepsilon_\perp$ for a dielectric material inside the channels. Figure 2H shows the resulting curves for the three studied devices in Fig. 2, A to C. By projecting the measured capacitive signals (symbols on the y axis of Fig. 2H) onto the x axis, we find $\varepsilon_\perp \approx 15.5$, 4.4, and 2.3 for $h \approx$ 10 nm, 3.8 nm, and 1.4 nm, respectively. We emphasize that $\varepsilon_\perp$ is the only unknown in our model, as all the other parameters were determined experimentally. Also, some devices exhibited small (1 to 3 Å) residual sagging in the filled state (see, e.g., Fig. 2, A to C). If not taken into account, this effect could lead to systematic albeit small errors in determining $\varepsilon_\perp$ (by effectively shifting the calculated curves in the y direction). Our calculations included this residual sagging (fig. S5).

We repeated such experiments and their analysis for more than 40 devices with h ranging from ~1 to 300 nm. The results are summarized in Fig. 3, which shows the observed $\varepsilon_\perp$ as a function of h. The bulk behavior ($\varepsilon_\perp \approx 80$) was recovered only for water as thick as ~100 nm, which shows that confinement could affect the dielectric properties of even relatively thick water layers (fig. S6). At smaller thicknesses, $\varepsilon_\perp$ evolved approximately linearly with h and approached a limiting value of ~2.1 ± 0.2 at $h < 2$ nm, where only a few layers of water could fit inside the channels. Note that the functional dependence in Fig. 3 was found independent of details of our experimental geometries such as thickness of the top hBN layer and the AFM tip radius (fig. S7).

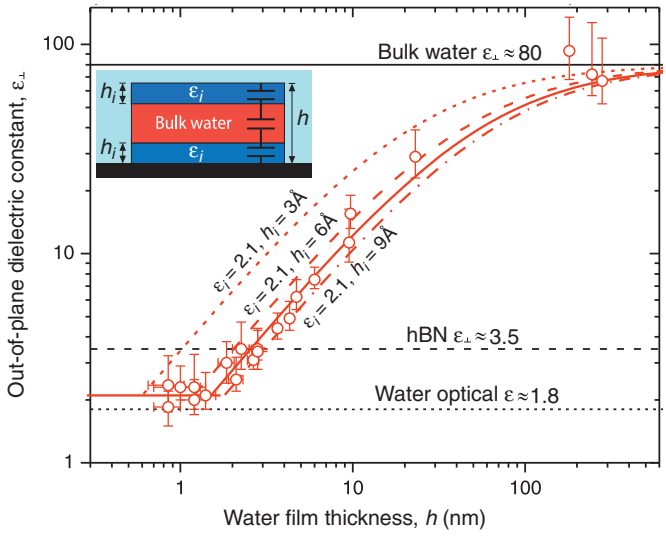

Fig. 3. Dielectric constant of water under strong confinement. Symbols denote $\varepsilon_\perp$ for water inside channels with different values of h. The y-axis error is the uncertainty in $\varepsilon_\perp$ found from the analysis as described in Fig. 2H. The x-axis error bars show the uncertainty in the water thickness including the residual sagging. Red curves: Calculated $\varepsilon_\perp(h)$ behavior for the model sketched in the inset. It assumes the presence of a near-surface layer with $\varepsilon_i = 2.1$ and thickness h_i, whereas the remainder of the channel contains the ordinary bulk water. Solid curve: Best fit yielding $h_i = 7.4$ Å. The dotted, dashed, and dashed-dotted curves are for $h_i = 3$ Å, 6 Å, and 9 Å, respectively. Horizontal lines: Dielectric constants of bulk water (solid) and hBN (dashed). The dielectric constant of water at optical frequencies (square of its refractive index) is shown by the dotted line. The inset explains our capacitance model with different ε values for the bulk and interfacial water.

The dielectric constant $\varepsilon_\perp \approx 2.1$ measured for few-layer water is exceptionally small. Not only is it much smaller than that of bulk water ($\varepsilon_{bulk} \approx$ 80) and proton-disordered ice phases such as ordinary ice I_h ($\varepsilon \approx 99$) (*27*, *28*), but the value is also smaller than that in low-temperature proton-ordered ices ($\varepsilon \approx 3$ to 4) (*27*). Moreover, the observed $\varepsilon_\perp$ is small even in comparison with the high-frequency dielectric constant ε_∞ resulting from dipolar relaxation [$\varepsilon_\infty \approx 4$ to 6 for liquid water (*29*, *30*) and $\varepsilon_\infty \approx 3.2$ for ice I_h (*27*, *28*)]. Nonetheless, $\varepsilon_\perp \approx 2.1$ lies (as it should) above $\varepsilon \approx$ 1.8 for water at optical frequencies (*27*, *30*), which is the contribution resulting from the electronic polarization. The above comparison implies that the dipole rotational contribution is completely suppressed, at least in the direction perpendicular to the atomic planes of the confining channels. This result agrees with the MD simulations that find water dipoles to be oriented preferentially parallel to moderately hydrophobic surfaces such as hBN and graphite (*12*–*14*). The small $\varepsilon_\perp$ suggests that the hydrogen-bond contribution, which accounts for the unusually large $\varepsilon_\infty \approx 4$ to 6 in bulk water (*29*, *30*), is also suppressed. The remaining polarizability can be attributed mostly to the electronic contribution (which is not expected to change under the confinement) plus a small contribution from atomic dipoles, similar to the case of nonassociated liquids (*30*).

Although the observed $\varepsilon_\perp$ remains anomalously small (<20) over a wide range of h up to 20 nm (Fig. 3), polarization suppression does not necessarily extend over the entire volume of the confined water. Indeed, the capacitance response can come from both interfacial and inner molecules, effectively averaging their contributions over the channel thickness. To this end, we recall that water near solid surfaces is believed to have a pronounced layered structure that extends ~10 Å into the bulk (*12*–*17*). Accordingly, the observed dependence $\varepsilon_\perp(h)$ could be attributed to a cumulative effect from the thin near-surface layer with the low dielectric constant ε_i, whereas the rest of the water has the normal, bulk polarizability, $\varepsilon_{bulk} \approx 80$. The overall effect can be described by three capacitors in series (inset of Fig. 3). This model yields the effective $\varepsilon_\perp = h/[2h_i/\varepsilon_i + (h - 2h_i)/\varepsilon_{bulk}]$, where h_i is the thickness of the near-surface layer. Its ε_i can be taken as ~2.1 in the limit of small h if we assume that the layered structure does not change much with increasing h (*13*) and is similar at both the graphite and hBN surfaces, as predicted by MD simulations (*14*). Figure 3 shows that the proposed simple model describes well the experimental data, allowing an estimate for the thickness h_i of interfacial water with the suppressed polarization (*24*) (fig. S8). Within experimental error, our data yield $h_i \approx 7.5 \pm 1.5$ Å, in agreement with the expected layered structure of water (*14*–*17*). In other words, the electrically dead layer extends two to three molecular diameters away from the surface. This result is also consistent with the thickness h = 1.5 to 2 nm where the limiting value $\varepsilon_\perp \approx$ 2.1 is reached (see Fig. 3). This h is approximately twice h_i and can be understood as the distance at which the near-surface layers originating from top and bottom walls merge.

We have measured the dielectric constant of water confined at the nanoscale and found it to be anomalously low. Because water exhibits a distinct layered structure near all surfaces, independently of their hydrophilicity (*31*), it is reasonable to expect that confined and interfacial water have a strongly suppressed $\varepsilon_\perp$ not only near moderately hydrophobic surfaces (such as those studied in this work) but in most cases. Our results are important for better understanding of long-range interactions in biological systems, including those responsible for the stability of macromolecules such as DNA and proteins, and of the electric double layer that plays a critical role in areas such as electrochemistry and energy storage. The results can also be used to fine-tune parameters in future atomistic simulations of confined water.

REFERENCES AND NOTES

1. J. N. Israelachvili, *Intermolecular and Surface Forces* (Academic Press, ed. 3, 2011).
2. S. Leikin, V. A. Parsegian, D. C. Rau, R. P. Rand, *Annu. Rev. Phys. Chem.* **44**, 369–395 (1993).
3. B. Honig, A. Nicholls, *Science* **268**, 1144–1149 (1995).
4. O. Stern, *Elektrochem. Angew. Phys. Chem.* **30**, 508–516 (1924).
5. B. E. Conway, J. O'M. Bockris, I. A. Ammar, *Trans. Faraday Soc.* **47**, 756–766 (1951).
6. J. B. Hubbard, L. J. Onsager, *J. Chem. Phys.* **67**, 4850–4857 (1977).
7. A. Chandra, *J. Chem. Phys.* **113**, 903–905 (2000).
8. C. Zhang, F. Gygi, G. Galli, *J. Phys. Chem. Lett.* **4**, 2477–2481 (2013).
9. A. Schlaich, E. W. Knapp, R. R. Netz, *Phys. Rev. Lett.* **117**, 048001 (2016).
10. D. Ben-Yaakov, D. Andelman, R. Podgornik, *J. Chem. Phys.* **134**, 074705 (2011).
11. D. J. Bonthuis, R. R. Netz, *Langmuir* **28**, 16049–16059 (2012).
12. C. Y. Lee, J. A. McCammon, P. J. Rossky, *J. Chem. Phys.* **80**, 4448–4455 (1984).
13. G. Cicero, J. C. Grossman, E. Schwegler, F. Gygi, G. Galli, *J. Am. Chem. Soc.* **130**, 1871–1878 (2008).
14. G. Tocci, L. Joly, A. Michaelides, *Nano Lett.* **14**, 6872–6877 (2014).
15. J. N. Israelachvili, R. M. Pashley, *Nature* **306**, 249–250 (1983).
16. M. F. Toney *et al.*, *Nature* **368**, 444–446 (1994).
17. J.-J. Velasco-Velez *et al.*, *Science* **346**, 831–834 (2014).

18. H.-B. Cui *et al*., *Angew. Chem. Int. Ed.* **44**, 6508–6512 (2005).
19. A. R. Haidar, A. K. Jonscher, *J. Chem. Soc. Faraday Trans. I* **82**, 3535–3551 (1986).
20. J. L. Aragones, L. G. MacDowell, C. Vega, *J. Phys. Chem. A* **115**, 5745–5758 (2011).
21. A. K. Geim, I. V. Grigorieva, *Nature* **499**, 419–425 (2013).
22. B. Radha *et al*., *Nature* **538**, 222–225 (2016).
23. A. Esfandiar *et al*., *Science* **358**, 511–513 (2017).
24. See supplementary materials.
25. L. Fumagalli, D. Esteban-Ferrer, A. Cuervo, J. L. Carrascosa, G. Gomila, *Nat. Mater.* **11**, 808–816 (2012).
26. K. K. Kim *et al*., *ACS Nano* **6**, 8583–8590 (2012).
27. V. F. Petrenko, R. W. Whitworth, *Physics of Ice* (Oxford Univ. Press, 1999).
28. G. P. Johari, *Contemp. Phys.* **22**, 613–642 (1981).
29. N. E. Hill, *Trans. Faraday Soc.* **59**, 344–346 (1963).
30. N. E. Hill, W. E. Vaughan, A. H. Price, M. Davies, *Dielectric Properties and Molecular Behaviour* (Van Nostrand Reinhold, 1969).
31. O. Björneholm *et al*., *Chem. Rev.* **116**, 7698–7726 (2016).

ACKNOWLEDGMENTS

We thank N. Walet, P. Carbone, L. Lue, and A. Michaelides for useful discussions. **Funding:** Supported by the Engineering and Physical Sciences Research Council, Lloyd's Register Foundation, Graphene Flagship, European Research Council, and Royal Society. G.G. acknowledges support from Ministerio de Industria, Economia y Competitividad (MINECO, grant TEC2016-79156-P) and ICREA Academia Award. **Author contributions:** L.F. proposed and directed the research with help from A.K.G. and K.S.N.; A.E. fabricated most of the devices with contributions from S.H., A.J., Q.Y., and B.R.; L.F. carried out experiments and data analysis; P.A. helped with image acquisition and processing; R.F., G.G., and L.F. implemented finite-element numerical calculations; T.T. and K.W. provided hBN; L.F. and A.K.G. wrote the manuscript; and all authors contributed to discussions. **Competing interests:** We declare no such interests. **Data and materials availability:** All data needed to evaluate the conclusions in the paper are present in the paper and supplementary materials.

SUPPLEMENTARY MATERIALS

www.sciencemag.org/content/360/6395/1339/suppl/DC1
Materials and Methods
Supplementary Text
Figs. S1 to S8
References (*32*–*45*)

24 February 2018; accepted 3 May 2018
10.1126/science.aat4191

GRAVITATION

A precise extragalactic test of General Relativity

Thomas E. Collett[1]*, Lindsay J. Oldham[2], Russell J. Smith[3], Matthew W. Auger[2], Kyle B. Westfall[1,4], David Bacon[1], Robert C. Nichol[1], Karen L. Masters[1,5], Kazuya Koyama[1], Remco van den Bosch[6]

Einstein's theory of gravity, General Relativity, has been precisely tested on Solar System scales, but the long-range nature of gravity is still poorly constrained. The nearby strong gravitational lens ESO 325-G004 provides a laboratory to probe the weak-field regime of gravity and measure the spatial curvature generated per unit mass, γ. By reconstructing the observed light profile of the lensed arcs and the observed spatially resolved stellar kinematics with a single self-consistent model, we conclude that γ = 0.97 ± 0.09 at 68% confidence. Our result is consistent with the prediction of 1 from General Relativity and provides a strong extragalactic constraint on the weak-field metric of gravity.

General Relativity (GR) postulates that mass deforms space-time, so that light passing near to a massive object is deflected. If two galaxies are almost perfectly aligned, the deformation of space-time near the center of the foreground galaxy can be large enough that multiple images of the background galaxy are observed. Such alignments are called strong gravitational lenses. In the case of a spherical foreground lens and a perfect alignment of lens and source, the background galaxy is distorted into an Einstein ring. The radius of this ring, the Einstein radius, is a function of the mass of the lens, the amount of spatial curvature produced per unit mass, and a ratio of three angular diameter distances between the observer, lens, and source.

Angular diameter distances are calculated from the redshifts (inferred from the wavelength shift of spectral lines owing to the expansion of the Universe) of the lens, z_l, and source, z_s, and the cosmological parameters of our Universe (*1*). Therefore, the combination of a nonlensing measurement of the mass of a strong lensing galaxy and a measurement of the Einstein radius constrains the amount of spatial curvature produced per unit mass and tests whether GR is the correct theory of gravity.

In the limit of a weak gravitational field, the metric of space-time is characterized by two potentials (*2*)—the Newtonian potential, Φ, and the curvature potential, Ψ—so that the comoving distance element is

$$ds^2 = a^2(\tau)\left[-(1+2\Phi)d\tau^2 + (1-2\Psi)g_{ij}dx^i dx^j\right] \quad (1)$$

where τ is the conformal time, x^i and x^j are the spacelike coordinates, g_{ij} is the three-metric of constant-curvature spaces, and $a(\tau)$ is the scale factor of the Universe.

In GR, the two potentials are the same, but many alternative gravity models invoked to explain the accelerated expansion of the Universe [such as $f(R)$ gravity (*3*)] predict the ratio of the two potentials ($\gamma = \Psi/\Phi$) to be scale-dependent. These alternative models of gravity remove the need for a dark energy to accelerate the expansion of the Universe. Testing the scale dependence of γ therefore discriminates between GR and these alternative gravities. The motion of nonrelativistic objects is governed by the Newtonian potential, whereas the motion of relativistic particles is sensitive to both potentials (*2*). Measuring γ therefore requires observations of the motions of both relativistic and nonrelativistic particles around the same massive object.

On Solar System scales, the GR prediction for γ has been verified to high precision. By measuring the travel time of radio photons passing close to the Sun, the Cassini mission found $\gamma = 1 + (2.1 \pm 2.3) \times 10^{-5}$ (*4*). However, the extragalactic constraints on GR are much less precise. On scales of 10 to 100 Mpc, γ has been constrained to just 20% precision (*5*–*7*) by combining measurements of weak gravitational lensing and redshift space distortions. On megaparsec scales, 30% constraints on γ have been achieved using the mass profiles of clusters (*8*, *9*).

On kiloparsec scales, strong gravitational lensing, combined with stellar kinematics in the lens,

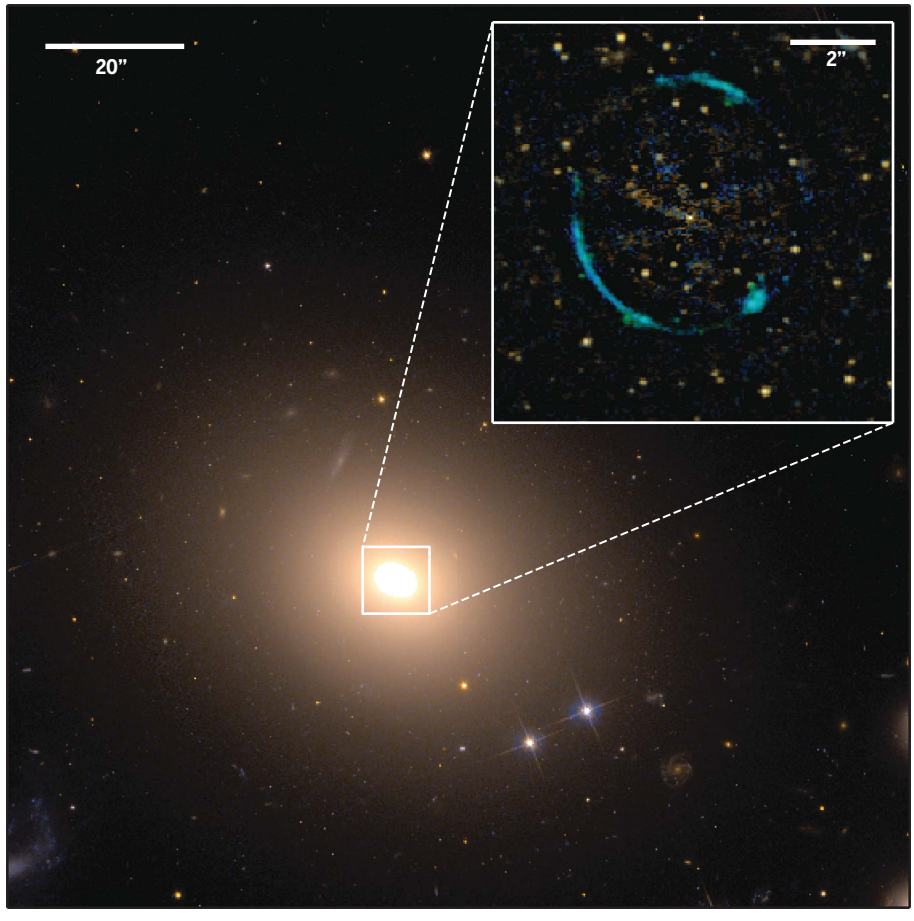

Fig. 1. Color composite image of ESO325-G004. Blue, green, and red channels are assigned to the F475W, F606W, and F814W HST imaging. The inset shows a F475W and F814W composite of the arcs of the lensed background source after subtraction of the foreground lens light. Scale bars are in arc seconds.

allows a test of the weak-field metric of gravity. The kinematics are sensitive only to the Newtonian potential, whereas the lensing is sensitive to the sum of the potentials. The deflection angle of light, $\hat{\boldsymbol{\alpha}}(\mathbf{x})$, caused by a galaxy with surface mass density $\Sigma(\mathbf{x})$, is given by

$$\hat{\boldsymbol{\alpha}}(\mathbf{x}) = \frac{2G}{c^2}(1+\gamma)\int \mathrm{d}^2\mathbf{x}'\Sigma(\mathbf{x}')\frac{\mathbf{x}-\mathbf{x}'}{|\mathbf{x}-\mathbf{x}'|^2} \quad (2)$$

where G is the gravitational constant, and c is the speed of light. Here, γ is explicitly assumed to be constant over the length scales relevant for lensing. In this case, the lensing and dynamical masses are related by

$$M_{\mathrm{dyn}} = \frac{1+\gamma}{2}M^{\mathrm{GR}}_{\mathrm{lensing}} \quad (3)$$

where M_{dyn} is the mass derived from the dynamics, and $M^{\mathrm{GR}}_{\mathrm{lensing}}$ is the mass derived from lensing and assuming GR is correct.

Previous studies have combined Einstein radius measurements with stellar velocity dispersions to infer constraints on γ (*10*, *11*). Recent work (*12*) used a sample of 80 lenses to infer $\gamma = 0.995 \pm 0.04$ (statistical) $\pm$ 0.25 (systematic) at 68% confidence. The systematic uncertainties are much larger than the statistical uncertainties, because the result relies on assumptions about the density profile of the lenses and the orbits of the stars within the lenses. The large distances to the lenses in these samples ($0.1 < z_l < 1$) make a more detailed study of their kinematics impractical with current instruments.

The nearby (lens redshift $z_l = 0.035$) galaxy ESO 325-G004 (hereafter, E325) is located at right ascension $13^{\mathrm{h}}43^{\mathrm{m}}33^{\mathrm{s}}.2$, declination $-38°10'34''$ (J2000 equinox). Hubble Space Telescope (HST) imaging of E325 serendipitously revealed the presence of an Einstein ring with a 2.95″ radius around the center of the galaxy (*13*), shown in Fig. 1. Follow-up observations have revealed that the source is an extended star-forming galaxy at source redshift $z_s = 2.1$ (*14*). E325 provides a laboratory for testing GR on kiloparsec scales because the small distance to the lens enables spatially resolved measurements of the stellar kinematics; this places tight constraints on the three-dimensional mass structure of the lens. E325 also has an extended arc system, which provides tight constraints on the two-dimensional surface mass profile of the lens. The small distance also means that the Einstein ring appears in the baryon-dominated central region of the lens galaxy: The uncertain distribution of dark matter is much less important than for more distant lenses.

E325 has previously been observed with the Advanced Camera for Surveys on the HST (*13*). We used the HST image observed in the red F814W filter to describe the light profile of the galaxy for our mass modeling, and we produced an image of the arc light by subtracting the F814W image from that in the blue F475W filter, with the F814W image radially rescaled to account for a slight color gradient in the lens galaxy (*15*). Previous strong lensing constraints on γ have relied only on Einstein radius measurements (*10*–*12*), yielding a constraint only on the total lensing mass within the Einstein ring. However, the extended arcs in E325 also allow for a detailed reconstruction of the unlensed

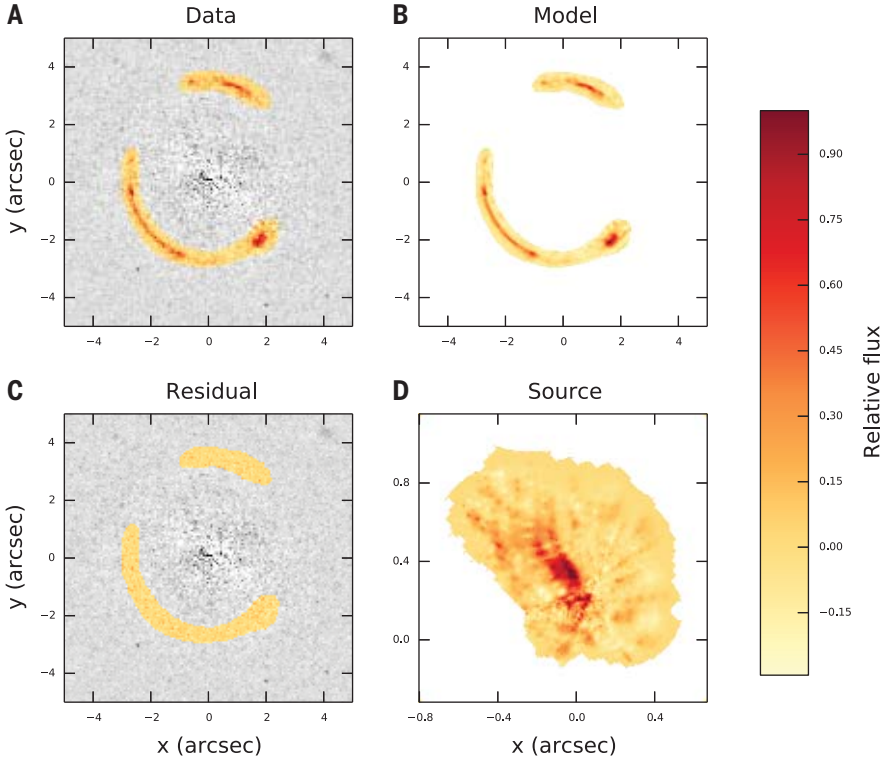

Fig. 2. Best-fitting reconstruction of the lensed arcs in E325. (**A**) The foreground-subtracted F475W HST image (*15*). We analyzed only the data shown in color. (**B**) The best fit model of the lens. (**C**) The difference after subtracting the model from the data. (**D**) The reconstruction of the unlensed source for the best-fitting model. In all panels, the units are in arc seconds, with the lens centered at (0, 0). The color bar shows the relative flux for all the images.

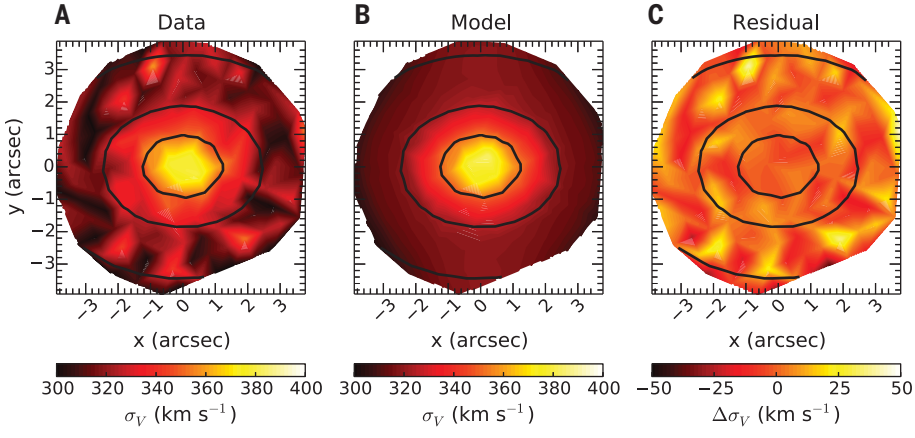

Fig. 3. Two-dimensional velocity dispersion profile for E325. (**A**) The observed MUSE velocity dispersion (σ_V) data. (**B**) Kinematics predicted by our best-fitting model. (**C**) The residual difference between the data and model.

[1]Institute of Cosmology and Gravitation, University of Portsmouth, Burnaby Road, Portsmouth PO1 3FX, UK. [2]Institute of Astronomy, University of Cambridge, Madingley Road, Cambridge CB3 0HA, UK. [3]Centre for Extragalactic Astronomy, University of Durham, Durham DH1 3LE, UK. [4]University of California Observatories–Lick Observatory, University of California–Santa Cruz, 1156 High Street, Santa Cruz, CA 95064, USA. [5]Department of Physics and Astronomy, Haverford College, 370 Lancaster Avenue, Haverford, PA 19041, USA. [6]Max Planck Institute for Astronomy, Königstuhl 17, 69117 Heidelberg, Germany.
***Corresponding author. Email: thomas.collett@port.ac.uk**

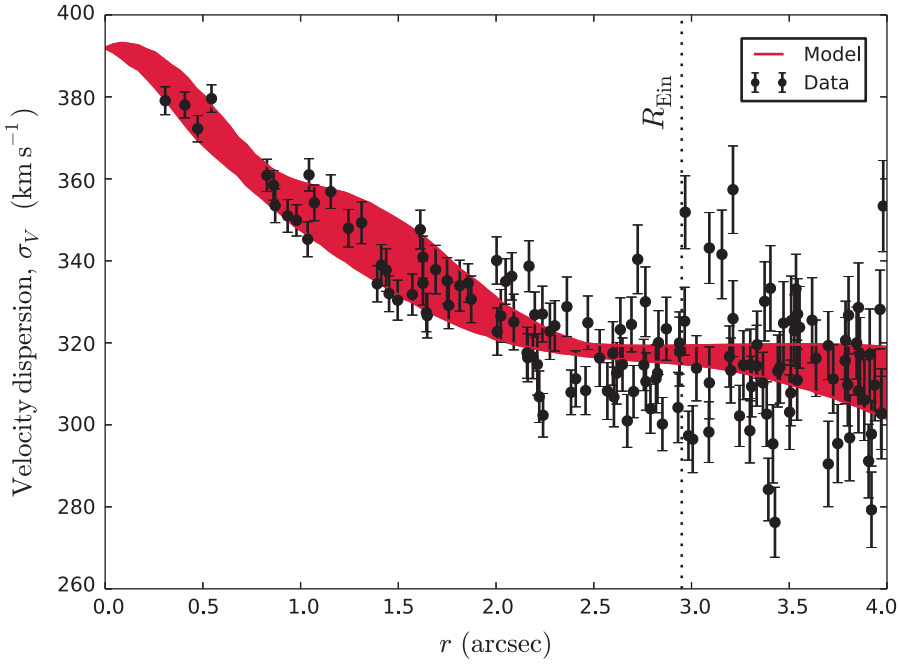

Fig. 4. One-dimensional velocity dispersion profile for E325, as a function of radial distance *r* from the lens center. Black circles show observed values from the MUSE data for the 0.6″ pixels used in the analysis; error bars are 1σ statistical uncertainties. The red band shows the range of velocity dispersions at each *r* predicted by our best-fitting model. The width of the band is due to azimuthal variation in the velocity dispersion, not the statistical uncertainty. The dotted vertical line indicates the Einstein radius.

source from the HST observations. This reconstruction places additional constraints on the radial magnification across the image plane wherever lensed images are present (*16*). The radial magnification is a weighted integral of the mass within the Einstein ring; hence, reconstructing the arcs excludes many density profiles that would have the same Einstein radius but produce arcs of different shapes and widths. This approach is now mature in studies of strong lenses where high-precision constraints are required (*17*–*20*).

To constrain the dynamical mass, we used observations acquired with the Multi Unit Spectroscopic Explorer (MUSE) (*21*) on the European Southern Observatory (ESO) Very Large Telescope to obtain spatially resolved spectroscopy across the lens (*15*). From the spectra, we extracted the velocity dispersion of the stars in each pixel. We use Jeans axisymmetric modeling (*22*) to infer the dynamical mass of the lens from these data (*15*).

We simultaneously fit a 20-parameter model to both the MUSE and the HST data (*15*). The parameters describe the mass-to-light ratio of the stellar component observed with the HST, including a mass-to-light gradient, a dark matter halo, and a central supermassive black hole. We also include parameters that describe external lensing shear from masses close to the line of sight, the radial profile of the stellar orbital anisotropy, and the unknown inclination of the lens galaxy with respect to the line of sight. The final parameter of our model is γ, the ratio of the Newtonian and curvature potentials. We assume that this ratio is constant across the relevant length scales of this lens. The smallest angular scale that the MUSE data resolve corresponds to a physical scale of 100 pc in the lens plane, and the Einstein radius corresponds to 2000 pc.

By sampling the posterior probability of our model fit to the data, using a Markov chain Monte Carlo method (*23*), we infer the uncertainties on the model parameters. Our best-fitting reconstruction of the HST image is shown in Fig. 2. Our model simultaneously reproduces the observed lensing and dynamical data. Our reconstruction of the MUSE data is shown in Figs. 3 and 4.

Within the constraints of our fiducial model, we infer that it is only possible to simultaneously reconstruct the lensing and kinematics if the stellar mass-to-light ratio of the lens increases within the central kiloparsec, with an observed F814W-band stellar mass-to-light ratio at large radius of $2.8 \pm 0.1 M_\odot/L_\odot$ (in units of solar mass over solar luminosity; consistent with a Milky Way–like stellar initial mass function), rising to $6.6 \pm 0.1 M_\odot/L_\odot$ in the center (consistent with an excess of mass in low-luminosity stars relative to the Milky Way). We infer that the central black hole has a mass of $3.8 \pm 0.1 \times 10^9\ M_\odot$, consistent with expectations (*24*) given the mass of E325. We find that the lens must be inclined close to the plane of the sky, with an inclination angle of 90 ± 15°. The typical orbits of the stars are mildly radial at most radii, although they are poorly constrained in the central 0.5 kpc. The dark matter in our fiducial model only accounts for 3^{+3}_{-2}% of the mass within the Einstein radius, consistent with expectations extrapolating from higher-redshift lenses (*25*), given that the 2.95″ Einstein radius is a quarter of the 13″ radius that contains half of the light of the lens.

Our fiducial model assumes that the dark matter follows the Navarro-Frenk-White (NFW) profile (*26*) that is found in cosmological dark matter–only simulations; however, the baryonic processes of galaxy formation are capable of resculpting the dark matter profile (*27*–*29*). An alternative model without a stellar mass-to-light gradient is also able to reconstruct the data, although the central dark matter density would have to fall with radius to the power −2.6 ($\rho_{\rm DM} \propto r^{-2.6}$)—much steeper than the fiducial ($\rho_{\rm DM} \propto r^{-1}$) profile. In this model, the baryons are consistent with a Milky Way–like stellar initial mass function, and the dark matter accounts for 31 ± 4% of the mass within the Einstein radius (*15*).

We also investigated another model that does not partition the mass into baryonic and dark matter; this model also required a steeply rising total mass-to-light ratio in the central regions. Our current data cannot distinguish between highly concentrated dark matter, a steep stellar mass-to-light gradient, and an intermediate solution, but E325 is definitely not consistent with a NFW dark matter halo and a constant stellar mass-to-light ratio.

In our fiducial model, we find $\gamma = 0.978^{+0.010}_{-0.015}$ at 68% confidence, with the uncertainties estimated from the Markov chain Monte Carlo analysis. Owing to the small statistical uncertainties, we also carried out a thorough analysis of our systematic uncertainty relating to the parameterization of the lens model.

In principle, the parameterization of the mass profile should not affect the inferred value of γ, because both the lensing and the kinematics are sensitive to the total mass distribution, rather than the partition between dark matter, black hole, and baryons. The alternative models investigated (*15*) show an excess scatter on γ of 0.01, in addition to the statistical uncertainties.

Our model assumes the fiducial cosmology from the Planck satellite's cosmic microwave background observations (*1*). Our inference of the lensing mass is inversely proportional to the assumed value of the current expansion rate of the Universe, H_0. The low redshift of the lens causes our inference on γ to be almost independent of the other cosmological parameters. The 1.3% uncertainty on the Planck determination of H_0 is equivalent to a 2.6% uncertainty on γ.

Our dynamical model assumes a particular stellar spectral library to extract the kinematics. For our data, there is a 2.2% systematic shift between velocity dispersions measured with theoretically motivated stellar libraries (*30*) and those empirically derived from observations of Milky Way stars (*31*). This translates to a 4.4% uncertainty on the dynamical mass and hence 8.8% uncertainty on γ. This systematic uncertainty dominates the final uncertainty on γ.

By simultaneously reconstructing the extended light profile of the arcs and spatially resolved

kinematics of E325, we precisely constrained γ with a single system. The high-resolution data allow us to fit for both the density profile and the anisotropy profile of the lens, removing these as sources of systematic uncertainty that had limited previous strong lensing constraints on γ (*10*–*12*). We conclude that $\gamma = 0.97 \pm 0.09$ (68% confidence limits), including our identified systematic uncertainties. This constraint on the ratio of the two potentials outside the Solar System confirms the prediction of GR in the local Universe for galactic masses and kiloparsec scales. Our result implies that large deviations from $\gamma = 1$ can only occur on scales greater than ~2 kpc, thereby excluding alternative gravity models that produce the observed accelerated expansion of the Universe but predict $\gamma \neq 1$ on galactic scales.

REFERENCES AND NOTES

1. Planck Collaboration, *Astron. Astrophys.* **594**, A13 (2016).
2. E. Bertschinger, *Philos. Trans. R A Math. Phys. Eng. Sci.* **369**, 4947–4961 (2011).
3. W. Hu, I. Sawicki, *Phys. Rev. D* **76**, 064004 (2007).
4. B. Bertotti, L. Iess, P. Tortora, *Nature* **425**, 374–376 (2003).
5. Y.-S. Song *et al.*, *Phys. Rev. D* **84**, 083523 (2011).
6. F. Simpson *et al.*, *Mon. Not. R. Astron. Soc.* **429**, 2249–2263 (2013).
7. C. Blake *et al.*, *Mon. Not. R. Astron. Soc.* **456**, 2806–2828 (2016).
8. H. Wilcox *et al.*, *Mon. Not. R. Astron. Soc.* **452**, 1171–1183 (2015).
9. L. Pizzuti *et al.*, *J. Cosmol. Astropart. Phys.* **2016**, 023 (2016).
10. A. S. Bolton, S. Rappaport, S. Burles, *Phys. Rev. D* **74**, 061501 (2006).
11. J. Schwab, A. S. Bolton, S. A. Rappaport, *Astrophys. J.* **708**, 750–757 (2010).
12. S. Cao *et al.*, *Astrophys. J.* **835**, 92 (2017).
13. R. J. Smith, J. P. Blakeslee, J. R. Lucey, J. Tonry, *Astrophys. J.* **625**, L103–L106 (2005).
14. R. J. Smith, J. R. Lucey, *Mon. Not. R. Astron. Soc.* **434**, 1964–1977 (2013).
15. Materials and methods are available as supplementary materials.
16. T. E. Collett, thesis, University of Cambridge, Cambridge, UK, 2015.
17. S. H. Suyu *et al.*, *Astrophys. J.* **766**, 70 (2013).
18. S. Vegetti, L. V. E. Koopmans, A. Bolton, T. Treu, R. Gavazzi, *Mon. Not. R. Astron. Soc.* **408**, 1969–1981 (2010).
19. T. E. Collett, M. W. Auger, *Mon. Not. R. Astron. Soc.* **443**, 969–976 (2014).
20. K. C. Wong *et al.*, *Mon. Not. R. Astron. Soc.* **465**, 4895–4913 (2017).
21. R. Bacon *et al.*, *Proc. SPIE* **7735**, 773508 (2010).
22. M. Cappellari, *Mon. Not. R. Astron. Soc.* **390**, 71–86 (2008).
23. D. Foreman-Mackey, D. W. Hogg, D. Lang, J. Goodman, *Publ. Astron. Soc. Pac.* **125**, 306–312 (2013).
24. N. J. McConnell, C.-P. Ma, *Astrophys. J.* **764**, 184 (2013).
25. M. W. Auger *et al.*, *Astrophys. J.* **721**, L163–L167 (2010).
26. J. F. Navarro, C. S. Frenk, S. D. M. White, *Astrophys. J.* **462**, 563 (1996).
27. G. R. Blumenthal, S. M. Faber, R. Flores, J. R. Primack, *Astrophys. J.* **301**, 27 (1986).
28. O. Y. Gnedin, A. V. Kravtsov, A. A. Klypin, D. Nagai, *Astrophys. J.* **616**, 16–26 (2004).
29. M. G. Abadi, J. F. Navarro, M. Fardal, A. Babul, M. Steinmetz, *Mon. Not. R. Astron. Soc.* **407**, 435–446 (2010).
30. C. Conroy, P. van Dokkum, *Astrophys. J.* **747**, 69 (2012).
31. F. Valdes, R. Gupta, J. A. Rose, H. P. Singh, D. J. Bell, *Astrophys. J. Suppl. Ser.* **152**, 251–259 (2004).

ACKNOWLEDGMENTS

We are grateful to S. Carniari for help with reducing the MUSE data and to D. Newman for discussions. We thank the three anonymous referees for their constructive feedback. **Funding:** T.E.C. is funded by a Dennis Sciama Fellowship from the University of Portsmouth. R.J.S. acknowledges support from the STFC through grant ST/P000541/1. D.B., R.C.N., K.L.M., and K.K. are supported by STFC through grant ST/N000688/1. K.K. is supported by the European Research Council (ERC) (grant agreement 646702 "CosTesGrav"). Numerical computations were performed on the SCIAMA High Performance Compute (HPC) cluster, which is supported by the ICG, SEPNet, and the University of Portsmouth. **Author contributions:** T.E.C. performed the lensing and dynamical modeling, led the proposal for the MUSE data, and wrote the paper. L.J.O. implemented the Jeans modeling of E325, extracted the MUSE velocity dispersions, and cowrote the paper. R.J.S. performed the initial kinematic fits and produced the lens-subtracted HST data. M.W.A. reduced the HST and MUSE data. K.B.W. helped design and implement the MUSE observations. All authors provided ideas throughout the project and commented on the manuscript and observing proposal. **Competing interests:** The authors have no competing interests. **Data and materials availability:** This work is based on observations made with ESO telescopes at the La Silla Paranal Observatory; those data are available at http://archive.eso.org under program ID 097.A-0987(A). This work is also based on observations made with the NASA/ESA Hubble Space Telescope and obtained from the Hubble Legacy Archive, http://hla.stsci.edu [under programs GO 10429 (PI: Blakeslee) and GO 10710 (PI: Noll)], which is a collaboration between the Space Telescope Science Institute (STScI/NASA), the Space Telescope–European Coordinating Facility (ST-ECF/ESA), and the Canadian Astronomy Data Centre (CADC/NRC/CSA). Our lens modeling code, PYLENS, is available at http://github.com/tcollett/pylens. The MGE_FIT_SECTORS software and JAM dynamical modeling code are available at www-astro.physics.ox.ac.uk/~mxc/software/. The ensemble sampler EMCEE is available at http://dfm.io/emcee/. The output parameters of our models are given in tables S2 to S4.

SUPPLEMENTARY MATERIALS

www.sciencemag.org/content/360/6395/1342/suppl/DC1
Materials and Methods
Figs. S1 to S6
Tables S1 to S4
References (*32*–*65*)

29 June 2017; accepted 26 April 2018
10.1126/science.aao2469

ANTHROPOLOGY

New genus of extinct Holocene gibbon associated with humans in Imperial China

Samuel T. Turvey[1]*, Kristoffer Bruun[2], Alejandra Ortiz[3], James Hansford[1,4], Songmei Hu[5], Yan Ding[5], Tianen Zhang[5], Helen J. Chatterjee[2]

Although all extant apes are threatened with extinction, there is no evidence for human-caused extinctions of apes or other primates in postglacial continental ecosystems, despite intensive anthropogenic pressures associated with biodiversity loss for millennia in many regions. Here, we report a new, globally extinct genus and species of gibbon, *Junzi imperialis*, described from a partial cranium and mandible from a ~2200- to 2300-year-old tomb from Shaanxi, China. *Junzi* can be differentiated from extant hylobatid genera and the extinct Quaternary gibbon *Bunopithecus* by using univariate and multivariate analyses of craniodental morphometric data. Primates are poorly represented in the Chinese Quaternary fossil record, but historical accounts suggest that China may have contained an endemic ape radiation that has only recently disappeared.

A Warring States–period tomb excavated in 2004 at Shenheyuan, Xi'an (formerly the ancient capital Chang'an), Shaanxi—possibly attributable to Lady Xia, grandmother of China's first emperor Qin Shihuang (259–210 BCE)—contains 12 pits with animal remains (Fig. 1) (*1*, *2*). Similar tomb menageries are known from other Chinese high-status burials of comparable age (*3*). Pit K12 contains skeletons of leopard (*Panthera pardus*), lynx (*Lynx lynx*), Asiatic black bear (*Ursus thibetanus*), crane (*Grus* sp.), domestic mammals and birds (*1*), and a gibbon (Shaanxi Provincial Institute of Archaeology, Shenheyuan M1K12:3).

Gibbons and siamangs (Hylobatidae) include four living genera (*Hoolock*, *Hylobates*, *Nomascus*, and *Symphalangus*) consisting of 20 species (*4*, *5*). Six extant species are known historically from China (*5*, *6*). Gibbons were considered culturally important throughout Chinese history; their perceived "noble" characteristics made them symbols of scholar-officials (*junzi*), and they became high-status pets from the Zhou Dynasty (1046–256 BCE) (*7*). They are extremely scarce in China's Pleistocene-Holocene record, and most premodern remains are isolated teeth or postcrania insufficiently diagnostic for species-level or genus-level identification (*8*, *9*). The most complete Quaternary Chinese hylobatid is a left mandibular fragment from Chongqing (AMNH-18534), probably early-middle Pleistocene in age, described in 1923 as an extinct genus and species, *Bunopithecus sericus* (*10*). By contrast, M1K12:3 includes a partial facial skeleton (missing the posterior neurocranium) with complete anterior dentition, left-right PM3-4, and right M1-2; an associated right M3; a partial mandible with almost complete anterior dentition (missing left I2), left-right pm3-4, and right m1-2; and nondiagnostic right distal forelimb elements (Fig. 1).

Destructive sampling of M1K12:3 was not possible because of the single specimen's protected archaeological status, and previous attempts to amplify DNA from Chinese Holocene samples have often proved unsuccessful because of poor biomolecule preservation under subtropical conditions (*11*), so we conducted multivariate and univariate morphometric analyses to determine its affinities to other hylobatids. First, we conducted canonical variate analyses (CVAs) using 16 cranial landmarks shared between M1K12:3 and a dataset including all extant hylobatid genera (*Hoolock*, $n = 53$; *Hylobates*, $n = 327$; *Nomascus*, $n = 34$; and *Symphalangus*, $n = 63$) (*12*, *13*). We partially restored a three-dimensional scan of the M1K12:3 cranium before analysis through mirror-imaging and reference-based reconstruction of the zygomatic bone, zygomatic arch, posterior maxilla, and posterior frontal (*13*). Landmarks are distributed across nearly the entire remaining or restored cranial surface. All CVAs were performed by using genus as the classifying variable when assessing the position of M1K12:3 in morphospace.

Permutation tests (10,000 rounds) for between-group Procrustes and Mahalanobis distances show significant differentiation between all extant genera ($P < 0.0001$, all comparisons) and between M1K12:3 and extant genera (Fig. 2, Table 1, and table S1). CV1 (60.90% variation) is associated with expansion of the facial region and primarily separates *Symphalangus*, the largest, most morphologically distinct hylobatid. CV2 (23.04% variation) represents shape changes to the frontal, orbit, and infraorbital region and strongly differentiates M1K12:3 from extant genera owing to its expanded upper anterior neurocranium: M1K12:3 exhibits a more superior position of the frontal posterior margin (bregma, stephanion), the anterior margin (glabella, upper orbital rim) has undergone an inferior shift, the zygomaxillary suture is shortened to give a narrower cheekbone, and molar dentition is more widely set together with an inferior shift (table S2). Posterior probabilities indicate extremely high classification accuracy (96 to 97%) (table S3), with M1K12:3 consistently classified as a separate group.

We collected molar (M1-3, m1-2) landmark data [homologous landmarks at main cusp tips, 20 (upper) or 22 (lower) semilandmarks along outline], tooth crown areas (maximum occlusal area), polygon areas (ratio from lines connecting cusps relative to total occlusal area), and cusp angles (calculated from homologous landmark coordinates) from M1K12:3 (*13*). We compared these data with a new dataset containing morphometric data for 789 hylobatid molars representing 279 individuals (*Hoolock*, $n = 77$; *Hylobates*, $n = 129$; *Nomascus*, $n = 41$; and *Symphalangus*, $n = 32$), including all extant Chinese species and AMNH-18534 (*13*).

Permutation tests (10,000 rounds) for Mahalanobis distances again show significant differentiation between all extant genera ($P < 0.001$, all comparisons), although Procrustes distances do not consistently differentiate extant genera, especially *Nomascus* (table S5). M1K12:3 is statistically differentiated from extant genera in several features, including occlusal area (significantly larger M2, M3, and m2 than *Hylobates*; significantly smaller M1, m1, and m2 than *Symphalangus*); larger M3 paracone angle than that of *Nomascus*; and smaller protoconid, metaconid, entoconid, and/or hypoconid angles than those of all genera (fig. S4 and tables S6 and S7). CVAs derived from semilandmark data demonstrate the distinctive molar shape of M1K12:3. M3, m1, and m2 all fall outside the range of extant hylobatid variation (Fig. 2) and have high CVA classification accuracy (76 to 86%) (table S3). Permutation tests for Procrustes and Mahalanobis distances show significant differentiation between M1K12:3 and extant hylobatids for upper and/or lower molar outline; pairwise distances are greater than between extant genera (Table 1 and table S1). CVA for m2, the only tooth shared by M1K12:3 and AMNH-18534, demonstrates that these specimens are also morphologically distinct (Fig. 2); *Bunopithecus* shows a very different relationship to extant hylobatids compared with M1K12:3, with a likely close relationship to *Hoolock* (*10*).

Although these analyses cannot reconstruct M1K12:3's phylogenetic affinities, even genomic analyses have proved unable to clarify higher-order hylobatid relationships, possibly because living genera diverged through near-instantaneous radiation ~5 million years ago (*14*). However, cranial and molar data clearly differentiate M1K12:3 from living hylobatids and the only other Chinese Quaternary hylobatid. We therefore describe M1K12:3 as a new extinct genus and species,

[1]Institute of Zoology, Zoological Society of London, Regent's Park, London NW1 4RY, UK. [2]Department of Genetics, Evolution and Environment, University College London, Gower Street, London WC1E 6BT, UK. [3]Institute of Human Origins, School of Human Evolution and Social Change, Arizona State University, Tempe, AZ 85281, USA. [4]Ocean and Earth Science, National Oceanography Centre Southampton, University of Southampton Waterfront Campus, Southampton SO14 3ZH, UK. [5]Shaanxi Provincial Institute of Archaeology, Xi'an 710054, China.
*Corresponding author. Email: samuel.turvey@ioz.ac.uk

Junzi imperialis (*15*). Although other Holocene primate losses are known (21 extinctions in "ecologically naïve" Madagascan and Caribbean island faunas, with two species persisting beyond 1500 CE) (*16*, *17*), the disappearance of *J. imperialis* constitutes the first documented postglacial extinction of an ape or of any continental primate.

Gibbons are today restricted to southwestern China (*6*), with the closest populations >1200 km from Chang'an and separated by major drainages (Fig. 1). Large rivers can represent barriers to gene flow in hylobatids (*18*), providing biogeographic support for evolutionary differentiation of central Chinese gibbons. Chang'an was an important regional power center under the Qin State and became China's political and economic center during the Han Dynasty (*19*); gibbons could therefore have been transported to Chang'an as trade items or tributes. However, other mammals from the Shenheyuan tomb still occur in Shaanxi (*6*), suggesting a similar local origin for M1K12:3. Contemporary accounts describe gibbons being caught near Chang'an into the 10th century (*7*), and gibbon survival in Shaanxi until the 18th century (*20*). Southern Shaanxi represents the northern limit of China's subtropical forest ecoregion and retains remnant populations of primates and other mammals (such as giant pandas) that co-occurred with gibbons in Quaternary assemblages (*6*, *21*).

Global ecosystems have experienced extreme human-caused biodiversity loss in recent centuries, with extinction rates elevated by several orders of magnitude; it is increasingly accepted that a mass extinction is underway (*22*, *23*). Eastern and southeast Asian biotas have been disrupted disproportionately; this region contains the most threatened mammals (*4*), and 73% of Asian primates are threatened compared with 60% globally (*24*). In China, two gibbon species (*Hylobates lar* and *Nomascus leucogenys*) have recently disappeared, surviving species are all critically endangered, and the Hainan gibbon (*Nomascus hainanus*) may be the world's rarest mammal with ~26 surviving individuals (*4*).

The background mammalian extinction rate is estimated at 1.8 extinctions/million species/year (*22*). Because 525 Holocene-Recent primates, including 27 apes, are recognized (*5*, *24*, *25*), expected background extinction rates are 9.45×10^{-4}/year for primates, and 4.86×10^{-5}/year for apes. We could therefore expect 11.1 background primate extinctions and 57% probability of background ape extinction across the 11,700-year Holocene [although only 45% probability of primate extinction and 2% probability of ape extinction since 1500 CE, the International Union for Conservation of Nature (IUCN) threshold used to assess human-caused extinctions (*4*), and the period into which *J. imperialis* likely persisted]. A hypothesis of "natural" rather than anthropogenically mediated extinction of *J. imperialis* therefore cannot be discarded completely. However, few extinctions across the climatically stable Holocene can even questionably be interpreted as nonanthropogenic (*16*). Central Chinese landscapes have supported among the world's highest human densities for millennia (*19*) and experienced extensive Holocene mammal extinctions (*21*). The discovery of M1K12:3 in a tomb provides direct evidence of human exploitation, and extensive deforestation occurred near Chang'an during the late Imperial period, with remaining high-elevation forests representing suboptimal gibbon habitat (*26*). Analysis of predictors of Chinese Holocene mammal range loss has shown that best-supported models include an index of anthropogenic impact (*21*), and reconstruction of historical gibbon decline across China demonstrates extinction following a wavefront of directional pressures that matches known human population expansion (*20*).

Although primates are disproportionately threatened today (*24*), previous studies suggest that they have not experienced elevated levels of past extinction (*27*). However, they are underrepresented in Quaternary archives, which remain understudied across most areas of primate distribution (*8*, *21*). Our description of *J. imperialis* suggests that past human-caused primate diversity loss may be underestimated, with important implications for understanding extinction vulnerability and informing conservation (*24*). Our findings also emphasize the extreme vulnerability of hylobatids even compared with other primates. Historical records document former gibbon occurrence across central and southern China (*7*, *20*), in areas separated from distributions of extant species and *J. imperialis* by major drainages (Fig. 1). These populations may represent undescribed extinct species, suggesting a much greater historical loss of global ape diversity. We encourage further investigation of Asian environmental

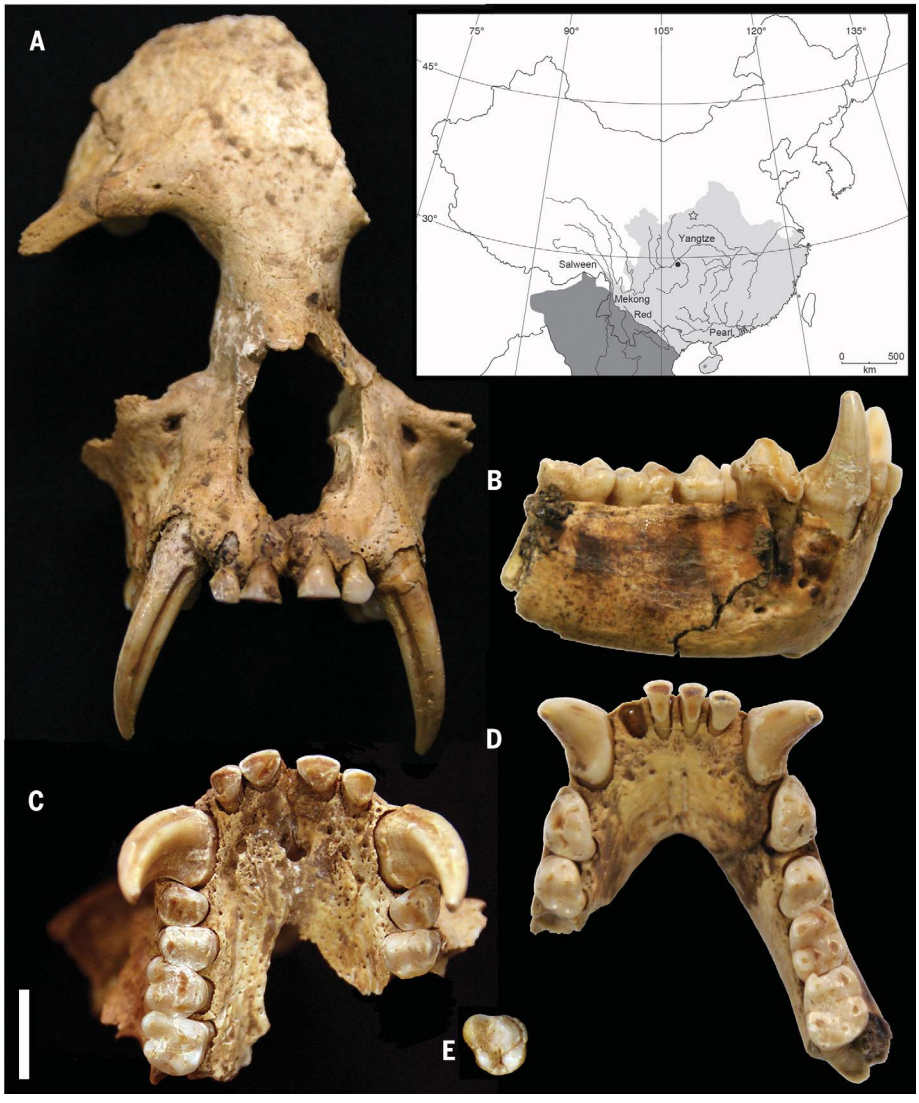

Fig. 1. Cranium and mandible of *Junzi imperialis* holotype (M1K12:3). (**A**) Cranium, anterior view. (**B**) Mandible, lateral view. (**C**) Upper dentition, occlusal view. (**D**) Lower dentition, occlusal view. (**E**) Right M3. Scale bar, 10 mm. (Inset) Modern distribution of hylobatids [dark gray; modified from (*18*)] and historical distribution across China [light gray; modified from (*20*)], showing Chang'an (star), *Bunopithecus sericus* collection locality (solid circle), and major rivers.

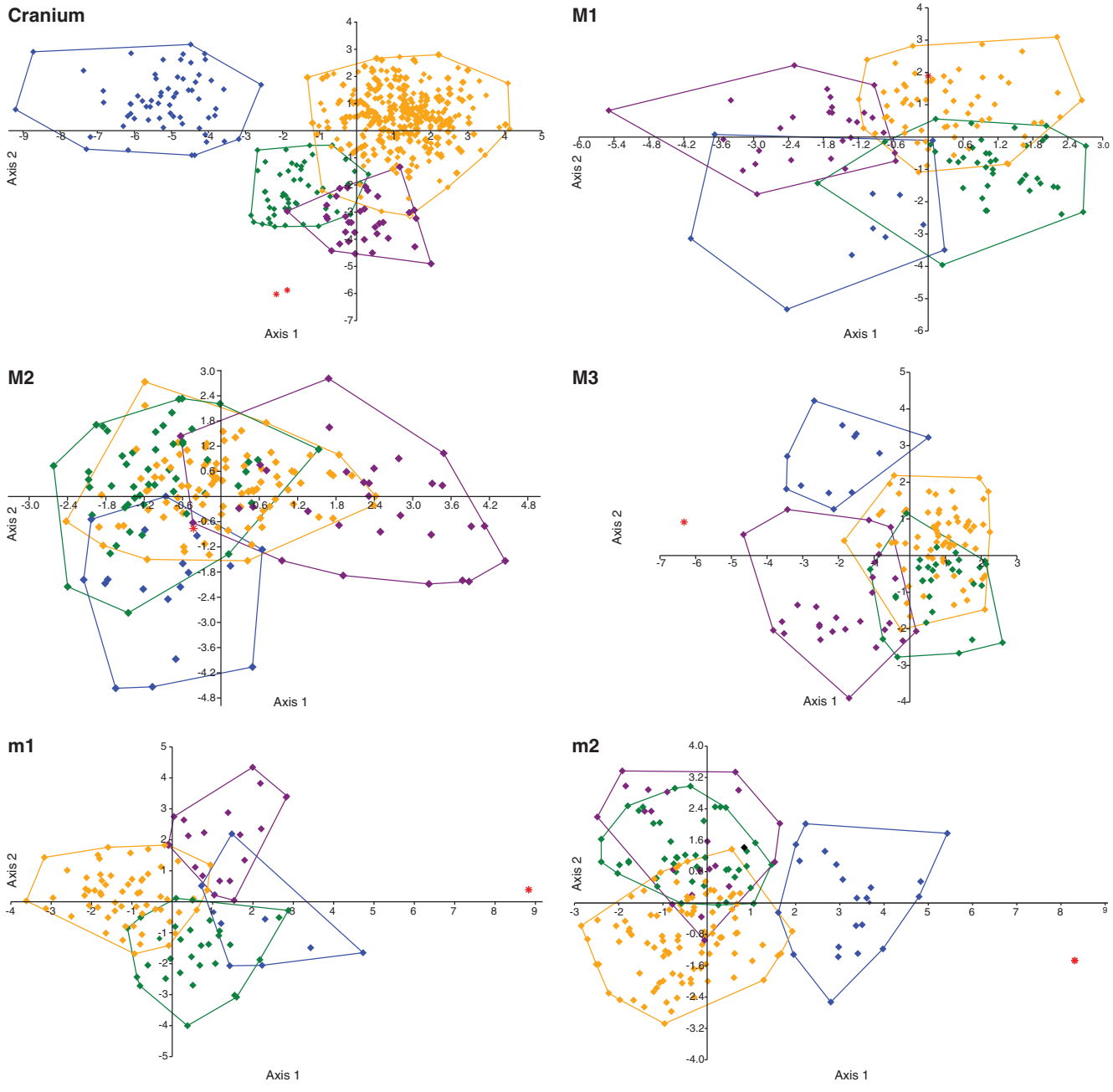

Fig. 2. Plots of first two canonical variates (CV1 and CV2) of hylobatid cranial and molar analyses. M1K12:3, red; *Bunopithecus*, black (m2 only); *Hoolock*, green; *Hylobates*, orange; *Nomascus*, purple; *Symphalangus*, blue. Cranial plot includes both reconstructions of M1K12:3.

Table 1. Comparisons between M1K12:3 and extant hylobatids for permutation tests (10,000 rounds) of cranial and molar Procrustes and Mahalanobis distances.

Extant hylobatid genus	Procrustes distance						Mahalanobis distance					
	Cranium	M1	M2	M3	m1	m2	Cranium	M1	M2	M3	m1	m2
Hoolock	>0.001*	0.164	0.116	0.117	0.222	0.092	>0.001*	0.099	0.075	0.030*	0.005*	0.006*
Hylobates	>0.0001*	0.345	0.165	0.191	0.053	0.035*	>0.0001*	0.161	0.128	0.034*	0.010*	0.003*
Nomascus	0.001*	0.437	0.263	0.152	0.399	0.141	>0.001*	0.296	0.401	0.062	0.018*	0.042*
Symphalangus	>0.001*	0.030*	0.065	0.054	0.823	0.343	>0.001*	0.126	>0.001*	0.052	0.088	0.004*

*Significant difference.

archives to reconstruct past human-caused biodiversity loss in this global conservation hotspot and provide new insights for understanding faunal vulnerability and resilience in order to help prevent future extinctions.

REFERENCES AND NOTES

1. T. Zhang, N. Hou, Y. Ding, *Zhongguo Wenwubao* **2006**, 1–2 (2006).
2. Y. Ding, *Kaogu Yu Wenwu* **2009**, 62–66 (2009).
3. X. Wang, *Kaogu Yu Wenwu* **1983**, 89–91 (1983).
4. IUCN, *The IUCN Red List of Threatened Species. Version 2017-2* (IUCN, 2017).
5. P. F. Fan *et al.*, *Am. J. Primatol.* **79**, e22631 (2017).
6. A. T. Smith, Y. Xie, Eds., *A Guide to the Mammals of China* (Princeton Univ. Press, 2008).
7. R. H. Van Gulik, *The Gibbon in China: An Essay in Animal Lore* (E. J. Brill, 1967).
8. N. G. Jablonski, G. Chaplin, "The fossil record of gibbons" in *The Gibbons: New Perspectives on Small Ape Socioecology and Population Biology*, D. Whittaker, S. Lappan, Eds. (Springer, 2009), pp. 110–130.
9. Y. Gu, *Hum. Evol.* **4**, 509–514 (1989).
10. A. Ortiz *et al.*, *PLOS ONE* **10**, e0131206 (2015).
11. S. T. Turvey *et al.*, *J. Biogeogr.* **43**, 2250–2260 (2016).
12. N. Creel, H. Preuschoft, "Cranial morphology of the lesser apes" in *Gibbon and Siamang, Vol. 4*, D. M. Rumbaugh, Ed. (Karger, 1976), pp. 219–303.
13. Materials and methods are available as supplementary materials.
14. L. Carbone *et al.*, *Nature* **513**, 195–201 (2014).
15. Systematic paleontology is available as supplementary materials.
16. S. T. Turvey, *Holocene Extinctions* (Oxford Univ. Press, 2009).
17. S. B. Cooke, A. L. Rosenberger, S. Turvey, *Proc. Natl. Acad. Sci. U.S.A.* **108**, 2699–2704 (2011).
18. V. N. Thinh *et al.*, *BMC Evol. Biol.* **10**, 74 (2010).
19. L. Liu, X. Chen, *The Archaeology of China: From the Late Paleolithic to the Early Bronze Age* (Cambridge Univ. Press, 2012).
20. S. T. Turvey, J. J. Crees, M. M. I. Di Fonzo, *Proc. R. Soc. B* **282**, 20151299 (2015).
21. S. T. Turvey, J. J. Crees, Z. Li, J. Bielby, J. Yuan, *Proc. R. Soc. B* **284**, 20171979 (2017).
22. A. D. Barnosky *et al.*, *Nature* **471**, 51–57 (2011).
23. G. Ceballos *et al.*, *Sci. Adv.* **1**, e1400253 (2015).
24. A. Estrada *et al.*, *Sci. Adv.* **3**, e1600946 (2017).
25. A. Nater *et al.*, *Curr. Biol.* **27**, 3487–3498.e10 (2017).
26. R. B. Marks, *China: An Environmental History* (Rowman & Littlefield, 2017).
27. S. T. Turvey, S. A. Fritz, *Philos. Trans. R. Soc. Lond. B Biol. Sci.* **366**, 2564–2576 (2011).

ACKNOWLEDGMENTS

Access to collections was provided by the Institute of Zoology, Beijing; Kunming Institute of Zoology; South China Institute of Endangered Animals; Natural History Museum, London; American Museum of Natural History; Center for the Study of Human Origins; National Museum of Natural History; Museum of Comparative Zoology; and the Zoological Museum, Vietnam National University. We thank J. Korsgaard, C. Kimock, H. Ma, and B. Garrod for assistance. **Funding:** Research was supported by a Royal Society University Research Fellowship (UF080320/130573). **Author contributions:** S.T.T. and H.J.C. designed the research; J.H., A.O., S.H., Y.D., T.Z., S.T.T., and K.B. collected data; K.B., A.O., and H.J.C. analyzed data; and S.T.T., A.O., and H.J.C. wrote the paper. **Competing interests:** None declared. **Data and materials availability:** All data needed to evaluate the conclusions in the paper are present in the paper or the supplementary materials.

SUPPLEMENTARY MATERIALS

www.sciencemag.org/content/360/6395/1346/suppl/DC1
Materials and Methods
Supplementary Text
Figs. S1 to S4
Tables S1 to S7
References (*28*–*44*)

26 July 2017; accepted 3 May 2018
10.1126/science.aao4903

NEUROSCIENCE

Locally coordinated synaptic plasticity of visual cortex neurons in vivo

Sami El-Boustani[1]*†‡, Jacque P. K. Ip[1]†, Vincent Breton-Provencher[1], Graham W. Knott[2], Hiroyuki Okuno[3]§, Haruhiko Bito[4], Mriganka Sur[1]*

Plasticity of cortical responses in vivo involves activity-dependent changes at synapses, but the manner in which different forms of synaptic plasticity act together to create functional changes in neurons remains unknown. We found that spike timing–induced receptive field plasticity of visual cortex neurons in mice is anchored by increases in the synaptic strength of identified spines. This is accompanied by a decrease in the strength of adjacent spines on a slower time scale. The locally coordinated potentiation and depression of spines involves prominent AMPA receptor redistribution via targeted expression of the immediate early gene product Arc. Hebbian strengthening of activated synapses and heterosynaptic weakening of adjacent synapses thus cooperatively orchestrate cell-wide plasticity of functional neuronal responses.

Neuronal circuits in the brain are subject to changes driven by sensory inputs (*1*, *2*) or motor learning (*3*–*5*), causing cells to modify their responses to individual inputs while maintaining a stable level of activity (*6*). Homeostatic plasticity stabilizes the output firing rate of single neurons by uniformly scaling up or down the strength of all synapses (*6*, *7*). Other forms of compensatory plasticity can also act locally at dendritic stretches (*8*–*14*) or even at single synapses (*15*–*17*). Synaptic potentiation at specific dendritic locations could be coordinated with heterosynaptic depression of nearby synapses within short stretches of the same dendrite to cooperatively implement functional plasticity of single-cell responses (*18*). It is unknown whether locally coordinated synaptic plasticity occurs in vivo and whether it has a role in shaping neuronal responses.

Cortical plasticity induced by sensory deprivation or enrichment (*2*) results in large-scale functional and structural changes across many neurons and synapses. We developed a controlled paradigm for inducing plasticity at identified synapses on single neurons in the primary visual cortex (V1) of awake juvenile mice (postnatal day 28 to 35). We reasoned that pre-before-post pairing at specific synapses, via visual stimuli presented at a target location closely followed by channelrhodopsin-2 (ChR2)–driven spiking of an individual neuron, would induce Hebbian potentiation of excitatory synapses responding to the target stimulus and consequently shift the receptive field at the soma (Fig. 1, A and B). We characterized excitatory synaptic inputs to V1 layer 2/3 neurons in response to sparse noise stimuli (*19*) (Fig. 1, C to E). Evoked excitatory postsynaptic currents (EPSCs) typically responded to stimulus onset or offset (Fig. 1F). Onset responses lasted for about 200 ms with a peak response at 65 to 130 ms (mean, 96.3 ± 7.4 ms; n = 8 neurons). To ensure that the peak synaptic input led the ChR2 action potential, we induced postsynaptic spiking 150 ms after visual stimulus onset to potentiate responses to the target stimulus and avoid post-before-pre pairing. Such ChR2-induced spiking corresponded to a peak excitatory postsynaptic potential to spike time difference of 20 to 85 ms, which overlaps with time windows used in previous studies to induce response potentiation (*20*, *21*).

To induce and measure receptive field plasticity over extended periods of time, we electroporated the calcium indicator mRuby2-P2A-GCaMP6s (*22*) and the opsin ChR2-mCherry (*23*) in single neurons (*19*) (Fig. 1, G and H). ChR2 allowed precise control of neuronal spikes (Fig. 1I; n = 7 neurons; number of spikes per pulse = 1.2 ± 0.32). We used the GCaMP6s signal to map receptive fields measured at the soma (Fig. 1, J and K, and fig. S1, A and B). We then determined a target location close to the peak receptive field response location. Repeated presentations of the target stimulus were paired with single blue light pulses to elicit ChR2 spikes (60 pairings). Receptive fields were measured again 1 to 2 hours postpairing. For most neurons, the receptive field center of mass shifted toward the target stimulus (Fig. 1, K and L). These changes were not observed when ChR2 stimulation was not paired with the target stimulus (*19*) (Fig. 1L). Receptive field shifts could not be explained by changes in eye position (fig. S2) and did not induce functional changes in the network (fig. S3). Receptive field shifts could also be achieved with other pairing rates and durations (fig. S4).

We next investigated the structural basis of receptive field plasticity at the synaptic level. We used dendritic spine volume changes as a structural proxy for long-term potentiation or depression (*24*–*26*). By comparing dendritic spines pre- and postpairing, we observed bidirectional volume changes within dendritic stretches (Fig. 2A). These changes were not caused by drifts in the imaging planes (fig. S5). Spines exhibiting structural long-term potentiation (sLTP) or depression (sLTD) were compared with those in control experiments in the absence of ChR2 ($ChR2^-$; Fig. 2, B and C). We quantified changes in spine volume by using the normalized difference (δV) between the integrated spine fluorescence signal relative to the shaft pre- and postpairing, and we defined a threshold for pairing-induced sLTP and sLTD in $ChR2^+$ neurons ($\delta V = \pm 0.25$, corresponding to spines that exceeded the 97th percentile of the $ChR2^-$ distribution; fig. S6). We then backtracked the temporal evolution of significantly potentiated or depressed spines (Fig. 2D). sLTP spines rapidly increased in volume immediately after pairing, and this was followed by a moderate increase over the next 2 hours. In contrast, sLTD spines showed an initial small decrease in volume that was amplified over the next 2 hours until the average volume change for sLTD and sLTP spines became approximately balanced. The density of sLTD spines was significantly correlated with, and was greater than, the density of sLTP spines in individual dendrites (Fig. 2E). sLTD spine density was significantly larger at short sLTP-sLTD distances (*19*), indicating that sLTD spines were preferentially located around sLTP spines (Fig. 2F).

We reconstructed stretches of dendrite from $ChR2^+$ and $ChR2^-$ neurons with electron microscopy (EM) (Fig. 2, G and J) and compared spines that were well isolated in two-photon images (*19*). All two-photon–imaged spines on these dendrites were identified by EM. For both the $ChR2^+$ and $ChR2^-$ dendrite, EM spine volumes were highly correlated with the spine fluorescence signal postpairing (Fig. 2, H and K). Consistent with the observation that structural plasticity caused by pairing resulted in both increases and decreases of spine volumes in $ChR2^+$ neurons, whereas volumes remained stable in $ChR2^-$ neurons, prepairing signals showed significantly larger dispersion around the best fit for the $ChR2^+$ dendrite (Fig. 2H) but were equivalent to postpairing signals for the $ChR2^-$ dendrite (Fig. 2K). EM spine volume was highly correlated with synaptic surface area, consistent

[1]Department of Brain and Cognitive Sciences, Picower Institute for Learning and Memory, Massachusetts Institute of Technology, Cambridge, MA 02139, USA. [2]Bio Electron Microscopy Laboratory, School of Life Sciences, École Polytechnique Fédérale de Lausanne, Lausanne 1015, Switzerland. [3]Medical Innovation Center, Kyoto University Graduate School of Medicine, Sakyo-ku, Kyoto 606-8507, Japan. [4]Department of Neurochemistry, Graduate School of Medicine, The University of Tokyo, Hongo 7-3-1, Bunkyo-ku, Tokyo 113-0033, Japan.
***Corresponding author. Email: msur@mit.edu (M.S.); elbousta@mit.edu (S.E.-B.)** †These authors contributed equally to this work. ‡Present address: Brain Mind Institute, School of Life Sciences, Ecole Polytechnique Fédérale de Lausanne, Lausanne 1015, Switzerland. §Present address: Department of Biochemistry and Molecular Biology, Graduate School of Medical and Dental Sciences, Kagoshima University, 8-35-1 Sakuragaoka, Kagoshima 890-8544, Japan.

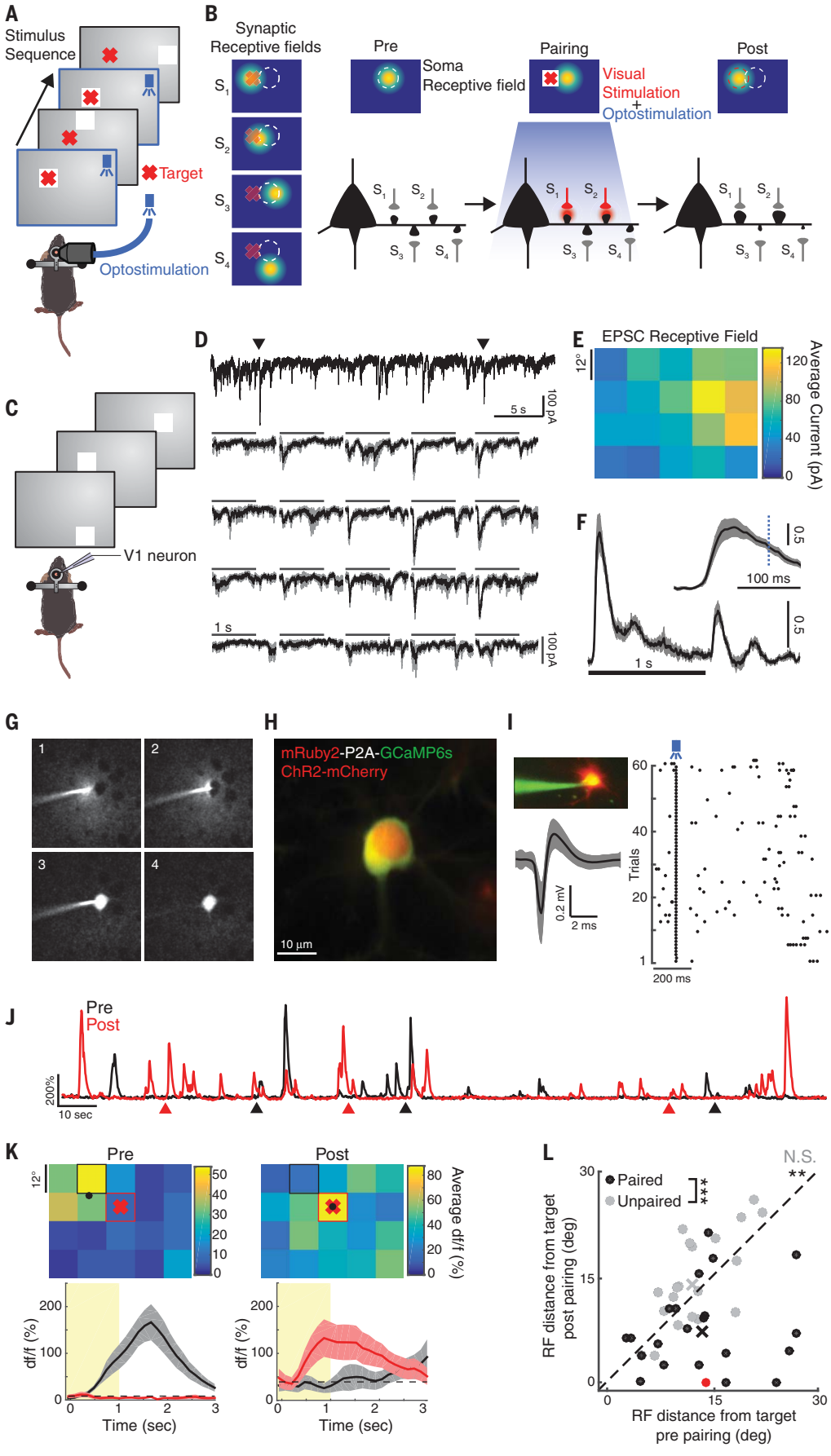

Fig. 1. Induction of receptive field plasticity in V1 neurons. (**A**) Pairing protocol (white squares, visual stimuli). (**B**) Effect of pairing on a neuron's receptive field and its dendritic spines (S_1 to S_4). (**C**) Whole-cell recording during sparse noise stimuli. (**D**) Top, excitatory current trace of a recorded neuron. Bottom, average EPSC for each stimulus location (gray shading, SEM). (**E**) Receptive field obtained by averaging EPSCs between 50 and 150 ms. (**F**) EPSC in *z*-score averaged over all neurons and stimulus locations (n = 8 neurons). Gray shading, SEM; dotted blue line, 150 ms. (**G**) Single-cell electroporation in vivo. (**H**) Neuron expressing mRuby2-P2A-GCaMP6s and ChR2-mCherry. (**I**) Loose-patch recording of a $ChR2^+$ neuron spiking to single blue light pulses. Spike waveforms are shown (gray shading, standard deviation). (**J**) Calcium df/*f* (fluorescence signal changes relative to baseline) traces obtained from soma. Arrowheads, onset of visual stimuli, presented prepairing at the preferred location (black) and postpairing at the target location (red). (**K**) Top, receptive fields from the traces in (J). Preferred stimulus locations are shown with black (pre) and red (post) squares. Black dots, center of mass. Red crosses, target stimulus. Bottom, response time course in squared locations. Shaded areas, SEM. Black dashed line, baseline df/*f* level. (**L**) Distance between the target and receptive field center of mass pre- and postpairing (black; n = 22 neurons; N = 23 mice; paired Wilcoxon test, $^{**}P < 0.01$). Red dot, example in (K). X, average shift. Control neurons with unpaired ChR2-visual stimulation are shown in gray (n = 21 neurons; N = 11 mice; P = 0.06; N.S., not significant). Receptive field shifts were significantly different between paired and unpaired populations (unpaired Kruskal-Wallis test, $^{***}P < 0.001$).

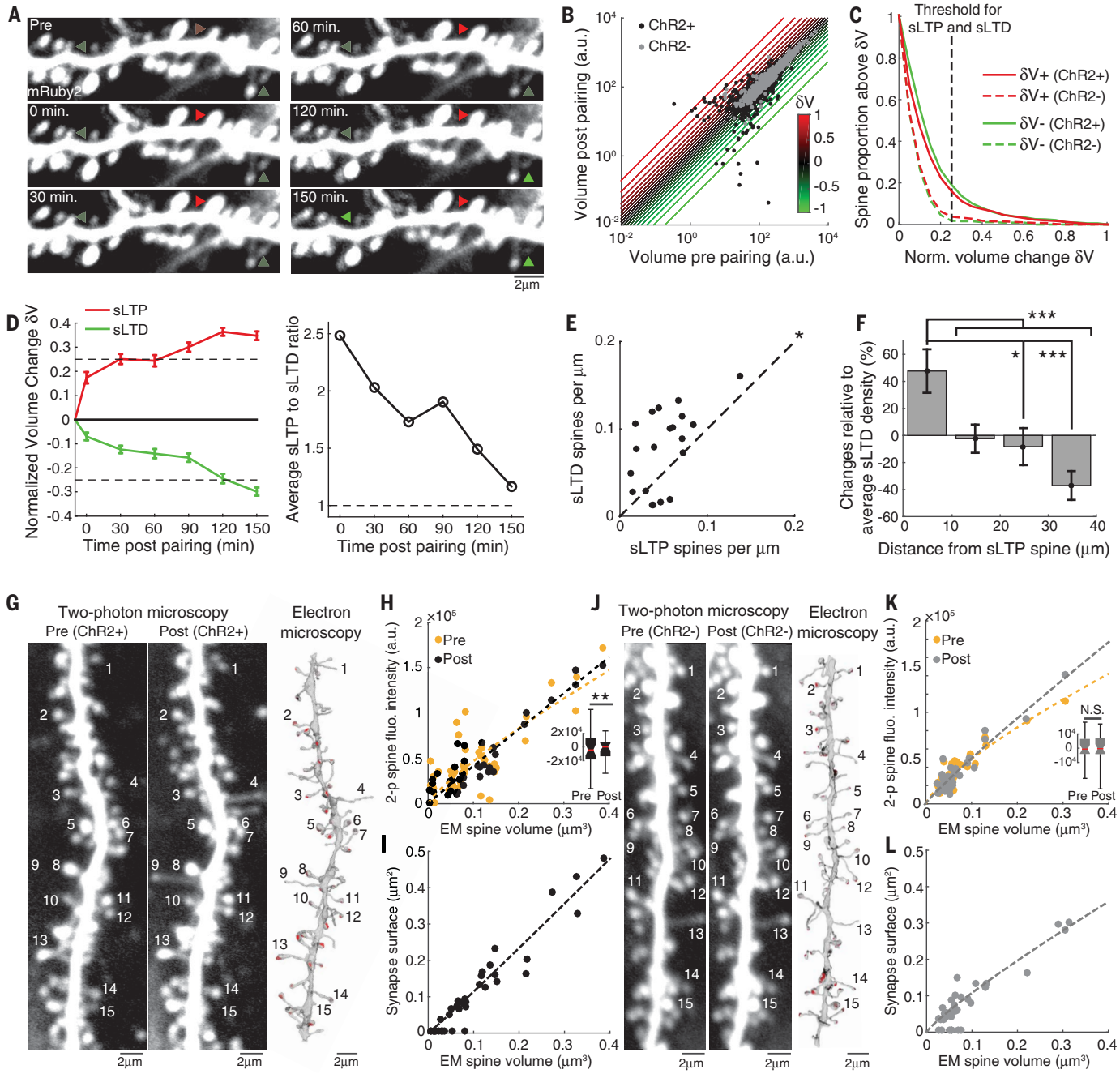

Fig. 2. Hebbian potentiation and heterosynaptic depression in stretches of dendrite. (**A**) Time-lapse dendritic imaging. Arrowheads correspond to sLTP (red) and sLTD (green) spines. (**B**) Spine volumes pre- and postpairing (>2 hours) for ChR2$^+$ (n = 1498 spines) and ChR2$^-$ (n = 845 spines) neurons. a.u., arbitrary units. (**C**) Proportion of enlarged (δV+) and shrunken (δV–) spines above different δV values (variance F-test between ChR2$^+$ and ChR2$^-$, $P < 0.001$). Black dashed line, sLTP and sLTD threshold $\delta V = \pm 0.25$. (**D**) Left, average normalized volume change over time for sLTP (n = 110) and sLTD (n = 98) spines. Dashed lines, threshold. Right, sLTP-to-sLTD volume change ratio. (**E**) sLTP and sLTD spine density per dendrite (n = 20 dendrites; Pearson coefficient = 0.55, $P < 0.05$; paired Wilcoxon test, $^*P < 0.05$). (**F**) sLTD spine density variation relative to the mean as a function of distance from sLTP spines [n = 103 sLTP spines; one-way analysis of variance (ANOVA), $P < 0.01$; unpaired Kruskal-Wallis test, $^{***}P < 0.001$ and $^*P < 0.05$ with Bonferroni correction]. (**G**) ChR2$^+$ dendrite imaged pre- and postpairing and reconstructed by EM after the experiment, postpairing. (**H**) Spine volume measured with EM compared to two-photon fluorescence signal [n = 36 spines; EM versus post, coefficient of determination (r^2) = 0.85; EM versus pre, r^2 = 0.57]. Lines depict best-fit power functions. Inset, distribution of fit residuals (unpaired variance F-test, $^{**}P < 0.01$). (**I**) Spine volume versus synaptic surface area (n = 36 spines; r^2 = 0.91). Some small spines lacked synapses, as has been previously reported (*33*). (**J** to **L**) Same as (G) to (I) for a ChR2$^-$ neuron (n = 33 spines; EM versus post, r^2 = 0.88; EM versus pre, r^2 = 0.85; unpaired variance F-test). Spine volume versus synapse area is shown in (L) (n = 39 spines; r^2 = 0.92). Error bars, SEM.

with the hypothesis that synaptic weight is reflected in spine volume (Fig. 2, I and L, and fig. S7).

We investigated the functional signature associated with structural changes to evaluate whether they were consistent with receptive field plasticity measured at the soma. GCaMP6s activity in individual spines was used to measure input-specific receptive fields (Fig. 3, A to C). Spine receptive fields were heterogeneously distributed along dendritic stretches (fig. S8). We hypothesized that sLTP spines should have their receptive field centers overlapping the visual target because of Hebbian plasticity, whereas nearby sLTD spines would have receptive field centers located away from the target because of heterosynaptic, potentially cooperative, plasticity. Spines with receptive fields overlapping the target stimulus indeed increased in volume (Fig. 3, D and E), whereas neighboring spines with receptive fields away from the target were reduced (Fig. 3, D and F). Structural changes were accompanied by consistent changes in GCaMP6s signal amplitude (fig. S9). The average receptive field for sLTP spines was sharp and centered on the target, whereas the average receptive field for sLTD spines was distributed broadly away from and around the target (Fig. 3G). The distribution of sLTP and sLTD spines as a function of their receptive field distance from the target confirmed that as distance increased, the effect on spine size shifted from sLTP to sLTD (Fig. 3H).

We next electroporated SEP-GluA1—an AMPA receptor (AMPAR) subunit 1 tagged with a pH-sensitive form of green fluorescent protein (GFP), Super Ecliptic pHluorin (SEP) (*27*, *28*)—into single neurons to restrict the signal to membrane-inserted receptors, together with ChR2 and a volume-filling marker, DsRed2. Because the GCaMP6s signal would occlude GFP-tagged proteins, we electroporated GCaMP6s alone into neighboring neurons to determine a pairing target location for inducing plasticity in the $ChR2^+$ neuron (Fig. 4A) (neighboring neurons in V1 share a substantial proportion of their subthreshold receptive field; fig. S10). A strong and distinct SEP fluorescence signal was observed at the surface of individual spines (Fig. 4B, left). Comparing changes in SEP-GluA1 enrichment with volume changes in individual spines more than 2 hours after the pairing protocol, we found a significant positive correlation (Fig. 4, C to E). Positive or negative changes in volume thus reflect corresponding modifications of spine synaptic weight through AMPAR expression changes.

Arc, the protein encoded by the immediate gene *Arc*, is involved in AMPAR endocytosis (*29*). Arc preferentially interacts with the inactive β isoform of CaMKII and acts as an inverse tag of plasticity (*30*) that could potentially mediate heterosynaptic depression in dendritic segments (*31*). We used a monomeric enhanced GFP (mEGFP)–tagged Arc (mEGFP-Arc) probe (*30*) to study the molecular dynamics of Arc after the pairing protocol (Fig. 4B, right). Arc enrichment in spines was increased in sLTD spines and decreased in sLTP spines (Fig. 4, C to E). To test whether Arc mediates heterosynaptic depression, we delivered small hairpin RNA (shRNA; figs. S11 and S12) to deplete Arc in single neurons. Neurons in which Arc was knocked down displayed spines filled with SEP-GluA1 (Fig. 4, F and G), which was homogenously distributed along dendrites, compared with control neurons, where SEP-GluA1 was sparsely and focally distributed (Fig. 4H). To relate Arc expression to calcium signaling in spines (*30*) (fig. S13), we additionally knocked down CaMKIIβ (fig. S11). Dendrites with reduced CaMKIIβ displayed reduced spine-specific Arc expression (Fig. 4, I to K). Knockdown of Arc in neurons expressing GCaMP6s and ChR2 prevented displacement of receptive fields toward the target after pairing (Fig. 4L and fig. S12), consistent with impaired functional plasticity (*32*). In contrast to control neurons, the density of sLTP spines was not significantly different

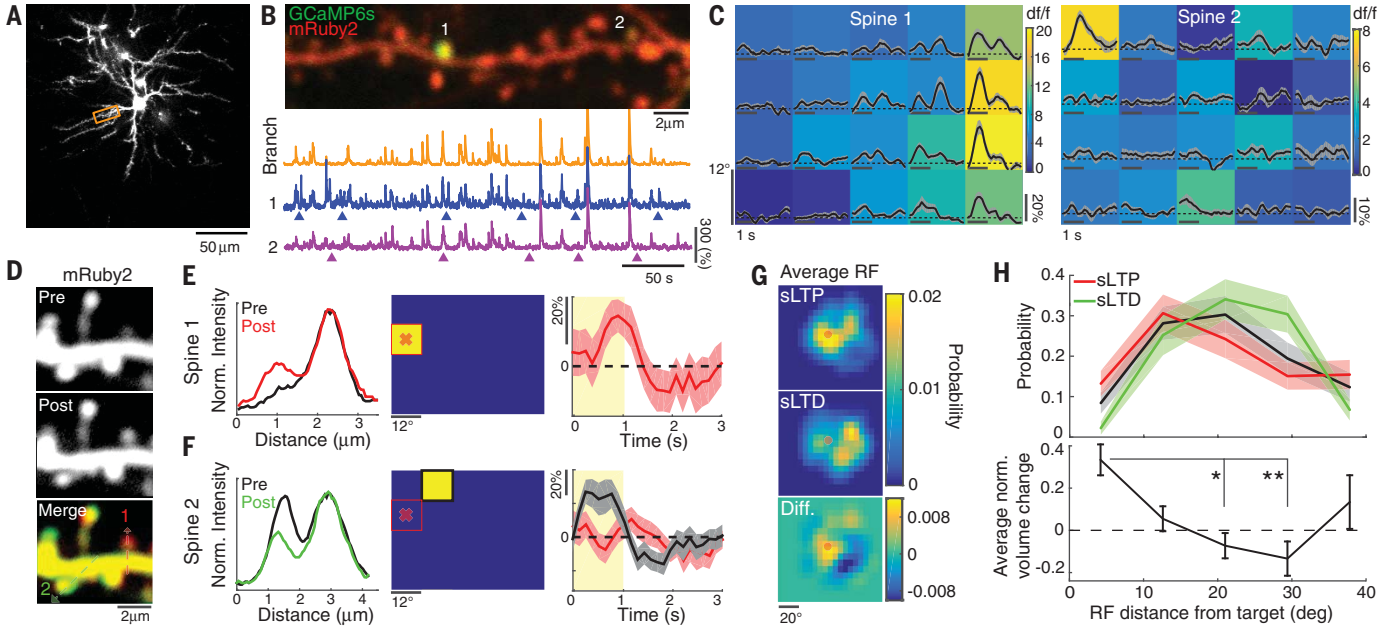

Fig. 3. Functional identification of sLTP and sLTD dendritic spines. (**A**) Neuron expressing mRuby2-P2A-GCaMP6s. (**B**) Top, dendritic stretch from within the rectangle in (A). Bottom, calcium traces for two spines and their corresponding branch. Arrowheads, onset of preferred stimuli. (**C**) Receptive fields for spines in (B). Gray shading, SEM. Color map, time-averaged response. (**D**) Dendritic segment with nearby sLTP ("1") and sLTD ("2") spines. (**E**) Left, profiles from the dashed red line in (D). Middle, receptive field of the spine. Red cross, target position. Right, response time course for the preferred stimulus. Shaded areas, SEM. (**F**) Same as (E) for the sLTD spine in (D). Left, profiles from the dashed green line. Right, response time course for the preferred stimulus (gray) and for the target stimulus location (red). (**G**) Average normalized receptive field centered on the target for sLTP (n = 94) and sLTD (n = 87) spines. Bottom, difference between distributions. (**H**) Top, distribution of receptive field distances from the target. Black distribution, randomized spine identity. Shaded areas, standard deviation. Bottom, average normalized volume change as a function of receptive field distance from the target for all sLTP and sLTD spines (n = 181 spines; one-way ANOVA, $P < 0.01$; $^*P < 0.05$ and $^{**}P < 0.01$ with Bonferroni correction). Error bars, SEM.

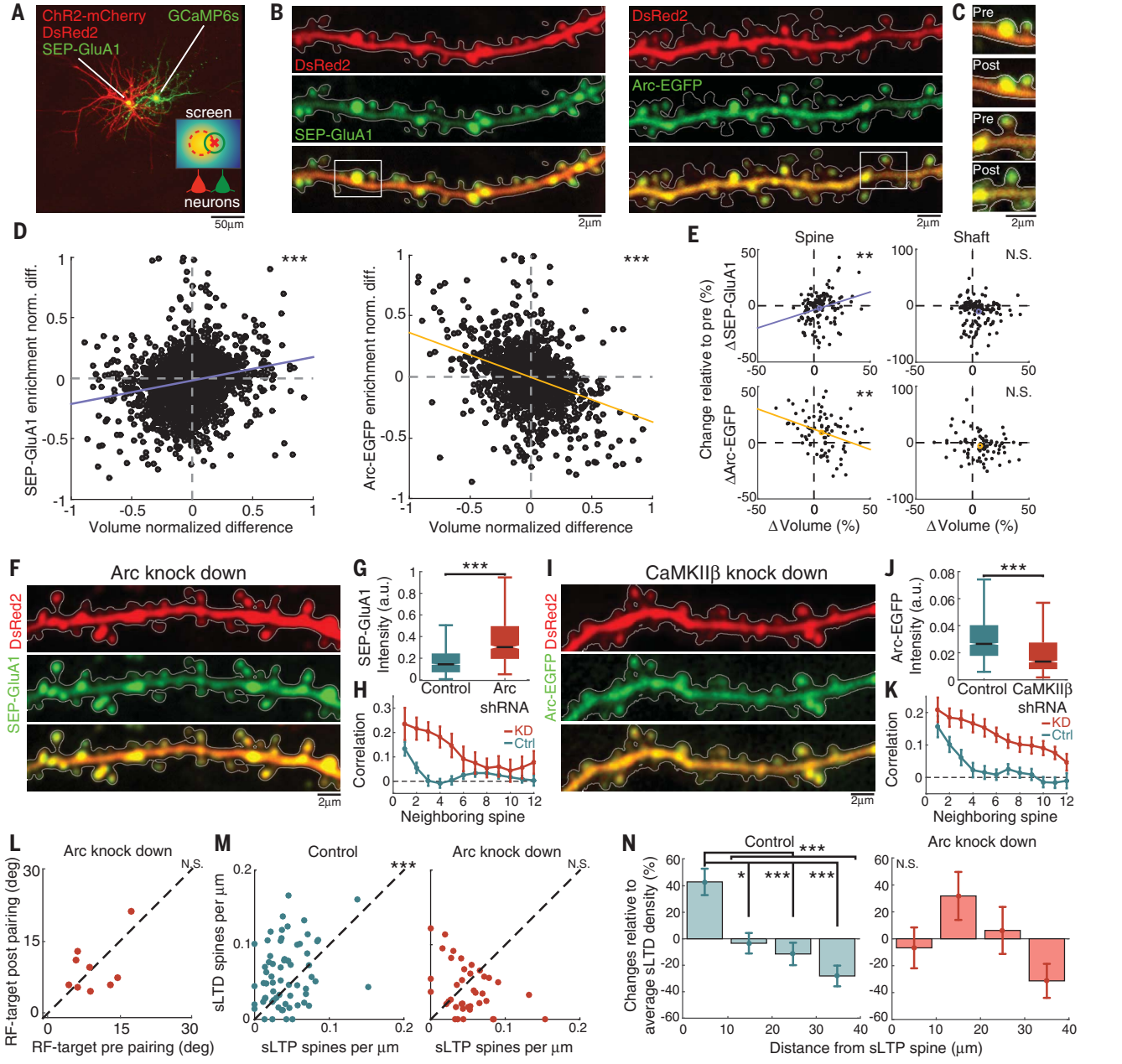

Fig. 4. Role of Arc in regulating plasticity of V1 neurons. (**A**) Neuron expressing ChR2-mCherry, DsRed2, and SEP-GluA1 in close proximity to a neuron expressing GCaMP6s. (**B**) Dendrites expressing SEP-GluA1 (left) or Arc-EGFP (right). (**C**) Spines corresponding to white rectangles in (B). (**D**) Comparison between normalized change in volume and SEP-GluA1 (left) or Arc-EGFP (right) enrichment (SEP-GluA1: n = 4354 spines from 17 neurons, N = 12 mice; Pearson coefficient = 0.22, ***P < 0.001) (Arc-EGFP: n = 1719 spines from 16 neurons, N = 8 mice; Pearson coefficient = −0.37, ***P < 0.001). (**E**) Relative volume changes compared with relative SEP-GluA1 (top; n = 122 dendrites) or Arc-EGFP (bottom; n = 81 dendrites) enrichment changes averaged over all spines or measured in the dendritic shaft (Pearson coefficient = 0.27, **P < 0.01 for SEP-GluA1 and −0.29, **P < 0.01 for Arc-EGFP). Purple and orange lines, best linear fits. Circles, average values. (**F**) Dendrite expressing SEP-GluA1 and Arc shRNA-DsRed2. (**G**) Distributions of spine SEP-GluA1 average intensity when Arc is endogenously expressed or knocked down [n = 960 spines from three neurons for knockdown (KD); n = 2669 spines from 11 neurons for control (Ctrl); Kruskal-Wallis test, ***P < 0.001]. (**H**) SEP-GluA1 intensity correlation with neighboring spines. (**I** to **K**) Same as (F) to (H) in control or CaMKIIβ KD dendrites expressing Arc-EGFP (n = 2053 spines from four neurons for KD; n = 2550 spines from 11 neurons for Ctrl; Kruskal-Wallis test, ***P < 0.001). (**L**) Distance between the target and receptive field pre- and postpairing for the Arc KD condition (n = 9 neurons, N = 7 mice; paired Wilcoxon test). (**M**) sLTP and sLTD spine density per dendrite for control (n = 66 dendrites; Pearson coefficient = 0.31, P < 0.05; paired Wilcoxon test, ***P < 0.001) and Arc KD (n = 39 dendrites; Pearson coefficient = −0.37, P < 0.05; paired Wilcoxon test, not significant) conditions. (**N**) sLTD spine density variation relative to the mean as a function of distance from sLTP spines for the control (average over n = 253 sLTP spines; one-way ANOVA, P < 0.001; unpaired Kruskal-Wallis test, ***P < 0.001 and *P < 0.05 with Bonferroni correction) and Arc KD conditions (average over n = 142 sLTP spines; one-way ANOVA, not significant). Dendrites in the control condition either express a scrambled Arc shRNA plasmid fused with DsRed (n = 46 dendrites) or mRuby2-P2A-GCaMP6s (n = 20 dendrites). Error bars, SEM.

from the density of sLTD spines for neurons with Arc knockdown (Fig. 4M). The spatial organization of sLTD spines around sLTP spines was impaired in Arc knockdown dendrites compared with controls (Fig. 4N), demonstrating that Arc helps organize the distribution of potentiated and depressed spines that underlies plasticity of neuronal responses. Local bidirectional plasticity of functionally identified spines was also observed in experiments where vision from the deprived eye was restored after monocular deprivation (fig. S15). Thus, Arc-mediated heterosynaptic plasticity takes place under physiological conditions and constitutes a mechanism for local coordination of synaptic plasticity that drives functional plasticity of neurons with heterogeneous synaptic inputs (fig. S16).

REFERENCES AND NOTES

1. H. Ko *et al*., *Nature* **496**, 96–100 (2013).
2. J. S. Espinosa, M. P. Stryker, *Neuron* **75**, 230–249 (2012).
3. S. X. Chen, A. N. Kim, A. J. Peters, T. Komiyama, *Nat. Neurosci.* **18**, 1109–1115 (2015).
4. J. Cichon, W.-B. Gan, *Nature* **520**, 180–185 (2015).
5. A. Hayashi-Takagi *et al*., *Nature* **525**, 333–338 (2015).
6. G. G. Turrigiano, S. B. Nelson, *Nat. Rev. Neurosci.* **5**, 97–107 (2004).
7. K. Ibata, Q. Sun, G. G. Turrigiano, *Neuron* **57**, 819–826 (2008).
8. W. Ju *et al*., *Nat. Neurosci.* **7**, 244–253 (2004).
9. W. C. Oh, L. K. Parajuli, K. Zito, *Cell Rep.* **10**, 162–169 (2015).
10. M. A. Sutton *et al*., *Cell* **125**, 785–799 (2006).
11. W.-J. Bian, W.-Y. Miao, S.-J. He, Z. Qiu, X. Yu, *Cell* **162**, 808–822 (2015).
12. J. Winnubst, J. E. Cheyne, D. Niculescu, C. Lohmann, *Neuron* **87**, 399–410 (2015).
13. J. N. Bourne, K. M. Harris, *Hippocampus* **21**, 354–373 (2011).
14. A. Govindarajan, R. J. Kelleher, S. Tonegawa, *Nat. Rev. Neurosci.* **7**, 575–583 (2006).
15. J. C. Béïque, Y. Na, D. Kuhl, P. F. Worley, R. L. Huganir, *Proc. Natl. Acad. Sci. U.S.A.* **108**, 816–821 (2011).
16. Q. Hou, D. Zhang, L. Jarzylo, R. L. Huganir, H.-Y. Man, *Proc. Natl. Acad. Sci. U.S.A.* **105**, 775–780 (2008).
17. M. C. Lee, R. Yasuda, M. D. Ehlers, *Neuron* **66**, 859–870 (2010).
18. I. Rabinowitch, I. Segev,*Trends Neurosci.* **31**, 377–383 (2008).
19. Supplementary materials.
20. C. D. Meliza, Y. Dan, *Neuron* **49**, 183–189 (2006).
21. V. Pawlak, D. S. Greenberg, H. Sprekeler, W. Gerstner, J. N. D. Kerr, *eLife* **2**, e00012 (2013).
22. T. Rose *et al*., *Science* **352**, 1319–1322 (2016).
23. F. Zhang *et al*., *Nature* **446**, 633–639 (2007).
24. M. Matsuzaki, N. Honkura, G. C. R. Ellis-Davies, H. Kasai, *Nature* **429**, 761–766 (2004).
25. C. D. Harvey, K. Svoboda, *Nature* **450**, 1195–1200 (2007).
26. Y. Zhang, R. H. Cudmore, D.-T. Lin, D. J. Linden, R. L. Huganir, *Nat. Neurosci.* **18**, 402–407 (2015).
27. C. D. Kopec, B. Li, W. Wei, J. Boehm, R. Malinow, *J. Neurosci.* **26**, 2000–2009 (2006).
28. H. Makino, R. Malinow, *Neuron* **72**, 1001–1011 (2011).
29. S. Chowdhury *et al*., *Neuron* **52**, 445–459 (2006).
30. H. Okuno *et al*., *Cell* **149**, 886–898 (2012).
31. C. Mullins, G. Fishell, R. W. Tsien, *Neuron* **89**, 1131–1156 (2016).
32. C. L. McCurry *et al*., *Nat. Neurosci.* **13**, 450–457 (2010).
33. G. W. Knott, A. Holtmaat, L. Wilbrecht, E. Welker, K. Svoboda, *Nat. Neurosci.* **9**, 1117–1124 (2006).

ACKNOWLEDGMENTS

We thank R. Neve, B. Bartelle, and A. Jasanoff for their assistance with plasmid preparation and testing; J. Petravicz for performing the eyelid sutures for monocular deprivation experiments; M. Yildirim for providing two-photon point spread function measurements; K. Li for his assistance with optical intrinsic imaging; O. Marre, J. Mayrhofer, and C. Gasselin for their comments on the manuscript; and V. Jayaraman, R. A. Kerr, D. S. Kim, L. L. Looger, and K. Svoboda from the GENIE Project, Janelia Farm Research Campus, Howard Hughes Medical Institute (HHMI), for the distribution of GCaMP6. **Funding:** This work was supported by Marie Curie postdoctoral fellowship FP7-PEOPLE-2010-IOF (to S.E.-B.), a Human Frontier Science Program Long-Term Fellowship (to J.P.K.I.), AMED-CREST (to H.B.), KAKENHI grants (15H04258 to H.O. and 15H02358 and 17H06312 to H.B.), and NIH grants NS090473 and EY007023, NSF grant EF1451125, the Simons Center for the Social Brain, and the Picower Institute Innovation Fund (to M.S.). **Author contributions:** S.E.-B., J.P.K.I., and M.S. conceived experiments. S.E.-B. performed single-cell electroporation. S.E.-B. and J.P.K.I. performed surgeries and carried out in vivo experiments. S.E.-B. performed data analysis. M.S. and J.P.K.I. contributed to analysis of experiments. V.B.-P. performed intracellular recordings in vivo and eye-tracking controls. G.W.K. performed the EM and analysis. H.O. and H.B. designed and provided the Arc-EGFP plasmid and the CaMKIIβ shRNA and controls. S.E.-B., J.P.K.I., V.B.-P., and M.S. wrote the paper. **Competing interests:** The authors declare no competing interests. **Data and materials availability:** All data needed to evaluate the conclusions of the paper are in the paper or the supplementary materials or are available at www.surlab.org. pGL4.11-Arc7000-mGFP-Arc-UTRs, CaMKIIβ shRNA vector, and control shRNA vector are available from H.B. under a material transfer agreement with the University of Tokyo.

SUPPLEMENTARY MATERIALS

www.sciencemag.org/content/360/6395/1349/suppl/DC1
Materials and Methods
Figs. S1 to S16
References (*34*–*49*)

13 June 2017; resubmitted 7 March 2018
Accepted 8 May 2018
10.1126/science.aao0862

EVOLUTIONARY BIOLOGY

Adaptive introgression underlies polymorphic seasonal camouflage in snowshoe hares

Matthew R. Jones[1]*, L. Scott Mills[2,3,4], Paulo Célio Alves[2,5,6], Colin M. Callahan[1], Joel M. Alves[5,7], Diana J. R. Lafferty[2,4,8], Francis M. Jiggins[7], Jeffrey D. Jensen[9,10], José Melo-Ferreira[5,6]*, Jeffrey M. Good[1,2]*

Snowshoe hares (*Lepus americanus*) maintain seasonal camouflage by molting to a white winter coat, but some hares remain brown during the winter in regions with low snow cover. We show that cis-regulatory variation controlling seasonal expression of the *Agouti* gene underlies this adaptive winter camouflage polymorphism. Genetic variation at *Agouti* clustered by winter coat color across multiple hare and jackrabbit species, revealing a history of recurrent interspecific gene flow. Brown winter coats in snowshoe hares likely originated from an introgressed black-tailed jackrabbit allele that has swept to high frequency in mild winter environments. These discoveries show that introgression of genetic variants that underlie key ecological traits can seed past and ongoing adaptation to rapidly changing environments.

Many species undergo reversible changes in morphology, physiology, and behavior to cope with the challenges of seasonal environments. These critical components of phenotypic plasticity often track the environment through the photoperiod-dependent release of hormones (*1*). However, circannual rhythms can become desynchronized when abiotic conditions change rapidly (*2*), leading to declines in population fitness (*3*). The capacity of species to adapt to rapidly changing environments will depend in part on the proximate and ultimate causes of variation underlying seasonal traits (*4*, *5*), which remain poorly understood at the molecular level (*1*, *2*).

At least 21 bird and mammal species undergo autumn molts from brown to white coats (*6*–*8*) as part of a suite of plastic trait responses to seasonal environments. We used natural variation in seasonal camouflage of the snowshoe hare (*Lepus americanus*) to understand the genetic basis of this critical seasonal trait. Autumn molts to white winter coats are cued by photoperiod (*8*) and generally track seasonal snow cover (*7*). Direct estimates of hare survival have shown that mismatch between coat color and snow cover increases predation (*3*). White winter coats predominate across the snowshoe hare range, but some populations molt into brown winter coats (Fig. 1). In the Pacific Northwest (PNW), shifts in the probability of white coats coincide with a gradient in snow cover from warmer coastal to colder inland environments, consistent with local selection for seasonal camouflage, with color morphs co-occurring across a broad polymorphic zone (Fig. 1C) (*7*).

To dissect the genetic basis of polymorphic seasonal camouflage, we used whole-genome sequences for a winter-white hare from Montana (MT, 33x coverage) (*9*, *10*) and a winter-brown hare from Washington (WA, 22x coverage) and constructed a reference through iterative mapping (*11*) to the rabbit genome (*9*, *12*). We then sequenced 80 whole exomes (62 Mb, 21 ± 7.6x coverage per individual) from two regions in the PNW polymorphic zone (WA, n = 26; Oregon, hereafter OR, n = 26; each region 50% winter-white), a monomorphic winter-white locality in MT (n = 14), and a monomorphic winter-brown locality in British Columbia (BC, n = 14; table S1). If the polymorphic zone represents admixture between previously isolated populations, then genetic structure could obscure genotype-phenotype associations (*13*). Analysis of 38,694 unlinked single-nucleotide polymorphisms (SNPs) revealed geographic structure (Fig. 1C), but genome-wide genetic differentiation (fixation index, F_{ST}) between winter-brown and winter-white individuals was ~0 within polymorphic localities (table S2). The polymorphic zone also showed no evidence of admixture on the basis of linkage disequilibrium patterns (fig. S1) or allele sharing with other populations (table S3) (*14*). Thus, geographic variation for winter coat color in the PNW likely reflects primary intergradation across a gradient in snow cover.

We tested 513,812 SNPs for coat color associations across polymorphic populations and identified a single outlier region on chromosome 4 in perfect association with winter coat color ($P = 4.24 \times 10^{-10}$, dominant association test; Fig. 2A, fig. S2, and data S1) (*12*). We then augmented exome data with low-coverage whole-genome resequencing of polymorphic zone hares (~20x per color morph). Coat color associations based on genotype likelihoods (15,173,804 SNPs) (*15*) confirmed a single outlier region (fig. S3) localized to a ~225-kb interval of elevated F_{ST} between color morphs. This interval was centered on the pigmentation gene *Agouti* and two flanking genes, *Ahcy* and *Eif2s2*, neither of which are known to be directly involved in coat color (Fig. 2B). Winter-brown hares were homozygous (n = 26) for brown-associated alleles (hereafter *a*), whereas winter-white hares were either heterozygous (n = 24) or homozygous (n = 2) for the alternative allele (hereafter *A*; Fig. 2C). We then induced autumn molts in 18 captive wild-caught hares (WA, n = 11; MT, n = 7) and found perfect concordance between *Agouti* genotypes and winter coat colors (Fig. 2C and table S4). This experiment included a heterozygous (*Aa*) wild-caught winter-white female from WA that gave birth in captivity to both winter-white and winter-brown offspring (Fig. 2D). Therefore, winter coat color segregates as a dominant locus in both wild and captive animals.

The agouti signaling protein (ASIP) antagonizes the melanocortin-1 receptor (MC1R) in follicular melanocytes, shifting melanogenesis toward lighter pheomelanin pigments or inhibiting pigment production (*16*). MC1R mutations suppress expression of winter-white coats in dark or blue color morphs of arctic foxes, suggesting that ASIP-MC1R interactions are involved in the development of seasonal color molts (*17*). *Agouti* is typically expressed as ventral- or hair cycle–specific isoforms distinguished by alternative 5′ untranslated regions (5′UTRs; Fig. 2B) (*18*). Both isoforms have been associated with lighter dorsal pelage (*19*, *20*). We hypothesized that the development of winter-white coats, which mostly lack pigments (*8*), is controlled by isoform-specific up-regulation of *Agouti* during the autumn molt. To test this, we quantified allele-specific expression of both isoforms and the tightly linked *Ahcy* locus in dorsal skin biopsies from three captive heterozygous hares (*Aa*) undergoing brown-to-white molts. Quantitative polymerase chain reaction (qPCR) verified expression of *Ahcy* and the *Agouti* hair-cycle isoform, whereas expression of the ventral isoform was negligible (Fig. 3A and tables S5 and S6). Targeted pyrosequencing revealed highly skewed expression toward the white (*A*) allele of the *Agouti* hair-cycle isoform ($P < 0.0001$, Student's t test), indicative of cis-regulatory variation, whereas *Ahcy* showed equal allelic expression (Fig. 3B and table S7). These data suggest that winter-white coats develop because of increased expression of *Agouti* during the autumn molt, which fits with our observed dominance relationships and previous studies on the evolution of lighter pelage in deer mice (*19*, *20*). Our findings directly link *Agouti* expression and the evolution of seasonal

[1]Division of Biological Sciences, University of Montana, Missoula, MT 59812, USA. [2]Wildlife Biology Program, University of Montana, Missoula, MT 59812, USA. [3]Office of Research and Creative Scholarship, University of Montana, Missoula, MT 59812, USA. [4]Fisheries, Wildlife, and Conservation Biology Program, Department of Forestry and Environmental Resources, North Carolina State University, Raleigh, NC 27695, USA. [5]CIBIO, Centro de Investigação em Biodiversidade e Recursos Genéticos, InBIO Laboratório Associado, Universidade do Porto, 4485-661 Vairão, Portugal. [6]Departamento de Biologia, Faculdade de Ciências da Universidade do Porto, 4169-007 Porto, Portugal. [7]Department of Genetics, University of Cambridge, Cambridge CB2 3EH, UK. [8]Department of Biology, Northern Michigan University, Marquette, MI 49855, USA. [9]School of Life Sciences, Ecole Polytechnique Fédérale de Lausanne, 1015 Lausanne, Switzerland. [10]School of Life Sciences, Arizona State University, Tempe, AZ 85281, USA.
***Corresponding author. Email: matthew2.jones@umontana.edu (M.R.J.); jmeloferreira@cibio.up.pt (J.M.-F.); jeffrey.good@umontana.edu (J.M.G.)**

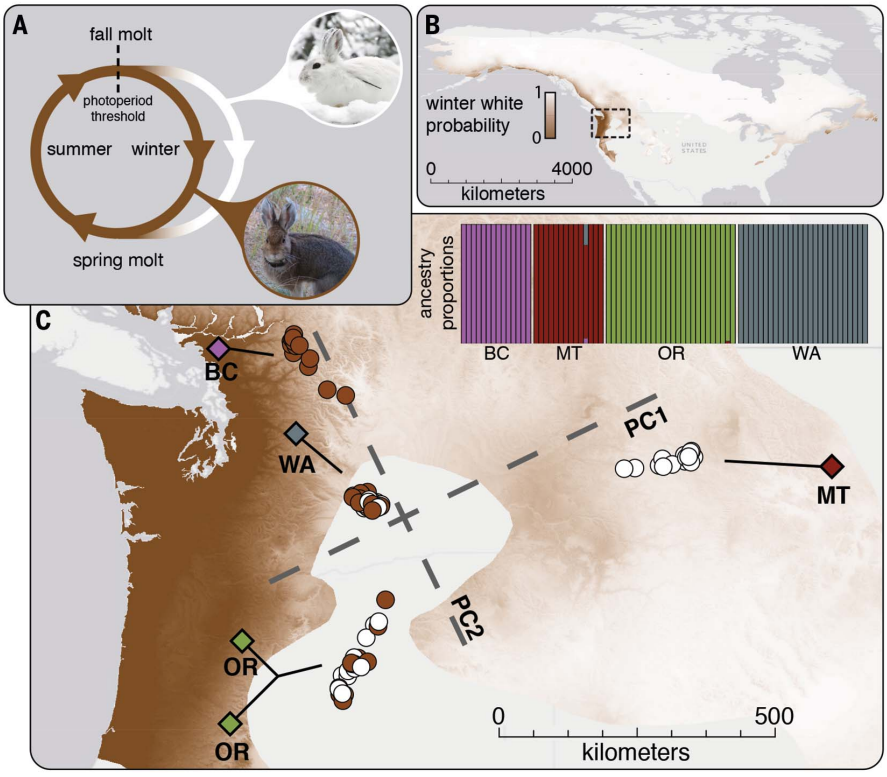

Fig. 1. Winter coat color polymorphism and population structure in snowshoe hares. (**A**) Alternative winter color morphs in snowshoe hares. [Photo credit: L. Scott Mills research photo] (**B**) The modeled range-wide probability of winter-white coats, adapted from (*7*). (**C**) Magnification of region outlined in (B) shows principle components (PC1, 7.42%, and PC2, 5.27%; coat color represented as brown and white circles) and population ancestry plots of 38,694 unlinked SNPs derived from 80 exomes sampled from five localities (colored diamonds) overlaid on the probability of winter-white coats in the PNW.

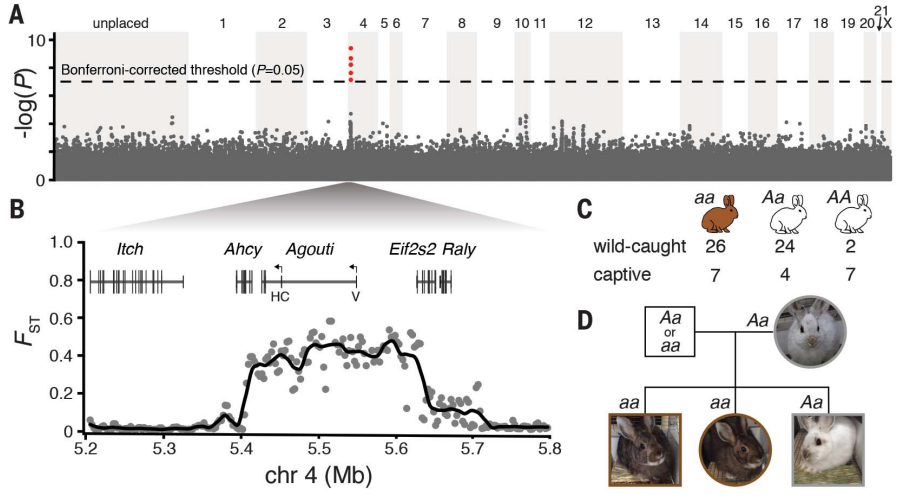

Fig. 2. The genetic basis of winter coat color polymorphism. (**A**) Exome SNP associations ($-\log_{10}$ of *P* values, assuming dominant minor allele; 513,812 SNPs) for polymorphic zone individuals. Red points above the dashed line exceed the Bonferroni-corrected threshold of $P = 0.05$. (**B**) Gene structures of *Itch*, *Ahcy*, *Agouti*, *Eif2s2*, and *Raly* across the associated interval on chromosome 4 (chr 4) and alternative *Agouti* transcription start sites (arrows) corresponding to hair-cycle (HC) and ventral (V) 5′UTRs. Sliding window averages of F_{ST} (5 kb with 2.5-kb step) between winter-white and winter-brown individuals with low-coverage whole genomes (15,173,804 SNPs). (**C**) Dominance of winter coat color inferred from *Agouti* genotypes of wild (OR and WA; Hardy-Weinberg $\chi^2 = 1.6$, $P = 0.21$) and captive (WA and MT) hares. (**D**) Pedigree and genotypes of a mixed-phenotype family (paternal genotype is unknown but inferred to carry the *a* allele). [Photo credit: Diana J. R. Lafferty and Matthew R. Jones]

camouflage in snowshoe hares and suggest that cis-regulatory evolution plays an important role in the origin of seasonal traits.

Comparison of winter-white (MT) and winter-brown (WA) genomes revealed notably elevated levels of absolute genetic divergence across *Agouti* (*Agouti* $d_{XY} = 1.6\%$; genome-wide $d_{XY} = 0.41\%$; $P < 0.0001$, randomization test; Fig. 4A and fig. S4), indicating that the color polymorphism did not arise from a recent de novo mutation. Alternatively, elevated divergence could reflect either the long-term maintenance of polymorphism or introgression from another species (*21*, *22*). Six of the 32 species of hares and jackrabbits (genus *Lepus*) have winter-white molts, but evolutionary relationships within this rapid radiation are poorly resolved (*23*). To examine the origins of winter coat color variants, we combined whole-genome sequences of two additional winter-white snowshoe hares from Pennsylvania and Utah, two winter-brown black-tailed jackrabbits (*L. californicus*) from Nevada, and a previously sequenced winter-white mountain hare (*L. timidus*) from Europe (*10*). Phylogenetic analyses (*24*) predicted a very rare topology at *Agouti* that clustered individuals by winter coat color (Fig. 4B and fig. S5). Pairwise divergence between all winter-brown and winter-white individuals was significantly elevated across a known cis-regulatory region of *Agouti* (*25*, *26*) ~40-kb upstream of the transcription start site of the hair-cycle isoform ($P < 0.001$, randomization test; Fig. 4A and fig. S4). Divergence peaked across a ~20-kb interval ($d_{XY} = 2.2$ to 2.4%) that included a 1033-base insertion on the winter-white haplotype and a ~4.3-kb deletion on the winter-brown haplotype (fig. S4). Additional functional data are needed to determine if either of these candidate mutations underlie the observed cis-regulatory differences in *Agouti* expression (Fig. 3B).

The elevated interspecific divergence between color groups suggests that the winter-white and winter-brown *Agouti* alleles may have arisen relatively early in *Lepus* (*21*). By contrast, divergence within color groups was strongly reduced across a larger interval encompassing *Agouti* (Fig. 4A and fig. S6), indicating that winter coat color alleles may have been shared through hybridization. In support of this hypothesis, we found low, but significant, levels of genome-wide introgression (*27*) between snowshoe hares and both black-tailed jackrabbits and mountain hares (table S8). Window-based analyses of absolute divergence and derived-allele sharing (*28*) identified the *Agouti* interval among the strongest genome-wide signatures of introgression in both winter-brown and winter-white clusters (fig. S7).

Previous studies demonstrated mitochondrial DNA introgression from black-tailed jackrabbits, a western North American prairie-scrub species, into PNW snowshoe hares and speculated that hybridization may have contributed to the evolution of brown winter coats in snowshoe hares (*29*, *30*). Consistent with this, winter-brown snowshoe hares unambiguously nested within black-tailed jackrabbit variation at *Agouti* (Fig. 4B and fig. S5B), resulting in a 174-kb interval of

significantly reduced divergence between species (d_{XY} = 0.42 versus 1.2% genome-wide; P < 0.001, randomization test) embedded within a 236-kb interval of significant admixture (proportion of introgression, $\hat{f}_{hom}$ = 0.71; Fig. 4A). Strong selection at a locus in the ancestral population can reduce divergence between species (*31*), resulting in false inferences of introgression (*28*); however, coalescent simulations of shared polymorphism with and without selection in the ancestral population indicate that such shallow divergence is highly unlikely in the absence of interspecific gene flow (Fig. 4C and fig. S8). We also detected introgression within the winter-white *Agouti* group (figs. S7 and S8). Resolving the origin and functional relevance of the winter-white signatures awaits further investigation, given that three other North American *Lepus* species undergo some degree of seasonal coat color change (*7*).

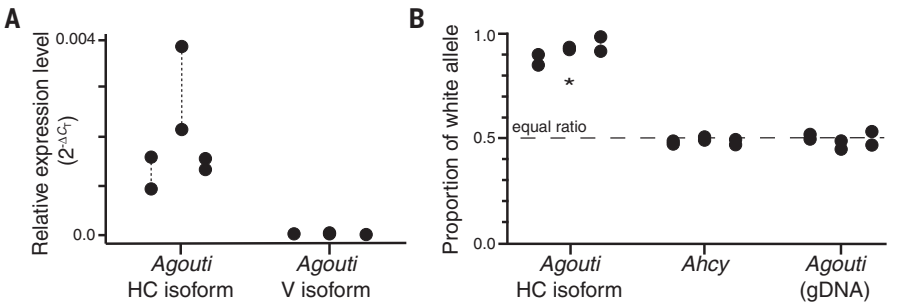

Fig. 3. *Agouti* expression in snowshoe hares during autumn molts. (**A**) The relative expression level ($2^{-\Delta C_T}$, where ΔC_T is the difference in the qPCR cycle threshold relative to *Gapdh*, a constitutively expressed control gene) of hair-cycle (HC) and ventral (V) *Agouti* isoforms in molting skin of winter-white (*Aa*) snowshoe hares. (**B**) Relative abundance of the winter-white allele in the same skin samples for *Agouti* hair-cycle transcripts, *Ahcy* transcripts, and *Agouti* genomic DNA (gDNA). The asterisk indicates that white-allele proportions were significantly increased in *Agouti* transcripts compared to *Ahcy* transcripts and *Agouti* genomic DNA (P < 0.00001, Student's t test). Pairs of points represent technical replicates.

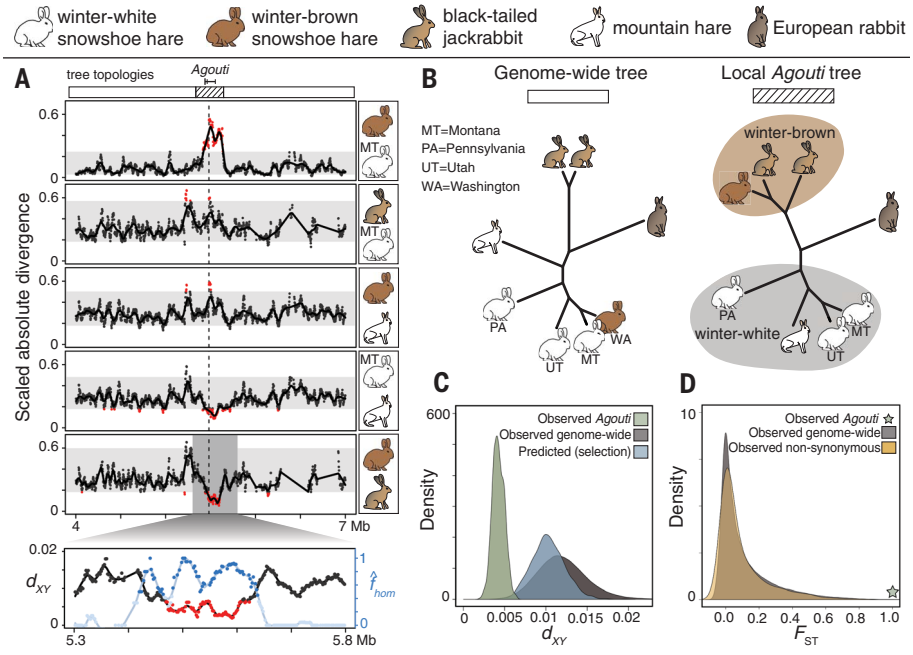

Fig. 4. The evolution of winter coat color alleles in hares and jackrabbits. (**A**) Estimated tree topologies across the *Agouti* region [top, see (B)]. Pairwise comparisons of mutation-scaled absolute genetic divergence in 20-kb sliding windows (dashed line indicates location of candidate insertion-deletion mutations). Gray rectangles represent 99.8% bootstrap quantiles, and red points are windows with one-tailed P < 0.001 based on randomization tests. Bottom plot shows a finer scale of absolute divergence in black (d_{XY}, red points with one-tailed P < 0.001) and the fraction of introgression in blue ($\hat{f}_{hom}$, dark blue points with z score > 4) between black-tailed jackrabbits and the WA winter-brown snowshoe hare. (**B**) The most common genome-wide topology (white) and the local *Agouti* topology (hatched; rabbit outgroup). Brown- and gray-shaded regions indicate winter-brown and winter-white groups, respectively. (**C**) Distributions of d_{XY} between the winter-brown snowshoe hare and black-tailed jackrabbits genome-wide (gray), at *Agouti* (green), and under simulations of strong ancestral selection (blue). (**D**) Distributions of SNP F_{ST} values between BC (monomorphic winter-brown) and MT (monomorphic winter-white) hares genome-wide (gray) and for nonsynonymous SNPs (yellow). The green star indicates F_{ST} = 1 at a diagnostic *Agouti* SNP.

To link introgression with local adaptation, we tested for selective sweeps on the basis of allele frequency skews (*32*) while controlling for demographic history (fig. S9 and table S9). We detected a hard sweep overlapping *Agouti* in winter-brown individuals from the polymorphic zone but no evidence for a sweep in winter-white individuals (figs. S10 and S11). We estimate that the sweep of the winter-brown allele in the PNW occurred 3000 to 15,000 years ago, after the retreat of the Cordilleran ice sheet (*33*). High inferred selection coefficients (s) on the introgressed winter-brown *Agouti* background ($\overline{s_{WA}}$ = 0.024, $\overline{s_{OR}}$ = 0.015; fig. S11C) and fixation of alternative *Agouti* alleles between monomorphic winter-brown (BC) and winter-white (MT) localities (Fig. 4D), despite high gene flow (table S9), indicate that seasonal camouflage is maintained under strong local selection.

Despite widespread evidence of hybridization between animal species, introgression has rarely been directly linked to ecological adaptation (*34*–*36*). We have shown that introgression has shaped locally adaptive seasonal camouflage in snowshoe hares. Recurrent introgression of coat color variants could facilitate evolutionary responses to environmental change within populations as well as the long-term maintenance of adaptive variation among species, similar to adaptive polymorphisms of beak morphology across the radiation of Darwin's finches (*22*, *34*). The evolution of winter-brown coats in snowshoe hares may have enabled their persistence in environments with more ephemeral seasonal snow after the end of the last glacial maximum. Temperate snow-cover duration is predicted to dramatically decrease over the next century under most models of climate change (*37*), which may further intensify directional selection for winter-brown camouflage (*3*, *6*). Thus, the establishment of this dynamic color polymorphism through introgression is likely to be a critical component of ongoing adaptation to rapidly changing seasonal environments (*7*) in this iconic ecological model.

REFERENCES AND NOTES

1. M. E. Visser, S. P. Caro, K. van Oers, S. V. Schaper, B. Helm, *Philos. Trans. R. Soc. Lond., B, Biol. Sci.* **365**, 3113–3127 (2010).
2. B. Helm *et al.*, *Proc. Biol. Sci.* **280**, 20130016 (2013).
3. M. Zimova, L. S. Mills, J. J. Nowak, *Ecol. Lett.* **19**, 299–307 (2016).
4. W. E. Bradshaw, C. M. Holzapfel, *Mol. Ecol.* **17**, 157–166 (2008).
5. A. A. Hoffmann, C. M. Sgrò, *Nature* **470**, 479–485 (2011).
6. L. S. Mills *et al.*, *Proc. Natl. Acad. Sci. U.S.A.* **110**, 7360–7365 (2013).
7. L. S. Mills *et al.*, *Science* **359**, 1033–1036 (2018).
8. M. Zimova *et al.*, *Biol. Rev. Camb. Philos. Soc.* 10.1111/brv.12405 (2018).
9. M. Carneiro *et al.*, *Science* **345**, 1074–1079 (2014).

10. F. A. Seixas, thesis, University of Porto, Porto, Portugal, and University of Montpellier, Montpellier, France (2017).
11. B. A. J. Sarver *et al*., *Genome Biol. Evol.* **9**, 726–739 (2017).
12. Materials and methods are available as supplementary materials.
13. J. K. Pritchard, M. Stephens, N. A. Rosenberg, P. Donnelly, *Am. J. Hum. Genet.* **67**, 170–181 (2000).
14. D. Reich *et al*., *Nature* **488**, 370–374 (2012).
15. T. S. Korneliussen, A. Albrechtsen, R. Nielsen, *BMC Bioinformatics* **15**, 356 (2014).
16. E. Le Pape *et al*., *Proc. Natl. Acad. Sci. U.S.A.* **106**, 1802–1807 (2009).
17. D. I. Våge *et al*., *Peptides* **26**, 1814–1817 (2005).
18. H. Vrieling, D. M. Duhl, S. E. Millar, K. A. Miller, G. S. Barsh, *Proc. Natl. Acad. Sci. U.S.A.* **91**, 5667–5671 (1994).
19. C. R. Linnen, E. P. Kingsley, J. D. Jensen, H. E. Hoekstra, *Science* **325**, 1095–1098 (2009).
20. M. Manceau, V. S. Domingues, R. Mallarino, H. E. Hoekstra, *Science* **331**, 1062–1065 (2011).
21. R. F. Guerrero, M. W. Hahn, *Mol. Ecol.* **26**, 5362–5368 (2017).
22. F. Han *et al*., *Genome Res.* **27**, 1004–1015 (2017).
23. J. Melo-Ferreira *et al*., *Syst. Biol.* **61**, 367–381 (2012).
24. N. Zamani *et al*., *BMC Genomics* **14**, 347 (2013).
25. D. M. J. Duhl, H. Vrieling, K. A. Miller, G. L. Wolff, G. S. Barsh, *Nat. Genet.* **8**, 59–65 (1994).
26. C. R. Linnen *et al*., *Science* **339**, 1312–1316 (2013).
27. E. Y. Durand, N. Patterson, D. Reich, M. Slatkin, *Mol. Biol. Evol.* **28**, 2239–2252 (2011).
28. S. H. Martin, J. W. Davey, C. D. Jiggins, *Mol. Biol. Evol.* **32**, 244–257 (2015).
29. E. Cheng, K. E. Hodges, J. Melo-Ferreira, P. C. Alves, L. S. Mills, *Mol. Ecol.* **23**, 2929–2942 (2014).
30. J. Melo-Ferreira, F. A. Seixas, E. Cheng, L. S. Mills, P. C. Alves, *Mol. Ecol.* **23**, 4617–4630 (2014).
31. T. E. Cruickshank, M. W. Hahn, *Mol. Ecol.* **23**, 3133–3157 (2014).
32. P. Pavlidis, D. Živkovic, A. Stamatakis, N. Alachiotis, *Mol. Biol. Evol.* **30**, 2224–2234 (2013).
33. J. J. Clague, T. S. James, *Quat. Sci. Rev.* **21**, 71–87 (2002).
34. S. Lamichhaney *et al*., *Science* **352**, 470–474 (2016).
35. Y. Song *et al*., *Curr. Biol.* **21**, 1296–1301 (2011).
36. C. Pardo-Diaz *et al*., *PLOS Genet.* **8**, e1002752 (2012).
37. G. T. Pederson *et al*., *Science* **333**, 332–335 (2011).

ACKNOWLEDGMENTS

We thank E. Cheng, K. Garrison, and P. Zevit for assistance with sample collection. We thank R. Bracewell, T. Brekke, M. Carneiro, Z. Clare-Salzler, M. Dean, E. Kopania, M. S. Ferreira, N. Herrera, E. Larson, M. Nachman, B. Payseur, B. Sarver, and members of the NSF EPSCoR UNVEIL network for helpful discussion. R. Bracewell, B. Cole, T. Cosart, L. Farelo, E. Larson, S. Laurent, T. Max, S. Pfeifer, B. Sarver, and K. Zarn provided computational or laboratory support. A. Kumar assisted with the preparation of Fig. 1. Sequencing was performed at the University of Montana Genomics Core (supported by a grant from the M. J. Murdock Charitable Trust), the CIBIO-InBIO University of Porto New-Gen sequencing platform, the University of Oregon Genomics and Cell Characterization Core Facility, the HudsonAlpha Institute for Biotechnology, and Novogene Technology Co., Ltd. Computational resources were provided by the University of Montana Genomics Core and the Vital-IT Center for high-performance computing of the SIB Swiss Institute of Bioinformatics. **Funding:** This work was funded by a National Science Foundation (NSF) Graduate Research Fellowship (DGE-1313190), a NSF Doctoral Dissertation Improvement Grant (DEB-1702043), NSF Graduate Research Opportunities Worldwide, Portuguese Fundação para a Ciência e a Tecnologia (FCT) project grant "CHANGE" (PTDC/BIA-EVF/1624/2014, supported by National Funds), NSF EPSCoR (OIA-1736249), NSF (DEB-1743871), a FCT Investigator Grant (IF/00033/2014, supported by POPH-QREN funds from ESF and Portuguese MCTES/FCT), FLAD (Luso-American Development Foundation; PORTUGAL–U.S. Research Networks Program), the Drollinger-Dial Foundation, an American Society of Mammalogists Grant-in-Aid of Research, a Swiss Government Excellence Scholarship, and European Union's Seventh Framework Programme (CIBIO New-Gen sequencing platform; grant agreement 286431).
Author contributions: M.R.J., L.S.M., P.C.A., J.D.J., J.M.-F., and J.M.G. designed the study. J.M.G. coordinated the study. M.R.J., C.M.C., J.M.A., and D.J.R.L. generated data. J.M.A. and F.M.J. helped develop the exome capture experiments. M.R.J. performed data analyses under the guidance of J.M.G., J.M.-F., and J.D.J. M.R.J. and J.M.G. wrote the paper with input from the other authors. All authors approved the manuscript before submission.
Competing interests: None declared. **Data and materials availability:** Original sequence data are available in the Sequence Read Archive (www.ncbi.nlm.nih.gov/sra) under BioProject PRJNA420081 (SAMN08146448 to SAMN08146534). Previously generated whole-genome sequence data of snowshoe hare (SAMN02782769 and SAMN07526959) and mountain hare (SAMN07526960) are also available in the Sequence Read Archive.

SUPPLEMENTARY MATERIALS

www.sciencemag.org/content/360/6395/1355/suppl/DC1
Materials and Methods
Figs. S1 to S11
Tables S1 to S9
References (*38*–*82*)
Data S1

21 November 2017; accepted 1 May 2018
10.1126/science.aar5273

PINS

RESTORING HOPE

Since the first Deep Brain Stimulation initiative of Tsinghua Univeristy in 2000, PINS Medical has gradually established a multinational corporation with headquarter based in Beijing and international business center in Singapore. As an innovative high-tech enterprise with focus on neuromodulation, a variety of clinical products have been developed to date, which include stimulators for deep brain, vagus nerve, spinal cord and sacral nerve stimulation therapies. PINS Medical devotes itself to providing cutting-edge treatments for patients who suffer from neurological disorders such as Parkinson's Disease, Epilepsy, Chronic Pain and OAB, etc.

As part of the "National Engineering Laboratory for Neuromodulation", PINS Medical works in close cooperation with Tsinghua University and the numerous affiliated clinical centers, becoming a center of attraction for a wide range of professional talents in areas of clinical research, innovative R&D and business management. Since 2008, PINS Medical has developed rapidly in becoming a leading brand in neuromodulation within the Chinese market, due to the success of its creative research platform that efficiency links basic research, R&D of novel products, clinical testing and market entry.

With an outstanding reputation as a high-tech healthcare corporation, PINS Medical has a primary mission for providing innovative, high-quality products and services for patients to improve quality of life. PINS, which stands for Programmable Implanted Neuromodulation Stimulator, is also an abbreviation of "Patient Is No.1 alwayS". This clearly presents the goal of PINS Medical for "restoring hope", not simply as an innovation company but also across society to citizens.

Looking into the future with the continuous rise in incidence of neuropsychiatric disorders and increased social burden across the globe, PINS Medical along with local governments, research centers, companies and top academic scientists, are now developing and promoting innovative therapies worldwide.

www.pinsmedical.com info@pinsmedical.cn

Local project members

e-kakashi established in CIAT experimental field

Smart and Sustainable Agriculture with IoT

e-kakashi

PS Solutions

Through SATREPS *(1)*, PS Solutions Corp., an IT solution provider, is participating in CIAT *(2)*, a project developing rice crops and farming systems optimized for Colombia.

e-kakashi, an Agricultural Internet of Things (IoT)

Why is an IT company and not an agricultural or chemical company being tasked to solve food problems in Colombia? The answer is **e-kakashi**, a powerful IoT tool designed by PS Solutions Corp. **e-kakashi** collects environmental data and integrates it with farming data to give crop growers the best solutions to a wide range of field conditions.

“We must listen to the crops”, says **e-kakashi** developer Dr. Takashi Togami, “to know when they are thirsty or sick. Like children, with special attention and care, plants will grow, bloom and produce well.”

In partnership with Hitachi, Ltd., **e-kakashi** is combined with sensors that can measure environmental factors that influence crops, such as air temperature and humidity, soil temperature and moisture, and solar irradiance. Data is collected at a specific field and combined with previous scientific data about cultivation to create **ek-Recipe**, a tool Dr. Togami describes as a science-based e-farming manual. **ek-Recipe** helps the user optimize cultivation. Another tool of **e-kakashi**, **ek-Navigation**, supports decision making for the cultivation.

The benefits of using **e-kakashi** were demonstrated in 2016 for the cultivation of Koshihikari, a rice crop grown in Japan, Australia and the United States. **ek-Navigation** calculated that an accumulated temperature of 1000°C upon panicle initiation would prompt harvesting. In combination with this prediction, **ek-Navigation** calculated the best crop would come with an accumulated irradiance over 750 MJ when the crop is ripening. The powerful and unique feature of **e-kakashi** is its capability to turn collective farming experiences into indices for optimal cultivation.

Reduction of Environmental Footprint

However, **e-kakashi** goes beyond simple cultivation management. It also contributes to solving environmental problems such as unstable water supplies and greenhouse gas emission such as methane. Controlling water levels during plant growth could have a significant effect on methane emissions *(3)*. In collaboration with Tokyo Electron Device Limited, PS Solutions Corp. has been developing **e-kakashi** to track and calculate optimal water levels at each phase of plant growth as a way to both enhance agriculture productivity and reduce methane emissions. “Agriculture has a great negative impact on the global environment. Integrating scientific knowledge and technology can minimize that impact and still realize sustainable agriculture,” says Dr. Togami.

Plants Suitable for Local Environments

PS Solutions Corp. was invited to take part in the Colombia project by Dr. Manabu Ishitani (a senior scientist at CIAT) and Dr. Satoshi Ogawa (JICA expert *(4)*). In this project, **e-kakashi** is contributing to the development of cultivation technology for rice crops most suitable to the Colombian environment. With the help of **e-kakashi**, a new variety of rice whose roots grow diagonally to reach water-rich soil was made using marker assisted selection *(5)* and cultivation technology. The benefits of this effort are not only more nutritious and environmentally-friendly crops, but also jobs for locals. “Besides better farming, we see our technology as a way to fight poverty with smart agriculture,” says Dr. Togami.

References

1. SATREPS, Science and Technology Research Partnership for Sustainable Development, a research program jointly run by JST (Japan Science and Technology Agency), AMED (Japan Agency for Medical Research and Development), and JICA (Japan International Cooperation Agency).
2. CIAT, International Center for Tropical Agriculture.
3. Minamikawa, K., Tokida, T., Sudo, S., Padre, A., Yagi, K. (2015) Guidelines for measuring CH4 and N2O emissions from rice paddies by a manually operated closed chamber method. National Institute for Agro-Environmental Sciences, Tsukuba, Japan
4. JICA, Japan International Cooperation Agency
5. Y. Uga et al., “Control of root system architecture by DEEPER ROOTING 1 increases rice yield under drought conditions.” Nature Genetics 45, 1097-102 (2013).

Science Robotics Meeting in Japan 2018

–Challenges and Opportunities of Robotics–

The world's first "*Science Robotics* Meeting" was jointly held by the American journal *Science* and the American Association for the Advancement of Science (AAAS) for three days from March 12 to 14, 2018, at Plaza Heisei (Tokyo International Exchange Center) in Odaiba, Tokyo. The purpose of this meeting was to have researchers and businesses, as well as users, discuss the frontline of R&D in robotics, which is attracting growing global attention, and to share a future vision of society in which humans and robots coexist.

The *Science* Robotics Meeting gathered together first-rate experts in robotics from around the world. Those involved in R&D for various fields, including industry, medicine, and transportation (e.g., self-driving cars), exchanged the latest information on robotic technologies, operating software, and actions for robot diffusion.

On Day One, the Opening Memorial Lecture was delivered by Dr. Guang-Zhong Yang, editor of *Science Robotics* and director and co-founder of the Hamlyn Center at Imperial College London. Dr. Yang pointed to the importance of clarifying future orientation of robot development and sharing with potential users and others how robots can contribute to the future.

The Keynote Lecturers included, on Day Two, Dr. Mark Raibert, founder and chief executive officer of Boston Dynamics, famous for ambulatory robots, who presented the latest updates on the company's robot development, and on Day Three, Dr. Rodney Brooks, in charge of Robotics at MIT's Computer Science and Artificial Intelligence Lab. Dr. Brooks highlighted the significance of robot development for solving problems facing the world, such as climate change and an increasingly older population, indicating research themes that should be tackled in the future, including driverless vehicles and robot caregivers.

Such communications by international speakers were matched by Japanese corporate sponsors and participants who seized the opportunity to present the current status of their R&D efforts to the rest of the world. The following are summaries of the activities by Fujitsu Limited, JIG-SAW, PS Solutions, and AXION RESEARCH, in the field of artificial intelligence (AI) development.

Fujitsu: AI development and robotics services connecting people with ICT

Fujitsu Limited is an all-around Information and Communication Technology (ICT) company that makes network equipment ranging from cell phones to super computers and offers cloud and other services.

The Tokyo-headquartered multinational has been developing robots since the 1970s, starting with industrial robots and advancing to spacecraft robotic arms and humanoid robots in the 1990s. More recently, the company launched cute teddy-bear robots designed to interact with and respond to humans.

Today, Fujitsu is focusing on the development of platforms that connect robots with AI.

Mr. Hirotaka Hara (Fujitsu)

Mr. Hirotaka Hara, Fujitsu's representative director and senior vice president- AI Service Business Unit, says, "For future robotic development, controlling interfaces with humans will be crucial. We're hoping to develop AI seamlessly with robots, focusing on where robots and humans meet."

Fujitsu's involvement with AI goes back a long way, as attested by the number of its AI-related patent applications, which is "one of the largest among Japanese information technology (IT) vendors," according to Mr. Hara.

Fujitsu's effort in this area has resulted in Robopin, a robot designed to function as a receptionist, and the human-centric AI technology, Zinrai. Mr. Hara explains that Fujitsu's goal with Zinrai is to "realize AI that truly helps and works with humans," eventually arriving at the stage where AI enables humans to "predict the unpredictable."

One application of Zinrai is an automatic scoring system for gymnastics competitions. The growing complexity of techniques is making it extremely difficult for judges to give fair and accurate scores. The Zinrai system comprising 3D laser sensors and AI automatically recognizes techniques and gives scores. Its trial use is scheduled for the 2018 Gymnastics World Cup, as a step to an official adoption at the 2020 Summer Olympics in Tokyo.

JIG-SAW: Software-aided eyesight restoration

Established in 2001, JIG-SAW offers management services for cloud servers, Internet of Things (IoT) devices, communication chips, and modules. The company provides auto-sensing and auto-direction services, drawing on its foundation of software, hardware, and signal control technologies. Its corporate mission is "Supporting the world where all is connected with the Internet."

To fulfill this mission in the field of medicine, JIG-SAW is currently pursuing an eyesight restoration project called "NEW.VISION." Mr. Katsuya Sakamoto, manager of JIG-SAW's Business Strategy Division, says the company wants to "enable the visually impaired to recognize scenes, human expressions, and read and write." For the project, JIG-SAW is collaborating with the laboratory of Dr. Hiroshi Tomita of the Department of Biological Sciences, the Faculty of Science and Engineering at Iwate University in Morioka, Japan.

Dr. Tomita is an authority on research into the human application of the visual regeneration technique using the light-sensitive genes of green algae. The gene therapy technique that he developed can make ganglion cells perceive light. At present, however, this method can only cover the perception of green and blue among the three primary colors. The vividness of regained eyesight will depend on how signals of the color red are reproduced. JIG-SAW is charged with the development of software that modulates this reproduction.

Mr. Katsuya Sakamoto (JIG-SAW)

Concretely, it involves, says Mr. Sakamoto, "converting visual images captured by camera into 'visible' images by software and sending the signals directly to the brain to stabilize the level of visual reproduction." JIG-SAW obtained a Japanese patent for this concept in June 2017 as "prism glasses using a color signal control algorithm." R&D for smart glasses carrying the same software is also underway.

Expectations are high that, in addition to visual regeneration, the software may also be used for auditory reconstruction and tactile simulation.

PS Solutions: IoT and AI for smart farming

From left to right: Drs. Norio Yamaguchi, Kyosuke Yamamoto, and Takashi Togami (PS Solutions)

PS Solutions, a SoftBank Group company that develops and provides IT solutions, has developed e-kakashi for agriculture ("*kakashi*" is the Japanese word for scarecrow). The company intends to further develop this system that collects data as an agricultural IoT solution so that it will become fully capable of analyzing collected data using AI to guide and eventually automate crop cultivation.

Dr. Norio Yamaguchi, a fellow at PS Solutions, says, "Data plus analysis make it possible to grow crops without relying on experience and intuition. Data analysis plus AI will make it possible for the system to determine, for example, when to open or close vinyl greenhouse windows and how much to open them and automatically do so, instead of farmers personally opening or closing the windows based on data."

For this, however, the amount of data stored by e-kakashi is "still insufficient for fully operational output, although it has data on 85 million counts," says Dr. Kyosuke Yamamoto, senior chief engineer at the Agricultural Science Lab of the company's Critical Process Systems (CPS) Business Division. Opportunities for data collection are few and far between in the case of rice growing, for example, since it takes place only once or twice a year. For this reason, PS Solutions is also conducting R&D to establish methods that enable efficient learning with a small amount of data by combining machine learning and plant science.

Regarding the company's future orientation, Dr. Takashi Togami, director of the Agricultural Science Lab says, "We want to propose cultivation methods that are optimal for different kinds of plants and for each stage of growth. We hope to accomplish this by combining scientific knowledge with data on the growth of plants." The company is thus actively collecting and analyzing differences between its proposals founded on botanical science and actions actually taken by farmers based on their experience and intuition. By learning such findings with AI, PS Solutions hopes eventually to realize AI that can replace experience and intuition.

AXION RESEARCH: AI-based assessment of disease risk

AXION RESEARCH, a startup company established in December 2016, conducts Big Data analysis, with the use of wearable devices in some cases, on the theme of "Scientific Health."

Mr. Tomoyoshi Sato (AXION RESEARCH)

Mr. Tomoyoshi Sato, chief executive officer, says about the use of AI in the field of healthcare, "If you can visualize your physical condition and see how close to or far from your ideal physical condition, you're more likely to remain healthy or regain good health easily even if you do become ill. Predicting a path on which you shift from good health to disease and being attentive to your health maintenance can improve you and your family's quality of life (QoL)."

According to Mr. Sato, (1) the annual number of deaths caused by disease hardly changes from year to year because there is always a fixed number of persons shifting from good to poor health; (2) various kinds of stress and lack of sleep lower a person's immunity, accelerating the risk of shift to disease; and (3) if robots and AI understand human emotion and personalities, they can serve as reliable partners who provide sincere advice on health maintenance.

Based on these hypotheses, AXION RESEARCH is currently developing AXiR Engine, a prediction engine for healthcare. It will visualize a person's status of health and risk of disease and predicts his or her change from good to poor and ill health. Changing lifestyle or seeking medical attention in early stages according to the risk of disease thus indicated can enhance the person's QoL.

For this, Mr. Sato envisages "getting human personalities, values, and thought patterns to be recognized and learned to realize meaningful human–AI communication." To do so, the company intends to utilize existing natural language processing technology and develop systems to capture slight emotional shifts based on verbal communication, vocal registers, and patterns of movement of facial muscles.

AXION RESEARCH is seeking partners for R&D and technological development.

HUMAN VACCINES PROJECT

MICHELSON MEDICAL RESEARCH FOUNDATION

The Inaugural Winners of the Michelson Prizes for Human Immunology and Vaccine Research

Dr. Patricia Therese Illing
Monash University

Spliced peptides: Novel candidates for effective influenza immunity?

Dr. Ansuman Satpathy
Stanford University

Epigenomic mechanisms of vaccine-induced immunity

Dr. Laura Kate Mackay
The Peter Doherty Institute for Infection and Immunity

Targeting tissue-resident immune cells for enhanced immune protection

Could you be the next Michelson Prize winner?

More Information:

www.humanvaccinesproject.org/michelsonprizes

The Michelson Prizes for Human Immunology and Vaccine Research are **$150,000 awards that support young investigators applying disruptive research concepts** to significantly advance the development of future vaccines and immunotherapies.

Winners were selected via a rigorous, global competition and will receive their awards at the 1st annual conference on the *'The Future of Vaccine Development'* at the Michelson Center for Convergent Bioscience at the University of Southern California in June.

Information about the 2019 Michelson Prizes will be published in the fall of 2018. **If you are a researcher under the age of 35 with an innovative research concept, we encourage you to apply.**

Present your work to the world

Are you a representative of the upcoming generation of thought leaders in your field? Together we look forward to your application for the new Sartorius & *Science* Prize for Regenerative Medicine & Cell Therapy.

Apply now!

www.passionforscience.com/prize

The Sartorius & *Science* Prize for Regenerative Medicine & Cell Therapy

Awarded by sartorius Science

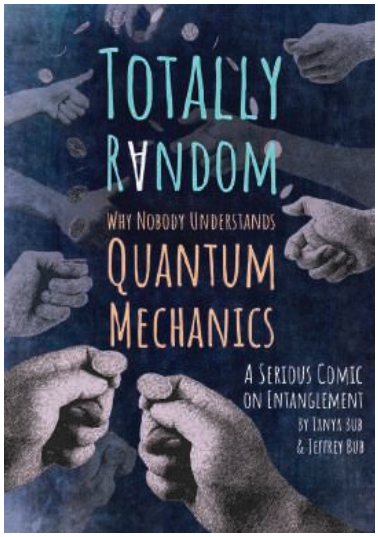

"What a delight! *Totally Random* explores some of the strangest features of quantum theory—and introduces some of the most important new devices that exploit quantum weirdness—in a way that is accessible, smart, and funny. An entanglement page-turner!"
—David Kaiser, author of *How the Hippies Saved Physics*

Paper $22.95

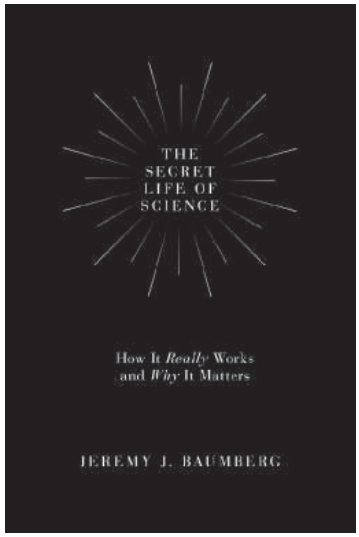

"None of this is news to those of us living within the ecosystem, but it is high time that an insider brings the dysfunctional and diseased aspects of Big Science to the attention of the educated public. . . . A refreshing and important read for scientists and policymakers alike."
—A. Zee, author of *On Gravity: A Brief Tour of a Weighty Subject*

Cloth $29.95

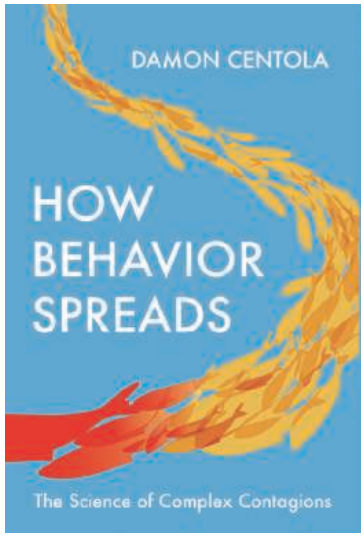

"Clearly and elegantly written, brimming with fresh ideas, and based on cutting-edge experimental techniques, *How Behavior Spreads* is an essential addition to the core bookshelves of social scientists who care about networks and social change."
—Paul DiMaggio, Princeton University

Cloth $35.00

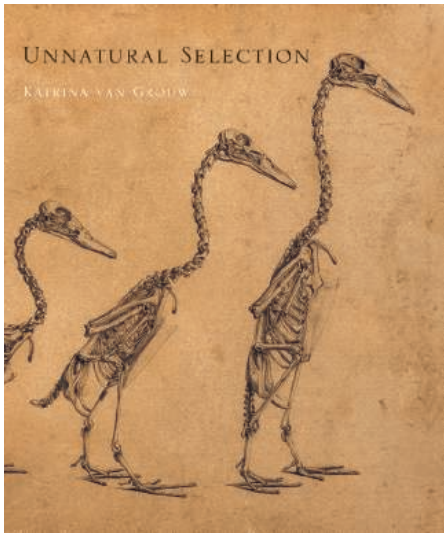

"Combining art, history, and science, this idiosyncratic book is very engaging and exceptionally clear. The illustrations, more than just appropriate and accurate, are marvelous."
—Henry S. Horn, professor emeritus of ecology and evolutionary biology, Princeton University

Cloth $45.00

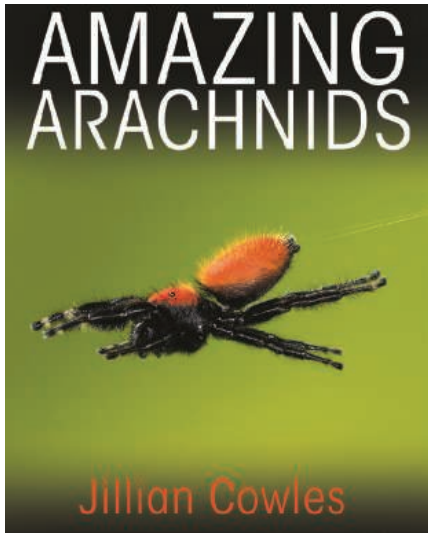

"Cowles has assembled a fascinating collection of phenomena pertaining to arachnids and presented it with a narrative that is simply a joy to read."
—W. David Sissom, West Texas A&M University

Cloth $45.00

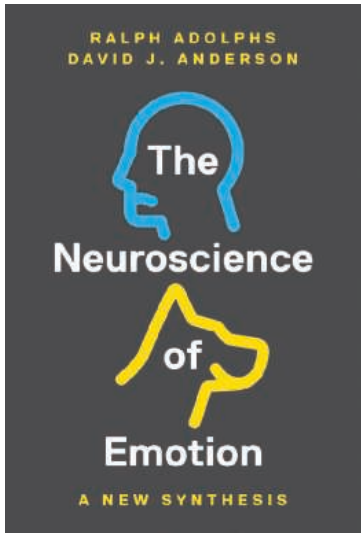

"Adolphs and Anderson, who have built their respective reputations on the study of human and animal emotions, have written the best and most comprehensive text yet on the subject. This is an indispensable book."
—Antonio Damasio, author of *The Strange Order of Things: Life, Feeling, and the Making of Cultures*

Cloth $45.00

SCIENCE TRANSCENDING BOUNDARIES

AAAS | ANNUAL MEETING
Washington, DC | Feb. 14–17, 2019

aaas.org/meetings

Dear Colleagues:

Many lines are drawn in today's world: within our communities, within global society, and within science itself. The 2019 AAAS Annual Meeting theme, Science Transcending Boundaries, considers how science can bring together people, ideas, and solutions from across real and artificial borders, disciplines, sectors, ideologies, and traditions.

On behalf of the AAAS Board of Directors, I urge you to join us in Washington, DC, February 14-17, 2019, where this theme will be explored through interdisciplinary scientific sessions, renowned speakers, and in-depth discussions. The AAAS Annual Meeting is the most widely reported global science gathering and the premier event at which you can network with future collaborators across disciplines.

We look forward to seeing you in Washington. Registration and housing open in August.

Margaret A. Hamburg, M.D.

Margaret A. Hamburg
AAAS President
Foreign Secretary, National Academy of Medicine

HOW FAR WILL YOUR ESSAY TAKE YOU?

Apply for the *Science* & SciLifeLab Prize for Young Scientists — an annual prize awarded to early-career scientists. The prize is presented in four categories: Cell and Molecular Biology, Genomics and Proteomics, Ecology and Environment, and Translational Medicine.

The winners will have their essays published by *Science*, win up to USD 30,000 and be invited to a week in Sweden to attend the award ceremony. Get ready for a life-changing moment in your scientific career.

SCIENCEPRIZE.SCILIFELAB.SE

Science & SciLifeLab PRIZE
For Young Scientists

Knut och Alice Wallenbergs Stiftelse

Science AAAS

SciLifeLab

Raman Imaging Software

WITec Suite FIVE is a software suite that enables an integrated functionality incorporating the various WITec techniques and measurement modes such as Raman, AFM, SNOM, Raman–AFM, Raman–SEM, fluorescence, and combinations thereof. It includes a powerful software environment for data acquisition, evaluation, and processing of even large data volumes and 3D scans. The novel consolidated wizard guides the user through the entire experiment, from initial settings and acquisition to data and image postprocessing, and simplifies the generation of high-quality images. WITec's unique handheld controller, EasyLink, provides a tactile and immediate interface for directing the automated translation stage, objective turret, illumination, and focus. WITec Suite FIVE transforms the user experience, enabling the researcher to move from setup to results with unprecedented ease.

WITec Instruments
For info: 865-984-4445
www.witec.de/products/accessories/software-witec-suite

Freeze Dryer

The LyoCapsule Freeze Dryer is a lyophilization instrument that delivers results comparable to larger R&D freeze dryers. Its small chamber incorporates a unique cylindrical inner chamber, or "capsule," to hold the vials, and uses wall temperature control to ensure that edge vials dry under the same process conditions as the center vial. This mini freeze dryer can process small quantities of costly materials such as developmental biological drugs, and requires far less material preparation time while still facilitating robust and cost-effective cycle development. The unit can accommodate 2-mL to 20-mL vials; seven 20-mL vials can fit comfortably on the circular shelf. In addition, it offers robust process-monitoring tools including chamber- and condenser-capacitance manometers, a Pirani gauge, product thermocouples, SMART Freeze Drying technology, and tunable diode laser absorption spectroscopy (TDLAS) as an add-on option.

SP Scientific
For info: 800-431-8232
www.spscientific.com

Single-Cell WGA Kit

CovCheck Multiplex Human Kit is a PCR kit for determining human single-cell, whole-genome amplification (WGA) success with high throughput. It provides a ready-to-use set of end-point PCR primers in a convenient 96-well plate format, complete with optimized PCR reagents including a premium hot-start *Taq* polymerase. The plate includes 16 identical sets of 24 different primer pairs multiplexed in six reactions, which will amplify small portions from each human chromosome, allowing coverage analysis of 16 independent whole-genome amplifications simultaneously.

Expedeon
For info: 844-611-3656
www.expedeon.com

Biological Shaker

The Innova S44i biological shaker from Eppendorf is now moving shaker technology forward—designed with an intelligent new drive for years of dependable operation. It is specifically developed for laboratories that are short on space but have high demands for sample cultivation, and its industry-leading load-speed and capacity threshold make it ideal for growing microbiological and phototrophic organisms. The Innova S44i comes with a responsive touchscreen interface for effortless operation. It is easy to define operating parameters and to view performance history, alarm status, trend graphs, or event history directly on the display. Built-in user management allows the controlled access, operation, and traceability that are required in highly regulated laboratories. The built-in USB drive enables all data and events from the Innova S44i to be transferred for documentation or later evaluation. The new shaker can be integrated into a central monitoring and data management software using VisioNize software from Eppendorf.

Eppendorf
For info: 800-645-3050
www.eppendorf.com

Sample Recognition Software

LiveID software enables real-time classification of samples using direct-analysis mass spectrometry (MS). Information is provided to the user immediately at the time of analysis, enabling informed, real-time decision-making, and removing doubt from sample identity. LiveID can be used with high-resolution time-of-flight MS data generated from a Waters Xevo G2-XS or SYNAPT G2-Si MS fitted with a rapid evaporative ionization mass spectrometry (REIMS) source. Applications are extensive and include confirmation of sample authenticity for foods and bulk chemicals, food fraud, plant phenotyping in herbicide research, microbe classification, and bioengineering research.

Waters
For info: 800-252-4752
www.waters.com

Purified Cancer Exosome Samples

AMS Biotechnology (AMSBIO) has introduced a range of purified cancer exosome samples to help researchers study the role of exosomes in cancer development and metastasis. The purified tumor exosomes can be used for RNA or protein-analysis techniques such as quantitative reverse transcription-PCR (qRT-PCR), microarray, and mass spectrometry. AMSBIO also offers purified tumor exosomal RNA that is ready-to-use for next-generation sequencing. Our purified tumor exosome range includes samples from bladder, breast, colorectal, Crohn's disease, diabetes type 1, kidney, leukemia, liver, melanoma, nasopharyngeal, non-Hodgkin lymphoma, prostate, psoriasis, rheumatoid arthritis, systemic lupus, thyroid, and uterine corpus cancers. This product range is for research use only. Exosomes—small endosome-derived lipid nanoparticles actively secreted by exocytosis—have been shown to have pleiotropic physiological and pathological functions, and play significant roles in diverse pathological conditions such as cancer and infectious and neurodegenerative diseases.

AMS Biotechnology
For info: +44-(0)-1235-828200
www.amsbio.com/exosomes.aspx

Electronically submit your new product description or product literature information! Go to www.sciencemag.org/about/new-products-section for more information.

Newly offered instrumentation, apparatus, and laboratory materials of interest to researchers in all disciplines in academic, industrial, and governmental organizations are featured in this space. Emphasis is given to purpose, chief characteristics, and availability of products and materials. Endorsement by *Science* or AAAS of any products or materials mentioned is not implied. Additional information may be obtained from the manufacturer or supplier.

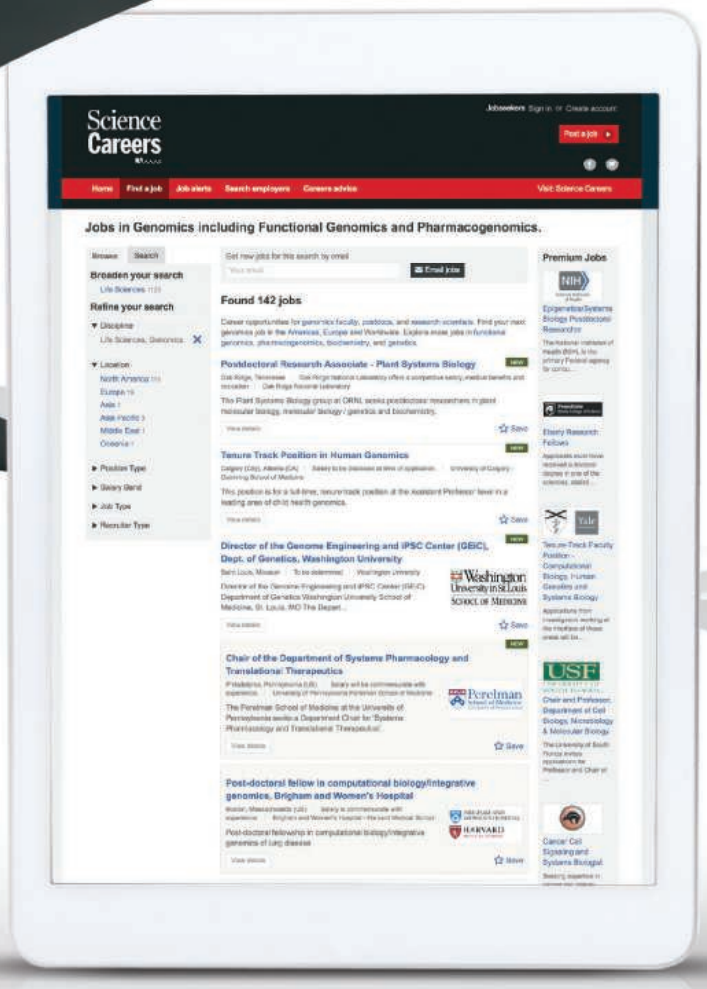

Step up your job search with *Science* Careers

- Access thousands of job postings
- Sign up for job alerts
- Explore career development tools and resources

Search jobs on **ScienceCareers.org** today

NEW ENGLAND BioLabs® Inc.

be INSPIRED
drive DISCOVERY
stay GENUINE

We've spread our wings.

Monarch® Nucleic Acid Purification Kits Now available for DNA & RNA

Designed with sustainability in mind, Monarch® Nucleic Acid Purification Kits are the perfect complement to many molecular biology workflows. Available for DNA & RNA purification, with buffers and columns available separately, Monarch kits are optimized for excellent performance, convenience and value. Quickly and easily recover highly pure, intact DNA and RNA in minutes. Available kits include:

- Monarch Plasmid Miniprep Kit
- Monarch DNA Gel Extraction Kit
- Monarch PCR & DNA Cleanup Kit (5 µg)
- **NEW** MONARCH TOTAL RNA MINIPREP KIT – optimized for use with a variety of sample types, including cells, tissues, blood, and more

Make the change and migrate to Monarch today.

Interested in trying a sample of our new Monarch Total RNA Miniprep Kit?

Learn more at
NEBMonarch.com

Science Careers

SCIENCE CAREERS ADVERTISING

For full advertising details, go to ScienceCareers.org and click For Employers, or call one of our representatives.

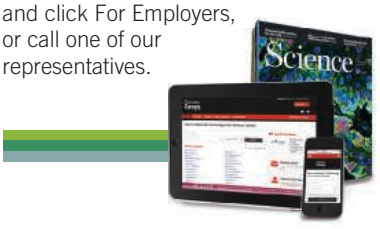

AMERICAS

+1 202 326-6577
+1 202 326-6578
advertise@sciencecareers.org

EUROPE, INDIA, AUSTRALIA, NEW ZEALAND, REST OF WORLD

+44 (0) 1223 326527
advertise@sciencecareers.org

CHINA, KOREA, SINGAPORE, TAIWAN, THAILAND

+86 131 4114 0012
advertise@sciencecareers.org

JAPAN

+81 3-6459-4174
advertise@sciencecareers.org

CUSTOMER SERVICE

AMERICAS

+1 202 326-6577

REST OF WORLD

+44 (0) 1223 326528

advertise@sciencecareers.org

ScienceCareers
FROM THE JOURNAL SCIENCE AAAS

ScienceCareers.org

POSITIONS OPEN

Postdoctoral Scientist – Virology
Cedars-Sinai Medical Center (CSMC)
Los Angeles, California

The Center of Neurovirology and Vaccine Development of Ophthalmology Research Laboratories within CSMC, departments of Surgery and Biological Sciences, is offering postdoctoral opportunities for highly motivated individuals. The candidates should have strong molecular virology background and familiar with techniques such as multi-color flow cytometry, cell isolation, tissue culture, ELISA, RT-PCR and animal handling and breeding. The successful candidate will participate in studies to define immune-regulatory pathways that control the innate and adaptive immune responses involved in HSV-1 latency-reactivation. Also, we expect applicants to have at least one or two first author virology-immunology related published articles. The lab is equipped with state-of-the-art research facilities and equipment. Must be eligible to work in the U.S. Interested individuals should submit their resume and 3 references and address it to Dr. Homayon Ghiasi to the following requisition website:

https://jobs.cedars-sinai.edu/job/los-angeles/postdoctoral-scientist/252/8032774

For information about Dr. Ghiasi's lab see website:

http://bio.csmc.edu/view/15051/Homayon-Ghiasi.aspx

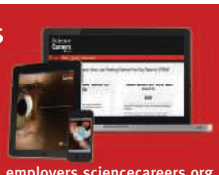

GBIF Global Biodiversity Information Facility

Recruitment of Executive Secretary for the Global Biodiversity Information Facility (GBIF)

GBIF seeks a visionary leader to head its Secretariat in Copenhagen, Denmark. GBIF is an international collaboration among countries and international organisations to provide free and open access to biodiversity data worldwide: www.gbif.org.

The Executive Secretary defines strategies, implements work programmes, oversees GBIF staff and operations, liaises with the Governing Board, and builds key networks and collaborations for GBIF's future development.

For a full description of the position, required skills, and application procedures, see:
https://www.gbif.org/news/Sw3gUiGs6aMIAkU86mACw

Application deadline is 24 July 2018 at 23:59 CEST (GMT +2).

Special Job Focus:

Chemistry

Issue date: July 27

Book ad by July 12

Ads accepted until July 20 if space allows

129,562
subscribers in print every week

62,906
yearly unique active job seekers searching for chemistry

40,352
yearly applications submitted for chemistry positions

What makes *Science* the best choice for recruiting?

- Read and respected by 400,000 readers around the globe
- 80% of readers read *Science* more often than any other journal
- Your ad dollars support AAAS and its programs, which strengthens the global scientific community.

Why choose this Chemistry Focus for your advertisement?

- Relevant ads lead off the career section with a special "Chemistry" banner
- Bonus distribution to:
  American Chemical Society Fall, August 19–23, Boston, MA.

Expand your exposure. Post your print ad online to benefit from:

- Link on the job board homepage directly to chemistry jobs
- Dedicated landing page for jobs in chemistry
- Additional marketing driving relevant job seekers to the job board.

To book your ad:
advertise@sciencecareers.org

The Americas
+ 202 326 6577

Europe
+44 (0) 1223 326527

Japan
+81 3 6459 4174

China/Korea/Singapore/ Taiwan
+86 131 4114 0012

Produced by the *Science*/AAAS Custom Publishing Office.

ScienceCareers
FROM THE JOURNAL SCIENCE AAAS

SCIENCECAREERS.ORG

FOR RECRUITMENT IN SCIENCE, THERE'S ONLY ONE *SCIENCE*.

Associate Scientist/Scientist, Principal Investigator Population Research, Sanford Research

The Population Health Group within Sanford Research invites applications for an Associate Scientist/Scientist, Principal Investigator within Sanford Research in Sioux Falls, SD. Sanford Research is the non-profit research branch under Sanford Health.

As the public health and social/behavioral science arm of Sanford Research the Population Health Group (approximately 25 people) is comprised of investigators with considerable federal funding for over 10 years for community-based research projects, with an emphasis in American Indian and rural population health. Sanford Research looks to recruit an Associate Scientist/Scientist (equivalent to Associate Professor/Professor), with eligibility for commensurate rank within the Sanford School of Medicine at The University of South Dakota. Ideal candidates will have an existing research portfolio in population health, health disparities, or a similar field of study. The candidate will also become the Principal Investigator of a new NIH-funded Center for Biomedical Research Excellence (CoBRE) program development grant, titled the Transdisciplinary Center for Population Health (TCPH). In this role the candidate will mentor junior faculty, oversee relevant scientific cores, and utilize the CoBRE and institutional resources to grow and sustain the Center. This candidate would also have the opportunity to engage in translational health services research leveraging Sanford's integrated data warehouse (clinical and claims data) to inform healthcare delivery. Ideal candidates will have a strong record of independent investigator-initiated grant funding and ideally program grant funding in population health (or a similar field), managing large budgets, mentoring early-career investigators to funding success, and experience in developing collaborations with various communities and institutional partners.

Significant institutional support includes:

- Comprehensive compensation package will be tailored to the individual's qualifications
- Space and state-of-the-art facilities
- Access to integrated healthcare data
- Opportunity to recruit multiple new faculty (2-6) over time to build/expand the Center as current project leaders graduate from the CoBRE Program

Application

Sanford Health is an Equal Opportunity/Affirmative Action Employer. Applicants should submit a single PDF that includes: 1) a cover letter that outlines qualifications, including previous mentoring experiences, 2) curriculum vita, and 3) a statement of research interests and future research plans with specific details on the relevance of their research to population health. Applications will be accepted until the position is filled. Address materials and questions to Search Committee Chair: Dr. DenYelle Kenyon, 2301 E. 60th St. N., Sioux Falls, SD 57014, CHOPR@sanfordhealth.org.

SANFORD HEALTH

019036-00722 6/18

THE UNIVERSITY OF BRITISH COLUMBIA

Faculty of Medicine

CAREER OPPORTUNITY

Department of Cellular & Physiological Sciences Assistant Professor (Tenure Track)

The Department of Cellular & Physiological Sciences (www.cellphys.ubc.ca), part of the Faculty of Medicine at the University of British Columbia invites applications for a tenure track position at the Assistant Professor level. Our internationally recognized research faculty have strengths in investigating the molecular and cellular processes underlying complex biological systems and human disease. We seek an outstanding candidate interested in studying the cellular/molecular basis of chronic and complex conditions such as cancer, diabetes, obesity and cardiovascular disease, with a focus on cell biology, cell signaling or metabolism.

The successful applicant will have a PhD or equivalent, excellent communication skills, a track record of excellence in research, commitment to innovative teaching methods and curriculum development. They will be expected to establish an independent research program and to compete nationally and internationally for operating grants. The successful candidate will be assigned research space in a modern, highly collaborative, multidisciplinary team environment within the Life Science Institute (www.lsi.ubc.ca). They will have access to state of the art core facilities within the LSI and other research centers on the UBC campus, and will also be eligible to apply for infrastructure funds for highly specialized equipment.

A generous start-up package will be provided along with protected time within the first years of the appointment to establish a competitive research program. Teaching excellence is expected as is broad contribution to the educational missions of the department at the undergraduate and graduate levels, including the medical undergraduate program. All positions are subject to budgetary approval.

A letter of application, accompanied by a detailed curriculum vitae and names of three references and a statement of research interests should be directed to:

Edwin D. Moore, Ph.D.
Professor and Head
Department of Cellular & Physiological Sciences
2350 Health Sciences Mall
Vancouver, BC V6T 1Z3

The deadline for applications to be received is **September 15, 2018**. The anticipated start date for this position is July 1, 2019, or a date to be mutually agreed upon.

The University of British Columbia is a global centre for research and teaching, consistently ranked among the top 20 public universities in the world and 3rd largest university in Canada with an economic impact of 12.5 billion to the provincial economy. Since 1915, UBC's West Coast spirit has embraced innovation and challenged the status quo. Its entrepreneurial perspective encourages students, staff and faculty to challenge convention, lead discovery and explore new ways of learning. At UBC, bold thinking is given a place to develop into ideas that can change the world. As one of the world's leading universities, The University of British Columbia creates an exceptional learning environment that fosters global citizenship, advances a civil and sustainable society, and supports outstanding research to serve the people of British Columbia, Canada and the world.

Equity and diversity are essential to academic excellence. An open and diverse community fosters the inclusion of voices that have been underrepresented or discouraged. We encourage applications from members of groups that have been marginalized on any grounds enumerated under the B.C. Human Rights Code, including sex, sexual orientation, gender identity or expression, racialization, disability, political belief, religion, marital or family status, age, and/or status as a First Nation, Metis, Inuit, or Indigenous person. All qualified candidates are encouraged to apply; however Canadians and permanent residents will be given priority.

www.cps.med.ubc.ca/

10 ways that *Science* Careers can help advance your career

1. Register for a free online account on **ScienceCareers.org**.
2. Search thousands of job postings and find your perfect job.
3. Sign up to receive e-mail alerts about job postings that match your criteria.
4. Upload your resume into our database and connect with employers.
5. Watch one of our many webinars on different career topics such as job searching, networking, and more.
6. Download our career booklets, including Career Basics, Careers Beyond the Bench, and Developing Your Skills.
7. Complete an interactive, personalized career plan at "my IDP."
8. Visit our Career Forum and get advice from career experts and your peers.
9. Research graduate program information and find a program right for you.
10. Read relevant career advice articles from our library of thousands.

Visit **ScienceCareers.org** today — all resources are free

Science Careers
FROM THE JOURNAL SCIENCE AAAS

SCIENCECAREERS.ORG

WORKING LIFE

By **Michael L. Smith**

Dinner without reservations

When my Ph.D. adviser recommended that I organize the dinner for a visiting speaker, I enthusiastically agreed. I was thinking of asking this scientist to be my postdoc adviser, and hosting would be a good way to get to know him. But restaurant dinners—the norm for visiting speakers—had always felt stuffy and overly formal to me. I couldn't hear beyond my immediate neighbors, I couldn't mingle, and I couldn't linger for postdinner discussion. So I proposed an alternative: hosting dinner at my home. I reasoned that I could do the cooking and accommodate a larger group. Best of all, we would not have to worry about restaurant constraints. I had a month to prepare. Easy peasy.

But as the day approached, I worried that maybe I had bitten off more than I could chew. In addition to cleaning my house, grocery shopping, and preparing the meal, I was surprised to find that this simple but unconventional event required approval from 11 different university offices and departments. If I light candles, will I need to rent a fire extinguisher from the university's environmental health and safety department? If I serve alcohol, will I check IDs at the door or in my living room? Will my mini-speaker count as amplified sound? Our brilliant departmental administrator guided me through the paperwork. As for the rest of it, I was pretty much on my own.

After the speaker gave his seminar—an inspiring talk delivered to a packed house, laden with impressive data and visuals—I was convinced that his lab would be good for me academically. I rushed home to prepare dinner, eager to figure out whether he was someone I could work with and to make an impression as both a scientist and a host.

As the guests arrived, I was prepared with light snacks and drinks. But as I zipped between the living room and the kitchen—checking on the main dish, adjusting the music, and making sure that everyone had what they needed—I grew concerned that my hosting duties were keeping me from participating fully in the conversation. Would the speaker remember me in a positive light if I contacted him months later? Would my occasional comments be enough to leave an impression? If not, maybe he would notice that the flan had the perfect consistency, because I pressure cooked it for exactly 6 minutes in my *flanera*. That's the sort of attention to detail that you want in a postdoc.

As the night went on long after restaurant staff would have booted us out, I became convinced that—despite the complications and stress—hosting at home had indeed beaten the restaurant experience. Yes, I may have slightly burned the bottom of the enchiladas, but no one seemed to mind. And if anyone didn't like my heavy use of cilantro, well, they kept it to themselves.

"Hosting at home had indeed beaten the restaurant experience."

Most important, it was a lively evening with people mingling informally, unrestricted by set seating. Everyone got a chance to chat with the speaker, which gave me the opportunity to see how he interacted with other students, his perspective on their research, and his general gestalt. Hosting a dinner party might not be for everyone. But in my case, getting to know this person was a top priority, and the effort was worth it.

Could I have had my cake and eaten it, too, hosting at home without having to scramble between hosting duties? I should have listened to my roommate's advice: KISS, for "Keep it simple, stupid." That means preparing the entire meal beforehand so that it requires only reheating before eating. For drinks, stick to beer and wine, not cocktails. As for ambiance, set it and forget it: Just put a playlist on low in the background.

And what ever happened with that visiting speaker? I've just started a postdoc in his lab, so he must have liked something about that evening. Maybe it was my savvy discussion of science. More likely, it was the flan, because I just found out that he hates cilantro. ■

Michael L. Smith is a postdoctoral researcher in the Department of Collective Behavior at the Max Planck Institute for Ornithology in Konstanz, Germany. Send your career story to SciCareerEditor@aaas.org.

ILLUSTRATION: ROBERT NEUBECKER